University of Strathclyde

Department of Naval Architecture, Ocean and Marine Engineering

PERIDYNAMIC MODELING OF FIRE DAMAGE IN COMPOSITES

by

Yan Gao

A thesis submitted in fulfillment of the requirements for the degree of Doctor of Philosophy

July 2020

This thesis is the result of the author's original research. It has been composed by the author and has not been previously submitted for examination which has led to the award of a degree.

Singed: Date:

Table of Contents

Abstract

The predictions of composite materials responses in fire environments are important in terms of safety. This reality problem can be simplified as a thermal fluid-structure interaction problem in terms of mathematical modelling. The thermo-fluid model is used to simplify the physical properties of fire. The classical continuum mechanics has difficulty in predicting crack propagations because of the singularities of differential equations at discontinuities. Therefore, the peridynamic theory which uses the integral governing equations is a good choice to predict the damage in composite materials. It will bring convenience to simulate the composite response in fire environments using a monolithic methodology. Consequently, in the current study, both thermo-fluid modelling for fire and thermomechanical damage modelling in composites are simulated by using peridynamic theory. Therefore, the following models are developed step by step to achieve the final target.

Firstly, a fully coupled thermomechanical ordinary state-based peridynamic model is developed for isotropic materials. Both the deformation effect on the temperature field and the temperature effect on deformation are taken into consideration. Then the fully coupled ordinary state-based peridynamic model for isotropic materials is extended to laminated composites. Besides, a bond-based peridynamic laminate model was applied to predict the responses of a 13-ply composite under a pressure shock loading.

Secondly, regarding the fluid model to represent fire, a peridynamic model is developed for Newtonian single-phase fluid low Reynold's number laminar flow. The high temperature should also be considered which is one of the typical properties of fire. Therefore, the heat transfer is incorporated into the fluid model to represent the thermal properties of fire. Based on the single-phase fluid peridynamic model, peridynamic model for multi-phase fluid flows is also developed. The Navier-Stokes equations including the surface tension forces are reformulated into their integral forms.

Thirdly, by combining the developed single-phase fluid peridynamic model and the ordinary state-based peridynamic solid model, a fluid-structure interaction model is developed for the simulation of weakly compressible viscous fluid and elastic structure interactions. Subsequently, the heat transfer is incorporated into the fluid-structure interaction model to predict the composite response under a fire scenario. The ISO temperature-time curve is utilized to present the high temperature which is induced by fire. The thermal degradation properties of the composite materials are also included in the numerical peridynamic composite model. Finally, the composite response under fire scenario is predicted.

Acknowledgements

I would like to thank to:

- My first supervisor, Dr Selda Oterkus, for her full support and encouragement. It is my great honour to cooperate with her and do my postgraduate research under her supervision. Thanks to her open mind, idea and generous financial support, I had an enjoyable and unforgettable time in Glasgow.
- My second supervisor, Dr Erkan Oterkus, for providing guidance and kind help throughout my postgraduate research.
- All my friends and all the staff in the Naval Architecture, Ocean and Marine Engineering Department.
- My parents for their unconditional love, support and encouragement throughout my life.

List of Figures

List of Tables

Nomenclature

General denotation	
$\mathbf{x}$	Vector defining the coordinate of a point in the undeformed configuration (m)
$\mathbf{x}'$	Vector defining the coordinate of a family member of point $\mathbf{x}$ in the undeformed configuration (m)
$\mathbf{y}$	Vector defining the coordinate of a point in the deformed configuration (m)
$\mathbf{y}'$	Vector defining the coordinate of a family member of point $\mathbf{x}$ in the deformed configuration (m)
t	Time (s)
$\mathbf{u}(\mathbf{x},t)$	Displacement associated with point $\mathbf{x}$ at time t (m)
$\mathbf{v}(\mathbf{x},t)$	Velocity associated with point $\mathbf{x}$ at time t $(\mathrm{m/s})$
$\ddot{\mathbf{u}}(\mathbf{x},t), \mathbf{a}(\mathbf{x},t)$	Acceleration associated with point $\mathbf{x}$ at time t $(\mathrm{m/s^2})$
$\rho(\mathbf{x},t)$	Density associated with point $\mathbf{x}$ at time t $(\mathrm{kg/m^3})$
V'	Volume of point $\mathbf{x}'$ $(\mathrm{m^3})$
h_{thick}	Thickness of an object in two dimensional problems (m)

Peridynamic theory related denotation	
$\boldsymbol{\xi}$	Initial relative position (m)
$\boldsymbol{\eta}$	Relative displacement (m)
H_x	Interaction domain of point $\mathbf{x}$
δ	Horizon size (m)
$\mathbf{t}$	Peridynamic force density exerted from $\mathbf{x}$ to $\mathbf{x}'$ $(\mathrm{N/m^6})$
$\mathbf{t}'$	Peridynamic force density exerted from $\mathbf{x}'$ to $\mathbf{x}$ $(\mathrm{N/m^6})$

$\mathbf{f}(\boldsymbol{\xi}, \boldsymbol{\eta}, t)$	Bond-based Peridynamic force density associated with $\boldsymbol{\xi}$ and $\boldsymbol{\eta}$ $\left(\mathrm{N/m^6}\right)$
$\mathbf{b}(\mathbf{x}, t)$	Volumetric body force associated with point $\mathbf{x}$ at time t $\left(\mathrm{N/m^6}\right)$
c	Bond constant in bond-based peridynamic theory $\left(\mathrm{N/m^6}\right)$
s	Bond stretch
s_c	Critical bond stretch

Solid mechanics related denotation

θ	Dilatation of a solid peridynamic point
E	Elastic modulus $\left(\mathrm{Pa}\right)$
K_θ	Bulk modulus $\left(\mathrm{Pa}\right)$
μ	Second Lamé constant $\left(\mathrm{Pa}\right)$
ν	Poisson's ratio
E_1	Elastic modulus in fibre direction for composites $\left(\mathrm{Pa}\right)$
E_2	Elastic modulus in transverse direction for composites $\left(\mathrm{Pa}\right)$
G_{12}	Shear modulus $\left(\mathrm{Pa}\right)$
G_{IC}	Critical energy release rate for first failure mode $\left(\mathrm{J/m^2}\right)$
G_{IIC}	Critical energy release rate for second failure mode $\left(\mathrm{J/m^2}\right)$

Thermodynamics related denotation

$T(\mathbf{x}, t)$	Temperature change of point $\mathbf{x}$ at time t $\left(\mathrm{K}\right)$
Θ_0	Reference temperature $\left(\mathrm{K}\right)$
$\Theta(\mathbf{x}, t)$	Absolute temperature of point $\mathbf{x}$ at time t $\left(\mathrm{K}\right)$
α	Linear thermal expansion coefficient $\left(\mathrm{K^{-1}}\right)$
k_T	Thermal conductivity $\left(\mathrm{W/mK}\right)$
c_v	Specific heat capacity under constant volume $\left(\mathrm{J/kgK}\right)$
c_p	Specific heat capacity under constant pressure $\left(\mathrm{J/kgK}\right)$

β_{cl}	Thermal modulus in classical thermodynamics $\left(\mathrm{Pa/K}\right)$
$\mathbf{q}$	Heat flux $\left(\mathrm{W/m^2}\right)$
Fluid mechanics part related denotation	
$\boldsymbol{\sigma}$	Total stress $\left(\mathrm{N/m^2}\right)$
μ	Dynamic viscosity coefficient (second lame constant) $\left(\mathrm{kg/ms}\right)$
$\dot{\boldsymbol{\varepsilon}}$	Shear strain rate $\left(\mathrm{s^{-1}}\right)$
p	Pressure $\left(\mathrm{Pa}\right)$
e	Internal energy $\left(\mathrm{J}\right)$
c_s	Artificial speed of sound $\left(\mathrm{m/s}\right)$
γ	Ratio of specific heat capacity
Re	Reynolds number
Pr	Prandtl number
Ec	Eckert number
Nu	Nusselt number
Ra	Rayleigh number
Gr	Grashof number
Ri	Richardson number
Ma	Mach number

1. Introduction

This chapter contains four sections. Section 1.1 presents the background of the composite materials, fire properties, and damage prediction methods. Section 1.2 presents the objective of this research, while the thesis structure is provided in Section 1.3. Finally, a summary of the content in this chapter is given in the last section.

1.1. Background

The composite materials are widely applied to construct offshore structures such as oil platform and offshore wind turbine etc. due to their high-performance mechanical properties [1]. However, the concerns regarding their response to fire come into the academic research field since the composite materials are usually flammable. Therefore, in terms of safety, it is meaningful to investigate the composite response in fire environments [2]. The failure prediction of the composite materials due to fire is one of the important aspects. However, it is a quite complex problem since multi-fields are involved in this subject, e.g. solid mechanics including composite mechanics, thermodynamics, fluid mechanics, thermochemistry and so on [3]. It will be difficult to consider every factor of the composite firing process for numerical simulations. Therefore, the composite firing process can be simplified as a thermal fluid-structure interaction for numerical study.

The peridynamic theory (PD) [4] is able to predict the failure or damage because its governing equations that use an integral form are meaningful even at discontinuities. Therefore, the peridynamic theory can be utilized to predict the composite damage in the fire environments. However, there is no peridynamic model available in the published literature to solve the thermal fluid structure interaction problems. Furthermore, one remaining issue is that the PD theory is originally proposed for solid mechanics. Hence even the PD fluid model is quite a few in published literature. Consequently, the extension of the application field of the PD theory is required firstly. Then the coupling of the PD fluid model and PD solid model can be conducted to solve the final problem. As a result, several PD models are developed including the composite model and fluid models. The coupling approach of the fluid, solid, and heat

is developed in the PD form. Finally, the composite response in fire environment is predicted by using the developed PD models.

1.2. Research objective

The objectives of this research are:

- Developing an ordinary state-based peridynamic (OSB PD) fully coupled thermoelastic model to simulate isotropic materials behaviour under thermomechanical loadings. The coupling term between the mechanical field and the thermal field is considered bi-directionally. This work forms the foundation of the composite model introduced in Chapter 4. The results regarding this study are provided in Chapter 3 and published as a journal paper [5].
- Developing OSB PD fully coupled thermoelastic formulation for laminated composites by extending the isotropic material model in Chapter 3. The results regarding this study are provided as a part of Chapter 4 and published as a journal paper [6]. The formulation is reduced to a bond-based peridynamic (BB PD) fully coupled thermoelastic form to investigate the behaviour of laminates under extreme loading conditions such as underwater explosions. The study provides an application example of the peridynamic model provided in Chapter 4 in ocean engineering fields. The results are provided as a part of Chapter 4 and published as a journal paper [7].
- Developing a non-local Lagrangian model based on the peridynamic differential operator (PDDO) for fluid low Reynold's number laminar flow. This study forms the foundation of the fire model. To the author's knowledge, this is the first time that the peridynamic differential operator is used to solve the Navier-Stokes equations. Furthermore, this work is one of the earliest researches regarding the peridynamic applications on fluid mechanics. The results are provided as a part of Chapter 5 and published as a journal paper [8].
- Developing a non-local Eulerian model based on the peridynamic differential operator for fluid flow coupled with heat transfer problems. This

work is conducted based on the previous fluid model. The results are provided as a part of Chapter 5 and published as a journal paper [9].

- Developing a multiphase fluid model based on the developed single-phase fluid model in Chapter 5. The surface tension force is included in the multiphase fluid model. The method of the surface tension force modelling provides the basic idea for the fluid-structure interface numerical treatments. Thus, this study provides one of the fundamental models for fluid-structure interaction model in Chapter 7. The results are provided in Chapter 6 and the related manuscript is under review.
- Developing a fluid-structure interaction model by combining the previous solid model in Chapter 3 and the fluid model in Chapter 5. The coupling methodology is developed based on the numerical treatments for the multiphase fluid interface in Chapter 6. The corresponding methods and simulation results are provided in Chapter 7. And the related manuscript is under review.
- Based on the above PD models, a thermal fluid-structure interaction of composites for fire scenario is simulated as a comprehensive case in Chapter 8. The thermal degradation properties of the composites are taken into consideration. The composite damage is predicted by direct fire contact and indirect fire contact. The thermal interaction between the fire-heated air and composites is simulated via convection and radiation interface boundary conditions. And the related manuscript is under review.

In conclusion, the ultimate goal of this research is to propose a monolithic methodology based on the peridynamic theory to simulate the thermal fluid-structure interaction, e.g. composite material damage in fire environments.

1.3. Thesis structure

This thesis is structured in the following chapters and a brief outline of the content of each chapter is given below:

- Chapter 1 Introduction.

This chapter provides basic information regarding the research background, the research objective, and the structure of this thesis.

- Chapter 2 Literature Review

  This chapter represents the traditional peridynamic theory and the peridynamic differential operator. For the peridynamic theory, the bond-based form and the ordinary state-based form are reviewed. As to the peridynamic differential operator, the theoretical foundation, the derivation and construction process are provided. Furthermore, an accuracy test is performed for the peridynamic differential operator to investigate the accuracy of the approximation for first and the second derivatives.

- Chapter 3 OSB Fully Coupled Thermomechanical PD Model for Isotropic Materials

  This chapter describes the OSB PD thermomechanical model for isotropic materials. The non-dimensional form of the PD model is also provided. Validation of the model is conducted by solving some benchmark problems and comparing the simulation results with other numerical solutions. The three-point bending problem, plate crack propagation, and the Kolthoff problem are simulated in a fully coupled thermoelastic fashion [5].

- Chapter 4 Fully Coupled Thermomechanical PD Model for Composites Material

  This chapter presents a fully coupled ordinary state-based peridynamic model for laminated composites. The formulation includes a coupling of both thermal and mechanical fields. To verify the proposed model, numerical simulations for benchmark problems are carried out and their results are compared with ANSYS solutions. Various loading conditions, e.g. uniform and linear temperature load, pressure shocks are considered for single layer laminar and multi-layer laminates. Finally, the crack propagation paths and temperature distributions are predicted for shock loading conditions [6, 7].

- Chapter 5 Isothermal and Non-isothermal Fluid Laminar Flow Simulation

  This chapter provides a non-local model for fluid flow both in isothermal condition and non-isothermal condition. The fluid flow governing equations, i.e. Navier-Stokes equations, are reformulated in the integral formulation by using the peridynamic differential operator. Then the numerical simulation algorithms in the total Lagrangian description, updated Lagrangian description, and Eulerian description are provided. The numerical model is validated by solving the benchmark problems in fluid mechanics, e.g. hydrostatic problem, Poiseuille flow, Couette flow, shear driven cavity flow, Taylor-Green vortex, water dam breakage, natural convection, and mixed convection problems [8, 9].

- Chapter 6 Multi-phase Fluid Flow Numerical Simulation

  This chapter provides a non-local model for multi-phase fluid flow based on the peridynamic differential operator. This is an extension work based on the non-local model for single-phase fluid flow in Chapter 5. The surface tension force existing on the interface of different fluids is modelled by the peridynamic differential operator. Some benchmark problems for multi-phase fluid flows are solved to validate the proposed model, i.e. two-phase hydrostatic problem, two-phase Poiseuille flow, two-dimensional droplet deformation.

- Chapter 7 Fluid-Structure Interaction Numerical Simulation

  This chapter presents a new monolithic methodology based on the PD theory for simulating fluid-structure interactions. The fluid model developed in Chapter 5 is adopted. The ordinary state-based PD isotropic material model reviewed in Section 2.1.2 is employed. The fluid motion and elastic structure deformation are predicted simultaneously by using a novel interaction algorithm. To validate the developed fluid-structure interaction model, a dam collapsed under a rubber gate is simulated.

- Chapter 8 Coupled Thermo-fluid-mechanical Peridynamic Model for Analysing Composite under Fire Scenarios

  This chapter presents a thermal fluid-structure simulation of composites in a fire environment by using the developed peridynamic model. The thermal degradation property of the composites is also taken into consideration. There are two simulation cases provided, i.e. composite directly under fire temperature boundary condition and the composite indirectly under fire boundary condition via fire-heated air. The fluid and composite interact via the thermal field by considering the convection and radiation on the interface.

- Chapter 9 Conclusion

  This chapter reviews the research achievements, summarises the research novelty and contribution. The gaps and recommended future work are listed. The publications from the PhD thesis are provided, and the final remarks are drawn.

1.4. Summary

Damage prediction is a challenging topic since the classical continuum mechanics (CCM) mathematical model is meaningless at discontinuities. Therefore, the peridynamic theory is adopted in this study for composite damage modelling to overcome the shortcomings of classical continuum mechanics. The fire scenario prediction is another challenging topic in fluid mechanics. To solve the composite damage under fire scenario in a monolithic methodology, the fire is simplified as a heat-conducting fluid and modelled by the PD theory. The following objectives of this thesis research are the proposing of 1) OSB PD model for fully coupled thermomechanics for isotropic materials, 2) OSB PD model for fully coupled thermomechanics for composite materials, 3) single-phase viscous fluid PD model, 4) heat-conducting viscous fluid PD model, 5) multi-phase viscous fluid PD model, 6) fluid-structure interaction PD model, 7) thermal fluid and structure interaction PD model.

2. Literature Review

2.1. Peridynamic theory

The peridynamics (PD) proposed by Silling and Askari [4] is a non-local, mesh-free Lagrangian method, which provides an alternative formulation for the continuum mechanics. PD is based on integral-differential equations as opposed to the partial differential equations of classical continuum mechanics [4]. Therefore, no singular stress or strain will be created at discontinuities. The equation will be valid everywhere within the body. This is one of its advantages over the classical numerical simulation methods such as the finite element method (FEM). Here, the basic concepts of the PD theory are reviewed [10].

As shown in Fig. 2-1, each material point is identified by its location represented by a coordinate $\mathbf{x}$ in an undeformed state. The body region is R, and the interaction domain of material point $\mathbf{x}$ is called neighbourhood and is denoted by $H_{\mathbf{x}}$. The maximum interaction distance is called horizon size and denoted by δ. The length of the horizon is the measure of nonlocal behaviour. The other material points in $H_{\mathbf{x}}$, i.e. $\mathbf{x}'$, are called the family members of $\mathbf{x}$. Furthermore, $\mathbf{y}$ and $\mathbf{y}'$ represent the positions of $\mathbf{x}$ and $\mathbf{x}'$ in the deformed configuration. Hence, the displacements of points $\mathbf{x}$ and family member $\mathbf{x}'$ are $\mathbf{u}(\mathbf{x})=\mathbf{y}-\mathbf{x}$ and $\mathbf{u}'=\mathbf{u}(\mathbf{x}')=\mathbf{y}'-\mathbf{x}'$, respectively. As illustrated in Fig. 2-1, the initial relative position vector is denoted as

$$\boldsymbol{\xi}=\mathbf{x}'-\mathbf{x} \tag{2.1}$$

Consequently, the relative displacement between $\mathbf{x}$ and $\mathbf{x}'$ can be defined as

$$\boldsymbol{\eta}=\mathbf{u}(\mathbf{x}')-\mathbf{u}(\mathbf{x})=(\mathbf{y}'-\mathbf{y})-(\mathbf{x}'-\mathbf{x}) \tag{2.2}$$

The equation of motion for point $\mathbf{x}$ in PD form is expressed as [10]

$$\rho(\mathbf{x})\ddot{\mathbf{u}}(\mathbf{x},t)=\int_{H_{\mathbf{x}}}\left(\mathbf{t}(\mathbf{u}'-\mathbf{u},\mathbf{x}'-\mathbf{x},t)-\mathbf{t}'(\mathbf{u}-\mathbf{u}',\mathbf{x}-\mathbf{x}',t)\right)\mathrm{d}V'+\mathbf{b}(\mathbf{x},t) \tag{2.3}$$

where $\rho(\mathbf{x})$ represents density, V' represents the volume of point $\mathbf{x}'$, $\ddot{\mathbf{u}}(\mathbf{x},t)$ represents the acceleration of point $\mathbf{x}$ at time t, $\mathbf{b}(\mathbf{x},t)$ represents the volumetric body force. The integration on the right-hand side of Eq. (2.3) represents the total PD force density acting on point $\mathbf{x}$. The acceleration of the central point is calculated by the force exerted from its family members, indicating a non-local behaviour. In the deformed configuration, $\mathbf{t}'$ is the PD force density function exerted from point $\mathbf{x}'$ to point $\mathbf{x}$. Similarly, $\mathbf{t}$ is the PD force density function acting at the material point $\mathbf{x}'$ from point $\mathbf{x}$. Depending on the magnitude and direction of the PD forces $\mathbf{t}$ and $\mathbf{t}'$, the PD theory can be classified into two subdomains, i.e. bond-based peridynamics (BB-PD) and state-based peridynamics (SB-PD). The BB-PD and ordinary state-based (OSB-PD) theory are used in this study, which will be explained in the following subsections.

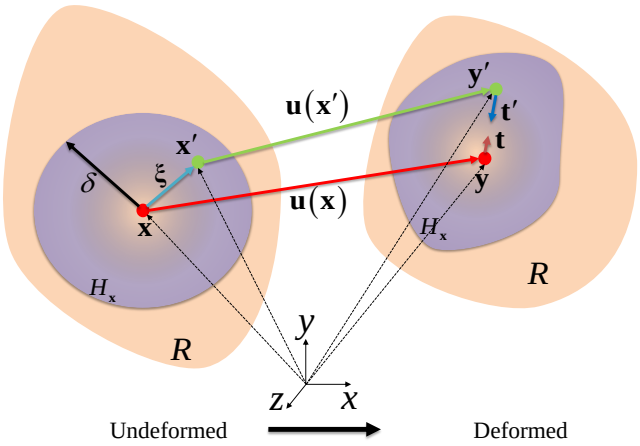

Fig. 2-1 Interaction of the point of interest $\mathbf{x}$ with its family member $\mathbf{x}'$

2.1.1. Bond-based PD theory

The material body R can be discretised by a set of material points. The material point i is the central point and material point j is one of its family members. The coordinates of point i in the undeformed and deformed configurations are $\mathbf{x}_i$ and $\mathbf{y}_i$, respectively. The corresponding displacement is denoted by $\mathbf{u}_i$. The bold symbols are used to represent vectors. The same notation is applied to other material points, e.g. j. The initial relative position and relative displacement vectors are defined as

$\boldsymbol{\xi}_{ij} = \mathbf{x}_j - \mathbf{x}_i$ and $\boldsymbol{\eta}_{ij} = \mathbf{u}_j - \mathbf{u}_i$. Then the relative position in the deformed configuration is $\mathbf{y}_j - \mathbf{y}_i = \boldsymbol{\xi}_{ij} + \boldsymbol{\eta}_{ij}$.

It should be noted that in bond-based PD, the pairwise PD forces $\mathbf{t}$ and $\mathbf{t}'$ are forced to be equal in magnitude and parallel in direction, i.e. $\mathbf{t} = -\mathbf{t}'$. As a result, the discretised form of Eq.(2.3) becomes

$$\rho(\mathbf{x}_i)\ddot{\mathbf{u}}(\mathbf{x}_i, t) = \sum_{j=1}^{N_i} 2\mathbf{t}\left(\mathbf{u}_j - \mathbf{u}_i, \mathbf{x}_j - \mathbf{x}_i, t\right)V_j + \mathbf{b}(\mathbf{x}_i, t) \tag{2.4}$$

where N_i is the total number of family members for point i. In BB-PD theory, a pairwise PD force density $\mathbf{f}$ is defined as

$$\mathbf{f}\left(\mathbf{u}_j - \mathbf{u}_i, \mathbf{x}_j - \mathbf{x}_i, t\right) = 2\mathbf{t}\left(\mathbf{u}_j - \mathbf{u}_i, \mathbf{x}_j - \mathbf{x}_i, t\right) = c\left(s_{ij} - \alpha\frac{\left(T_i + T_j\right)}{2}\right)\frac{\mathbf{y}_j - \mathbf{y}_i}{\left|\mathbf{y}_j - \mathbf{y}_i\right|} \tag{2.5}$$

As a result, the equation of motion Eq.(2.3) is expressed in bond-based PD form as [10]

$$\rho(\mathbf{x}_i)\ddot{\mathbf{u}}(\mathbf{x}_i, t) = \left(\sum_{j=1}^{N_i} c\left(s_{ij} - \alpha\frac{\left(T_i + T_j\right)}{2}\right)\frac{\mathbf{y}_j - \mathbf{y}_i}{\left|\mathbf{y}_j - \mathbf{y}_i\right|}V_j\right) + \mathbf{b}(\mathbf{x}_i, t) \tag{2.6}$$

in which α is the linear thermal expansion coefficient of the material. The term T_i represents the temperature change of point $\mathbf{x}_i$ with respect to the initial temperature, $T_i = \Theta(\mathbf{x}_i, t) - \Theta(\mathbf{x}_i, t = 0)$. Similarly, T_j is the temperature change of point $\mathbf{x}_j$. The term s_{ij} is the PD bond stretch which represents the deformation status of the PD bond between material points $\mathbf{x}_i$ and $\mathbf{x}_j$. It can be defined as [10]

$$s_{ij} = \frac{\left|\mathbf{y}_j - \mathbf{y}_i\right| - \left|\mathbf{x}_j - \mathbf{x}_i\right|}{\left|\mathbf{x}_j - \mathbf{x}_i\right|} \tag{2.7}$$

The term c is the PD constant which can be calculated by equalling the strain energy densities obtained from PD theory and CCM. The formulations of c for different dimensional problems are provided as [10]

$$c=\begin{cases}\dfrac{2E}{A_{area}\delta^2}, & \text{for 1D problems}\\ \dfrac{12K_\theta}{\pi h_{thick}\delta^3}, & \text{for 2D problems}\\ \dfrac{18K_\theta}{\pi\delta^4}, & \text{for 3D problems}\end{cases} \tag{2.8}$$

where A_{area} is the cross-section area for 1D problems and h_{thick} is the thickness for 2D problems.

The BB-PD theory does not distinguish the shear deformation and bulk deformation. Hence, the Poisson's ratio is forced to be 1/3 in two dimensional (2D) analysis and 1/4 in three dimensional (3D) analysis [10].

2.1.2. Ordinary state-based PD theory

In order to overcome the limitation of BB-PD theory on the material properties, state-based peridynamic theory is proposed by Silling et al. [11]. The ordinary state-based expressions for PD force functions are presented as provided in [12]

$$\mathbf{t}\left(\mathbf{u}_j-\mathbf{u}_i,\mathbf{x}_j-\mathbf{x}_i,t\right)=\frac{1}{2}\left[4\delta\frac{ad\Lambda_{ij}}{\left|\mathbf{x}_j-\mathbf{x}_i\right|}\left(\theta_i-n\alpha T_i\right)+4\delta b\left(s_{ij}-\alpha T_i\right)\right]\frac{\mathbf{y}_j-\mathbf{y}_i}{\left|\mathbf{y}_j-\mathbf{y}_i\right|} \tag{2.9a}$$

and

$$\mathbf{t}\left(\mathbf{u}_i-\mathbf{u}_j,\mathbf{x}_i-\mathbf{x}_j,t\right)=-\frac{1}{2}\left[4\delta\frac{ad\Lambda_{ji}}{\left|\mathbf{x}_i-\mathbf{x}_j\right|}\left(\theta_j-n\alpha T_j\right)+4\delta b\left(s_{ji}-\alpha T_j\right)\right]\frac{\mathbf{y}_i-\mathbf{y}_j}{\left|\mathbf{y}_i-\mathbf{y}_j\right|} \tag{2.9b}$$

with

$$n = \begin{cases} 2, \text{for } 2\text{D} \\ 3, \text{for } 3\text{D} \end{cases} \tag{2.9c}$$

$$\Lambda_{ij} = \left(\frac{\mathbf{y}_j - \mathbf{y}_i}{\left| \mathbf{y}_j - \mathbf{y}_i \right|} \right) \cdot \left(\frac{\mathbf{x}_j - \mathbf{x}_i}{\left| \mathbf{x}_j - \mathbf{x}_i \right|} \right) \tag{2.9d}$$

The dilatations, θ_i for point $\mathbf{x}_i$ and θ_j for point $\mathbf{x}_j$, are defined as

$$\theta_i = \left(\sum_{j=1}^{N_i} d\delta \left(s_{ij} - \alpha T_i \right) \Lambda_{ij} V_j \right) + n\alpha T_i \tag{2.10a}$$

$$\theta_j = \left(\sum_{i=1}^{N_j} d\delta \left(s_{ji} - \alpha T_j \right) \Lambda_{ji} V_i \right) + n\alpha T_j \tag{2.10b}$$

The relationship between the PD material parameters, i.e. a, b and d, and classical material parameters are listed as provided in [12];

$$a = 0, b = \frac{E}{2A_{area}\delta^3}, d = \frac{1}{2A_{area}\delta^2} \text{ for 1D} \tag{2.11a}$$

$$a = \frac{1}{2}\left(K_\theta - 2\mu \right), b = \frac{6\mu}{\pi h_{thick}\delta^4}, d = \frac{2}{\pi h_{thick}\delta^3} \text{ for 2D} \tag{2.11b}$$

$$a = \frac{1}{2}\left(K_\theta - \frac{5}{3}\mu \right), b = \frac{15\mu}{2\pi\delta^5}, d = \frac{9}{4\pi\delta^4} \text{ for 3D} \tag{2.11c}$$

By plugging Eq. (2.9) into Eq.(2.3), the equation of motion for ordinary state-based PD formulation in discretised form can be written as [12]

$$\rho(\mathbf{x}_i)\ddot{\mathbf{u}}(\mathbf{x}_i, t) = \left(\sum_{j=1}^{N_i} \left[\begin{array}{l} \dfrac{2\delta d \Lambda_{ij}}{\left| \mathbf{x}_j - \mathbf{x}_i \right|} \left(a\left(\theta_i + \theta_j \right) - n\alpha \left(T_i + T_j \right) \right) \\ +4\delta b \left(s_{ij} - \alpha \dfrac{\left(T_i + T_j \right)}{2} \right) \end{array} \right] \frac{\mathbf{y}_j - \mathbf{y}_i}{\left| \mathbf{y}_j - \mathbf{y}_i \right|} V_j \right) + \mathbf{b}\left(\mathbf{x}_i, t \right) \tag{2.12}$$

2.1.3. Peridynamic failure criteria

Since PD equations are formulated without any spatial derivatives, PD theory is suitable to be applied for failure prediction. Once the stretch between material points exceed the critical stretch value, s_c, the bond will be broken and will be removed permanently. At the same time, the force between these two points becomes zero. The critical stretch value for bond failure is related to the critical energy release rate G_c [12];

$$s_c = \begin{cases} \sqrt{\dfrac{G_c}{\left(3\mu + \left(\dfrac{3}{4}\right)^4 \left(K_\theta - 2\mu\right)\right)\delta}} & \text{for 3D} \\ \sqrt{\dfrac{G_c}{\left(\dfrac{6}{\pi}\mu + \dfrac{16}{9\pi^2}\left(K_\theta - 2\mu\right)\right)\delta}} & \text{for 2D} \end{cases} \tag{2.13}$$

A history-dependent damage function $\chi\left(\mathbf{x}_i, \mathbf{x}_j, t\right)$ is implemented for each interaction between the material points [12]. The value of the function $\chi\left(\mathbf{x}_i, \mathbf{x}_j, t\right)$ will be set to be zero when the bond is broken.

$$\chi\left(\mathbf{x}_i, \mathbf{x}_j, t\right) = \begin{cases} 1, \left(s_{ij} - \alpha \dfrac{T_i + T_j}{2}\right) < s_c \\ 0, \left(s_{ij} - \alpha \dfrac{T_i + T_j}{2}\right) \geq s_c \end{cases} \tag{2.14}$$

The local damage at a point represents the weighted ratio of the number of broken interactions to the total number of interactions. Therefore, the crack propagation path can be presented by the local damage value as [13]

$$\varphi\left(\mathbf{x}_i, t\right) = 1 - \frac{\sum_{j=1}^{N_i} \chi\left(\mathbf{x}_i, \mathbf{x}_j, t\right) V_j}{\sum_{j=1}^{N_i} V_j} \tag{2.15}$$

2.2. Peridynamic differential operator

It can be inferred from the previous section that the PD form of the material parameters is required for PD material modelling, which is calculated by equalling the strain energy density obtained from classical continuum mechanics and PD expressions. Based on the PD concepts, a peridynamic differential operator is recently proposed by Madenci et al. [14]. It is derived based on Taylor series expansion and orthogonal function properties. Being different from the bond-based PD theory, the peridynamic differential operator does not have any constraint on material properties. Furthermore, it can be directly applied to reformulate the partial differential equations to their integral forms. The classical physical parameters can be directly used without converting into their PD expressions, which avoids the derivation process required by the bond-based and ordinary state-based peridynamic theory. In addition, it does not have any limitation on the order of the partial derivatives both for time and space. For example, the second-order derivatives can be directly approximated by one integration by using the PD differential operator which corresponds to the second-order derivative. As a result, the error of the PD result is reduced by using fewer integrations, compared to non-ordinary state-based PD. Furthermore, the PD differential operator functions are also forced to be orthogonal to each term in the Taylor series expansion [14]. Therefore, when determining the expressions of the PD differential operators, both lower and higher-order terms are considered.

The theoretical foundation and derivation of PDDO will be briefly presented for 2D problems in Section 2.2.1 and an accuracy test for PDDO is conducted in Section 2.2.2.

2.2.1. PD differential operator for 2D

The simulations involved in this thesis are for 2D, therefore peridynamic differential operator [14] for two-dimensional space up to second-order derivative is provided in an explicit form.

The Taylor series expansion up to second-order derivatives for two-dimensional space is expressed in an explicit form as

$$f\left(\mathbf{x}+\boldsymbol{\xi}\right)-f\left(\mathbf{x}\right)=\xi_1\frac{\partial f\left(\mathbf{x}\right)}{\partial x_1}+\xi_2\frac{\partial f\left(\mathbf{x}\right)}{\partial x_2}+\frac{1}{2}\xi_1^2\frac{\partial^2 f\left(\mathbf{x}\right)}{\partial x_1^2}+\frac{1}{2}\xi_2^2\frac{\partial^2 f\left(\mathbf{x}\right)}{\partial x_2^2}+\xi_1\xi_2\frac{\partial^2 f\left(\mathbf{x}\right)}{\partial x_1\partial x_2}+R_{\mathbf{x},2}\left(\boldsymbol{\xi}\right) \tag{2.16}$$

where $\boldsymbol{\xi}=\xi_1\mathbf{e}_1+\xi_2\mathbf{e}_2$ with $\mathbf{e}_1$ and $\mathbf{e}_2$ representing the unit vectors in x and y directions. The term $R_{\mathbf{x},2}\left(\boldsymbol{\xi}\right)$ is the remainder for Taylor series as

$$R_{\mathbf{x},2}\left(\boldsymbol{\xi}\right)=\sum_{|n_1+n_2|=3}\frac{1}{n_1!n_2!}\frac{\partial^3 f\left(\mathbf{x}+\alpha\boldsymbol{\xi}\right)}{\partial x_1^{n_1}\partial x_2^{n_2}}\xi_1^{n_1}\xi_2^{n_2},\ \text{for some}\ \alpha\in\left(0,1\right) \tag{2.17}$$

Note that $R_{\mathbf{x},2}\left(\boldsymbol{\xi}\right)=O\left(\left|\boldsymbol{\xi}\right|^3\right)$ and it is assumed to be negligible. The non-local form with the help of PD differential operator will be derived for following differentials [14].

$$\frac{\partial f\left(\mathbf{x}\right)}{\partial x_1},\frac{\partial f\left(\mathbf{x}\right)}{\partial x_2},\frac{\partial^2 f\left(\mathbf{x}\right)}{\partial x_1^2},\frac{\partial^2 f\left(\mathbf{x}\right)}{\partial x_2^2},\frac{\partial^2 f\left(\mathbf{x}\right)}{\partial x_1\partial x_2} \tag{2.18}$$

Since the derivatives are up to the second-order, PD differential operator $g^{p_1p_2}\left(\boldsymbol{\xi}\right)$ will be used to represent the PD nonlocal expressions up to the second-order derivatives.

Multiplying $g^{p_1p_2}\left(\boldsymbol{\xi}\right)$ by Eq. (2.16) and integrating over the horizon results in [14]

$$\begin{aligned}&\int_{H_{\mathbf{x}}}g^{p_1p_2}\left(\boldsymbol{\xi}\right)\left(f\left(\mathbf{x}+\boldsymbol{\xi}\right)-f\left(\mathbf{x}\right)\right)\mathrm{d}V'\\&=\int_{H_{\mathbf{x}}}\xi_1\frac{\partial f\left(\mathbf{x}\right)}{\partial x_1}g^{p_1p_2}\left(\boldsymbol{\xi}\right)\mathrm{d}V'+\int_{H_{\mathbf{x}}}\xi_2\frac{\partial f\left(\mathbf{x}\right)}{\partial x_2}g^{p_1p_2}\left(\boldsymbol{\xi}\right)\mathrm{d}V'\\&+\int_{H_{\mathbf{x}}}\frac{1}{2}\xi_1^2\frac{\partial^2 f\left(\mathbf{x}\right)}{\partial x_1^2}g^{p_1p_2}\left(\boldsymbol{\xi}\right)\mathrm{d}V'+\int_{H_{\mathbf{x}}}\frac{1}{2}\xi_2^2\frac{\partial^2 f\left(\mathbf{x}\right)}{\partial x_2^2}g^{p_1p_2}\left(\boldsymbol{\xi}\right)\mathrm{d}V'\\&+\int_{H_{\mathbf{x}}}\xi_1\xi_2\frac{\partial^2 f\left(\mathbf{x}\right)}{\partial x_1\partial x_2}g^{p_1p_2}\left(\boldsymbol{\xi}\right)\mathrm{d}V'\end{aligned} \tag{2.19}$$

where $0 < p_1 + p_2 \le 2$. By enforcing the orthogonality conditions for each PD differential operator as [14]

for $g^{10}(\boldsymbol{\xi})$:

$$\begin{aligned}&\int_{H_{\mathbf{x}}} \xi_1 g^{10}(\boldsymbol{\xi})\,\mathrm{d}V' = 1, \int_{H_{\mathbf{x}}} \xi_2 g^{10}(\boldsymbol{\xi})\,\mathrm{d}V' = 0, \int_{H_{\mathbf{x}}} \frac{1}{2}\xi_1^2 g^{10}(\boldsymbol{\xi})\,\mathrm{d}V' = 0,\\ &\int_{H_{\mathbf{x}}} \frac{1}{2}\xi_2^2 g^{10}(\boldsymbol{\xi})\,\mathrm{d}V' = 0, \int_{H_{\mathbf{x}}} \xi_1\xi_2 g^{10}(\boldsymbol{\xi})\,\mathrm{d}V' = 0\end{aligned} \tag{2.20a}$$

for $g^{01}(\boldsymbol{\xi})$:

$$\begin{aligned}&\int_{H_{\mathbf{x}}} \xi_1 g^{01}(\boldsymbol{\xi})\,\mathrm{d}V' = 0, \int_{H_{\mathbf{x}}} \xi_2 g^{01}(\boldsymbol{\xi})\,\mathrm{d}V' = 1, \int_{H_{\mathbf{x}}} \frac{1}{2}\xi_1^2 g^{01}(\boldsymbol{\xi})\,\mathrm{d}V' = 0,\\ &\int_{H_{\mathbf{x}}} \frac{1}{2}\xi_2^2 g^{01}(\boldsymbol{\xi})\,\mathrm{d}V' = 0, \int_{H_{\mathbf{x}}} \xi_1\xi_2 g^{01}(\boldsymbol{\xi})\,\mathrm{d}V' = 0\end{aligned} \tag{2.20b}$$

for $g^{20}(\boldsymbol{\xi})$:

$$\begin{aligned}&\int_{H_{\mathbf{x}}} \xi_1 g^{20}(\boldsymbol{\xi})\,\mathrm{d}V' = 0, \int_{H_{\mathbf{x}}} \xi_2 g^{20}(\boldsymbol{\xi})\,\mathrm{d}V' = 0, \int_{H_{\mathbf{x}}} \frac{1}{2}\xi_1^2 g^{20}(\boldsymbol{\xi})\,\mathrm{d}V' = 1\\ &\int_{H_{\mathbf{x}}} \frac{1}{2}\xi_2^2 g^{20}(\boldsymbol{\xi})\,\mathrm{d}V' = 0, \int_{H_{\mathbf{x}}} \xi_1\xi_2 g^{20}(\boldsymbol{\xi})\,\mathrm{d}V' = 0\end{aligned} \tag{2.20c}$$

for $g^{02}(\boldsymbol{\xi})$:

$$\begin{aligned}&\int_{H_{\mathbf{x}}} \xi_1 g^{02}(\boldsymbol{\xi})\,\mathrm{d}V' = 0, \int_{H_{\mathbf{x}}} \xi_2 g^{02}(\boldsymbol{\xi})\,\mathrm{d}V' = 0, \int_{H_{\mathbf{x}}} \frac{1}{2}\xi_1^2 g^{02}(\boldsymbol{\xi})\,\mathrm{d}V' = 0,\\ &\int_{H_{\mathbf{x}}} \frac{1}{2}\xi_2^2 g^{02}(\boldsymbol{\xi})\,\mathrm{d}V' = 1, \int_{H_{\mathbf{x}}} \xi_1\xi_2 g^{02}(\boldsymbol{\xi})\,\mathrm{d}V' = 0\end{aligned} \tag{2.20d}$$

for $g^{11}(\boldsymbol{\xi})$:

$$\begin{aligned}&\int_{H_{\mathbf{x}}} \xi_1 g^{11}(\boldsymbol{\xi})\,\mathrm{d}V' = 0, \int_{H_{\mathbf{x}}} \xi_2 g^{11}(\boldsymbol{\xi})\,\mathrm{d}V' = 0, \int_{H_{\mathbf{x}}} \frac{1}{2}\xi_1^2 g^{11}(\boldsymbol{\xi})\,\mathrm{d}V' = 0,\\ &\int_{H_{\mathbf{x}}} \frac{1}{2}\xi_2^2 g^{11}(\boldsymbol{\xi})\,\mathrm{d}V' = 0, \int_{H_{\mathbf{x}}} \xi_1\xi_2 g^{11}(\boldsymbol{\xi})\,\mathrm{d}V' = 1\end{aligned} \tag{2.20e}$$

the following relations can be obtained from Eq. (2.19) as [14]

$$\textit{for } g^{10}(\boldsymbol{\xi}): \qquad \int_{H_{\mathbf{x}}} g^{10}(\boldsymbol{\xi})\big(f(\mathbf{x}+\boldsymbol{\xi})-f(\mathbf{x})\big)\mathrm{d}V' = \frac{\partial f(\mathbf{x})}{\partial x_1} \tag{2.21a}$$

$$\textit{for } g^{01}(\boldsymbol{\xi}): \qquad \int_{H_{\mathbf{x}}} g^{01}(\boldsymbol{\xi})\big(f(\mathbf{x}+\boldsymbol{\xi})-f(\mathbf{x})\big)\mathrm{d}V' = \frac{\partial f(\mathbf{x})}{\partial x_2} \tag{2.21b}$$

$$\textit{for } g^{20}(\boldsymbol{\xi}): \qquad \int_{H_{\mathbf{x}}} g^{20}(\boldsymbol{\xi})\big(f(\mathbf{x}+\boldsymbol{\xi})-f(\mathbf{x})\big)\mathrm{d}V' = \frac{\partial^2 f(\mathbf{x})}{\partial x_1^2} \tag{2.21c}$$

$$\textit{for } g^{02}(\boldsymbol{\xi}): \qquad \int_{H_{\mathbf{x}}} g^{02}(\boldsymbol{\xi})\big(f(\mathbf{x}+\boldsymbol{\xi})-f(\mathbf{x})\big)\mathrm{d}V' = \frac{\partial^2 f(\mathbf{x})}{\partial x_2^2} \tag{2.21d}$$

$$\textit{for } g^{11}(\boldsymbol{\xi}): \qquad \int_{H_{\mathbf{x}}} g^{11}(\boldsymbol{\xi})\big(f(\mathbf{x}+\boldsymbol{\xi})-f(\mathbf{x})\big)\mathrm{d}V' = \frac{\partial^2 f(\mathbf{x})}{\partial x_1 \partial x_2} \tag{2.21e}$$

In conclusion, the differentials in local form are reformulated into their non-local form as [14]

$$\begin{Bmatrix} \dfrac{\partial f(\mathbf{x})}{\partial x_1} \\ \dfrac{\partial f(\mathbf{x})}{\partial x_2} \\ \dfrac{\partial^2 f(\mathbf{x})}{\partial x_1^2} \\ \dfrac{\partial^2 f(\mathbf{x})}{\partial x_2^2} \\ \dfrac{\partial^2 f(\mathbf{x})}{\partial x_1 \partial x_2} \end{Bmatrix} = \int_{H_{\mathbf{x}}} \big(f(\mathbf{x}+\boldsymbol{\xi})-f(\mathbf{x})\big) \begin{Bmatrix} g^{10}(\boldsymbol{\xi}) \\ g^{01}(\boldsymbol{\xi}) \\ g^{20}(\boldsymbol{\xi}) \\ g^{02}(\boldsymbol{\xi}) \\ g^{11}(\boldsymbol{\xi}) \end{Bmatrix} \mathrm{d}V' \tag{2.22}$$

where the term g represents the PD differential operator for each derivative, such as $g^{10}(\boldsymbol{\xi})$ is the PD differential operator for $\partial f(\mathbf{x})/\partial x_1$.

The PD differential operator functions, $g^{p_1 p_2}(\boldsymbol{\xi})$, are chosen as [14]

for $g^{10}(\boldsymbol{\xi}): g^{10}(\boldsymbol{\xi}) = \left(a_{10}^{10}\right) w\xi_1 + \left(a_{01}^{10}\right) w\xi_2 + \left(a_{20}^{10}\right) w\xi_1^2 + \left(a_{02}^{10}\right) w\xi_2^2 + \left(a_{11}^{10}\right) w\xi_1\xi_2$ (2.23a)

for $g^{01}(\boldsymbol{\xi}): g^{01}(\boldsymbol{\xi}) = \left(a_{10}^{01}\right) w\xi_1 + \left(a_{01}^{01}\right) w\xi_2 + \left(a_{20}^{01}\right) w\xi_1^2 + \left(a_{02}^{01}\right) w\xi_2^2 + \left(a_{11}^{01}\right) w\xi_1\xi_2$ (2.23b)

for $g^{20}(\boldsymbol{\xi}): g^{20}(\boldsymbol{\xi}) = \left(a_{10}^{20}\right) w\xi_1 + \left(a_{01}^{20}\right) w\xi_2 + \left(a_{20}^{20}\right) w\xi_1^2 + \left(a_{02}^{20}\right) w\xi_2^2 + \left(a_{11}^{20}\right) w\xi_1\xi_2$ (2.23c)

for $g^{02}(\boldsymbol{\xi}): g^{02}(\boldsymbol{\xi}) = \left(a_{10}^{02}\right) w\xi_1 + \left(a_{01}^{02}\right) w\xi_2 + \left(a_{20}^{02}\right) w\xi_1^2 + \left(a_{02}^{02}\right) w\xi_2^2 + \left(a_{11}^{02}\right) w\xi_1\xi_2$ (2.23d)

for $g^{11}(\boldsymbol{\xi}):\ g^{11}(\boldsymbol{\xi}) = \left(a_{10}^{11}\right) w\xi_1 + \left(a_{01}^{11}\right) w\xi_2 + \left(a_{20}^{11}\right) w\xi_1^2 + \left(a_{02}^{11}\right) w\xi_2^2 + \left(a_{11}^{11}\right) w\xi_1\xi_2$ (2.23e)

or expressed in a compact form as [14]

$$\begin{Bmatrix} g^{10}(\boldsymbol{\xi}) \\ g^{01}(\boldsymbol{\xi}) \\ g^{20}(\boldsymbol{\xi}) \\ g^{02}(\boldsymbol{\xi}) \\ g^{11}(\boldsymbol{\xi}) \end{Bmatrix} = \begin{bmatrix} a_{10}^{10} & a_{01}^{10} & a_{20}^{10} & a_{02}^{10} & a_{11}^{10} \\ a_{10}^{01} & a_{01}^{01} & a_{20}^{01} & a_{02}^{01} & a_{11}^{01} \\ a_{10}^{20} & a_{01}^{20} & a_{20}^{20} & a_{02}^{20} & a_{11}^{20} \\ a_{10}^{02} & a_{01}^{02} & a_{20}^{02} & a_{02}^{02} & a_{11}^{02} \\ a_{10}^{11} & a_{01}^{11} & a_{20}^{11} & a_{02}^{11} & a_{11}^{11} \end{bmatrix} \begin{Bmatrix} w\xi_1 \\ w\xi_2 \\ w\xi_1^2 \\ w\xi_2^2 \\ w\xi_1\xi_2 \end{Bmatrix} \tag{2.24}$$

where $a_{q_1 q_2}^{p_1 p_2}$ represents the coefficients of the polynomials with $0 < q_1 + q_2 \le 2$. The weighted function w is defined as [14]

$$w = e^{-(2|\xi|/\delta)^2} \tag{2.25}$$

By substituting Eq. (2.23a) into the orthogonality conditions provided in Eq. (2.20a) the following equations for $g^{10}(\boldsymbol{\xi})$ can be obtained as [14]

$$\begin{aligned} &\left(a_{10}^{10}\right)\int_{H_x} w\xi_1^2 \mathrm{d}V' + \left(a_{01}^{10}\right)\int_{H_x} w\xi_1\xi_2 \mathrm{d}V' + \left(a_{20}^{10}\right)\int_{H_x} w\xi_1^3 \mathrm{d}V' \\ &+ \left(a_{02}^{10}\right)\int_{H_x} w\xi_1\xi_2^2 \mathrm{d}V' + \left(a_{11}^{10}\right)\int_{H_x} w\xi_1^2\xi_2 \mathrm{d}V' = 1 \end{aligned} \tag{2.26a}$$

$$\begin{aligned} &\left(a_{10}^{10}\right)\int_{H_x} w\xi_1\xi_2 \mathrm{d}V' + \left(a_{01}^{10}\right)\int_{H_x} w\xi_2^2 \mathrm{d}V' + \left(a_{20}^{10}\right)\int_{H_x} w\xi_1^2\xi_2 \mathrm{d}V' \\ &+ \left(a_{02}^{10}\right)\int_{H_x} w\xi_2^3 \mathrm{d}V' + \left(a_{11}^{10}\right)\int_{H_x} w\xi_1\xi_2^2 \mathrm{d}V' = 0 \end{aligned} \tag{2.26b}$$

$$\left(a_{10}^{10}\right)\int_{H_x} w\xi_1^3 \mathrm{d}V' + \left(a_{01}^{10}\right)\int_{H_x} w\xi_1^2\xi_2 \mathrm{d}V' + \left(a_{20}^{10}\right)\int_{H_x} w\xi_1^4 \mathrm{d}V' + \left(a_{02}^{10}\right)\int_{H_x} w\xi_1^2\xi_2^2 \mathrm{d}V' + \left(a_{11}^{10}\right)\int_{H_x} w\xi_1^3\xi_2 \mathrm{d}V' = 0 \tag{2.26c}$$

$$\left(a_{10}^{10}\right)\int_{H_x} w\xi_1\xi_2^2 \mathrm{d}V' + \left(a_{01}^{10}\right)\int_{H_x} w\xi_2^3 \mathrm{d}V' + \left(a_{20}^{10}\right)\int_{H_x} w\xi_1^2\xi_2^2 \mathrm{d}V' + \left(a_{02}^{10}\right)\int_{H_x} w\xi_2^4 \mathrm{d}V' + \left(a_{11}^{10}\right)\int_{H_x} w\xi_1\xi_2^3 \mathrm{d}V' = 0 \tag{2.26d}$$

$$\left(a_{10}^{10}\right)\int_{H_x} w\xi_1^2\xi_2 \mathrm{d}V' + \left(a_{01}^{10}\right)\int_{H_x} w\xi_1\xi_2^2 \mathrm{d}V' + \left(a_{20}^{10}\right)\int_{H_x} w\xi_1^3\xi_2 \mathrm{d}V' + \left(a_{02}^{10}\right)\int_{H_x} w\xi_1\xi_2^3 \mathrm{d}V' + \left(a_{11}^{10}\right)\int_{H_x} w\xi_1^2\xi_2^2 \mathrm{d}V' = 0 \tag{2.26e}$$

Similarly, by substituting Eq. (2.23b-e) into the orthogonality conditions provided in Eq. (2.20b-e), the following relations can be obtained [14]

$$\mathbf{A}\mathbf{a} = \mathbf{b} \tag{2.27}$$

with

$$\mathbf{A} = \int_{H_x} \begin{bmatrix} w\xi_1^2 & w\xi_1\xi_2 & w\xi_1^3 & w\xi_1\xi_2^2 & w\xi_1^2\xi_2 \\ w\xi_1\xi_2 & w\xi_2^2 & w\xi_1^2\xi_2 & w\xi_2^3 & w\xi_1\xi_2^2 \\ w\xi_1^3 & w\xi_1^2\xi_2 & w\xi_1^4 & w\xi_1^2\xi_2^2 & w\xi_1^3\xi_2 \\ w\xi_1\xi_2^2 & w\xi_2^3 & w\xi_1^2\xi_2^2 & w\xi_2^4 & w\xi_1\xi_2^3 \\ w\xi_1^2\xi_2 & w\xi_1\xi_2^2 & w\xi_1^3\xi_2 & w\xi_1\xi_2^3 & w\xi_1^2\xi_2^2 \end{bmatrix} \mathrm{d}V' \tag{2.28a}$$

$$\mathbf{a} = \begin{bmatrix} a_{10}^{10} & a_{10}^{01} & a_{10}^{20} & a_{10}^{02} & a_{10}^{11} \\ a_{01}^{10} & a_{01}^{01} & a_{01}^{20} & a_{01}^{02} & a_{01}^{11} \\ a_{20}^{10} & a_{20}^{01} & a_{20}^{20} & a_{20}^{02} & a_{20}^{11} \\ a_{02}^{10} & a_{02}^{01} & a_{02}^{20} & a_{02}^{02} & a_{02}^{11} \\ a_{11}^{10} & a_{11}^{01} & a_{11}^{20} & a_{11}^{02} & a_{11}^{11} \end{bmatrix} \tag{2.28b}$$

$$\mathbf{b} = \begin{bmatrix} 1 & 0 & 0 & 0 & 0 \\ 0 & 1 & 0 & 0 & 0 \\ 0 & 0 & 2 & 0 & 0 \\ 0 & 0 & 0 & 2 & 0 \\ 0 & 0 & 0 & 0 & 1 \end{bmatrix} \tag{2.28c}$$

After solving for the unknown coefficient $\mathbf{a}$, the non-local form of derivatives of function f can be found.

2D PDDO can be easily generalized into the 3D PDDO as [14]

$$\begin{Bmatrix} \dfrac{\partial f(\mathbf{x})}{\partial x_1} \\ \dfrac{\partial f(\mathbf{x})}{\partial x_2} \\ \dfrac{\partial f(\mathbf{x})}{\partial x_3} \\ \dfrac{\partial^2 f(\mathbf{x})}{\partial x_1^2} \\ \dfrac{\partial^2 f(\mathbf{x})}{\partial x_2^2} \\ \dfrac{\partial^2 f(\mathbf{x})}{\partial x_3^2} \\ \dfrac{\partial^2 f(\mathbf{x})}{\partial x_1 \partial x_2} \\ \dfrac{\partial^2 f(\mathbf{x})}{\partial x_1 \partial x_3} \\ \dfrac{\partial^2 f(\mathbf{x})}{\partial x_2 \partial x_3} \end{Bmatrix} = \int_{H_{\mathbf{x}}} \left(f(\mathbf{x}+\boldsymbol{\xi}) - f(\mathbf{x}) \right) \begin{Bmatrix} g^{100}(\boldsymbol{\xi}) \\ g^{010}(\boldsymbol{\xi}) \\ g^{001}(\boldsymbol{\xi}) \\ g^{200}(\boldsymbol{\xi}) \\ g^{020}(\boldsymbol{\xi}) \\ g^{002}(\boldsymbol{\xi}) \\ g^{110}(\boldsymbol{\xi}) \\ g^{101}(\boldsymbol{\xi}) \\ g^{011}(\boldsymbol{\xi}) \end{Bmatrix} \mathrm{d}V' \tag{2.29}$$

where

$$\begin{Bmatrix} g^{100}(\boldsymbol{\xi}) \\ g^{010}(\boldsymbol{\xi}) \\ g^{001}(\boldsymbol{\xi}) \\ g^{200}(\boldsymbol{\xi}) \\ g^{020}(\boldsymbol{\xi}) \\ g^{002}(\boldsymbol{\xi}) \\ g^{110}(\boldsymbol{\xi}) \\ g^{101}(\boldsymbol{\xi}) \\ g^{011}(\boldsymbol{\xi}) \end{Bmatrix} = \left(\mathbf{A}^{-1}\mathbf{b} \right)^T \begin{bmatrix} w\xi_1 \\ w\xi_2 \\ w\xi_3 \\ w\xi_1^2 \\ w\xi_2^2 \\ w\xi_3^2 \\ w\xi_1\xi_2 \\ w\xi_1\xi_3 \\ w\xi_2\xi_3 \end{bmatrix} \tag{2.30a}$$

$$\mathbf{A}=\int_{H_x} w\begin{bmatrix} \xi_1^2 & \xi_1\xi_2 & \xi_1\xi_3 & \xi_1^3 & \xi_1\xi_2^2 & \xi_1\xi_3^2 & \xi_1^2\xi_2 & \xi_1^2\xi_3 & \xi_1\xi_2\xi_3 \\ \xi_1\xi_2 & \xi_2^2 & \xi_2\xi_3 & \xi_1^2\xi_2 & \xi_2^3 & \xi_2\xi_3^2 & \xi_1\xi_2^2 & \xi_1\xi_2\xi_3 & \xi_2^2\xi_3 \\ \xi_1\xi_3 & \xi_2\xi_3 & \xi_3^2 & \xi_1^2\xi_3 & \xi_2^2\xi_3 & \xi_3^3 & \xi_1\xi_2\xi_3 & \xi_1\xi_3^2 & \xi_2\xi_3^2 \\ \xi_1^3 & \xi_1^2\xi_2 & \xi_1^2\xi_3 & \xi_1^4 & \xi_1^2\xi_2^2 & \xi_1^2\xi_3^2 & \xi_1^3\xi_2 & \xi_1^3\xi_3 & \xi_1^2\xi_2\xi_3 \\ \xi_1\xi_2^2 & \xi_2^3 & \xi_2^2\xi_3 & \xi_1^2\xi_2^2 & \xi_2^4 & \xi_2^2\xi_3^2 & \xi_1\xi_2^3 & \xi_1\xi_2^2\xi_3 & \xi_2^3\xi_3 \\ \xi_1\xi_3^2 & \xi_2\xi_3^2 & \xi_3^3 & \xi_1^2\xi_3^2 & \xi_2^2\xi_3^2 & \xi_3^4 & \xi_1\xi_2\xi_3^2 & \xi_1\xi_3^3 & \xi_2\xi_3^3 \\ \xi_1^2\xi_2 & \xi_1\xi_2^2 & \xi_1\xi_2\xi_3 & \xi_1^3\xi_2 & \xi_1\xi_2^3 & \xi_1\xi_2\xi_3^2 & \xi_1^2\xi_2^2 & \xi_1^2\xi_2\xi_3 & \xi_1\xi_2^2\xi_3 \\ \xi_1^2\xi_3 & \xi_1\xi_2\xi_3 & \xi_1\xi_3^2 & \xi_1^3\xi_3 & \xi_1\xi_2^2\xi_3 & \xi_1\xi_3^3 & \xi_1^2\xi_2\xi_3 & \xi_1^2\xi_3^2 & \xi_1\xi_2\xi_3^2 \\ \xi_1\xi_2\xi_3 & \xi_2^2\xi_3 & \xi_2\xi_3^2 & \xi_1^2\xi_2\xi_3 & \xi_2^3\xi_3 & \xi_2\xi_3^3 & \xi_1\xi_2^2\xi_3 & \xi_1\xi_2\xi_3^2 & \xi_2^2\xi_3^2 \end{bmatrix} dV' \tag{2.30b}$$

$$\mathbf{b}=\begin{bmatrix} 1 & 0 & 0 & 0 & 0 & 0 & 0 & 0 & 0 \\ 0 & 1 & 0 & 0 & 0 & 0 & 0 & 0 & 0 \\ 0 & 0 & 1 & 0 & 0 & 0 & 0 & 0 & 0 \\ 0 & 0 & 0 & 2 & 0 & 0 & 0 & 0 & 0 \\ 0 & 0 & 0 & 0 & 2 & 0 & 0 & 0 & 0 \\ 0 & 0 & 0 & 0 & 0 & 2 & 0 & 0 & 0 \\ 0 & 0 & 0 & 0 & 0 & 0 & 1 & 0 & 0 \\ 0 & 0 & 0 & 0 & 0 & 0 & 0 & 1 & 0 \\ 0 & 0 & 0 & 0 & 0 & 0 & 0 & 0 & 1 \end{bmatrix} \tag{2.30c}$$

$$\boldsymbol{\xi}=\xi_1\mathbf{e}_1+\xi_2\mathbf{e}_2+\xi_3\mathbf{e}_3 \tag{2.30d}$$

with $\mathbf{e}_1$, $\mathbf{e}_2$ and $\mathbf{e}_3$ representing the unit vectors in the x, y, and z directions.

2.2.2. PPDO model accuracy test for 2D

2.2.2.1 The effect of particle distribution on PDDO accuracy

The PDDO accuracy is tested for first and second order derivatives both for uniform and non-uniform particle distributions. In this way, the effect of the non-uniform particle distribution which frequently exists in fluid flow simulation on the PDDO accuracy is investigated.

In order to test the higher-order derivatives approximation accuracy, a function is set as an object

$$f\left(x,y\right)=x^2+2y^3 \tag{2.31}$$

with the variable domain of $x\in\left[0,2\right]$ and $y\in\left[0,2\right]$. The exact solutions for the derivatives are easy to obtain as

$$\begin{aligned}&\frac{\partial f\left(x,y\right)}{\partial x}=2x;\frac{\partial f\left(x,y\right)}{\partial y}=6y^2;\\&\frac{\partial^2 f\left(x,y\right)}{\partial x^2}=2;\frac{\partial^2 f\left(x,y\right)}{\partial y^2}=12y;\frac{\partial^2 f\left(x,y\right)}{\partial x\partial y}=0\end{aligned} \tag{2.32}$$

In the numerical implementation, the domain is discretized by 21×21 particles with both uniform and non-uniform distributions, as shown in Fig. 2-2. The non-uniform distribution is generated from a standard normal distribution [15].

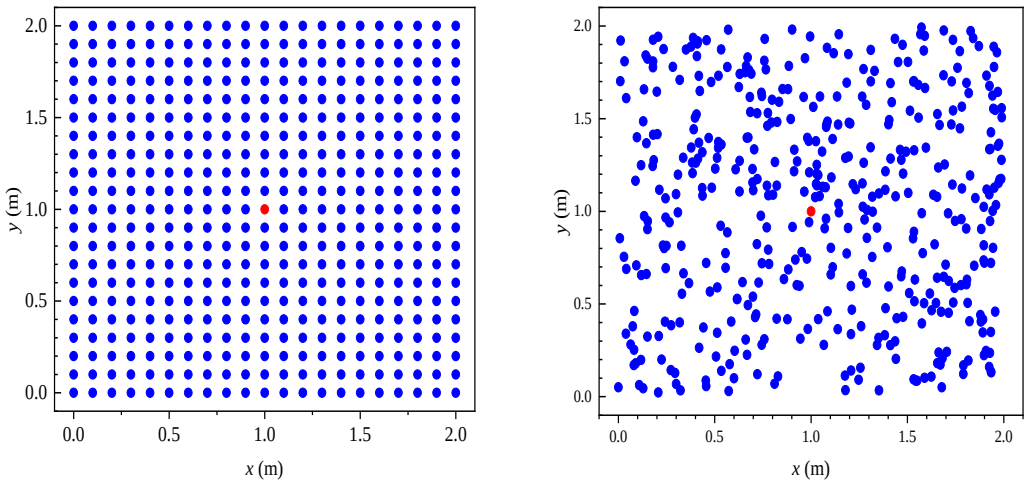

Fig. 2-2 (a) Uniform (b) non-uniform particle distributions

The red point located at $\left(1,1\right)$ in Fig. 2-2 is set to be the point of interest, whose derivatives are shown in Table 1 for exact and PDDO solutions with their relative errors.

Table 1 Comparison of derivatives at $(x, y) = (1,1)$ with exact value and PDDO solution with 21×21 particles

Method		$\partial f/\partial x$	$\partial f/\partial y$	$\partial^2 f/\partial x^2$	$\partial^2 f/\partial^2 y$	$\partial^2 f/\partial x \partial y$
Exact Solution		2	6	2	12	0
PDDO Uniform	value	2	6.0536	2	12	3.719E-15
	error	(0)	(0.89%)	(0)	(0)	(-)
PPDO Non-uniform	value	2.0005	6.0572	1.9738	11.9924	-0.06672
	error	(0.028%)	(0.95%)	(1.31%)	(0.063%)	(-)

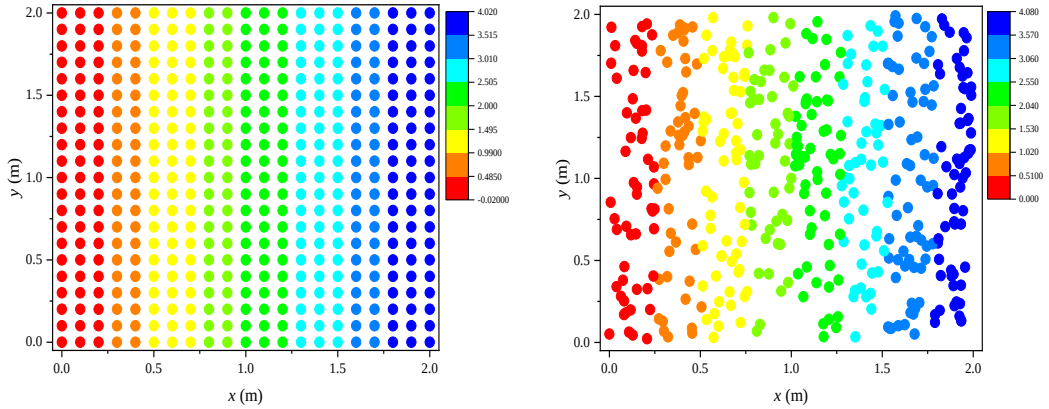

(a) Uniform (b) Non-uniform

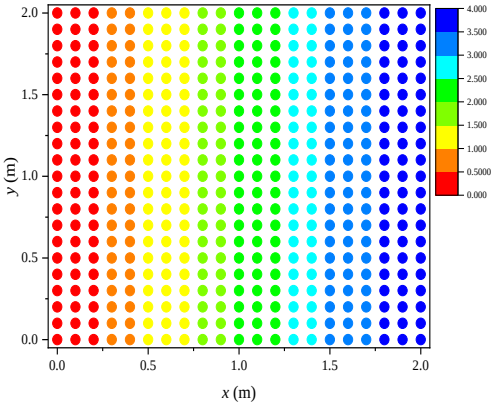

(c) Exact

Fig. 2-3 (a) Uniform (b) non-uniform particle distributions, and (c) exact values for $\partial f/\partial x$

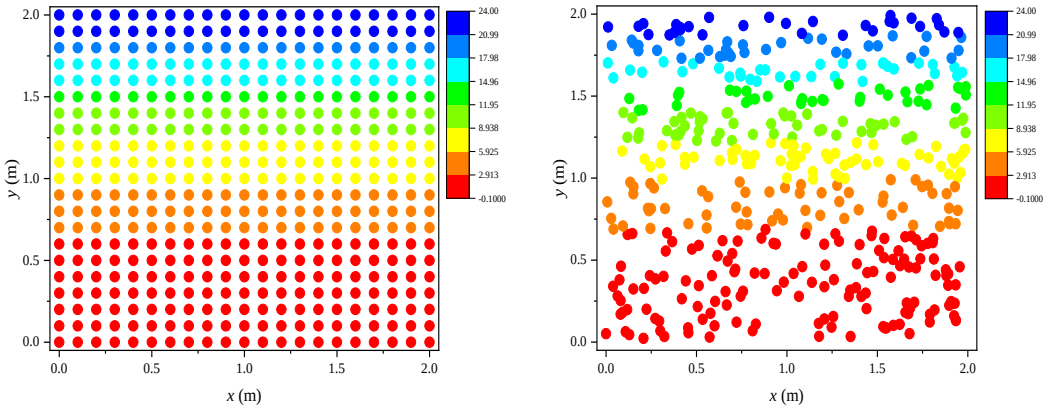

(a) Uniform (b) Non-uniform

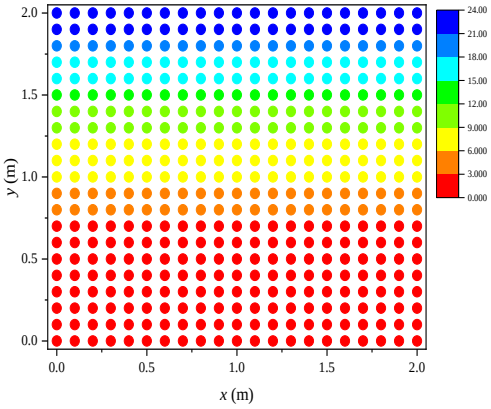

(c) Exact

Fig. 2-4 (a) Uniform (b) non-uniform particle distributions, and (c) exact values for $\partial f / \partial y$

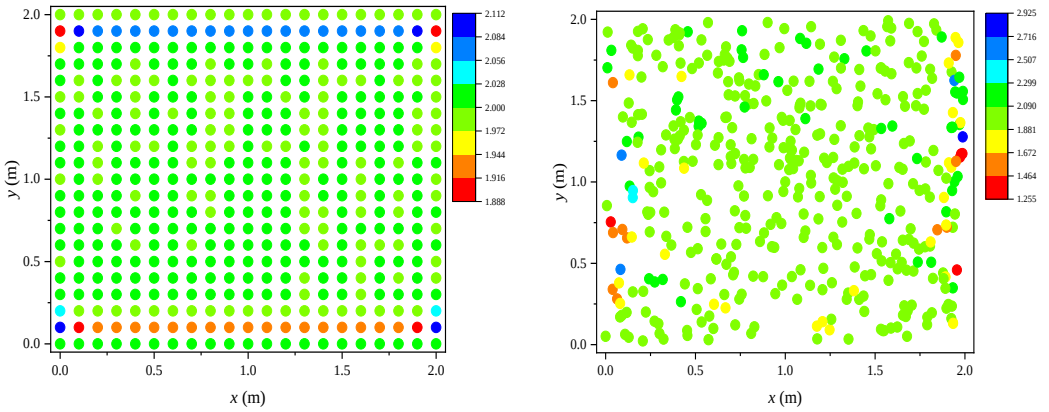

(a) Uniform (b) Non-uniform

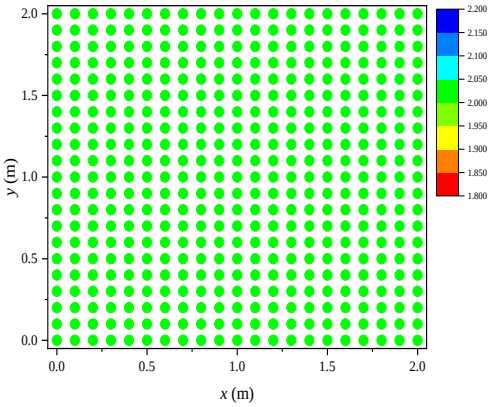

(c) Exact

Fig. 2-5 (a) Uniform (b) non-uniform particle distributions, and (c) exact values for $\partial^2 f/\partial x^2$

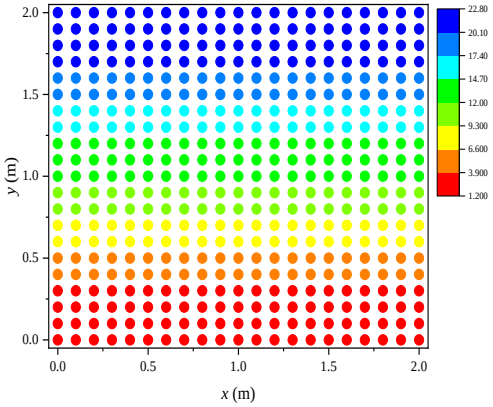

(a) Uniform

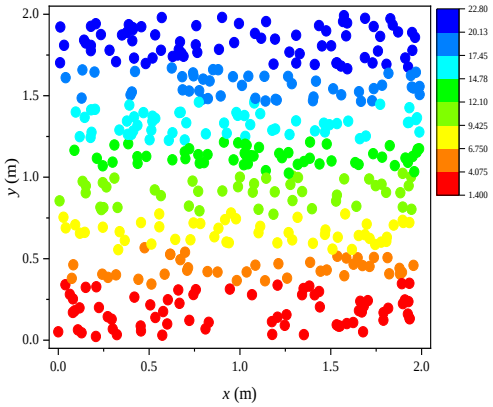

(b) Non-uniform

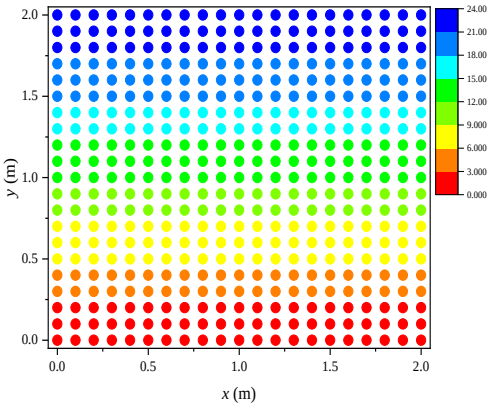

(c) Exact

Fig. 2-6 (a) Uniform (b) non-uniform particle distributions, and (c) exact values for $\partial^2 f/\partial y^2$

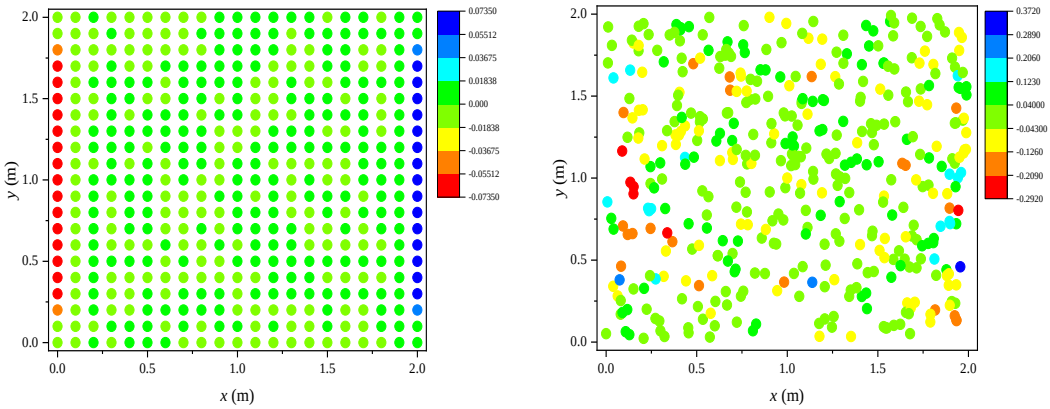

(a) Uniform (b) Non-uniform

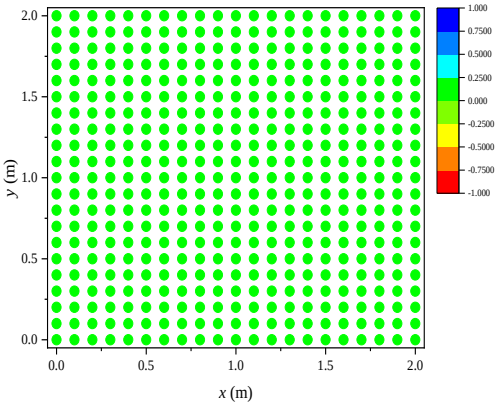

(c) Exact

Fig. 2-7 (a) Uniform (b) non-uniform particle distributions, and (c) exact values for $\partial^2 f/\partial x\partial y$

It can be observed from Table 1 that the accuracy of the PDDO both for first and second-order derivatives is acceptable. However, the irregularity of the particle distribution will increase the numerical error compared to the regular particle distribution as shown in Fig. 2-3-Fig. 2-7. Therefore, the techniques that redistribute the particles in a nearly uniform fashion is necessary for the PDDO simulations.

2.2.2.2 PDDO prediction accuracy test for function value prediction

The non-uniform particles as shown in Fig. 2-2 (b) are treated as the original particles. The uniform distributed particles as shown in Fig. 2-2 (a) are set as the new particles. The function Eq.(2.31) is given to the non-uniform particles in Fig. 2-2 (b). The distribution of the function values $f(x,y)$ of these non-uniform particles is shown in Fig. 2-10 (a). The function values of the uniform particles should be predicted

by using the derivatives on the non-uniform particle positions calculated by PDDO. The procedure is provided in Fig. 2-8.

The positions of the uniform and non-uniform distributed particles are provided in Fig. 2-9 (a). The uniform distributed particles are set as the interest points with their family members being the non-uniform distributed points, as illustrated in Fig. 2-9 (b). Particle i represents the particle of interest belonging to the uniform distribution system, and particle j represents the particle belonging to the non-uniform distribution system within the horizon of particle i. Besides, the particles belonging to the uniform distribution are not the family members of particle i, although they are located within the horizon.

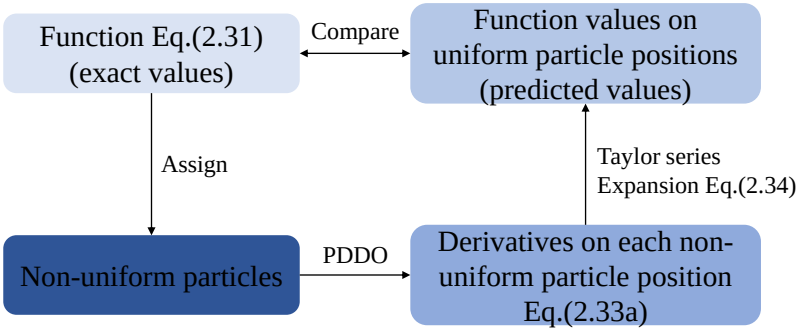

Fig. 2-8 Function value prediction procedure

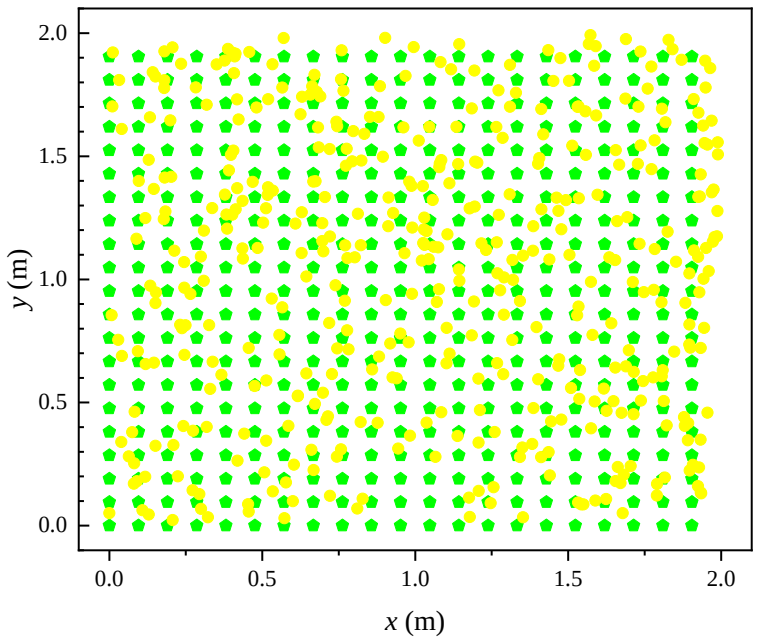

(a)

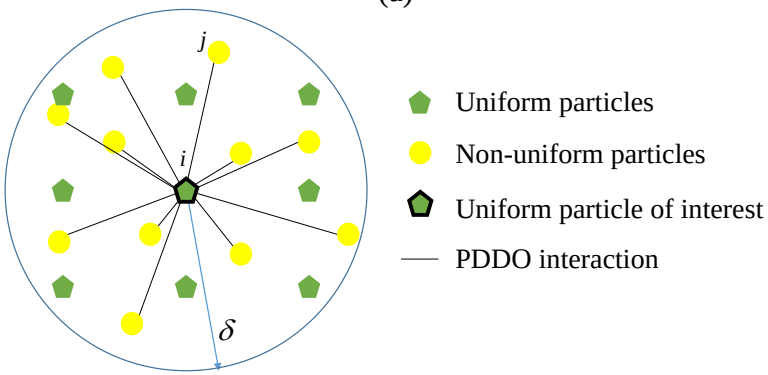

(b)

Fig. 2-9 (a) Uniform and non-uniform distributed particle positions, (b) illustration of PDDO interaction between uniform particles and non-uniform particles

First, the derivatives of function $f(x,y)$ on the positions of non-uniform distributed particles are predicted by PDDO in the realm of non-uniform distribution particle system. For example, for particle j belonging to the non-uniform particle distribution system, the derivatives are calculated according to Eq.(2.33) as

$$\begin{bmatrix} f_{,x}^{PDDO}\left(x_j^{nu},y_j^{nu}\right) \\ f_{,y}^{PDDO}\left(x_j^{nu},y_j^{nu}\right) \\ f_{,xx}^{PDDO}\left(x_j^{nu},y_j^{nu}\right) \\ f_{,yy}^{PDDO}\left(x_j^{nu},y_j^{nu}\right) \\ f_{,xy}^{PDDO}\left(x_j^{nu},y_j^{nu}\right) \end{bmatrix} = \sum_{k=1}^{N_j}\left(f\left(x_k^{nu},y_k^{nu}\right)-f\left(x_j^{nu},y_j^{nu}\right)\right)\begin{bmatrix} g^{10}\left(\xi_{jk}\right) \\ g^{01}\left(\xi_{jk}\right) \\ g^{20}\left(\xi_{jk}\right) \\ g^{02}\left(\xi_{jk}\right) \\ g^{11}\left(\xi_{jk}\right) \end{bmatrix} V_k \qquad (2.33a)$$

with

$$\begin{bmatrix} g^{10}\left(\xi_{jk}\right) \\ g^{01}\left(\xi_{jk}\right) \\ g^{20}\left(\xi_{jk}\right) \\ g^{02}\left(\xi_{jk}\right) \\ g^{11}\left(\xi_{jk}\right) \end{bmatrix} = \left(A^{-1}\begin{bmatrix} 1 & 0 & 0 & 0 & 0 \\ 0 & 1 & 0 & 0 & 0 \\ 0 & 0 & 2 & 0 & 0 \\ 0 & 0 & 0 & 2 & 0 \\ 0 & 0 & 0 & 0 & 1 \end{bmatrix}\right)^T \begin{bmatrix} w\left(\xi_{jk}^1\right) \\ w\left(\xi_{jk}^2\right) \\ w\left(\xi_{jk}^1\right)^2 \\ w\left(\xi_{jk}^2\right)^2 \\ w\left(\xi_{jk}^1\right)\left(\xi_{jk}^2\right) \end{bmatrix} \qquad (2.33b)$$

$$A=\sum_{k=1}^{N_j} w \begin{bmatrix} \left(\xi_{jk}^1\right)^2 & \left(\xi_{jk}^1\right)\left(\xi_{jk}^2\right) & \left(\xi_{jk}^1\right)^3 & \left(\xi_{jk}^1\right)\left(\xi_{jk}^2\right)^2 & \left(\xi_{jk}^1\right)^2\left(\xi_{jk}^2\right) \\ \left(\xi_{jk}^1\right)\left(\xi_{jk}^2\right) & \left(\xi_{jk}^2\right)^2 & \left(\xi_{jk}^1\right)^2\left(\xi_{jk}^2\right) & \left(\xi_{jk}^2\right)^3 & \left(\xi_{jk}^1\right)\left(\xi_{jk}^2\right)^2 \\ \left(\xi_{jk}^1\right)^3 & \left(\xi_{jk}^1\right)^2\left(\xi_{jk}^2\right) & \left(\xi_{jk}^1\right)^4 & \left(\xi_{jk}^1\right)^2\left(\xi_{jk}^2\right)^2 & \left(\xi_{jk}^1\right)^3\left(\xi_{jk}^2\right) \\ \left(\xi_{jk}^1\right)\left(\xi_{jk}^2\right)^2 & \left(\xi_{jk}^2\right)^3 & \left(\xi_{jk}^1\right)^2\left(\xi_{jk}^2\right)^2 & \left(\xi_{jk}^2\right)^4 & \left(\xi_{jk}^1\right)\left(\xi_{jk}^2\right)^3 \\ \left(\xi_{jk}^1\right)^2\left(\xi_{jk}^2\right) & \left(\xi_{jk}^1\right)\left(\xi_{jk}^2\right)^2 & \left(\xi_{jk}^1\right)^3\left(\xi_{jk}^2\right) & \left(\xi_{jk}^1\right)\left(\xi_{jk}^2\right)^3 & \left(\xi_{jk}^1\right)^2\left(\xi_{jk}^2\right)^2 \end{bmatrix} V_k \tag{2.33c}$$

$$\xi_{jk}=\left(\left(\xi_{jk}^1\right)^2+\left(\xi_{jk}^2\right)^2\right)^{1/2}=\left(\left(x_k^{nu}-x_j^{nu}\right)^2+\left(y_k^{nu}-y_j^{nu}\right)^2\right)^{1/2} \tag{2.33d}$$

where superscript *nu* represents the non-uniform particle. Particle k represents the family member of particle j belonging to the non-uniform distributed system. N_j is the total number of the family members of particle j which belongs to the non-uniform distributed system. The terms ξ_{jk}^1 and ξ_{jk}^2 are defined as $\xi_{jk}^1=x_k^{nu}-x_j^{nu}$ and $\xi_{jk}^2=y_k^{nu}-y_j^{nu}$.

Subsequently, the function value on the position of particle i (shown in Fig. 2-9 (b)) can be predicted by using the derivatives on the position of particle j by using Taylor series expansion as (as shown in Eq.(2.16))

$$\begin{aligned} \left(f\left(x_i^u,y_i^u\right)\right)^{corrected} &= f\left(x_j^{nu},y_j^{nu}\right)+f_{,x}^{PDDO}\left(x_j^{nu},y_j^{nu}\right)\left(x_i^u-x_j^{nu}\right) \\ &+f_{,y}^{PDDO}\left(x_j^{nu},y_j^{nu}\right)\left(y_i-y_j^{nu}\right)+\frac{1}{2}f_{,xx}^{PDDO}\left(x_j^{nu},y_j^{nu}\right)\left(x_i^u-x_j^{nu}\right)^2 \\ &+\frac{1}{2}f_{,yy}^{PDDO}\left(x_j^{nu},y_j^{nu}\right)\left(y_i^u-y_j^{nu}\right)^2+f_{,xy}^{PDDO}\left(x_j^{nu},y_j^{nu}\right)\left(x_i^u-x_j^{nu}\right)\left(y_i^u-y_j^{nu}\right) \end{aligned} \tag{2.34}$$

where superscript *u* represents the uniform particle and *nu* represents the non-uniform particle. By using Eq. (2.34), and by using the non-uniform family members (j) located at $\left(x_j^{nu},y_j^{nu}\right)$ of particle (i) located at $\left(x_i^u,y_i^u\right)$, one corrected function value at $\left(x_i^u,y_i^u\right)$ can be obtained for each family of (i) (such as (j)). Therefore, the

predicted function value at $\left(x_i^u, y_i^u\right)$ can be obtained by averaging the corrected values as

$$\left(f\left(x_i^u, y_i^u\right)\right)^{predicted} = \frac{\sum_{j=1}^{N_{i,nu}} \left(f\left(x_i^u, y_i^u\right)\right)^{corrected}}{N_{i,nu}}$$

$$= \frac{\sum_{j=1}^{N_{i,nu}} \left(\begin{array}{l} f\left(x_j^{nu}, y_j^{nu}\right) + f_{,x}^{PDDO}\left(x_j^{nu}, y_j^{nu}\right)\left(x_i^u - x_j^{nu}\right) \\ + f_{,y}^{PDDO}\left(x_j^{nu}, y_j^{nu}\right)\left(y_i - y_j^{nu}\right) + \frac{1}{2} f_{,xx}^{PDDO}\left(x_j^{nu}, y_j^{nu}\right)\left(x_i^u - x_j^{nu}\right)^2 \\ + \frac{1}{2} f_{,yy}^{PDDO}\left(x_j^{nu}, y_j^{nu}\right)\left(y_i^u - y_j^{nu}\right)^2 + f_{,xy}^{PDDO}\left(x_j^{nu}, y_j^{nu}\right)\left(x_i^u - x_j^{nu}\right)\left(y_i^u - y_j^{nu}\right) \end{array} \right)}{N_{i,nu}} \quad (2.35)$$

where $N_{i,nu}$ is the total number of the non-uniform family members of particle located at $\left(x_i^u, y_i^u\right)$.

The function values assigned to the non-uniform particles, $f\left(x_j^{nu}, y_j^{nu}\right)$ and predicted for the uniform particles, $\left(f\left(x_i^u, y_i^u\right)\right)^{predicted}$ are plotted in Fig. 2-10 and Fig. 2-11 for resolutions 21×21 and 51×51, respectively.

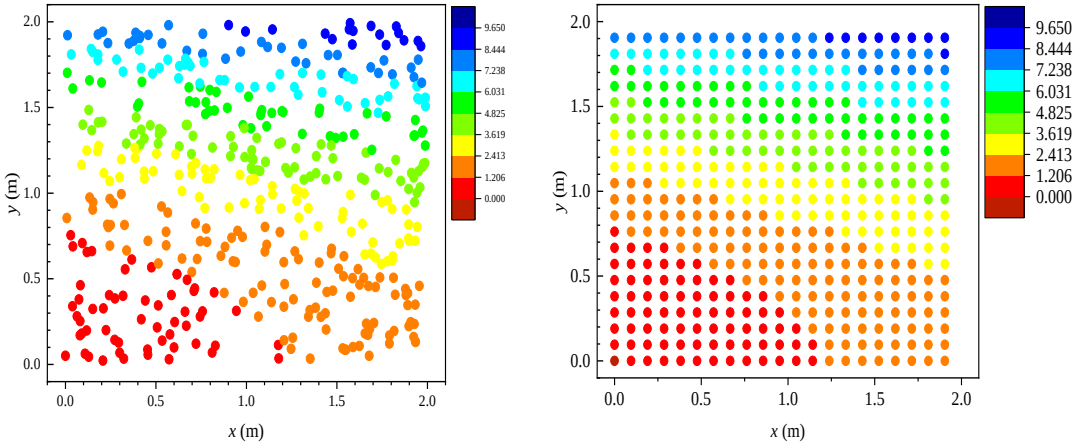

(a) (b)

Fig. 2-10 Function value, for (a) non-uniform particles (assigned), $f\left(x_j^{nu}, y_j^{nu}\right)$ and (b) uniform particles (predicted), $\left(f\left(x_i^u, y_i^u\right)\right)^{predicted}$ for resolution 21×21

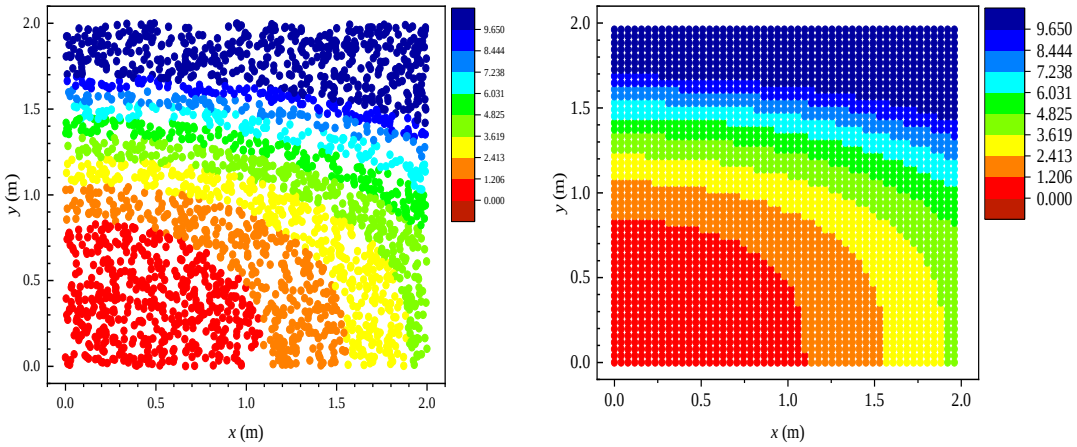

(a) (b)

Fig. 2-11 Function value for (a) non-uniform particles (assigned), $f\left(x_j^{nu}, y_j^{nu}\right)$ and (b) uniform particles (predicted), $\left(f\left(x_i^u, y_i^u\right)\right)^{predicted}$ for resolution 51×51

The total L_2-norm error of the uniform particle set is calculated as

$$\varepsilon_r = \sqrt{\frac{\sum_i \left(f^{predicted}\left(x_i^u, y_i^u\right) - f^{exact}\left(x_i^u, y_i^u\right)\right)^2}{\sum_i \left(f^{exact}\left(x_i^u, y_i^u\right)\right)^2}} \tag{2.36}$$

By comparing the error for different resolutions as $\varepsilon_r = 0.31\%$ for 21×21, $\varepsilon_r = 0.0670\%$ for 41×41, and $\varepsilon_r = 0.0374\%$ for 51×51, as shown in Fig. 2-12, it can be concluded that a higher resolution results in a more accurate solution.

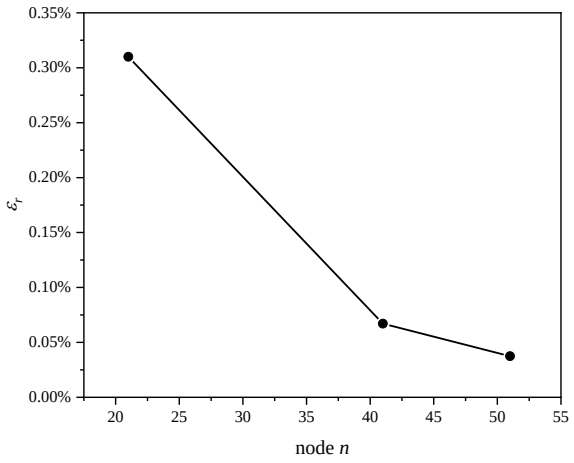

Fig. 2-12 L_2-norm error plot for different resolutions

3. Ordinary State Based Fully Coupled Thermomechanical PD Model for Isotropic Materials

3.1. Introduction

Due to the development of aerospace and mechanical industries in recent years, mechanical and thermal shock loadings become typical and important loading types. For example, the gas turbine engine casing of an aircraft can experience a temperature rise as high as $1700^{\circ}C$ within an extremely short period [16]. In the analyses with such loading conditions, the thermomechanical coupling effects often play a crucial role and as a consequence, they should be considered both in thermal and structural fields [17]. Not only the effect of temperature on deformation but also the effect of deformation on the temperature field is non-negligible. Therefore, fully coupled thermoelasticity analyses are necessary when dealing with such types of problems.

The basic theory of linear coupled thermoelasticity is well understood and fully developed for many years. Biot [18] first introduced a coupling item in heat conduction equation to solve the coupled problem of thermoelasticity. Later, Herrmann [19] generalized Biot's principle to a three-dimensional anisotropic body. Recently, Jabbari et al. [20, 21] gave exact equations for classical coupled thermoelasticity in cylindrical and spherical coordinates. Although some analytical solutions are provided for some simple problems, many complex problems have not been completely solved with analytical methods [22]. Therefore, numerical methods such as FEM and boundary element method (BEM) have been widely applied to get approximate solutions [23]. For example, Cannarozzi and Ubertini [24] conducted FEM analyses for linear coupled quasi-static thermoelastic problems with a mixed variation method. Displacement and temperature acted as primary variables in their research. On the other hand, stress and heat flux acted as dual variables which were also involved directly in their analysis. Tehrani and Eslami [25] studied the coupling coefficients and relaxation time effects on thermal and elastic wave motion by using BEM. When the fracture is involved in the fully coupled analyses, temperature distribution around crack tips becomes a major concern. The high energy concentration around a moving crack produces high amount

of heat energy and results in unneglectable temperature increase. Atkinson and Craster [26] deduced some simple and asymptotic temperature distributions for the region near crack tips during crack propagation. Weichert and Schönert [27] investigated the temperature near the crack tips in brittle materials with very small plastic zones and high crack velocities. The crack tips were simulated as heat generation sources and consequently, the temperature distributions were predicted. An experimental study conducted by Bhalla et al. [28] estimated the temperature distribution near the crack tips. A temperature increase was observed in their experiments. Miehe et.al [29] presented a continuum phase-field model for brittle fracture in thermoelasticity. A bending numerical simulation test considering the crack growth and dissipative heat generation was provided, and its corresponding temperature field was discussed.

When a discontinuity is involved in thermoelastic problems, the aforementioned numerical simulation methods based on the classical mechanical theory predict unbounded stresses and energy densities. Even for linear elastic fracture mechanics (LEFM) and dislocation dynamics, supplemental constitutive equations are needed to determine the motion of a dislocation. On the contrary, peridynamics [4, 30] is a nonlocal theory that includes damage as part of the material response. As a consequence, the PD equations remain valid where crack or discontinues merges [31]. Therefore, PD theory is especially suitable for problems with discontinues, thus it is adopted in this study. The crack nucleation and propagation has been investigated by many researchers in the realm of PD theory [32-38], but most of them are only in the mechanical field. In the thermal field, Oterkus et.al [39] derived the formulation of thermal diffusion with PD theory and utilized it to capture the fuel pellet cracking [40]. Bobaru and Duangpanya [41, 42] studied the heat conduction in bodies with and without discontinuities in bond-based PD theory. Regarding the thermomechanics, fully coupled bond-based PD theory was formulated by Oterkus et.al [43], Oterkus [44], Madenci and Oterkus [45]. Furthermore, they successfully applied their model to predict crack propagation [46, 47]. However, due to the aforementioned limitation of the BB-PD model on material properties [13], an ordinary state-based PD model is necessary for thermomechanical problems.

Regarding the fully coupled thermomechanical analysis, the ordinary state-based PD model has not been explicitly provided, only the expression in bond-based theory is available in the published literature [44, 48]. Therefore, in this section, ordinary state-based fully coupled PD thermoelastic equations with explicit formulations of PD parameters are provided in Section 3.2. Then these equations are cast into their corresponding non-dimensional forms in Section 3.3.

3.2. The OSB thermomechanical isotropic PD model

The ordinary state-based PD model for mechanical deformation prediction is provided in Section 2.1.2. In this section, the OSB-PD thermal model is discussed. For the point of interested i, the heat conduction equation in the fully coupled thermomechanical PD model is [43]

$$\rho c_v \dot{T}\left(\mathbf{x}_i,t\right)=\sum_{j=1}^{N_i}\left(\kappa\frac{\Theta\left(\mathbf{x}_j,t\right)-\Theta\left(\mathbf{x}_i,t\right)}{\left|\mathbf{x}_j-\mathbf{x}_i\right|}-\Theta_0\beta\left(\mathbf{x}_j-\mathbf{x}_i\right)\dot{e}\left(\mathbf{x}_j-\mathbf{x}_i\right)\right)V_j+h_s\left(\mathbf{x}_i,t\right) \quad (3.1)$$

where $h_s\left(\mathbf{x}_i,t\right)$ is the rate of heat generation per unit volume. In the above equation, κ is defined as PD micro-conductivity with its definitions being listed as [39, 43, 49]

$$\kappa=\frac{2k_T}{A_{area}\delta^2} \text{ for 1D} \quad (3.2a)$$

$$\kappa=\frac{6k_T}{\pi h_{thick}\delta^3} \text{ for 2D} \quad (3.2b)$$

$$\kappa=\frac{6k_T}{\pi\delta^4} \text{ for 3D} \quad (3.2c)$$

The second term within the summation of Eq. (3.1) represents the deformation coupling effect on temperature. The time rate of change of stretch extension, $\dot{e}\left(\mathbf{x}_j-\mathbf{x}_i\right)$, can be defined as

$$\dot{e}\left(\mathbf{x}_j-\mathbf{x}_i\right)=\frac{\mathbf{y}_j-\mathbf{y}_i}{\left|\mathbf{y}_j-\mathbf{y}_i\right|}\cdot\left(\dot{\mathbf{u}}_j-\dot{\mathbf{u}}_i\right) \tag{3.3}$$

The term β is the PD thermal modulus and its formulation in OSB-PD theory is derived as follows (details provided in Appendix A). The physical meaning and theory foundation of the PD thermal modulus are fully discussed by Oterkus et al. [43]. In this section, the same derivation approach is adopted. The initial form of the ordinary state-based PD force function for point $\mathbf{x}_i$ is shown in Eq. (2.9a). In another form, being similar to the derivation conducted by Oterkus et al. [43, 44], the PD force function can be divided into two parts as [43, 44]

$$\mathbf{t}=\mathbb{k}\cdot\mathbf{u}-\mathbf{B}T \tag{3.4}$$

The first part on the right-hand side includes only the structural deformation, and the second part is related to temperature effect. In Eq. (3.4), $\mathbb{k}$ is called the modulus state [50], the term $\mathbf{B}T$ represents the effects of thermal state on deformation.

By plugging the dilatation term in Eq. (2.10a) into the PD force function Eq. (2.9a) results

$$\mathbf{t}\left(\mathbf{u}_j-\mathbf{u}_i,\mathbf{x}_j-\mathbf{x}_i,t\right)=\left[2\delta\frac{d\Lambda_{ij}}{\left|\mathbf{x}_j-\mathbf{x}_i\right|}a\left(\sum_{j=1}^{N_i}d\delta\left(s_{ij}-\alpha T_i\right)\Lambda V_j\right)+2\delta b\left(s_{ij}-\alpha T_i\right)\right]\frac{\mathbf{y}_j-\mathbf{y}_i}{\left|\mathbf{y}_j-\mathbf{y}_i\right|} \tag{3.5}$$

After rewriting the PD force function by splitting into pure mechanical and thermal part Eq. (3.5) becomes

$$\begin{aligned}\mathbf{t}=&\left[\left(\frac{2a\delta^2d^2\Lambda_{ij}}{\left|\mathbf{x}_j-\mathbf{x}_i\right|}\sum_{j=1}^{N_i}s\Lambda_{ij}V_j+2\delta bs_{ij}\right)\frac{\mathbf{y}_j-\mathbf{y}_i}{\left|\mathbf{y}_j-\mathbf{y}_i\right|}\right]\\&-\left[\left(\frac{2a\delta^2d^2\Lambda_{ij}}{\left|\mathbf{x}_j-\mathbf{x}_i\right|}\sum_{j=1}^{N_i}\Lambda_{ij}V_j+2\delta b\right)\left(\alpha\frac{\mathbf{y}_j-\mathbf{y}_i}{\left|\mathbf{y}_j-\mathbf{y}_i\right|}\right)\right]T_i\end{aligned} \tag{3.6}$$

By comparing Eqs. (3.4) and (3.6), local thermal modulus of the bond between $\mathbf{x}$ and $\mathbf{x}'$ can be obtained as

$$\beta\left(\mathbf{x}_j-\mathbf{x}_i\right)=\left(\frac{2a\delta^2d^2\Lambda_{ij}}{\left|\mathbf{x}_j-\mathbf{x}_i\right|}\sum_{j=1}^{N_i}\Lambda_{ij}V_j+2\delta b\right)\alpha \tag{3.7}$$

with $\mathbf{B}=\beta\dfrac{\mathbf{y}_j-\mathbf{y}_i}{\left|\mathbf{y}_j-\mathbf{y}_i\right|}$ [43, 44]. Substituting the PD parameters provided in Eq. (2.11), the explicit form of the local OSB thermal modulus, β, for different dimensions can be obtained as

$$\beta=\frac{E\alpha}{A_{area}\delta^2}\ \text{for 1D} \tag{3.8a}$$

$$\beta\left(\mathbf{x}_j-\mathbf{x}_i\right)=\frac{4\alpha}{\pi h_{thick}\delta^3}\left(\frac{K_\theta-2\mu}{\pi h_{thick}\delta}\frac{\Lambda_{ij}}{\left|\mathbf{x}_j-\mathbf{x}_i\right|}\sum_{j=1}^{N_i}\Lambda_{ij}V_j+3\mu\right)\ \text{for 2D} \tag{3.8b}$$

$$\beta\left(\mathbf{x}_j-\mathbf{x}_i\right)=\frac{3\alpha}{\pi\delta^4}\left(\frac{\left(27K_\theta-45\mu\right)}{16\pi\delta^2}\frac{\Lambda_{ij}}{\left|\mathbf{x}_j-\mathbf{x}_i\right|}\sum_{j=1}^{N_i}\Lambda_{ij}V_j+5\mu\right)\ \text{for 3D} \tag{3.8c}$$

Furthermore, for the bond-based restriction ($a=0$) [10], the OSB-PD thermal modulus will reduce to its bond-based form, where $\beta_b=2\delta b\alpha$ or $\beta_b=1/2\left(c\alpha\right)$ [43, 44] with c being the bond-based PD material constant [10] as provided in Eq. (2.8).

3.3. Non-dimensional form of OSB PD model

The governing equation can be put in a non-dimensional form by using non-dimensional variables [51]. Therefore, the fully coupled PD equations are cast into their non-dimensional forms by adopting the approach proposed by Sackman [52] and Oterkus et al. [43].

Regarding the heat conduction equation, the diffusivity is defined as the characteristic length/time quantity and the characteristic length/time is the elastic wave speed [52]

$$\gamma = \frac{k_T}{\rho c_v} = \frac{l^{*2}}{t^*} \tag{3.9}$$

$$\tilde{a} = \sqrt{\frac{\lambda + 2\mu}{\rho}} = \frac{l^*}{t^*} \tag{3.10}$$

where λ and μ are Lame's constants. Combining the characteristic length/time scale leads to characteristic length and time as follows [52]

$$l^* = \gamma / \tilde{a} \tag{3.11a}$$

$$t^* = \gamma / \tilde{a}^2 \tag{3.11b}$$

As explained in [43, 52] following non-dimensional forms can be used

Length related variables:

$$x = \frac{\gamma}{\tilde{a}}\bar{x}, \delta = \frac{\gamma}{\tilde{a}}\bar{\delta}, A = \left(\frac{\gamma}{\tilde{a}}\right)^2 \bar{A}, V = \left(\frac{\gamma}{\tilde{a}}\right)^3 \bar{V} \tag{3.12}$$

Displacement:

$$u = \left(\frac{\gamma}{\tilde{a}}\right)\frac{\beta_{cl}\theta_o}{(\lambda + 2\mu)}\bar{u} \tag{3.13}$$

Stretch:

$$s = \frac{\beta_{cl}\theta_o}{(\lambda + 2\mu)}\bar{s} \tag{3.14}$$

Time:

$$t = \left(\frac{\gamma}{\tilde{a}^2} \right) \bar{t} \tag{3.15}$$

Velocity-related variables:

$$\mathrm{v} = \frac{\beta_{cl}\theta_o}{(\lambda + 2\mu)} \tilde{a} \bar{\mathrm{v}} \quad \text{and} \quad \dot{e} = \frac{\beta_{cl}\theta_o}{(\lambda + 2\mu)} \tilde{a} \bar{\dot{e}} \tag{3.16}$$

And the temperature:

$$T = \Theta_0 \bar{T} \tag{3.17}$$

By using the above non-dimensional parameters and substituting the peridynamic parameters listed in Section 2.1.2 into Eq. (2.12) and Eq. (3.1), the non-dimensional form of the fully coupled equations can be achieved by utilizing the non-dimensional parameters given in Eq. (3.9)-Eq. (3.17) as

1D analysis

$$\dot{\bar{T}}_i = \frac{2}{\bar{A}\bar{\delta}^2} \sum_{j=1}^{N_i} \left(\frac{\bar{T}_j - \bar{T}_i}{\left| \bar{\mathbf{x}}_j - \bar{\mathbf{x}}_i \right|} - \epsilon \frac{\bar{\dot{e}}}{2} \right) \bar{V}_j + \bar{h}_s \text{ for 1D} \tag{3.18a}$$

$$\bar{\ddot{\mathbf{u}}}(\mathbf{x}_i, t) = \frac{2}{\bar{A}\bar{\delta}^2} \sum_{j=1}^{N_i} \left(\bar{s}_{ij} - \frac{\bar{T}_i + \bar{T}_j}{2} \right) \frac{\bar{\mathbf{y}}_j - \bar{\mathbf{y}}_i}{\left| \bar{\mathbf{y}}_j - \bar{\mathbf{y}}_i \right|} \bar{V}_j + \bar{\mathbf{b}}(\mathbf{x}_i, t) \text{ for 1D} \tag{3.18b}$$

2D analysis

$$\dot{\bar{T}}_i = \frac{6}{\pi \bar{h} \bar{\delta}^3} \sum_{j=1}^{N_i} \left(\frac{\bar{T}_j - \bar{T}_i}{\left| \bar{\mathbf{x}}_j - \bar{\mathbf{x}}_i \right|} - \frac{\epsilon \bar{\dot{e}}}{1+\nu} \left[1 - \nu + \left(\nu - \frac{1}{3} \right) \frac{\Lambda_{ij}}{\pi \bar{h} \bar{\delta} \left| \bar{\mathbf{x}}_j - \bar{\mathbf{x}}_i \right|} \sum_{j=1}^{N_i} \Lambda_{ij} V_j \right] \right) \bar{V}_j + \bar{h}_s \text{ for 2D} \tag{3.19a}$$

$$\ddot{\bar{\mathbf{u}}}\left(\mathbf{x}_i,t\right)=\frac{2}{\pi\bar{h}\bar{\delta}^3\left(1+\nu\right)}\sum_{j=1}^{N_i}\left[\begin{array}{l}\dfrac{3\nu-1}{\pi\bar{h}\bar{\delta}\left|\bar{\mathbf{x}}_j-\bar{\mathbf{x}}_i\right|}\Lambda_{ij}\left(\bar{\theta}_i+\bar{\theta}_j\right)\\ +6\left(1-\nu\right)\left(\left(1+\nu\right)\bar{s}_{ij}-\dfrac{\bar{T}_i+\bar{T}_j}{2}\right)\end{array}\right]\frac{\bar{\mathbf{y}}_j-\bar{\mathbf{y}}_i}{\left|\bar{\mathbf{y}}_j-\bar{\mathbf{y}}_i\right|}\bar{V}_j+\bar{\mathbf{b}}\left(\mathbf{x}_i,t\right)\text{for 2D}$$

(3.19b)

with

$$\bar{\theta}_i=\sum_{j=1}^{N_i}\left[\left(1+\nu\right)\bar{s}_{ij}-\bar{T}_i\right]\Lambda_{ij}\bar{V}_j\text{ for 2D}\qquad\text{(3.19c)}$$

3D analysis

$$\dot{\bar{T}}=\frac{6}{\pi\bar{\delta}^4}\sum_{j=1}^{N_i}\left(\frac{\bar{T}_j-\bar{T}_i}{\left|\bar{\mathbf{x}}_j-\bar{\mathbf{x}}_i\right|}-\frac{\epsilon\dot{\bar{e}}}{16\left(1+\nu\right)}\left[\begin{array}{l}20\left(1-2\nu\right)\\ +27\left(\nu-\dfrac{1}{4}\right)\dfrac{\Lambda_{ij}}{\left|\bar{\mathbf{x}}_j-\bar{\mathbf{x}}_i\right|\pi\bar{\delta}^2}\displaystyle\sum_{j=1}^{N_i}\Lambda_{ij}V_j\end{array}\right]\right)\bar{V}_j+\bar{h}_s\text{ for 3D}$$

(3.20a)

$$\ddot{\bar{\mathbf{u}}}\left(\mathbf{x}_i,t\right)=\frac{3}{\left(1+\nu\right)\pi\bar{\delta}^4}\sum_{j=1}^{N_i}\left[\begin{array}{l}\dfrac{27}{8}\left(\nu-\dfrac{1}{4}\right)\dfrac{\Lambda_{ij}\left(\bar{\theta}_i+\bar{\theta}_j\right)}{\pi\bar{\delta}^2\left|\bar{\mathbf{x}}_j-\bar{\mathbf{x}}_i\right|}\\ +5\left(1-2\nu\right)\left(\dfrac{1+\nu}{1-\nu}\bar{s}_{ij}-\dfrac{\bar{T}_i+\bar{T}_j}{2}\right)\end{array}\right]\frac{\bar{\mathbf{y}}_j-\bar{\mathbf{y}}_i}{\left|\bar{\mathbf{y}}_j-\bar{\mathbf{y}}_i\right|}\bar{V}_j+\bar{\mathbf{b}}\left(\mathbf{x}_i,t\right)\text{ for 3D}$$

(3.20b)

with

$$\bar{\theta}_i=\sum_{j=1}^{N_i}\left[\frac{1+\nu}{1-\nu}\bar{s}_{ij}-\bar{T}_i\right]\Lambda_{ij}\bar{V}_j\text{ for 3D}\qquad\text{(3.20c)}$$

In the above equations, the non-dimensional variables are denoted with an overscore. The parameters $\bar{\dot{T}}_i$ and $\bar{\dot{T}}_j$ are the rate of temperature changes at material point $\bar{\mathbf{x}}_i$ and $\bar{\mathbf{x}}_j$, respectively. The non-dimensional coupling coefficient, ϵ, measures the strength

of the coupling effect on temperature distribution due to deformation. It can be defined as [52]

$$\epsilon = \frac{\beta_{cl}^2 \Theta_0}{\rho c_v \left(\lambda + 2\mu\right)} \tag{3.21}$$

3.4. Numerical implementation

In a dimensional simulation, the accelerations and temperature changes of PD material points are updated according to Eq.(2.12) and Eq.(3.1). In a non-dimensional simulation, the accelerations and temperature changes of PD material points are updated according to Section 3.3. Explicit time integration is used to find the temperature, velocity and displacement profile at each time step [44]. The numerical procedure is provided in Fig. 3-1 for dimensional simulations as an example. In Fig. 3-1, N_t represent the total number of the time step, n represents the current number of the time step, and N_{node} represents the total number of PD points.

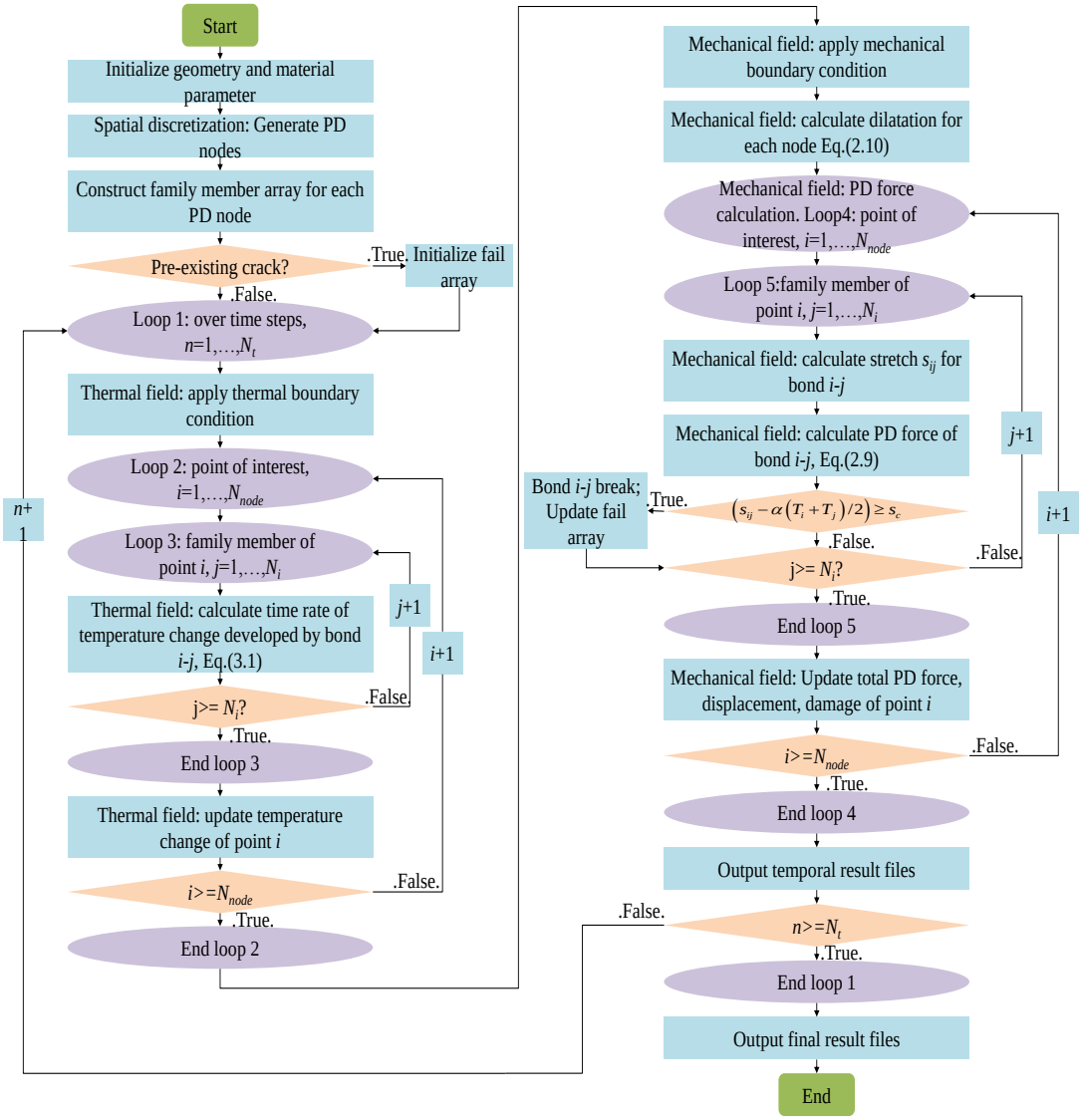

Fig. 3-1 Flowchart for the numerical procedure

3.5. Verification simulation cases

In this section, peridynamic simulations are conducted using the proposed model. The validity of the fully coupled thermomechanical equations is established by comparing the PD solutions with previously considered BEM and ANSYS solutions. Firstly, a dimensionless isotropic plate is imposed with three types of loadings, i.e. pressure shock loading, thermal shock loading and their combination. The results from PD solution are in agreement with the ones from an existing BEM solution. Secondly, a dimensional isotropic square plate is separately subjected to a tension pressure shock loading and a combination of compression and tension pressure shock loading. The

temperature and displacement responses from PD solution coincide very well with ANSYS solution. The present two-dimensional PD model is thus validated via these numerical simulations both in dimensional and non-dimensional forms. As a next verification problem, a block is investigated with a temperature boundary condition. Good agreements are obtained by comparing PD and ANSYS solutions. Hence, the non-dimensional form of the equations is validated both for two and three-dimensional problems.

3.5.1. Plate subjected to shock loading

The validity of the non-dimensional thermoelastic PD equations for 2D problems is established by constructing PD solutions for an existing BEM solution provided by Hosseini-Tehrani and Eslami [53]. The same geometry model, boundary conditions, and loading conditions are adopted as in [53]. As shown in Fig. 3-2, a thin plate with a non-dimensional geometry $\bar{L}=10, \bar{W}=10$ and thickness $\bar{h}=1$ is subject to a shock loading on the edge of $\bar{x}=-\bar{L}/2$ and fixed on the edge of $\bar{x}=\bar{L}/2$. The edges of $\bar{y}=\bar{W}/2$ and $\bar{y}=-\bar{W}/2$ are traction free. Furthermore, at $\bar{x}=-\bar{L}/2$ the plate is subjected to temperature boundary condition and all other three edges are insulated. The Poisson's ratio is set to be 0.17. Regarding the PD discretization, the grid size is $\Delta x=0.05$ and the horizon size is chosen as $\delta=3.015\Delta x$. The uniform time step size is 5.0×10^{-4} with total simulation time $\bar{t}_{total}=6$. The boundary condition is implemented by using fictitious layers [54]. The applied loads are implemented on a real boundary layer [54]. Since there is no heat source in this simulation case, $\bar{h}_s=0$.

The initial conditions are:

$$\bar{u}_{\bar{x}}\left(\bar{x},\bar{y},\ \bar{t}=0\right)=\bar{u}_{\bar{y}}\left(\bar{x},\bar{y},\bar{t}=0\right)=0 \tag{3.22a}$$

$$\bar{T}\left(\bar{x},\bar{y},\bar{t}=0\right)=0 \tag{3.22b}$$

with $\bar{u}_{\bar{x}}$ and $\bar{u}_{\bar{y}}$ representing the non-dimensional displacement components in the x and y directions, respectively.

The shock loading conditions are:

Loading 1: Pressure shock

$$\bar{P}\left(\bar{x}=-\bar{L}/2,\bar{y},\bar{t}\right)=5\bar{t}e^{-2\bar{t}} \tag{3.23a}$$

$$\bar{T}\left(\bar{x}=-\bar{L}/2,\bar{y},\bar{t}\right)=0 \tag{3.23b}$$

Loading 2: Thermal shock

$$\bar{P}\left(\bar{x}=-\bar{L}/2,\bar{y},\bar{t}\right)=0 \tag{3.24a}$$

$$\bar{T}\left(\bar{x}=-\bar{L}/2,\bar{y},\bar{t}\right)=5\bar{t}e^{-2\bar{t}} \tag{3.24b}$$

Loading 3: Combined pressure and thermal shock

$$\bar{P}\left(\bar{x}=-\bar{L}/2,\bar{y},\bar{t}\right)=5\bar{t}e^{-2\bar{t}} \tag{3.25a}$$

$$\bar{T}\left(\bar{x}=-\bar{L}/2,\bar{y},\bar{t}\right)=5\bar{t}e^{-2\bar{t}} \tag{3.25b}$$

where $\bar{t}$ represents the non-dimensional time. The applied pressure load is in the positive x direction, as illustrated in Fig. 3-2.

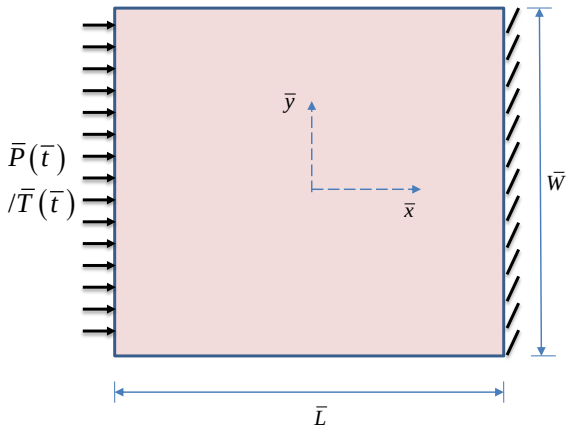

Fig. 3-2 A thin plate subjected to shock loading conditions

Fig. 3-3 to Fig. 3-5 provide the thermal and mechanical responses at $\bar{t} = 3$ and $\bar{t} = 6$ along the horizontal centreline of the plate for 3 different loading conditions. The coupling coefficient $\epsilon = 0$ represents the uncoupled case, where the effect of deformation on temperature field is ignored. Fig. 3-3(a) represents the temperature distribution when the plate is subjected to pure pressure shock loading (loading condition 1). As can be seen from the figure, when $\epsilon = 0$ no temperature change is observed. On the other hand, when $\epsilon = 0.1$ both temperature drop and temperature rise are observed, which are induced by the applied pressure shock due to coupling effect. The magnitude of the temperature change is relatively small, within the range between -0.02 to 0.05. As time progresses, the peak position of the temperature distribution moves towards a positive x direction. Fig. 3-3(b) represents the dimensionless axial displacement along the horizontal centreline at $\bar{t} = 3$ and $\bar{t} = 6$. The wave fronts at these two time points are observed. There are slight differences between the displacement predictions from the coupled and uncoupled cases. As time progresses, the difference becomes larger. Therefore, it could be inferred that due to coupling effect, the temperature change induced by deformation does affect the deformation. The same conclusion is obtained from the simulation cases with loading condition 2 as can be seen from Fig. 3-4. Due to the heating effect by the applied thermal loading, the plate experiences an expansion state. Subsequently, the tension loading creates a cooling effect. Therefore, when compared with the uncoupled case, the relatively lower temperature change is observed in the coupled case. Consequently, the lower temperature change gives rise to a smaller deformation response. This conclusion can also be applied to loading condition 3, whose results are presented in Fig. 3-5.

In conclusion, good agreements are obtained for three types of loadings. For both the thermal and mechanical fields, the results from ordinary state-based PD predictions agree well with those from BEM solutions obtained by Hosseini-Tehrani and Eslami [53]. Therefore, via these numerical simulations, the present non-dimensional PD model is validated for 2D problems.

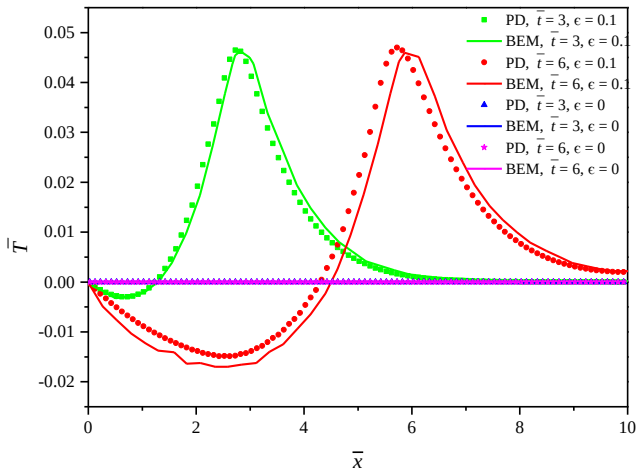

(a)

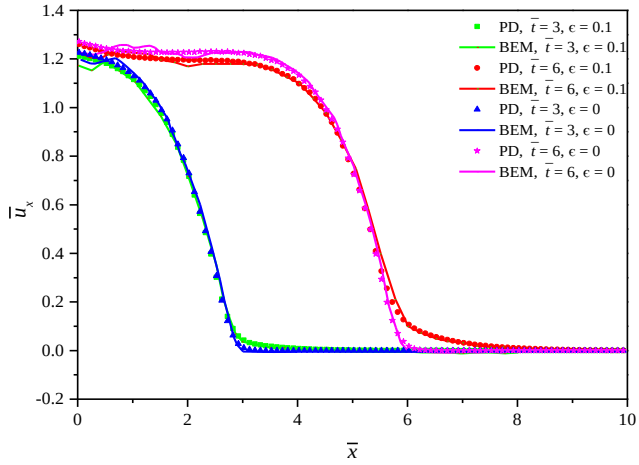

(b)

Fig. 3-3 Comparison of BEM method [53] and PD solutions (a) Temperature change distributions; (b) Displacements along the horizontal centreline of the plate for loading condition 1

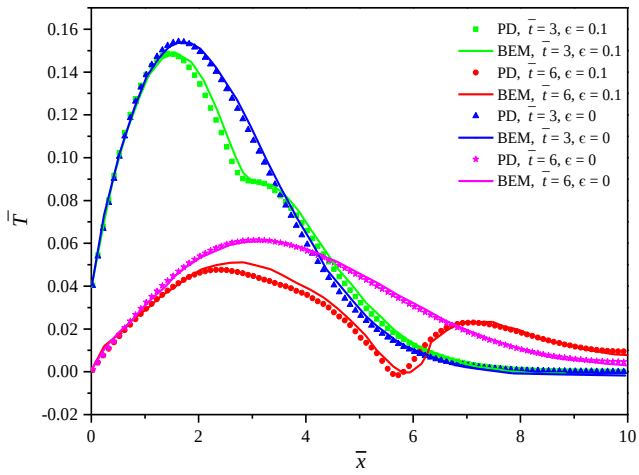

(a)

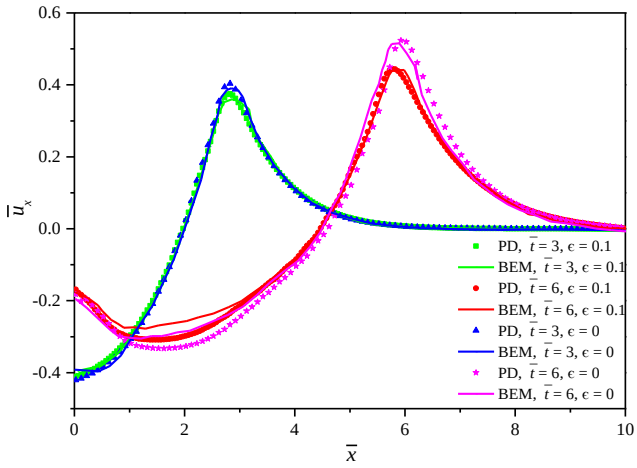

(b)

Fig. 3-4 Comparison of BEM method [53] and PD solutions (a) Temperature change distributions; (b) Displacements along the horizontal centreline of the plate for loading condition 2

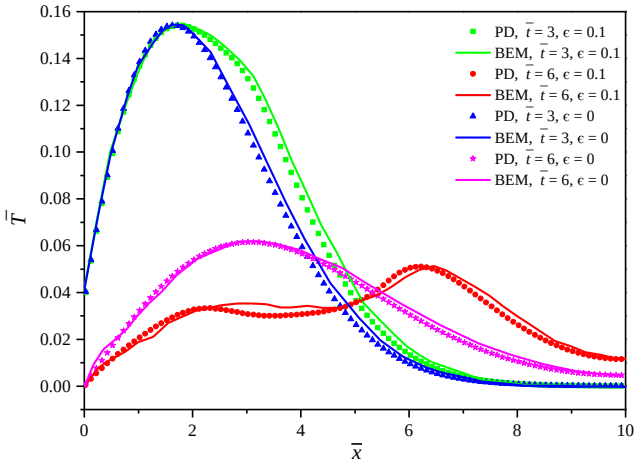

(a)

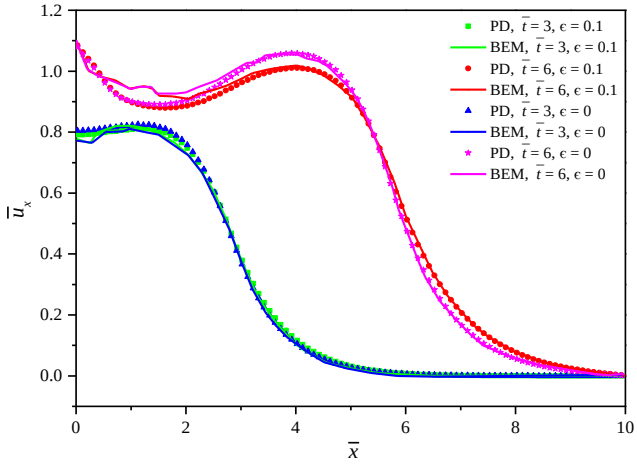

(b)

Fig. 3-5 Comparison of BEM method [53] and PD solutions (a) Temperature change distributions; (b) Displacements along the horizontal centreline of the plate for loading condition 3

3.5.2. Plate subjected to pressure loading

Thermal and deformation responses of a square plate under two types of pressure shocks are analysed. The geometry dimensions of the plate are $L = W = 0.1\,\mathrm{m}$, with the thickness being 0.001 m. The material is chosen as carbon steel and its material properties are given as: elastic modulus $E = 200\,\mathrm{GPa}$, Poisson's ratio $\nu = 0.17$, thermal expansion coefficient $\alpha = 11.5\times10^{-6}\ \mathrm{K}^{-1}$, density $\rho = 7870\,\mathrm{kg/m}^3$, specific heat capacity $c_v = 472\,\mathrm{J/(kgK)}$, and thermal conductivity $k_T = 51.9\,\mathrm{W/(mK)}$. The reference temperature is $\Theta_0 = 285\,\mathrm{K}$. The grid size is $\Delta x = 0.0005\,\mathrm{m}$ and the horizon size is chosen as $\delta = 3.015\Delta x$. The time step size is $0.001\,\mu\mathrm{s}$ with total simulation time $8\,\mu\mathrm{s}$. On the other hand, directly coupled plane element PLANE 223 is utilized in the ANSYS model. The number of nodes 80×80 and time step size is $0.16\,\mu\mathrm{s}$ for the ANSYS model.

The initial conditions are:

$$u_x(x, y, t=0) = u_y(x, y, t=0) = 0 \tag{3.26a}$$

$$T(x, y, t=0) = 0 \tag{3.26b}$$

The shock loading conditions are:

Loading 1:

$$P(x = -L/2, y, t) = -10^{20}t^2\ \mathrm{Pa} \tag{3.27}$$

Loading 2:

$$P(x = -L/2, y, t) = 10^9 \sin\left(\frac{\pi}{2}t\times10^6\right)\ \mathrm{Pa} \tag{3.28}$$

Fig. 3-6 and Fig. 3-7 provide the temperature and deformation responses along the horizontal centreline of the plate under two loading conditions. Since only the mechanical loadings are applied, the temperature changes are induced due to the coupling term in the heat flow equation. As shown in Fig. 3-6(a) and Fig. 3-7(a), there is a remarkable agreement between PD and ANSYS solutions. When the plate is subjected to loading condition 1, the temperature drop is observed due to tension loading as it can be seen from Fig. 3-6(a). As time progresses, temperature change increases to a final value of $6.5\,\mathrm{K}$. When the plate is subjected to loading condition 2, temperature increases where there is local compression, and temperature drops where there is local tension.

Under both loading conditions displacement fields obtained from PD and ANSYS simulations match very well. Furthermore, it should be noted that even though carbon steel has a relatively small coupling coefficient, i.e. $\epsilon = 0.002861$, the generated temperature change due to mechanical shock loading is considerable. Therefore, if a large strain rate exists, i.e. shock loading is applied, fully coupled thermomechanical analysis should be taken into consideration.

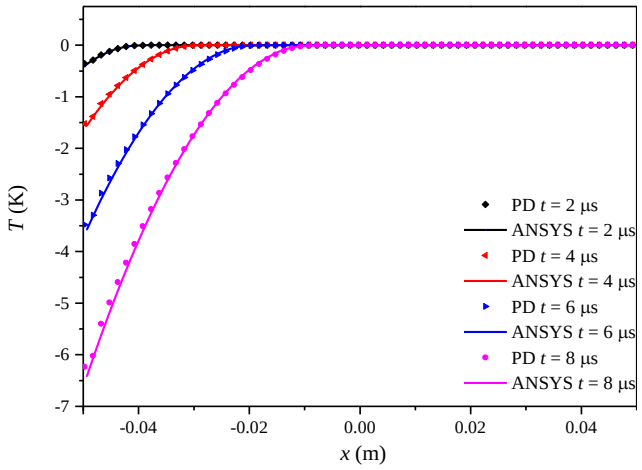

(a)

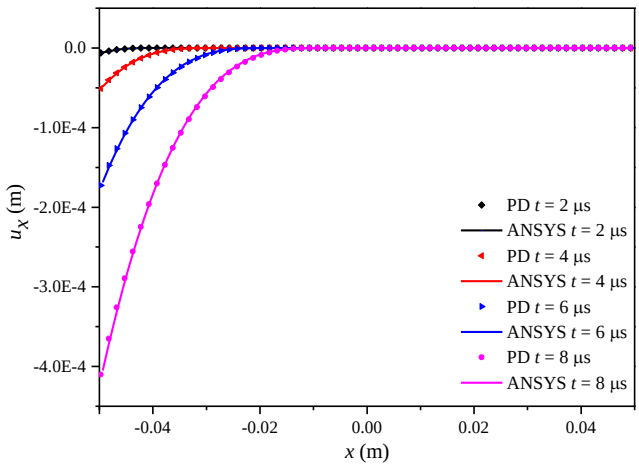

(b)

Fig. 3-6 Comparison of ANSYS and PD solutions (a) Temperature change distributions (b) Displacements along the horizontal centreline of the plate for loading condition 1

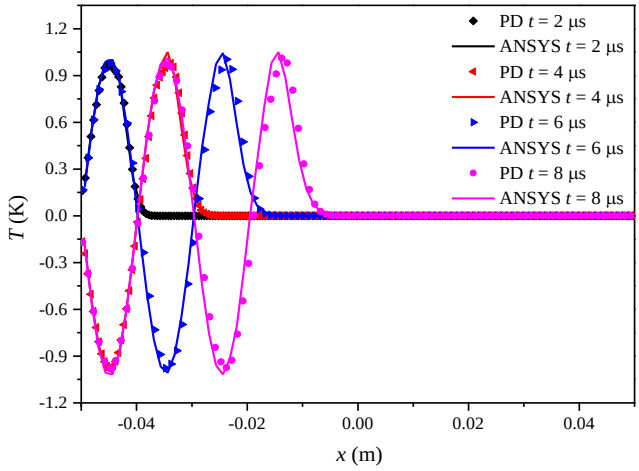

(a)

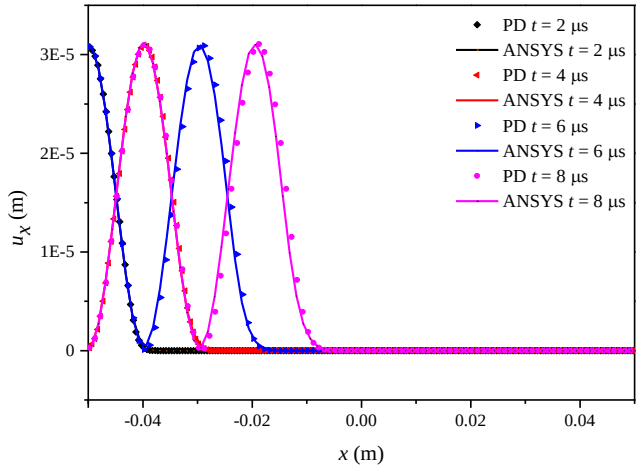

(b)

Fig. 3-7 Comparison of ANSYS and PD solutions (a) Temperature change distributions (b) Displacements along the horizontal centreline of the plate for loading condition 2.

3.5.3. Block subjected to thermal loading

In order to validate the proposed PD model for 3D problems, a block subjected to temperature boundary condition is investigated. As shown in Fig. 3-8, the dimensionless length, width and height of the block are 5, 0.15 and 0.15, respectively. The Poisson's ratio is set as 0.33 and the coupling coefficient is 1.0. Regarding the PD model, the grid size is $\Delta x = 0.0125$ and the horizon is chosen as $\delta = 3.015\Delta x$. The integration time step size is $\pi/4\times10^{-4}$ and the total simulation time is π. On the other hand, directly coupled solid element type SOLID 226 is adopted with a mesh size of 0.05 and time step size of 0.02π in ANSYS model.

The block is clamped at $x = \bar{L}$. The block is gradually heated at $x = 0$ and all other surfaces are insulated. The temperature boundary condition is defined as $\bar{T} = \sin(\bar{t})$, where $\bar{t}$ is the dimensionless time. A fictitious layer is used to implement boundary conditions [55].

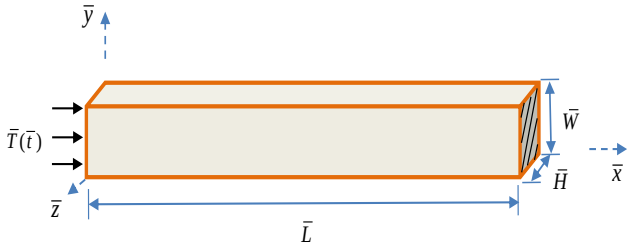

Fig. 3-8 Block under thermal loading

The temperature distributions and horizontal displacements along the line of $y = \bar{W}/2$ and $z = \bar{H}/2$ are presented in Fig. 3-9 (a) and (b) at dimensionless time of $\bar{t} = \pi/4, \pi/2, 3\pi/4, \pi$ respectively. The results which are obtained from ANSYS solutions are also provided for comparison. It could be seen that both the temperature and displacement distributions match very well, indicating the capability of the derived

PD formulations to accurately predict the thermal and mechanical responses for three-dimensional problems.

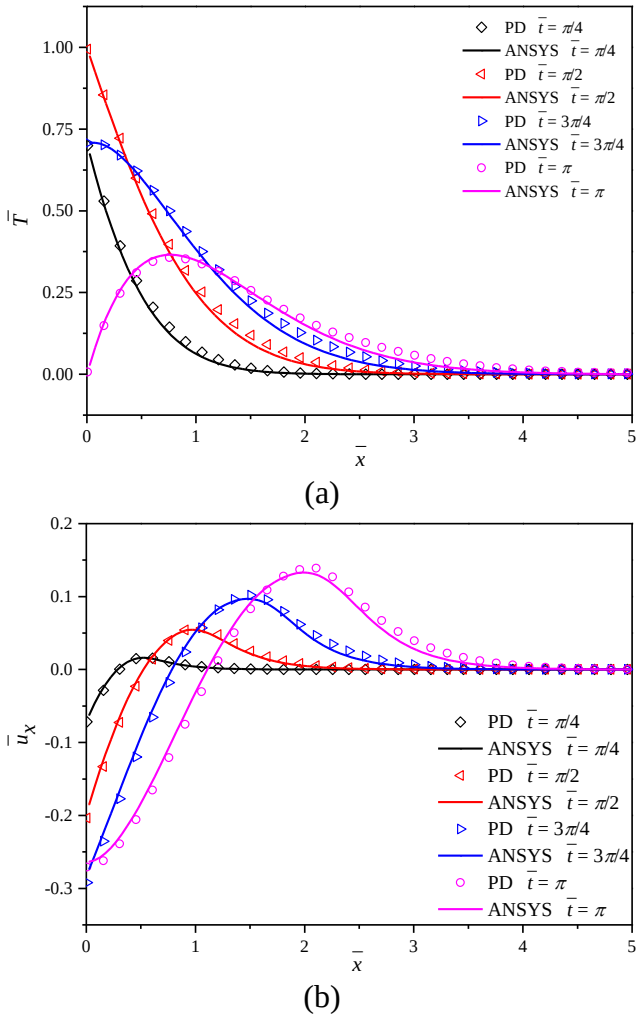

Fig. 3-9 Comparison of ANSYS and PD solutions (a) Temperature change distributions (b) Horizontal displacements along the centreline of the block

Derived formulations and explicit expressions of PD parameters including their dimensional and non-dimensional forms are validated through these numerical simulations.

3.6. Numerical results for damage prediction

Peridynamics is a reformulation of classical equations that is better suited for modelling bodies with discontinuities. The proposed model is further employed for failure prediction including fully coupled analysis. First, a three-point bending test is

considered to predict the temperature distribution and deformed shape. Then a plate with a pre-existing central crack is subjected to a pressure shock loading condition. The temperature and structural responses without crack propagation are verified against the ANSYS solution. Then the crack propagation is simulated, and its path is compared with the one from a pure mechanical simulation. In this way, the coupling term effect on crack propagation is estimated and analysed. Therefore, analysis involving cracks are considered in this section by using the developed PD model. Finally, a numerical simulation based on Kalthoff experiment [56] is carried out. The crack path predicted by the PD model is compared with the result of the experiment.

3.6.1. Three-point bending simulation

Three-point bending test of a simply supported beam is simulated under prescribed displacement condition as illustrated in Fig. 3-10. The origin of the coordinate system is located in the middle of the beam. The material properties are related to rubber-like material, the shear modulus is $1\,\text{MPa}$, Poisson's ratio $\nu = 0.45$, thermal expansion coefficient $\alpha = 1\times10^{-3}\,\text{K}^{-1}$, thermal conductivity $k_T = 0.1\,\text{W/(mK)}$, density $\rho = 906.5\,\text{kg/m}^3$, specific heat capacity $c_v = 1103.14\,\text{J/(kgK)}$ [57]. The critical stretch value is $s_c = 0.1724$. The reference temperature is $\Theta_0 = 293\,\text{K}$. The dimensions of the beam are $L = 40\,\text{mm}$, $W = 10\,\text{mm}$, and thickness $h = 0.5\,\text{mm}$. A pre-existing crack with length being $a = 1\,\text{mm}$ is located in the middle of the beam at $y = -W/2$. The supports are placed $b = 4\,\text{mm}$ inwards from the outer edges. A prescribed displacement is applied in the middle of the beam at $y = W/2$ as $u = (t/t_{total})u_{\max}$, where t_{total} is the total simulation time, $t_{total} = 0.01\,\text{s}$ and $u_{\max} = 6\,\text{mm}$. The uniform PD grid size is $\Delta x = 0.5\,\text{mm}$ and the horizon is $\delta = 3.015\Delta x$. The time step size is $1\times10^{-6}\,\text{s}$ and the total simulation time is $t_{total} = 0.01\,\text{s}$.

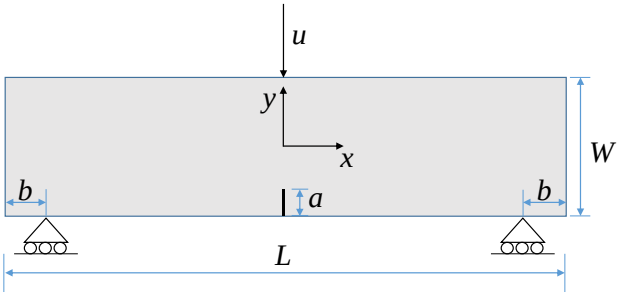

Fig. 3-10 Geometry of three-point bending test

Fig. 3-11 and Fig. 3-12 present the damage plots and corresponding temperature distributions at $t = 0.007\,\mathrm{s}$ and $t = 0.01\,\mathrm{s}$. It can be observed from Fig. 3-11 (a) and Fig. 3-12 (a) that the initial crack grows in the vertical direction. Fig. 3-11 (b) and Fig. 3-12 (b) present the corresponding temperature distributions. As expected, the temperature rise is observed where the local compression is expected and the temperature drop is observed near the crack surfaces where there is local tension.

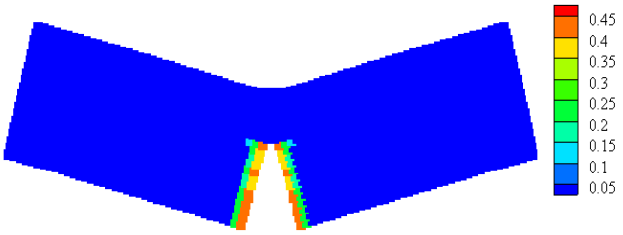

(a)

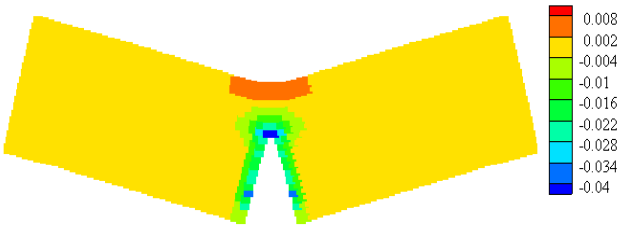

(b)

Fig. 3-11 (a) Damage plot and (b) temperature change (K) in deformed configuration at $t = 0.007\,\mathrm{s}$ (displacement scale factor is 1)

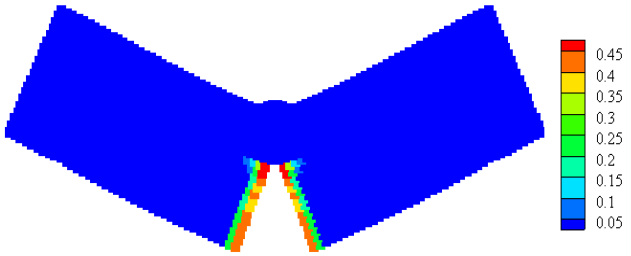

(a)

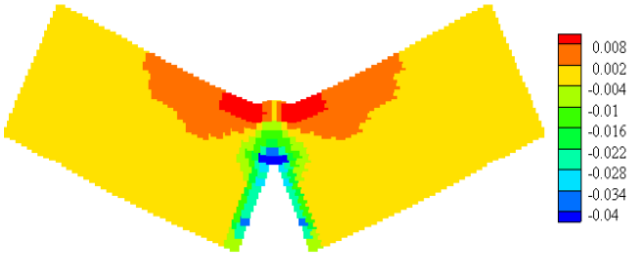

(b)

Fig. 3-12 (a) Damage plot and (b) temperature change (K) in deformed configuration at $t = 0.01\,\mathrm{s}$ (displacement scale factor is 1)

3.6.2. Plate with a crack subjected to pressure shock loading

Based on the previous example in Section 3.5.2, damage propagation is predicted for a plate with a pre-existing crack of length 0.02 m, as shown in Fig. 3-13. The geometry, material properties, and boundary condition are identical to those in Section 3.5.2.

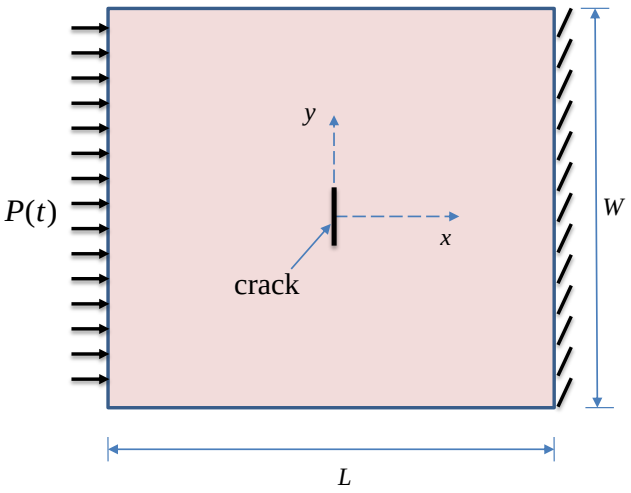

Fig. 3-13 An isotropic plate with a pre-existing central crack under pressure shock loading

The pressure shock loading is specified as

$$P(t)=\begin{cases}-1\times10^{14}t\ \left(\text{Pa}\right)\ , t<t_0\\ -1\times10^{14}t_0\ \left(\text{Pa}\right), t>t_0\end{cases} \tag{3.29}$$

where $t_0=8\,\mu\text{s}$. The total node number in x or y direction for the PD model is set to be 500 with a grid size of 0.2 mm. Thus the critical stretch value s_c is calculated as 0.0213 with G_c being $42320\ \text{J/m}^2$. The horizon is $\delta=3.015\Delta x$. The time step size is set as 10^{-9} s and the total simulation time is $30\ \mu\text{s}$. On the other hand, directly coupled plane element type PLANE223 is applied in the ANSYS model with the grid size of $\Delta x=0.00125$ and time step size of $0.6\,\mu\text{s}$.

In order to better understand the existence of crack surface on the temperature and deformation field, initial failure is not allowed. The horizontal displacement predictions at different time steps are shown in Fig. 3-14, Fig. 3-15, and Fig. 3-16. It is observed that the peridynamic results coincide very well with ANSYS solutions. The displacement distribution along x axis propagates uniformly in the vertical direction before the elastic wave reaches the crack, as shown in Fig. 3-14. After the elastic wave reaches the crack surface, displacements become non-uniform due to the

discontinuity of the displacements along the crack surface as it can be seen from Fig. 3-15 and Fig. 3-16.

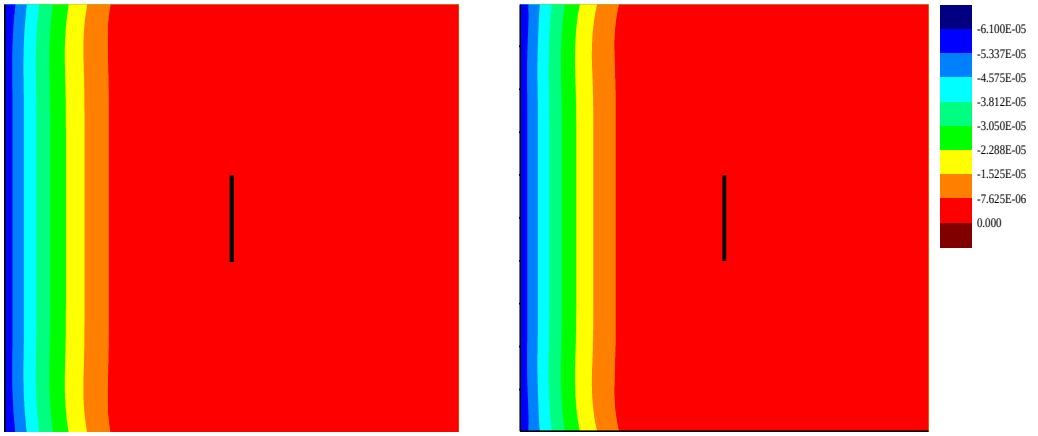

(a) (b)

Fig. 3-14 Horizontal displacements (m) (a) ANSYS and (b) PD results at $t = 7\,\mu s$

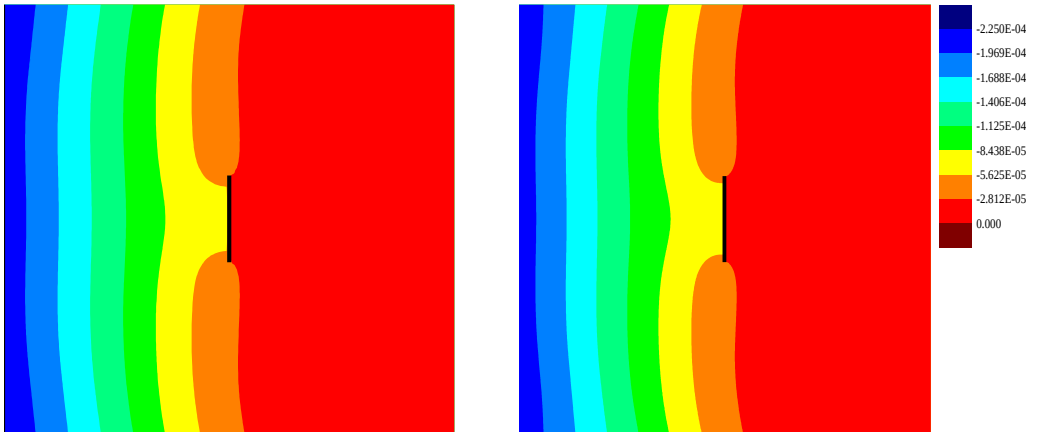

(a) (b)

Fig. 3-15 Horizontal displacements (m) (a) ANSYS and (b) PD results at $t = 15\,\mu s$

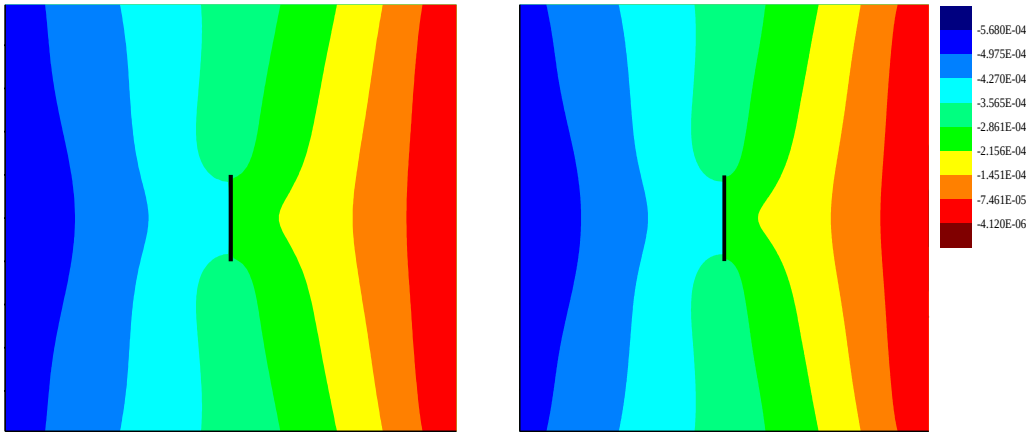

(a) (b)

Fig. 3-16 Horizontal displacements (m) (a) ANSYS and (b) PD results at $t = 30\,\mu s$

Fig. 3-17, Fig. 3-18, and Fig. 3-19 present the induced temperature distributions due to the applied loading. It is observed that the peridynamic results agree very well with ANSYS solutions. The temperature distributions along x axis propagate almost uniformly in the vertical direction before the thermal wave reaches the crack, as shown in Fig. 3-17. After the thermal wave reaches or passes the crack, thermal waves get disturbed by the existence of the crack. The higher temperature drop is observed near the crack tip as can be seen from Fig. 3-18 and Fig. 3-19. This also indicates the stress concentration near the crack tips. Besides, the region near the crack tips is under tension, indicating a tendency of a crack growing in the vertical direction. The crack surfaces experience local compression. Therefore, temperature rises are observed in these regions as it can be seen from Fig. 3-19.

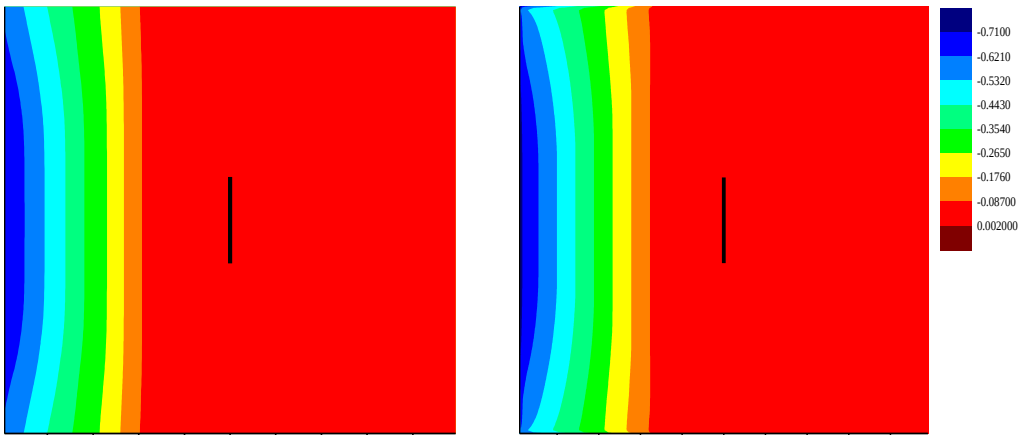

(a) (b)

Fig. 3-17 Temperature change distributions (K) (a) ANSYS and (b) PD results at $t = 7\ \mu s$

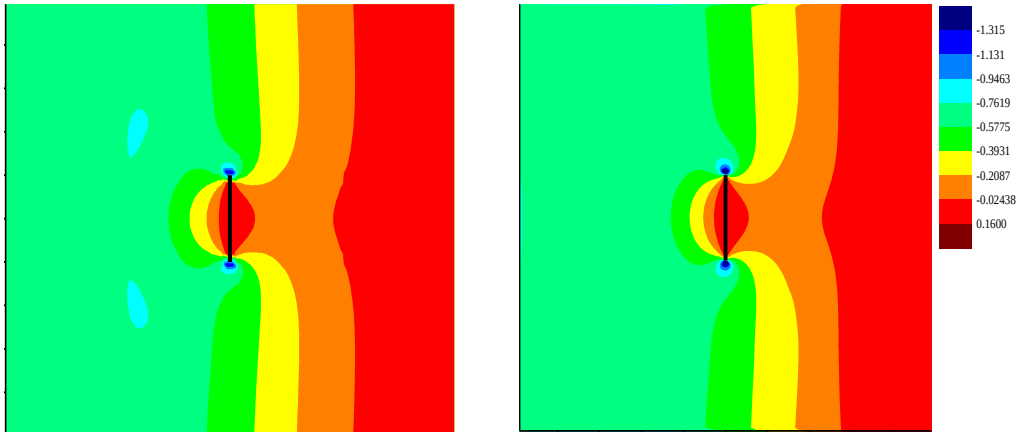

(a) (b)

Fig. 3-18 Temperature change distributions (K) (a) ANSYS and (b) PD results at $t = 15\ \mu s$

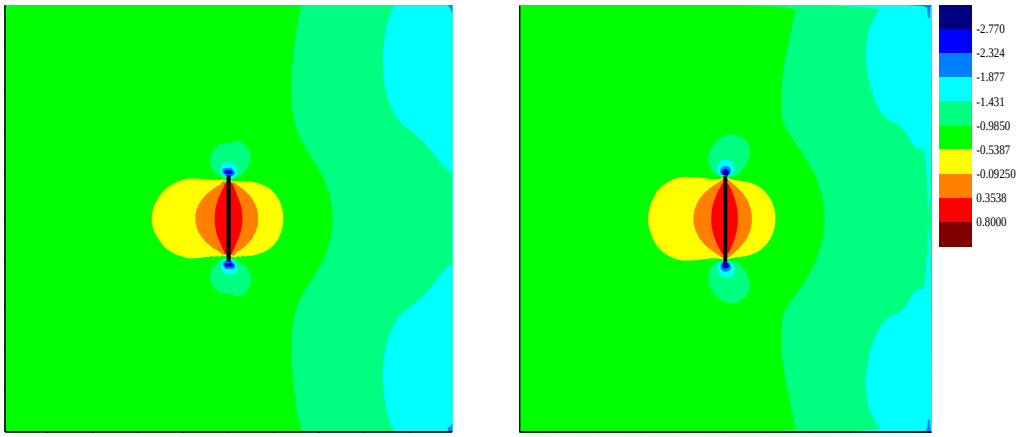

(a) (b)

Fig. 3-19 Temperature change distributions (K) (a) ANSYS and (b) PD results at $t = 30\ \mu s$

After verification of temperature and deformation field for a plate with a pre-existing crack. As a next example, crack propagation is allowed. The crack configurations at different time steps are provided in Fig. 3-20 to Fig. 3-22. Crack propagation patterns are compared with coupled and uncoupled cases. Temperature distributions at corresponding stages from coupled cases are also provided.

In the early stage, the cracks grow in similar patterns for both simulation cases. Crack start to propagate earlier for the uncoupled case (Fig. 3-20). Cracks both begin to propagate at around 16 μs . Up to 28 μs , the cracks propagate in a self-similar manner for both coupled and uncoupled cases. Cracks start branching at around 28 μs (Fig. 3-21) and split into visible asymmetrical branches (Fig. 3-22). Besides, the branches for uncoupled case grow faster than the coupled case.

For the coupled case, it is clear that before 16 μs the temperature distribution is the same as the one obtained from the simulation without crack propagation. However, temperature drops at the crack tips move as the crack propagates (Fig. 3-21 (c)- Fig. 3-22 (c)). The cooling region at the crack tips creates temperature-induced local compression at these regions. Furthermore, the temperature rise around the crack surfaces creates local tension against the compression created by the pressure shock loading. In conclusion, the induced temperature change due to deformation influences the crack growth in the opposite direction against the applied mechanical loading, leading to a reduced degree of crack propagation response. Hence, a different crack pattern from the uncoupled simulation is obtained.

In conclusion, if shock loadings are applied, large strain rates are created, and thus the coupling term should be considered for more accurate crack propagation predictions.

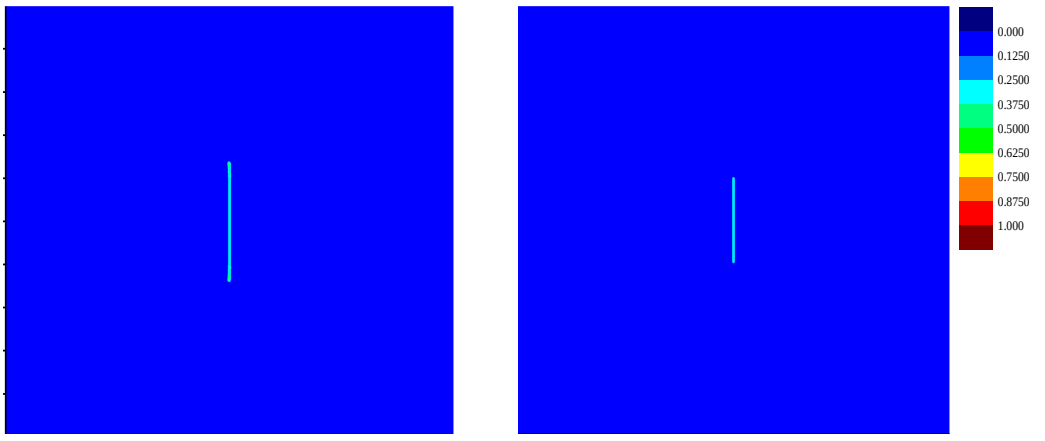

(a) (b)

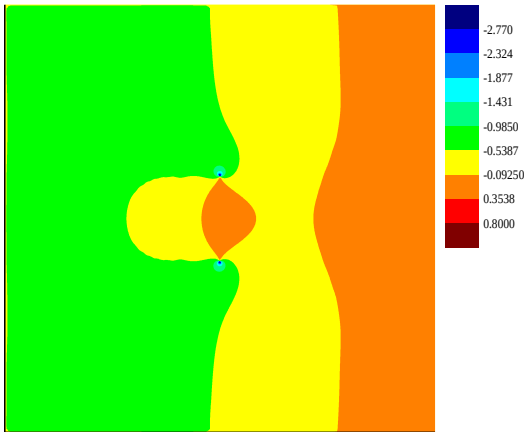

(c)

Fig. 3-20 Damage plots for (a) uncoupled case, (b) coupled case and (c) corresponding temperature change (K) distributions at $t = 16\,\mu s$

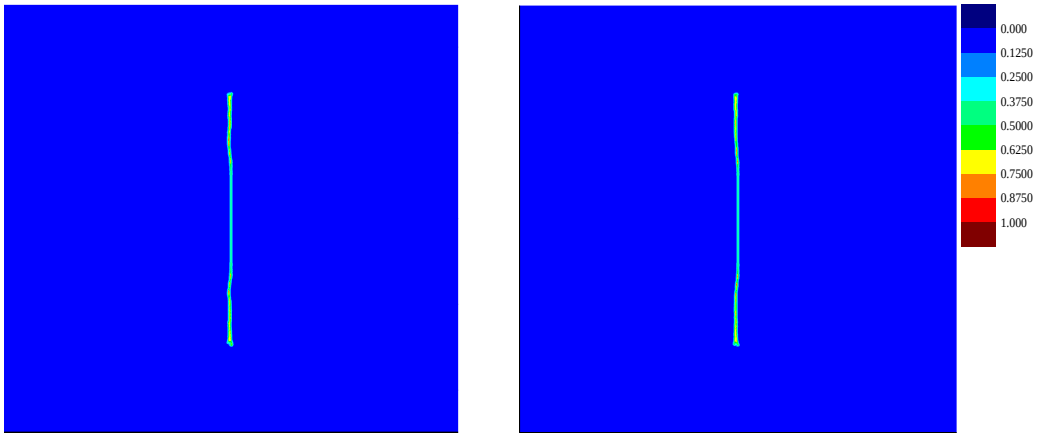

(a) (b)

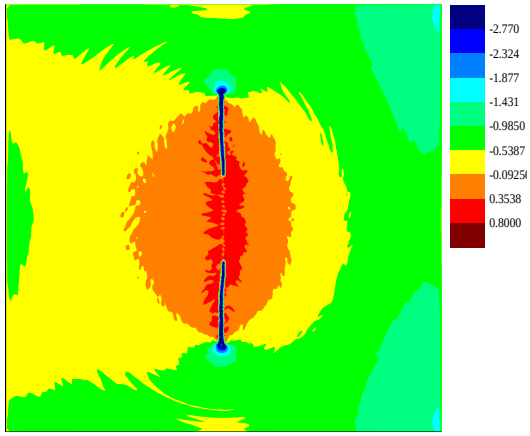

(c)

Fig. 3-21 Damage plots for (a) uncoupled case, (b) coupled case and (c) corresponding temperature change (K) distributions at $t = 28\,\mu s$

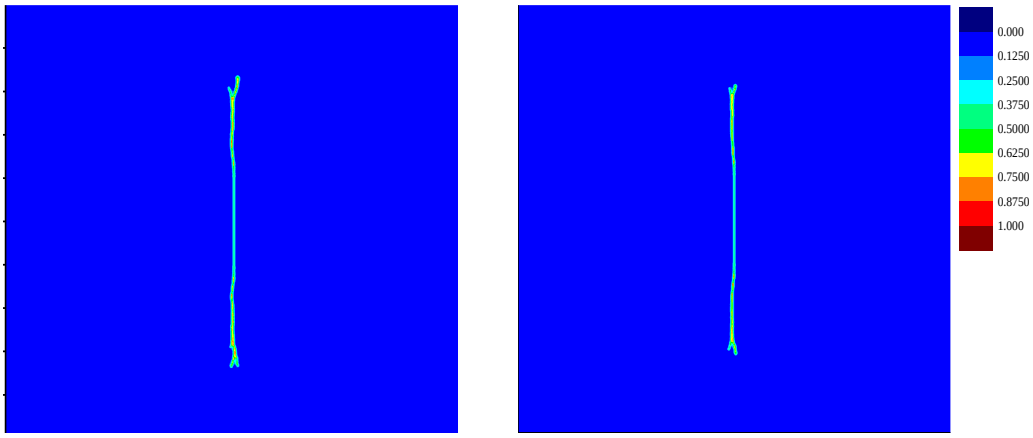

(a) (b)

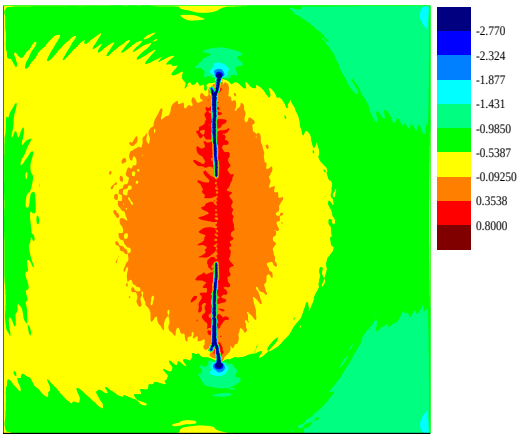

(c)

Fig. 3-22 Damage plots for (a) uncoupled case, (b) coupled case and (c) corresponding temperature change (K) distributions at $t = 30\,\mu s$

3.6.3. Kalthoff problem simulation

Kalthoff and Winkler [58] and Kalthoff [56, 59] performed a series of experiments where pre-notched plates were subjected to dynamic shear loads. In the experiments, a cylindrical projectile impacted on the notched side of the plate with a constant velocity $\mathbf{V}_0$ parallel to the axis of the notch. The pre-existing crack in the upper half steel plate was observed to grow in an angle of approximately 70^o counter-clockwise with the notch axis. The failure is in a brittle fracture mode under a lower strain rate. These experiments have been successfully simulated by numerical methods such as

phase-field simulation [60], finite element method [61]. In addition, Silling [62] and Dipasquale et al. [63] used PD to numerically simulate the Kalthoff problem within the realm of the mechanical field. In this section, a fully coupled thermomechanical simulation is conducted based on the Kalthoff experiment.

The problem is symmetric so that only the upper half plate is modelled. As shown in Fig. 3-23, a square plate is modelled with $L = W = 100\,\text{mm}$ and its thickness is $1\,\text{mm}$. A pre-existing crack of length being $50\,\text{mm}$ is located above the x axis with the distance of $25\,\text{mm}$. Due to the symmetric conditions, the lower horizontal edge of the plate is fixed in the y direction, i.e. $u_y\left(x, y = 0, t\right) = 0$. The other boundaries are free. All the boundaries are thermally insulated. The impact is simulated by imposing a constant velocity to the nodes on the left surface between the crack and the lower horizontal boundary in the PD model. The velocity is parallel to the x direction and its magnitude is

$$\left|\mathbf{v}_0\right| = \begin{cases} \left(t/t_0\right) v_0 & t \le t_0 \\ v_0 & t > t_0 \end{cases} \tag{3.30}$$

where $\left|\mathbf{v}_0\right|$ represent the magnitude of the applied velocity with $v_0 = 16.5\,\text{m/s}$ and $t_0 = 1\,\mu\text{s}$ [60]. The properties of the elastic material are $E = 190\,\text{GPa}$, $\rho = 8000\,\text{kg/m}^3$, $\nu = 0.3$, $c_v = 477\,\text{J/}\left(\text{kgK}\right)$, $\alpha = 17.6\times10^{-6}\,\text{K}^{-1}$, $k_T = 16.2\,\text{W/}\left(\text{mK}\right)$. The critical energy release rate is $G_c = 2.213\times10^4\,\text{J/m}^2$. The reference temperature is $\Theta_0 = 285\,\text{K}$. As to the PD discretization, the mesh size is $\Delta x = 0.0005\,\text{m}$ and the horizon is chosen as $\delta = 3.015\Delta x$. The time step size is $0.01\,\mu\text{s}$ and the total simulation time is $90\,\mu\text{s}$. The critical stretch value is calculated as $s_c = 0.0103$.

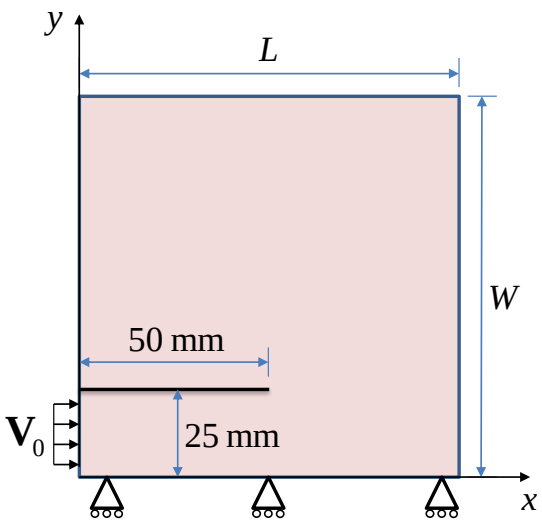

Fig. 3-23 The geometry and boundary conditions for Kalthoff problem

The crack is observed to propagate at $t = 20\,\mu s$. The crack evolution at different times is provided in Fig. 3-24. The angle between the crack path and the positive x direction is observed to be 68^{o}, which is close to the corresponding result of the Kalthoff experiment. Furthermore, the temperature change distribution evolutions are provided in Fig. 3-25. The maximum stretch distributions in deformed configurations are presented in Fig. 3-26. It can be observed temperature rises near the crack and temperature drops in the crack, which agrees with the conclusions drawn in the last two simulation cases.

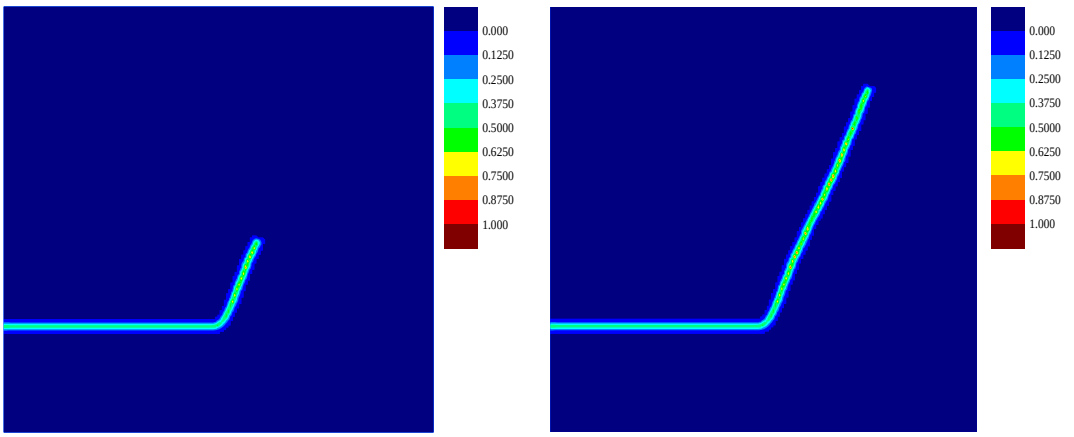

(a) (b)

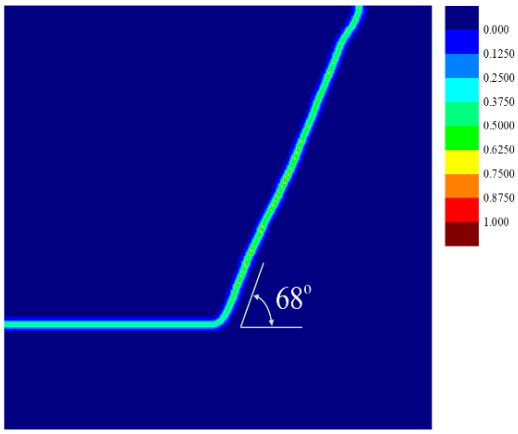

(c)

Fig. 3-24 Crack evolution at different times, (a) $t = 40\ \mu s$; (b) $t = 65\ \mu s$;(c) $t = 90\ \mu s$

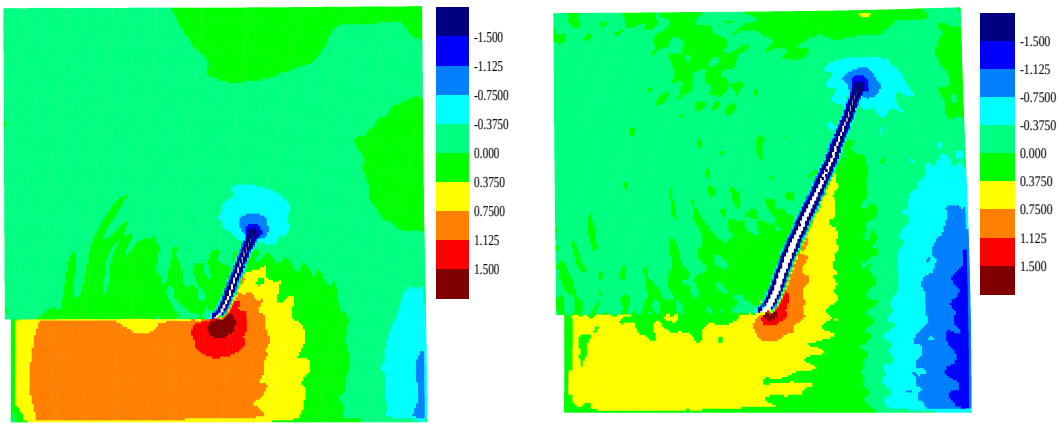

(a) (b)

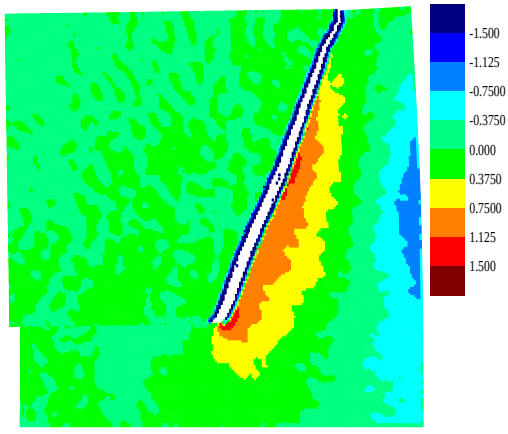

(c)

Fig. 3-25 Temperature change (K) distributions at different times (displacement scale factor is 3), (a) $t = 40\ \mu s$; (b) $t = 65\ \mu s$;(c) $t = 90\ \mu s$.

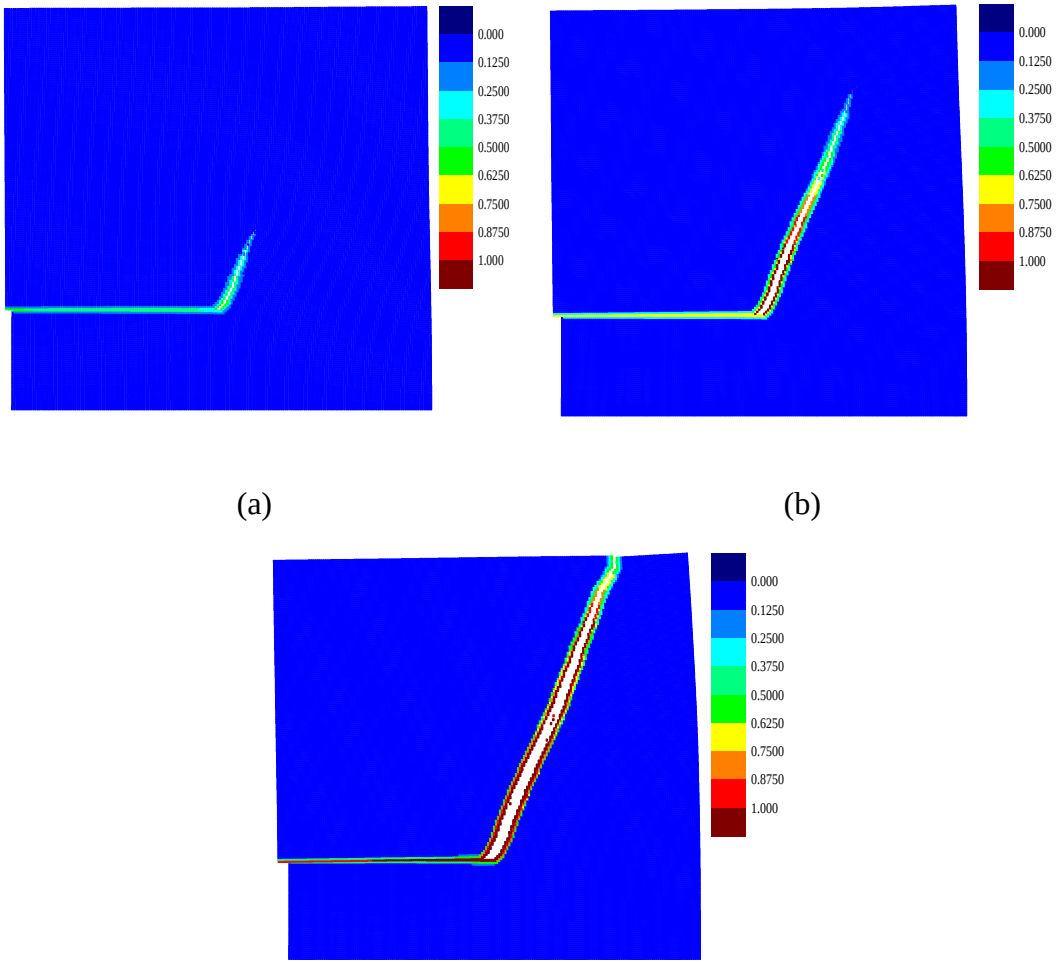

Fig. 3-26 Maximum stretch distributions in deformed configurations (displacement scale factor is 3) at different times, (a) $t = 40\,\mu s$; (b) $t = 65\,\mu s$; (c) $t = 90\,\mu s$.

3.7. Summary

In this chapter, fully coupled thermoelastic equations in ordinary state-based peridynamic theory are provided, including their non-dimensional forms. To verify the PD model, some benchmark problems are solved by using both peridynamics and FEM solutions. The good agreement between PD and other methods indicates the validity of the proposed PD model. Finally, crack propagation patterns are predicted for three-point bending test, Kalthoff problem, and a plate with a pre-existing crack subjected to a pressure load. The following conclusions are drawn:

1. The ordinary state-based fully coupled thermomechanical PD model introduced in this chapter is capable of predicting temperature and displacement responses accurately both for dimensional and non-dimensional problems.

2. When shock loadings are applied, the coupling effect on displacements and temperature should be taken into consideration for more accurate results.

3. The coupling terms do have an effect on crack propagation when shock loadings are applied. Therefore, fully coupled analysis is necessary in such cases.

4. Fully Coupled Thermomechanical PD Model for Composites Material

4.1. Introduction

In recent years, high-performance composite materials like fibre-reinforced composites (FRCs) and carbon-carbon composites (CCCs) are increasingly used in aerospace and mechanical industries, especially for the working environments with mechanical shocks and large temperature variations [64]. The analyses of this type of problems have been carried out in the past using the uncoupled or semi-coupled thermoelasticity theory. It is assumed that the deformation induces relatively small temperature changes, and hence can be conveniently neglected. Only the effect of the temperature on the deformation field is considered. However, the coupling coefficient of composites is much larger than the metal materials. Furthermore, the coupling effect on temperature is significant under the loading conditions like a sudden change of temperature or a mechanical shock. Therefore, the deformation effect on the temperature field is crucial in these cases. The uncoupled or semi-coupled analysis may not be accurate enough, and the employment of the fully coupled thermoelasticity theory is necessary in these cases [65].

Many research achievements in the realm of fully coupled thermoelasticity are presented in the literature regarding composite materials. This problem becomes complex because of the anisotropic property of composite materials. Stanley [66] presented an experiment to test the thermoelastic constants of composite materials under compressive loading. Basic equations of linear thermoelasticity of composite material were established in Ene's work [67]. Besides, a simple form of coupling constant was introduced to estimate the coupling effect for composite materials. In addition to the analytical and experimental methods, numerical methods are also popular in this field. Rao and Sinha [68] dealt with the coupled thermomechanical analysis of composites beams using FEM, presenting different results from uncoupled analyses. Moreover, the coupled thermoelastic response of a composite plate subjected to thermal shock was studied by Mukherjee and Sinha [69] using FEM. Khan et al. [70] compared the temperature profiles from different FE models in the

thermomechanical analysis of composites. Comparatively, boundary element method (BEM) was adopted by Kögl and Gaul [71] to investigate the coupling effect of composites. They stated that when linear elements were used, the BEM had an improved accuracy than FEM. Fully coupled thermomechanical analyses of one layer or equivalent single-layer plate were given by Brischetto and Carrera [72], providing a wise approach for multi-layered composites.

In addition to thermoelasticity, failure analysis is also a hot topic in composite research. It is a challenging task to predict damage in composites. Composites can be defined as two or more materials combined to form a single material [73]. There are several kinds of failure exist in laminated composites materials, e.g. fibre/matrix debonding damage, fibre breakage in tension, as well as fibre bulking in compression, interlaminar delamination, and penetration due to impact [74]. Therefore, the inhomogeneous nature of composites must be taken into consideration in the analysis, to predict the corresponding failure modes. Furthermore, the stacking sequence and thickness also have an important effect on the failure initiation and evolution [75]. Although many mathematical models and computational methods have been developed to predict these failure mechanisms, a high challenge still exist because of the adoption of continuum damage mechanics. Being different from the aforementioned numerical methods, i.e. BEM and FEM, peridynamic (PD) theory is a new numerical method based on non-local continuum theory. Therefore, the PD theory is suitable for simulating cracks for composite materials. Oterkus and Madenci [76-78] successfully applied the bond-based PD theory for composite materials. Kilic et al. [79] predicted the crack propagation in centre-cracked composites laminates using a bond-based PD theory. Although bond-based PD theory has been successfully employed in analysing composite materials, the material property is limited to having a fixed Poisson's ratio [4]. Additionally, the major shear stiffness G_{12} of a lamina is also forced to be a fixed value related to the elastic modulus in fibre direction and transverse direction [80]. Consequently, if bond-based peridynamic theory is utilized in analysing fibre reinforced composite lamina, four independent material constants $\left(E_1, E_2, G_{12}, \nu_{12}\right)$ will reduce to two independent constants $\left(E_1, E_2\right)$ [80]. On the other hand, state-based peridynamic theory [11] which eliminates these limitations.

Although various formulations are available for state-based PD composites modelling, most of them are limited to mechanical analysis. Oterkus and Madenci [46] provided a fully coupled analysis of a fibre-reinforced lamina. And then the model was extended to multi-layer laminates by Gao and Oterkus [7]. But the bond-based peridynamic theory is used for both models. To the authors' knowledge, fully coupled formulas and analyses for laminates are currently not available in ordinary state-based peridynamic framework.

To address this concern, the focus of this chapter is on fully coupled analysis of composite materials with ordinary state-based peridynamic theory. Oterkus et al. [39] derived the heat conduction equation with ordinary state-based peridynamic theory. Moreover, fully coupled thermomechanical equations for isotopic materials were proposed by Oterkus et al. [43] using bond-based peridynamic theory and extended to ordinary state-based peridynamic form by Gao and Oterkus [5]. Based on the previous work, in this chapter, both thermal and deformation fields are derived using ordinary state-based peridynamic theory. The directional dependency of composite material properties, as well as the coupling effect on temperature, is taken into account. Then the fully coupled thermomechanical numerical simulations are presented in Section 4.2. Subsequently, the validation cases are conducted in Section 4.3. Furthermore, the bond-based fully coupled thermomechanical PD model is applied to simulate the damage of composites under underwater explosion in Section 4.4.

4.2. PD composite model

Regarding the fully coupled thermomechanical problems, the PD formulations are derived based on irreversible thermodynamics, i.e. the conservation of energy and the free energy density function. The general form of the fully coupled thermomechanical equations based on peridynamic theory is given in [43-46, 48] and Chapter 3. However, the fully coupled thermomechanical composite model in ordinary state-based PD framework has not been established so far. The following section represents the derivation of fully coupled thermomechanical formulations for ordinary state-based peridynamics for composites by taking into account their directional properties.

4.2.1. Single-layer PD composite model

In this section, fully coupled ordinary state-based peridynamic single layer composite (lamina) model is developed in which the orthotropic property of lamina is taken into consideration. As shown in Fig. 4-1, it is presumed that the PD bonds are divided into three types according to their bond directions: fibre direction denoted by F, transverse direction denoted by T, and arbitrary direction denoted by FT [10, 80, 81]. Besides, the fibre angle is denoted by Φ. The bond angle with respect to the positive x direction is denoted by φ.

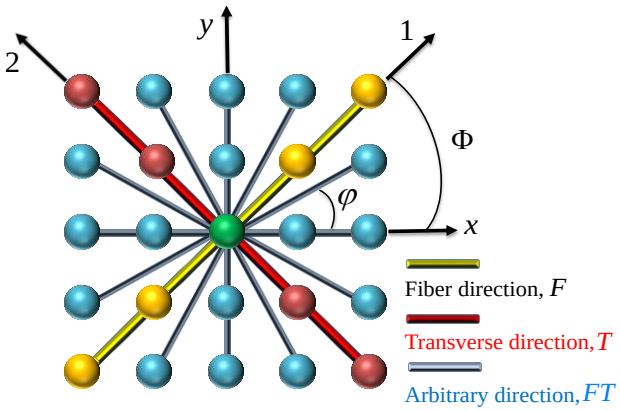

Fig. 4-1 Interaction of a family of material points for a fibre-reinforced lamina.

PD force density function provided in [10, 82] is modified by including the thermal effects as;

$$\mathbf{t}\left(\mathbf{u}_j-\mathbf{u}_i,\mathbf{x}_j-\mathbf{x}_i,t\right)=2\delta\left[\begin{array}{l}\dfrac{d\Lambda_{ij}}{\left|\mathbf{x}_j-\mathbf{x}_i\right|}a\left(\theta_i-\left(\alpha_1+\alpha_2\right)T_i\right)\\+\left(\mu_F b_F\left(\mathbf{x}_i\right)+\mu_T b_T\left(\mathbf{x}_i\right)+b_{FT}\right)\left(s_{ij}-\alpha_\varphi T_i\right)\end{array}\right]\frac{\mathbf{y}_j-\mathbf{y}_i}{\left|\mathbf{y}_j-\mathbf{y}_i\right|} \quad (4.1a)$$

and

$$\mathbf{t}\left(\mathbf{u}_i-\mathbf{u}_j,\mathbf{x}_i-\mathbf{x}_j,t\right)=-2\delta\left[\left[\begin{array}{l}\dfrac{d\Lambda_{ij}}{\left|\mathbf{x}_j-\mathbf{x}_i\right|}a\left(\theta_j-\left(\alpha_1+\alpha_2\right)T_j\right)\\+\left(\mu_F b_F\left(\mathbf{x}_j\right)+\mu_T b_T\left(\mathbf{x}_j\right)+b_{FT}\right)\left(s_{ji}-\alpha_\varphi T_j\right)\end{array}\right]\right]\frac{\mathbf{y}_j-\mathbf{y}_i}{\left|\mathbf{y}_j-\mathbf{y}_i\right|} \quad (4.1b)$$

where

$$\mu_F = \begin{cases} 1 & \left(\mathbf{x}_j - \mathbf{x}_i\right) /\!/ \text{ fibre direction} \\ 0 & \text{otherwise} \end{cases} \tag{4.2a}$$

with

$$\mu_T = \begin{cases} 1 & \left(\mathbf{x}_j - \mathbf{x}_i\right) \perp \text{ fibre direction} \\ 0 & \text{otherwise} \end{cases} \tag{4.2b}$$

In Eq.(4.1), α_1 and α_2 represent the thermal expansion coefficients in fibre and transverse direction, respectively. Thereby, α_φ represents the thermal expansion coefficient in any direction as [76]

$$\alpha_\varphi = \alpha_x \cos^2\left(\varphi\right) + \alpha_y \sin^2\left(\varphi\right) + \alpha_{xy} \sin\left(\varphi\right)\cos\left(\varphi\right) \tag{4.3}$$

with [83]

$$\alpha_x = \alpha_1 \cos^2\left(\Phi\right) + \alpha_2 \sin^2\left(\Phi\right) \tag{4.4a}$$

$$\alpha_y = \alpha_1 \sin^2\left(\Phi\right) + \alpha_2 \cos^2\left(\Phi\right) \tag{4.4b}$$

In Eq.(4.1), θ_i and θ_j are the dilatations of point i and j, respectively [10, 80]. The dilatation for a single layer PD model is also modified by including the thermal effects as

$$\theta_i = d\delta \sum_{j=1}^{N_{ply}} \left(s_{ij} - \alpha_\varphi T_i\right) \Lambda_{ij} V_j + \left(\alpha_1 + \alpha_2\right) T_i \tag{4.5}$$

with $d = \dfrac{2}{\pi h_{thick} \delta^3}$ and N_{ply} representing the total number of the family members within the same layer. The parameters s_{ij} and Λ_{ij} [10, 80] are defined in Eq.(2.7) and (2.9d).

In Eq.(4.1), the peridynamic parameters b_F , b_T and b_{FT} are associated with deformation of collective points in the fibre, transverse and other directions, respectively. The peridynamic parameters in Eq.(4.1) are defined as [10]:

$$a = \frac{1}{2}\left(Q_{12} - Q_{66}\right) \tag{4.6a}$$

$$b_{FT} = \frac{6Q_{66}}{\pi h_{thick}\delta^4} \tag{4.6b}$$

$$b_F\left(\mathbf{x}_i\right) = \frac{\left(Q_{11} - Q_{12} - 2Q_{66}\right)}{2\delta\sum_{j=1}^{N_F}\left|\mathbf{x}_j - \mathbf{x}_i\right|V_j} \tag{4.6c}$$

$$b_T\left(\mathbf{x}_i\right) = \frac{\left(Q_{22} - Q_{12} - 2Q_{66}\right)}{2\delta\sum_{j=1}^{N_T}\left|\mathbf{x}_j - \mathbf{x}_i\right|V_j} \tag{4.6d}$$

where N_F , N_T are the total number of bonds in the fibre and transverse direction respectively (Fig. 4-1). The reduced stiffness matrix, $[Q]$, is defined as [1]

$$[Q] = \begin{bmatrix} Q_{11} & Q_{12} & 0 \\ Q_{21} & Q_{22} & 0 \\ 0 & 0 & Q_{66} \end{bmatrix} \tag{4.7}$$

with

$$Q_{11} = \frac{E_1}{1-\nu_{12}\nu_{21}}, Q_{22} = \frac{E_2}{1-\nu_{12}\nu_{21}}, Q_{12} = \frac{\nu_{12}E_2}{1-\nu_{12}\nu_{21}}, Q_{66} = G_{12} \tag{4.8}$$

In Eq. (4.8), E_1 , E_2 , G_{12} , ν_{12} and ν_{21} represent the elastic modulus in the fibre direction, the elastic modulus in the transverse direction, major shear modulus, major Poisson's ratio and minor Poisson's ratio, respectively.

Similarly, the directional dependency properties are also taken into consideration in the heat equation given in Eq.(3.1). Therefore, thermal micro conductivity proposed by Oterkus and Madenci [46] for a lamina is adopted as

$$\kappa = \begin{cases} \kappa_f + \kappa_m & \text{for fibre direction} \\ \kappa_m & \text{otherwise.} \end{cases} \tag{4.9}$$

where κ_m and κ_f represent the peridynamic micro conductivities for fibre and other directions as [46]

$$\kappa_m = \frac{6k_2}{\pi h_{thick} \delta^3} \tag{4.10}$$

and

$$\kappa_f\left(\mathbf{x}_i\right) = \frac{2\left(k_1 - k_2\right)}{\sum_{j=1}^{N_F} \left|\mathbf{x}_j - \mathbf{x}_i\right| V_j} \tag{4.11}$$

In Eq. (4.10) and Eq.(4.11), k_1 and k_2 represent the thermal conductivities in CCM for fibre and transverse direction.

PD thermal moduli in fibre and other directions are defined as (derivation process is provided in Appendix B)

$$\beta = \begin{cases} \beta_f + \beta_m & \text{for fibre direction} \\ \beta_m & \text{otherwise.} \end{cases} \tag{4.12}$$

with

$$\beta_m = \frac{3\left(Q_{12}\alpha_1 + Q_{22}\alpha_2\right)}{\pi h_{thick} \delta^3} \tag{4.13}$$

and

$$\beta_f\left(\mathbf{x}_i\right)=\frac{\left(Q_{11}\alpha_1+Q_{12}\alpha_2\right)-\left(Q_{12}\alpha_1+Q_{22}\alpha_2\right)}{\sum_{j=1}^{N_F}\left|\mathbf{x}_j-\mathbf{x}_i\right|V_j} \tag{4.14}$$

As a summary, the ordinary state-based PD formulation for a single layer is given as;

$$\begin{aligned}\rho\ddot{\mathbf{u}}(\mathbf{x}_i,t)=\sum_{j=1}^{N_{ply}}2\delta&\left[\begin{array}{l}\dfrac{d\Lambda_{ij}}{\left|\mathbf{x}_j-\mathbf{x}_i\right|}a\left(\theta_i+\theta_j-\left(\alpha_1+\alpha_2\right)\left(T_i+T_j\right)\right)\\+\left(\mu_F b_F\left(\mathbf{x}_i\right)+\mu_T b_T\left(\mathbf{x}_i\right)+b_{FT}\right)\left(s_{ij}-\alpha_\varphi T_i\right)\\+\left(\mu_F b_F\left(\mathbf{x}_j\right)+\mu_T b_T\left(\mathbf{x}_j\right)+b_{FT}\right)\left(s_{ji}-\alpha_\varphi T_j\right)\end{array}\right]\frac{\mathbf{y}_j-\mathbf{y}_i}{\left|\mathbf{y}_j-\mathbf{y}_i\right|}V_j\\&+\mathbf{b}(\mathbf{x}_i,t)\end{aligned} \tag{4.15}$$

$$\rho c_v\dot{T}(\mathbf{x}_i,t)=\sum_{j=1}^{N_{ply}}\left[\begin{array}{l}\left(\mu_F\kappa_f\left(\mathbf{x}_i\right)+\kappa_m\right)\dfrac{\Theta_j-\Theta_i}{\left|\mathbf{x}_j-\mathbf{x}_i\right|}\\-\Theta_0\left(\mu_F\beta_f\left(\mathbf{x}_i\right)+\beta_m\right)\dot{e}\left(\mathbf{x}_j-\mathbf{x}_i\right)\end{array}\right]V_j+\rho q_b(\mathbf{x}_i,t) \tag{4.16}$$

Here Θ_j and Θ_k represent the temperatures at point j and k, respectively.

4.2.2. Multi-layer PD composite model

The PD mechanical model developed by Oterkus and Madenci [10, 76] for composite laminates is adopted in this subsection. As illustrated in Fig. 4-2, each ply in a laminate is modelled by one-layer PD nodes (shown in blue, red, and yellow colour for different plies). The multi-layer laminate is modelled by assembling the single-layer models according to the stacking sequence. Due to the directionally dependent properties of the laminate, four kinds of PD bonds are defined in the model: in-plane fibre bonds, in-plane matrix bonds, interlayer normal bonds, and interlayer shear bonds [10, 76]. Additional bonds, also called interlayer bonds, are added to connect points between neighbouring plies. The in-plane bonds have already been discussed in the single-layer model, so only the latter two bonds belonging to interlayer bonds will be explained in this section. The grid size is represented by Δx.

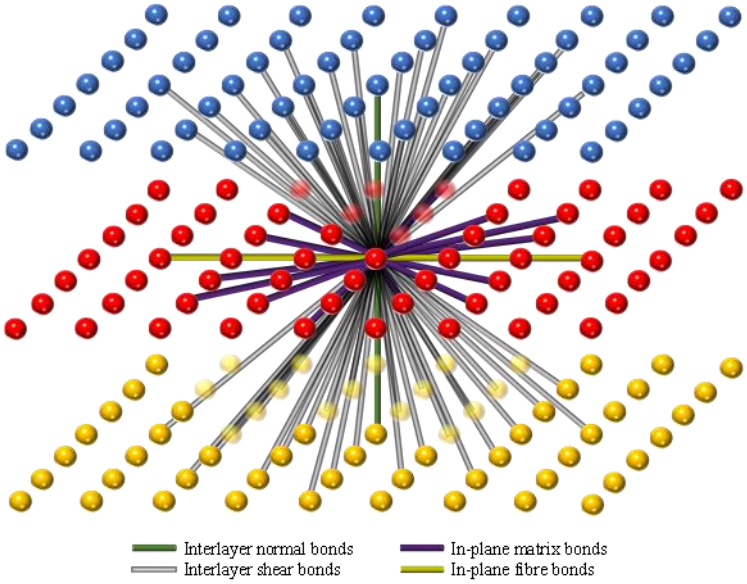

Fig. 4-2 Illustration of PD laminate model for $\delta = 3\Delta x$ and fibre direction, $\Phi = 0$.

As illustrated in Fig. 4-2, the equation of motion for material point k in n^{th} ply can be expressed as [10]

$$\rho\ddot{\mathbf{u}}_k^n = \sum_{j=1}^{N_{ply}} \left(\mathbf{t}_{kj}^n - \mathbf{t}_{jk}^n \right) V_j^n + \sum_{m=n+1,n-1} \mathbf{P}_k^{nm} V_k^m + 2 \sum_{m=n+1,n-1} \sum_{j=1}^{N_{shear}} \mathbf{q}_{kj}^{nm} V_j^m + \mathbf{b}_k^n \qquad (4.17)$$

where $\mathbf{P}_k^{nm}$ represents the PD force density vector due to transverse normal bond and $\mathbf{q}_{kj}^{nm}$ is the force density vector associated with transverse shear deformation. The superscripts, n and m, represent the sequence number of the layer where the material point is located. The term N_{shear} represents the number of family members connecting to $\mathbf{x}_k$ through interlayer shear bonds. It should be noted that the first term on the right-hand side of Eq. (4.17) is presented in Section 4.2.1.

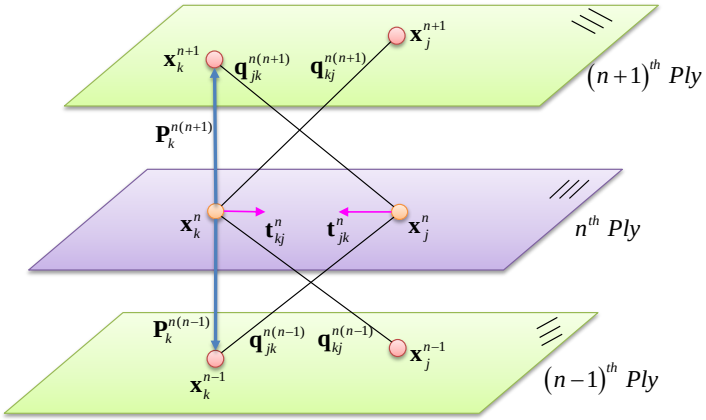

Fig. 4-3 Representation of interactions of material point k in multi-layer composite model.

In the transverse normal deformation, the laminate (resin-rich layer) is treated as the matrix material in its thickness direction [10]. Therefore, the material properties in the thickness direction are assumed the same as the material properties of the matrix, i.e.

$$E_z = E_m, G_z = G_m \text{ and } \alpha_z = \alpha_m \tag{4.18}$$

where the subscript m represents the matrix material. The transverse normal force density function [10] including the thermal effects is represented as

$$\mathbf{P}_k^{nm} = 4b_N \hat{\delta}\left(s_k^{nm} - \alpha_m T_{avg,k}^{nm}\right)\frac{\mathbf{y}_k^m - \mathbf{y}_k^n}{\left|\mathbf{y}_k^m - \mathbf{y}_k^n\right|} \tag{4.19}$$

where $\mathbf{P}_k^{nm}$ represents the force density between point k in n^{th} ply and its corresponding point in m^{th} ply with the same in-plane coordinate. The term $\hat{\delta}$ is the horizon in the transverse normal direction. The term $T_{avg,k}^{nm}$ is the average temperature change of point $\mathbf{x}_k^n$ and $\mathbf{x}_k^m$. The transverse normal peridynamic parameter, b_N, is given as [10];

$$b_N = \frac{E_m}{\hat{\delta}\left[\left(h_{n+1} + h_n\right)V_k^{n+1} + \left(h_{n-1} + h_n\right)V_k^{n-1}\right]} \tag{4.20}$$

where h_{n+1}, h_n and h_{n-1} are illustrated in Fig. 4-4(a).

Similarly, transverse shear bond force density function can be modified by including the thermal effects as;

$$\mathbf{q}_{kj}^{nm} = 4b_S\tilde{\delta}\left(\left(s_{kj}^{nm} - \alpha_m T_{avg,kj}^{nm}\right) - \left(s_{jk}^{nm} - \alpha_m T_{avg,jk}^{nm}\right)\right)\frac{\mathbf{y}_j^m - \mathbf{y}_k^n}{\left|\mathbf{y}_j^m - \mathbf{y}_k^n\right|} \qquad (4.21a)$$

or

$$\mathbf{q}_{kj}^{nm} = 4b_S\tilde{\delta}\frac{\phi_{kj}^{nm}\left(h_m + h_n\right)}{\left|\mathbf{x}_j^m - \mathbf{x}_k^n\right|}\frac{\mathbf{y}_j^m - \mathbf{y}_k^n}{\left|\mathbf{y}_j^m - \mathbf{y}_k^n\right|} \qquad (4.21b)$$

with

$$\phi_{kj}^{nm} = \left|\mathbf{x}_j^m - \mathbf{x}_k^n\right|\frac{\left(s_{kj}^{nm} - \alpha_m T_{avg,kj}^{nm}\right) - \left(s_{jk}^{nm} - \alpha_m T_{avg,jk}^{nm}\right)}{h_m + h_n} \qquad (4.21c)$$

where h_m and h_n are the thickness of m^{th} and n^{th} layer in the laminate, respectively. Here m^{th} layer represents the one layer above or one layer below the n^{th} layer (Fig. 4-4(a)). Thereby, ϕ_{kj}^{nm} represents the average shear angle in the interlayer shear direction. s_{kj}^{nm} is the stretch between nodes $\mathbf{x}_k^n$ and $\mathbf{x}_j^m$, and $T_{avg,kj}^{nm}$ is the average temperature difference between nodes $\mathbf{x}_k^n$ and $\mathbf{x}_j^m$, with respect to the initial temperature. The term $\mathbf{q}_{kj}^{nm}$ is the transverse shear force density vector between material point k in n^{th} ply and material point j in m^{th} ply. The horizon size in transverse shear direction, $\tilde{\delta}$, is defined as $\tilde{\delta} = \sqrt{\delta^2 + \hat{\delta}^2}$ (Fig. 4-4(b)). The term b_S is a PD parameter and it is given as [10];

$$b_S = \frac{G_m}{8\pi\tilde{\delta}} \frac{1}{\left\{\left(\frac{h_{n+1}+h_n}{2}\right)^3\left[\left(\delta^2+2\left(\frac{h_{n+1}+h_n}{2}\right)^2\right)/\sqrt{\delta^2+\left(\frac{h_{n+1}+h_n}{2}\right)^2}-\left(h_{n+1}+h_n\right)\right]\right.}$$
$$\left.+\left(\frac{h_{n-1}+h_n}{2}\right)^3\left[\left(\delta^2+2\left(\frac{h_{n-1}+h_n}{2}\right)^2\right)/\sqrt{\delta^2+\left(\frac{h_{n-1}+h_n}{2}\right)^2}-\left(h_{n-1}+h_n\right)\right]\right\} \tag{4.22}$$

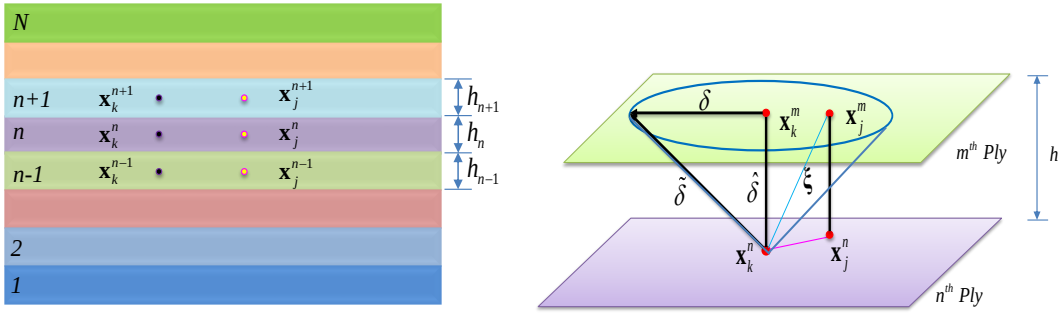

(a) (b)

Fig. 4-4 (a) Illustration of each lamina in a laminate with N representing the total number of layers; (b) Horizon in transverse shear direction

In this chapter, the multi-layer laminates composed by uniform thickness (h_{thick}) plies are considered. As a result, Eq.(4.20) for the expression of b_N and Eq.(4.22) for the expression of b_S can be simplified as

$$b_N = \frac{E_m}{2h_{thick}\hat{\delta}\left[V_k^{n+1}+V_k^{n-1}\right]} \tag{4.23}$$

and

$$b_S = \frac{G_m}{8\pi\tilde{\delta}} \frac{1}{2h_{thick}^3\left(\left(\delta^2+2h_{thick}^2\right)/\sqrt{\delta^2+h_{thick}^2}-2h_{thick}\right)} \tag{4.24}$$

Similarly, the effect of interlayer thermal bonds is considered in the coupled heat equation by modifying Eq.(4.16) as

$$\rho c_v \dot{T}\left(\mathbf{x}_k^n, t\right) = \sum_{j=1}^{N_{ply}} \left[\left(\mu_F \kappa_f\left(\mathbf{x}_k^n\right) + \kappa_m\right) \frac{\Theta\left(\mathbf{x}_j^n, t\right) - \Theta\left(\mathbf{x}_k^n, t\right)}{\left|\mathbf{x}_j^n - \mathbf{x}_k^n\right|} - \Theta_0 \left(\mu_F \beta_f\left(\mathbf{x}_k^n\right) + \beta_m\right) \dot{e}_{jk}^n \right] V_j^n$$
$$+ \sum_{m=n+1,\, n-1} \left[\kappa_{inter} \frac{\Theta\left(\mathbf{x}_k^m, t\right) - \Theta\left(\mathbf{x}_k^n, t\right)}{\left|\mathbf{x}_k^m - \mathbf{x}_k^n\right|} - \Theta_0 \beta_{inter} \dot{e}_{k,z}^{nm} \right] V_k^m$$
$$+ \sum_{m=n+1,\, n-1} \sum_{j=1}^{N_{inter}} \left[\kappa_{inter} \frac{\Theta\left(\mathbf{x}_j^m, t\right) - \Theta\left(\mathbf{x}_k^n, t\right)}{\left|\mathbf{x}_j^m - \mathbf{x}_k^n\right|} - \Theta_0 \beta_{inter} \dot{e}_{kj,z}^{nm} \right] V_j^m + \rho q_b\left(\mathbf{x}_k^n, t\right) \tag{4.25}$$

The second and third terms on the right-hand side of Eq. (4.25) represents the heat flow between adjacent layers. N_{inter} is the family member number those connect to $\mathbf{x}_k^n$ through interlayer thermal bonds. Rate of change of bond extension is considered only through the thickness direction for interlayer thermal bonds. Interlayer PD micro conductivity and PD thermal modulus are given as

$$\kappa_{inter} = \frac{k_m}{2\pi h_{thick}^3 \left(\tilde{\delta} - h_{thick}\right)} \tag{4.26}$$

and

$$\beta_{inter} = \frac{E_m \alpha_m}{4\pi h_{thick}^3 \left(\tilde{\delta} - h_{thick}\right)} \tag{4.27}$$

The derivation process for κ_{inter} and β_{inter} is given in Appendix B. And their surface correction factor formulations are provided in Appendix C.

4.2.3. Reduced bond-based model

Based on the previous state-based PD multilayer laminate model, the reduced bond-based PD formulation is derived in this section. The discretized form of the PD equation of motion for a material point $\mathbf{x}_k^n$ in the n layer of a laminate can be written as

$$\rho\ddot{\mathbf{u}}\left(\mathbf{x}_k^n,t\right)=\sum_{j=1}^{N_{ply}}\left(\mu_F c_f\left(\mathbf{x}_k^n\right)+c_m\right)\left(s_{kj}^n-\alpha_\vartheta T_{kj}^n\right)\frac{\mathbf{y}_j^n-\mathbf{y}_k^n}{\left|\mathbf{y}_j^n-\mathbf{y}_k^n\right|}V_j^n$$
$$+\sum_{m=n+1,\,n-1}c_{in}\left(s_k^{nm}-\alpha_m T_k^{nm}\right)\frac{\mathbf{y}_k^m-\mathbf{y}_k^n}{\left|\mathbf{y}_k^m-\mathbf{y}_k^n\right|}V_k^m \tag{4.28}$$
$$+\sum_{m=n+1,\,n-1}\sum_{j=1}^{N_{shear}}c_{is}\phi\left(\Delta x\right)^2\frac{\mathbf{y}_j^m-\mathbf{y}_k^n}{\left|\mathbf{y}_j^m-\mathbf{y}_k^n\right|}V_j^m+\mathbf{b}\left(\mathbf{x}_k^n,t\right)$$

The first three terms on the right-hand side of Eq.(4.28) represent the PD forces developed by in-plane bonds (including fibre bonds and matrix bonds), interlayer normal bonds, and interlayer shear bonds in sequence. If the bond direction is parallel to the fibre direction, μ_F is equal to 1, otherwise, it is 0. c_f, c_m, c_{in}, and c_{is} are PD material constants associated with in-plane fibre bonds, in-plane matrix bonds, interlayer normal bonds, and interlayer shear bonds, respectively. The definitions for PD material constants are listed as [10, 76]

$$c_f\left(\mathbf{x}_k^n\right)=\frac{2E_1\left(E_1-E_2\right)}{\left(E_1-\frac{1}{9}E_2\right)\left(\sum_{j=1}^{N_F}\left|\mathbf{x}_j^n-\mathbf{x}_k^n\right|V_j^n\right)} \tag{4.29}$$

$$c_m=\frac{8E_1E_2}{\left(E_1-\frac{1}{9}E_2\right)\pi h_{thick}\delta^3} \tag{4.30}$$

$$c_{in}=\frac{E_m}{h_{thick}V} \tag{4.31}$$

$$c_{is}=\frac{2G_m}{\pi h_{thick}\left(\delta^2+h_{thick}^2\ln\left(h_{thick}^2/\tilde{\delta}^2\right)\right)} \tag{4.32}$$

It is assumed that a material point interacts with other points in adjacent plies through interlayer normal bonds and interlayer shear bonds. Therefore, the horizon of the interlayer normal bond is taken as equal to the thickness of one-ply, h_{thick}. In Eq.(4.29), N_F represents the total number of family members those connect to the

material point with fibre bonds. In Eq. (4.31), the value of V can be calculated as the average volume of material points connected through interlayer normal bonds. As to the thermal expansion coefficient α_ϑ, the same formulation Eq.(4.3) developed in [84] is utilized. α_m represents the thermal expansion coefficient of the matrix material. In Eq. (4.28), ϕ represents the shear angle of the diagonal shear bonds.

It should be noted that because of the adoption of bond-based PD theory, the four material constants existing in a laminate, i.e., E_1, E_2, ν_{12}, and G_{12}, reduce to two constants: E_1 and E_2 [76, 80]. The major Poisson's ratio ν_{12} is limited to 1/3, and the major shear modulus is $G_{12} = \dfrac{\nu_{12} E_2}{1-\nu_{12}\nu_{21}}$ with $\nu_{12}/E_1 = \nu_{21}/E_2$.

Regarding the bond-based thermal model, the heat conduction equation given for a laminate is

$$\begin{aligned}\rho c_v \dot{T}\left(\mathbf{x}_k^n, t\right) = & \sum_{j=1}^{N_{ply}} \left[\begin{array}{l} \left(\mu_F \kappa_f\left(\mathbf{x}_k^n\right) + \kappa_m\right) \dfrac{\Theta\left(\mathbf{x}_j^n, t\right) - \Theta\left(\mathbf{x}_k^n, t\right)}{\left|\mathbf{x}_j^n - \mathbf{x}_k^n\right|} \\ -\Theta_0\left(\mu_F \beta_f\left(\mathbf{x}_k^n\right) + \beta_m\right) \dot{e}_{kj}^n \end{array} \right] V_j^n \\ & + \sum_{m=n+1,\, n-1} \left[\kappa_{inter} \frac{\Theta\left(\mathbf{x}_k^m, t\right) - \Theta\left(\mathbf{x}_k^n, t\right)}{\left|\mathbf{x}_k^m - \mathbf{x}_k^n\right|} - \Theta_0 \beta_{in} \dot{e}_k^{nm} \right] V_k^m \\ & + \sum_{j=1}^{N_{shear}} \left[\kappa_{inter} \frac{\Theta\left(\mathbf{x}_j^m, t\right) - \Theta\left(\mathbf{x}_k^n, t\right)}{\left|\mathbf{x}_j^m - \mathbf{x}_k^n\right|} - \Theta_0 \beta_{is} \dot{e}_{kj}^{nm} \right] V_j^m + \rho q_b\left(\mathbf{x}_k^n, t\right) \end{aligned} \tag{4.33}$$

where κ_{inter} represents the micro-conductivity for both interlayer normal and shear bonds defined by Eq.(4.26).

The PD thermal modulus β depends on the PD material bond constant [43, 44, 46]. PD thermal modulus for in-plane bonds and interlayer bonds can be expressed as

$$\beta_f = \frac{1}{2} c_f \alpha_\vartheta \tag{4.34}$$

$$\beta_m = \frac{1}{2} c_m \alpha_g \tag{4.35}$$

$$\beta_{in} = \frac{1}{2} c_{in} \alpha_g \tag{4.36}$$

$$\beta_{is} = \frac{1}{2} c_{is} \alpha_g \tag{4.37}$$

where β_f, β_m, β_{in} and β_{is} are associated with in-plane fibre bonds, in-plane matrix bonds, interlayer normal bonds, and interlayer shear bonds.

4.2.4. Failure criteria

The general PD failure criteria are provided in Section 2.1.3. Due to the anisotropic material properties of the laminates, the failure criteria should be modified correspondingly. The mode mixity effects can be captured by the selected failure criteria, which is demonstrated by Vazic et al. [38]. The PD predictions for failure mode ranging from pure mode I to pure model II are consistent with the experiments [85]. Because of the four different types of PD bonds in a multi-layer composites model, four different critical stretch values are needed in the failure analyses. The critical stretch values are considered as [10, 86]

$$s_m = \sqrt{\frac{G_{IC}}{\left(\frac{6}{\pi}\mu_m + \frac{16}{9\pi^2}\left(K_m - 2\mu_m\right)\right)\delta}} \tag{4.38}$$

$$s_{ft} = \frac{\sigma_{1t}}{E_1}; s_{fc} = \frac{\sigma_{1c}}{E_1} \tag{4.39}$$

$$s_{in} = \sqrt{\frac{2G_{IC}}{h_{thick} E_m}} \tag{4.40}$$

$$\phi_{is} = \sqrt{\frac{G_{IIC}}{h_{thick} G_m}} \tag{4.41}$$

where s_m, s_f, s_{in}, ϕ_{is} are the critical stretch values for matrix bonds, fibre bonds, interlayer normal bonds, and interlayer shear bonds, respectively. The material constants K_m and μ_m are bulk modulus and Lamé constant of the matrix material. Besides, G_{IC} and G_{IIC} are critical energy release rate for the first and second failure mode in classical fracture mechanics, respectively. The terms σ_{1t} and σ_{1c} are the longitudinal tension and compression strength properties of a single ply. The critical stretch in Eq.(4.39) has a similar meaning of critical strain in the context of classical continuum mechanics. On the other hand, the critical stretches given in Eqs. (4.38), (4.40), (4.41) are obtained by equating the energies required to eliminate all PD interactions across the crack surfaces to the mode I or mode II critical energy release rates. Thus, the failure criteria mentioned in Eqs. (4.38), (4.40), (4.41) are energy-based [10]. By applying the above failure criteria, it can be observed that the fibre bonds can fail both in tension and compression. The matrix bonds, interlayer normal bonds, and interlayer shear bonds are only allowed to fail in tension.

Eq. (4.38) and (4.39) are related to the intralaminar failure mode. Eq. (4.38) corresponds to matrix damage and splitting failure mode. Eq. (4.39) corresponds to fibre damage. Eq.(4.40) and (4.41) are related to the interlaminar failure mode. Eq. (4.40) corresponds to interlaminar mode-I fracture and Eq. (4.41) corresponds to interlaminar mode-II fracture as shown in Fig. 4-5.

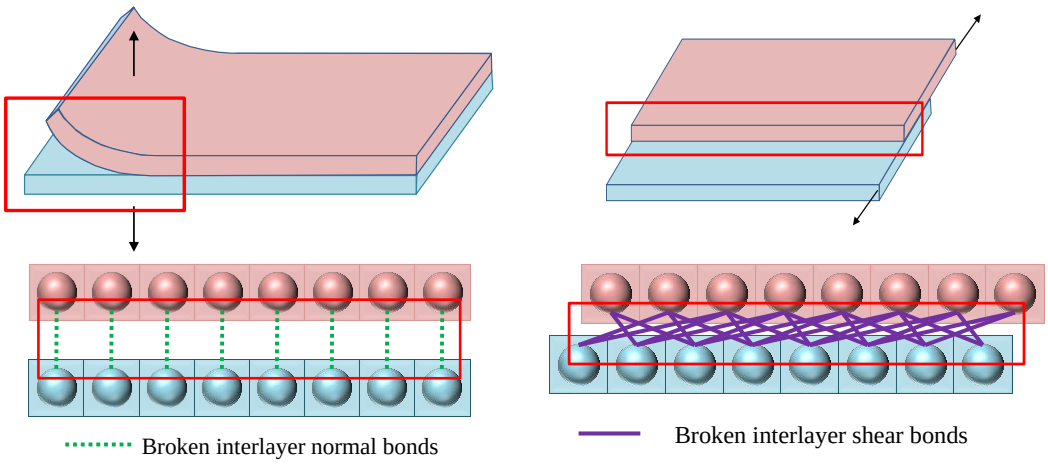

Fig. 4-5 Interlaminar failure modes: (a) Mode-I Fracture; (b) Mode-II Fracture

The history-dependent failure function, χ in Eq. (2.14), is defined for each interaction to indicate the bond breakage, i.e. being 1 for intact bond and being zero for a broken bond, as [10, 40, 86]

$$\chi_f\left(\mathbf{x}_j^n-\mathbf{x}_k^n,\mathbf{y}_j^n-\mathbf{y}_k^n,t\right)=\begin{cases}1,\ \text{for}\left(s_{kj}-\alpha_1 T_{avg,kj}\right)<s_{ft}\ \text{and}\left(s_{kj}-\alpha_1 T_{avg,kj}\right)>s_{fc}\\ 0,\ \text{for}\left(s_{kj}-\alpha_1 T_{avg,kj}\right)\geq s_{ft}\ \text{or}\left(s_{kj}-\alpha_1 T_{avg,kj}\right)\leq s_{fc}\end{cases} \quad (4.42)$$

$$\chi_m\left(\mathbf{x}_j^n-\mathbf{x}_k^n,\mathbf{y}_j^n-\mathbf{y}_k^n,t\right)=\begin{cases}1,\ \text{for}\left(s_{kj}-\alpha_\varphi T_{avg,kj}\right)<s_m\\ 0,\ \text{for}\left(s_{kj}-\alpha_\varphi T_{avg,kj}\right)\geq s_m\end{cases} \quad (4.43)$$

$$\chi_{in}\left(\mathbf{x}_k^m-\mathbf{x}_k^n,\mathbf{y}_k^m-\mathbf{y}_k^n,t\right)=\begin{cases}1,\ \text{for}\left(s_k^{nm}-\alpha_m T_{avg,k}^{nm}\right)<s_{in}\\ 0,\ \text{for}\left(s_k^{nm}-\alpha_m T_{avg,k}^{nm}\right)\geq s_{in}\end{cases} \quad (4.44)$$

$$\chi_{is}\left(\mathbf{x}_j^m-\mathbf{x}_k^n,\mathbf{y}_j^m-\mathbf{y}_k^n,t\right)=\begin{cases}1,\ \text{for}\ \phi_{kj}^{nm}<\phi_{is}\\ 0,\ \text{for}\ \phi_{kj}^{nm}\geq\phi_{is}\end{cases} \quad (4.45)$$

where χ_f, χ_m, χ_{in} and χ_{is} are related to fibre bonds, matrix bonds, interlayer normal bonds, interlayer shear bonds. As a result, Eqs. (4.1), (4.5), (4.19), and (4.21b) with including the failure functions Eq.(4.42)-(4.45) are expressed as

$$\mathbf{t}\left(\mathbf{u}_j^n-\mathbf{u}_k^n,\mathbf{x}_j^n-\mathbf{x}_k^n,t\right)=2\delta\left[\begin{array}{l}\dfrac{d\Lambda_{kj}^n}{\left|\mathbf{x}_j^n-\mathbf{x}_k^n\right|}a\left(\theta_k^n-\left(\alpha_1+\alpha_2\right)T_k^n\right)\\ +\left(\begin{array}{l}\chi_f\mu_F b_F\left(\mathbf{x}_k^n\right)\\ +\chi_m\mu_T b_T\left(\mathbf{x}_k^n\right)+\chi_m b_{FT}\end{array}\right)\left(s_{kj}^n-\alpha_\varphi T_k^n\right)\end{array}\right]\frac{\mathbf{y}_j^n-\mathbf{y}_k^n}{\left|\mathbf{y}_j^n-\mathbf{y}_k^n\right|} \quad (4.46a)$$

$$\mathbf{t}\left(\mathbf{u}_k^n-\mathbf{u}_j^n,\mathbf{x}_k^n-\mathbf{x}_j^n,t\right)=-2\delta\left[\begin{array}{l}\dfrac{d\Lambda_{jk}^n}{\left|\mathbf{x}_k^n-\mathbf{x}_j^n\right|}a\left(\theta_j^n-\left(\alpha_1+\alpha_2\right)T_j^n\right)\\ +\left(\begin{array}{l}\chi_f\mu_F b_F\left(\mathbf{x}_j^n\right)\\ +\chi_m\mu_T b_T\left(\mathbf{x}_j^n\right)+\chi_m b_{FT}\end{array}\right)\left(s_{jk}^n-\alpha_\varphi T_j^n\right)\end{array}\right]\frac{\mathbf{y}_j^n-\mathbf{y}_k^n}{\left|\mathbf{y}_j^n-\mathbf{y}_k^n\right|} \quad (4.46b)$$

$$\theta_k^n = d\delta\sum_{j=1}^{N_{ply}} \chi_d \left(s_{kj}^n - \alpha_\varphi T_k^n\right)\Lambda_{kj}^n V_j^n + \left(\alpha_1+\alpha_2\right)T_k^n,\ \chi_d = \begin{cases} \chi_f, \text{ for fibre direction} \\ \chi_m, \text{ for other directions} \end{cases} \tag{4.47}$$

$$\mathbf{P}_k^{nm} = 4b_N\hat{\delta}\chi_{in}\left(s_k^{nm} - \alpha_m T_{avg,k}^{nm}\right)\frac{\mathbf{y}_k^m - \mathbf{y}_k^n}{\left|\mathbf{y}_k^m - \mathbf{y}_k^n\right|} \tag{4.48}$$

$$\mathbf{q}_{kj}^{nm} = 4b_S\tilde{\delta}\chi_{is}\frac{\phi_{kj}^{nm}\left(h_m + h_n\right)}{\left|\mathbf{x}_j^m - \mathbf{x}_k^n\right|}\frac{\mathbf{y}_j^m - \mathbf{y}_k^n}{\left|\mathbf{y}_j^m - \mathbf{y}_k^n\right|} \tag{4.49}$$

Correspondingly, for each kind of PD bond damage the local damage parameter Eq. (2.15) becomes as [13];

$$\varphi_f\left(\mathbf{x}_k^n, t\right) = 1 - \frac{\sum_{j=1}^{N_F}\chi_f\left(\mathbf{x}_j^n - \mathbf{x}_k^n, \mathbf{y}_j^n - \mathbf{y}_k^n, t\right)V_j^n}{\sum_{j=1}^{N_F} V_j^n} \tag{4.50a}$$

$$\varphi_m\left(\mathbf{x}_k^n, t\right) = 1 - \frac{\sum_{j=1}^{N_{ply}}\chi_m\left(\mathbf{x}_j^n - \mathbf{x}_k^n, \mathbf{y}_j^n - \mathbf{y}_k^n, t\right)V_j^n}{\sum_{j=1}^{N_{ply}} V_j^n} \tag{4.50b}$$

$$\varphi_{in}\left(\mathbf{x}_k^n, t\right) = 1 - \frac{\sum_{m=n+1,n-1}\chi_{in}\left(\mathbf{x}_k^m - \mathbf{x}_k^n, \mathbf{y}_k^m - \mathbf{y}_k^n, t\right)V_k^m}{\sum_{m=n+1,n-1} V_k^m} \tag{4.50c}$$

$$\varphi_{is}\left(\mathbf{x}_k^n, t\right) = 1 - \frac{\sum_{j=1}^{N_{shear}}\chi_{is}\left(\mathbf{x}_j^m - \mathbf{x}_k^n, \mathbf{y}_j^m - \mathbf{y}_k^n, t\right)V_j^m}{\sum_{j=1}^{N_{shear}} V_j^m} \tag{4.50d}$$

4.3. Simulation cases

In order to validate the derived ordinary state-based thermomechanical PD formulations, several numerical simulations are conducted, and then the results are

mainly compared with those obtained from ANSYS solutions. Firstly, in Section 4.3.1, temperature changes are imposed on the composite models to estimate the equation of motion which includes the thermal loading. Secondly, heat transfer simulations in multi-layer composites are implemented in Section 4.3.2, in order to validate the developed PD thermal model for multi-layer composites. Thirdly, pressure shock loads are applied in fully coupled thermomechanical analyses in Sections 4.3.3. The emphasis is put on the predictions of the displacements and the temperature, which act as primary variables in the simulations. And the validity of the fully coupled thermomechanical PD model is investigated by the comparisons of the simulation results with the ANSYS solution. Finally, in Section 4.3.4, failure analyses with central pre-existing cracks on the models are carried out. The crack propagation paths and the temperature distribution evolutions are predicted.

During the numerical simulations, the composite material is chosen as graphite/epoxy. The material properties are listed in Table 2 [1]. The length and width of the single-layer composite model specified as $0.1\,\mathrm{m}$. The thickness of the single-layer model is $0.001\,\mathrm{m}$. The multi-layer composite model is constructed with three single-layer models with a ply stacking sequence of $\left[0/90^{\circ}/0\right]$, as illustrated in Fig. 4-6. Each ply is modelled as a two-dimensional orthotropic structure with one node in the thickness direction. The models are discretized into 200 subdomains both in x and y directions, leading to a space between material points, Δx, as $5\times10^{-4}\,\mathrm{m}$. High accuracy and desired numerical efficiency can be achieved by adopting this grid size. The in-plane horizon is chosen as $\delta = 3.015\Delta x$, which is recommended by [13] and [10]. The origin of the coordinate system is set at the middle of the bottom ply as illustrated in Fig. 4-6. The reference temperature is $\Theta_0 = 285\,\mathrm{K}$.

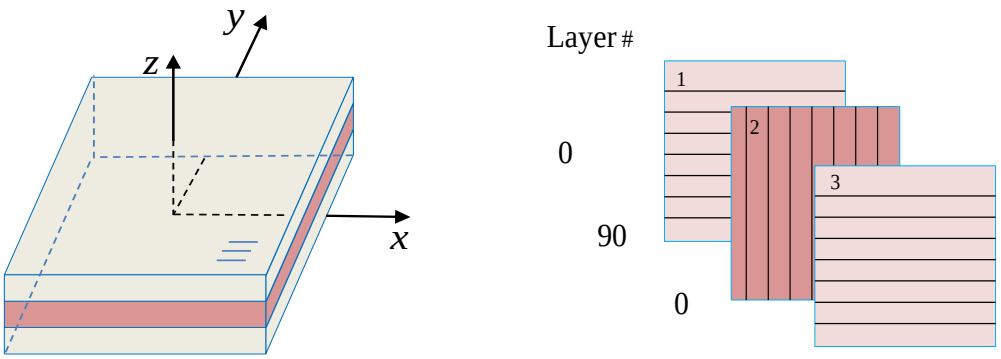

Fig. 4-6 Multi-layer composite model with a stacking sequence $\left[0/90^{\circ}/0\right]$.

Table 2 Material property of composites [1]

Mechanical Properties		Thermal Properties	
Longitudinal elastic modulus $E_1\left(\text{GPa}\right)$	181	Longitudinal coefficient of thermal expansion $\alpha_1\left(\mu\text{m/m/K}\right)$	0.02
Transverse elastic modulus $E_2\left(\text{GPa}\right)$	10.3	Transverse coefficient of thermal expansion $\alpha_2\left(\mu\text{m/m/K}\right)$	22.5
Shear modulus $G_{12}\left(\text{GPa}\right)$	7.17	Longitudinal thermal conductivity $k_1\left(\text{W/m/K}\right)$	8.3075
Major Poisson's ratio ν_{12}	0.28	Transverse thermal conductivity $k_2\left(\text{W/m/K}\right)$	0.7575
Mass density $\rho\left(\text{kg/m}^3\right)$	1620	Specific heat $c_v\left(\text{J/kg/K}\right)$	1092.728
Elastic modulus of matrix material $E_m\left(\text{GPa}\right)$	3.4	Thermal conductivity of matrix material $k_m\left(\text{W/m/K}\right)$	0.2
Shear modulus of matrix material $G_m\left(\text{GPa}\right)$	1.308	Thermal expansion coefficient of matrix material $\alpha_m\left(\mu\text{m/m/K}\right)$	63

4.3.1. Composite subject to temperature change

In this section, temperature changes are imposed on both the single-layer and multi-layer composite models. All four edges of both composite models are free to deform, and they are insulated. An adaptive dynamic relaxation (ADR) approach introduced by Kilic and Madenci [87] is utilized for the quasi-static analyses. A unit time step size is used to save computational time [10]. The displacements predictions are compared with the ones from ANSYS or classical laminate theory (CLT) [88] solutions.

4.3.1.1 Constant temperature change

As a first case, simple loading condition, i.e. a constant temperature change of $50\ \mathrm{K}$, being applied to single-layer composite with a fibre orientation of $\Phi=0^{o}$ is considered. The analytical solution based on the CLT for a single layer ply can be calculated as [89];

$$u_x\left(x, y=0\right)=\alpha_1\left(\Delta T\right)x \tag{4.51a}$$

$$u_y\left(x=0, y\right)=\alpha_2\left(\Delta T\right)y \tag{4.51b}$$

The term u_x and u_y represent the horizontal and vertical components of displacement.

During the numerical simulations, convergence study is utilised by tracing the displacements of a point as shown in Fig. 4-7. The horizontal and vertical displacements predictions along the central lines of the single-layer model are provided in Fig. 4-8. The good agreements indicate the successful application of the state-based PD equation of motion by considering the effect of temperature on the mechanical field.

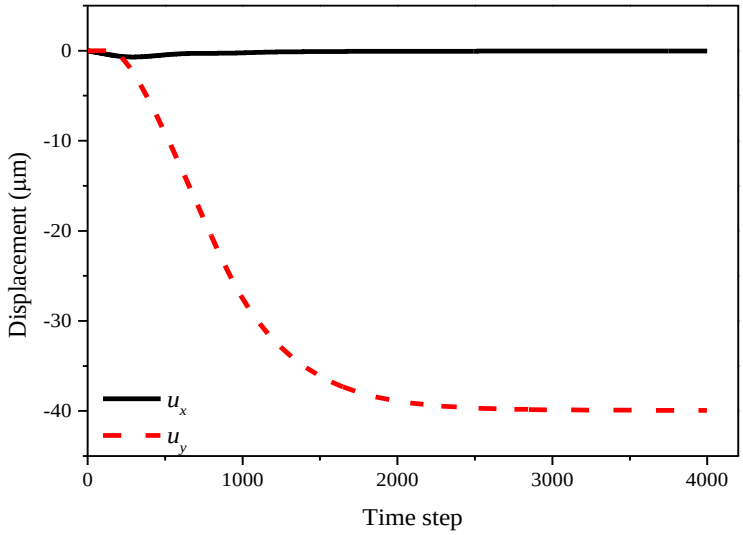

Fig. 4-7 Convergence study by tracing the displacements of the material point at $x=-0.0495\mathrm{m}$ and $y=-0.0355\mathrm{m}$.

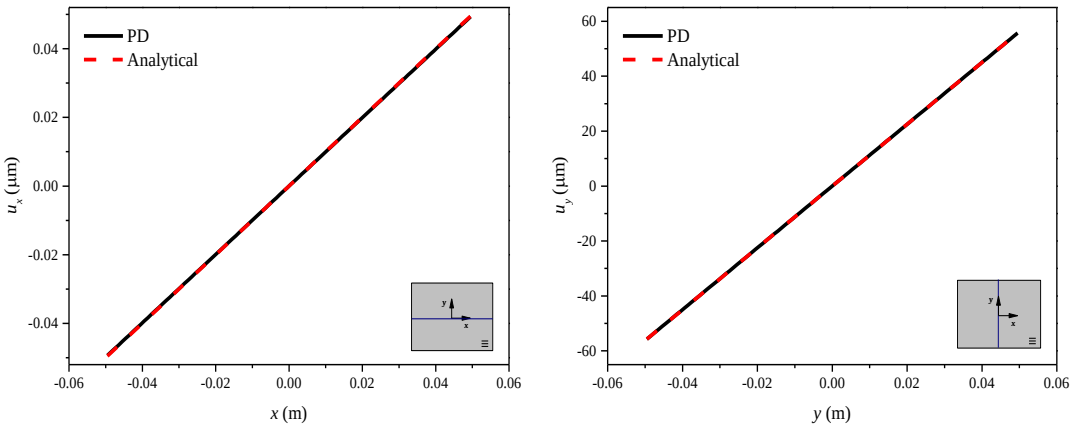

(a) (b)

Fig. 4-8 (a) Horizontal (b) Vertical displacements along the central lines of the single-layer model subjected to constant temperature change.

As a second case, the same constant temperature change is imposed on the multi-layer composite model. The analytical solution based on the CLT for multi-layer composite model can be calculated as [89];

$$u_x = \alpha_x^* (\Delta T) x \tag{4.52a}$$

$$u_y = \alpha_y^* (\Delta T) y \tag{4.52b}$$

$$u_z = \alpha_m (\Delta T) z \tag{4.52c}$$

where α_x^* and α_y^* are the thermal expansion coefficients of the laminate with respect to the global coordinate system. They can be presented as [89]

$$\{\alpha^*\} = [A]^{-1} \sum_{k=1}^{N} \left[\bar{Q}\right]^k \{\alpha\}_{xy}^k h_k \tag{4.53a}$$

with

$$\{\alpha^*\} = \{\alpha_x^*, \alpha_y^*, \alpha_{xy}^*\} \tag{4.53b}$$

and

$$[A] = \sum_{k=1}^{N} \left[\bar{Q}\right]^k h_k \tag{4.53c}$$

where $\left[\bar{Q}\right]^k$ is the reduced transformed stiffness matrix as defined in Eq. (4.7), $\{\alpha\}_{xy}^k$ is the thermal expansion coefficient vector with respect to the global coordinate system and h_k is the thickness of the k^{th} layer. In ANSYS, the solid element type SOLID186 is utilized in the static analysis. The mesh size in x and y directions are 2×10^{-3} m with three elements in the z direction.

The displacement components along the midline of the multi-layer composite model obtained from PD, ANSYS and analytical simulations are compared and presented in Fig. 4-9. It can be easily observed that the results from these methods agree very well. Thus, the PD equation of motion for multi-layer composite under a constant temperature change is validated. There is a slight difference between PD results and classical ones near the boundary due to the PD surface effect [90]. It should be noted that the deformation of multi-layer composite differs significantly from the single-layer because of the orientation of each ply in the stacking sequence.

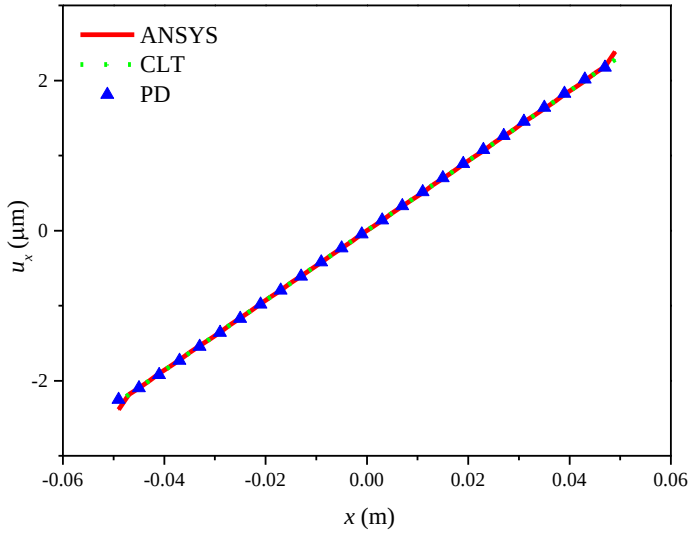

(a)

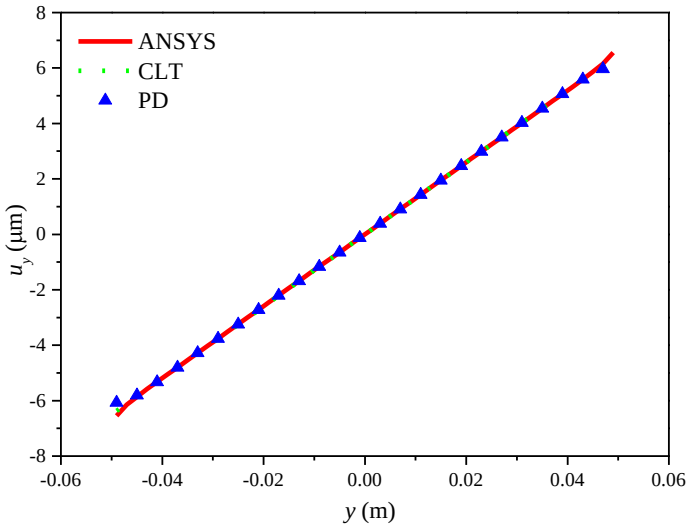

(b)

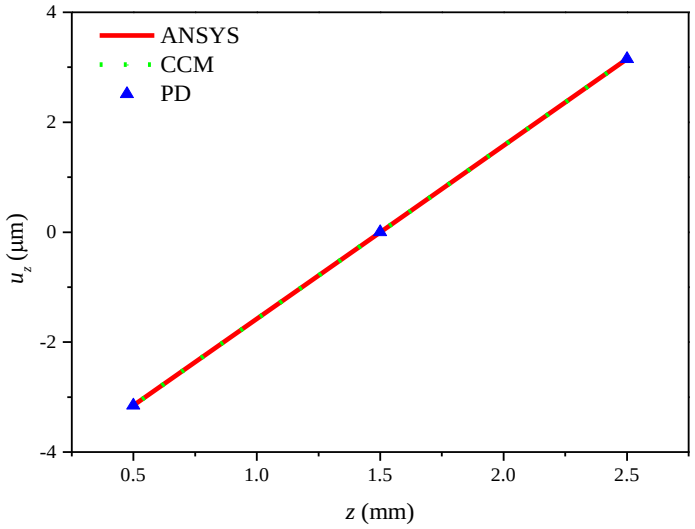

(c)

Fig. 4-9 (a) Horizontal (b) Vertical (c) Out of plane displacements along the central lines of the multi-layer model subjected to constant temperature change.

4.3.1.2 Linear temperature change

The thermal loading is changed to a linear temperature change, $\Delta T = 500x\,(\mathrm{K})$ with x representing the horizontal location. As a first case, the non-uniform temperature change is applied for the single-layer composite model. In ANSYS, the plane element type PLANE182 with the plane stress assumption is utilized in the static analysis. The mesh size is 1×10^{-3} m with only one element in the thickness direction. As shown in

Fig. 4-10 and Fig. 4-11, the horizontal and vertical displacements predictions from peridynamic solutions are in agreement with the ANSYS predictions.

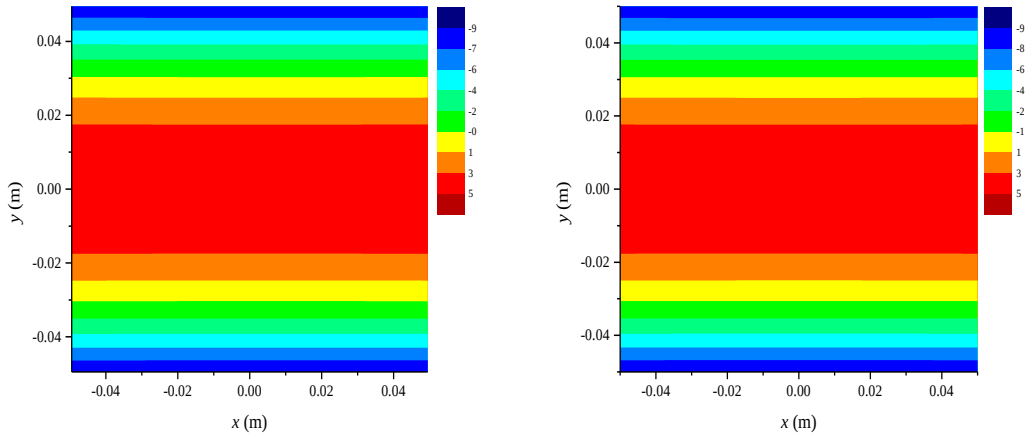

(a) (b)

Fig. 4-10 Horizontal displacements, u_x (μm) (a) PD and (b) ANSYS results

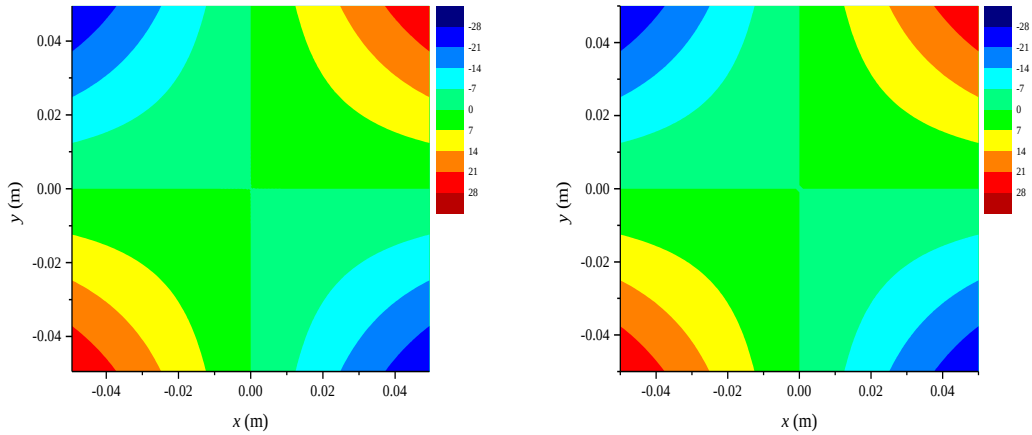

(a) (b)

Fig. 4-11 Vertical displacements, u_y (μm) (a) PD and (b) ANSYS results

As a second case, the same linear temperature change is applied to the multi-layer composite model. The ANSYS model is the same as described in Section 4.3.1.1. The displacements components are compared with ANSYS predictions, as shown in Fig. 4-12 to Fig. 4-17. Due to symmetric fibre orientations of the composite, the horizontal and vertical displacements distributions are the same for top and bottom plies. As expected, the displacement in the thickness direction, the top and bottom plies have deformation in the opposite direction. The transverse displacement of the middle ply is observed as zero. It can be inferred from Fig. 4-16 and Fig. 4-17 that a delamination

tendency exists on the right side due to higher temperatures. Good agreements are also obtained with ANSYS solutions.

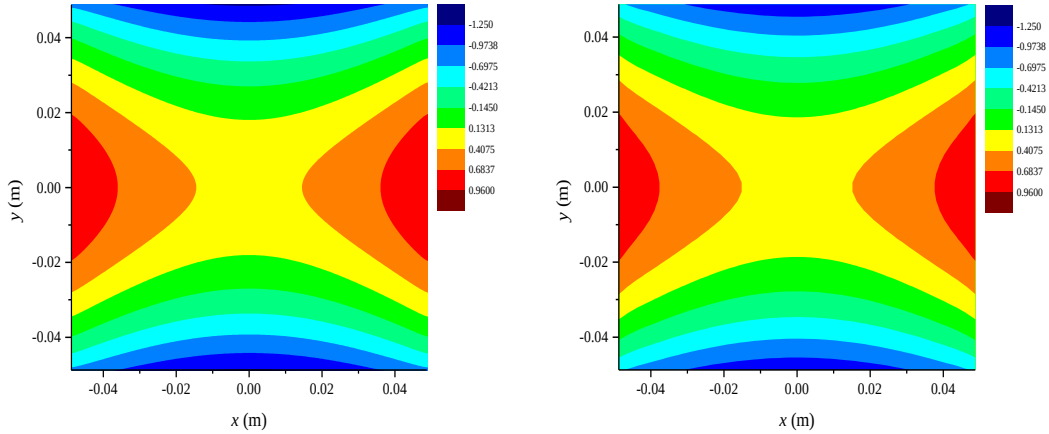

(a) (b)

Fig. 4-12 Horizontal displacements, u_x (μm) (a) PD (b) ANSYS results for bottom ply.

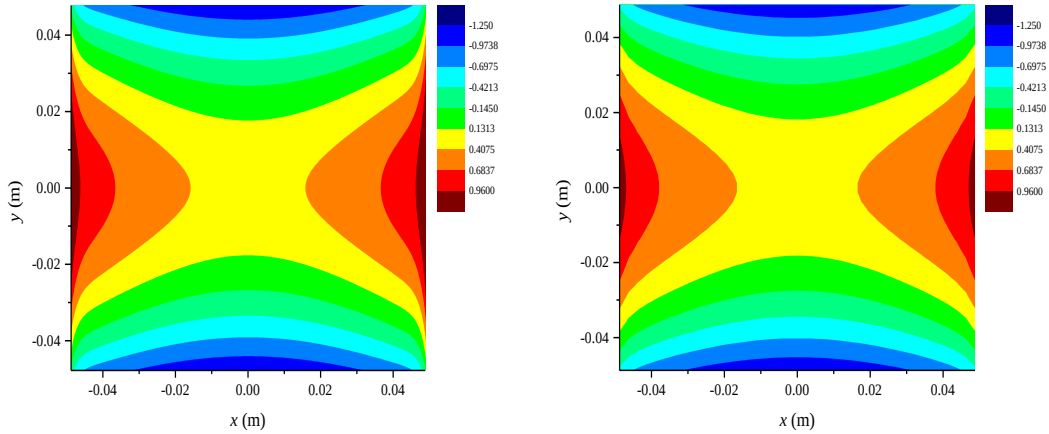

(a) (b)

Fig. 4-13 Horizontal displacements, u_x (μm) (a) PD (b) ANSYS results for middle ply

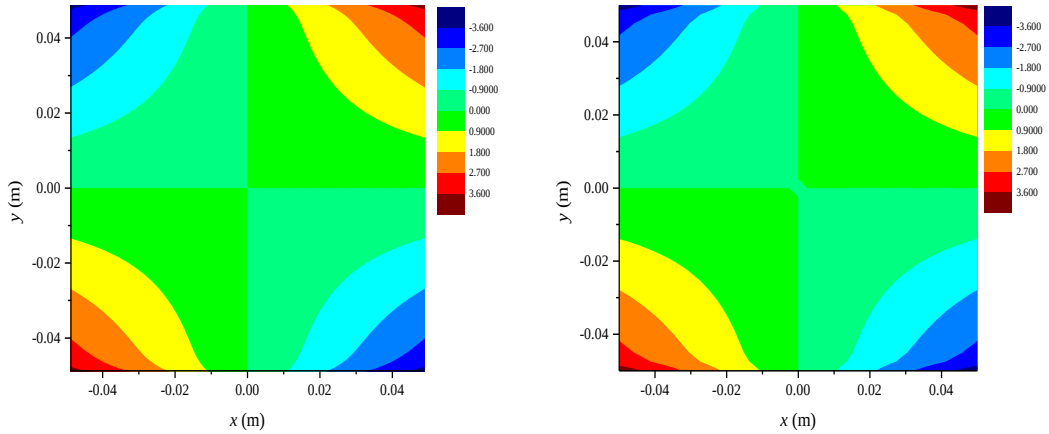

(a) (b)

Fig. 4-14 Vertical displacements, u_y (μm) (a) PD (b) ANSYS results for bottom ply.

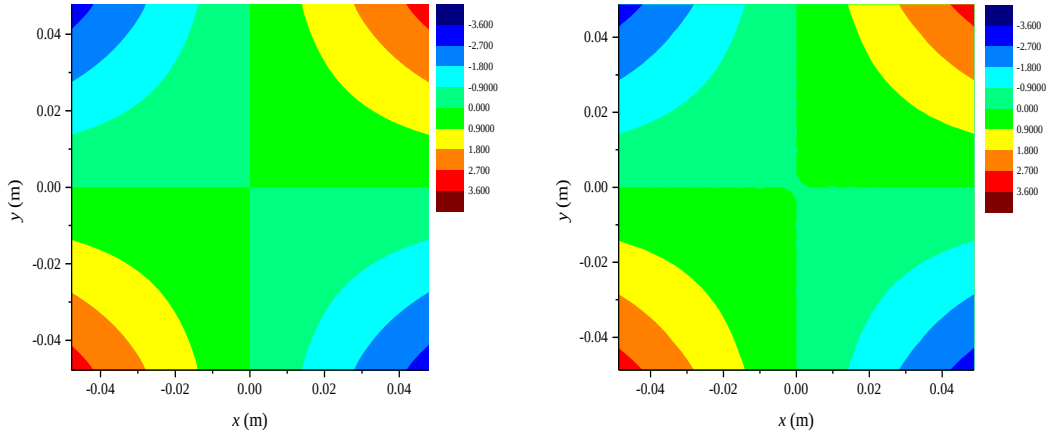

(a) (b)

Fig. 4-15 Vertical displacements, u_y (μm) (a) PD (b) ANSYS for middle ply.

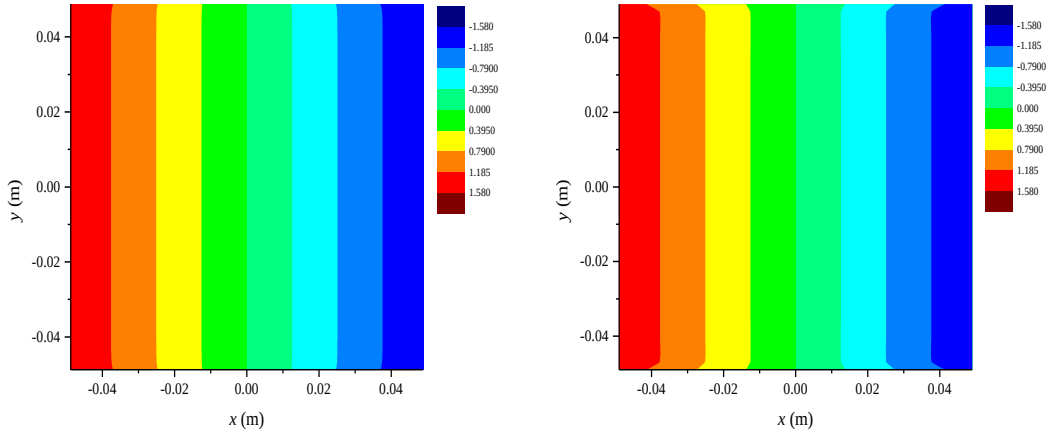

(a) (b)

Fig. 4-16 Transverse displacement, u_z (μm) (a) PD (b) ANSYS for bottom ply.

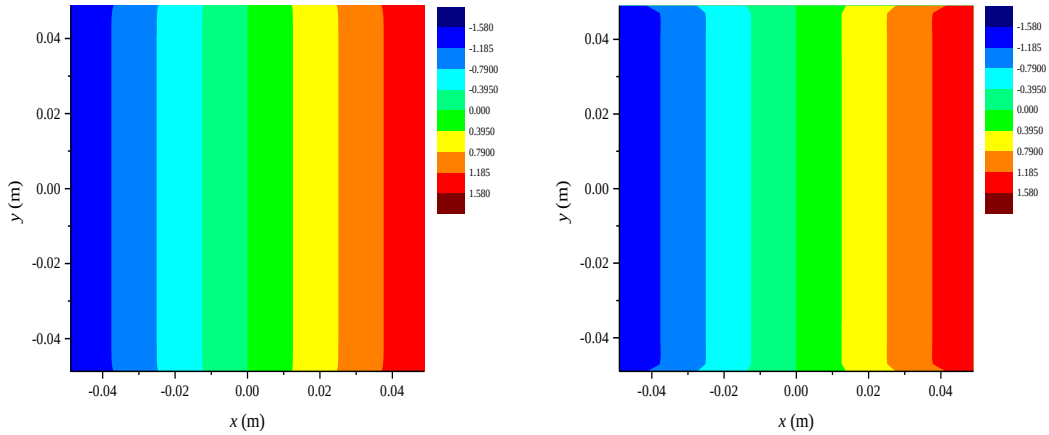

(a) (b)

Fig. 4-17 Transverse displacement, $u_z\ (\mu\text{m})$ (a) PD (b) ANSYS for top ply.

4.3.2. Heat transfer in composites

In this section, pure heat transfer analyses in the single and multi-layer composite model are tested in order to validate the proposed multi-layer PD thermal model.

4.3.2.1 Composite subject to heat flux on the top ply

Constant heat flux $5000\ \text{W/m}^2$ is applied to the top ply of the multi-layer model. The composite model is initially at the reference temperature, Θ_0. The total simulation time is $t = 50\,\text{s}$ and the time step size in PD solution is defined as $\text{d}t = 0.01\,\text{s}$. On the other hand, the element type SOLID278 is utilized in the transient thermal ANSYS analysis. A grid 60×60 in the *x*-*y* plane with three elements in the *z* direction is chosen in the ANSYS model. In addition, the time step size used in ANSYS model is $2.5\,\text{s}$. The temperature change distribution predictions during the simulation process are compared with those from ANSYS simulations, as shown from Fig. 4-18 to Fig. 4-20. The remarkable match indicates the successful application of the PD interlayer heat flow formulation.

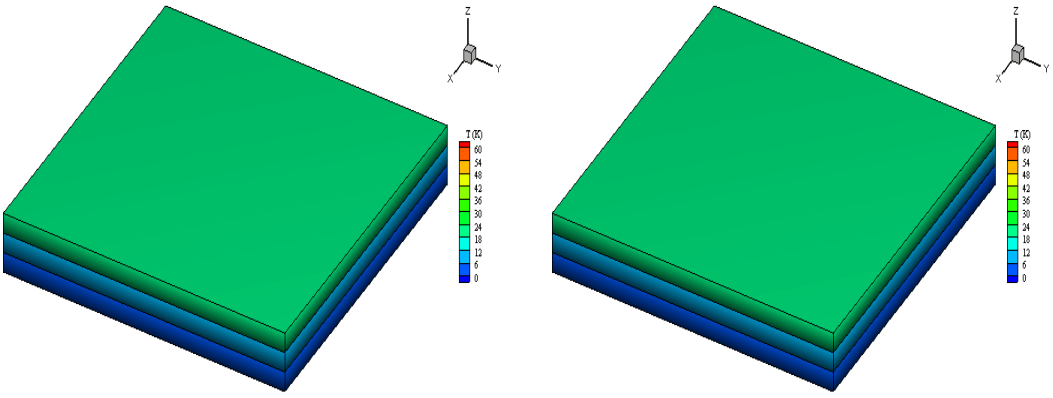

(a) (b)

Fig. 4-18 Temperature change distributions at $t = 10\,\text{s}$ (a) PD (b) ANSYS results

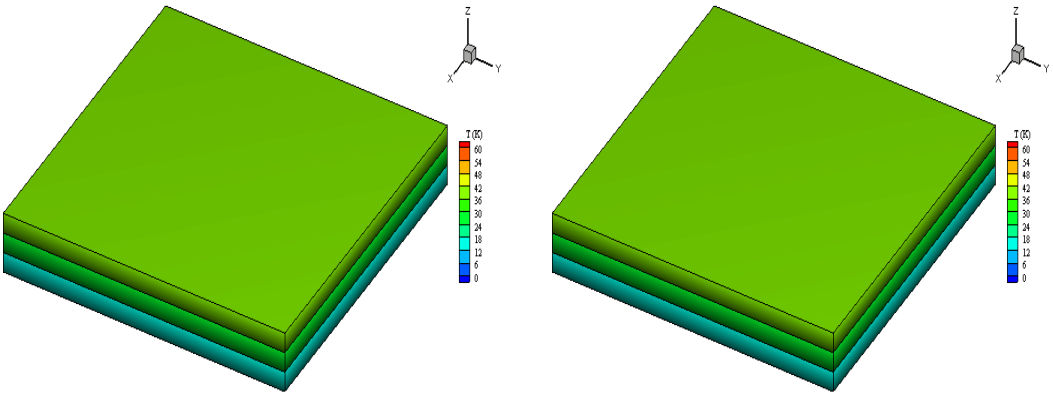

(a) (b)

Fig. 4-19 Temperature change distributions at $t = 30\,\mathrm{s}$ (a) PD (b) ANSYS results

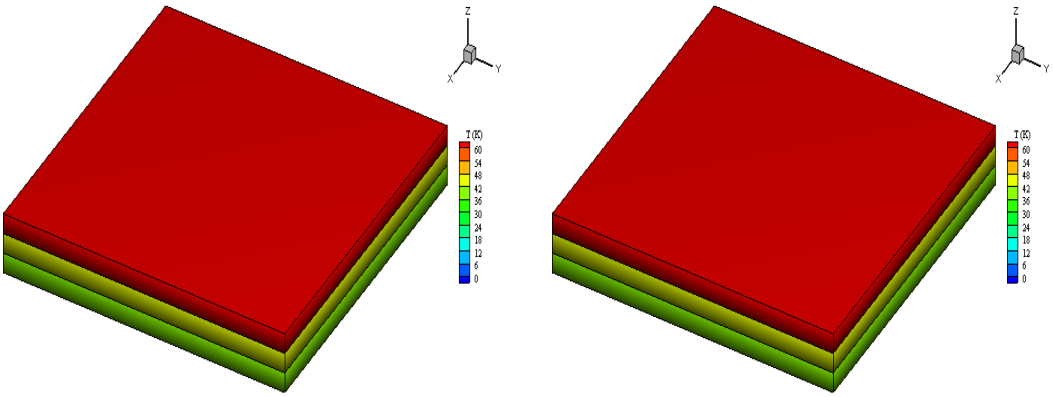

(a) (b)

Fig. 4-20 Temperature change distributions at $t = 50\,\mathrm{s}$ (a) PD (b) ANSYS results

4.3.2.2 Composite subject to a temperature boundary condition

In order to verify the PD heat conduction model for in-plane and transverse directions, a temperature boundary condition $\Delta T = (y + 100z)t\,(\mathrm{K})$ is applied at $x = -L/2$, where x, y and z represent the coordinate components and t is the simulation time. The composite model is initially at the reference temperature, Θ_0. The total simulation time is $300\,\mathrm{s}$ and the time step size in PD solution is $\mathrm{d}t = 0.01\,\mathrm{s}$. The SOLID278 element type is chosen for the ANSYS model with a time step size $10\,\mathrm{s}$. The ANSYS model is constructed with 40 elements in x and y directions and 3 elements in z direction. The PD results of temperature distributions are compared with the ANSYS solutions, as shown from Fig. 4-21 to Fig. 4-23. Good agreement is achieved, thus the PD thermal model of the laminate is validated.

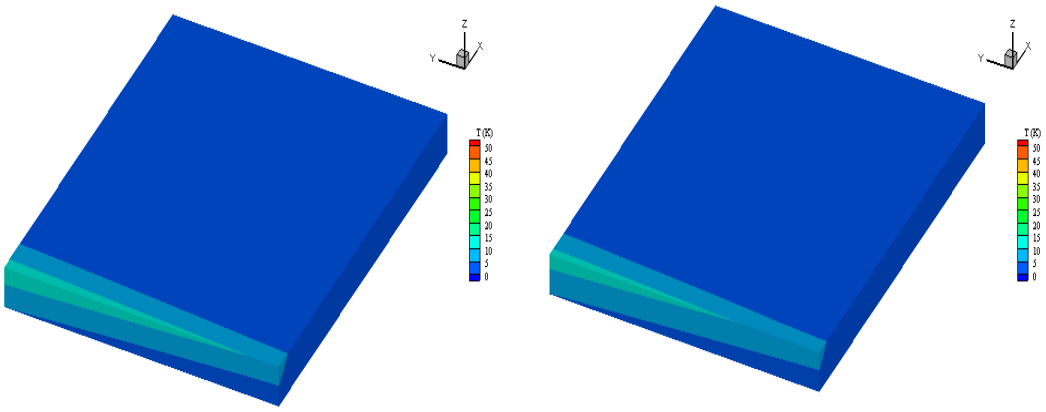

(a) (b)

Fig. 4-21 Temperature change distributions at $t = 50\,\mathrm{s}$ (a) PD (b) ANSYS results

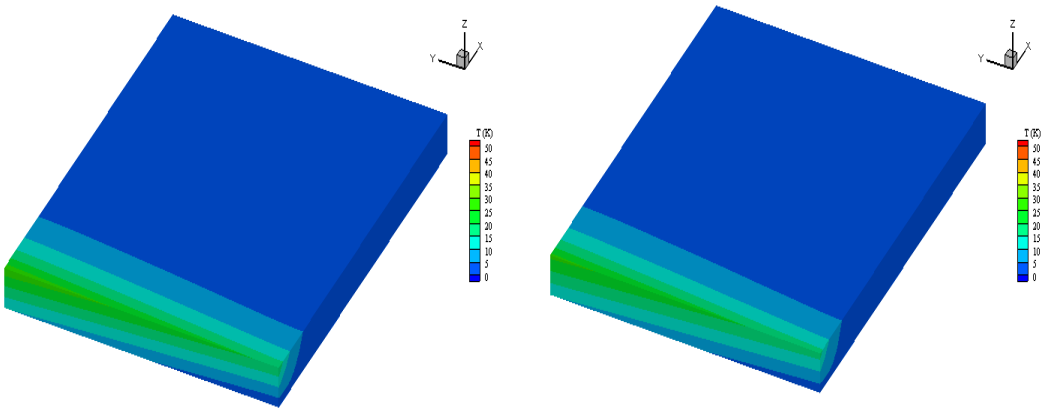

(a) (b)

Fig. 4-22 Temperature change distributions at $t = 100\,\mathrm{s}$ (a) PD (b) ANSYS results

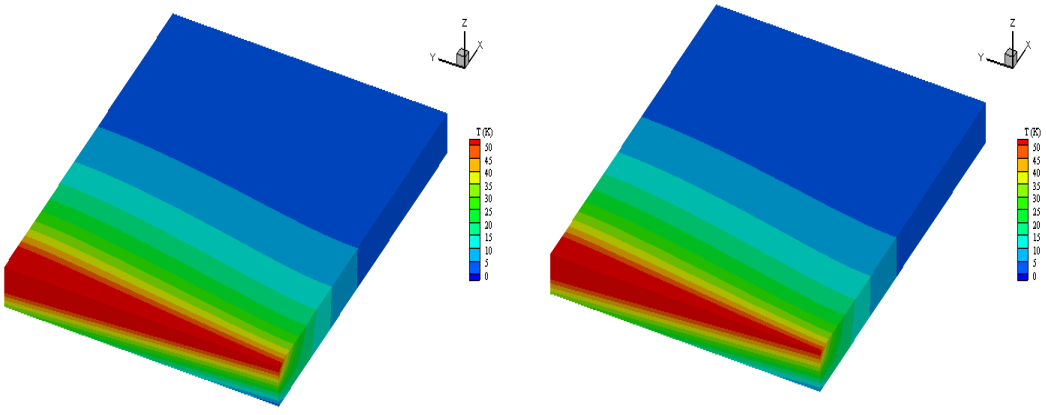

(a) (b)

Fig. 4-23 Temperature change distributions at $t = 300\,\mathrm{s}$ (a) PD (b) ANSYS results.

4.3.3. Composites subject to pressure shock

In order to validate the fully coupled thermomechanical PD formulations, the deformation and thermal responses of single-layer and multi-layer composite models under pressure shock loads are investigated. As illustrated in Fig. 4-24, the plate is fixed on the right edge and it is subjected to pressure loading on the left edge. The plate is insulated at the top, bottom and right edges.

The initial conditions are:

$$u_x\left(x,y,z,t=0\right)=u_y\left(x,y,z,t=0\right)=u_z\left(x,y,z,t=0\right)=0 \tag{4.54a}$$

$$T\left(x,y,z,t=0\right)=0 \tag{4.54b}$$

The boundary conditions are:

$$u_x\left(x=L/2,\,y,\,z,\,t\right)=u_y\left(x=L/2,\,y,\,z,\,t\right)=u_z\left(x=L/2,\,y,\,z,\,t\right)=0 \tag{4.55a}$$

$$\sigma_{xx}\left(x,\,y=\pm W/2,\,z,\,t\right)=\sigma_{yy}\left(x,\,y=\pm W/2,\,z,\,t\right)=\sigma_{zz}\left(x,\,y=\pm W/2,\,z,\,t\right)=0 \tag{4.55b}$$

$$\sigma_{xx}\left(x=-L/2,y,t\right)=P\left(t\right) \tag{4.55c}$$

$$T_{,x}\left(x=\pm L/2,\,y=\pm W/2,\,z,\,t\right)=0 \tag{4.55d}$$

$$T_{,y}\left(x=\pm L/2,\,y=\pm W/2,\,z,\,t\right)=0 \tag{4.55e}$$

$$T_{,z}\left(x=\pm L/2,\,y=\pm W/2,\,z,\,t\right)=0 \tag{4.55f}$$

where u_z represents the displacement in z direction.

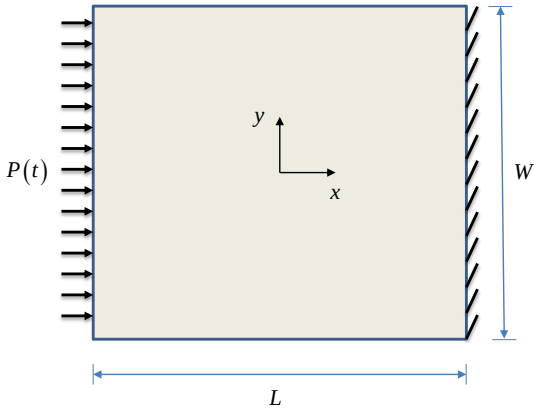

Fig. 4-24 The top view of composite models under a pressure shock.

4.3.3.1 Single-layer composite subject to pressure shock

Pressure shock loading is applied to the single-layer composite model for 2 different cases.

Case 1:

$$P(t)=10^{10}\sin\left(\pi t\times10^{6}\right)\text{ Pa; for fibre angle }\Phi=0^{o} \tag{4.56a}$$

Case 2:

$$P(t)=-10^{14}t\text{ Pa; for fibre angle }\Phi=90^{o} \tag{4.56b}$$

The induced temperature changes and horizontal displacements along the central line of the ply are predicted with the newly developed fully coupled thermomechanical model. The results are compared with ANSYS solutions by using a directly coupled method [91]. The directly coupled element PLANE223 is utilized in the transient thermomechanical analysis. The mesh size is 2×10^{-4} m and the time step size is 8×10^{-8} s in ANSYS solution.

Fig. 4-25 and Fig. 4-26 provide the temperature change distributions and horizontal displacements for 2 different cases. In case 1, a compressive wave is generated. As the wave moves to the right, the temperature rise is observed where there is local compression, on the other hand, the temperature drop is observed where there is local

tension. On the other hand, in case 2 temperature drop is observed due to applied tension loading. The observed temperatures coincide with the theory and experimental results [92]. As seen from Fig. 4-25-Fig. 4-26, the induced temperature changes and horizontal displacements match very well with ANSYS solutions.

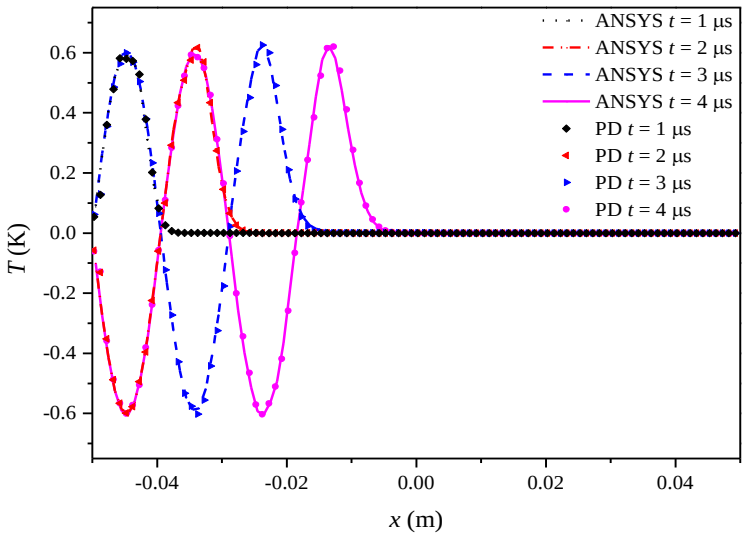

(a)

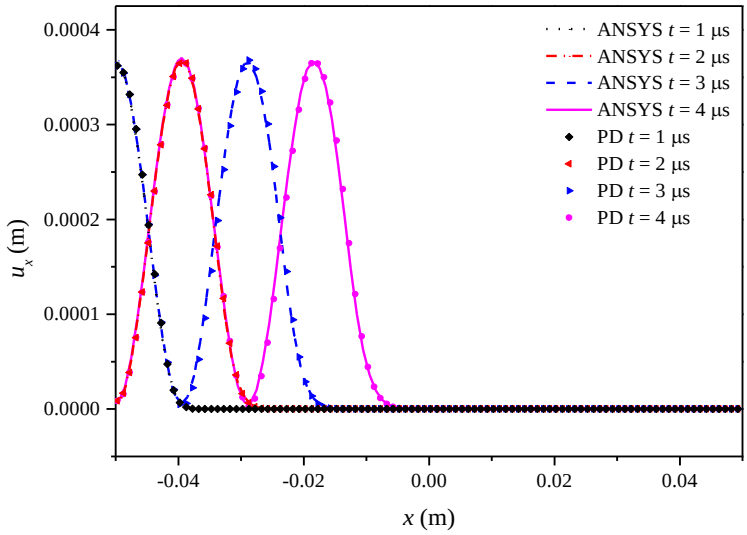

(b)

Fig. 4-25 (a) Temperature change distributions (b) horizontal displacements at $y = 0$ for case 1

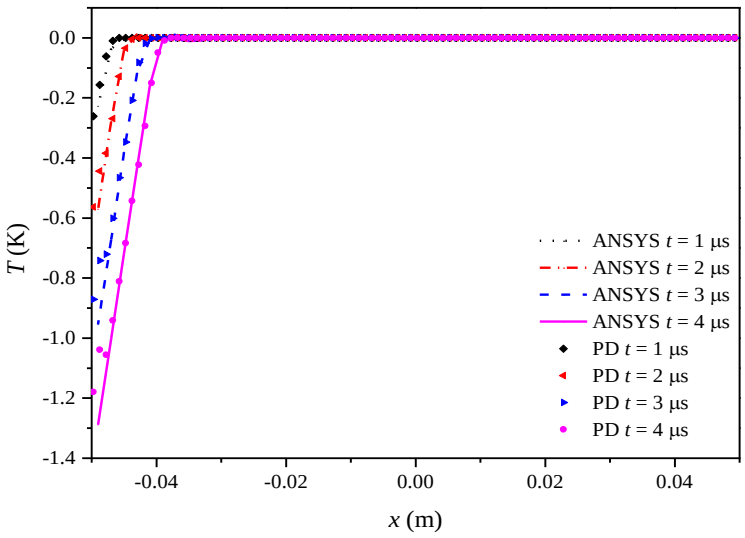

(a)

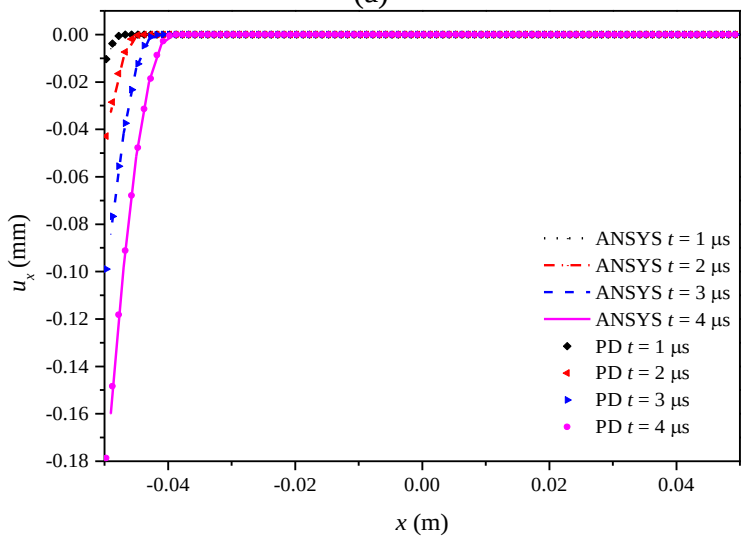

(b)

Fig. 4-26 (a) Temperature change distributions (b) horizontal displacements at $y = 0$ for case 2

4.3.3.2 Multi-layer composite subject to pressure shock

In order to validate the proposed PD fully coupled thermomechanical model for multi-layer composites, a pressure shock loading is applied to the multi-layer model as:

$$P(t) = -10^{16} t \text{ Pa} \tag{4.57}$$

The induced temperature changes and displacements along the central lines of all three plies are predicted with the proposed PD model. Furthermore, the results are

compared with ANSYS solutions by using coupled element type SOLID226. The mesh size and time step remain the same with the ones from the multi-layer composite as in Section 4.3.1.

Fig. 4-27 and Fig. 4-28 are the horizontal displacements and temperature change distributions of each ply, respectively. Due to the symmetry stacking sequence and loading condition, the top ply and bottom behave similarly. As it can be seen in Fig. 4-27, the displacements of the middle ply are slightly larger than the bottom ply due to fibre orientation since the fibres in the middle ply are perpendicular to the loading direction, on the other hand, the fibres in the top and bottom plies are in the loading direction. Similarly, in terms of the temperature field, temperature changes of the middle ply are also much larger than the bottom ply as seen in Fig. 4-28. As time progresses, sudden temperature variations are observed near the boundary. Although there are little discrepancies between the PD and ANSYS results in the later stage especially in the middle ply, such variations are also captured in PD results.

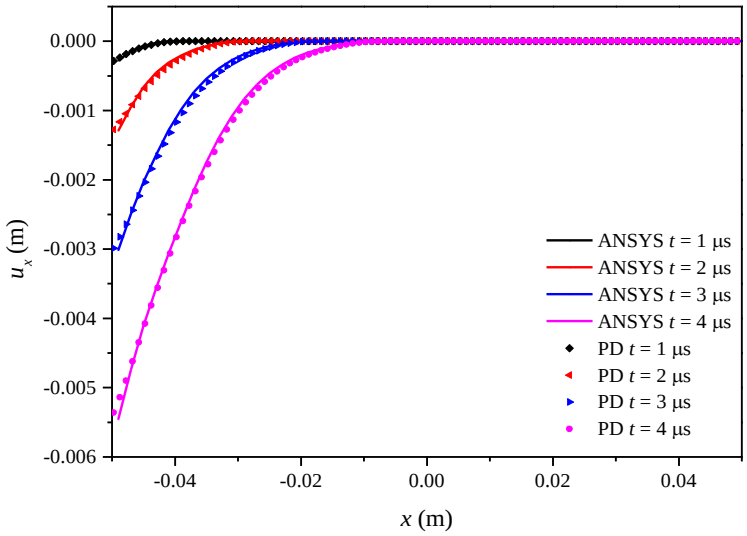

(a)

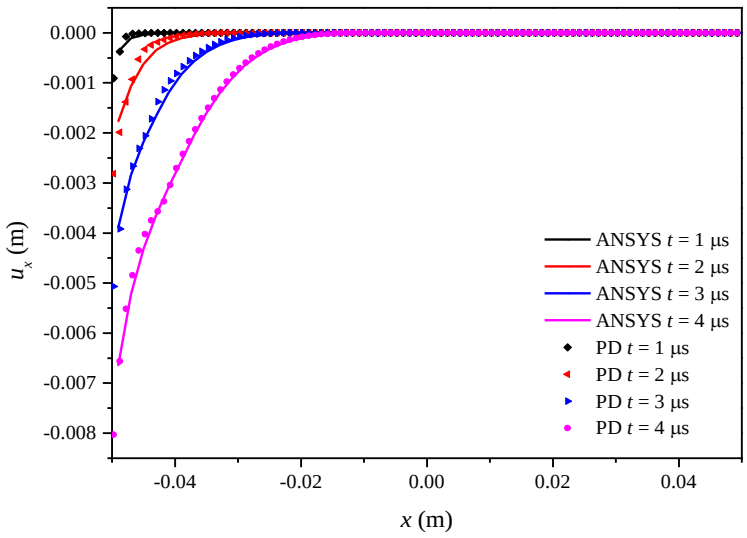

(b)

Fig. 4-27 Horizontal displacements at $y = 0$ (a) bottom ply (b) middle ply

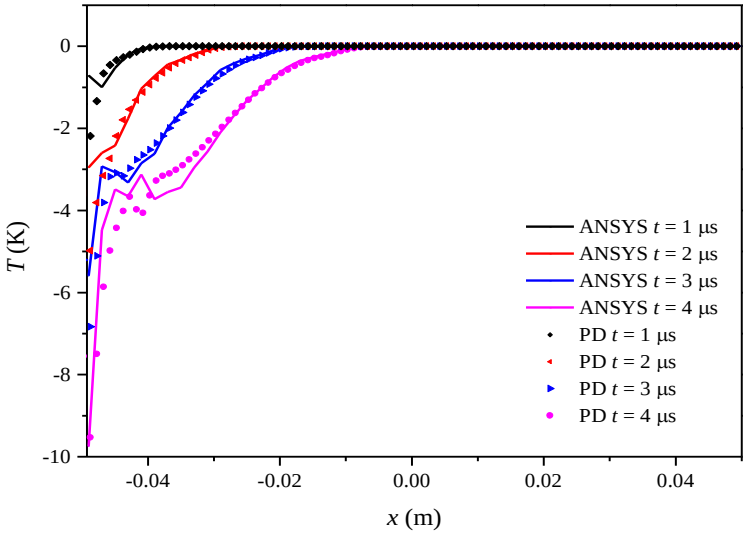

(a)

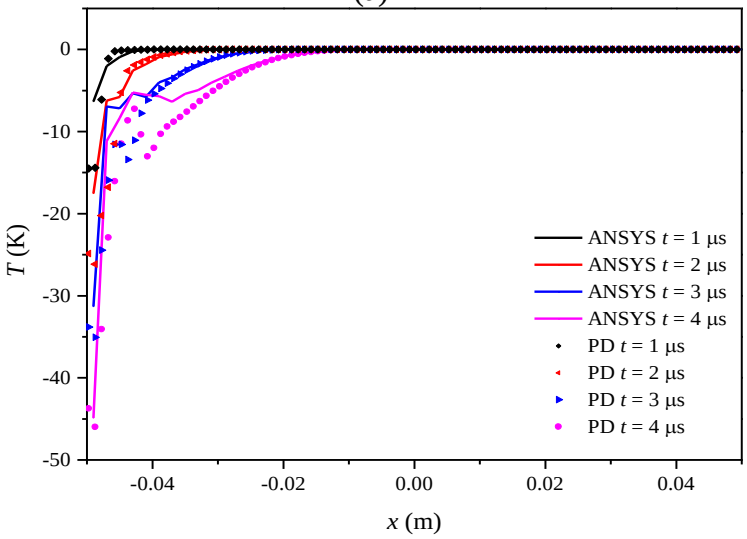

(b)

Fig. 4-28 Temperature change distributions at $y = 0$ (a) bottom ply (b) middle ply

4.3.4. Crack propagation predictions of composites

After verifying the developed PD thermomechanical formulations for both single and multi-layer composites, in this section, damage patterns and corresponding temperature change distributions for single layer and multi-layer composite model at different integration times are presented with a pre-existing crack size of $2a = 2.0$ cm as seen in Fig. 4-29. The initial and boundary conditions are identical to those from Section 4.3.3. PD discretization is achieved with a uniform grid of 300×300. The critical stretch values are calculated as $s_m = 0.0177$ and $s_{in} = 0.03734$ with $G_{IC} = 2.37 \times 10^{-3}$ MPa/m [76]. The critical stretch value of fibre bond is assumed to be twice the matrix bond, i.e $s_f = 0.0354$. The critical stretch value of interlayer shear bonds is calculated as $\phi_{is} = 0.1043$ with $G_{IIC} = 7.11 \times 10^{-3}$ MPa/m [86]. The simulation time is chosen as $14\ \mu$s with time step size 10^{-9} s.

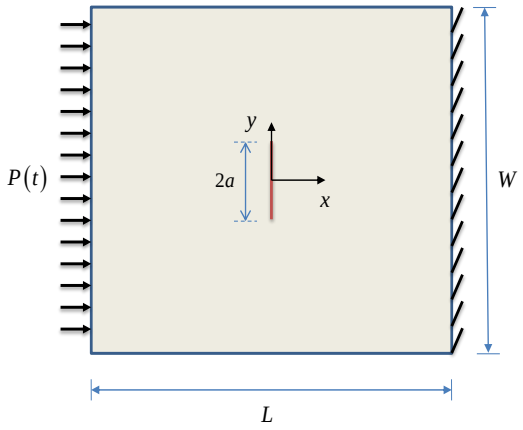

Fig. 4-29 Top view of a composite model with a central crack under a tension pressure shock.

4.3.4.1 Single-layer composite with a central crack

Pressure shock loading is applied to the single-layer composite with a crack for 2 different cases.

Case 1:

$$P(t) = -3\times10^{14}\left(tH(t_0 - t) + t_0 H(t - t_0)\right) \text{ Pa; for fibre direction } \Phi=0^{o} \quad (4.58a)$$

Case 2:

$$P(t) = -5\times10^{12}\left(tH(t_0 - t) + t_0 H(t - t_0)\right) \text{ Pa; for fibre direction } \Phi=90^{o} \quad (4.58b)$$

where $t_0 = 4.0\,\mu s$.

The damage plots and temperature change distributions at different time steps are provided from Fig. 4-30 to Fig. 4-32 for case 1. As shown in Fig. 4-30(a), the crack begins to propagate at $t = 8\,\mu s$. Coinciding with the predictions in previous solutions [79, 80], the crack grows along the fibre direction which is perpendicular to the pre-existing crack direction. From this figure, it can also be noticed that the cracks on either side of the pre-existing crack tips grow equally. It indicates the fibre/matrix debonding [93] failure mode, which arises from in-plane shear stress in the matrix. A similar failure pattern is observed in the experiments conducted by Bogert et al.[94]. As presented in Fig. 4-32(b), temperature increases near the crack, which agrees with the conclusion in [95]. There is a temperature drop due to local tension near the crack tip. On the other hand, there is a temperature rise along the crack surfaces due to local compression. The temperature change distribution has a similar pattern as the crack growth.

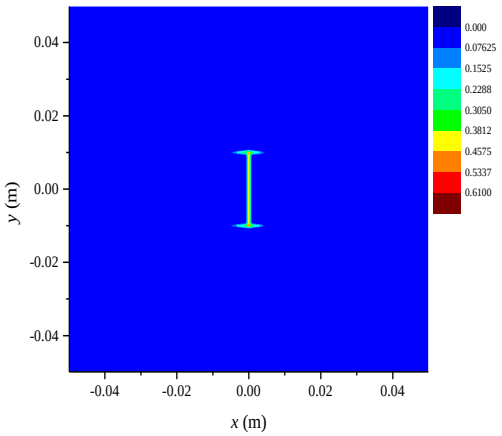

(a)

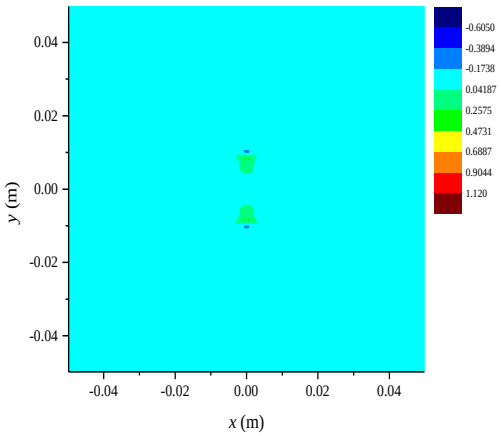

(b)

Fig. 4-30 (a) Matrix damage plot (b) Temperature change distributions (K) for case 1 at $t = 8\,\mu\mathrm{s}$.

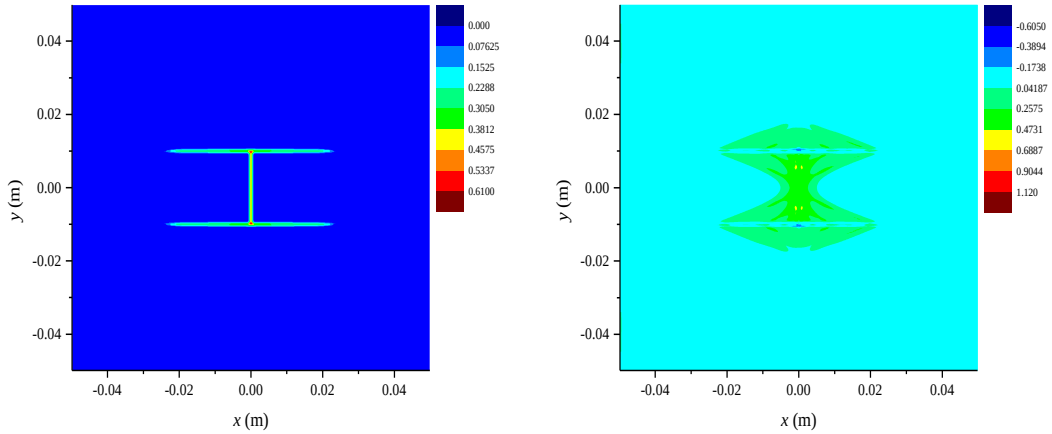

(a) (b)

Fig. 4-31 (a) Matrix damage plot (b) Temperature change distributions (K) for case 1 at $t = 11\,\mu\mathrm{s}$.

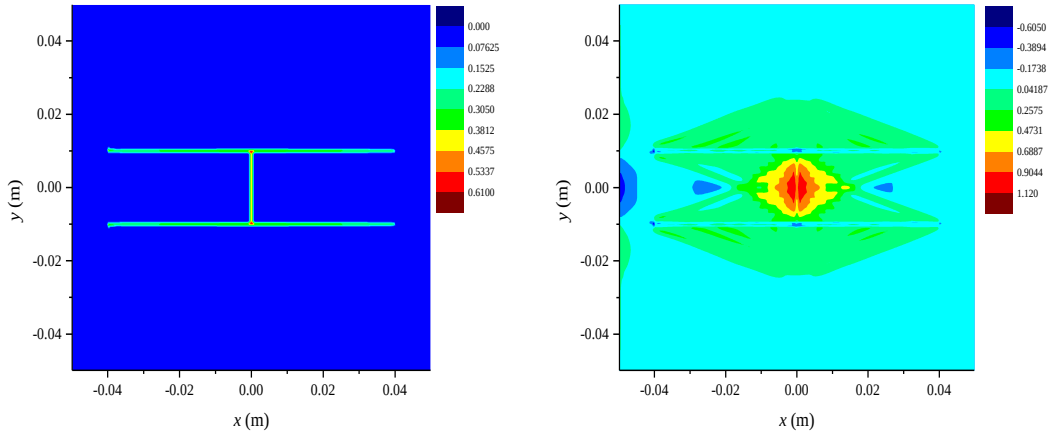

(a) (b)

Fig. 4-32 (a) Matrix damage plot (b) Temperature change distributions (K) for case 1 at $t = 14\,\mu\mathrm{s}$.

The crack growth and temperature change predictions at different time steps are provided from Fig. 4-33 to Fig. 4-35 for case 2. Similar to case 1, the crack propagates along the fibre direction, indicating the fibre/matrix debonding. Only the splitting failure mode is observed in the PD prediction, which is consistent with the experimental observations from [96, 97]. The temperature drops at crack tips are observed from Fig. 4-33 to Fig. 4-35.

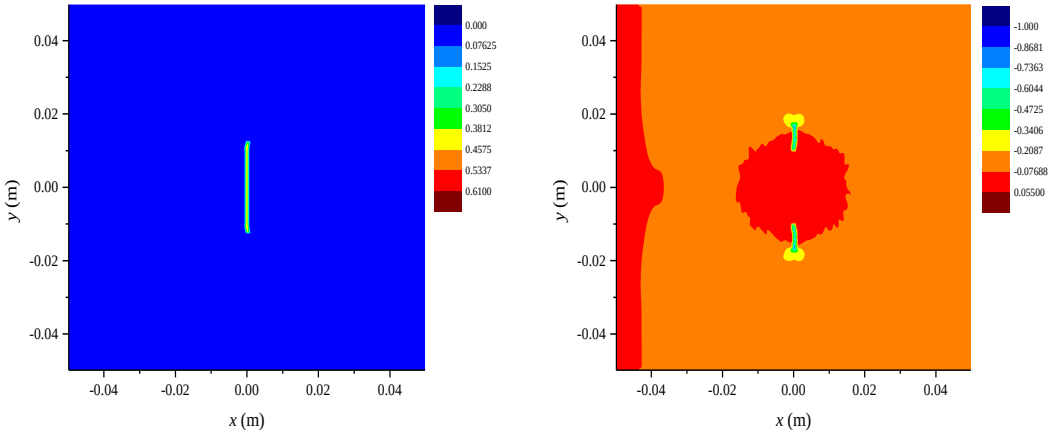

(a) (b)

Fig. 4-33 (a) Matrix damage plot (b) Temperature change distributions (K) for case 2 at $t = 7.5\,\mu\mathrm{s}$

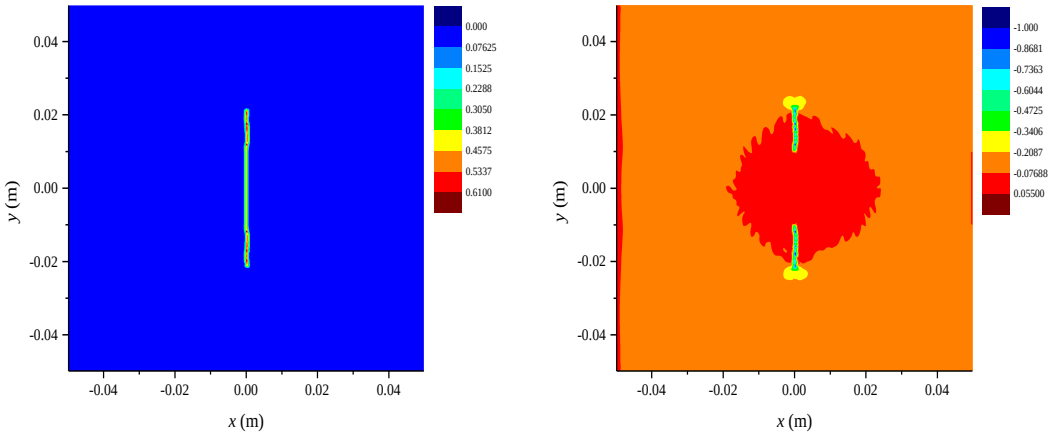

(a) (b)

Fig. 4-34 (a) Matrix damage plot (b) Temperature change distributions (K) for case 2 at $t = 8\,\mu\mathrm{s}$.

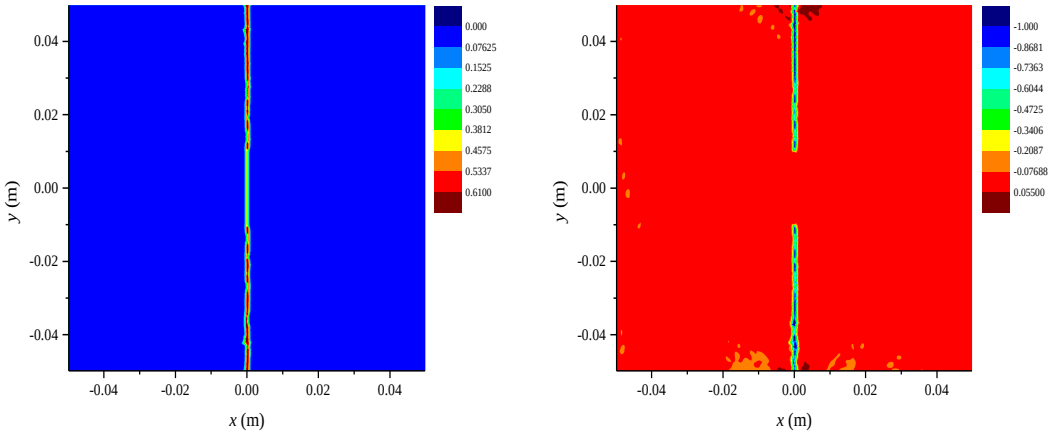

(a) (b)

Fig. 4-35 (a) Matrix damage plot (b) Temperature change distributions (K) for case 2 at $t = 10.5\,\mu\mathrm{s}$.

4.3.4.2 Multi-layer composite with a central crack

In this section, the crack propagation in a multi-layer composite is investigated. The load that is applied to investigate the damage pattern is given as;

$$P(t) = -3\times10^{14}\left(tH\left(t_0 - t\right) + t_0 H\left(t - t_0\right)\right)\ \text{Pa} \tag{4.59}$$

with $t_0 = 4\,\mu\text{s}$.

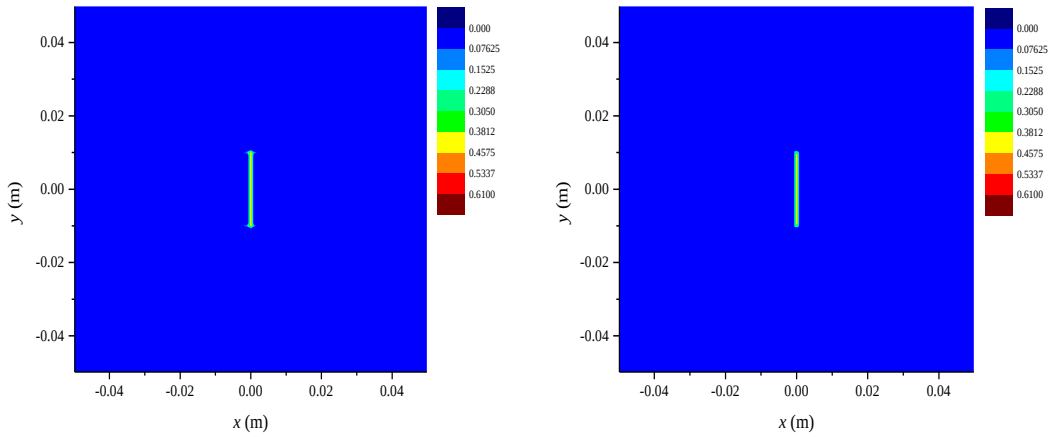

(a) (b)

Fig. 4-36 Matrix damage plot of (a) bottom ply and (b) middle ply at $t = 8\,\mu\text{s}$.

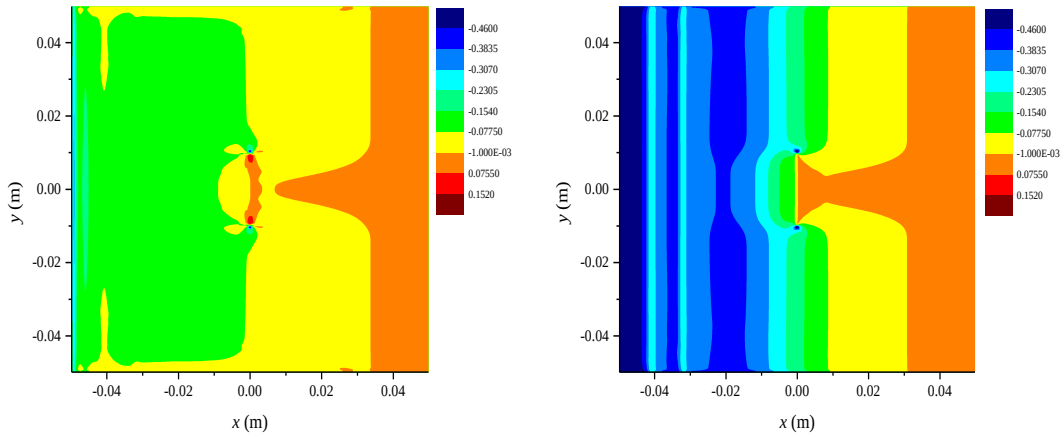

(a) (b)

Fig. 4-37 Temperature change distributions (K) for (a) bottom ply and (b) middle ply at $t = 8\,\mu\text{s}$.

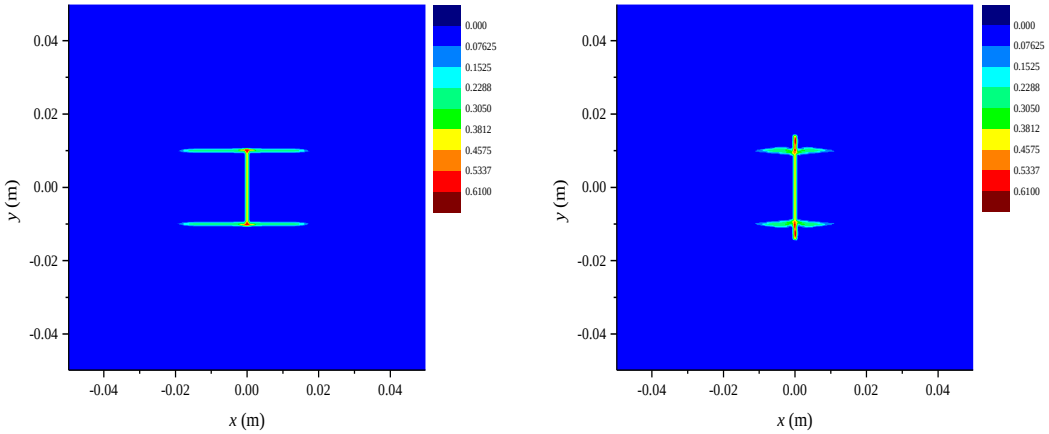

(a) (b)

Fig. 4-38 Matrix damage plot of (a) bottom ply and (b) middle ply at $t = 11\,\mu s$.

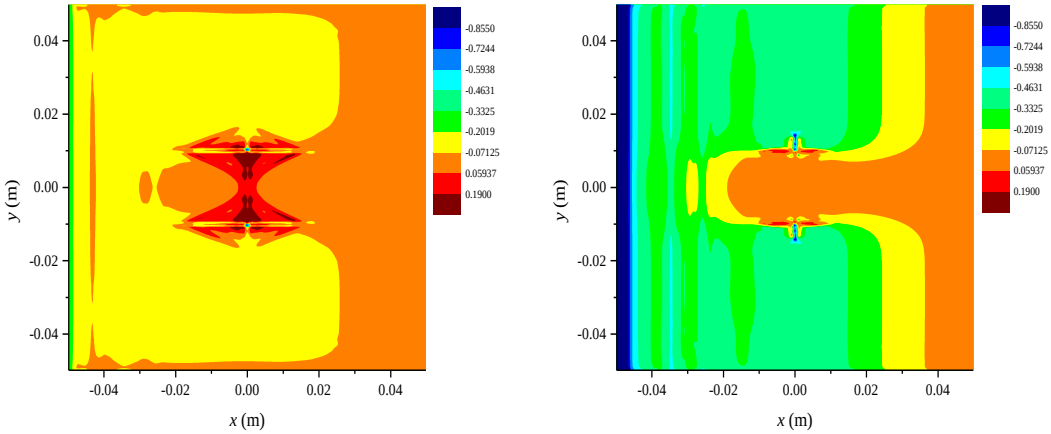

(a) (b)

Fig. 4-39 Temperature change distributions (K) for (a) bottom ply and (b) middle ply at $t = 11\,\mu s$.

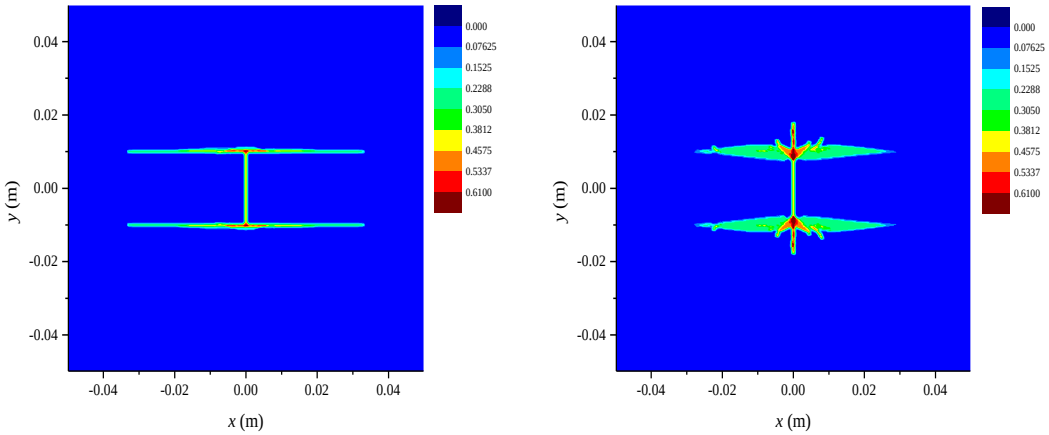

(a) (b)

Fig. 4-40 Matrix damage plot of (a) bottom ply and (b) middle ply at $t = 14\,\mu s$.

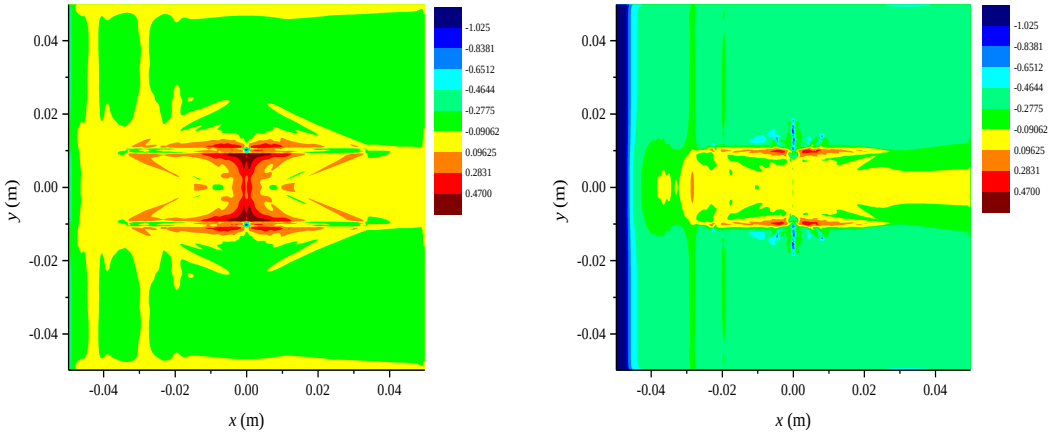

(a) (b)

Fig. 4-41 Temperature change distributions (K) for (a) bottom ply and (b) middle ply at $t = 14\,\mu\mathrm{s}$.

The damage plots for in-plane matrix bonds and their corresponding temperature change distributions at different time steps are presented from Fig. 4-36 to Fig. 4-41. For the laminate, an "H" type splitting failure mode is observed for all plies, which agrees with the findings in [76] and the experimental results in [98]. It is observed that the matrix breakage in the top or bottom plies shown in Fig. 4-40 (a) is similar to damage pattern obtained for a single layer composite model with $\Phi = 0^{\circ}$ fibre direction as shown in Fig. 4-32 (a). However, as shown in Fig. 4-40 (b)), the middle ply apparently has a bigger damage zone than the other two plies, which is consistent with the conclusions in [99]. This is due to the alignment of the fibres. Since the fibres are not aligned with the loading direction in the middle ply, the extent of damage is bigger than the other two layers. This is also indicating the different damage levels in multi-layer composites. Furthermore, the crack grows both in the fibre direction and in the transverse direction in the middle ply, presenting a different crack growth path compared with the predictions from the analysis of the single-layer composite model with $\Phi = 90^{\circ}$ as shown in Fig. 4-35 (a). As a result, a complex damage mode is presented in the middle ply [93]. The interaction between the plies is taken into account through interlayer bonds. It is also observed that the crack pattern has an influence on the induced temperature distribution.

4.4. Marine composites under shock loads

Nowadays, composite materials have been increasingly used in marine structures because of their high-performance properties. During their service time, they may be exposed to extreme loading conditions such as underwater explosions. Temperature changes induced by pure mechanical shock loadings cannot be neglected especially when smart composite materials are employed for condition monitoring of critical systems in a marine structure. Considering this fact, both the thermal loading effect on deformation and the deformation effect on temperature need to be taken into consideration. Consequently, an analysis conducted in a fully coupled thermomechanical manner is necessary. Peridynamics is a newly proposed non-local theory which can predict failures without extra assumptions. Therefore, a fully coupled thermomechanical peridynamic model is developed for laminated composites materials. In this study, numerical analysis of a 13-ply laminated composite subjected to an underwater explosion is conducted by using the developed model. The pressure shocks generated by the underwater explosion are applied on the top surface of the laminate for uniform and non-uniform load distributions. The damage is predicted and compared with existing experimental results. The simulation results obtained from the uncoupled case are also provided for comparison. Thus, the coupling term effects on crack propagation paths are investigated. Furthermore, the corresponding temperature distributions are also investigated.

4.4.1. Introduction

Laminated composite materials have many outstanding mechanical, physical, and chemical properties. For example, they are an easily fabricated and cost-effective alternative to some other monolithic materials [100]. Therefore, in recent years, composites have become common materials in marine industries. One application is for the construction of military vessels [101]. Composite materials can provide low-radar signatures for stealth operations. In addition, the low electro-magnetic signature these materials provide can reduce the possibility of detonating magnetic sea mines [102]. However, due to the special working conditions for military vessels, the composite materials may be subjected to some severe environments, such as

mechanical shock loads, large temperature variations, and exposures [103]. Hence, the damage level of composites induced by such extreme loading conditions becomes a critical factor with regards to the safety issue in the designation of the vessels. As a result, the failure analyses of composite materials under shock loadings draws a lot of interest and has been investigated for years.

In addition to the complexity of the composite material properties, shock loadings, which result in high strain rates, also give rise to additional complexity in the analysis. Large safety factors are typically used in composite structure design to make sure no damage will occur, resulting in a conservative solution or over-design [104]. Therefore, a good understanding of the responses of composite materials under shock loadings (i.e., explosions) is necessary for the balance between safety and economy issues.

There are three major methods to investigate the responses of composite materials under explosions: the experimental method, the analytical method, and the numerical simulation method. As to the experiment method, there are two kinds of experimental tests, according to the scale, i.e., a full-scale test and a laboratory-scale test. The full-scale explosive tests can provide important information on survivability, damage tolerance, and failure modes [105]. They are necessary to validate the results of analytical and numerical simulations [106]. In 1989, a 3 m × 3 m composite plate was tested under an underwater blast, to be investigated in full scale [107]. However, the full-scale tests are performed infrequently, due to high costs. For this reason, the explosive test in the laboratory scale is adopted for the research. A divergent shock tube was designed to investigate the responses of a clamped test plate under shock loadings [108]. Thus, plane wave fronts and wave parameters were easily controlled and repeated. LeBlanc and Shukla used a tube filled with water to reproduce the underwater explosive loads [109]. Wadley [110] developed another test method to investigate the compressive responses of multi-layered lattices during underwater shock loadings. Analytical methods are generally adopted in the initial design state of composite structures, which give relatively faster solutions compared to the other two methods. Rabczuk et al. [111] proposed a simplified method to investigate the effects of fluid-structure interaction in composite structures subjected to dynamic underwater loads. Hoo Fatt and Palla [112] derived analytical solutions for transient response and

damage initiation of a composite panel subjected to blast loading. However, analytical solutions are mainly limited to special and simple cases. In contrast, numerical simulation methods can be applied to various types of loadings, complicated geometries of structures, and complex boundary conditions. Kazancı [113] conducted a review of the available numerical achievements regarding the simulation of composite plates under a blast load. The finite element method (FEM) [114], smooth particle hydrodynamics (SPH) [115], and the finite strip method (FSM) [116] have all been applied to model composite materials.

When explosion loads are applied to the test plate, the plate experiences high strain rate stages. Therefore, the coupling effect of deformation on temperature cannot be neglected, which may have an effect on the crack propagation path with the induced temperature changes. Therefore, a fully coupled thermomechanical composite model is necessary for the simulation of thermal and mechanical responses of composites under shock loadings. Here, a fully coupled approach means both the temperature effects on deformation and the deformation effects on temperature are included in the simulation [18]. In this section, the responses of a 13-ply composite plate subjected to an underwater explosion load are studied, by considering the fully coupled thermomechanical effects. The crack propagation evolutions are predicted and compared with uncoupled cases. The predicted temperature distributions are also provided.

4.4.2. Numerical simulation

4.4.2.1 Problem description

The bond-based PD laminate model provided in Section 4.2.3 is implemented in FORTRAN program to predict the responses of a 13 ply laminate subjected to shock loading which was previously considered by Diyaroglu et al. [86]. Note that, in this study, the temperature changes due to mechanical deformations and their effects on damage evolution are taken into account by solving fully coupled thermomechanical equations whereas thermal effects are ignored in [86]. The heat conduction equation and the equation of motion are solved simultaneously for each time increment by using explicit time integration. The composite material properties are provided in Table 3.

Table 3. Material properties of 13 plies composite material [86].

Mechanical Properties		Thermal Properties	
$E_1\,(\mathrm{GPa})$	39.3	$\alpha_1\,(\mu\mathrm{m/m/K})$	8.6
$E_2\,(\mathrm{GPa})$	9.7	$\alpha_2\,(\mu\mathrm{m/m/K})$	22.1
$G_{12}\,(\mathrm{GPa})$	3.32	$k_1\,(\mathrm{W/mK})$	10.4
Poisson's ratio ν_{12}	0.33	$k_2\,(\mathrm{W/mK})$	0.89
$\rho\,(\mathrm{kg/m^3})$	1850	$c_v\,(\mathrm{J/(kg\cdot K)})$	879
$E_m\,(\mathrm{GPa})$	3.792	$\alpha_m\,(\mu\mathrm{m/m/K})$	63
$G_m\,(\mathrm{GPa})$	1.422	$k_m\,(\mathrm{W/mK})$	0.34
Poisson's ratio ν_m	0.33	$\Theta_0\,(\mathrm{K})$	285

Because of the adoption of bond-based PD, the major shear modulus changed to be 3.32 GPa according to the constraint on material constants. As illustrated in Fig. 4-42, the 13 ply test plate is in a circle shape with outer radius, $R_{out}=132.715\,\mathrm{mm}$ and inner radius, $R_{in}=114.3\,\mathrm{mm}$. The thickness of each ply in the laminate is the same as $h=0.254\,\mathrm{mm}$. The region between the inner circle and outer circle is constrained in top and bottom plies and is left free for other plies. The constraint is implemented by applying six bolts with a radius of $r=4\,\mathrm{mm}$. Thus the fixed end allows the specimen to absorb the full energy of the applied load. The stacking sequence is $\left[0/90/0/90/0/90/\bar{0}\right]$ (shown in Fig. 4-42).

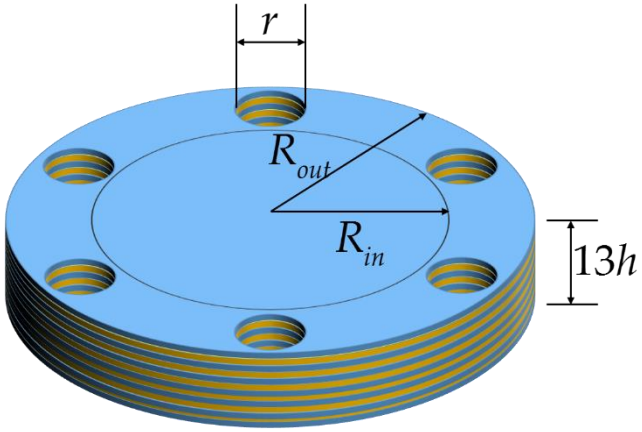

Fig. 4-42 Geometry dimension illustration of the test laminate. (Blue colour represents 0^o and yellow colour represents 90^o plies).

The PD discretization of one-ply is presented in Fig. 4-43. The grid size is $\Delta x = 2.6543\times10^{-3}$ m. The horizon size is chosen as $\delta = 3.015\Delta x$. The material points located within the bolt regions are deleted in order to represent the actual shape of the test plate. Based on such discretization, the critical stretch value related to bonds failures can be calculated [75]. The critical energy release rate for matrix failure is $G_{IC} = 11.85\times10^{-3}$ MPa, thus s_m is calculated as $s_m = 1.47\times10^{-2}$. The tension and compression strength properties are $\sigma_{1t} = 965$ MPa and $\sigma_{1c} = -883$ MPa. Therefore, the critical stretch value for fibre failure in tension is $s_{ft} = 2.46\times10^{-2}$ and in compression is $s_{fc} = -2.25\times10^{-2}$. As to the interlayer bonds, the critical stretch values are calculated as $s_{in} = 7.015\times10^{-2}$ with $G_{IC} = 2.73\times10^{-3}$ MPa and $\phi_{is} = 0.14$ with $G_{IIC} = 7.11\times10^{-3}$ MPa. The time step size for explicit time integration is $\Delta t = 7.69\times10^{-8}$ s. The total simulation time is set 0.3641×10^{-3} s.

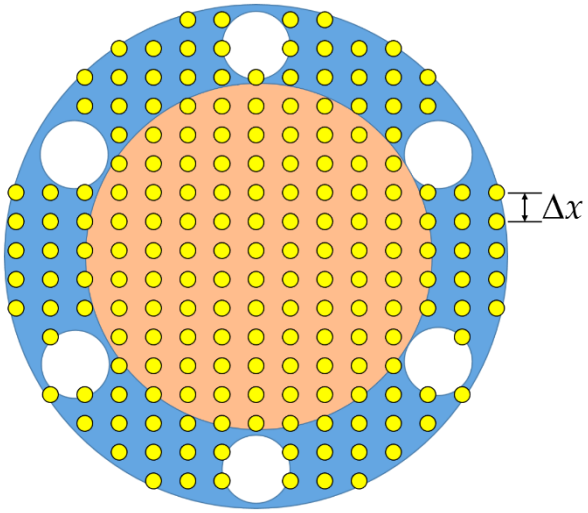

Fig. 4-43 Illustration of PD discretization for one ply (blue colour represents the fixed boundary region and orange colour represents the inner part).

Several dynamic loadings generated by explosions are modelled by using different time-dependent pressure functions. The pressure shock applied in the experiment conducted by LeBlanc and Shukla [104] is utilized here. The charge which is equivalent to 1.32 g TNT is located at 5.25 m away from the test plate. The pressure

wave is caused by the rapid expansion of explosive gases. The speed of these gases can be approximated as the speed of sound in water [117]. The pressure linearly increases until it reached its peak value, $P_{\max}$, followed by the exponential decay, expressed in Eq.(4.60) and shown in Fig. 4-44. Here $P_{\max}$ is set to be 9.65 MPa.

$$P(t)=\begin{cases} P_{\max}\times\left(t/4\times10^{-5}\right), t<0.04\times10^{-3}\ \text{s} \\ P_{\max}, \qquad 0.04\times10^{-3}\ \text{s}<t<0.08\times10^{-3}\ \text{s} \\ P_{\max}e^{-1000(t-0.08)/0.2}, \quad 0.04\times10^{-3}\ \text{s}<t<1\times10^{-3}\ \text{s} \end{cases} \tag{4.60}$$

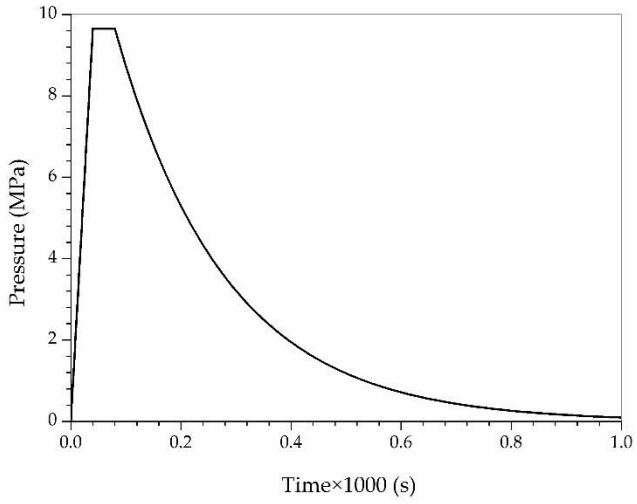

Fig. 4-44 Pressure load distribution for the test plate.

Generally, there are two approaches for modelling the shock load depending on the distance (stand-off distance) between the charge source and the object of interest [113]. The explosion load is assumed to be uniform if the stand-off distance is long enough, which is termed as a far-field explosion. On the contrary, the near-field explosion adopts non-uniform load distribution. There are also two approaches to simulate the non-uniform pressure shock loads, i.e., decoupling the load and the structural response and coupling the load and response. In this subsection, a non-uniform pressure load simulated and decoupled approach is utilized, i.e., the pressure shock load is in a form of $P(r,t)=P_1(r)P_2(t)$. A non-uniform distribution of shock loading over the plate is simulated by adopting the pressure distribution derived by Turkmen and Mecitoglu [118] as

$$P(r) = -0.0005r^4 + 0.01r^3 - 0.0586r^2 - 0.001r + 1 \tag{4.61}$$

where r represents the distance from the collective node to the centre of the test plate. The test plate adopted here is slightly larger than the one in [118]. Consequently, the distribution profile is extended by 0.83 cm correspondingly, as illustrated in Fig. 4-45. Finally, the explosion load is defined as

$$P(r,t) = \begin{cases} P(t)\begin{pmatrix} -0.0005(r-0.83)^4 + 0.01(r-0.83)^3 \\ -0.0586(r-0.83)^2 - 0.001(r-0.83) + 1 \end{pmatrix}, & r > 0.83\,\text{cm} \\ P(t), & r < 0.83\,\text{cm} \end{cases} \tag{4.62}$$

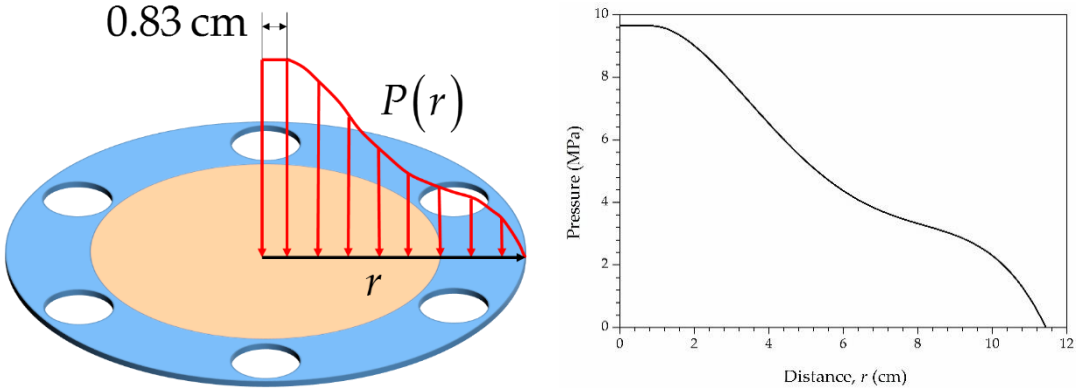

(a) (b)

Fig. 4-45 (a) Illustration of non-uniform pressure distribution over the top ply and (b) pressure profile.

4.4.2.2 Subjected to uniform pressure loading

First, the test laminate is subjected to uniform pressure load, $P(t)$ without allowing failure. The regions between the inner circle and outer circle are fixed in three dimensions for all plies. During the simulation, the central points in each ply experience the same vertical (z) displacement evolutions. Therefore, the vertical displacement evolution of the central point on the top ply is plotted in Fig. 4-46(a). It can be observed that the test plate firstly deforms in the negative z-direction, then it will recover to some extent with a velocity in the positive z-direction. The largest deformation occurs at approximately 3700 time steps, corresponding to

0.28453×10^{-3} s . The vertical displacement distribution over the top ply at 0.28453×10^{-3} s is shown in Fig. 4-46(b).

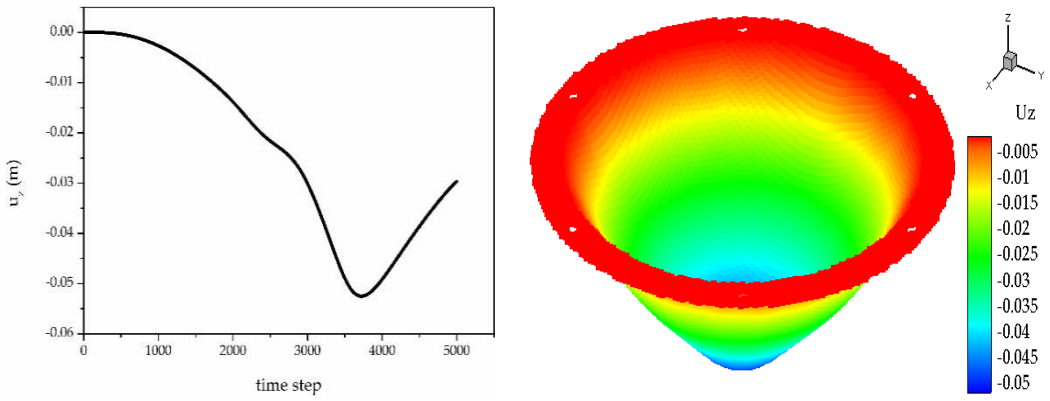

(a) (b)

Fig. 4-46 (a) Variation of the displacement in *z* direction of the central point as a function of time; (b) Vertical displacement distribution for the top ply at 0.28453×10^{-3} s .

Fully coupled thermomechanical simulation under the uniform pressure load $P(t)$, i.e., far-field explosion, is also investigated for further comparison. The crack propagations and temperature change distributions at 0.1538×10^{-3} s are provided in Fig. 4-47 for top ply, Fig. 4-48 for middle ply, and Fig. 4-49 for bottom ply. It can be inferred from the matrix damage plots that all the plies in the laminate experience the tear failure near the constraint boundary condition. Furthermore, the damage region in the bottom ply is larger than the top ply, indicting a combination of tension failure mode and tear failure mode. As to the temperature distribution, the temperature increases near cracks are observed for all plies, which are more obvious in the top ply provided in Fig. 4-47(b). The temperature drop is also observed in a tension state, which is obvious in the bottom ply provided in Fig. 4-49(b).

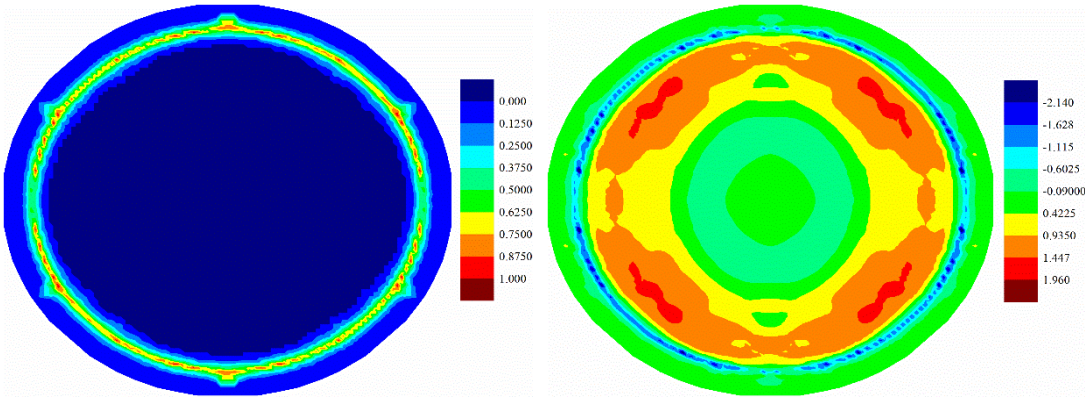

(a) (b)

Fig. 4-47 (a) Matrix damage and (b) temperature change distribution (K) of top ply at 0.1538×10^{-3} s.

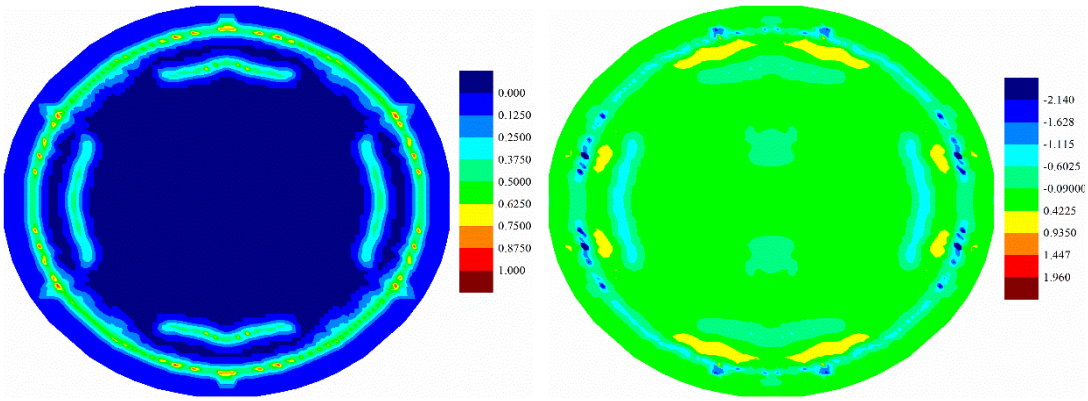

(a) (b)

Fig. 4-48 (a) Matrix damage and (b) temperature change distribution (K) of middle (7th) ply at 0.1538×10^{-3} s.

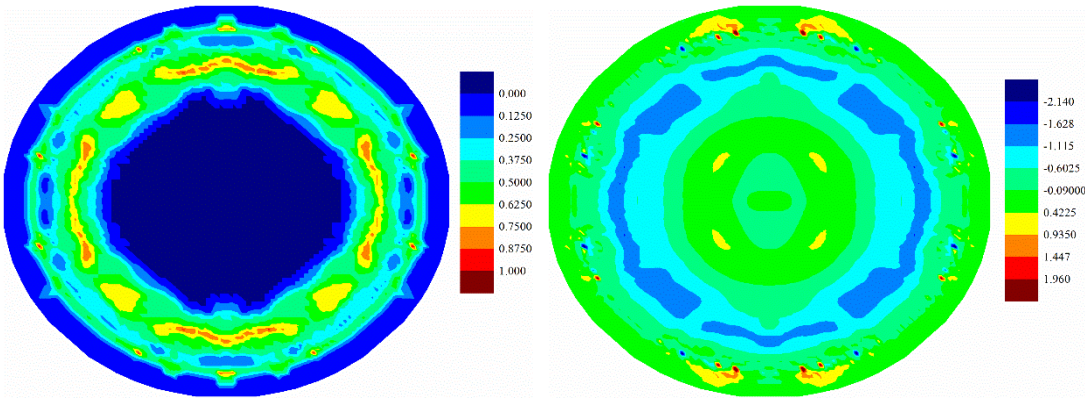

(a) (b)

Fig. 4-49 (a) Matrix damage and (b) temperature change distribution (K) of bottom ply at 0.1538×10^{-3} s.

4.4.2.3 Subjected to uniform non-uniform pressure load

In this section, the test laminate is subjected to non-uniform pressure load $P(r,t)$, i.e., near field explosion. The matrix damage and temperature distribution in deformed shape are provided in Fig. 4-50. Matrix damage predictions at 0.28453×10^{-3} s and 0.3461×10^{-3} s obtained from coupled and uncoupled cases are shown from Fig. 4-51 to Fig. 4-56.

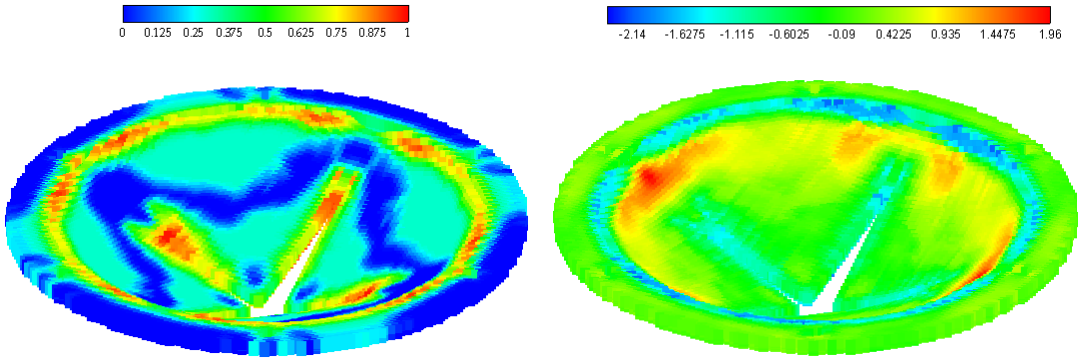

(a) (b)

Fig. 4-50 (a) Matrix damage and (b) temperature change distribution (K) of the laminate at 0.3461×10^{-3} s.

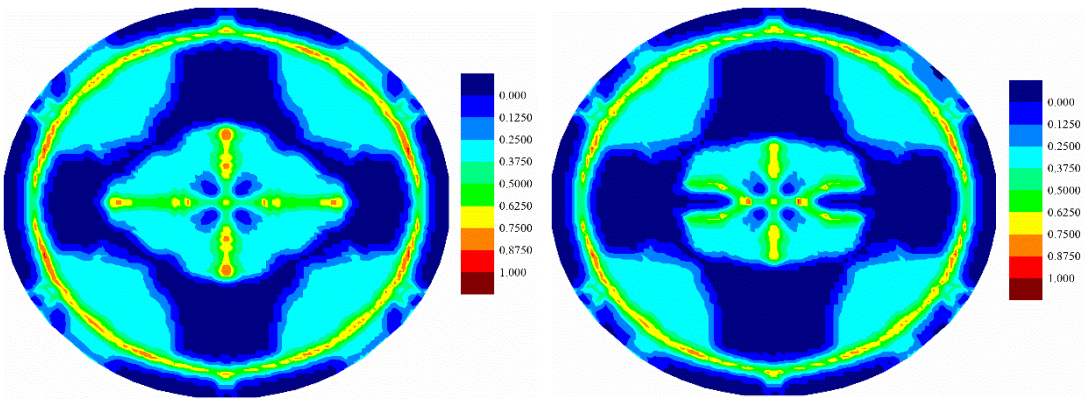

(a) (b)

Fig. 4-51 Matrix damage comparison of top ply for (a) coupled case and (b) uncoupled case at 0.28453×10^{-3} s.

For the fully coupled simulation case, by comparing the damage of the plies at different times, it is obvious that the damaged zone gets larger as time progresses. The damage patterns are different for each ply when compared at the same time. The cracks mainly occur near the clamped boundary region for the top ply, indicating a tear failure mode. On the other hand, the central part experiences the largest level of damage for

the bottom ply, indicating a tension failure mode. Consequently, the different force states give rise to a different level of damages. However, for all plies, the crack propagations present a cross-shaped pattern. It can be explained that the fibre direction of each ply is either zero or 90 degrees. The matrix damage occurs parallel to the fibre direction. For a ply with fibre direction being zero, the matrix crack will occur along the horizontal direction. However, the fibre directions for its adjacent plies are 90 degrees. Hence, the matrix crack will also occur in the vertical direction due to the contribution of the interlayer bonds. Consequently, the final cracks are in cross shapes. The damages present highest levels near the central vertical lines for all plies. This phenomenon is also observed in the experiment [109], as shown in Fig. 4-57. As it can be seen from Fig. 4-47 to Fig. 4-49, there are damages around the bolt holes and these damages were also observed in experiments [109] as it can be seen in Fig. 4-57.

As shown in Fig. 4-51 to Fig. 4-56, different damage patterns are observed for coupled and uncoupled cases. As time progresses, temperature change increases and the differences in damage plots become more obvious. Considering the small temperature changes induced by the applied pressure shock, the coupling term effect on damage is significant. It can be inferred that the difference in damage due to coupling effect will become more significant with larger strain rates. Temperature decreases where there is local tension and as a result, local compression is created due to temperature drop which reduces the extent of damage observed by the uncoupled cases (Fig. 4-51 to Fig. 4-56).

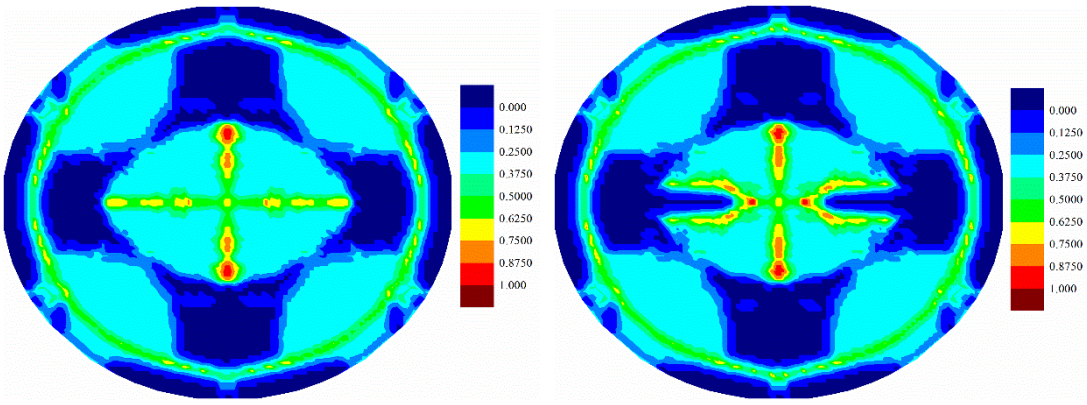

(a) (b)

Fig. 4-52 Matrix damage comparison of middle (7th) ply for (a) coupled case and (b) uncoupled case at 0.28453×10^{-3} s.

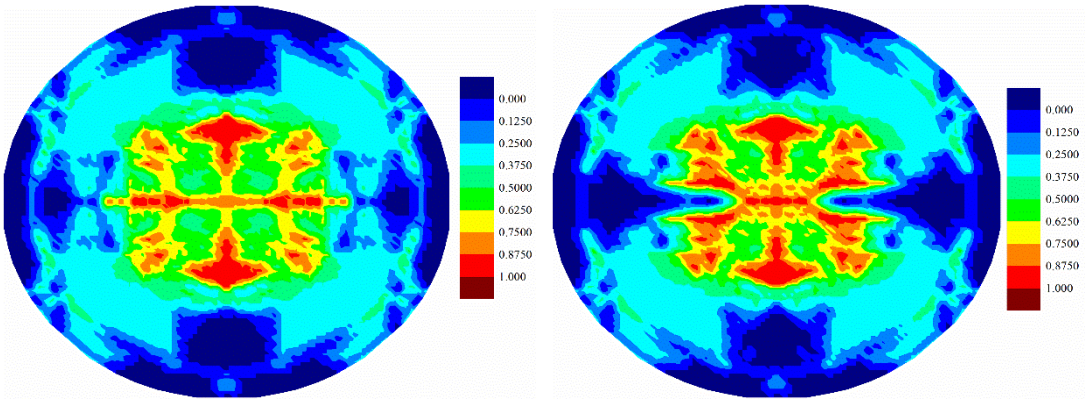

(a) (b)

Fig. 4-53 Matrix damage comparison of bottom ply for (a) coupled case and (b) uncoupled case at 0.28453×10^{-3} s.

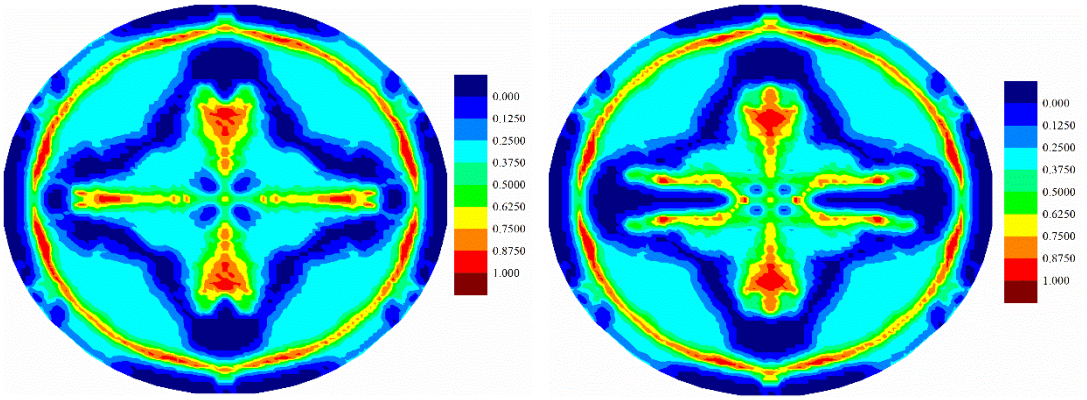

(a) (b)

Fig. 4-54 Matrix damage comparison of top ply for (a) coupled case and (b) uncoupled case at 0.3461×10^{-3} s.

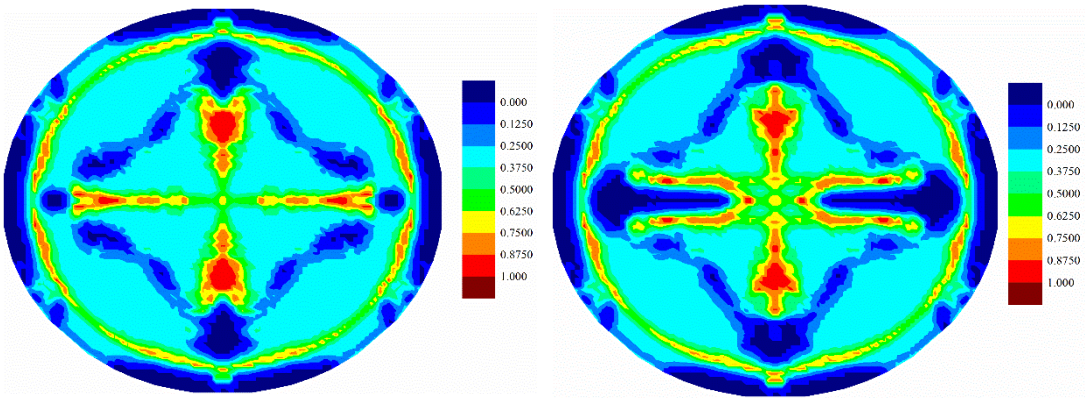

(a) (b)

Fig. 4-55 Matrix damage comparison of middle (7th) ply for (a) coupled case and (b) uncoupled case at 0.3461×10^{-3} s.

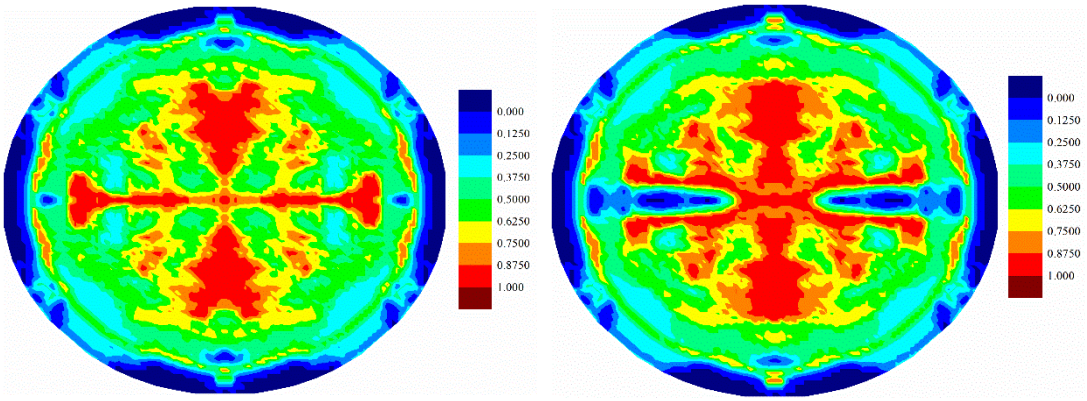

(a) (b)

Fig. 4-56 Matrix damage comparison of bottom ply for (a) coupled case and (b) uncoupled case at 0.3461×10^{-3} s .

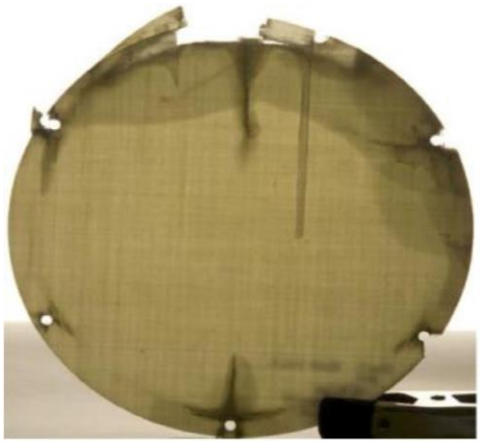

Fig. 4-57 Material damage during test [109].

The extent of damage in interlayer shear bonds was also investigated, and only slight differences were observed in the top few plies between the coupled and uncoupled cases (Fig. 4-58). The middle ply experienced the most severe damage, as shown in Fig. 4-59. Thus, it can be inferred that the interlayer shear bond damages occur mainly in the middle plies of the test laminate. Hence, it can be concluded that there is delamination failure in the middle plies.

Temperature changes induced by the applied pressure shock loading are presented for different plies in Fig. 4-60 to Fig. 4-62. It is observed that as the loading increased, the temperature changes of PD nodes increased. For all plies, the temperature change profiles all have similar patterns as the corresponding crack damage patterns. As shown in Fig. 4-60 to Fig. 4-62, there is a temperature rise where there is local compression, and there is a temperature drop where there is local tension, as explained

in [10]. In the top ply, most of the region was under compression and temperature rise was observed; on the other hand, the bottom ply was mostly under tension, and a consequent temperature drop was observed, as shown in Fig. 4-62. In the cracked surfaces, temperature drops were observed because of the local tension; however, the temperature rise was observed near the crack tips. Thus, the crack propagation paths do have effects on the temperature distributions.

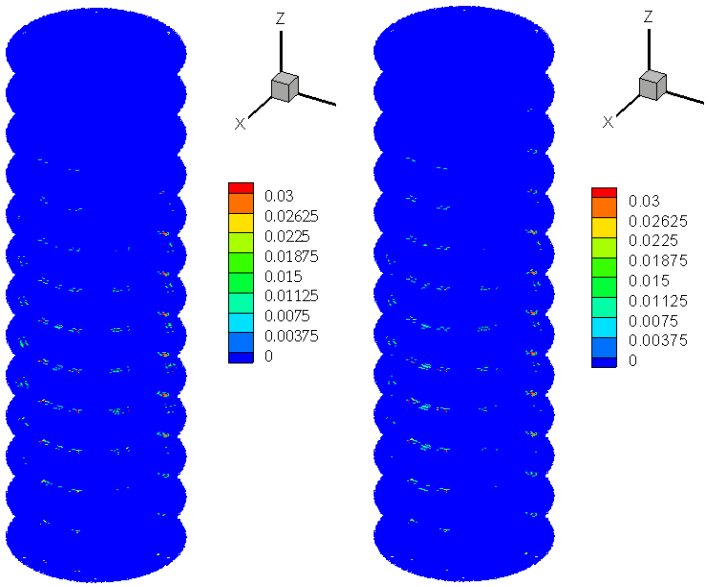

(a) (b)

Fig. 4-58 Interlayer shear damage comparison for (a) coupled case and (b) uncoupled case at 0.3461×10^{-3} s .

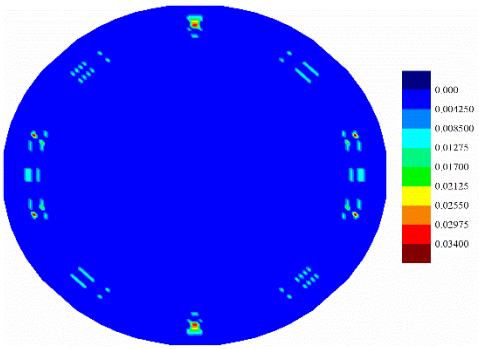

Fig. 4-59 Interlayer shear damage of middle ply in coupled case at 0.3461×10^{-3} s .

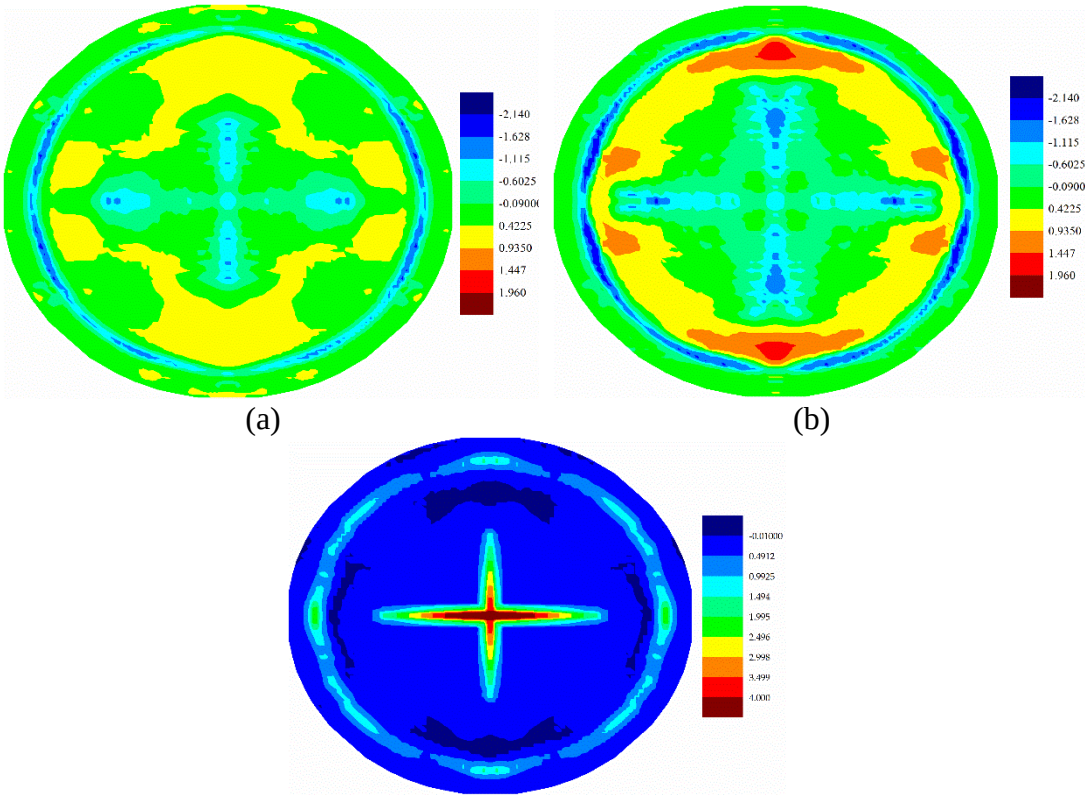

(a) (b)

(c)

Fig. 4-60 (a) Distribution of temperature change (K) of top ply at 0.28453×10^{-3} s; (b) Distribution of temperature change (K) of top ply at 0.3461×10^{-3} s; (c) Maximum stretch distribution of top ply at 0.3461×10^{-3} s.

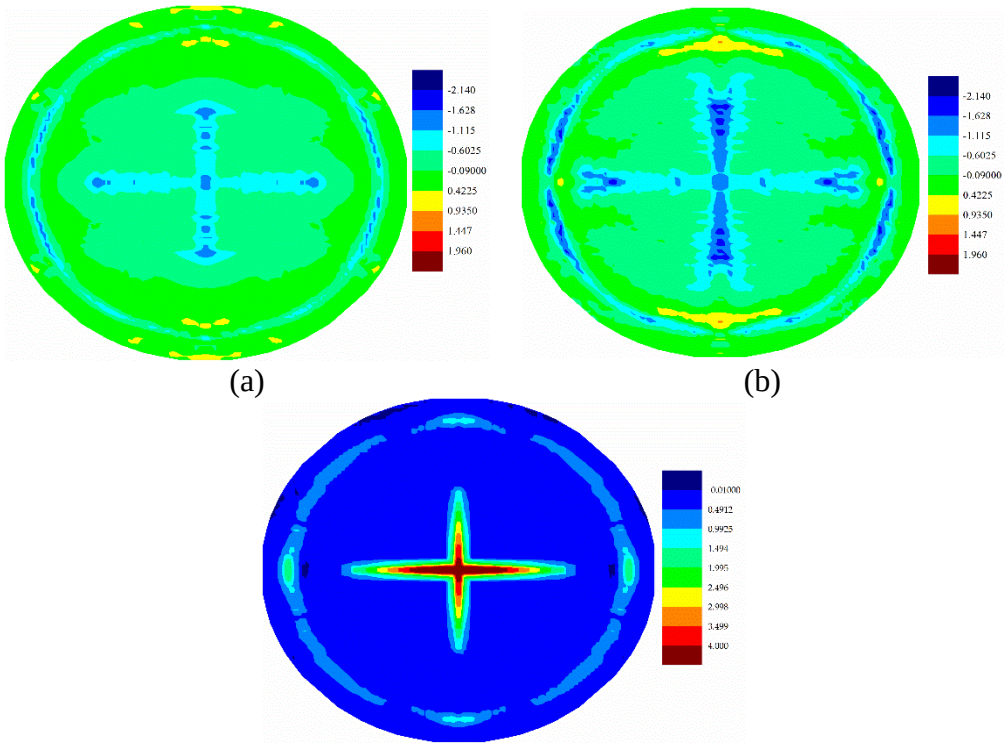

(a) (b)

(c)

Fig. 4-61 (a) Distribution of temperature change (K) of middle ply at 0.28453×10^{-3} s ; (b) Distribution of temperature change (K) of middle ply at 0.3461×10^{-3} s ; (c) Maximum stretch distribution of middle ply at 0.3461×10^{-3} s .

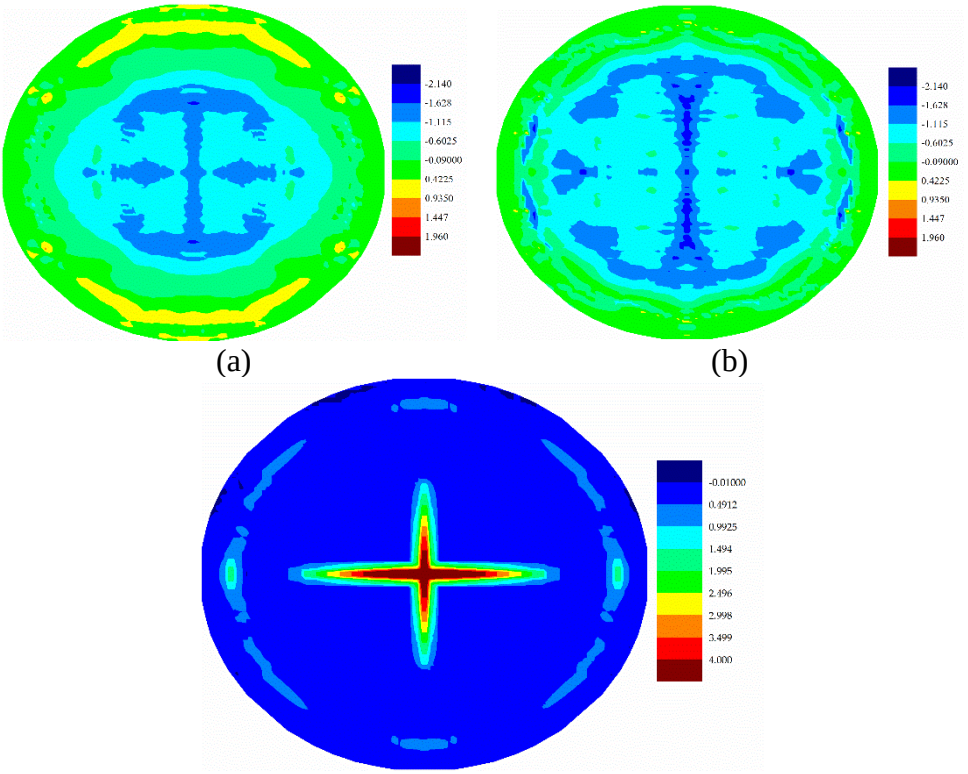

(a) (b)

(c)

Fig. 4-62 (a) Distribution of temperature change (K) of bottom ply at 0.28453×10^{-3} s ; (b) Distribution of temperature change (K) of bottom ply at 0.3461×10^{-3} s ; (c) Maximum stretch distribution of bottom ply at 0.3461×10^{-3} s .

4.5. Summary

In this chapter, a fully coupled thermomechanical model formulated by ordinary state-based peridynamic theory is proposed both for single layer and multi-layer composites. Subsequently, numerical simulations of some benchmark problems are conducted for the validation of the developed model. The temperature and deformation fields are investigated by considering the coupling effects in both fields. Consequently, the present model is validated by comparing peridynamic simulations with ANSYS results. Finally, failure analyses are conducted with pre-existing cracks on single layer and multi-layer models. The progressive crack propagations and temperature distribution evolutions are discussed. As an application case, a bond-based PD

laminate model was applied to predict the responses of a 13-ply composite under a pressure shock loading.

The following conclusions can be drawn:

1. The present model in the framework of ordinary state-based peridynamic theory is capable of predicting the deformation of multi-layer composites under thermal loads.

2. The developed PD thermal model can be applied in heat conduction simulations for multi-layer composites.

3. The proposed fully coupled ordinary state-based thermomechanical model can be applied to predict the crack propagation for composites. The induced temperature distribution evolution can also be predicted.

5. Isothermal and Non-isothermal Fluid Laminar Flow Simulation

5.1. Introduction

The fluid and structure interaction is often encountered in ocean engineering, e.g. floating structures and water waves interactions [119], sloshing in a water tank [120], green water impact [121] etc. The fluid motion is a crucial issue because of the fluid-induced movements such as heaving and rolling of the offshore structures. Sometimes the fluid may even also cause considerable pressure loadings on the offshore structure and make local damages of these structures [119]. Therefore, an accurate fluid motion prediction is necessary for a fluid-structure interaction simulation in the field of ocean engineering. Peridynamics [4] has been applied on the numerical simulations of offshore structure damage in the ocean engineering field, e.g. the ship-ice interaction [122-124]. It will be beneficial to simulate both the structure and fluid with the same methodology, e.g. peridynamics. Therefore, a peridynamic fluid model is provided in this section which can be further incorporated into the peridynamic solid model to simulate the fluid and structure interactions.

The Eulerian approach is adopted in most computational fluid dynamics (CFD) methodologies. Since CFD can solve fluid flow problems with any boundary and initial conditions, it has been widely used in academic research [125]. There are two types of computational Lagrangian approaches: total Lagrangian approach and updated Lagrangian approach. The total Lagrangian approach uses the initial configuration as the reference configuration, while the updated Lagrangian approach adopts the current configuration as the reference configuration. Smoothed Particle Hydrodynamics (SPH), which is an updated Lagrangian approach, is another widely used method for fluid flow simulations [126, 127]. SPH is a mesh-free particle method, and it does not need a grid to calculate spatial derivatives [128]. In addition, it is easy to work with and can give reasonable accuracy. Therefore, it draws a lot of attention in recent years.

Since the PD is originally proposed for structural mechanical problems, it is generally applied to predict fracture in solids [4, 10, 76, 78, 129]. Later on, the peridynamic theory has been applied in other fields [130]. However, the application of PD on fluid mechanics has not been extensively studied, only a few PD fluid models are available in the published literature [55, 131-134]. A state-based peridynamic formulation is presented by Katiyar et al. [135] to simulate the fluid flow in porous media. Later on, the model is applied to simulate the growth of fluid-driven cracks in porous and fractured media [134]. A fully coupled poroelastic peridynamic formulation is introduced by Oterkus et al. [55] to simulate fluid-filled fractures. In their model, the coupling effect of porous fluid flow and deformation of porous media is considered to predict the behaviour of fluid-filled fractures. However, in these PD models, the fluid flow was limited to porous flow. Therefore, the developed PD fluid models cannot be utilized for general fluid flow simulations. An Eulerian form of peridynamic model is presented to by Silling et al. [133] to simulate the shockwaves. In their model, the peridynamic forces are defined in the deformed configuration to simulate strong shock waves and fluid response for very large deformations. An updated Lagrangian PD model based on the state-based peridynamics concept is applied as Updated Lagrangian Particle Hydrodynamics (ULPH) to simulate Newtonian fluid flow [132]. In this chapter, the peridynamic differential operator is used to simulate low Reynolds number flow problems. Besides, a PPDO model is also developed to solve the problems of fluid flow coupled with heat transfer.

This chapter is organized as follows. Section 5.2 describes the developed non-local operator by using the peridynamic differential operator. Section 5.3 describes the non-local form of Navier-Stokes equations that are derived based on their local forms by using non-local velocity operator. Section 5.4 presents the numerical algorithms in the total Lagrangian description, updated Lagrangian description, and Euler description. In addition, the treatments regarding numerical simulation are explained. Section 5.5 presents a set of classical isothermal fluid flow problems, i.e. Couette flow, Poiseuille flow, Taylor Green vortex, shear driven cavity, and dam collapse problems, which are numerically simulated with the developed model. Subsequently, non-isothermal fluid flow simulation, i.e. a natural convection problem, a mixed convection problem, and

a pure heat conduction problem, are numerically conducted in Section 5.6. Finally, the conclusions are drawn in Section 5.7.

5.2. Non-local operator by using PD differential operator

In this section, the non-local form of velocity divergence, gradient, and second derivatives are developed to approximate their corresponding local operators. The non-local derivatives will be utilized in the derivation of the non-local form of Navier-Stokes equations in Section 5.3. PD differential operator tensors which are expressed in the matrix form are introduced as

For 3D

$$\mathbf{g}_1(\boldsymbol{\xi}) = \left[g^{100}(\boldsymbol{\xi})\, g^{010}(\boldsymbol{\xi})\, g^{001}(\boldsymbol{\xi}) \right] \tag{5.1a}$$

and

$$\mathbf{g}_2(\boldsymbol{\xi}) = \begin{bmatrix} g^{200}(\boldsymbol{\xi}) & g^{110}(\boldsymbol{\xi}) & g^{101}(\boldsymbol{\xi}) \\ g^{110}(\boldsymbol{\xi}) & g^{020}(\boldsymbol{\xi}) & g^{011}(\boldsymbol{\xi}) \\ g^{101}(\boldsymbol{\xi}) & g^{011}(\boldsymbol{\xi}) & g^{002}(\boldsymbol{\xi}) \end{bmatrix} \tag{5.1b}$$

For 2D

$$\mathbf{g}_1(\boldsymbol{\xi}) = \begin{bmatrix} g^{10}(\boldsymbol{\xi}) & g^{01}(\boldsymbol{\xi}) \end{bmatrix} \tag{5.1c}$$

and

$$\mathbf{g}_2(\boldsymbol{\xi}) = \begin{bmatrix} g^{20}(\boldsymbol{\xi}) & g^{11}(\boldsymbol{\xi}) \\ g^{11}(\boldsymbol{\xi}) & g^{02}(\boldsymbol{\xi}) \end{bmatrix} \tag{5.1d}$$

where $\mathbf{g}_1(\boldsymbol{\xi})$ and $\mathbf{g}_2(\boldsymbol{\xi})$ represent the first-order and second-order PD differential operators up to second-order derivatives, respectively. The components in $\mathbf{g}_1(\boldsymbol{\xi})$ and $\mathbf{g}_2(\boldsymbol{\xi})$ matrices are provided in Eq.(2.24) and Eq.(2.30), respectively. The analytical

expression of the 2D PDDO is provided in Appendix D. These matrices can also be expressed as

For 3D

$$\mathbf{g}_1(\boldsymbol{\xi}) = \begin{bmatrix} g_1^{(1)}(\boldsymbol{\xi}) & g_1^{(2)}(\boldsymbol{\xi}) & g_1^{(3)}(\boldsymbol{\xi}) \end{bmatrix} \tag{5.2a}$$

and

$$\mathbf{g}_2(\boldsymbol{\xi}) = \begin{bmatrix} g_2^{(1,1)}(\boldsymbol{\xi}) & g_2^{(1,2)}(\boldsymbol{\xi}) & g_2^{(1,3)}(\boldsymbol{\xi}) \\ g_2^{(2,1)}(\boldsymbol{\xi}) & g_2^{(2,2)}(\boldsymbol{\xi}) & g_2^{(2,3)}(\boldsymbol{\xi}) \\ g_2^{(3,1)}(\boldsymbol{\xi}) & g_2^{(3,2)}(\boldsymbol{\xi}) & g_2^{(3,3)}(\boldsymbol{\xi}) \end{bmatrix} \tag{5.2b}$$

For 2D

$$\mathbf{g}_1(\boldsymbol{\xi}) = \begin{bmatrix} g_1^{(1)}(\boldsymbol{\xi}) & g_1^{(2)}(\boldsymbol{\xi}) \end{bmatrix} \tag{5.2b}$$

and

$$\mathbf{g}_2(\boldsymbol{\xi}) = \begin{bmatrix} g_2^{(1,1)}(\boldsymbol{\xi}) & g_2^{(1,2)}(\boldsymbol{\xi}) \\ g_2^{(2,1)}(\boldsymbol{\xi}) & g_2^{(2,2)}(\boldsymbol{\xi}) \end{bmatrix} \tag{5.2b}$$

where the term $g_1^{(i)}(\boldsymbol{\xi})$ represents the elements in $\mathbf{g}_1(\boldsymbol{\xi})$ vector, $g_2^{(i,j)}(\boldsymbol{\xi})$ represents the elements in $g_2^{(i,j)}(\boldsymbol{\xi})$ matrix with $i, j = 1, 2, 3$.

Three-dimensional vectoral function for point $\mathbf{x}$ can be denoted as

$$\mathbf{f}(\mathbf{x}) = f_1(\mathbf{x})\mathbf{e}_1 + f_2(\mathbf{x})\mathbf{e}_2 + f_3(\mathbf{x})\mathbf{e}_3 \tag{5.3}$$

where the scalar values $f_1(\mathbf{x})$, $f_2(\mathbf{x})$ and $f_3(\mathbf{x})$ represent the projections of the function vector on the corresponding unit vectors.

5.2.1. Non-local form of divergence

The local form of divergence is defined as

$$\nabla \cdot \mathbf{f}(\mathbf{x}) = \frac{\partial f_1(\mathbf{x})}{\partial x_1} + \frac{\partial f_2(\mathbf{x})}{\partial x_2} + \frac{\partial f_3(\mathbf{x})}{\partial x_3} \tag{5.4}$$

As described by Eq.(2.29), by applying the first-order PD differential operator, $\mathbf{g}_1(\boldsymbol{\xi})$, the non-local form of the first-order derivatives can be evaluated as

$$\frac{\partial f_1(\mathbf{x})}{\partial x_1} = \int_{H_\mathbf{x}} \left(f_1(\mathbf{x}') - f_1(\mathbf{x}) \right) g_1^{(1)}(\boldsymbol{\xi}) \mathrm{d}V' \tag{5.5a}$$

$$\frac{\partial f_2(\mathbf{x})}{\partial x_2} = \int_{H_\mathbf{x}} \left(f_2(\mathbf{x}') - f_2(\mathbf{x}) \right) g_1^{(2)}(\boldsymbol{\xi}) \mathrm{d}V' \tag{5.5b}$$

$$\frac{\partial f_3(\mathbf{x})}{\partial x_3} = \int_{H_\mathbf{x}} \left(f_3(\mathbf{x}') - f_3(\mathbf{x}) \right) g_1^{(3)}(\boldsymbol{\xi}) \mathrm{d}V' \tag{5.5c}$$

Therefore, the non-local form of divergence can be expressed by using PD differential operator as

$$\begin{aligned} \nabla \cdot \mathbf{f}(\mathbf{x}) = & \int_{H_\mathbf{x}} \left(f_1(\mathbf{x}') - f_1(\mathbf{x}) \right) g_1^{(1)}(\boldsymbol{\xi}) \mathrm{d}V' + \int_{H_\mathbf{x}} \left(f_2(\mathbf{x}') - f_2(\mathbf{x}) \right) g_1^{(2)}(\boldsymbol{\xi}) \mathrm{d}V' \\ & + \int_{H_\mathbf{x}} \left(f_3(\mathbf{x}') - f_3(\mathbf{x}) \right) g_1^{(3)}(\boldsymbol{\xi}) \mathrm{d}V' \end{aligned} \tag{5.6}$$

Eq. (5.6) can also be written as

$$\nabla \cdot \mathbf{f}(\mathbf{x}) = \int_{H_\mathbf{x}} \begin{bmatrix} \left(f_1(\mathbf{x}') - f_1(\mathbf{x}) \right) g_1^{(1)}(\boldsymbol{\xi}) \\ + \left(f_2(\mathbf{x}') - f_2(\mathbf{x}) \right) g_1^{(2)}(\boldsymbol{\xi}) \\ + \left(f_3(\mathbf{x}') - f_3(\mathbf{x}) \right) g_1^{(3)}(\boldsymbol{\xi}) \end{bmatrix} \mathrm{d}V' \tag{5.7}$$

Subsequently, by considering the vector form of PD differential operator in Eq.(5.2a), the non-local form of divergence can be expressed in compact form as

$$\frac{\partial f_i(\mathbf{x})}{\partial x_i} = \int_{H_\mathbf{x}} g_1^{(i)}(\boldsymbol{\xi})\left(f_i(\mathbf{x}') - f_i(\mathbf{x})\right)\mathrm{d}V' \tag{5.8a}$$

or

$$\nabla\cdot\mathbf{f}(\mathbf{x}) = \int_{H_\mathbf{x}} \mathbf{g}_1(\boldsymbol{\xi})\cdot\left(\mathbf{f}(\mathbf{x}') - \mathbf{f}(\mathbf{x})\right)\mathrm{d}V' \tag{5.8b}$$

Fig. 5-1 presents the relative velocity vector, $\left(\mathbf{v}(\mathbf{x}') - \mathbf{v}(\mathbf{x})\right)$, first-order PD differential operator vector, $\mathbf{g}_1$, and their dot products as a function example.

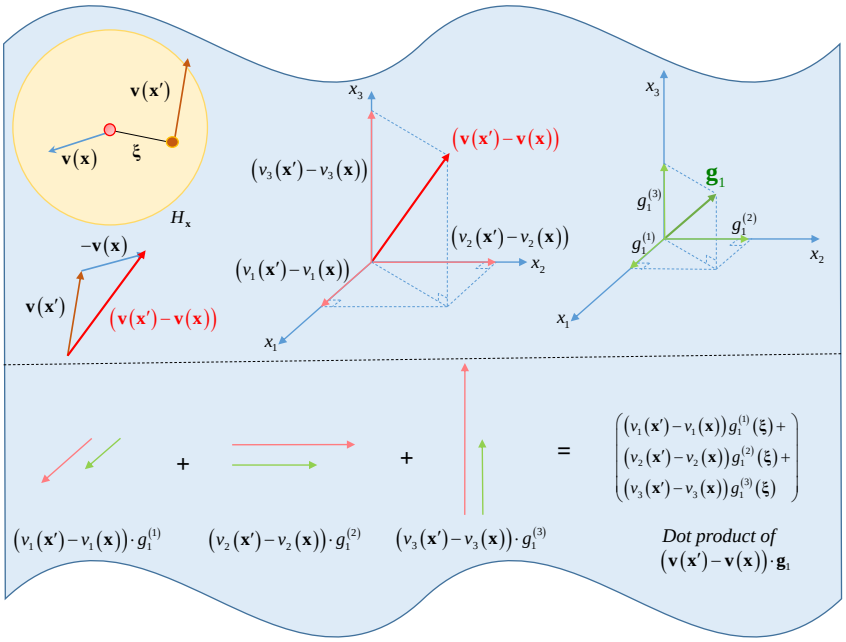

Fig. 5-1 Illustration of relative velocity vector $\left(\mathbf{v}(\mathbf{x}') - v(\mathbf{x})\right)$, first-order PD differential operator vector, $\mathbf{g}_1$ and their dot products

5.2.2. Non-local form of gradient

The local form of the gradient is defined as

$$\nabla \otimes \mathbf{f}(\mathbf{x}) = \frac{\partial f_i(\mathbf{x})}{\partial x_j} \mathbf{e}_i \otimes \mathbf{e}_j = \begin{bmatrix} \frac{\partial f_1(\mathbf{x})}{\partial x_1} & \frac{\partial f_1(\mathbf{x})}{\partial x_2} & \frac{\partial f_1(\mathbf{x})}{\partial x_3} \\ \frac{\partial f_2(\mathbf{x})}{\partial x_1} & \frac{\partial f_2(\mathbf{x})}{\partial x_2} & \frac{\partial f_2(\mathbf{x})}{\partial x_3} \\ \frac{\partial f_3(\mathbf{x})}{\partial x_1} & \frac{\partial f_3(\mathbf{x})}{\partial x_2} & \frac{\partial f_3(\mathbf{x})}{\partial x_3} \end{bmatrix} \tag{5.9}$$

where $i, j = 1,2,3$. The non-local expressions of the diagonal elements in the gradient matrix are already provided in Eq.(5.8a). Similarly, the non-local form derivatives in Eq. (5.9) can be expressed as

$$\frac{\partial f_i(\mathbf{x})}{\partial x_j} = \int_{H_\mathbf{x}} \left(f_i(\mathbf{x}') - f_i(\mathbf{x}) \right) g_1^{(j)}(\xi) \mathrm{d}V' \tag{5.10}$$

As a result, the non-local form for the gradient can be expressed by using PD differential operator as

$$\begin{aligned} &\nabla \otimes \mathbf{f}(\mathbf{x}) \\ &= \int_{H_\mathbf{x}} \begin{bmatrix} \left(f_1(\mathbf{x}') - f_1(\mathbf{x}) \right) g_1^{(1)}(\xi) & \left(f_1(\mathbf{x}') - f_1(\mathbf{x}) \right) g_1^{(2)}(\xi) & \left(f_1(\mathbf{x}') - f_1(\mathbf{x}) \right) g_1^{(3)}(\xi) \\ \left(f_2(\mathbf{x}') - f_2(\mathbf{x}) \right) g_1^{(1)}(\xi) & \left(f_2(\mathbf{x}') - f_2(\mathbf{x}) \right) g_1^{(2)}(\xi) & \left(f_2(\mathbf{x}') - f_2(\mathbf{x}) \right) g_1^{(3)}(\xi) \\ \left(f_3(\mathbf{x}') - f_3(\mathbf{x}) \right) g_1^{(1)}(\xi) & \left(f_3(\mathbf{x}') - f_3(\mathbf{x}) \right) g_1^{(2)}(\xi) & \left(f_3(\mathbf{x}') - f_3(\mathbf{x}) \right) g_1^{(3)}(\xi) \end{bmatrix} \mathrm{d}V' \end{aligned} \tag{5.11}$$

Subsequently, the matrix form in Eq. (5.11) can be converted to a compact form as

$$\nabla \otimes \mathbf{f}(\mathbf{x}) = \int_{H_\mathbf{x}} \left(\mathbf{f}(\mathbf{x}') - \mathbf{f}(\mathbf{x}) \right) \otimes \mathbf{g}_1(\xi) \mathrm{d}V' \tag{5.12}$$

5.2.3. Non-local form for second derivatives

Based on the non-local form of the first-order derivative provided in Section 5.2.1 and Section 5.2.2, the non-local form of the second derivatives is provided in this section.

The local form of Laplacian operator is defined as

$$\Delta\mathbf{f} = \nabla\cdot\left(\nabla\otimes\mathbf{f}\right) = \begin{bmatrix} \dfrac{\partial^2 f_1}{\partial x_1^2} + \dfrac{\partial^2 f_1}{\partial x_2^2} + \dfrac{\partial^2 f_1}{\partial x_3^2} \\ \dfrac{\partial^2 f_2}{\partial x_1^2} + \dfrac{\partial^2 f_2}{\partial x_2^2} + \dfrac{\partial^2 f_2}{\partial x_3^2} \\ \dfrac{\partial^2 f_3}{\partial x_1^2} + \dfrac{\partial^2 f_3}{\partial x_2^2} + \dfrac{\partial^2 f_3}{\partial x_3^2} \end{bmatrix} \tag{5.13}$$

As described Eq.(2.29), by applying the second-order PD differential operator, $\mathbf{g}_2\left(\boldsymbol{\xi}\right)$, the non-local form of the second-order derivatives can be evaluated as

$$\frac{\partial^2 f_i}{\partial x_j^2} = \int_{H_{\mathbf{x}}} \left(f_i\left(\mathbf{x}'\right) - f_i\left(\mathbf{x}\right)\right) g_2^{(j,j)}\left(\boldsymbol{\xi}\right) \mathrm{d}V' \tag{5.14}$$

where $i, j = 1,2,3$. After substituting Eq.(5.14) into Eq.(5.13), the non-local form of Laplacian becomes

$$\Delta\mathbf{f} = \int_{H_{\mathbf{x}}} \begin{bmatrix} \left(f_1\left(\mathbf{x}'\right) - f_1\left(\mathbf{x}\right)\right)\left(\sum_{j=1}^{3} g_2^{(j,j)}\left(\boldsymbol{\xi}\right)\right) \\ \left(f_2\left(\mathbf{x}'\right) - f_2\left(\mathbf{x}\right)\right)\left(\sum_{j=1}^{3} g_2^{(j,j)}\left(\boldsymbol{\xi}\right)\right) \\ \left(f_3\left(\mathbf{x}'\right) - f_3\left(\mathbf{x}\right)\right)\left(\sum_{j=1}^{3} g_2^{(j,j)}\left(\boldsymbol{\xi}\right)\right) \end{bmatrix} \mathrm{d}V' \tag{5.15}$$

By considering the operator matrix provided in Eq. (5.2b), the non-local form of Laplacian operator in Eq. (5.15) can be expressed in compact form as

$$\Delta\mathbf{f}\left(\mathbf{x}\right) = \int_{H_{\mathbf{x}}} \mathrm{Tr}\left(\mathbf{g}_2\left(\boldsymbol{\xi}\right)\right)\left(\mathbf{f}\left(\mathbf{x}'\right) - \mathbf{f}\left(\mathbf{x}\right)\right)\mathrm{d}V' \tag{5.16}$$

By using Eq. (5.9), the transpose of the gradient is defined as

$$\left(\nabla \otimes \mathbf{f}\right)^T = \begin{bmatrix} \dfrac{\partial f_1}{\partial x_1} & \dfrac{\partial f_2}{\partial x_1} & \dfrac{\partial f_3}{\partial x_1} \\ \dfrac{\partial f_1}{\partial x_2} & \dfrac{\partial f_2}{\partial x_2} & \dfrac{\partial f_3}{\partial x_2} \\ \dfrac{\partial f_1}{\partial x_3} & \dfrac{\partial f_2}{\partial x_3} & \dfrac{\partial f_3}{\partial x_3} \end{bmatrix} \tag{5.17}$$

Therefore, the divergence of the transpose of the gradient is

$$\nabla \cdot \left(\nabla \otimes \mathbf{f}\right)^T = \begin{bmatrix} \dfrac{\partial^2 f_1}{\partial x_1^2} + \dfrac{\partial^2 f_2}{\partial x_1 \partial x_2} + \dfrac{\partial^2 f_3}{\partial x_1 \partial x_3} \\ \dfrac{\partial^2 f_1}{\partial x_1 \partial x_2} + \dfrac{\partial^2 f_2}{\partial x_2^2} + \dfrac{\partial^2 f_3}{\partial x_2 \partial x_3} \\ \dfrac{\partial^2 f_1}{\partial x_1 \partial x_3} + \dfrac{\partial^2 f_2}{\partial x_2 \partial x_3} + \dfrac{\partial^2 f_3}{\partial x_3^2} \end{bmatrix} \tag{5.18}$$

Subsequently, the non-local form derivatives in Eq. (5.18) can be expressed as

$$\frac{\partial^2 f_i}{\partial x_j \partial x_k} = \int_{H_{\mathbf{x}}} \left(f_i(\mathbf{x}') - f_i(\mathbf{x}) \right) g_2^{(j,k)}(\boldsymbol{\xi}) \mathrm{d}V' \tag{5.19}$$

where $i, j, k = 1, 2, 3$. Eq.(5.18) can be converted into its non-local form as

$$\nabla \cdot \left(\nabla \otimes \mathbf{f}\right)^T = \int_{H_{\mathbf{x}}} \begin{bmatrix} \left(f_1(\mathbf{x}') - f_1(\mathbf{x}) \right) g_2^{(1,1)}(\boldsymbol{\xi}) + \left(f_2(\mathbf{x}') - f_2(\mathbf{x}) \right) g_2^{(1,2)}(\boldsymbol{\xi}) + \left(f_3(\mathbf{x}') - f_3(\mathbf{x}) \right) g_2^{(1,3)}(\boldsymbol{\xi}) \\ \left(f_1(\mathbf{x}') - f_1(\mathbf{x}) \right) g_2^{(2,1)}(\boldsymbol{\xi}) + \left(f_2(\mathbf{x}') - f_2(\mathbf{x}) \right) g_2^{(2,2)}(\boldsymbol{\xi}) + \left(f_3(\mathbf{x}') - f_3(\mathbf{x}) \right) g_2^{(2,3)}(\boldsymbol{\xi}) \\ \left(f_1(\mathbf{x}') - f_1(\mathbf{x}) \right) g_2^{(3,1)}(\boldsymbol{\xi}) + \left(f_2(\mathbf{x}') - f_2(\mathbf{x}) \right) g_2^{(3,2)}(\boldsymbol{\xi}) + \left(f_3(\mathbf{x}') - f_3(\mathbf{x}) \right) g_2^{(3,3)}(\boldsymbol{\xi}) \end{bmatrix} \mathrm{d}V' \tag{5.20}$$

Eq.(5.20) can be expressed in a compact form as

$$\nabla \cdot \left(\nabla \otimes \mathbf{f}(\mathbf{x})\right)^T = \int_{H_{\mathbf{x}}} \mathbf{g}_2(\boldsymbol{\xi}) \cdot \left(\mathbf{f}(\mathbf{x}') - \mathbf{f}(\mathbf{x})\right) \mathrm{d}V' \tag{5.21}$$

In conclusion, the comparison of the local form and the non-local form of the vectoral function derivatives are summarized as

Table 4 Comparison of local and non-local derivatives

Velocity derivatives	Local Form	Non-local form
$\nabla\cdot\mathbf{f}(\mathbf{x})$	$\sum_{i=1}^{3}\frac{\partial f_i(\mathbf{x})}{\partial x_i}$	$\int_{H_{\mathbf{x}}}\mathbf{g}_1(\boldsymbol{\xi})\cdot\left(\mathbf{f}(\mathbf{x}')-\mathbf{f}(\mathbf{x})\right)\mathrm{d}V'$
$\nabla\otimes\mathbf{f}(\mathbf{x})$	$\frac{\partial f_i(\mathbf{x})}{\partial x_j}\mathbf{e}_i\otimes\mathbf{e}_j,\ i,j=1,2,3$	$\int_{H_{\mathbf{x}}}\left(\mathbf{f}(\mathbf{x}')-\mathbf{f}(\mathbf{x})\right)\otimes\mathbf{g}_1(\boldsymbol{\xi})\mathrm{d}V'$
$\Delta\mathbf{f}(\mathbf{x})$	$\sum_{j=1}^{3}\frac{\partial^2 f_i(\mathbf{x})}{\partial x_j^2}\mathbf{e}_i,\ i=1,2,3$	$\int_{H_{\mathbf{x}}}\mathrm{Tr}\left(\mathbf{g}_2(\boldsymbol{\xi})\right)\left(\mathbf{f}(\mathbf{x}')-\mathbf{f}(\mathbf{x})\right)\mathrm{d}V'$
$\nabla\cdot\left(\nabla\otimes\mathbf{f}(\mathbf{x})\right)^T$	$\sum_{j=1}^{3}\frac{\partial^2 f_j(\mathbf{x})}{\partial x_i\partial x_j}\mathbf{e}_i,\ i=1,2,3$	$\int_{H_{\mathbf{x}}}\mathbf{g}_2(\boldsymbol{\xi})\cdot\left(\mathbf{f}(\mathbf{x}')-\mathbf{f}(\mathbf{x})\right)\mathrm{d}V'$

In this study, non-local operators both for the first and the second-order derivatives are provided. The non-local operators are derived by using second-order Taylor series expansion. If only the first-order derivative is considered and first-order Taylor series expansion is used, the non-local operators for the first-order derivatives, i.e. non-local gradient operator and non-local divergence operator, have the similar form as the ones from [132]. However, in the present study, the second-order Taylor series expansion is adopted and PD differential operator functions are directly determined by making them orthogonal to each term in the Taylor series expansion [14]. Therefore, the second-order terms have effects on the first-order operator due to the adoption of the orthogonal function properties. As a result, the formulations of the first-order operators, i.e. non-local gradient operator and divergence operator, becomes different from the ones in [132].

5.3. A non-local form of Navier-Stokes equations

In this section, the non-local form of Navier-Stokes equations which describe the Newtonian fluid laminar flow is derived by using the non-local operator developed in Section 5.2. The fluid flow is assumed as Newtonian fluid incompressible, viscous, laminar, two-dimensional, heat-conducting flow.

5.3.1. Conservation of mass

In classical fluid mechanics, the equation that describes the conservation of mass in local form is [136]

$$\frac{\mathrm{D}\rho}{\mathrm{D}t} = -\rho \nabla \cdot \mathbf{v} \tag{5.22}$$

where ρ is the fluid density. The non-local form of divergence operator in Table 4 is adopted to convert Eq. (5.22) into its non-local form as

$$\frac{\mathrm{D}\rho}{\mathrm{D}t} = -\rho \int_{H_{\mathbf{x}}} \mathbf{g}_1(\boldsymbol{\xi}) \cdot \left(\mathbf{v}(\mathbf{x}') - \mathbf{v}(\mathbf{x}) \right) \mathrm{d}V' \tag{5.23}$$

where the left-hand side represents the material derivative of density. In the Lagrangian description, the material derivative becomes

$$\frac{D\rho}{Dt} = \frac{\partial \rho}{\partial t} \tag{5.24}$$

Therefore, the non-local form of the conservation of mass in the Lagrangian description is

$$\frac{\partial \rho}{\partial t} = -\rho \int_{H_{\mathbf{x}}} \mathbf{g}_1(\boldsymbol{\xi}) \cdot \left(\mathbf{v}(\mathbf{x}') - \mathbf{v}(\mathbf{x}) \right) \mathrm{d}V' \tag{5.25}$$

In Euler description, the material derivative becomes

$$\frac{D\rho}{Dt} = \frac{\partial \rho}{\partial t} + \mathbf{v} \cdot \nabla \rho \tag{5.26}$$

Therefore, the non-local form of the conservation of mass in Euler description is

$$\frac{\partial \rho}{\partial t} = -\rho \int_{H_{\mathbf{x}}} \mathbf{g}_1(\boldsymbol{\xi}) \cdot \left(\mathbf{v}(\mathbf{x}') - \mathbf{v}(\mathbf{x}) \right) \mathrm{d}V' - \int_{H_{\mathbf{x}}} \left(\rho(\mathbf{x}') - \rho(\mathbf{x}) \right) \left(\mathbf{v}(\mathbf{x}) \cdot \mathbf{g}_1(\boldsymbol{\xi}) \right) \mathrm{d}V' \quad (5.27)$$

For incompressible flow, the conservation of mass becomes

$$\nabla \cdot \mathbf{v} = \frac{\partial v_1}{\partial x_1} + \frac{\partial v_2}{\partial x_2} + \frac{\partial v_3}{\partial x_3} = 0 \quad (5.28)$$

However, the time step size needs to be extremely small in numerical simulations [137-139]. As a result, the incompressible fluid flow is simulated as a weakly compressible fluid flow [138, 139]. The density is still updated according to Eq.(5.25) or Eq.(5.27).

5.3.2. Constitutive equations

The stress is defined as

$$\boldsymbol{\sigma} = -p\mathbf{I} + 2\mu\dot{\boldsymbol{\varepsilon}} \quad (5.29)$$

where p is the hydrostatic pressure, $\mathbf{I}$ is the second-order unit tensor, μ is the dynamic viscosity, and $\dot{\boldsymbol{\varepsilon}}$ is the shear strain rate. For incompressible fluid and compressible fluid flow, the expressions for stress are different. Therefore, the constitutive equations are discussed separately.

5.3.2.1 Incompressible fluid

The shear strain rate of the incompressible fluid is defined as

$$\dot{\boldsymbol{\varepsilon}} = \frac{1}{2}\left[\nabla \otimes \mathbf{v} + (\nabla \otimes \mathbf{v})^T \right] \quad (5.30)$$

Therefore, the stress $\boldsymbol{\sigma}$ is defined as [136]

$$\boldsymbol{\sigma} = -p\mathbf{I} + \mu\left(\nabla \otimes \mathbf{v} + (\nabla \otimes \mathbf{v})^T \right) \quad (5.31)$$

By using the non-local operator in Table 4, the non-local form of the shear strain rate is

$$\dot{\boldsymbol{\varepsilon}} = \frac{1}{2}\int_{H_{\mathbf{x}}} \left[\left(\mathbf{v}(\mathbf{x}') - \mathbf{v}(\mathbf{x})\right) \otimes \mathbf{g}_1(\boldsymbol{\xi}) + \mathbf{g}_1(\boldsymbol{\xi})^T \otimes \left(\mathbf{v}(\mathbf{x}') - \mathbf{v}(\mathbf{x})\right)^T \right] \mathrm{d}V' \quad (5.32)$$

As a result, the stress definition in Eq. (5.29) can be expressed as

$$\boldsymbol{\sigma} = -p\mathbf{I} + \mu\int_{H_{\mathbf{x}}} \left[\left(\mathbf{v}(\mathbf{x}') - \mathbf{v}(\mathbf{x})\right) \otimes \mathbf{g}_1(\boldsymbol{\xi}) + \mathbf{g}_1(\boldsymbol{\xi})^T \otimes \left(\mathbf{v}(\mathbf{x}') - \mathbf{v}(\mathbf{x})\right)^T \right] \mathrm{d}V' \quad (5.33)$$

Regarding the incompressible fluid flow, a prohibitively small time step size is required for stability in the pressure simulation [137]. Therefore, artificial compressibility methods [140] are introduced which makes the incompressible fluid weakly compressible. The Tait equation of state is adopted to model such flows, in which the pressure is an explicit function of local fluid density as [141]

$$p = B\left(\left(\frac{\rho_t}{\rho_0} \right)^{\gamma} - 1 \right) \quad (5.34)$$

where ρ_t represents the current local density, ρ_0 represents the initial density and γ represents the ratio of specific heat capacity which is $\gamma = 7$ for water and $\gamma = 1$ for gas.

In Eq. (5.34) B is a parameter which can be defined as [142]

$$B = \frac{\rho_0 c_s^2}{\gamma} \quad (5.35)$$

where c_s represents the speed of sound. The speed of sound can be approximated as [143]

$$c_s = \left|\mathbf{v}_f\right| / \sqrt{\eta} \quad (5.36)$$

with $\left|\mathbf{v}_f\right|$ representing the maximum magnitude of fluid flow velocity. The term η represents the density variation with a typical value being 0.01, indicating that density varies at most 1%. As a result, the speed of sound is assumed as 10 times of the maximum fluid velocity.

5.3.2.2 Compressible fluid

The shear strain rate for compressible fluid is defined as

$$\dot{\boldsymbol{\varepsilon}} = \frac{1}{2}\left[\nabla \otimes \mathbf{v} + \left(\nabla \otimes \mathbf{v}\right)^T\right] - \frac{1}{3}\left(\nabla \cdot \mathbf{v}\right)\mathbf{I} \tag{5.37}$$

By considering the non-local velocity operator in Table 4 and Eq.(5.32), the non-local form of the shear strain rate can be expressed as

$$\begin{aligned}\dot{\boldsymbol{\varepsilon}} = &\frac{1}{2}\int_{H_{\mathbf{x}}}\left[\left(\mathbf{v}\left(\mathbf{x}'\right)-\mathbf{v}\left(\mathbf{x}\right)\right)\otimes\mathbf{g}_1\left(\boldsymbol{\xi}\right)+\mathbf{g}_1\left(\boldsymbol{\xi}\right)^T\otimes\left(\mathbf{v}\left(\mathbf{x}'\right)-\mathbf{v}\left(\mathbf{x}\right)\right)^T\right]\mathrm{d}V' \\ &-\frac{1}{3}\int_{H_{\mathbf{x}}}\left[\left(\mathbf{g}_1\left(\boldsymbol{\xi}\right)\cdot\left(\mathbf{v}\left(\mathbf{x}'\right)-\mathbf{v}\left(\mathbf{x}\right)\right)\right)\mathbf{I}\right]\mathrm{d}V'\end{aligned} \tag{5.38}$$

As a result, the stress defined in Eq. (5.29) can be expressed as

$$\begin{aligned}\boldsymbol{\sigma} = &-p\mathbf{I}+\mu\int_{H_{\mathbf{x}}}\left[\left(\mathbf{v}\left(\mathbf{x}'\right)-\mathbf{v}\left(\mathbf{x}\right)\right)\otimes\mathbf{g}_1\left(\boldsymbol{\xi}\right)+\mathbf{g}_1\left(\boldsymbol{\xi}\right)^T\otimes\left(\mathbf{v}\left(\mathbf{x}'\right)-\mathbf{v}\left(\mathbf{x}\right)\right)^T\right]\mathrm{d}V' \\ &-\frac{2\mu}{3}\int_{H_{\mathbf{x}}}\left[\left(\mathbf{g}_1\left(\boldsymbol{\xi}\right)\cdot\left(\mathbf{v}\left(\mathbf{x}'\right)-\mathbf{v}\left(\mathbf{x}\right)\right)\right)\mathbf{I}\right]\mathrm{d}V'\end{aligned} \tag{5.39}$$

Regarding compressible fluid flow, the material derivative of pressure is [132]

$$\frac{\mathrm{D}p}{\mathrm{D}t} = -K_f \nabla \cdot \mathbf{v} \tag{5.40}$$

where K_f is the elastic bulk modulus of fluid.

The non-local velocity divergence operator in Table 4 is adopted to convert Eq.(5.40) into its non-local form as

$$\frac{\mathrm{D}p}{\mathrm{D}t} = -K_f \int_{H_\mathbf{x}} \left(\mathbf{g}_1(\boldsymbol{\xi}) \cdot \left(\mathbf{v}(\mathbf{x}') - \mathbf{v}(\mathbf{x}) \right) \right) \mathrm{d}V' \tag{5.41}$$

5.3.3. Conservation of momentum

The local form of the equation of motion is

$$\rho \frac{\mathrm{D}\mathbf{v}}{\mathrm{D}t} = \nabla \cdot \boldsymbol{\sigma} + \rho \mathbf{b} \tag{5.42}$$

where $\mathbf{b}$ represents the body force.

By using the definitions in Eq. (5.29) into Eq. (5.42), the equation of motion can be expressed in terms of pressure and shear strain rate as

$$\rho \frac{D\mathbf{v}}{Dt} = \nabla \cdot \left(-p\mathbf{I} + 2\mu \dot{\boldsymbol{\varepsilon}} \right) + \rho \mathbf{b} \tag{5.43}$$

By applying the Leibniz rule Eq. (5.43) can be written as

$$\rho \frac{D\mathbf{v}}{Dt} = -\nabla \cdot \left(p\mathbf{I} \right) + 2\mu \left(\nabla \cdot \dot{\boldsymbol{\varepsilon}} \right) + \dot{\boldsymbol{\varepsilon}} \nabla \cdot \left(2\mu \right) + \rho \mathbf{b} \tag{5.44}$$

The viscosity μ , in general, is a function of the thermodynamic state of fluid [136]. In this chapter, the dynamic viscosity μ is assumed to be constant, therefore Eq. (5.44) takes the form as

$$\rho \frac{D\mathbf{v}}{Dt} = -\nabla \cdot \left(p\mathbf{I} \right) + 2\mu \left(\nabla \cdot \dot{\boldsymbol{\varepsilon}} \right) + \rho \mathbf{b} \tag{5.45}$$

Similar to the non-local operators in Table 4, the non-local form of the first term on the right-hand side of Eq. (5.45) can be expressed as

$$\nabla \cdot \left(p\mathbf{I} \right) = \int_{H_\mathbf{x}} \left[\left(p(\mathbf{x}') - p(\mathbf{x}) \right) \mathbf{g}_1(\boldsymbol{\xi}) \right] \mathrm{d}V' \tag{5.46}$$

5.3.3.1 Incompressible fluid

By considering the shear strain rate expression provided in Eq.(5.30) for an incompressible fluid, the divergence of the shear strain rate can be expressed as

$$\nabla \cdot \dot{\boldsymbol{\varepsilon}} = \frac{1}{2} \nabla \cdot \left[\nabla \otimes \mathbf{v} + \left(\nabla \otimes \mathbf{v} \right)^T \right] \tag{5.47}$$

Eq. (5.47) can also be presented as

$$\nabla \cdot \dot{\boldsymbol{\varepsilon}} = \frac{1}{2} \left(\Delta \mathbf{v} + \nabla \cdot \left(\nabla \otimes \mathbf{v} \right)^T \right) \tag{5.48}$$

By applying the non-local second-order operators provided in Table 4, the non-local form of divergence of the shear strain rate can be obtained as

$$\nabla \cdot \dot{\boldsymbol{\varepsilon}} = \frac{1}{2} \int_{H_{\mathbf{x}}} \left[\mathrm{Tr}\left(\mathbf{g}_2 \left(\boldsymbol{\xi} \right) \right) \left(\mathbf{v}\left(\mathbf{x}' \right) - \mathbf{v}\left(\mathbf{x} \right) \right) + \mathbf{g}_2 \left(\boldsymbol{\xi} \right) \cdot \left(\mathbf{v}\left(\mathbf{x}' \right) - \mathbf{v}\left(\mathbf{x} \right) \right) \right] \mathrm{d}V' \tag{5.49}$$

By substituting Eq.(5.46) and Eq.(5.49) into Eq.(5.45), the non-local form of the equation of motion for an incompressible fluid can be obtained as

$$\begin{aligned} \rho \frac{D\mathbf{v}}{Dt} = & \int_{H_{\mathbf{x}}} \left\{ \mu \left[\mathrm{Tr}\left(\mathbf{g}_2 \left(\boldsymbol{\xi} \right) \right) \left(\mathbf{v}\left(\mathbf{x}' \right) - \mathbf{v}\left(\mathbf{x} \right) \right) + \mathbf{g}_2 \left(\boldsymbol{\xi} \right) \cdot \left(\mathbf{v}\left(\mathbf{x}' \right) - \mathbf{v}\left(\mathbf{x} \right) \right) \right] \right\} \mathrm{d}V' \\ & - \int_{H_{\mathbf{x}}} \left\{ \left(p\left(\mathbf{x}' \right) - p\left(\mathbf{x} \right) \right) \mathbf{g}_1 \left(\boldsymbol{\xi} \right) \right\} \mathrm{d}V' + \rho \mathbf{b} \end{aligned} \tag{5.50}$$

By using the incompressible flow constraint in Eq.(5.28), it can be proved that

$$\int_{H_{\mathbf{x}}} \left\{ \mathbf{g}_2 \left(\boldsymbol{\xi} \right) \cdot \left(\mathbf{v}\left(\mathbf{x}' \right) - \mathbf{v}\left(\mathbf{x} \right) \right) \right\} \mathrm{d}V' = 0 \tag{5.51}$$

Then conservation of momentum for incompressible fluid is

$$\rho \frac{D\mathbf{v}}{Dt} = \int_{H_{\mathbf{x}}} \left\{ \mu \mathrm{Tr}\left(\mathbf{g}_2 \left(\boldsymbol{\xi} \right) \right) \left(\mathbf{v}\left(\mathbf{x}' \right) - \mathbf{v}\left(\mathbf{x} \right) \right) - \left(p\left(\mathbf{x}' \right) - p\left(\mathbf{x} \right) \right) \mathbf{g}_1 \left(\boldsymbol{\xi} \right) \right\} \mathrm{d}V' + \rho \mathbf{b} \tag{5.52}$$

5.3.3.2 Compressible fluid

By considering the shear strain rate expression provided in Eq.(5.37) for compressible fluid, the divergence of the shear strain rate can be expressed as

$$\nabla\cdot\dot{\boldsymbol{\varepsilon}}=\frac{1}{2}\left(\Delta\mathbf{v}+\nabla\cdot\left(\nabla\otimes\mathbf{v}\right)^{T}\right)-\frac{1}{3}\nabla\cdot\left(\left(\nabla\cdot\mathbf{v}\right)\mathbf{I}\right) \tag{5.53}$$

It can be proved that $\nabla\cdot\left(\left(\nabla\cdot\mathbf{v}\right)\mathbf{I}\right)=\nabla\cdot\left(\nabla\otimes\mathbf{v}\right)^{T}$. By considering Eq. (5.49) and Table 4, the non-local form of the divergence of shear strain rate for compressible fluids can be obtained as

$$\begin{aligned}\nabla\cdot\dot{\boldsymbol{\varepsilon}}&=\int_{H_{\mathbf{x}}}\left\{\frac{1}{2}\left[\mathrm{Tr}\left(\mathbf{g}_{2}\left(\boldsymbol{\xi}\right)\right)\left(\mathbf{v}\left(\mathbf{x}'\right)-\mathbf{v}\left(\mathbf{x}\right)\right)+\mathbf{g}_{2}\left(\boldsymbol{\xi}\right)\cdot\left(\mathbf{v}\left(\mathbf{x}'\right)-\mathbf{v}\left(\mathbf{x}\right)\right)\right]\right\}\mathrm{d}V'\\&\quad-\int_{H_{\mathbf{x}}}\left\{\frac{1}{3}\left(\mathbf{g}_{2}\left(\boldsymbol{\xi}\right)\cdot\left(\mathbf{v}\left(\mathbf{x}'\right)-\mathbf{v}\left(\mathbf{x}\right)\right)\right)\right\}\mathrm{d}V'\\&=\int_{H_{\mathbf{x}}}\left\{\frac{1}{2}\mathrm{Tr}\left(\mathbf{g}_{2}\left(\boldsymbol{\xi}\right)\right)\left(\mathbf{v}\left(\mathbf{x}'\right)-\mathbf{v}\left(\mathbf{x}\right)\right)+\frac{1}{6}\mathbf{g}_{2}\left(\boldsymbol{\xi}\right)\cdot\left(\mathbf{v}\left(\mathbf{x}'\right)-\mathbf{v}\left(\mathbf{x}\right)\right)\right\}\mathrm{d}V'\end{aligned} \tag{5.54}$$

By substituting Eq.(5.46) and Eq. (5.54) into Eq. (5.45), the non-local form of the equation of motion for a compressible fluid can be obtained as

$$\rho\frac{D\mathbf{v}}{Dt}=\int_{H_{\mathbf{x}}}\left\{\begin{array}{l}\mu\left[\mathrm{Tr}\left(\mathbf{g}_{2}\left(\boldsymbol{\xi}\right)\right)\left(\mathbf{v}\left(\mathbf{x}'\right)-\mathbf{v}\left(\mathbf{x}\right)\right)+\frac{1}{3}\mathbf{g}_{2}\left(\boldsymbol{\xi}\right)\cdot\left(\mathbf{v}\left(\mathbf{x}'\right)-\mathbf{v}\left(\mathbf{x}\right)\right)\right]\\-\left(p\left(\mathbf{x}'\right)-p\left(\mathbf{x}\right)\right)\mathbf{g}_{1}\left(\boldsymbol{\xi}\right)\end{array}\right\}\mathrm{d}V'+\rho\mathbf{b} \tag{5.55}$$

As provided in Eq.(5.50) and (5.55), the conservation equation of momentum is directly expressed in terms of velocity and pressure, leading to the existence of the second-order derivatives. Due to the adoption of the corresponding PD differential operator for the second-order derivatives provided in Table 4, the acceleration can be directly calculated with one integration with second-order accuracy. The error introduced by the integration can be reduced compared to first-order approximations where the integration needs to be performed twice to calculate the acceleration. In addition, the computational time can also be reduced by using integration only once.

In the Lagrangian description, the material derivatives of velocity in Eq.(5.52) and Eq.(5.55) both for incompressible and compressible fluids can be simply replaced with the partial derivatives with respect to time, $\mathrm{D}\mathbf{v}/\mathrm{D}t = \partial\mathbf{v}/\partial t$. On the contrary, in Euler description, the material derivative of velocity is defined as [136]

$$\frac{\mathrm{D}\mathbf{v}}{\mathrm{D}t} = \frac{\partial \mathbf{v}}{\partial t} + \mathbf{v}\cdot\nabla\mathbf{v} \tag{5.56}$$

The non-local form of the term $\mathbf{v}\cdot\nabla\mathbf{v}$ can be calculated as

$$\begin{aligned}\mathbf{v}\cdot\nabla\mathbf{v} &= \begin{bmatrix} v_1\dfrac{\partial v_1}{\partial x_1} + v_2\dfrac{\partial v_1}{\partial x_2} + v_3\dfrac{\partial v_1}{\partial x_3} \\ v_1\dfrac{\partial v_2}{\partial x_1} + v_2\dfrac{\partial v_2}{\partial x_2} + v_3\dfrac{\partial v_2}{\partial x_3} \\ v_1\dfrac{\partial v_3}{\partial x_1} + v_2\dfrac{\partial v_3}{\partial x_2} + v_3\dfrac{\partial v_3}{\partial x_3} \end{bmatrix} = \begin{bmatrix} \int_{H_\mathbf{x}} \big(v_1(\mathbf{x}') - v_1(\mathbf{x})\big)\big(\mathbf{v}(\mathbf{x})\cdot\mathbf{g}_1(\boldsymbol{\xi})\big)\mathrm{d}V' \\ \int_{H_\mathbf{x}} \big(v_2(\mathbf{x}') - v_2(\mathbf{x})\big)\big(\mathbf{v}(\mathbf{x})\cdot\mathbf{g}_1(\boldsymbol{\xi})\big)\mathrm{d}V' \\ \int_{H_\mathbf{x}} \big(v_3(\mathbf{x}') - v_3(\mathbf{x})\big)\big(\mathbf{v}(\mathbf{x})\cdot\mathbf{g}_1(\boldsymbol{\xi})\big)\mathrm{d}V' \end{bmatrix} \\ &= \big(\mathbf{v}(\mathbf{x}') - \mathbf{v}(\mathbf{x})\big)\int_{H_\mathbf{x}} \big(\mathbf{v}(\mathbf{x})\cdot\mathbf{g}_1(\boldsymbol{\xi})\big)\mathrm{d}V'\end{aligned} \tag{5.57}$$

Therefore, the non-local form of the equation for the conservation of momentum in Euler description for incompressible and compressible fluids becomes

Incompressible:

$$\rho\frac{\partial\mathbf{v}}{\partial t} = \int_{H_\mathbf{x}} \begin{Bmatrix} \Big[\mu\mathrm{Tr}\big(\mathbf{g}_2(\boldsymbol{\xi})\big) - \rho\big(\mathbf{v}(\mathbf{x})\cdot\mathbf{g}_1(\boldsymbol{\xi})\big)\Big]\big(\mathbf{v}(\mathbf{x}') - \mathbf{v}(\mathbf{x})\big) \\ -\big(p(\mathbf{x}') - p(\mathbf{x})\big)\mathbf{g}_1(\boldsymbol{\xi}) \end{Bmatrix}\mathrm{d}V' + \rho\mathbf{b} \tag{5.58}$$

Compressible:

$$\rho\frac{\partial\mathbf{v}}{\partial t} = \int_{H_\mathbf{x}} \begin{Bmatrix} \Big[\mu\mathrm{Tr}\big(\mathbf{g}_2(\boldsymbol{\xi})\big) - \rho\big(\mathbf{v}(\mathbf{x})\cdot\mathbf{g}_1(\boldsymbol{\xi})\big)\Big]\big(\mathbf{v}(\mathbf{x}') - \mathbf{v}(\mathbf{x})\big) \\ +\dfrac{\mu}{3}\mathbf{g}_2(\boldsymbol{\xi})\cdot\big(\mathbf{v}(\mathbf{x}') - \mathbf{v}(\mathbf{x})\big) - \big(p(\mathbf{x}') - p(\mathbf{x})\big)\mathbf{g}_1(\boldsymbol{\xi}) \end{Bmatrix}\mathrm{d}V' + \rho\mathbf{b} \tag{5.59}$$

5.3.4. Conservation of energy

For the fluid flow coupled with heat transfer simulation, only the incompressible fluid flows in Euler description are considered. Therefore, the formulation of the conservation of energy here is only derived for incompressible fluids in Euler description. The local form of the conservation of energy is [136]

$$\rho\left(\frac{\partial e}{\partial t}+\mathbf{v}\cdot\nabla e\right)=-\nabla\cdot\mathbf{q}+\boldsymbol{\sigma}:\nabla\otimes\mathbf{v}+Q \tag{5.60}$$

where e is the internal energy, Q is the internal heat generation, and $\mathbf{q}$ is the heat flux vector defined as

$$\mathbf{q}=-k\left(\mathbf{x}\right)\cdot\nabla T \tag{5.61}$$

where $k\left(\mathbf{x}\right)$ is the thermal conductivity.

For thermodynamic systems, the internal energy assumed to be a function of temperature and density, i.e. $e=e\left(T,\rho\right)$. For constant density, the specific heat capacity under constant pressure, c_p, is equal to the specific heat capacity under constant volume, c_v, i.e. $c_v=c_p=C$ [136]. Consequently, the time rate of change of the internal energy can be evaluated as [136]

$$\frac{\partial e}{\partial t}+\mathbf{v}\cdot\nabla e=C\left(\frac{\partial T}{\partial t}+\mathbf{v}\cdot\nabla T\right)=C\left(\frac{\partial T}{\partial t}+v_1\frac{\partial T}{\partial x_1}+v_2\frac{\partial T}{\partial x_2}+v_3\frac{\partial T}{\partial x_3}\right) \tag{5.62}$$

where C represents the specific heat capacity. By using the definition of stress in Eq.(5.31), the term $\boldsymbol{\sigma}:\nabla\otimes\mathbf{v}$ can be written as [136]

$$\boldsymbol{\sigma}:\nabla\otimes\mathbf{v}=-p\mathbf{I}:\left(\nabla\otimes\mathbf{v}\right)+\mu\left(\nabla\otimes\mathbf{v}\right):\left(\nabla\otimes\mathbf{v}\right)+\mu\left(\nabla\otimes\mathbf{v}\right)^T:\left(\nabla\otimes\mathbf{v}\right) \tag{5.63}$$

or

$$\boldsymbol{\sigma}:\nabla\otimes\mathbf{v}=-p\left(\frac{\partial v_1}{\partial x_1}+\frac{\partial v_2}{\partial x_2}+\frac{\partial v_3}{\partial x_3}\right)+\mu\left(\begin{array}{l}2\left(\frac{\partial v_1}{\partial x_1}\right)^2+2\left(\frac{\partial v_2}{\partial x_2}\right)^2+2\left(\frac{\partial v_3}{\partial x_3}\right)^2\\+\left(\frac{\partial v_1}{\partial x_2}+\frac{\partial v_2}{\partial x_1}\right)^2+\left(\frac{\partial v_1}{\partial x_3}+\frac{\partial v_3}{\partial x_1}\right)^2+\left(\frac{\partial v_2}{\partial x_3}+\frac{\partial v_3}{\partial x_2}\right)^2\end{array}\right) \tag{5.64}$$

Substituting the incompressible condition Eq. (5.28) into Eq. (5.64) results in [136]

$$\boldsymbol{\sigma}:\nabla\otimes\mathbf{v}=\mu\left(\begin{array}{l}2\left(\frac{\partial v_1}{\partial x_1}\right)^2+2\left(\frac{\partial v_2}{\partial x_2}\right)^2+2\left(\frac{\partial v_3}{\partial x_3}\right)^2\\+\left(\frac{\partial v_1}{\partial x_2}+\frac{\partial v_2}{\partial x_1}\right)^2+\left(\frac{\partial v_1}{\partial x_3}+\frac{\partial v_3}{\partial x_1}\right)^2+\left(\frac{\partial v_2}{\partial x_3}+\frac{\partial v_3}{\partial x_2}\right)^2\end{array}\right) \tag{5.65}$$

By substituting Eq.(5.61), Eq.(5.62) and Eq.(5.65) into Eq.(5.60), the conservation of energy equation becomes [136]

$$\begin{aligned}\rho C\frac{\partial T}{\partial t}=&\frac{\partial k}{\partial x_1}\frac{\partial T}{\partial x_1}+\frac{\partial k}{\partial x_2}\frac{\partial T}{\partial x_2}+\frac{\partial k}{\partial x_3}\frac{\partial T}{\partial x_3}+k\left(\frac{\partial^2 T}{\partial x_1^2}+\frac{\partial^2 T}{\partial x_2^2}+\frac{\partial^2 T}{\partial x_3^2}\right)\\&-\rho C\left(v_1\frac{\partial T}{\partial x_1}+v_2\frac{\partial T}{\partial x_2}+v_3\frac{\partial T}{\partial x_3}\right)+Q\\&+\mu\left(\begin{array}{l}2\left(\frac{\partial v_1}{\partial x_1}\right)^2+2\left(\frac{\partial v_2}{\partial x_2}\right)^2+2\left(\frac{\partial v_3}{\partial x_3}\right)^2\\+\left(\frac{\partial v_1}{\partial x_2}+\frac{\partial v_2}{\partial x_1}\right)^2+\left(\frac{\partial v_1}{\partial x_3}+\frac{\partial v_3}{\partial x_1}\right)^2+\left(\frac{\partial v_2}{\partial x_3}+\frac{\partial v_3}{\partial x_2}\right)^2\end{array}\right)\end{aligned} \tag{5.66}$$

Therefore, by substituting the non-local form of the differentials provided in Table 4, the non-local form of conservation of energy becomes

$$
\begin{aligned}
&\rho(\mathbf{x})C\frac{\partial T(\mathbf{x})}{\partial t}= \\
&\sum_{i=1}^{3}\left(\int_{H_{\mathbf{x}}}\left(k(\mathbf{x}')-k(\mathbf{x})\right)g_1^{(i)}(\xi)\mathrm{d}V'\right)\left(\int_{H_{\mathbf{x}}}\left(T(\mathbf{x}')-T(\mathbf{x})\right)g_1^{(i)}(\xi)\mathrm{d}V'\right) \\
&+k(\mathbf{x})\int_{H_{\mathbf{x}}}\left(T(\mathbf{x}')-T(\mathbf{x})\right)\mathrm{Tr}\left(\mathbf{g}_2(\xi)\right)\mathrm{d}V' \\
&+\mu\left(\begin{array}{l}
2\sum_{i=1}^{3}\left(\int_{H_{\mathbf{x}}}\left(v_i(\mathbf{x}')-v_i(\mathbf{x})\right)g_1^{(i)}(\xi)\mathrm{d}V'\right)^2 \\
+\left(\int_{H_{\mathbf{x}}}\left(\left(v_1(\mathbf{x}')-v_1(\mathbf{x})\right)g_1^{(2)}(\xi)+\left(v_2(\mathbf{x}')-v_2(\mathbf{x})\right)g_1^{(1)}(\xi)\right)\mathrm{d}V'\right)^2 \\
+\left(\int_{H_{\mathbf{x}}}\left(\left(v_1(\mathbf{x}')-v_1(\mathbf{x})\right)g_1^{(3)}(\xi)+\left(v_3(\mathbf{x}')-v_3(\mathbf{x})\right)g_1^{(1)}(\xi)\right)\mathrm{d}V'\right)^2 \\
+\left(\int_{H_{\mathbf{x}}}\left(\left(v_2(\mathbf{x}')-v_2(\mathbf{x})\right)g_1^{(3)}(\xi)+\left(v_3(\mathbf{x}')-v_3(\mathbf{x})\right)g_1^{(2)}(\xi)\right)\mathrm{d}V'\right)^2
\end{array}\right) \\
&-\rho(\mathbf{x})C\int_{H_{\mathbf{x}}}\left(T(\mathbf{x}')-T(\mathbf{x})\right)\left(\mathbf{v}(\mathbf{x})\cdot\mathbf{g}_1(\xi)\right)\mathrm{d}V'+Q
\end{aligned}
\tag{5.67}
$$

If the thermal conductivity $k(\mathbf{x})$ is assumed to be uniform and constant, Eq.(5.67) reduces to

$$
\begin{aligned}
&\rho(\mathbf{x})C\frac{\partial T(\mathbf{x})}{\partial t}=k\int_{H_{\mathbf{x}}}\left(T(\mathbf{x}')-T(\mathbf{x})\right)\mathrm{Tr}\left(\mathbf{g}_2(\xi)\right)\mathrm{d}V' \\
&+\mu\left(\begin{array}{l}
2\sum_{i=1}^{3}\left(\int_{H_{\mathbf{x}}}\left(v_i(\mathbf{x}')-v_i(\mathbf{x})\right)g_1^{(i)}(\xi)\mathrm{d}V'\right)^2 \\
+\left(\int_{H_{\mathbf{x}}}\left(\left(v_1(\mathbf{x}')-v_1(\mathbf{x})\right)g_1^{(2)}(\xi)+\left(v_2(\mathbf{x}')-v_2(\mathbf{x})\right)g_1^{(1)}(\xi)\right)\mathrm{d}V'\right)^2 \\
+\left(\int_{H_{\mathbf{x}}}\left(\left(v_1(\mathbf{x}')-v_1(\mathbf{x})\right)g_1^{(3)}(\xi)+\left(v_3(\mathbf{x}')-v_3(\mathbf{x})\right)g_1^{(1)}(\xi)\right)\mathrm{d}V'\right)^2 \\
+\left(\int_{H_{\mathbf{x}}}\left(\left(v_2(\mathbf{x}')-v_2(\mathbf{x})\right)g_1^{(3)}(\xi)+\left(v_3(\mathbf{x}')-v_3(\mathbf{x})\right)g_1^{(2)}(\xi)\right)\mathrm{d}V'\right)^2
\end{array}\right) \\
&-\rho(\mathbf{x})C\int_{H_{\mathbf{x}}}\left(T(\mathbf{x}')-T(\mathbf{x})\right)\left(\mathbf{v}(\mathbf{x})\cdot\mathbf{g}_1(\xi)\right)\mathrm{d}V'+Q
\end{aligned}
\tag{5.68}
$$

5.3.5. Non-dimensional form for 2D problem

The governing equations in a non-dimensional form can be obtained by using the following non-dimensional parameters [144]

$$x_i^* = \frac{x_i}{L_0}, v_i^* = \frac{v_i}{v_0}, t^* = \frac{tv_0}{L_0}, \rho^* = \frac{\rho}{\rho_0}, \mu^* = \frac{\mu}{\mu_0}, k^* = \frac{k}{k_0}, T^* = \frac{T}{T_0}, p^* = \frac{p}{\rho_0 v_0^2}, g^* = \frac{gL_0}{v_0^2} \tag{5.69}$$

where the subscript $\left(_0\right)$ represents the reference variable and the superscript $\left(^*\right)$ represents the non-dimensional variable.

The non-dimensional form of the local governing equations in Euler description for two-dimensional problems by ignoring the internal heat generation can be written as

Conservation of mass

$$\frac{\partial \rho^*}{\partial t^*} + \left(v_1^* \frac{\partial \rho^*}{\partial x_1^*} + v_2^* \frac{\partial \rho^*}{\partial x_2^*} \right) = -\rho^* \left(\frac{\partial v_1^*}{\partial x_1^*} + \frac{\partial v_2^*}{\partial x_2^*} \right) \tag{5.70}$$

Conservation of momentum

$$\begin{bmatrix} \frac{\partial v_1^*}{\partial t^*} + v_1^* \frac{\partial v_1^*}{\partial x_1^*} + v_2^* \frac{\partial v_1^*}{\partial x_2^*} \\ \frac{\partial v_2^*}{\partial t^*} + v_1^* \frac{\partial v_2^*}{\partial x_1^*} + v_2^* \frac{\partial v_2^*}{\partial x_2^*} \end{bmatrix} = -\begin{bmatrix} \frac{\partial p^*}{\partial x_1^*} \\ \frac{\partial p^*}{\partial x_2^*} \end{bmatrix} + \frac{1}{\mathrm{Re}} \begin{bmatrix} \mu^* \left(\frac{\partial^2 v_1^*}{\partial x_1^{*2}} + \frac{\partial^2 v_1^*}{\partial x_2^{*2}} \right) \\ \mu^* \left(\frac{\partial^2 v_2^*}{\partial x_1^{*2}} + \frac{\partial^2 v_2^*}{\partial x_2^{*2}} \right) \end{bmatrix} + \begin{bmatrix} b_1^* \\ b_2^* \end{bmatrix} \tag{5.71}$$

Conservation of energy

$$\begin{aligned} \rho^* \left(\frac{\partial T^*}{\partial t^*} + v_1^* \frac{\partial T^*}{\partial x_1^*} + v_2 \frac{\partial T^*}{\partial x_2^*} \right) = {} & \frac{1}{\mathrm{Re}\,\mathrm{Pr}} \left(\frac{\partial k^*}{\partial x_1^*} \frac{\partial T^*}{\partial x_1^*} + \frac{\partial k^*}{\partial x_2^*} \frac{\partial T^*}{\partial x_2^*} \right) + \frac{k^*}{\mathrm{Re}\,\mathrm{Pr}} \left(\frac{\partial^2 T^*}{\partial x_1^{*2}} + \frac{\partial^2 T^*}{\partial x_2^{*2}} \right) \\ & + \frac{\mathrm{Ec}}{\mathrm{Re}} \mu^* \left(2 \left(\frac{\partial v_1^*}{\partial x_1^*} \right)^2 + 2 \left(\frac{\partial v_2^*}{\partial x_2^*} \right)^2 + \left(\frac{\partial v_1^*}{\partial x_2^*} + \frac{\partial v_2^*}{\partial x_1^*} \right)^2 \right) \end{aligned} \tag{5.72}$$

The non-dimensional parameters in Eqs. (5.70)-(5.72) are defined as

$$\mathrm{Re} = \frac{\rho_0 v_0 L_0}{\mu_0}, \mathrm{Pr} = \frac{\mu_0 C_0}{k_0}, \mathrm{Ec} = \frac{v_0^2}{C_0 T_0} \tag{5.73}$$

where Re is the Reynolds number, Pr is the Prandtl number, and Ec is the Eckert number.

Similarly, the non-local governing equations in Eqs.(5.70)-(5.72) can also be written into their non-dimensional forms with a constant thermal conductivity as

Conservation of mass

$$\frac{\partial \rho^*\left(\mathbf{x}^*\right)}{\partial t^*} = -\rho^*\left(\mathbf{x}^*\right)\int_{H_{\mathbf{x}^*}}\left(\left(v_1^*\left(\mathbf{x}'^*\right)-v_1^*\left(\mathbf{x}^*\right)\right)\mathrm{g}^{10}\left(\xi^*\right)+\left(v_2^*\left(\mathbf{x}'^*\right)-v_2^*\left(\mathbf{x}^*\right)\right)\mathrm{g}^{01}\left(\xi^*\right)\right)\mathrm{d}V'^* - \int_{H_{\mathbf{x}^*}}\left(\rho^*\left(\mathbf{x}'^*\right)-\rho\left(\mathbf{x}^*\right)\right)\left(v_1\left(\mathbf{x}^*\right)\mathrm{g}^{10}\left(\xi^*\right)+v_2\left(\mathbf{x}^*\right)\mathrm{g}^{01}\left(\xi^*\right)\right)\mathrm{d}V'^* \tag{5.74}$$

Conservation of momentum

$$\begin{aligned}\begin{bmatrix}\frac{\partial v_1^*\left(\mathbf{x}^*\right)}{\partial t^*}\\ \frac{\partial v_2^*\left(\mathbf{x}^*\right)}{\partial t^*}\end{bmatrix} &= -\begin{bmatrix}\int_{H_{\mathbf{x}^*}}\left(p^*\left(\mathbf{x}'^*\right)-p^*\left(\mathbf{x}^*\right)\right)g^{10}\left(\xi^*\right)\mathrm{d}V'^*\\ \int_{H_{\mathbf{x}^*}}\left(p^*\left(\mathbf{x}'^*\right)-p^*\left(\mathbf{x}^*\right)\right)g^{01}\left(\xi^*\right)\mathrm{d}V'^*\end{bmatrix}\\ &+\frac{\mu^*}{\mathrm{Re}}\begin{bmatrix}\int_{H_{\mathbf{x}^*}}\left(v_1^*\left(\mathbf{x}'^*\right)-v_1^*\left(\mathbf{x}^*\right)\right)\left(\mathrm{g}^{20}\left(\xi^*\right)+\mathrm{g}^{02}\left(\xi^*\right)\right)\mathrm{d}V'^*\\ \int_{H_{\mathbf{x}^*}}\left(v_2^*\left(\mathbf{x}'^*\right)-v_2^*\left(\mathbf{x}^*\right)\right)\left(\mathrm{g}^{20}\left(\xi^*\right)+\mathrm{g}^{02}\left(\xi^*\right)\right)\mathrm{d}V'^*\end{bmatrix}\\ &-\begin{bmatrix}\int_{H_{\mathbf{x}^*}}\left(v_1^*\left(\mathbf{x}'^*\right)-v_1^*\left(\mathbf{x}^*\right)\right)\left(v_1^*\left(\mathbf{x}^*\right)\mathrm{g}^{10}\left(\xi^*\right)+v_2^*\left(\mathbf{x}^*\right)\mathrm{g}^{01}\left(\xi^*\right)\right)\mathrm{d}V'^*\\ \int_{H_{\mathbf{x}^*}}\left(v_2^*\left(\mathbf{x}'^*\right)-v_2^*\left(\mathbf{x}^*\right)\right)\left(v_1^*\left(\mathbf{x}^*\right)\mathrm{g}^{10}\left(\xi^*\right)+v_2^*\left(\mathbf{x}^*\right)\mathrm{g}^{01}\left(\xi^*\right)\right)\mathrm{d}V'^*\end{bmatrix}+\begin{bmatrix}b_1^*\\ b_2^*\end{bmatrix}\end{aligned} \tag{5.75}$$

Conservation of energy

$$\rho^*\left(\mathbf{x}^*\right)\frac{\partial T^*\left(\mathbf{x}^*\right)}{\partial t^*}=\frac{k^*\left(\mathbf{x}^*\right)}{\mathrm{Re}\,\mathrm{Pr}}\int_{H_{\mathbf{x}^*}}\left(T^*\left(\mathbf{x}'^*\right)-T^*\left(\mathbf{x}^*\right)\right)\left(g^{20}\left(\xi^*\right)+g^{02}\left(\xi^*\right)\right)\mathrm{d}V'^*$$
$$+\frac{\mathrm{Ec}\mu^*}{\mathrm{Re}}\left(\begin{array}{l}2\left(\int_{H_{\mathbf{x}^*}}\left(v_1^*\left(\mathbf{x}'^*\right)-v_1^*\left(\mathbf{x}^*\right)\right)g^{10}\left(\xi^*\right)\mathrm{d}V'^*\right)^2\\+2\left(\int_{H_{\mathbf{x}^*}}\left(v_2^*\left(\mathbf{x}'^*\right)-v_2^*\left(\mathbf{x}^*\right)\right)g^{01}\left(\xi^*\right)\mathrm{d}V'^*\right)^2\\+\left(\int_{H_{\mathbf{x}^*}}\left(\left(v_1^*\left(\mathbf{x}'^*\right)-v_1^*\left(\mathbf{x}^*\right)\right)g^{01}\left(\xi^*\right)+\left(v_2^*\left(\mathbf{x}'^*\right)-v_2^*\left(\mathbf{x}^*\right)\right)g^{10}\left(\xi^*\right)\right)\mathrm{d}V'^*\right)^2\end{array}\right) \tag{5.76}$$
$$-\rho^*\left(\mathbf{x}^*\right)\int_{H_{\mathbf{x}^*}}\left(T^*\left(\mathbf{x}'^*\right)-T^*\left(\mathbf{x}^*\right)\right)\left(v_1^*\left(\mathbf{x}^*\right)g^{10}\left(\xi^*\right)+v_2^*\left(\mathbf{x}^*\right)g^{01}\left(\xi^*\right)\right)\mathrm{d}V'^*$$

where the non-dimensional relative position is calculated as $\xi^*=\mathbf{x}'^*-\mathbf{x}^*$.

The local Nusselt numbers are defined as

$$\mathrm{Nu}_{\mathrm{loc}}\left(x\right)=\left|\frac{\partial T^*}{\partial y^*}\right|_{y=\mathrm{loc}} \tag{5.77a}$$

$$\mathrm{Nu}_{\mathrm{loc}}\left(y\right)=\left|\frac{\partial T^*}{\partial x^*}\right|_{x=\mathrm{loc}} \tag{5.77b}$$

By applying the PD differential operator into Eq.(5.77), the Nusselt numbers can be calculated in the PD approach as

$$\mathrm{Nu}_{\mathrm{loc}}\left(x\right)=\left|\int_{H_{\mathbf{x}}}\left(T\left(\mathbf{x}'^*\right)-T\left(\mathbf{x}^*\right)\right)\mathrm{g}^{01}\left(\xi^*\right)\mathrm{d}V'^*\right|_{y=\mathrm{loc}} \tag{5.78a}$$

$$\mathrm{Nu}_{\mathrm{loc}}\left(y\right)=\left|\int_{H_{\mathbf{x}}}\left(T\left(\mathbf{x}'^*\right)-T\left(\mathbf{x}^*\right)\right)\mathrm{g}^{10}\left(\xi^*\right)\mathrm{d}V'^*\right|_{x=\mathrm{loc}} \tag{5.78b}$$

The average Nusselt numbers are defined as (L and W are the length and width in x and y direction, respectively)

$$\mathrm{Nu}_x=\frac{1}{L}\int_0^L\mathrm{Nu}_{\mathrm{loc}}\left(x\right)\mathrm{d}x \tag{5.79a}$$

$$\mathrm{Nu}_y = \frac{1}{W}\int_0^W \mathrm{Nu}_{\mathrm{loc}}(y)\mathrm{d}y \tag{5.79b}$$

5.4. Numerical implementation

In this section, the numerical implementation for fluid flow simulation is provided. There are two types of Lagrangian descriptions, i.e. total Lagrangian description and updated Lagrangian description. Both Lagrangian approaches have been discussed in state-based peridynamics [145]. Therefore, non-local Navier-Stokes equations are numerically implemented both in total and updated Lagrangian approaches. In addition, the Euler approach is provided for fluid flow coupled with heat transfer problems.

5.4.1. Kinematic quantities

The related kinematic quantities for numerical implementations are explained as follows. As shown in Fig. 5-2, point i represents the point of interest and point j represents one of its family members.

The definitions of relative kinematic quantities are shown in Fig. 5-2. The terms $\mathbf{x}$, $\mathbf{u}$, and $\mathbf{v}$ represent the position, displacement, and velocity vectors, respectively. The subscript $(_0)$ represents the initial configuration. On the other hand, the subscript $(_n)$ represents the current configuration. For example, $\mathbf{x}_0^i$ and $\mathbf{v}_0^i$ represent the position and the velocity vector for point i in the initial configuration, respectively. Here, $\boldsymbol{\xi}_0$, $\boldsymbol{\xi}_n$, $\boldsymbol{\xi}_{n+1}$ represent the relative position vectors in the initial, current, and updated configurations, respectively.

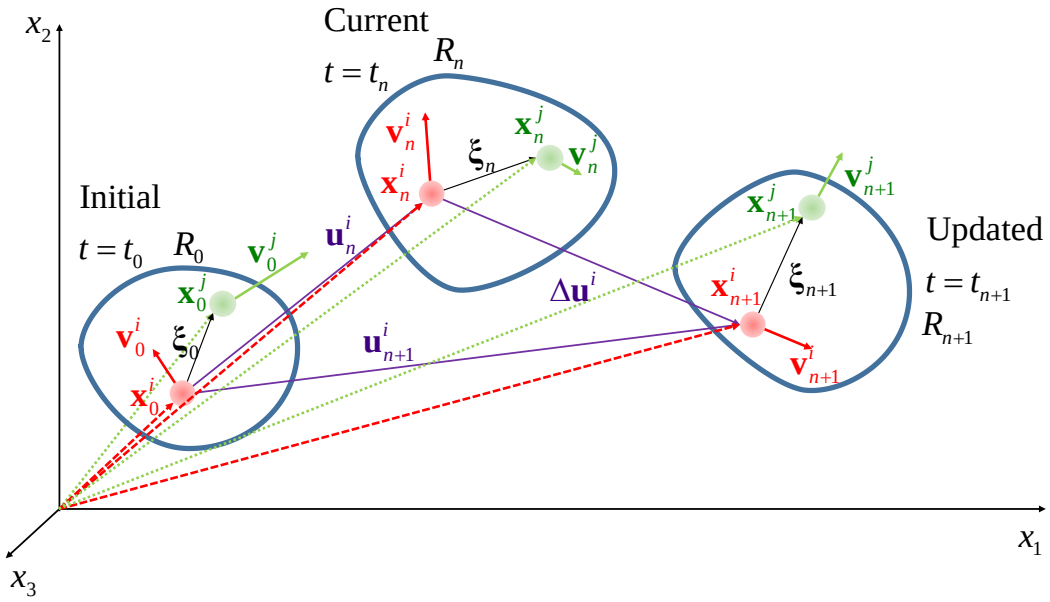

Fig. 5-2 Initial, current, and updated configurations in the fluid domain, R, for Lagrangian approach

For Euler description, the locations of the PD particles are not updated. The discretization for the Euler approach is provided in Fig. 5-3.

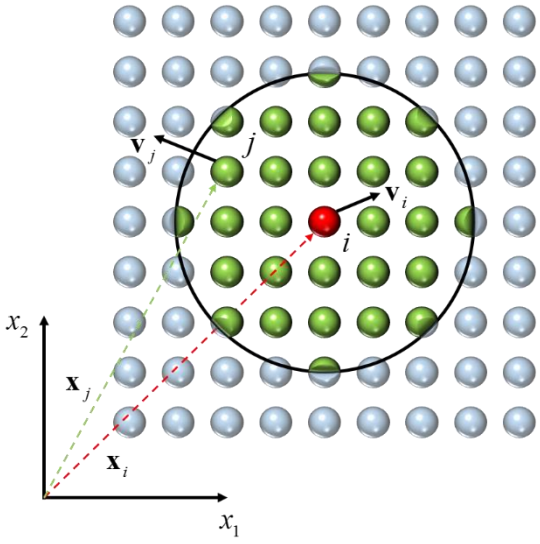

Fig. 5-3 PD discretization illustration: central point i and horizon $\delta = 3\Delta x$ with Δx being the point spacing distance

5.4.2. Total Lagrangian method

For numerical implementation, the integration is performed by using the discrete particles. Based on the derivations in Section 5.3, the algorithm in a total Lagrangian description is presented.

5.4.2.1 Governing equations in total Lagrangian description

In the total Lagrangian description, the governing equations in discretized form for incompressible fluid flows and compressible fluid flows are summarized as follows.

Conservation of Mass:

The discretized form of Eq. (5.23) can be evaluated as

$$\rho_{n+1}^{i} = \rho_{n}^{i} - \rho_{n}^{i}\Delta t\sum_{j=1}^{N_i}\left(\mathbf{g}_1\left(\boldsymbol{\xi}_0\right)\cdot\left(\mathbf{v}_n^j - \mathbf{v}_n^i\right)\right)V_0^j \tag{5.80}$$

where the subscript $\left(_n\right)$ represents the time step number, Δt represents the time step size, N_i represents the total number of family members of point i (red colour) and V_0^j represents the initial volume of point j (green colour). It should be noted that the density remains constant for incompressible fluid flow that is $\rho_{n+1}^{i} = \rho_0^i$.

Constitutive Equations for Pressure:

For incompressible fluid flow, the discretized form of Eq. (5.34) can be evaluated as

$$p_{n+1}^{i} = B\left(\left(\frac{\rho_{n+1}^{i}}{\rho_0^i}\right)^{\gamma} - 1\right) \tag{5.81}$$

For compressible fluid flow, the discretized form of Eq. (5.41) can be evaluated as

$$p_{n+1}^{i} = p_{n}^{i} - K_f\Delta t\sum_{j=1}^{N_i}\left(\mathbf{g}_1\left(\boldsymbol{\xi}_0\right)\cdot\left(\mathbf{v}_n^j - \mathbf{v}_n^i\right)\right)V_0^j \tag{5.82}$$

Conservation of Momentum:

For incompressible fluid flow, the discretized form of Eq. (5.50) can be evaluated as

$$\dot{\mathbf{v}}_{n+1}^{i}=\frac{1}{\rho_{n+1}^{i}}\sum_{j=1}^{N_i}\left[\mu\left(\mathrm{Tr}\left(\mathbf{g}_2\left(\xi_0\right)\right)\left(\mathbf{v}_n^j-\mathbf{v}_n^i\right)\right)-\left(p_n^j-p_n^i\right)\mathbf{g}_1\left(\xi_0\right)\right]V_0^j+\mathbf{b}_{n+1}^{i} \quad (5.83)$$

where $\dot{\mathbf{v}}^i$ represents the acceleration of point i.

For compressible fluid flow, the discretized form of Eq. (5.55) can be evaluated as

$$\dot{\mathbf{v}}_{n+1}^{i}=\frac{1}{\rho_{n+1}^{i}}\sum_{j=1}^{N_i}\left[\begin{array}{l}\mu\left(\mathrm{Tr}\left(\mathbf{g}_2\left(\xi_0\right)\right)\left(\mathbf{v}_n^j-\mathbf{v}_n^i\right)+\frac{1}{3}\mathbf{g}_2\left(\xi_0\right)\cdot\left(\mathbf{v}_n^j-\mathbf{v}_n^i\right)\right)\\-\left(p_n^j-p_n^i\right)\mathbf{g}_1\left(\xi_0\right)\end{array}\right]V_0^j+\mathbf{b}_{n+1}^{i} \quad (5.84)$$

Two kinds of time integration scheme can be utilized in the velocity and displacement updating: first-order scheme by using the Euler method and second-order scheme by using the Velocity Verlet algorithm [146].

First-order Euler method

the Forward Euler Method for Velocity:

$$\mathbf{v}_{n+1}^{i}=\mathbf{v}_n^i+\dot{\mathbf{v}}_{n+1}^{i}\Delta t \quad (5.85)$$

the Backward Euler Method for Displacement:

$$\mathbf{u}_{n+1}^{i}=\mathbf{u}_n^i+\mathbf{v}_{n+1}^{i}\Delta t \quad (5.86)$$

Second-order Velocity Verlet method [146]

$$\mathbf{v}_{n+1}^{i}=\mathbf{v}_n^i+\frac{1}{2}\left(\dot{\mathbf{v}}_{n+1}^{i}+\dot{\mathbf{v}}_n^i\right)\Delta t \quad (5.87)$$

$$\mathbf{u}_{n+1}^{i} = \mathbf{u}_{n}^{i} + \mathbf{v}_{n+1}^{i}\Delta t + \frac{1}{2}\dot{\mathbf{v}}_{n}^{i}\Delta t^{2} \tag{5.88}$$

5.4.2.2 Numerical algorithm for total Lagrangian description

The numerical algorithm for the total Lagrangian approach is provided in Fig. 5-4. Fig. 5-5(a) represents the PD differential operator construction, and Fig. 5-5(b) represents the boundary implementation. Since the total Lagrangian approach is adopted, the family members of each point remain the same during the time integration. The PD differential operator is constructed based on the initial configuration, i.e. peridynamic operator, $\mathbf{g}$ is a function of initial relative positions $\mathbf{g}\left(\xi_0\right)$. Therefore, the PD differential operator is constructed prior to the time integration, as shown in Fig. 5-4. During the numerical simulations, the PD differential operator associated with each PD bond is stored in a time-independent array. In addition, for PD differential operator construction, Math Kernel Library (MKL) [147] is utilized. The function 'DGESV' [148] which uses LU decomposition with partial pivoting and row interchanges is utilized for solving the coefficient matrix, $\mathbf{a}$, in Eq.(2.27).

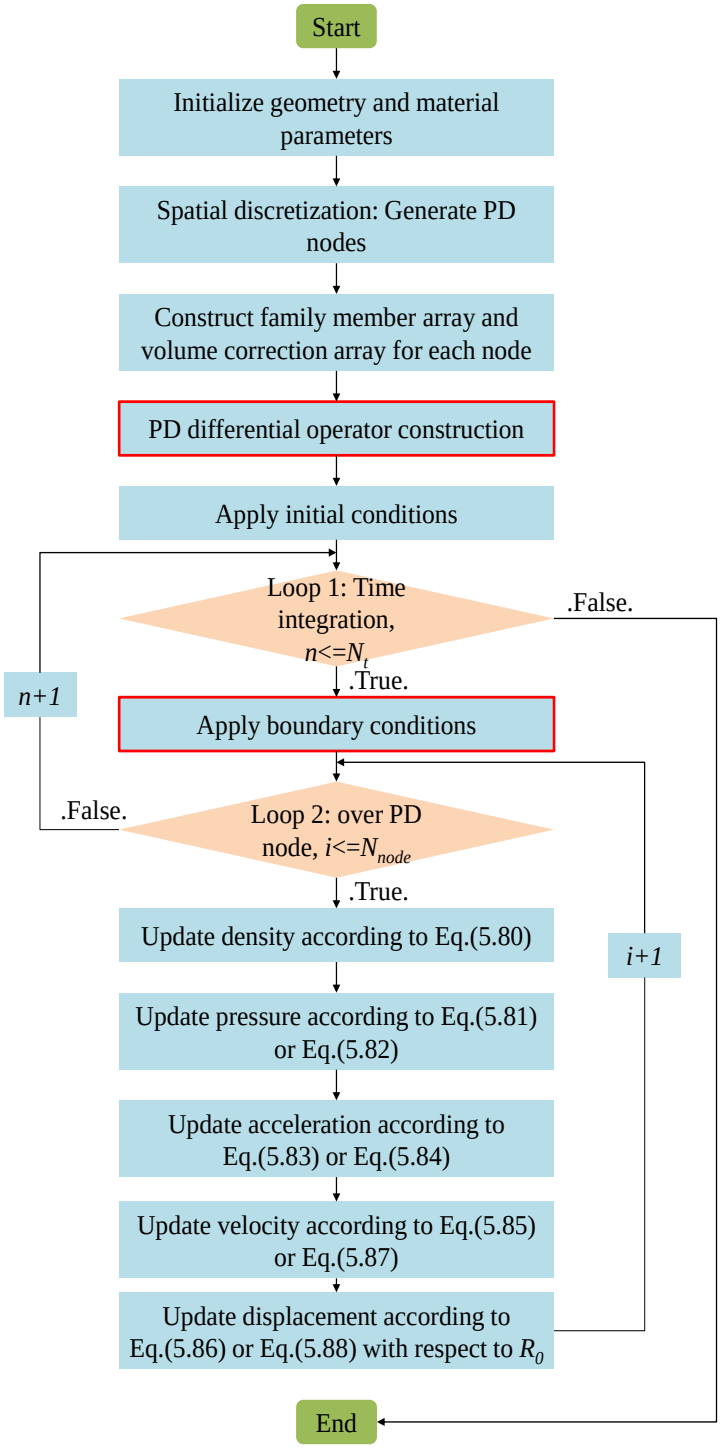

Fig. 5-4 Flowchart of the numerical algorithm for total Lagrangian approach

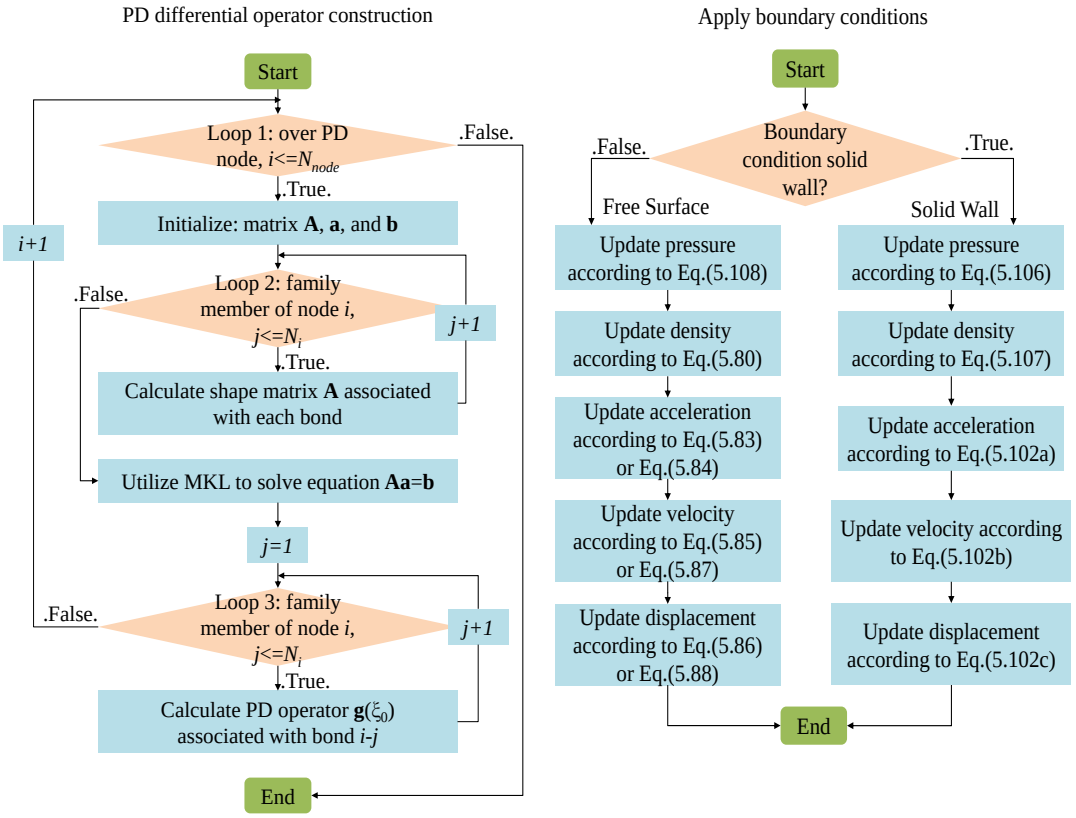

(a) (b)

Fig. 5-5 Flowchart for: (a) PD differential operator construction, and (b) boundary implementation

5.4.3. Updated Lagrangian method

In this section, the numerical algorithm for an updated Lagrangian description is developed for fluid flow simulations using the PD differential operator.

As shown in Fig. 5-6, point $\mathbf{x}$ is treated as the point of interest (shown in red colour) in a material body R. Since the long-range force is considered in the PD theory, the neighbourhood within which the central point $\mathbf{x}$ can interact with other points is denoted as $H_{\mathbf{x}}$, e.g. $H_{\mathbf{x}}^{n}$ at $t=t_n$ or $H_{\mathbf{x}}^{n+1}$ at $t=t_{n+1}$. The horizon δ keeps constant within time integration. It can be observed from the figure, at $t=t_n$, point $\mathbf{x}'$ (shown in green colour) is the family member of point $\mathbf{x}$, On the contrary, point $\mathbf{x}''$ locates outside the neighbourhood of point $\mathbf{x}$, leading to zero interact force. However, at time $t=t_{n+1}$, point $\mathbf{x}'$ goes out of the horizon domain and point $\mathbf{x}''$ comes into. Therefore,

the family members of point $\mathbf{x}$ are updated every time step when the updated Lagrangian description is adopted.

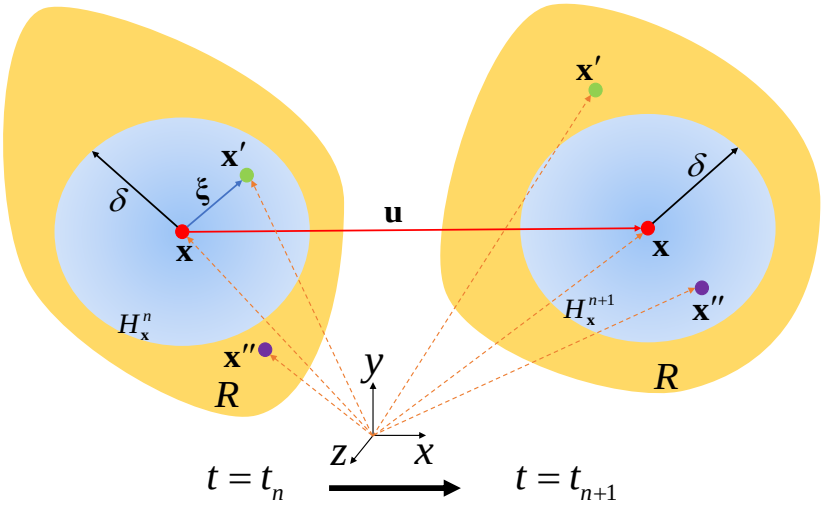

Fig. 5-6 Interaction of peridynamic central point $\mathbf{x}$ and its family member $\mathbf{x}'$ in current and updated configurations

5.4.3.1 Updated Lagrangian equations

The non-local fluid flow governing equations in the total Lagrangian description is already provided in Section 5.4.2. In the updated Lagrangian approach, the initial volume of point j, V_0^j, will be updated by using the current volume, V_n^j as

$$V_n^j = J_n V_0^j \tag{5.89}$$

where J_n is the determinant of Jacobian which is defined as

$$J_n = \det\left(\mathbf{F}_n\right) \tag{5.90}$$

In Eq.(5.90), $\mathbf{F}_n$ is the deformation gradients with respect to the initial configuration, which is defined as

$$\mathbf{F}_n = \frac{\partial \mathbf{x}_n}{\partial \mathbf{x}_0} \tag{5.91}$$

Similarly, the volume in the updated configuration V_{n+1}^{j} can be expressed in terms of initial volume as $\mathrm{d}V_{n+1}^{j} = J_{n+1}\mathrm{d}V_{0}^{j}$ with $J_{n+1} = \det\left(\mathbf{F}_{n+1}\right)$ and $\mathbf{F}_{n+1} = \partial\mathbf{x}_{n+1}/\partial\mathbf{x}_{0}$.

The volume in the updated configuration is related to the current configuration as

$$\mathrm{d}V_{n+1}^{j} = J_{n+1}J_{n}^{-1}\mathrm{d}V_{n}^{j} = \det\left(\Delta\mathbf{F}\right)\mathrm{d}V_{n}^{j} \tag{5.92}$$

where the relative deformation gradient $\Delta\mathbf{F}$ is defined as

$$\Delta\mathbf{F} = \frac{\partial\mathbf{x}_{n+1}}{\partial\mathbf{x}_{n}} = \frac{\partial\mathbf{x}_{n+1}}{\partial\mathbf{x}} / \frac{\partial\mathbf{x}_{n}}{\partial\mathbf{x}} = \mathbf{F}_{n+1}\mathbf{F}_{n}^{-1} \tag{5.93}$$

On the other hand, the non-local form of the deformation gradient tensor is defined in [149] by using the PD differential operator as

$$\mathbf{F} = \frac{\mathrm{Tr}\left(\mathbf{I}\right)}{m_{relF}}\int_{H_{\mathbf{x}}} w_{F}\left(\mathbf{y}'-\mathbf{y}\right)\otimes\left(\mathbf{x}'-\mathbf{x}\right)\mathrm{d}V' \tag{5.94}$$

with $w_{F} = \left(\delta/\left|\mathbf{x}'-\mathbf{x}\right|\right)^{2}$. The parameter $\mathbf{I}$ is the identity matrix with its trace $\mathrm{Tr}\left(\mathbf{I}\right)$ being 2 or 3 depending on the dimensions of the analysis. The parameter m_{relF} is evaluated as [149]

$$m_{relF} = V_{H}\delta^{2} \tag{5.95}$$

where V_{H} represents the volume of a sphere, $V_{H} = 4\pi\delta^{3}/3$ for 3D and volume of a disk, $V_{H} = h_{thick}\pi\delta^{2}$ for 2D with h_{thick} being the thickness of a disk [149]. Therefore, the non-local form of deformation gradient of point i for current and updated configurations are defined as [11, 132, 149]

$$\mathbf{F}_{n} = \frac{\mathrm{Tr}(\mathbf{I})}{m_{relF}}\int_{H_{n}^{i}} w_{F}\left(\boldsymbol{\xi}_{n}\right)\otimes\left(\boldsymbol{\xi}_{n}\right)\mathrm{d}V_{n}^{j} \tag{5.96}$$

and

$$\mathbf{F}_{n+1} = \frac{\mathrm{Tr}(\mathbf{I})}{m_{relF}} \int_{H_n^i} w_F\left(\xi_{n+1}\right) \otimes \left(\xi_n\right) \mathrm{d}V_n^j \tag{5.97}$$

By using the definition in Eq.(5.93), the non-local form of relative deformation gradient can be defined as

$$\Delta\mathbf{F} = \left[\int_{H_n^i} w_F\left(\xi_{n+1}\right) \otimes \left(\xi_n\right) \mathrm{d}V_n^j \right] \left[\int_{H_n^i} w_F\left(\xi_n\right) \otimes \left(\xi_n\right) \mathrm{d}V_n^j \right]^{-1} \tag{5.98}$$

Based on the developed non-local relative deformation gradient in Eq.(5.98), the volume for each material point is calculated by using Eq.(5.92).

5.4.3.2 Numerical algorithm for updated Lagrangian description

The numerical algorithm for the updated Lagrangian approach is provided in Fig. 5-7. And Fig. 5-8 represents the calculation of the relative deformation gradient. Within each time integration step, the coordinate of each node is updated as $\mathbf{x}_n = \mathbf{x}_0 + \mathbf{u}_n$. Therefore, the family members of each point are updated at each time step. The PD differential operator construction process is the same as Fig. 5-5 (a) except that the PD differential operator and the weighted function are constructed based on the current configuration, i.e. $\mathbf{g}$ and w are functions of the relative position in the current configuration $\mathbf{g}\left(\xi_n\right)$ and $w\left(\left|\xi_n\right|\right)$. Consequently, the PD differential operator associated with each bond is updated simultaneously for each time step. Therefore, in terms of computational time, it could be inferred that the updated Lagrangian program is more time consuming than the total Lagrangian program.

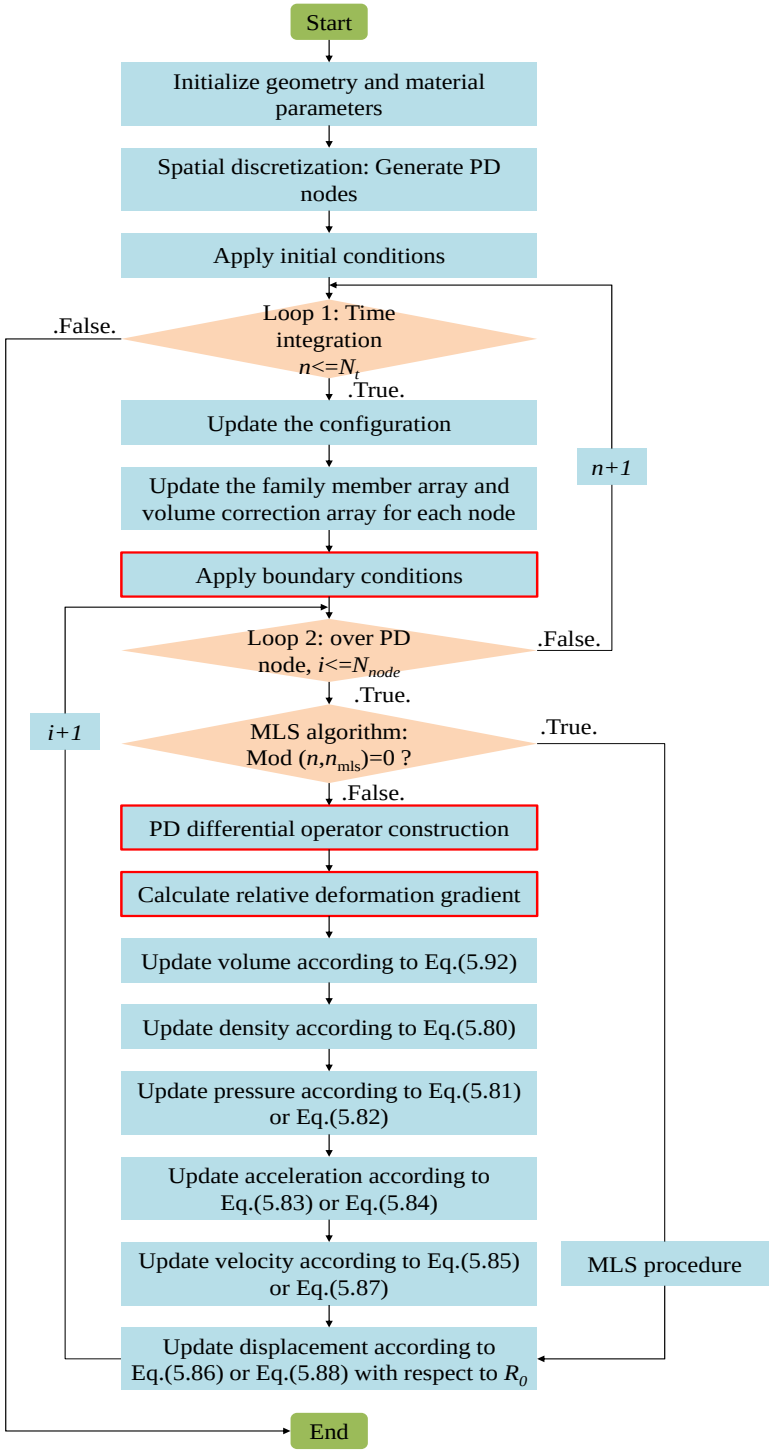

Fig. 5-7 Flowchart of the numerical algorithm for updated Lagrangian approach

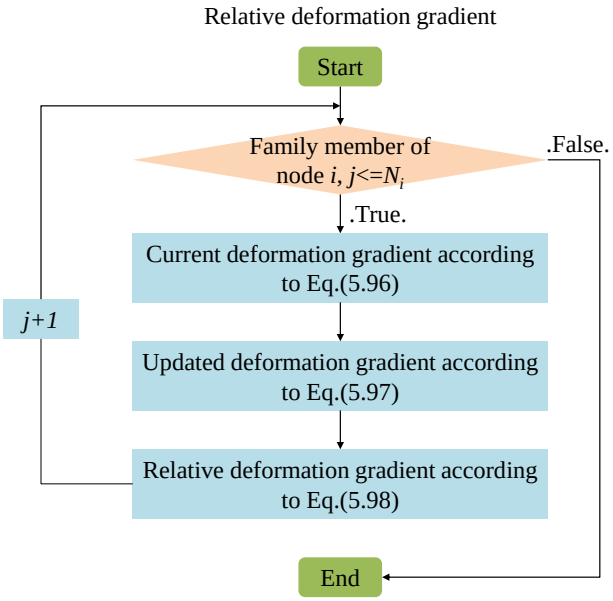

Fig. 5-8 Flowchart for relative deformation gradient calculation

5.4.4. Euler method

The fluid flow coupled with heat transfer problem is simulated in the Euler description. Therefore, in this section, the discretised form of the governing equations including the conservation of energy is provided.

5.4.4.1 Euler equations

The non-local form of the governing equations provided in Section 5.3 can be written in their discrete forms as;

Conservation of mass:

$$\rho_{n+1}^{i}=\rho_{n}^{i}-\Delta t\sum_{j=1}^{N_i}\left(\rho_{n}^{i}\left(\mathbf{g}_1\left(\boldsymbol{\xi}_0\right)\cdot\left(\mathbf{v}_{n}^{j}-\mathbf{v}_{n}^{i}\right)\right)+\left(\rho_{n}^{j}-\rho_{n}^{i}\right)\mathbf{v}_{n}^{i}\cdot\mathbf{g}_1\left(\boldsymbol{\xi}_0\right)\right)V_j \tag{5.99}$$

Conservation of momentum:

$$\dot{\mathbf{v}}_{n+1}^{i}=\frac{1}{\rho_{n+1}^{i}}\left\{\begin{array}{l}-\sum_{j=1}^{N_i}\left(p_n^j-p_n^i\right)\mathbf{g}_1\left(\xi_0\right)V_j+\mu\sum_{j=1}^{N_i}\left(\mathbf{v}_n^j-\mathbf{v}_n^i\right)\mathrm{Tr}\left(\mathbf{g}_2\left(\xi_0\right)\right)V_j\\-\rho_{n+1}^{i}\sum_{j=1}^{N_i}\left(\mathbf{v}_n^j-\mathbf{v}_n^i\right)\left(\mathbf{v}_n^i\cdot\mathbf{g}_1\left(\xi_0\right)\right)V_j\end{array}\right\}+\mathbf{b}_{n+1}^{i} \tag{5.100}$$

Conservation of Energy:

$$T_{n+1}^{i}=T_n^i+\frac{\Delta t}{\rho_{n+1}^{i}C}\left(\begin{array}{l}k\sum_{j=1}^{N_i}\left(T_n^j-T_n^i\right)\mathrm{Tr}\left(\mathbf{g}_2\left(\xi_0\right)\right)V_j\\+\mu\left(\begin{array}{l}2\sum_{\ell=1}^{3}\left(\sum_{j=1}^{N_i}\left(v_n^{\ell,j}-v_n^{\ell,i}\right)g_1^{\ell}\left(\xi_0\right)V_j\right)^2\\+\sum_{\lambda,\ell(\lambda<\ell)=1}^{3}\left(\sum_{j=1}^{N_i}\left(\begin{array}{l}\left(v_n^{\lambda,j}-v_n^{\lambda,i}\right)g_1^{\ell}\left(\xi_0\right)\\+\left(v_n^{\ell,j}-v_n^{\ell,i}\right)g_1^{\hbar}\left(\xi_0\right)\end{array}\right)V_j\right)^2\end{array}\right)\\-\rho_{n+1}^{i}C\sum_{j=1}^{N_i}\left(T_n^j-T_n^i\right)\left(\mathbf{v}_n^i\cdot\mathbf{g}_1\left(\xi_0\right)\right)V_j+Q\end{array}\right) \tag{5.101}$$

5.4.4.2 Numerical algorithm

The flowchart of the numerical algorithm is provided in Fig. 5-9. Firstly, the peridynamic differential operator is constructed as a function of the initial relative position. Therefore, the construction of peridynamic differential operator is conducted prior to the time integration. Secondly, both the thermal and flow fields are considered in the program. Thus, a flag array is constructed to indicate the material point interactions belonging to the thermal field or the flow field. Finally, the thermal field and the flow field are considered in a coupled manner.

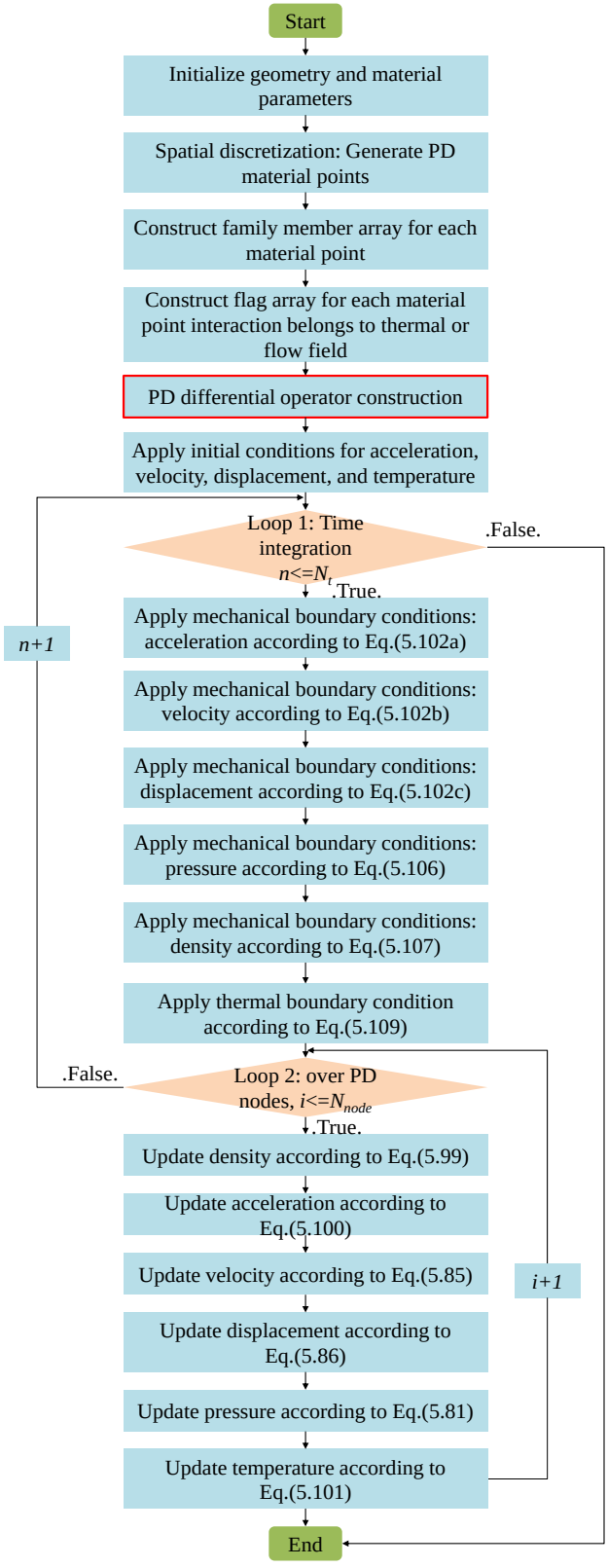

Fig. 5-9 Flowchart for numerical algorithm in Euler description for heat conducting fluid flow simulation

5.4.5. Boundary implementation

5.4.5.1 Solid boundary treatment

The implementation of a solid wall is a crucial issue in flow simulations. Fictitious layers [10, 39, 40, 150] can be used to implement the boundary conditions. As illustrated in Fig. 5-10, the fictitious layers (shown by red spheres) are located outside the boundary to simulate the solid wall. The thickness of the fictitious layers is chosen as the size of the horizon [151]. The positions of fictitious particles remain the same during the time integration [120, 152]. In Fig. 5-10, particle i represents the fictitious particles. Particle j represents one of its family members which belongs to fluid particles. The acceleration, velocity, and displacement of the fictitious particle i are defined as the same as the solid wall, i.e.

$$\dot{\mathbf{v}}_i = \dot{\mathbf{v}}_{solid\ wall} \tag{5.102a}$$

$$\mathbf{v}_i = \mathbf{v}_{solid\ wall} \tag{5.102b}$$

$$\mathbf{u}_i = \mathbf{u}_{solid\ wall} \tag{5.102c}$$

For the pressure evaluation of particle i, the formulation proposed by Adami et al. [152] is utilized. The viscous interaction between particle i and j is simply omitted [152]. In order to eliminate the penetration of fluid particles into the wall surface, the force balance at the wall interface is enforced as [152]

$$\frac{\mathrm{d}\mathbf{v}_j}{\mathrm{d}t} = -\frac{\nabla p_j}{\rho_j} + \mathbf{b} = \dot{\mathbf{v}}_i \tag{5.103}$$

where $\dot{\mathbf{v}}_i$ represents the acceleration of the solid particle i in the fictitious domain. The term p_j is the pressure of the fluid particle and ρ_j is the density of the fluid particle. According to [152], Eq. (5.103) can be further calculated as

$$\int \nabla p \cdot \mathbf{d}l = \rho_j \int \left(\mathbf{b} - \dot{\mathbf{v}}_i\right) \cdot \mathbf{d}l \tag{5.104}$$

where $\mathbf{d}l$ is a vectoral length element between fluid and fictitious particles [152]. For a single bond between the fluid and the fictitious particle, Eq.(5.104) takes the form as

$$p_i - p_j = \rho_j \left(\mathbf{b} - \dot{\mathbf{v}}_i\right) \cdot \xi_{ij} \tag{5.105}$$

where ξ_{ij} represents the relative position from the fluid particle to the dummy particle which can be expressed as $\xi_{ij} = \mathbf{x}_i - \mathbf{x}_j$, shown in Fig. 5-10. Consequently, the pressure of the fictitious particle i, p_i can be obtained by summation of all contributions of neighbouring fluid particles using the weighted function as [152]

$$p_i = \frac{\sum_{j=1}^{N_{i,fluid}} \left(p_j + \rho_j \left(\mathbf{b} - \dot{\mathbf{v}}_i\right) \cdot \xi_{ij}\right) w\left(\left|\xi_{ij}\right|\right)}{\sum_{j=1}^{N_{i,fluid}} w\left(\left|\xi_{ij}\right|\right)} \tag{5.106}$$

where $N_{i,fluid}$ represents the total number of the family member of particle i which belongs to fluid particles. The weighted function $w\left(\left|\xi_{ij}\right|\right)$ is defined as in Eq.(2.25).

Then the density of the fictitious particle i can be calculated by using Eq. (5.34) as

$$\rho_i = \rho_0 \left(\frac{p_i}{B} + 1\right)^{1/\gamma} \tag{5.107}$$

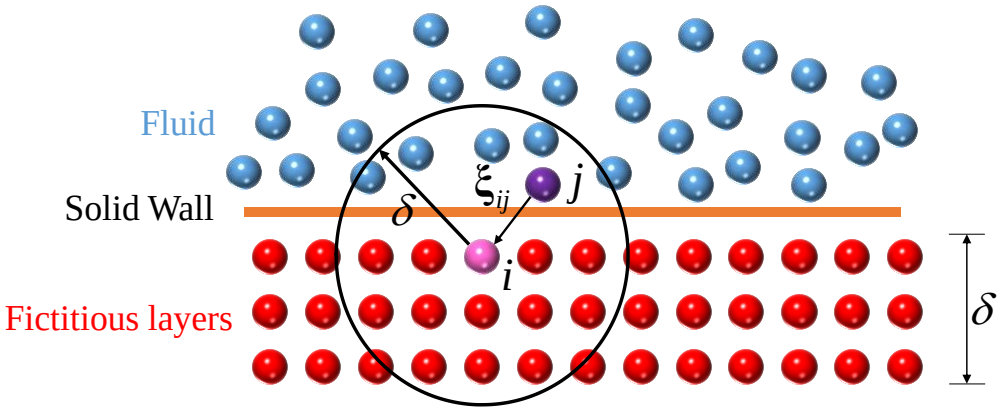

Fig. 5-10 Illustration of solid boundary implementation

5.4.5.2 Free surface boundary treatment

Similarly, the free surface boundary conditions are implemented by using dummy particles. Fictitious layer with its thickness being equal to the size of the horizon is added on the free surfaces. The material properties of the dummy particles are chosen the same as the fluid particles. The acceleration, velocity, displacement, and density are calculated for both fluid and dummy particles in the free surface. The only difference is that free surface pressure is applied to the fictitious layer as

$$p_{fictitious\ particles} = p_{free\ surface} = 0 \tag{5.108}$$

5.4.5.3 Temperature boundary treatment

The temperature on the boundary is denoted as T_{wall}. The temperature of the fictitious particle i is implemented as [39, 43, 150]

$$T_i = 2T_{wall} - T_j \tag{5.109}$$

The fictitious particle j is located at the same distance from the boundary as the fluid particles, i as shown in Fig. 5-11.

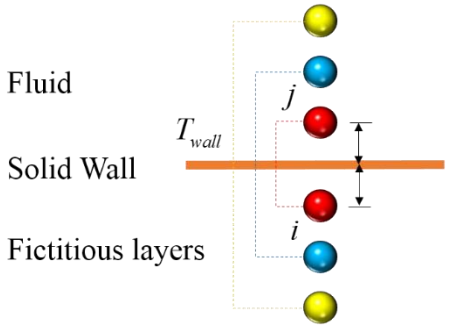

Fig. 5-11 Temperature boundary implementation (the pair of the fictitious particle and its corresponding fluid particle are shown in the same colour)

5.4.6. Numerical treatments

5.4.6.1 Initial damping

In order to improve the numerical stability of free surface flow simulation, such as dam collapse simulation, extra numerical implementations are used. First, damping time t_{damp} is chosen during which the acceleration of each PD node is multiplied by a factor $\zeta(t)$ as [152]

$$\zeta(t)=\begin{cases}0.5\left[\sin\left(\left(-0.5+t/t_{damp}\right)\pi\right)+1\right], & t<t_{damp}\\ 1, & t\geq t_{damp}\end{cases} \tag{5.110}$$

5.4.6.2 Moving least square scheme

The moving least square (MLS) algorithm is introduced to hydrodynamics by Dilts [153]. The MLS method [154] is adopted for every n_{MLS} time step to smooth the velocity and density profiles as

$$\mathbf{v}\left(\mathbf{x}_n^i\right)=\frac{\sum_j \mathbf{v}\left(\mathbf{x}_n^j\right) w_{MLS}\left(\mathbf{x}_n^i,\mathbf{x}_n^j\right)}{\sum_j w_{MLS}\left(\mathbf{x}_n^i,\mathbf{x}_n^j\right)} \tag{5.111}$$

$$\rho\left(\mathbf{x}_n^i\right)=\sum_j m_{mass} w_{MLS}\left(\mathbf{x}_n^i,\mathbf{x}_n^j\right) \tag{5.112}$$

with m_{mass} representing the initial mass of one PD particle, w_{MLS} is the smoothing weighted function which can be expressed as [154]

$$w_{MLS}\left(\mathbf{x}_n^i,\mathbf{x}_n^j\right)=\left[\beta_0\left(\mathbf{x}_n^i\right)+\beta_1\left(\mathbf{x}_n^i\right)\left(-\xi_{n,x}\right)+\beta_2\left(\mathbf{x}_n^i\right)\left(-\xi_{n,y}\right)\right] w_s\left(\mathbf{x}_n^i,\mathbf{x}_n^j\right) \tag{5.113}$$

with

$$\boldsymbol{\xi}_n=\xi_{n,x}\mathbf{e}_1+\xi_{n,y}\mathbf{e}_2 \tag{5.114a}$$

$$\boldsymbol{\beta}\left(\mathbf{x}_n^i\right)=\begin{pmatrix}\beta_0\\ \beta_1\\ \beta_2\end{pmatrix}=\mathbf{S}^{-1}\left(\mathbf{x}_n^i\right)\begin{bmatrix}1\\ 0\\ 0\end{bmatrix} \tag{5.114b}$$

$$\mathbf{S}\left(\mathbf{x}_n^i\right)=\sum_B w\left(\mathbf{x}_n^i,\mathbf{x}_n^j\right)\tilde{\mathbf{S}}\left(\mathbf{x}_n^i,\mathbf{x}_n^j\right) \tag{5.114c}$$

$$\tilde{\mathbf{S}}\left(\mathbf{x}_n^i,\mathbf{x}_n^j\right)=\begin{bmatrix}1 & -\xi_{n,x} & -\xi_{n,y}\\ -\xi_{n,x} & \left(\xi_{n,x}\right)^2 & \xi_{n,x}\xi_{n,y}\\ -\xi_{n,y} & \xi_{n,x}\xi_{n,y} & \left(\xi_{n,y}\right)^2\end{bmatrix} \tag{5.114d}$$

$$w_s\left(\mathbf{x}_n^i,\mathbf{x}_n^j\right)=e^{-\left(2|\xi_n|/\delta\right)^2} \tag{5.114e}$$

The flowchart for the MLS algorithm is provided in Fig. 5-12. If the remainder of the current time step number n divided by n_{MLS} is equal to zero, an additional MLS part will be added to the algorithm provided in Section 5.4.2 or 5.4.3. The density, velocity will be smoothed based on Eq.(5.112) and Eq.(5.111). As a result, the pressure and displacement will be recalculated according to the smoothed density and velocity.

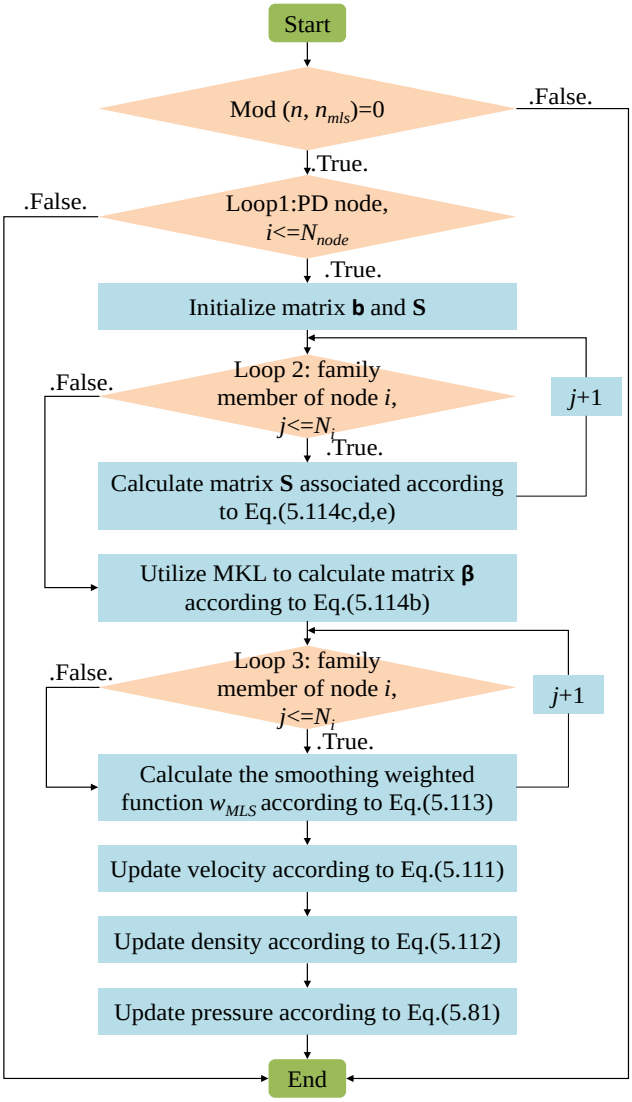

Fig. 5-12 Flowchart for the MLS algorithm

5.5. Isothermal fluid flow numerical simulations

In this section, numerical examples of several classical fluid flow problems are presented by using the proposed non-local PD formulations. The validation of the PD formulations is conducted by the comparisons between the PD results and those from other solutions. In all the following simulation cases, the fluid is water with density $\rho = 10^3$ kg/m^3 and dynamic viscosity $\mu = 10^{-3}$ kg/ms . Furthermore, the Mach numbers in all cases are less than 0.3 $(M < 0.3)$, leading to incompressible fluid flow. Therefore, the weakly compressible technique described in Section 5.3.2 is adopted for the pressure calculation.

5.5.1. Hydrostatic test

In the section, a hydrostatic simulation is conducted to study energy conservation. The fluid is in an open container with dimensions being $L \times W = 0.05\,\text{m} \times 0.03\,\text{m}$, as shown in Fig. 5-13 (a). The gravity acceleration being $|\mathbf{g}| = 9.8\,\text{m/s}^2$. The analytical solution of the hydrostatic pressure is calculated as $p_{analytical} = \rho|\mathbf{g}|(W - y)$ where y represents the vertical coordinate. For the PD discretization, as shown in Fig. 5-13 (b), 40×24 PD particles are in x and y directions with the initial particle spacing being $\Delta x = 1.25 \times 10^{-3}$ m. In order to save the computational time, only one fictitious layer is imposed to simulate the solid wall. The simulation time step size is chosen as $\Delta t = 10^{-5}$ s with total simulation time being $t = 1.5$ s. The Velocity Verlet algorithm is adopted.

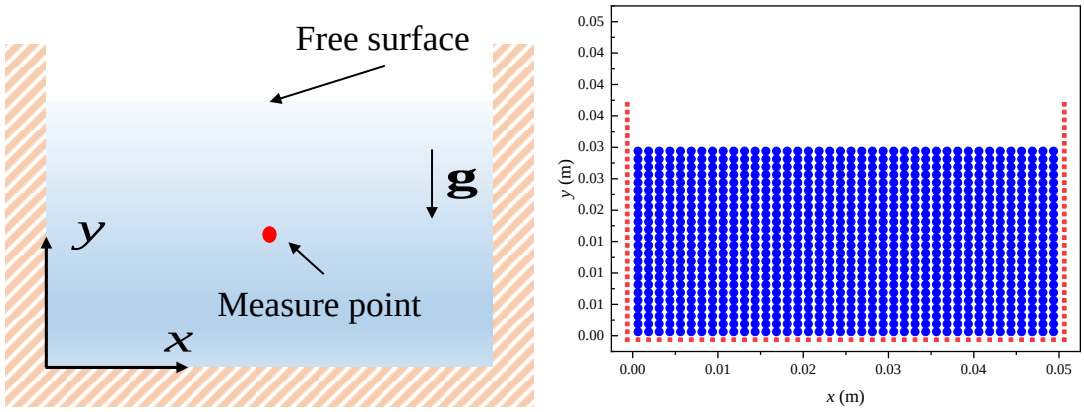

(a) (b)

Fig. 5-13 Schematic of the hydrostatic problem (a) geometry illustration and (b) PD discretization

The time history of the pressure of the measured point is presented in Fig. 5-14 (a), with the analytical solution being presented for comparison. The time history of the kinetic energy of the whole particles is shown in Fig. 5-14 (b). The pressure profile along the mid vertical line $x = 2.5 \times 10^{-2}$ m is compared with the analytical solution, as shown in Fig. 5-15 (a). Furthermore, the deformed configuration at the final time is presented in Fig. 5-15 (b). It can be observed that the PD predicted results agree well with the analytical solution. Thus, the capability of the present PD model for

simulating hydrostatic problems is demonstrated. In addition, the energy conservation of the model is also validated.

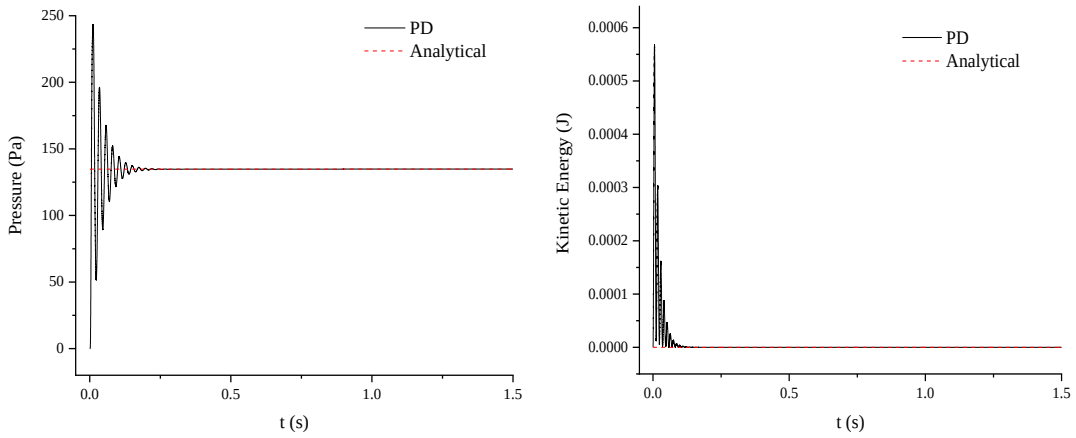

(a) (b)

Fig. 5-14 Time history of pressure (a) and kinetic history (b) of the measured point.

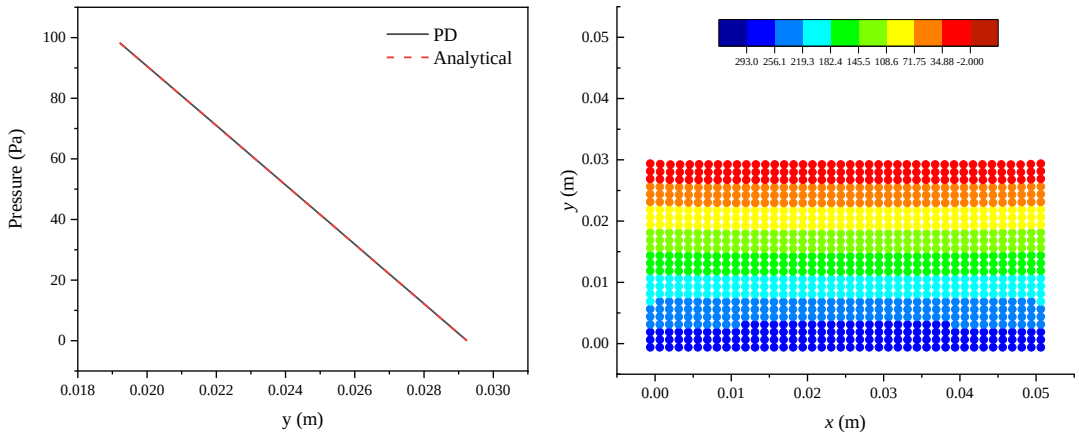

(a) (b)

Fig. 5-15 Pressure comparison on the mid vertical line $x = 2.5\times10^{-2}$ m (a) and deformed configuration (b)

5.5.2. Couette flow

First, the classical Couette flow is considered which involves fluid flow between two infinite plates with a stationary initial condition. As illustrated in Fig. 5-16 (a), the two plates (shown in orange colour) are located at $y = 0$ and $y = W$ with dimensions of $L = W = 10^{-3}$ m. The two vertical edges are free, and the body force is zero. At time

$t = 0$, the upper plate suddenly moves at a constant velocity $v_0 = 2.5\times10^{-5}$ m/s parallel to the x direction. The corresponding Reynolds number is;

$$\mathrm{Re} = \frac{v_0 W}{\nu} = 2.5\times10^{-2} \tag{5.115}$$

As shown in Fig. 5-16 (b), the mesh size of the PD discretization is represented by Δx. The horizon is chosen as $\delta = 3.015\Delta x$ [10, 14]. The time step size is chosen as 10^{-6} s and the total simulation time is 0.6 s. Fictitious boundary layers (represented by red nodes) with their thickness being $3\Delta x$ (horizon) are added to implement the solid wall boundary conditions, i.e.

$$v_x\left(x, y<0, t\right) = v_y\left(x, y<0, t\right) = 0 \tag{5.116a}$$

$$v_x\left(x, y>W, t\right) = 2.5\times10^{-5}\ \text{m/s},\ v_y\left(x, y>W, t\right) = 0 \tag{5.116b}$$

where v_x and v_y represent the horizontal and vertical velocities, respectively. Regarding the implementation of the other two vertical edges, if a PD node flows out of the right/left edge, it will immediately re-enter the opposite edge [132]. Therefore, the displacement of the material point flowing out from the edges can be modified as

$$u_x^{modified} = u_x - L, \text{ if } x>L \tag{5.117a}$$

$$u_x^{modified} = u_x + L, \text{ if } x<0 \tag{5.117b}$$

where u_x represents the horizontal displacement. Finally, the total Lagrangian algorithm described in Section 5.4.2 is applied to this problem.

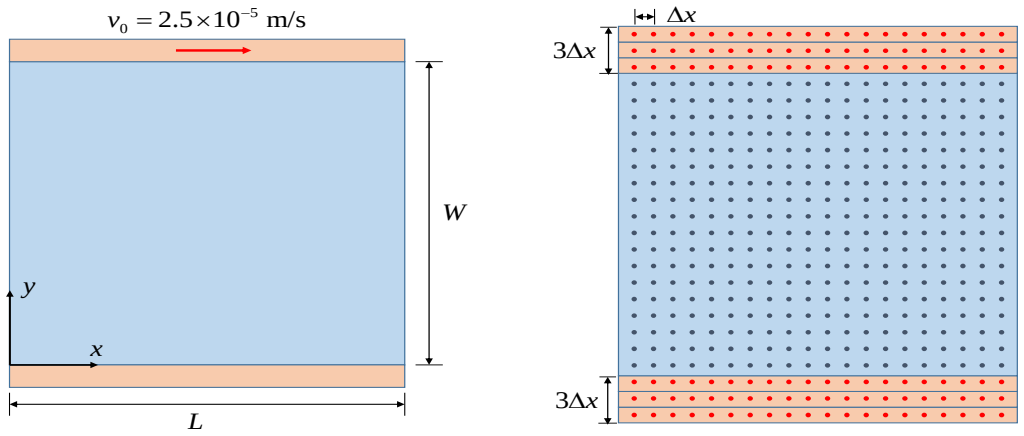

(a) (b)

Fig. 5-16 Couette flow simulation illustration (a) geometry illustration and (b) PD discretization

In order to validate the proposed non-local PD model, the PD predicted results are compared with the analytical series solution provided as [137]

$$v_x(y,t) = \frac{v_0}{W}y + \sum_{n=1}^{\infty}\frac{2v_0}{n\pi}(-1)^n \sin\left(\frac{n\pi}{W}y\right)\exp\left(-\nu\frac{n^2\pi^2}{W^2}t\right) \quad (5.118)$$

First, in order to estimate the sensitivity of mesh size on the accuracy, a mesh convergence study is performed by using a $n\times n$ mesh where $n = 50,100,200,400$. Fig. 5-17 shows the relative percentage error for the steady-state velocity at $x = L/2$ for different mesh sizes. The relative percentage error is calculated as [155]

$$\varepsilon_r(\%) = \sqrt{\frac{\sum\left(v_{PD} - v_{Analytical}\right)^2}{\sum\left(v_{Analytical}\right)^2}}\times 100 \quad (5.119)$$

As can be seen from the results, as the mesh size increases the velocity value converges. Even with coarse meshes, i.e. 50×50, the relative percentage error is approximate 1.5%.

Next, PD results are compared with analytical solutions provided in Eq.(5.118). Fig. 5-18 shows the comparison between the velocity profiles obtained by using the PD model and the series solution at different times by using 400×400 mesh. The steady-

state solution is represented at time $0.6\,\mathrm{s}$. It can be observed that the solutions from these two methods match very well, confirming the accuracy of the proposed non-local PD model. The horizontal velocity field for the steady-state is shown in Fig. 5-19. Consequently, the robustness of the proposed non-local PD model in the total Lagrangian description is verified.

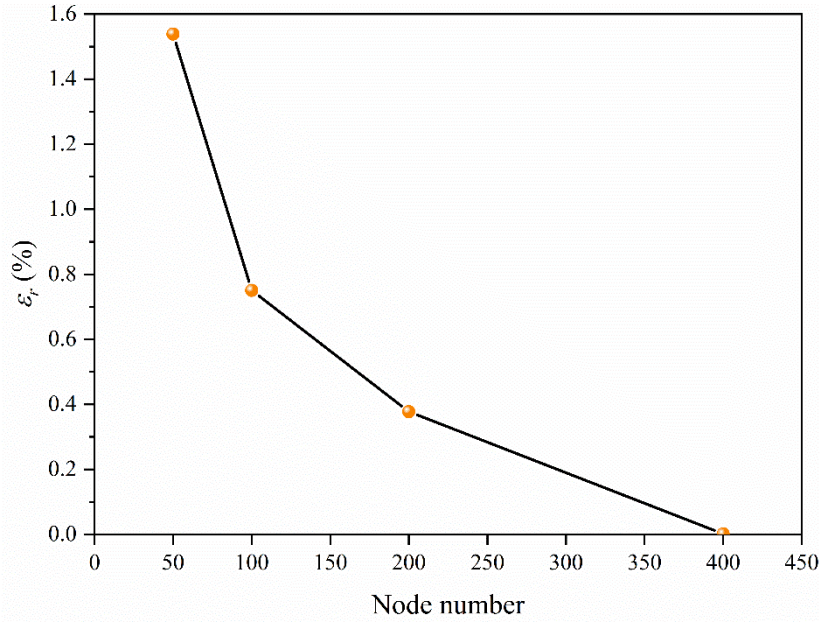

Fig. 5-17 Convergence study for PD solutions for Couette flow for different grid sizes at $t = 0.6\,\mathrm{s}$

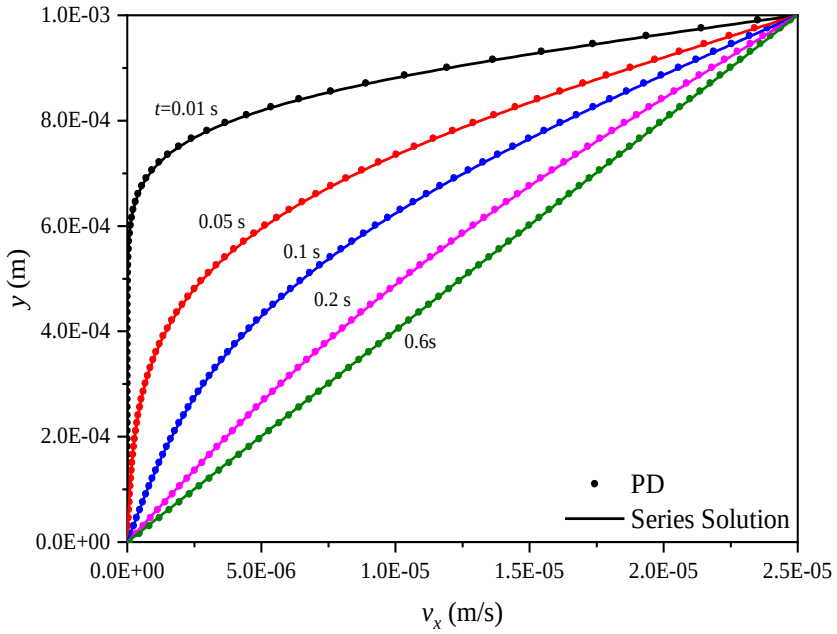

Fig. 5-18 Comparison of PD and series solutions for Couette flow

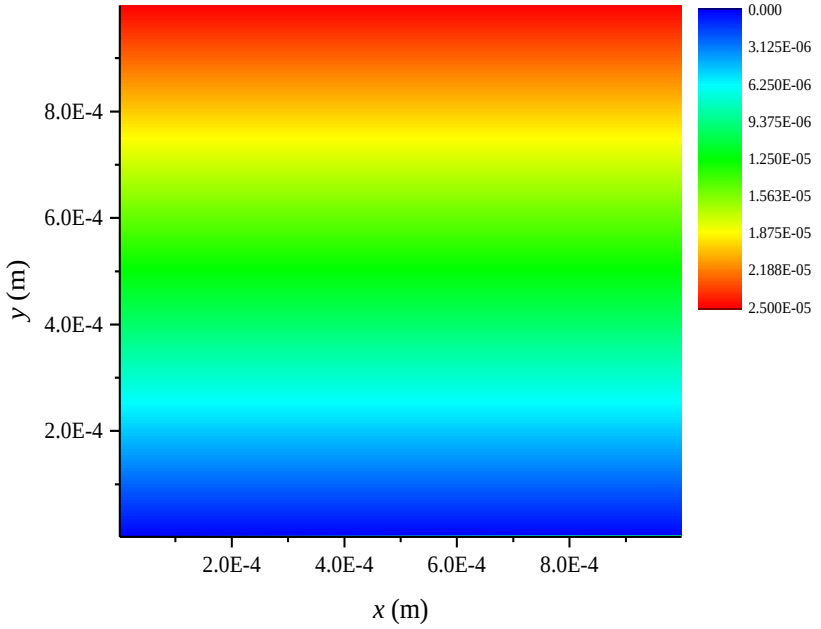

Fig. 5-19 Contour plot of horizontal velocity $v_x\left(\mathrm{m/s}\right)$ predicted by PD at $t=0.6\,\mathrm{s}$

5.5.3. Poiseuille flow

The second simulation case is Poiseuille flow between two stationary infinite plates at $y=0$ and $y=W$. The geometry is the same as the one from Couette flow, i.e.

$L = W = 10^{-3}$ m as shown in Fig. 5-16. The other two vertical edges are free. The fluid is initially at rest. Then a body force $F = 2\times10^{-4}$ m/s^2 parallel to the x direction is applied to drive the fluid to flow gradually, leading to a steady-state flow distribution finally.

In the numerical implementation, the same PD discretization model is adopted by using 400×400 mesh in the flow region with the horizon chosen as $\delta = 3.015\Delta x$. The constant time step size is 10^{-6} s and the total simulation time is 0.6 s. The solid wall boundary condition is implemented by using the fictitious layer as illustrated in Fig. 5-16 (b)

$$v_x\left(x, y<0, t\right) = v_y\left(x, y<0, t\right) = 0 \tag{5.120a}$$

$$v_x\left(x, y>W, t\right) = v_y\left(x, y>W, t\right) = 0 \tag{5.120b}$$

Besides, the vertical boundary implementation approach provided in Section 5.4.5 is also utilized. The total Lagrangian method described in Section 5.4.2 is adopted.

In order to validate the proposed PD model, the simulation results are compared with the time-dependent series solution provided as [137]

$$v_x\left(y,t\right) = \frac{F}{2\nu}y\left(y-W\right) + \sum_{n=0}^{\infty}\frac{4FW^2}{\nu\pi^3\left(2n+1\right)^3}\sin\left(\frac{\pi y}{W}\left(2n+1\right)\right)\exp\left(-\nu\frac{\left(2n+1\right)^2\pi^2}{W^2}t\right) \tag{5.121}$$

The horizontal velocity profiles obtained by the PD model are compared with the analytical solutions provided in Eq. (5.121), as shown in Fig. 5-20. Good agreements are also obtained in this case, validating the proposed non-local PD model. The horizontal velocity field is provided in Fig. 5-21 at time 0.6 s. As can be seen from the results, the maximum velocity is obtained as $v_0 = 2.5\times10^{-5}$ m/s which corresponds to the Reynold number as $\mathrm{Re} = 2.5\times10^{-2}$.

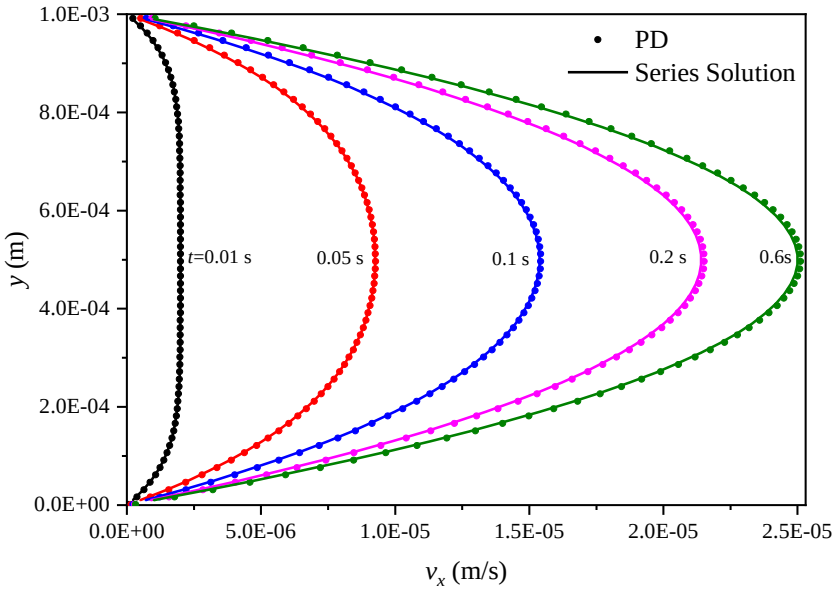

Fig. 5-20 Comparison of PD and series solutions for Poiseuille flow

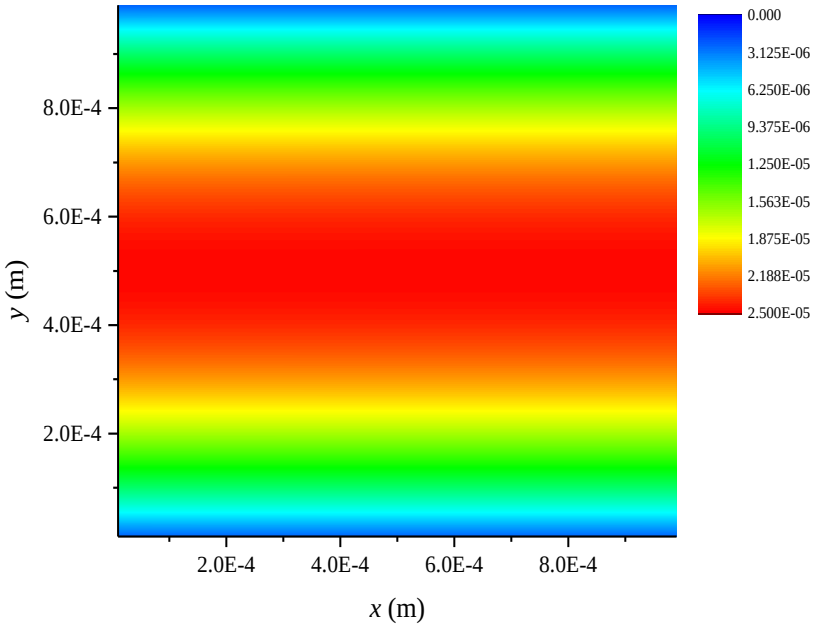

Fig. 5-21 Contour plot of horizontal velocity $v_x\left(\mathrm{m/s}\right)$ predicted by PD at $t=0.6\,\mathrm{s}$

5.5.4. Taylor-Green vortex

As a third simulation case, the two-dimensional Taylor-Green vortex at Re=1 is simulated by the proposed PD model in a total Lagrangian description. The geometry

of the fluid field is set as $[0,1]\times[0,1]$. The analytical solution of the velocity field is given as

$$v_1(x,y,t) = -v_0 e^{bt}\cos(2\pi x)\sin(2\pi y) \tag{5.122a}$$

$$v_2(x,y,t) = v_0 e^{bt}\sin(2\pi x)\cos(2\pi y) \tag{5.122b}$$

where the decay rate is $b = -8\pi^2/\mathrm{Re}$ [156] and v_0 is the maximum initial velocity magnitude.

As shown in Fig. 5-22 (b), four fictitious layers with their thicknesses being horizon are added outside the fluid field. The fictitious particles (shown in grey colour) are assorted into eight regions (numbered by yellow colour). Their physical parameters such as velocity etc. are forced to be equal to the fluid particles (shown in orange colour) in the same corresponding numbered region (shown in red colour). Therefore, the periodic boundary conditions in both x and y directions are implemented. As to the initial condition, as shown in Fig. 5-22 (a), the analytical velocity distribution at $t = 0$ is used with $v_0 = 0.04$ as

$$v_1(x,y,0) = -0.04\cos(2\pi x)\sin(2\pi y) \tag{5.123a}$$

$$v_2(x,y,0) = 0.04\sin(2\pi x)\cos(2\pi y) \tag{5.123b}$$

The time step size is chosen as $\mathrm{d}t = 1\times10^{-5}$ and the simulation time is $t = 0.05$. Three different mesh sizes are chosen as $\Delta x = 1/n$ with $n = 40, 50, 100$ to conduct the convergence study.

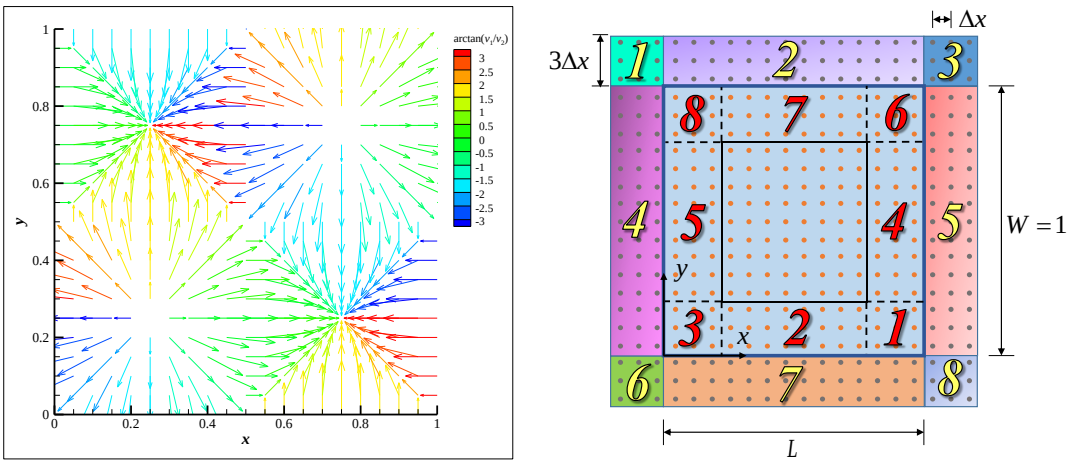

(a) (b)

Fig. 5-22 (a) Geometry illustration and initial velocity vector plot and (b) coordinate definition and boundary implementation for the Taylor Green vortex PD

A comparison of the decay of the maximum velocity magnitude is provided in Fig. 5-23. The exact solution and the remeshed smoothed particle hydrodynamics (rSPH) solution [157] are provided for comparison. It can be inferred that the PD predicted results agree well with the exact and rSPH solution. For the error analysis of the PD simulations, the relative error norm L_∞ is calculated as [156, 157]

$$L_\infty = \max_{t=0}^{T_{\max}} \left(\left| \frac{\max\left(\left| \mathbf{v}_i\left(t\right) \right| \right) - v_0 e^{bt}}{v_0 e^{bt}} \right| \right) \tag{5.124}$$

with $T_{\max}$ being the time where $\left(v_0 e^{bt}\right) = v_0/50$ [157]. The relative errors obtained by 40×40, 50×50, and 100×100 particles are provided in Fig. 5-24. The PD predicted velocity magnitude distributions obtained by PD and exact solutions at $t = 0.05$ with 100×100 particles are shown in Fig. 5-25.

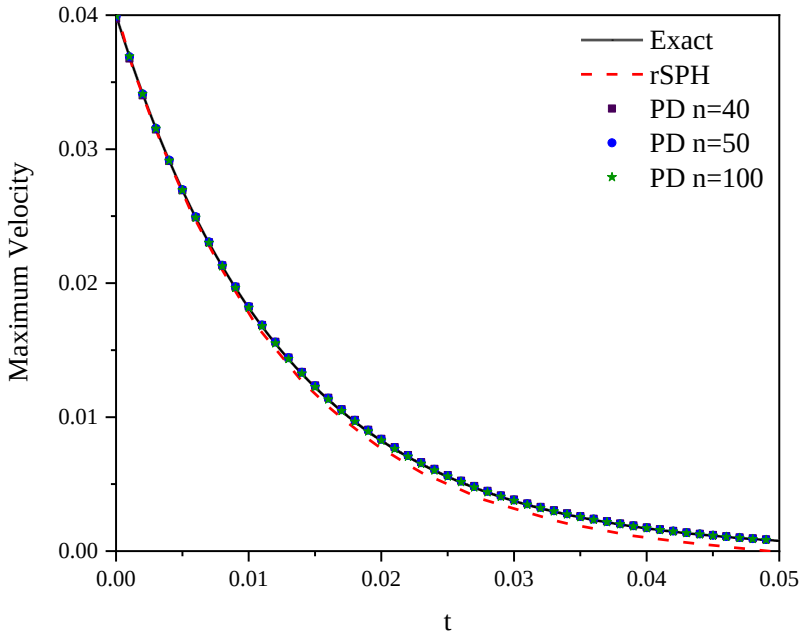

Fig. 5-23 Comparison of the maximum velocity between exaction solutions, rSPH solutions [157] and PD solutions.

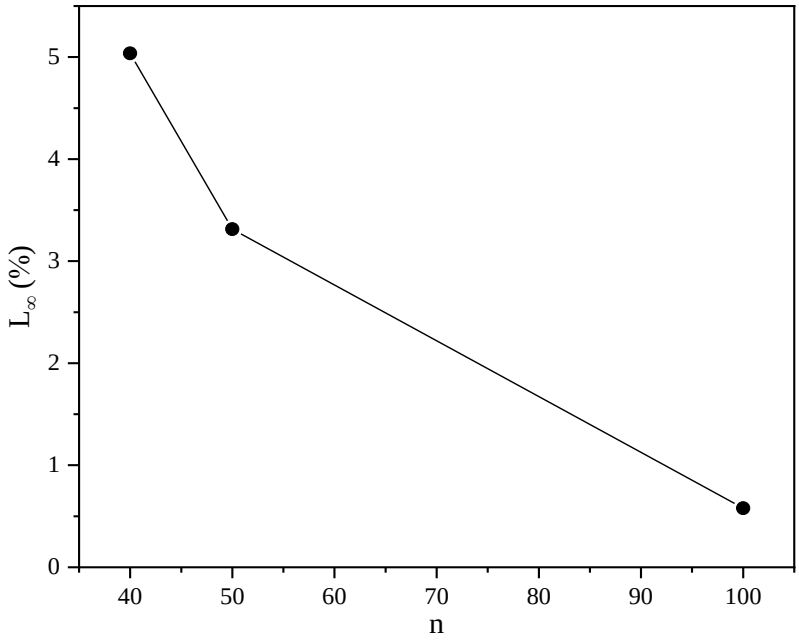

Fig. 5-24 Relative error of maximum velocity for different mesh sizes as *n*=40, 50, 100

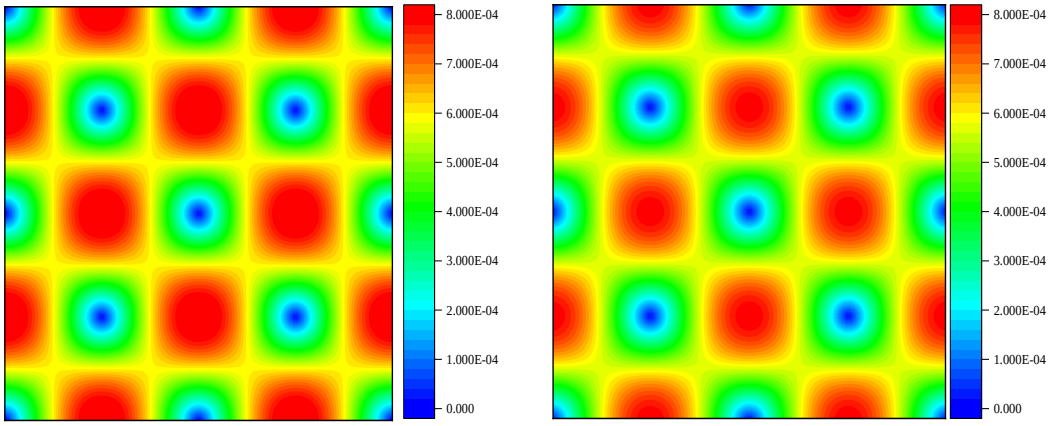

(a) (b)

Fig. 5-25 The velocity magnitude distribution at $t = 0.05$ with 100×100 particles for (a) PD solution and (b) exact solution.

5.5.5. Shear-driven cavity problem

The fourth simulation is regarding the shear-driven cavity problem. The fluid is initially at rest within a closed square cavity. The fluid flow is generated by moving the top side of the square cavity at a constant velocity, $v_0 = 10^{-3}$ m/s parallel to the x direction. As illustrated in Fig. 5-26, the geometry dimension is set as $L = W = 10^{-3}$ m. The PD mesh size is chosen as $\Delta x = L/n$ with n representing the particle number in one direction as $n = 40, 100$ for PD simulations. The horizon size $\delta = 3.015\Delta x$ is adopted. The time step size is chosen as 10^{-4} s and the total simulation time is 0.3 s. The solid boundary conditions are implemented as described in Section 5.4.5.1 (Eq.(5.106), Eq.(5.107)) by using fictitious layer, as shown in Fig. 5-26. During the simulation, the updated Lagrangian method described in Section 5.4.3 is adopted.

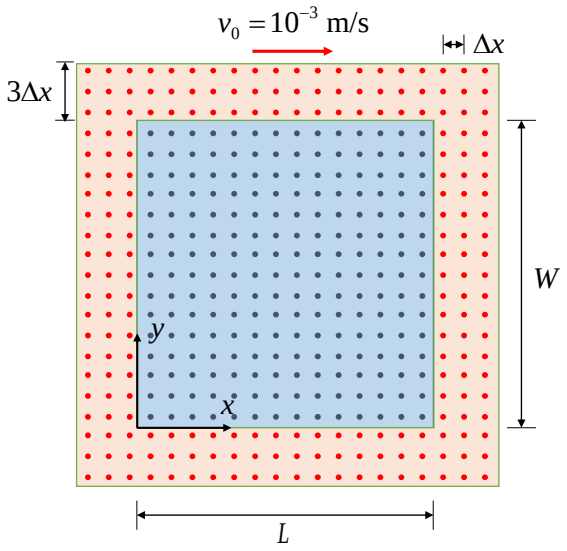

Fig. 5-26 Illustration of PD discretization for the shear-driven cavity problem

In order to validate the proposed PD model, the velocity profiles in steady-state condition, at $t = 0.3\,\mathrm{s}$ are compared with the previous literature. The reference data in [158] obtained by the finite difference method (FDM) and smoothed particle hydrodynamics (SPH), in [155] obtained by a Lagrangian gradient smoothing method (L-GSM) is provided in Fig. 5-27. In addition, the PD solutions by using different mesh sizes 40×40 and 100×100 are also provided. It can be observed that the PD results are close to the ones obtained by the other methods, proving the accuracy of the proposed PD model for the shear driven cavity problem. Besides, in Fig. 5-27 (a), for the non-dimensional vertical velocity profile in the region of $0.5<x<1.0$, the maximum vertical velocity magnitude predicted by PD is more close to the FDM solution than the ones in [155, 158] for the smoothing methods.

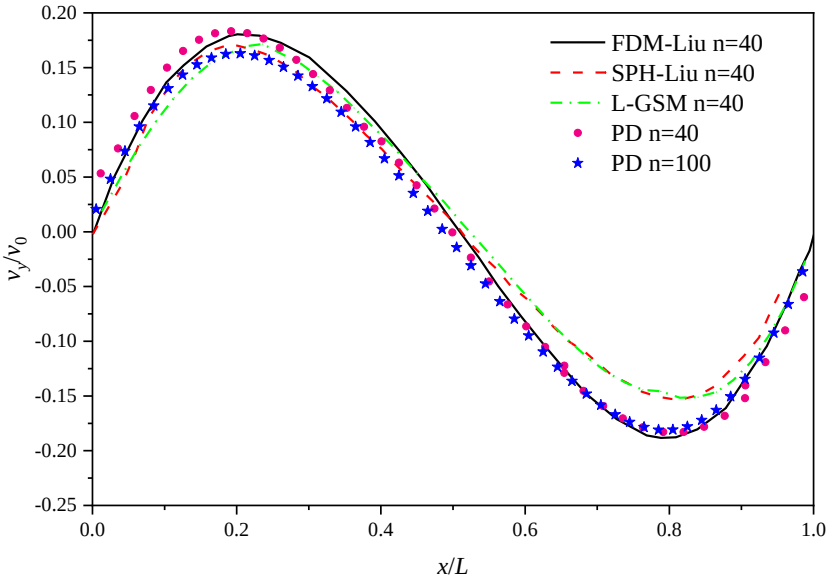

(a)

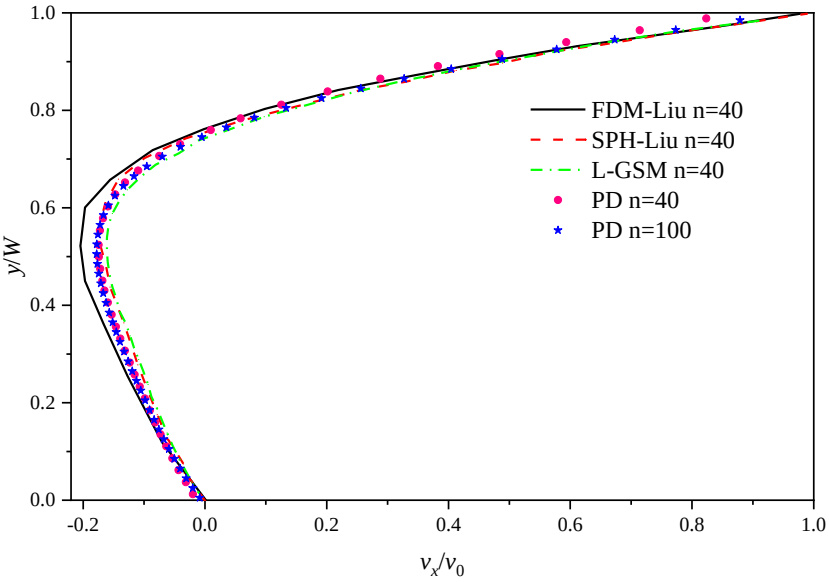

(b)

Fig. 5-27 Comparison of non-dimensional steady state PD velocity profiles with FDM and SPH data [158], L-GSM data [155], (a) vertical velocity at $y = W/2$ (b) horizontal velocity at $x = L/2$

The horizontal velocity distributions for each material point at time $t = 0.05\,\mathrm{s}$ and $t = 0.3\,\mathrm{s}$ are presented in Fig. 5-28. The vertical velocity vector field at time $t = 0.05\,\mathrm{s}$ and $t = 0.3\,\mathrm{s}$ are also provided in Fig. 5-29. It is observed that the fluid flow is in a recirculation pattern within the closed square and finally reaches its steady-state form.

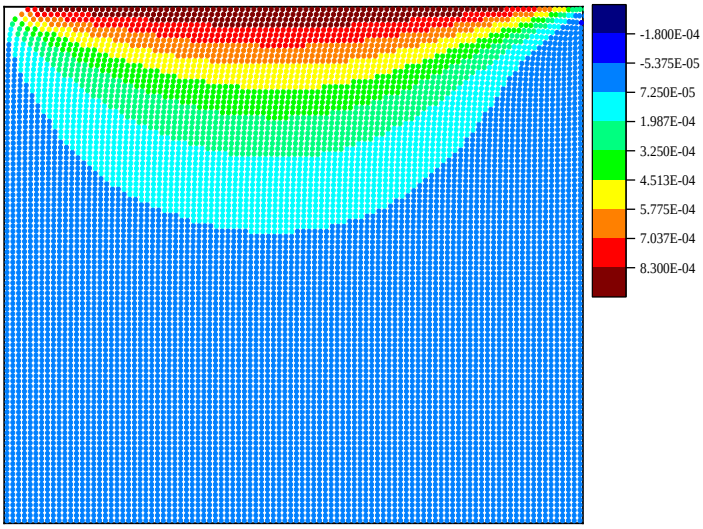

(a)

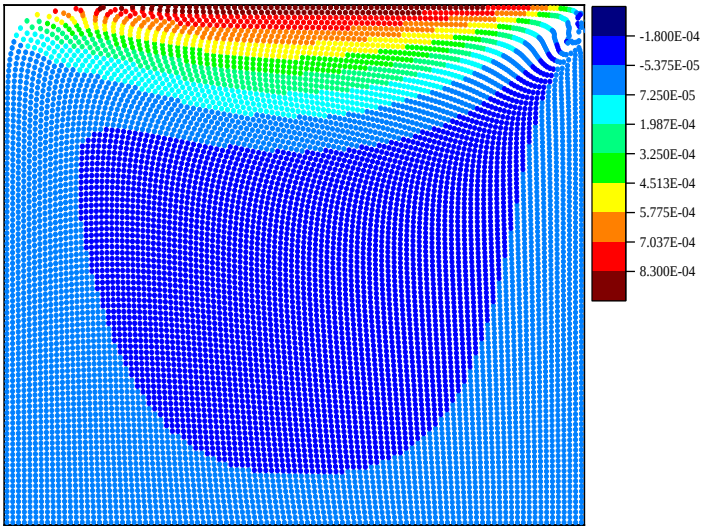

(b)

Fig. 5-28 Horizontal velocity $v_x\,(\mathrm{m/s})$ distribution and the particle positions predicted by PD for 100×100 mesh size at (a) $t=0.05\,\mathrm{s}$ and (b) at $t=0.3\,\mathrm{s}$

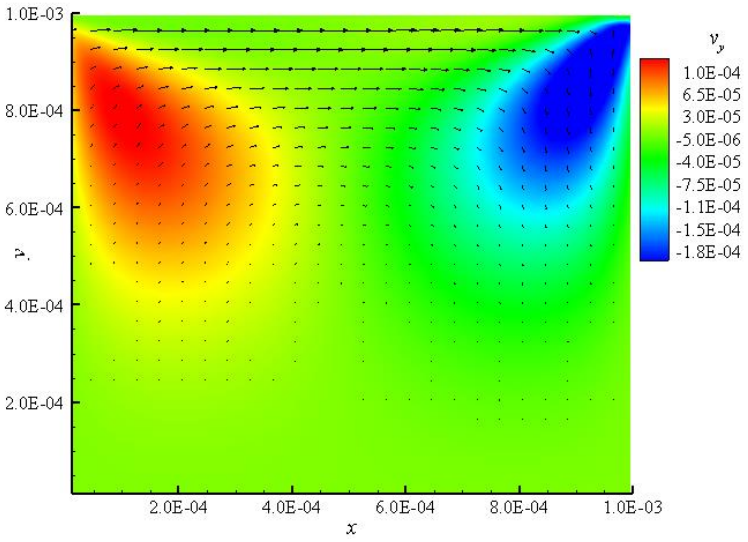

(a)

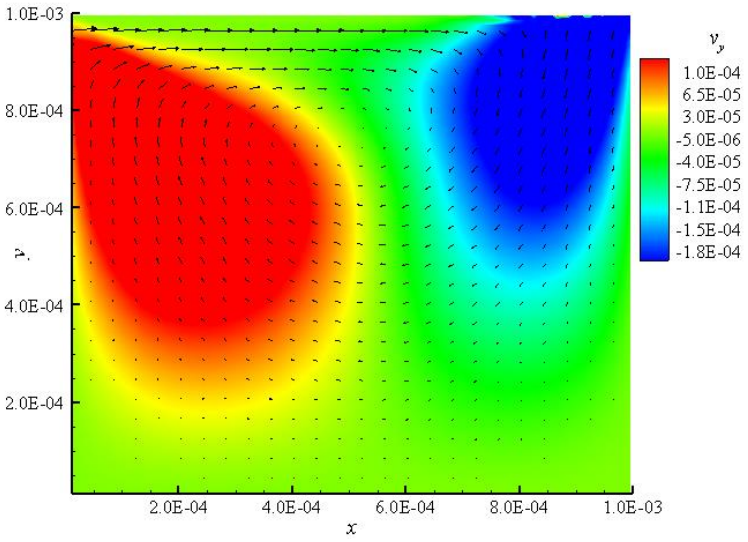

(b)

Fig. 5-29 Velocity vector field coloured by their vertical component magnitude predicted by PD for 100×100 mesh size at (a) $t=0.05\,\mathrm{s}$ (b) $t=0.3\,\mathrm{s}$

It can be observed that the particle distribution near the right upper corner is irregular to some extent. Therefore, the particle shifting technique (PST) [159] can be utilized to optimize the simulation results. Here, the solution of 40×40 particles at the steady-state with PST utilized is provided and compared with the initial one. The details on the application of PST is provided in Section 6.2.3.

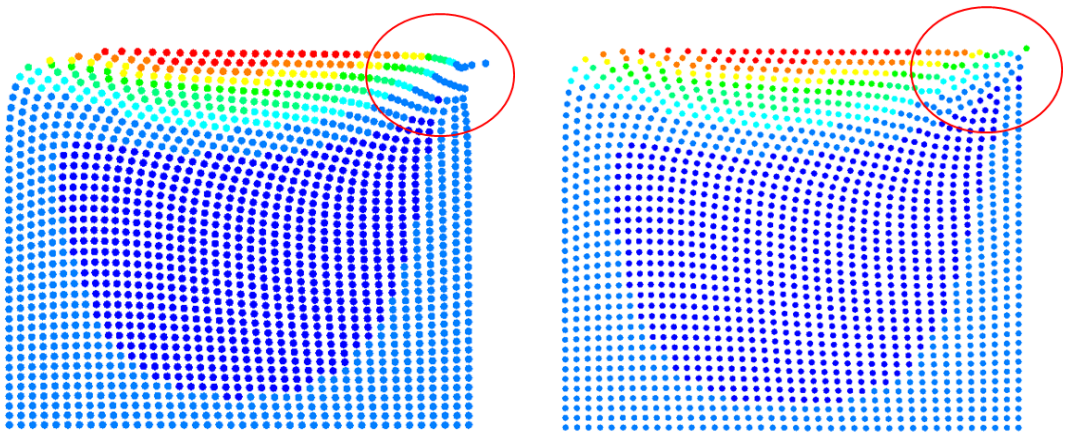

(a) (b)

Fig. 5-30 Particle distribution comparison (a) without and (b) with PST [159]

5.5.6. Dam collapse problem

To demonstrate the capability of the proposed PD formulations for predicting free surface flows, the classical dam collapse problem which has been extensively investigated [131, 154] is considered in this section. The dam break experiment conducted by S. Koshizuka and Y. Oka [160] is used for comparison. A two-dimensional flow generated after the breaking of a dam is simulated as shown in Fig. 5-31 (a). The geometry dimensions of the water column are $L = 0.146$ m for the width and $2L$ for height. The tank is open at the top with its width and height being $4L$ and L respectively. The flow is driven by the gravity and it is constraint by an open rectangle square. The gravitational acceleration is set as $g = 9.8\,\mathrm{m/s^2}$. Regarding the PD implementation shown in Fig. 5-31(b), the mesh size is chosen as $\Delta x = 4.867\times10^{-3}$ m (30×60 fluid particles) and the horizon is chosen as $\delta = 4.015\Delta x$. The time step size is $\mathrm{d}t = 2.5\times10^{-5}$ s with the total simulation time 0.4 s. As shown in Fig. 5-31 (b), fictitious layers (thickness being horizon) are added to implement the wall boundary conditions (shown in red colour). The acceleration, velocity, and displacements of the fictitious wall particles are set to be zero according to Eq.(5.102). The pressure and density of these fictitious wall particles are calculated according to Eq. (5.106) and Eq.(5.107). In this problem, B parameter in Eq. (5.34) is calculated by approximating the maximum magnitude of a fluid flow velocity as

$\left|\mathbf{v}_f\right| = \sqrt{2g(2L)} = 2.39$ m/s [142], leading to $B = 8.16\times10^4$ Pa . Also, zero pressure condition is applied for the free surface fictitious layers (shown in green colour) according to Eq.(5.108). The acceleration, velocity, displacement, and density of these free surface particles are calculated as real fluid particles. Besides, the updated Lagrangian description in Section 5.4.3 is adopted. The damping time in Eq.(5.110) to avoid the initial sudden movement is chosen as $t_{damp} = 100dt$. The MLS method described in Section 5.4.6 is applied with $n_{MLS} = 60$ for $t \le 0.3$ s and $n_{MLS} = 15$ for $t > 0.3$ s (when the water splashes the right vertical wall).

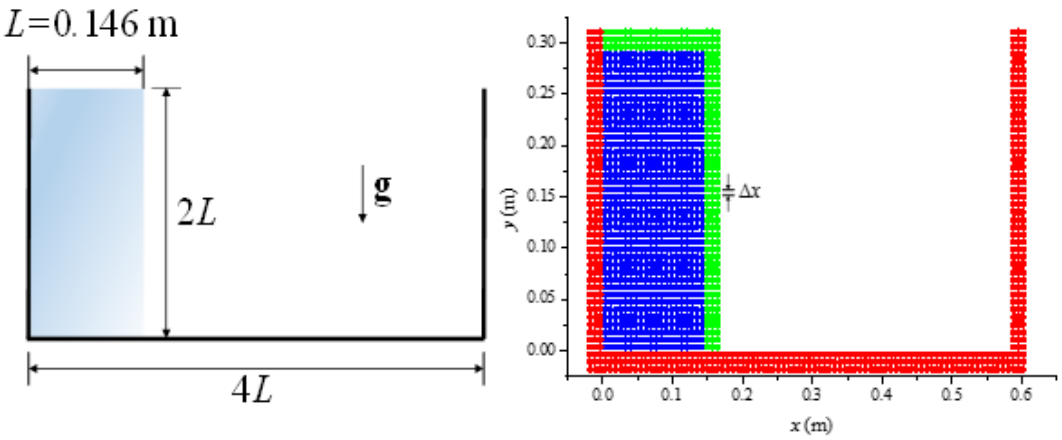

(a) (b)

Fig. 5-31 Sketch of the dam collapse problem (a) geometry model and (b) PD discretization model

Snapshots of vertical velocity profiles and the particle positions at different times are provided from Fig. 5-32 to Fig. 5-35 for both PD and experimental results. As shown in Fig. 5-36, the *x* position of the dam toe obtained by the PD simulation agrees well with the experiment results [161, 162]. It can be concluded that the proposed PD model is capable of predicting the classical dam collapse problem. It can be inferred from the numerical simulation results that there is void in the lower right corner of the fluid. The reason may be due to boundary pressure treatment for free surfaces. The pressures of the particles for free surfaces are directly set to be zero, while the pressure of the other fluid particles is calculated according to the equation of state. As a result,

it may produce discontinuities in the pressure profiles and lead to the voids in the lower right corner of the water column. In addition, the utilization of the MLS method may also bring some error and discontinuities on the fluid motion. The boundary treatments can be further improved by using constrained conditions for the fictitious layers [43, 44] or by incorporating the boundary conditions into the governing equations [14].

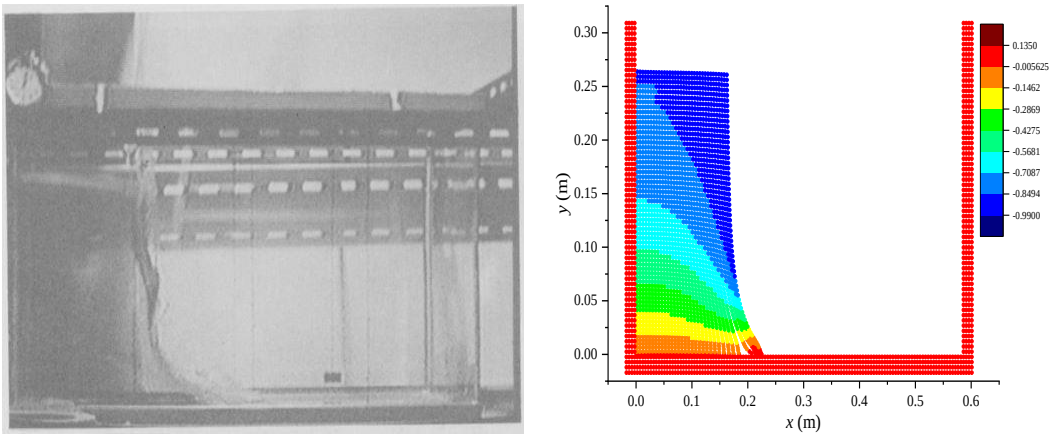

(a) (b)

Fig. 5-32 Comparison between (a) experimental result [160] and (b) PD predictions coloured by vertical velocity (m/s) at $t = 0.1\,\mathrm{s}$

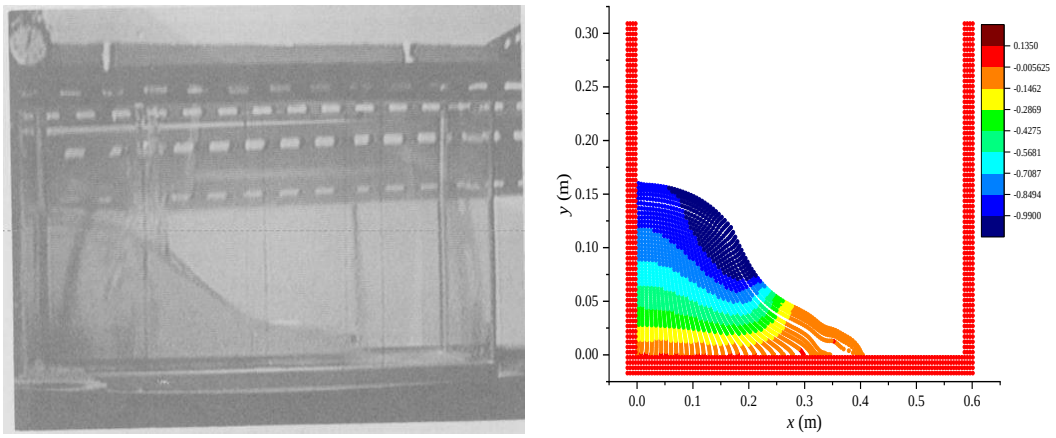

(a) (b)

Fig. 5-33 Comparison between (a) experimental result [160] and (b) PD predictions coloured by vertical velocity (m/s) at $t = 0.2\,\mathrm{s}$

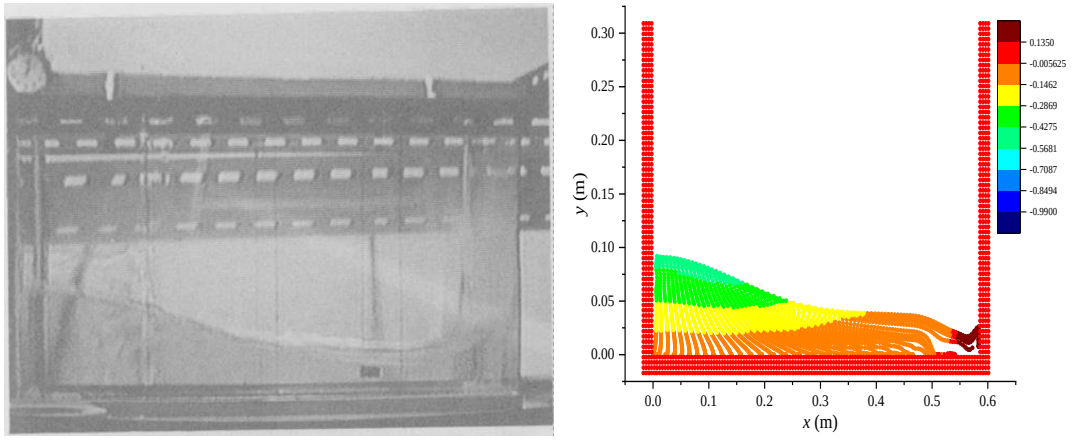

(a) (b)

Fig. 5-34 Comparison between (a) experimental result [160] and (b) PD predictions coloured by vertical velocity (m/s) at $t = 0.3\,\mathrm{s}$

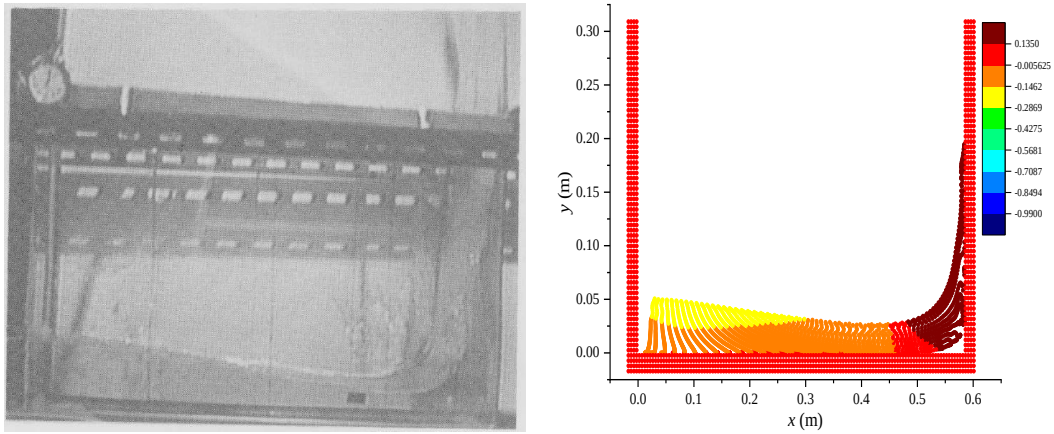

(a) (b)

Fig. 5-35 Comparison between (a) experimental result [160] and (b) PD predictions coloured by vertical velocity (m/s) at $t = 0.4\,\mathrm{s}$

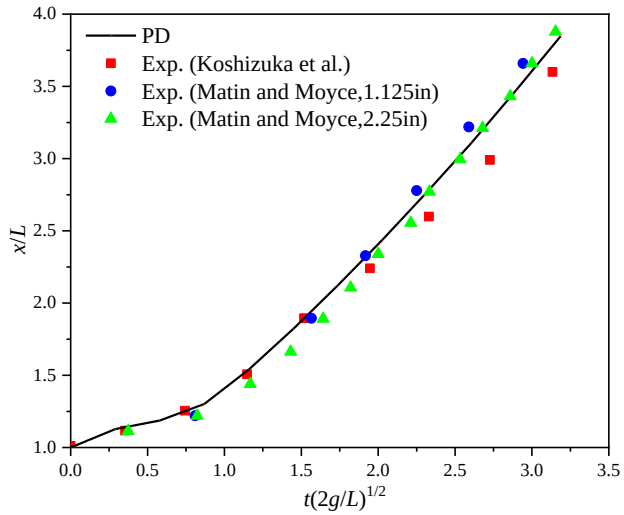

Fig. 5-36 Comparison of the *x* position of the dam toe for PD and experiment results [161, 162]

5.6. Non-isothermal fluid flow numerical simulation

In this section, three numerical simulations are conducted by applying the developed PD model. Firstly, heat conduction for a 2-D plate is conducted. The PD predicted results are compared with the solutions from ANSYS software. Secondly, natural convection in a cavity is simulated. Finally, mixed convection in a cavity is simulated. The predicted results from convection problems are compared with the ones from the previous literature.

5.6.1. Introduction

The problem of fluid flow coupled with heat transfer has been extensively studied. The convection problem is one of the typical problems within this field. Convection problems are generally divided into two categories, i.e. natural convection and forced convection, depending on the different types of driven forces. Temperature-induced buoyancy forces are responsible for the fluid flow in natural convection. On the other hand, the fluid flow is driven by lid motion in forced convection. A situation where both the natural and the forced convection are comparable is known as mixed convection. The natural and mixed convection problems are encountered in many engineering applications, e.g. the collection of solar energy, food processing, and safety of nuclear reactors et al. [163]. However, the predicting, understanding, and

controlling of such complex fluid and thermal systems are challengeable [164]. Due to the geometrical simplicity, the natural and mixed convection problems within an enclosed cavity have been extensively studied in the literature.

De Vahl Davis [165] provided a benchmark solution for the natural convection in a square cavity with constant temperature boundary conditions. The fluid flow was assumed to be laminar and the Boussinesq approximation was valid. The velocities, temperature, and rates of heat transfer had been obtained for Rayleigh numbers being up to 10^6. According to the experimental study in [166], the fluid flow will switch over to turbulence when the Rayleigh number is larger than 10^6. Later on, the study of the natural convection was extended to the turbulent field for Rayleigh number ranging from 10^6 to 10^{16} [167]. If the natural convection is driven by large temperature differences, the Boussinesq approximation is not applicable because of considerable density variations. Hence, a non-Boussinesq model was proposed by Szewc et al. [144] for such situations. Many numerical simulation methods have been applied for the natural convection simulation, i.e. the finite difference method (FDM) [165], the finite element method (FEM) and the discrete singular convolution (DSC) [168], the smoothed particle hydrodynamics (SPH) [144, 157, 169]. On the other hand, mixed convection in a square enclosed cavity is another benchmark problem. Moallemi and Jang [170] used the Semi-Implicit Method for Pressure-Linked Equations-revised (SIMPLER) [164] algorithm to investigate the effects of the Reynold number and Prandtl number on the flow and the heat transfer. The upper lid has a constant velocity and the bottom wall was heated. Later on, the situation in which the moving top wall was heated and the bottom wall was cooled was discussed by Iwatsu et al. [171]. In their work, the FDM was used to study the effect of the Richardson number, which provided a measure of the importance of natural convection relative to forced convection. FEM with a consistent splitting scheme was used by Wong [172] to simulate the buoyancy-opposing and buoyancy-aiding mixed convection problems. In addition, this benchmark problem has been discussed in extended configurations, e.g. in a two-sided lid-driven cavity [173] or an inclined driven cavity [174].

5.6.2. Pure heat conduction simulation

First, heat conduction in a 2-D plate is simulated. The length and width of the plate are $L = W = 0.1\,\mathrm{m}$. The thickness is $h = 0.001\,\mathrm{m}$. The material properties are set as: the thermal conductivity $k = 8.3075\,\mathrm{W/(mK)}$; the density $\rho = 1620\,\mathrm{kg/m^3}$; the specific heat capacity $c_v = 1092.728\,\mathrm{J/(kgK)}$. All four boundaries are subjected to a constant temperature $T = 10\,\mathrm{K}$. The initial temperature is zero. Without considering the velocity and internal heat generation terms, the governing equation Eq. (5.60) with a constant thermal conductivity for heat conduction becomes

$$\rho c_v \frac{\partial T}{\partial t} = k \Delta T \tag{5.125}$$

For PD implementation, the mesh size for the *x*-*y* plane is $\Delta x = 0.0005\,\mathrm{m}$. There is one layer in the thickness direction. The horizon is chosen as $\delta = 3.015 \Delta x$. Similar to the derivation performed by Silling and Askari [13] and Oterkus et al. [39], a von Newman stability condition is applied. The stability condition of the present model for heat conduction problems is obtained as

$$\mathrm{d}t \le \rho c_v \Big/ \left(k \sum_{j=1}^{N} \left(g^{20}(\xi) + g^{02}(\xi) \right) V_j \right) \tag{5.126}$$

As a result, the time step size is chosen as $\mathrm{d}t = 0.01\,\mathrm{s}$. The total simulation time is 40 s. The heat conduction is also simulated by using ANSYS software. The mesh size is chosen as $\Delta x = 0.001\,\mathrm{m}$ and the time step is $0.4\,\mathrm{s}$. The element type is chosen as PLANE55. The PD predicted temperature distribution is compared with ANSYS results as shown in Fig. 5-37. The good agreement validates the capability of the developed model for solving the pure two-dimensional heat transfer problem.

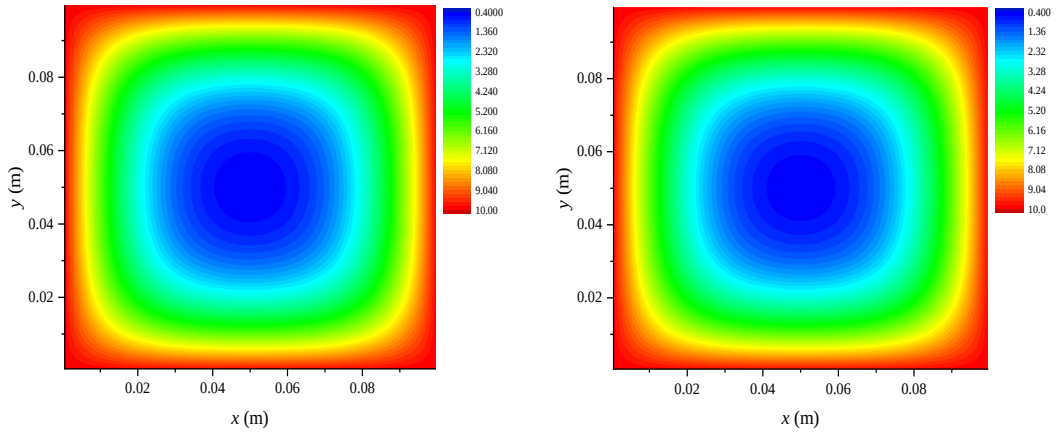

(a) (b)

Fig. 5-37 Temperature (K) distribution comparison between (a) ANSYS and (b) PD

5.6.3. Natural convection in a square cavity

Second, natural convection in a closed cavity is simulated in a non-dimensional form. A scheme of the two-dimensional natural convection problem, accompanying with the coordinate definitions and boundary conditions are shown in Fig. 5-38. For the initial state, the fluid is stationary and its temperature is zero. The boundary conditions are defined as

$$\text{at } x^* = 0:\ T^* = 1,\ v_1^* = v_2^* = 0 \tag{5.127a}$$

$$\text{at } x^* = 1:\ T^* = 0,\ v_1^* = v_2^* = 0 \tag{5.127b}$$

$$\text{at } y^* = 0:\ \partial T^*/\partial y^* = 0,\ v_1^* = v_2^* = 0 \tag{5.127c}$$

$$\text{at } y^* = 1:\ \partial T^*/\partial y^* = 0,\ v_1^* = v_2^* = 0 \tag{5.127d}$$

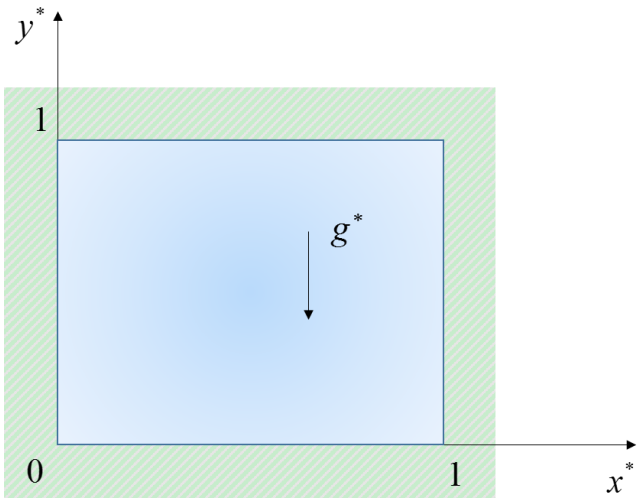

Fig. 5-38 Illustration for two-dimensional natural convection problem

For the natural convection in the cavity, the fluid flow is assumed to be weakly compressible. The fluid properties are assumed to be constant. Therefore, the viscous coefficient μ and the thermal conductivity k are uniform and constant for each PD point, i.e. $\mu = \mu_0; k = k_0$. The energy dissipation due to viscosity is neglected [144]. The Péclet number ($\mathrm{Pe}=\mathrm{RePr}$) is equal to 1 [144]. As a result, the non-dimensional parameters in Eq. (5.70) and Eq. (5.74) are

$$\mu^* = 1; k^* = 1; \mathrm{Ec} = 0; \mathrm{Re}\,\mathrm{Pr} = 1 \tag{5.128}$$

Furthermore, the Boussinesq approximation [175] is adopted. Hence, the value of non-dimensional gravity acceleration is approximated as

$$g^* = \mathrm{Ra}\,\mathrm{Pr}\,T^* \tag{5.129}$$

where Ra is the Rayleigh number defined as

$$\mathrm{Ra}=\frac{g\beta\Delta T L_0^3 \rho^2 C}{\mu k} \tag{5.130}$$

where β is the thermal expansion coefficient and ΔT is the temperature difference across the cavity.

Regarding the PD implementation, the mesh size is chosen as $\Delta x^* = 1/200$, and the horizon is chosen as $\delta^* = 3.015\Delta x^*$. The time step size is $\mathrm{d}t^* = 1\times10^{-5}$. The total simulation time is $t^* = 3$, leading to a steady-state of the fluid flow at the end of the simulation. The boundary implementation is illustrated in Fig. 5-39. Regarding the flow field, four fictitious layers are added to simulate the four solid walls. Their thicknesses are chosen as the size of the horizon. The accelerations, velocities, and displacements of the fictitious particles (shown in red colour) are zero. On the other hand, for the thermal field, two fictitious layers are added to implement the constant temperature boundary conditions. The temperature of the fictitious particle $\mathbf{x}'^*$ is set as [39]

$$T^*\left(x'^*, y^*, t^*\right) = 2 - T^*\left(x^*, y^*, t^*\right) \text{ for } x'^* + x^* = 0 \text{ and } y'^* = y^* \tag{5.131a}$$

$$T^*\left(x'^*, y^*, t^*\right) = -T^*\left(x^*, y^*, t^*\right) \text{ for } x'^* + x^* = 2 \text{ and } y'^* = y^* \tag{5.131b}$$

where $\mathbf{x}^*$ represents the corresponding fluid particle.

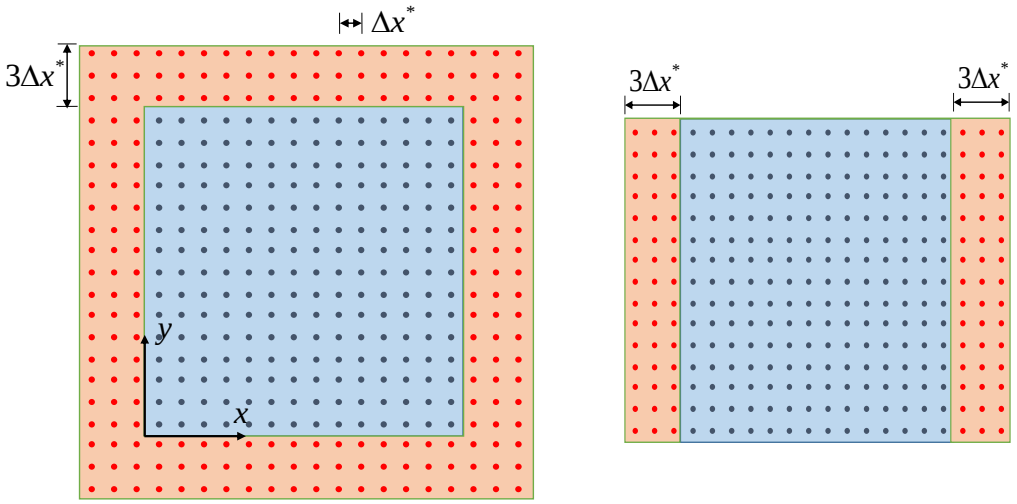

(a) (b)

Fig. 5-39 Illustrations of PD discretization and boundary implementation for (a) flow field and (b) thermal field

There are three simulation cases considered. The non-dimensional numbers in the mathematical model are set as $\mathrm{Ra} = 10^3, 10^4, 10^5$ and $\mathrm{Pr} = 0.71$. The simulation results are compared with the ones from the published literature. Firstly, the flow velocity and

temperature fields at the steady-state are provided in Fig. 5-40 for $Ra=10^3$, Fig. 5-41 for $Ra=10^4$, and Fig. 5-42 for $Ra=10^5$. The flow patterns and temperature distributions agree well with the solutions provided in [144, 165, 167, 168].

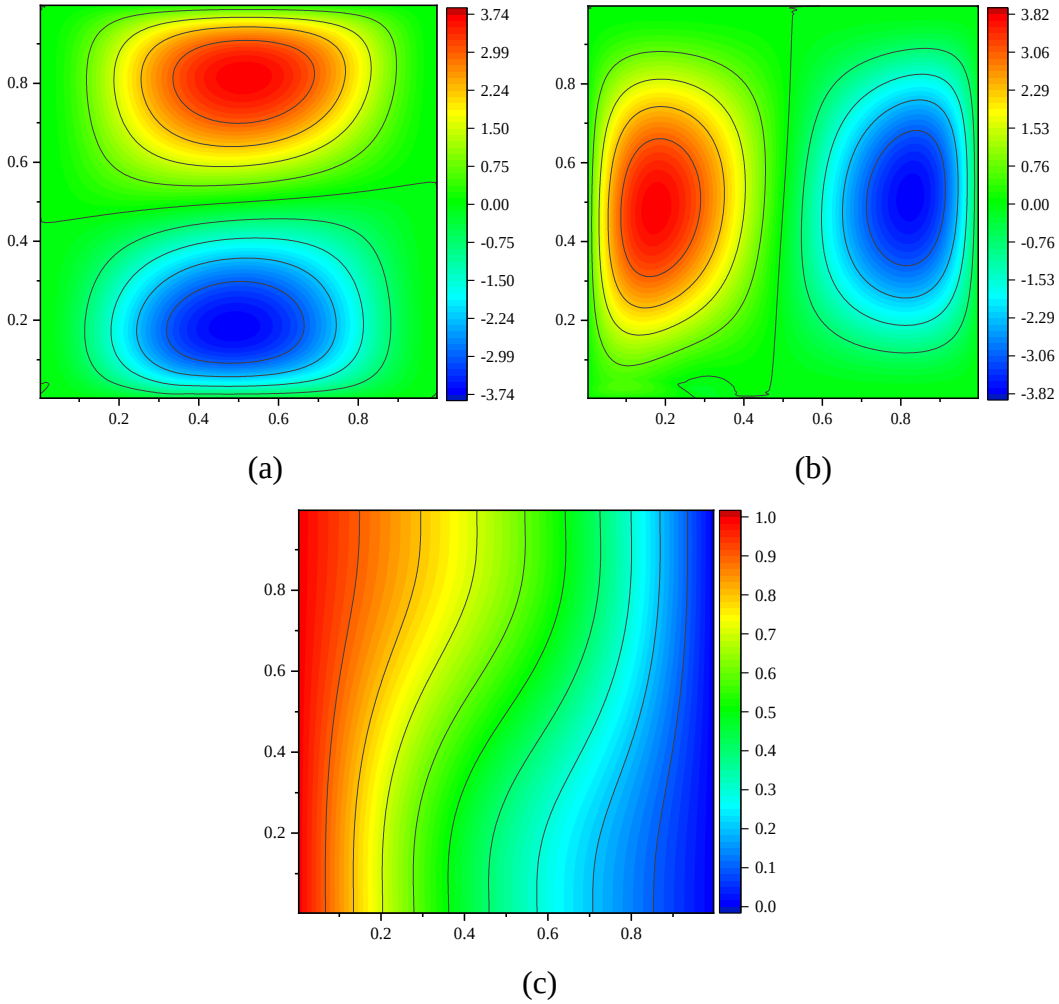

Fig. 5-40 Simulation results for $Ra=10^3$ and Pr=0.71: (a) horizontal velocity distribution, (b) vertical velocity distribution, and (c) temperature distribution

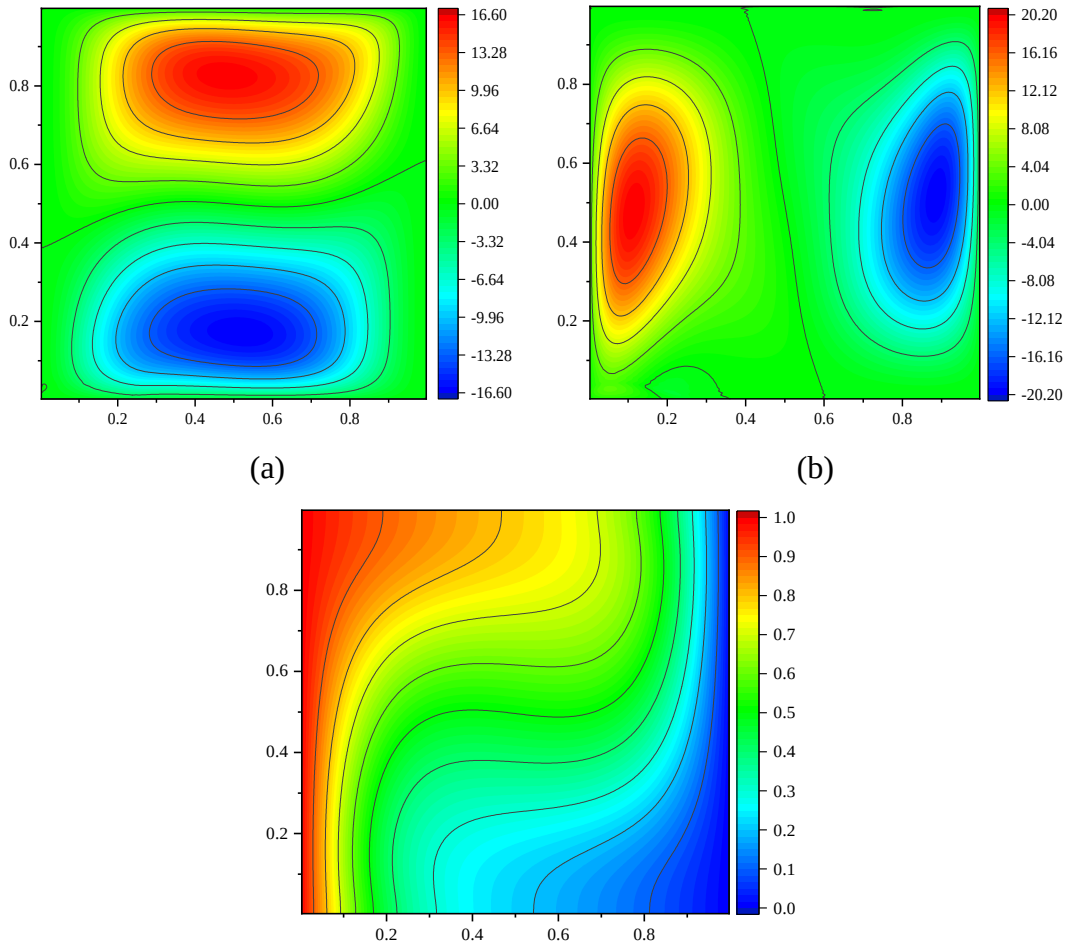

Fig. 5-41 Simulation results for Ra=10^4 and Pr=0.71: (a) horizontal velocity distribution, (b) vertical velocity distribution, and (c) temperature distribution

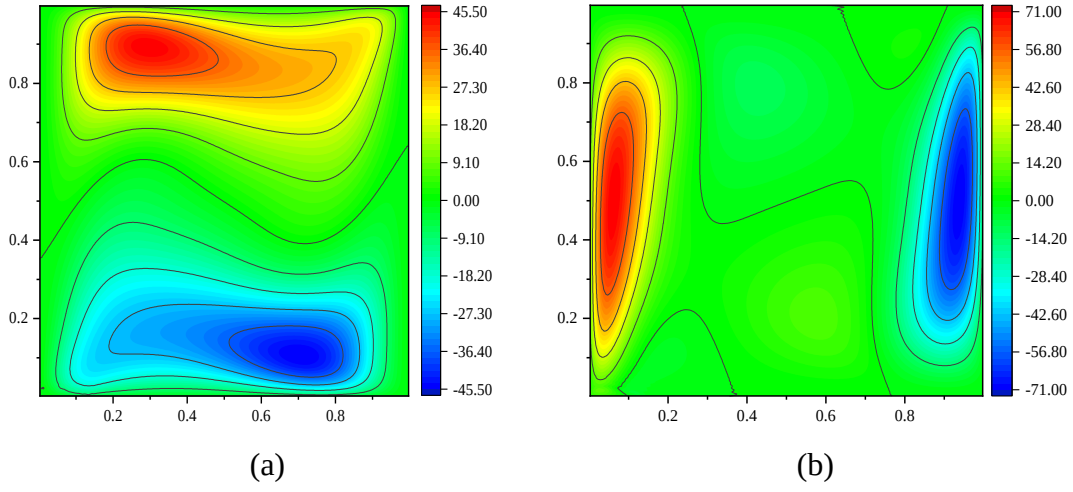

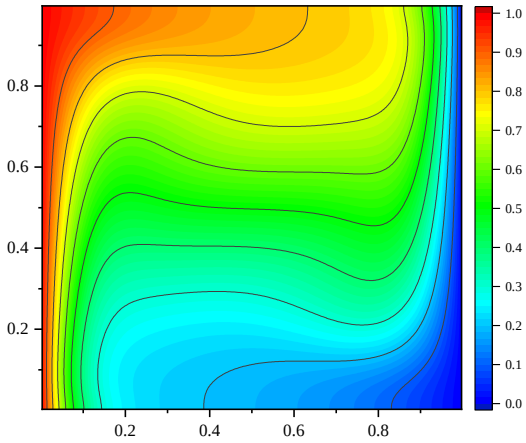

(c)

Fig. 5-42 Simulation results for Ra=10^5 and Pr=0.71: (a) horizontal velocity distribution, (b) vertical velocity distribution, and (c) temperature distribution

Later on, the profiles of horizontal velocity, vertical velocity, and temperature on the mid-plane are compared with the ones provided in [167] and [169], as shown in Fig. 5-43. In addition, the local Nusselt number along the hot wall ($x^* = 0$) is compared with the reference data provided in [169] obtained by ISPH, as shown in Fig. 5-44. It can be inferred from the figures that the PD predicted results agree well with the previous ones.

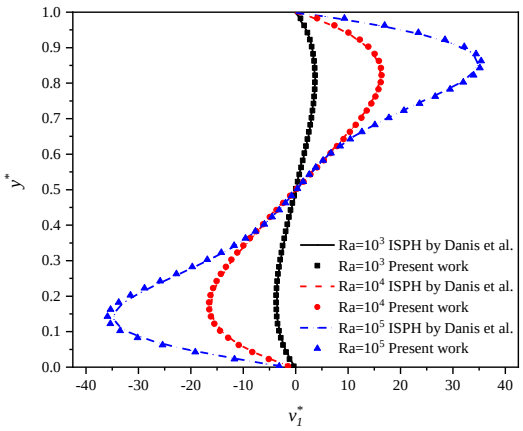

(a)

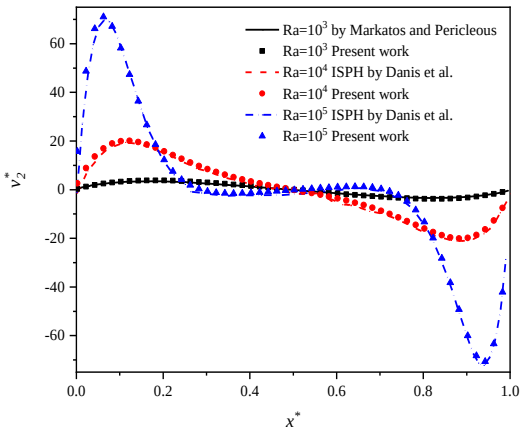

(b)

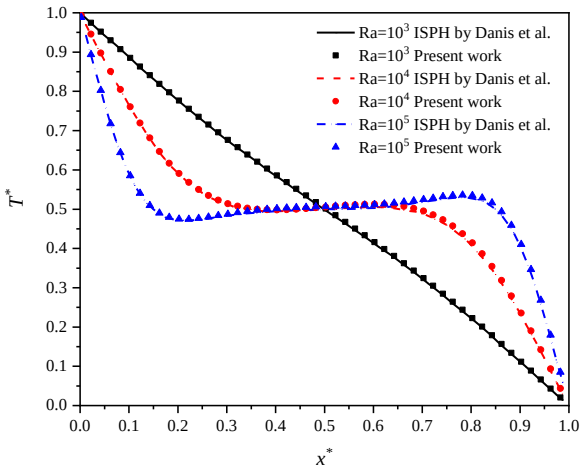

(c)

Fig. 5-43 Comparisons of dimensionless quantities (a) horizontal velocity on $x^* = 0.5$, (b) vertical velocity on $y^* = 0.5$, and (c) temperature on $y^* = 0.5$. Reference data is obtained by Danis et al. [169] and Markatos and Pericleous [167].

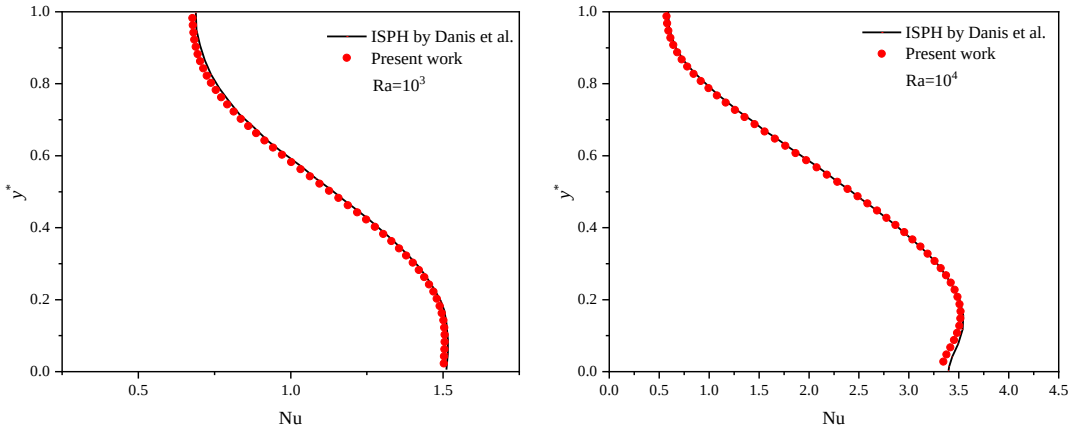

(a) (b)

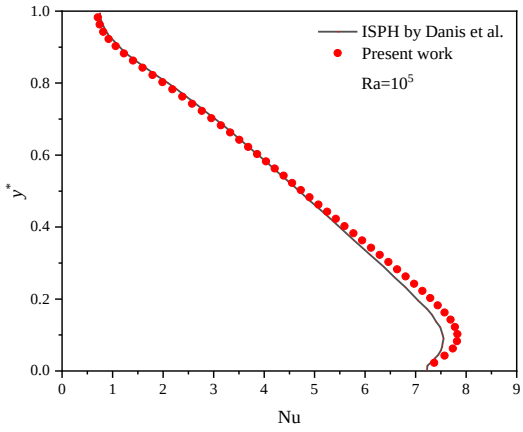

(c)

Fig. 5-44 Comparison of the local Nusselt number along with the hot wall ($x^* = 0$) for (a) Ra=10^3, (b) Ra=10^4, and (c) Ra=10^5. Reference data is from Danis et al. [169].

Finally, as a summary shown in Table 5, the representative quantities predicted by the PD model are compared with the available results obtained from finite difference method (FDM) [165], finite volume method (FVM) [167, 176], smoothed particle hydrodynamics (SPH) [157, 169], discrete singular convolution (DSC) [168].

Table 5 Comparison of the representative quantities.

	Present Work	[165]	[167]	[157]	[168]	[169]	[176]
Ra=10^3							
$v^*_{1,\max}$	3.731	3.649	3.544	3.431	3.643	3.666	4.077
$y^*_{\max}$	0.818	0.813	0.832	0.812	0.817	0.813	0.806
$v^*_{2,\max}$	3.796	3.697	3.593	3.511	3.686	3.720	4.130
$x^*_{\max}$	0.178	0.178	0.168	0.176	0.183	0.175	0.181
Nu_0	1.115	1.117	-	1.033	1.073	1.119	1.114
$\mathrm{Nu}_{\max}$	1.506	1.505	1.496	1.392	1.444	1.511	1.581
$\mathrm{Nu}_{\min}$	0.678	0.692	0.720	0.705	0.665	0.689	0.670
Ra=10^4							
$v^*_{1,\max}$	16.423	16.178	16.180	17.312	15.967	16.207	16.263
$y^*_{\max}$	0.828	0.823	0.832	0.823	0.817	0.825	0.818
$v^*_{2,\max}$	20.082	19.617	19.440	20.051	19.980	19.896	19.717
$x^*_{\max}$	0.118	0.119	0.113	0.112	0.117	0.113	0.119
Nu_0	2.253	2.238	-	2.081	2.155	2.257	2.245
$\mathrm{Nu}_{\max}$	3.519	3.528	3.482	3.448	3.441	3.543	3.539
$\mathrm{Nu}_{\min}$	0.574	0.586	0.643	0.541	0.528	0.584	0.583
Ra=10^5							
$v^*_{1,\max}$	35.441	34.730	35.730	-	33.510	34.745	35.173
$y^*_{\max}$	0.858	0.855	0.857	-	0.850	0.863	0.859
$v^*_{2,\max}$	70.987	68.59	69.08	-	70.81	70.448	69.746
$x^*_{\max}$	0.063	0.066	0.067	-	0.070	0.063	0.066
Nu_0	4.621	4.509	-	-	4.352	4.526	4.51
$\mathrm{Nu}_{\max}$	7.831	7.717	7.626	-	7.662	7.584	7.636

$\mathrm{Nu}_{\min}$	0.707	0.729	0.824	-	0.678	0.743	0.733

$v_{1,\max}^*$: the maximum horizontal velocity on the vertical mid-plane

$y_{\max}^*$: the corresponding vertical coordinate for the material point with $v_{1,\max}^*$

$v_{2,\max}^*$: the maximum vertical velocity on the horizontal mid-plane

$x_{\max}^*$: the corresponding horizontal coordinate for the material point with $v_{2,\max}^*$

Nu_0 : the average Nusselt number on the hot wall ($x^* = 0$)

$\mathrm{Nu}_{\max}$: the maximum value of the Nusselt number on the hot wall ($x^* = 0$)

$\mathrm{Nu}_{\min}$: the minimum value of the Nusselt number on the hot wall ($x^* = 0$)

From the comprehensive comparison between the present simulation results and the published literature, it can be concluded that the present model is able to accurately predict the two-dimensional natural convection problem in an enclosed square cavity for different values of Ra number.

5.6.4. Mixed convection in a square cavity

Thirdly, the problem of mixed convection in a lid-driven square cavity is simulated in a non-dimensional form. The geometry dimensions and the coordinate definition are the same as Fig. 5-38. The fluid is motionless at the initial state. An initial linear temperature field in the vertical direction is defined as [171]

$$T^*\left(x^*, y^*, t^*\right) = y^* \tag{5.132}$$

The boundary conditions are defined as

$$\text{On } x^* = 0\text{: } \partial T^*/\partial x^* = 0,\ v_1^* = v_2^* = 0 \tag{5.133a}$$

$$\text{On } x^* = 1\text{: } \partial T^*/\partial x^* = 0,\ v_1^* = v_2^* = 0 \tag{5.133b}$$

$$\text{On } y^* = 0\text{: } T^* = 0,\ v_1^* = v_2^* = 0 \tag{5.133c}$$

On $y^* = 1$: $T^* = 1$, $v_1^* = 1, v_2^* = 0$ (5.133d)

Being similar to the natural convection problem, for the mixed convection problem, the fluid properties are also assumed to be constant and the viscous dissipation is also neglected [171]. As a result, the non-dimensional parameters are

$$\mu^* = 1; k^* = 1; \mathrm{Ec} = 0 \tag{5.134}$$

Furthermore, the Boussinesq approximation [175] is also adopted. The non-dimensional gravity acceleration is approximated as

$$g^* = \frac{\mathrm{Gr}}{\mathrm{Re}^2} T^* = \mathrm{Ri} T^* \tag{5.135}$$

where Gr and Ri are the Grashof number and the Richardson number defined as

$$\mathrm{Gr} = \frac{\mathrm{Ra}}{\mathrm{Pr}}, \mathrm{Ri} = \frac{\mathrm{Gr}}{\mathrm{Re}^2} \tag{5.136}$$

For PD implementation, the mesh size is chosen as $\Delta x^* = 1/100$. The horizon is chosen as $\delta = 3.015\Delta x^*$. The time step size is $\mathrm{d}t^* = 1\times10^{-5}$ and the total simulation time is $t^* = 50$. The mixed convection problem reaches a steady state at the end of the simulation time. The boundary implementation approach is the same as the one in the natural convection simulation.

There are three simulation cases for the mixed convection problem. For all the cases, the Prandtl number and the Grashof number are fixed as $\mathrm{Pr} = 0.71$ and $\mathrm{Gr} = 100$. The Reynold number is set as Re=10, 100, 400 respectively. As a result, the Richardson number becomes Ri=1, 0.01, 0.000625 correspondingly. Therefore, by varying the Reynold number, the different Richardson numbers can be obtained.

In order to demonstrate the capability of the proposed model for solving the two-dimensional mixed convection in a square cavity problem, the steady solution for Re=400 (Ri =0.000625) is compared with the one provided by Iwatsu et al.[171]. The velocity profile comparisons are presented in Fig. 5-45. In addition, the comparison of

the temperature profiles and the local Nusselt number profiles are shown in Fig. 5-46. It can be inferred from the comparisons that the results agree well with the published literature [171], validating the present model.

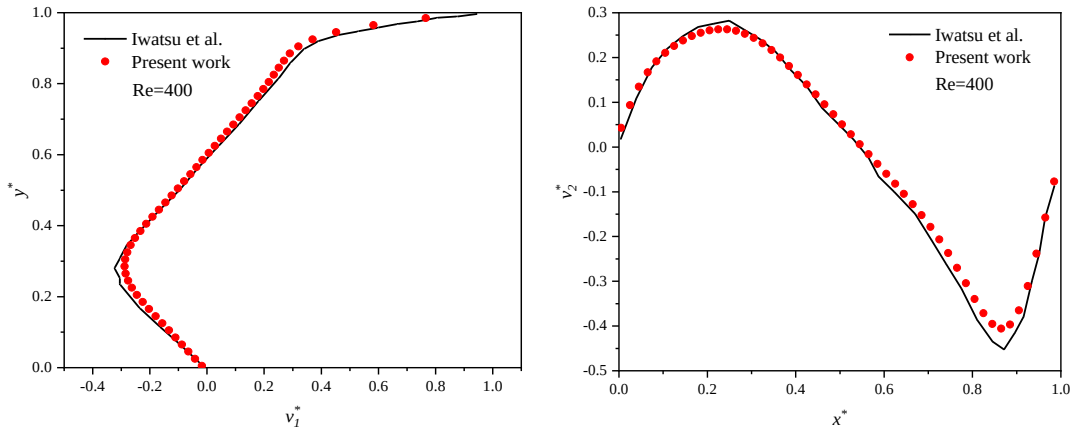

(a) (b)

Fig. 5-45 Comparison of velocity profiles for Re=400: (a) horizontal velocity on $x^* = 0.5$ and (b) vertical velocity on $y^* = 0.5$. Reference data is from Iwatsu et al. [171]

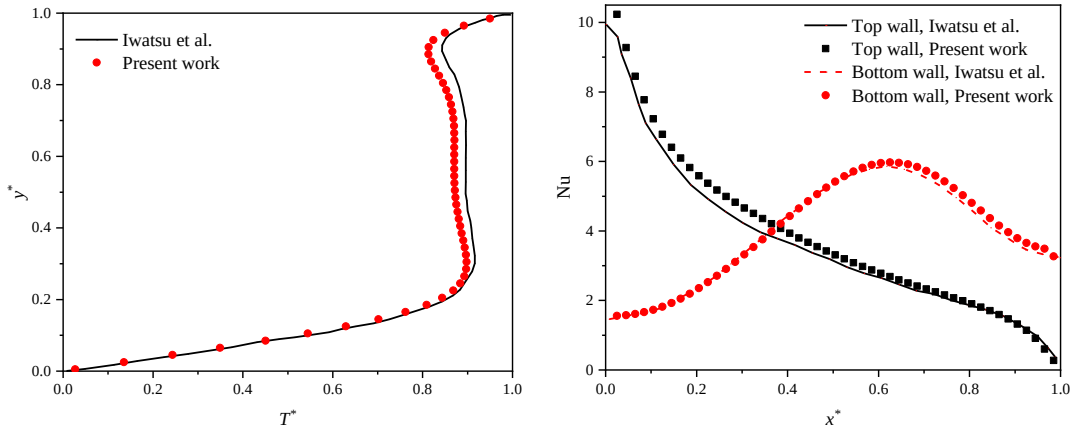

(a) (b)

Fig. 5-46 Comparison of thermal quantities for Re=400: (a) temperature profile on $x^* = 0.5$ and (b) local Nusselt profile at the top ($y^* = 1$) and bottom ($y^* = 0$) wall. Reference data is from Iwatsu et al. [171]

Later on, the average Nusselt numbers (Nu_{PD}) at the top wall of the cavity ($y^* = 1$) are provided in Table 6 for all the three cases. The comparison with Iwatsu et al. [171] (Nu_{ref}) is also provided. As can be seen from Table 6, the relative error between the PD and reference results is less than 0.3%. The relative error is calculated as

$$\varepsilon_r = \frac{\left|\mathrm{Nu}_{PD} - \mathrm{Nu}_{ref}\right|}{\mathrm{Nu}_{ref}} \tag{5.137}$$

Table 6 Average Nusselt number at the top wall for all the three cases

Re	Ri	Present work	Iwatsu et al. [171]	ε_r
		Nu_{PD}	Nu_{ref}	
10	1	1.014	-	-
100	0.01	1.937	1.94	0.15%
400	0.000625	3.849	3.84	0.23%

Furthermore, the velocity and temperature profiles on the mid-plane are provided in Fig. 5-47. The temperature distributions are provided in Fig. 5-48 for the three cases.

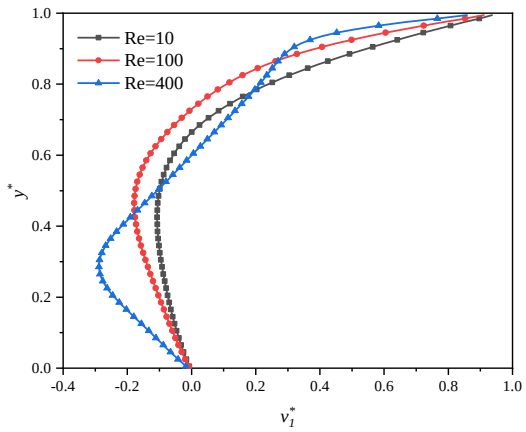

(a)

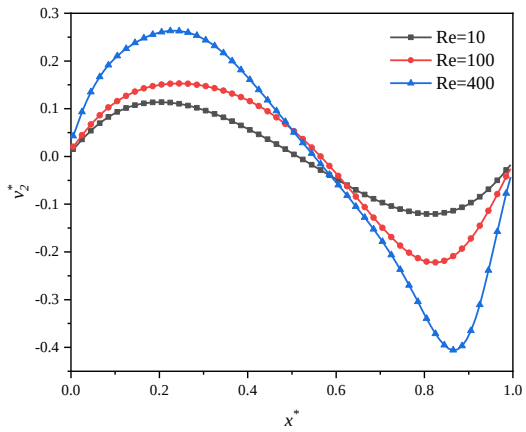

(b)

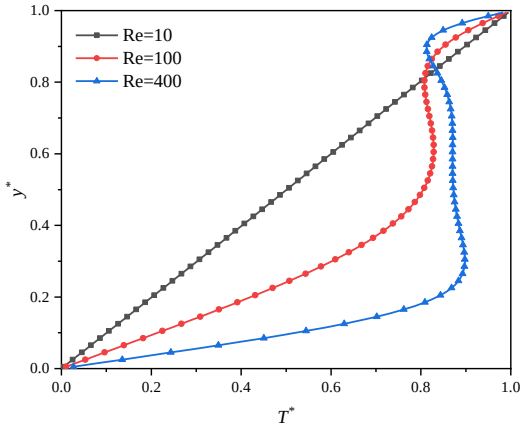

(c)

Fig. 5-47 Velocity and temperature profiles for all the three cases: (a) horizontal velocity on $x^* = 0.5$; (b) vertical velocity on $y^* = 0.5$; (c) temperature profile on $x^* = 0.5$.

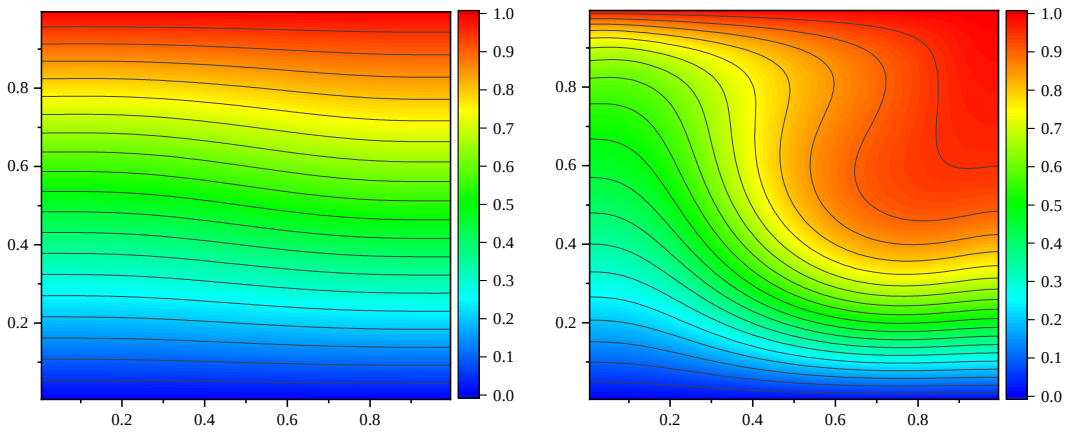

(a) (b)

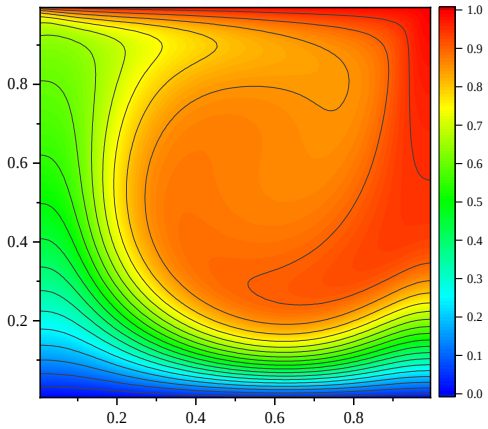

(c)

Fig. 5-48 Temperature field distribution for all the three cases: (a) Re=10, (b) Re=100, (c) Re=400

For a small value of Ri (Ri=0.000625 and Re=400 in this study), the fluid flow is dominated by the lid-driven force. The buoyancy effect is overwhelmed by the shear effect. For a low value of Ri (Ri=0.01 and Re=100 in this study), the buoyancy effect is comparable to the shear effect, leading to a mixed convection dominate situation. For an equivalent value of Ri (Ri=1 and Re=10 in this study), the buoyancy effect dominates the fluid flow, leading to a natural convection dominate simulation. The observations are consistent with the published literature [171, 177].

5.7. Summary

In this chapter, the fluid flow governing equations, i.e. Navier-Stokes equations, are reformulated into an integral form by using the peridynamic differential operator. Subsequently, the numerical algorithm in total and updated Lagrangian descriptions a well as Euler description are provided. Several classical fluid flow problems, i.e. Couette flow, Poiseuille flow, Taylor-Green Vortex, shear-driven cavity problem, are simulated by the proposed PD model. Furthermore, the developed PD model is applied to solve problems of free-surface flow as presented in the dam collapse problem. In addition, the developed model is applied to solve the pure heat conduction, the natural convection, and the mixed convection problems. The PD predicted results agree well with those obtained from other solutions, validating the capability of the proposed model for solving hydrodynamics including free surface flows problems and the coupled fluid flow and heat transfer phenomenon.

The present model can be further developed for other fluid flow problems such as multi-phase or multi-component fluid flow problems. Furthermore, since there are many existing PD models for solids, the fluid-structure interaction can be straightforwardly implemented by using the non-local models both for the fluid and the solid. The interaction can be inherently implemented because of the models' non-local behaviour.

6. Multi-phase Fluid Flow Numerical Simulation

Multi-phase fluid flow is a typical phenomenon in the engineering fields, such as oil and water flow in a pipe, gas-liquid flow in channels, combustions [178] etc.. Therefore, the problem of the multi-phase fluid flow has been intensively and extensively investigated for years.

For Euler grid-based methods, e.g. the volume of fluid (VOF) [179] and level set (LS) method [180], the unphysical re-initialization process is needed for large topological deformation [181]. Compared with the Euler methods, the Lagrangian particle methods, e.g. smoothed particle hydrodynamics (SPH) [182-185], moving particle semi-implicit (MPS) method [160, 186, 187], can simultaneously show and move the multi-phase fluid interface because of their intrinsic non-local property. Therefore, these particle methods have also been widely applied in the realm of the multi-phase fluid flow simulation. Taking the SPH method as an example, Monaghan and Rafiee [183] developed a simple SPH algorithm for multi-fluid flow with introducing a repulsive force on the interface to maintain the interface sharpness. The Incompressible SPH (ISPH) scheme is applied in [188] with a velocity divergence-free projection algorithm to solve the benchmark multi-fluid problems. The comparative study has been conducted for multi-phase fluid flow to estimate the available SPH techniques [189, 190]. The state-of-art SPH application for complex fluid flows is reviewed in [182, 191].

The PD can be applied to simulate the multi-phase fluid flows. Updated Lagrangian particle hydrodynamics (ULPH) is proposed by Tu et al. by using the non-ordinary state-based PD concept and updated Lagrangian scheme [132]. Subsequently, the ULPH has been extended to simulate the multi-phase fluid flow [192]. Wang and Zhang developed a PD-MPS method for multi-phase fluid flow simulations [187]. In the previous chapter, the PDDO has been applied to simulate the laminar fluid flow at low Reynold number [8] and heat-conducting fluid flow [9]. In this chapter, the previous work is extended for multi-phase fluid flows.

6.1. Governing equations for multiphase flow

In this study, the fluids are assumed to be weakly compressible, viscous, immiscible, Newtonian fluids under an isothermal laminar flow condition. The flow governing equations are reformulated to a Lagrangian form by using the peridynamic differential operator.

6.1.1. Classical governing equations

The governing equations for each fluid phase in the Lagrangian description are [193]

Continuity equation:

$$\frac{\partial \rho}{\partial t} = -\rho \nabla \cdot \mathbf{v} \tag{6.1}$$

Momentum equation:

$$\rho \frac{\partial \mathbf{v}}{\partial t} = -\nabla P + \mathbf{F}^V + \mathbf{F}^B + \mathbf{F}^S \tag{6.2}$$

where the variables are denoted as density ρ, time t, fluid velocity vector $\mathbf{v}$, pressure P, viscous stress $\mathbf{F}^V$, body force $\mathbf{F}^B$, and surface tension force $\mathbf{F}^S$.

The viscous stress $\mathbf{F}^V$ is defined as [193]

$$\mathbf{F}^V = \mu(\Delta \mathbf{v}) \tag{6.3}$$

where μ represents the dynamic viscosity.

According to the Continuum Surface Force model [194], the surface tension force is defined as

$$\mathbf{F}^S = \beta \kappa \hat{\mathbf{n}} \lambda + \nabla \beta \tag{6.4}$$

where β is the surface tension coefficient, $\hat{\mathbf{n}}$ is the unit normal towards the interface as shown in Fig. 6-1, κ is the curvature of the interface, and λ is the weight function representing the surface tension force magnitude distribution. The surface tension coefficient is set as a constant value. Therefore, the second term on the right-hand side of Eq. (6.4) which is the gradient of the surface tension coefficient becomes zero, i.e.

$$\nabla\beta = 0 \tag{6.5}$$

According to the Continuum Surface Force model [194], a colour function, s, is given to fluid n (n=1,2 as two-phase fluid flow) to identify the different phases (shown in different colours in Fig. 6-1). For example,

$$s = \begin{cases} 1, \text{ for fluid } 1 \\ 2, \text{ for fluid } 2 \end{cases} \tag{6.6}$$

Then, the gradient of the colour function representing the direction of the interface can be calculated as

$$\mathbf{c}_g = \nabla s \tag{6.7}$$

Consequently, the unit normal direction vector, $\hat{\mathbf{n}}$ in Eq.(6.4), can be calculated based on the normal direction vector provided in Eq.(6.7) as

$$\hat{\mathbf{n}} = \frac{\mathbf{c}_g}{|\mathbf{c}_g|} = \frac{\nabla s}{|\nabla s|} \tag{6.8}$$

The curvature of the interface in Eq. (6.4) can be calculated as the negative value of the divergence of the unit normal vector [194], i.e.

$$\kappa = -\nabla \cdot \hat{\mathbf{n}} \tag{6.9}$$

The weighted function λ in Eq. (6.4) represents the distribution of the magnitude of the surface tension force [193] (the magnitude decays as the distance to interface increases). Following the conventional choice, the weighted function is chosen as the magnitude of the gradient of the colour function as [193]

$$\lambda = \left|\mathbf{c}_g\right| = \left|\nabla s\right| \tag{6.10}$$

As a result, by substituting Eq.(6.5), Eq.(6.8), Eq.(6.9), and Eq.(6.10) into Eq.(6.4), the surface tension force can be expressed as

$$\mathbf{F}^S = \beta\kappa\hat{\mathbf{n}}\lambda + \nabla\beta = \beta\kappa\nabla s = \beta\left(-\nabla\cdot\left(\frac{\nabla s}{\left|\nabla s\right|}\right)\right)\nabla s \tag{6.11}$$

The above governing equations are closed with the equation of state. In the current chapter, two-phase fluid flows are considered, denoted as phase 1 for heavier fluid and phase 2 for lighter fluid. Therefore, for each fluid phase (denoted as a subscript *n* with *n*=1, 2), the equation of state can be expressed as [193]

$$P_n = P_{ref,n}\left(\left(\frac{\rho_n}{\rho_{0,n}}\right)^{\gamma_n} - 1\right) + P_{0,n} \tag{6.12}$$

where $\rho_{0,n}$ is the initial density of fluid *n*, γ_n is the material constant for fluid *n* ranging from 1 to 7. The term $P_{ref,n}$ is the reference pressure as [193]

$$P_{ref,n} = \frac{\rho_{0,n}c_n^2}{\gamma_n} \tag{6.13}$$

where c_n is the artificial speed of sound for fluid *n*. For both fluid phases, the reference pressures are set to be equal, i.e. $P_{ref,1} = P_{ref,2} = P_{ref}$. Besides, the artificial speed of sound for fluid 1, c_1, is chosen as the reference speed of sound. Therefore, the artificial speed of sound for fluid 2, c_2, is calculated as $c_2 = c_1\sqrt{\left(\gamma_2\rho_{0,1}/\gamma_1\rho_{0,2}\right)}$ [193].

The term $P_{0,n}$ in Eq.(6.12) is referred to as the background pressure to prevent negative pressure and tension instabilities [193, 195]. The adoption of the background pressure can keep the particle distribution uniformly to some extent. Therefore, it should not be too large to create extra particle resettlement and thus induce numerical

simulation errors [196]. For both fluids, the background pressure is chosen to be identical as $P_{0,1} = P_{0,2} = P_0 = 0.05P_{ref}$ for problems with no free surface flow and $P_{0,1} = P_{0,2} = 0$ for free surface flow problems [195].

6.1.2. PDDO governing equations

The non-local mathematical model is developed by reformulating the classical mathematical model by using PDDO.

The non-local form of the continuity equation, the pressure gradient term and the viscous force term in the momentum equation remain the same as in the single-phase flow as provided by Gao and Oterkus [8], and they can be presented as follows:

The non-local form of the continuity equation, i.e. Eq.(6.1):

$$\frac{\partial \rho(\mathbf{x})}{\partial t} = -\rho(\mathbf{x}) \int_{H_\mathbf{x}} \mathbf{g}_1(\boldsymbol{\xi}) \cdot \left(\mathbf{v}(\mathbf{x}') - \mathbf{v}(\mathbf{x})\right) \mathrm{d}V' \tag{6.14}$$

The non-local form of the pressure gradient in the momentum equation presented in Eq.(6.2):

$$\nabla P(\mathbf{x}) = \int_{H_\mathbf{x}} \left(P(\mathbf{x}') - P(\mathbf{x})\right) \mathbf{g}_1(\boldsymbol{\xi}) \mathrm{d}V' \tag{6.15}$$

The non-local form of viscous force in the momentum equation presented in Eq.(6.3):

$$\mathbf{F}^V = \int_{H_\mathbf{x}} \mu(\mathbf{x}) \left(\mathbf{v}(\mathbf{x}') - \mathbf{v}(\mathbf{x})\right) \mathrm{Tr}\left(\mathbf{g}_2(\boldsymbol{\xi})\right) \mathrm{d}V' \tag{6.16}$$

The derivation of the non-local form of surface tension force is presented as follows:

In order to develop the PDDO form of the surface tension force model, the gradient of the colour function, ∇s, should be firstly expressed by using the PDDO formulation as

$$\nabla s(\mathbf{x}) = \int_{H_\mathbf{x}} \left(s(\mathbf{x}') - s(\mathbf{x})\right) \mathbf{g}_1(\boldsymbol{\xi}) \mathrm{d}V' \tag{6.17}$$

However, due to the considerable density difference, the weighted function λ, i.e. $|\nabla s|$, can be modified to keep the continuity of the acceleration across the interface [193]. As a result, instead of using the colour function difference $\left(s(\mathbf{x}')-s(\mathbf{x})\right)$ in Eq.(6.17), the inter-particle colour index number can be utilized as [197]

$$\left(s(\mathbf{x}')-s(\mathbf{x})\right)=\mathbb{C}(\mathbf{x}',\mathbf{x})=\begin{cases}\dfrac{2\rho_{\mathbf{x},0}}{\rho_{\mathbf{x},0}+\rho_{\mathbf{x}',0}}, & \text{if } \mathbf{x} \text{ and } \mathbf{x}' \text{ belong to different phase}\\ 0, & \text{if } \mathbf{x} \text{ and } \mathbf{x}' \text{ belong to the same phase}\end{cases} \tag{6.18}$$

and Eq.(6.17) becomes [197]

$$\nabla s(\mathbf{x})=\int_{H_{\mathbf{x}}}\mathbb{C}(\mathbf{x}',\mathbf{x})\mathbf{g}_1(\xi)\mathrm{d}V' \tag{6.19}$$

where $\rho_{\mathbf{x},0}$ and $\rho_{\mathbf{x}',0}$ represent the initial densities of particle $\mathbf{x}$ and $\mathbf{x}'$, respectively. As a result, the colour function gradient in Eq. (6.7) becomes

$$\mathbf{c}_g(\mathbf{x})=\nabla s(\mathbf{x})=\int_{H_{\mathbf{x}}}\mathbb{C}(\mathbf{x}',\mathbf{x})\mathbf{g}_1(\xi)\mathrm{d}V' \tag{6.20}$$

Consequently, the weighted function in Eq. (6.10) which equals the magnitude of the normal direction vector becomes

$$\lambda=\left|\mathbf{c}_g(\mathbf{x})\right|=|\nabla s|=\left|\int_{H_{\mathbf{x}}}\mathbb{C}(\mathbf{x}',\mathbf{x})\mathbf{g}_1(\xi)\mathrm{d}V'\right| \tag{6.21}$$

and the unit normal vector $\hat{\mathbf{n}}$ Eq.(6.8) hence can be calculated as

$$\hat{\mathbf{n}}(\mathbf{x})=\frac{\mathbf{c}_g(\mathbf{x})}{\left|\mathbf{c}_g(\mathbf{x})\right|}=\frac{\nabla s}{|\nabla s|}=\frac{\int_{H_{\mathbf{x}}}\mathbb{C}(\mathbf{x}',\mathbf{x})\mathbf{g}_1(\xi)\mathrm{d}V'}{\left|\int_{H_{\mathbf{x}}}\mathbb{C}(\mathbf{x}',\mathbf{x})\mathbf{g}_1(\xi)\mathrm{d}V'\right|} \tag{6.22}$$

The curvature $\kappa(\mathbf{x})$ in Eq.(6.9) thus can be calculated by the PDDO formulation as

$$\kappa^*(\mathbf{x})=-\nabla\cdot\hat{\mathbf{n}}(\mathbf{x})=-\int_{H_{\mathbf{x}}}\left(\hat{\mathbf{n}}(\mathbf{x}')-\hat{\mathbf{n}}(\mathbf{x})\right)\cdot\mathbf{g}_1(\xi)\mathrm{d}V' \tag{6.23}$$

According to the explanation given in [198], the normal vector $\mathbf{n}$ may have erroneous direction and small value away from the interface, therefore a cut-off value ($\varepsilon = 1.0\times10^{-2}/\Delta x$ as suggested in [198]) is set for the normal vector $\mathbf{c}_g(\mathbf{x})$, smaller than which the unit normal vector $\hat{\mathbf{n}}(\mathbf{x})$ is set to be zero. A function $\mathbb{N}(\mathbf{x})$ is defined to indicate if the unit normal vector is zero as

$$\mathbb{N}(\mathbf{x}) = \begin{cases} 1, \text{ if } \left|\mathbf{c}_g(\mathbf{x})\right| > \varepsilon \\ 0, \text{ otherwise} \end{cases} \tag{6.24}$$

And the calculation of the unit normal vector $\hat{\mathbf{n}}(\mathbf{x})$ is set as

$$\hat{\mathbf{n}}(\mathbf{x}) = \begin{cases} \mathbf{c}_g(\mathbf{x}) / \left|\mathbf{c}_g(\mathbf{x})\right|, \text{ if } \mathbb{N}(\mathbf{x}) = 1 \\ 0, \text{ otherwise} \end{cases} \tag{6.25}$$

Therefore, the PDDO form of the unit normal direction $\hat{\mathbf{n}}(\mathbf{x})$ for particle $\mathbf{x}$ in Eq. (6.22) becomes as

$$\hat{\mathbf{n}}(\mathbf{x}) = \frac{\mathbf{c}_g(\mathbf{x})}{\left|\mathbf{c}_g(\mathbf{x})\right|} = \frac{\nabla s}{\left|\nabla s\right|} = \begin{cases} \dfrac{\int_{H_\mathbf{x}} \mathbb{C}(\mathbf{x}', \mathbf{x}) \mathbf{g}_1(\xi) \mathrm{d}V'}{\left|\int_{H_\mathbf{x}} \mathbb{C}(\mathbf{x}', \mathbf{x}) \mathbf{g}_1(\xi) \mathrm{d}V'\right|}, & \text{if } \mathbb{N}(\mathbf{x}) = 1 \\ 0, & \text{otherwise} \end{cases} \tag{6.26}$$

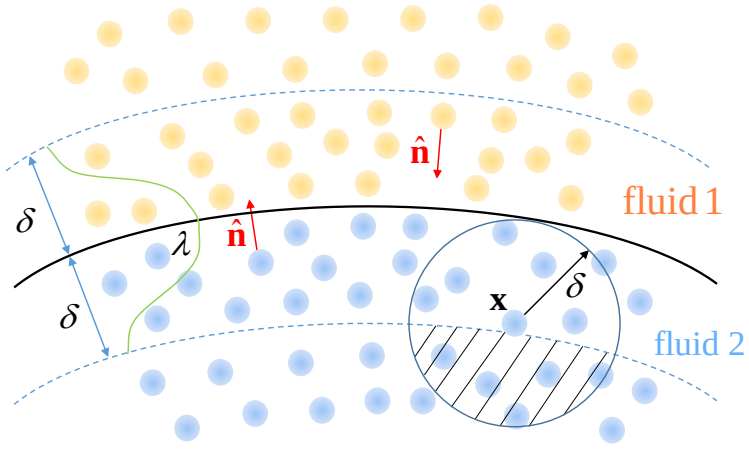

Fig. 6-1 Surface tension force in the multi-fluid interface region

The approach for curvature calculation provided in [198] is adopted to increase the approximation accuracy. An intermediate estimate of the curvature (the divergence of the unit normal vector $\nabla\cdot\hat{\mathbf{n}}$) is defined using a sum over neighbouring unit normal vectors as [198]

$$\kappa^{**}(\mathbf{x}) = -\left(\nabla\cdot\hat{\mathbf{n}}(\mathbf{x})\right)^{*} = -\int_{H_{\mathbf{x}}} \min\left(\mathbb{N}(\mathbf{x}),\mathbb{N}(\mathbf{x}')\right)\left(\hat{\mathbf{n}}(\mathbf{x}')-\hat{\mathbf{n}}(\mathbf{x})\right)\cdot\mathbf{g}_1(\xi)\,\mathrm{d}V' \quad (6.27)$$

The width of the multi-fluid interface region is defined as 2δ, as shown in Fig. 6-1. It can be referred from Fig. 6-1 that if the central point $\mathbf{x}$ is located at the edge of the interface transition region, the unit normal vectors of its family members located in the shaded region in Fig. 6-1 are forced to be zero. In other words, the neighbourhood of the interface region boundary particle is truncated. Being similar to surface correction for the boundary particles in peridynamic discretization and the approach adopted in [198], a correction factor for $\kappa^{**}(\mathbf{x})$ is proposed as

$$\varsigma^{*}(\mathbf{x}) = \frac{\int_{H_{\mathbf{x}}} \min\left(\mathbb{N}(\mathbf{x}),\mathbb{N}(\mathbf{x}')\right) w_0(\xi)\,\mathrm{d}V'}{\int_{H_{\mathbf{x}}} w_0(\xi)\,\mathrm{d}V'} \quad (6.28)$$

where w_0 represents the improved Gaussian weighted function as [154]

$$w_0(|\xi|) = \left(e^{-(|\xi|/h)^2} - e^{-9}\right) / \left(h^d \pi^{d/2}\left(1-10e^{-9}\right)\right), |\xi| < \delta \quad (6.29)$$

In Eq.(6.29), h represents the smoothing length [154] with its value being set as $h = 1.2\Delta x$. The parameter d represents the dimensionality of the problems as $d = 2$ for 2D problems. The term $\varsigma^{*}(\mathbf{x})$ can reflect the number density of particle $\mathbf{x}$ [198]. As a result, the curvature $\kappa(\mathbf{x})$ in Eq.(6.23) is modified as [198]

$$\kappa^{***}(\mathbf{x}) = \frac{\kappa^{**}(\mathbf{x})}{\varsigma^{*}(\mathbf{x})} = -\frac{\int_{H_{\mathbf{x}}} \min\left(\mathbb{N}(\mathbf{x}),\mathbb{N}(\mathbf{x}')\right)\left(\hat{\mathbf{n}}(\mathbf{x}')-\hat{\mathbf{n}}(\mathbf{x})\right)\cdot\mathbf{g}_1(\xi)\,\mathrm{d}V'}{\int_{H_{\mathbf{x}}} \min\left(\mathbb{N}(\mathbf{x}),\mathbb{N}(\mathbf{x}')\right) w_0(\xi)\,\mathrm{d}V' / \int_{H_{\mathbf{x}}} w_0(\xi)\,\mathrm{d}V'} \quad (6.30)$$

As shown in Fig. 6-1, it should be noted that the unit normal $\hat{\mathbf{n}}$ always points from the fluid phase itself to the other fluid phase. Consequently, for the calculation of the curvature, $\kappa(\mathbf{x})$ for central point $\mathbf{x}$, the unit normal direction vector $\hat{\mathbf{n}}(\mathbf{x}')$ for the family member $\mathbf{x}'$ is inverted if point $\mathbf{x}'$ and point $\mathbf{x}$ belong to different fluid phases. Hence, Eq.(6.30) is modified as

$$\kappa(\mathbf{x}) = -\frac{\int_{H_{\mathbf{x}}} \min\left(\mathbb{N}(\mathbf{x}), \mathbb{N}(\mathbf{x}')\right)\left(\varphi\hat{\mathbf{n}}(\mathbf{x}') - \hat{\mathbf{n}}(\mathbf{x})\right)\cdot\mathbf{g}_1(\xi)\mathrm{d}V'}{\int_{H_{\mathbf{x}}} \min\left(\mathbb{N}(\mathbf{x}), \mathbb{N}(\mathbf{x}')\right) w_0(\xi)\mathrm{d}V' / \int_{H_{\mathbf{x}}} w_0(\xi)\mathrm{d}V'} \tag{6.31}$$

with an additional parameter being added as [193]

$$\varphi = \begin{cases} -1, \text{ if } \mathbf{x} \text{ and } \mathbf{x}' \text{ belong to different phases} \\ 1, \quad \text{if } \mathbf{x} \text{ and } \mathbf{x}' \text{ belong to the same phases} \end{cases} \tag{6.32}$$

Finally, the surface tension force is expressed in PDDO form as

$$\begin{aligned} \mathbf{F}^S &= \beta\kappa\nabla s \\ &= -\beta\frac{\int_{H_{\mathbf{x}}} \min\left(\mathbb{N}(\mathbf{x}), \mathbb{N}(\mathbf{x}')\right)\left(\varphi\hat{\mathbf{n}}(\mathbf{x}') - \hat{\mathbf{n}}(\mathbf{x})\right)\cdot\mathbf{g}_1(\xi)\mathrm{d}V'}{\int_{H_{\mathbf{x}}} \min\left(\mathbb{N}(\mathbf{x}), \mathbb{N}(\mathbf{x}')\right) w_0(\xi)\mathrm{d}V' / \int_{H_{\mathbf{x}}} w_0(\xi)\mathrm{d}V'}\left(\int_{H_{\mathbf{x}}} \mathbb{C}(\mathbf{x}', \mathbf{x})\mathbf{g}_1(\xi)\mathrm{d}V'\right) \end{aligned} \tag{6.33}$$

In conclusion, the non-local form of the momentum equation Eq.(6.2) becomes

$$\begin{aligned} &\rho(\mathbf{x})\frac{\partial v(\mathbf{x})}{\partial t} = \\ &-\int_{H_{\mathbf{x}}}\left(\left(P(\mathbf{x}') - P(\mathbf{x})\right)\mathbf{g}_1(\xi)\right)\mathrm{d}V' + \int_{H_{\mathbf{x}}}\left(\mu(\mathbf{x})\left(\mathbf{v}(\mathbf{x}') - \mathbf{v}(\mathbf{x})\right)\mathrm{Tr}\left(\mathbf{g}_2(\xi)\right)\right)\mathrm{d}V' \\ &-\beta\frac{\int_{H_{\mathbf{x}}} \min\left(\mathbb{N}(\mathbf{x}), \mathbb{N}(\mathbf{x}')\right)\left(\varphi\hat{\mathbf{n}}(\mathbf{x}') - \hat{\mathbf{n}}(\mathbf{x})\right)\cdot\mathbf{g}_1(\xi)\mathrm{d}V'}{\int_{H_{\mathbf{x}}} \min\left(\mathbb{N}(\mathbf{x}), \mathbb{N}(\mathbf{x}')\right) w_0(\xi)\mathrm{d}V' / \int_{H_{\mathbf{x}}} w_0(\xi)\mathrm{d}V'}\left(\int_{H_{\mathbf{x}}} \mathbb{C}(\mathbf{x}', \mathbf{x})\mathbf{g}_1(\xi)\mathrm{d}V'\right) + \mathbf{F}^B \end{aligned} \tag{6.34}$$

6.2. Numerical implementation for multiphase fluid simulation

6.2.1. Discretised form of PDDO equations

In the numerical simulation, the updated Lagrangian description provided in Section 5.4.3 is adopted, as explained in [8]. Therefore, the reference configuration is referred to as the current configuration. The PDDO is reconstructed every time step based on the updated family member array. Correspondingly, the integral governing equations can also be expressed by using the discretized particles. The central point is denoted as i and its family member is denoted as j. Therefore, the continuity equation Eq.(6.14) is discretized as

$$\rho_i^{n+1} = \rho_i^n - \rho_i^n \Delta t \sum_{j=1}^{N_i} \left[\left(\mathbf{v}_j^n - \mathbf{v}_i^n \right) \cdot \mathbf{g}_1 \left(\boldsymbol{\xi}_{ij}^n \right) \right] V_j \tag{6.35a}$$

with

$$\boldsymbol{\xi}_{ij}^n = \mathbf{x}_j^n - \mathbf{x}_i^n \tag{6.35b}$$

where N_i represents the number of family members of point i and $\boldsymbol{\xi}_{ij}^n$ represents the relative position between particle i and j in the current configuration $t = t_n$.

The PDDO form of momentum equation, Eq.(6.34) becomes

$$\mathbf{a}_i^{n+1} = \frac{1}{\rho_{ij}^n} \begin{pmatrix} -\sum_{j=1}^{N_i} \left(P_j^n - P_i^n \right) \mathbf{g}_1 \left(\boldsymbol{\xi}_{ij}^n \right) V_j + \mu_{ij} \sum_{j=1}^{N_i} \left(\mathbf{v}_j^n - \mathbf{v}_i^n \right) \mathrm{Tr} \left(\mathbf{g}_2 \left(\boldsymbol{\xi}_{ij}^n \right) \right) V_j \\ -\beta \dfrac{\left(\sum_{j=1}^{N_i} \min \left(\mathbb{N}_i, \mathbb{N}_j \right) \left(\varphi \hat{\mathbf{n}}_j^n \text{-} \hat{\mathbf{n}}_i^n \right) \cdot \mathbf{g}_1 \left(\boldsymbol{\xi}_{ij}^n \right) V_j \right)}{\sum_{j=1}^{N_i} \min \left(\mathbb{N}_i, \mathbb{N}_j \right) w_0 \left(\boldsymbol{\xi}_{ij}^n \right) V_j / \sum_{j=1}^{N_i} w_0 \left(\boldsymbol{\xi}_{ij}^n \right) V_j} \left(\sum_{j=1}^{N_i} \mathbb{C}_{ij} \mathbf{g}_1 \left(\boldsymbol{\xi}_{ij}^n \right) V_j \right) \end{pmatrix} + \frac{1}{\rho_{ij}^n} \mathbf{F}^B \tag{6.36}$$

where $\mathbf{a}_i^{n+1}$ represents the acceleration of particle i in the updated configuration at $t = t_{n+1}$.

Interface implementation is a crucial step for the multi-phase fluid flow simulation. The discontinuities will present in the interface region. The non-local approximation near the discontinuous region will suffer numerical errors which will be more serious with higher-order schemes [188]. As a result, in order to prevent numerical oscillations and unphysical particle penetrations [191], the viscosity coefficient and the density for multi-phase interface interaction are smoothed in a harmonic mean interpolation as [152, 199]

$$\mu_{ij} = \frac{2\mu_i \mu_j}{\mu_i + \mu_j} \tag{6.37}$$

$$\rho_{ij} = \frac{2\rho_i \rho_j}{\rho_i + \rho_j} \tag{6.38}$$

where μ_i and μ_j represent the viscosity coefficients of particle i and j. Similarly, ρ_i and ρ_j are the densities for particle i and j, respectively.

The velocity and displacements can be predicted by using the Euler forward method (1st order) or the Velocity Verlet algorithm (2nd order) [200] as

Euler forward method:

$$\mathbf{v}_i^{n+1} = \mathbf{v}_i^n + \mathbf{a}_i^{n+1}\Delta t \tag{6.39a}$$

$$\mathbf{u}_i^{n+1} = \mathbf{u}_i^n + \mathbf{v}_i^{n+1}\Delta t \tag{6.39b}$$

$$\mathbf{x}_i^{n+1} = \mathbf{x}_i^0 + \mathbf{u}_i^{n+1} \tag{6.39c}$$

Velocity Verlet algorithm:

$$\mathbf{v}_i^{n+1} = \mathbf{v}_i^n + \frac{1}{2}\left(\mathbf{a}_i^{n+1} + \mathbf{a}_i^n\right)\Delta t \tag{6.40a}$$

$$\mathbf{u}_i^{n+1} = \mathbf{u}_i^n + \mathbf{v}_i^n \Delta t + \frac{1}{2}\mathbf{a}_i^n \Delta t^2 \tag{6.40b}$$

$$\mathbf{x}_i^{n+1} = \mathbf{x}_i^0 + \mathbf{u}_i^{n+1} \tag{6.40c}$$

where the displacement of particle i is denoted by $\mathbf{u}_i$. The term $\mathbf{x}_i^0$ represents the initial coordinate for particle i, and $\mathbf{x}_i^{n+1}$ represents the updated coordinate at $t = t_{n+1}$.

The time step size Δt should satisfy the CFL condition for kinetic, viscous, body force and surface tension force fields, shown as [195]

$$\Delta t < \min\left(\frac{h}{|\mathbf{V}_{\max}| + c_2}, \frac{1}{8}\frac{h^2}{\max\left(\mu_1/\rho_{0,1}, \mu_2/\rho_{0,2}\right)}, \frac{1}{4}\sqrt{\frac{h}{g}}, \frac{1}{4}\sqrt{\frac{\min\left(\rho_{0,1}, \rho_{0,2}\right)h^3}{2\pi\beta}} \right) \tag{6.41}$$

where h is the smoothing length, $|\mathbf{V}_{\max}|$ is the maximum fluid particle velocity, μ is the viscosity coefficient, ρ is the fluid density, g is the gravity acceleration, and β is the surface tension coefficient. The artificial speed of sound for the lighter fluid is larger than the one for the heavier fluid on the condition of same material constants $\gamma_1 = \gamma_2$. Therefore, the value of c_2 is used for the constraints on the time step size.

6.2.2. Boundary Treatment

6.2.2.1 Boundary conditions for solid wall

In the present work, the fictitious particles are employed to represent the solid boundaries as described in [8, 9].

Non-slip boundary conditions

The velocities of the fictitious wall particles can be calculated based on the velocities of the fluid particles. As illustrated in Fig. 6-2, for the non-slip solid boundary condition, the velocity of the solid fictitious particle i, is calculated as [152]

$$\mathbf{v}_i^n = 2\mathbf{v}_{wall} - \left(\sum_{j=1}^{N_1} w_0\left(\left|\boldsymbol{\xi}_{ij}^n\right|\right)\mathbf{v}_j^n + \sum_{k=1}^{N_2} w_0\left(\left|\boldsymbol{\xi}_{ij}^n\right|\right)\mathbf{v}_k^n \right) \tag{6.42}$$

where N_1 and N_2 represent the number of family members of material point i that belongs to fluid 1 and 2, respectively. Note that material point k and j cannot be fictitious wall particles, i.e. in Eq.(6.42) fictitious wall particles are not included in the family members of material point i.

Furthermore, particles j and k represent the family members of the solid particle i, where particle j belongs to fluid 1 and particle k belongs to fluid 2. Their velocities in the current configuration are denoted by $\mathbf{v}_j^n$ and $\mathbf{v}_k^n$, respectively. The parameter $\mathbf{v}_{wall}$ denotes the prescribed solid wall velocity. The second term on the right-hand side represents the weighted fluid velocity summation. In Eq. (6.42), w_0 represents the improved Gaussian weighted function as provided in Eq. (6.29).

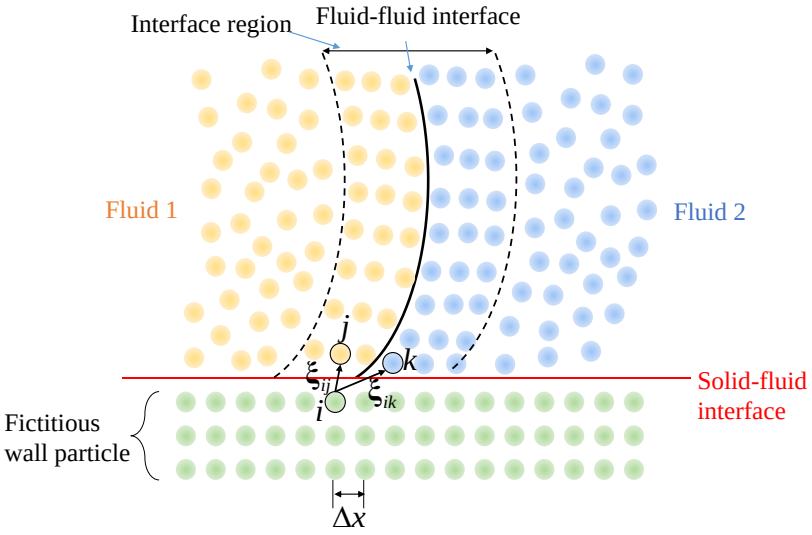

Fig. 6-2 Boundary and interface illustration

The pressure of the solid fictitious particle is calculated based on the fluid particles according to the formulation provided in [152] as

$$P_i = \frac{\sum_{j=1}^{N_1}\left(P_j + \left(\mathbf{F}_j^B - \rho_j \mathbf{a}_{wall}\right)\cdot\xi_{ij}^n\right) w_0\left(\xi_{ij}^n\right) + \sum_{k=1}^{N_2}\left(P_k + \left(\mathbf{F}_k^B - \rho_k \mathbf{a}_{wall}\right)\cdot\xi_{ik}^n\right) w_0\left(\left|\xi_{ik}^n\right|\right)}{\sum_{j=1}^{N_1} w_0\left(\left|\xi_{ij}^n\right|\right) + \sum_{k=1}^{N_2} w_0\left(\left|\xi_{ik}^n\right|\right)} \tag{6.43a}$$

$$\mathbf{F}_j^B = \rho_j \mathbf{g}; \mathbf{F}_k^B = \rho_k \mathbf{g}; \tag{6.43b}$$

where P_j and P_k represent the fluid pressure. $\mathbf{F}_j^B$ and $\mathbf{F}_k^B$ represent the body force of the fluid particles. In the current chapter, the body force is calculated as Eq. (6.43b) with $\mathbf{g}$ representing the gravitational acceleration. $\mathbf{a}_{wall}$ represents the acceleration of the solid wall. Please note that in Eq.(6.43a) fictitious wall particles are not included in the family members of material point i.

Slip boundary condition for solid wall

For the slip boundary condition, the viscous forces are neglected for fluid-solid particle interactions $\left(\mathbf{F}^v = 0\right)$ and the velocity of the fictitious wall particle is set as [152]

$$\mathbf{v}_i^n = \mathbf{v}_{wall} \tag{6.44}$$

The pressure of the fictitious solid particle is calculated according to Eq.(6.43a).

6.2.2.2 Boundary collision model

If the fluid particle penetrates the solid wall in the updated configuration, the velocity of the fluid particle needs to be corrected [201]. In this case, the boundary collision model [201] can be applied where the solid wall is simulated as a reflective boundary condition as

$$\left(\mathbf{v}_i^{n+1}\right)^{corrected} = \left(\mathbf{v}_i^{n+1}\right) - 2\left(\left(\mathbf{v}_i^{n+1} - \mathbf{v}_{wall}\right)\cdot\hat{\mathbf{n}}_{wall}\right)\hat{\mathbf{n}}_{wall}, \text{ if } \left(\mathbf{v}_i^{n+1} - \mathbf{v}_{wall}\right)\cdot\hat{\mathbf{n}}_{wall} < 0 \tag{6.45}$$

where $\hat{\mathbf{n}}_{wall}$ represents the unit normal direction of the solid wall, as shown in Fig. 6-3.

The velocity correction in Eq.(6.45) is illustrated in Fig. 6-3.

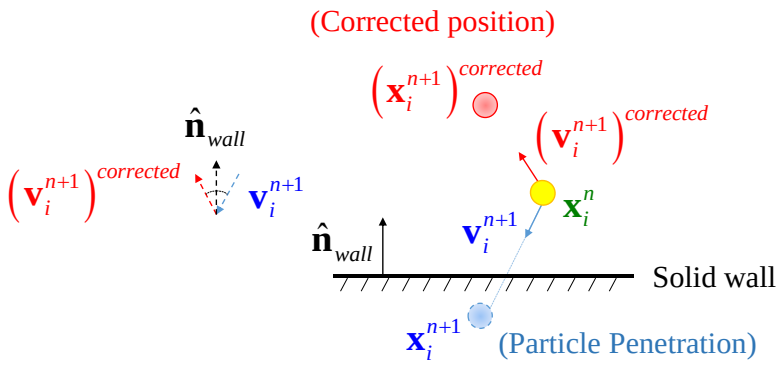

Fig. 6-3 Sketch for solid wall collision model

6.2.3. Particle shifting technology for preventing particle clustering

For the particle methods such as SPH, the instability problem may occur when the particle distribution becomes highly distorted [202]. The numerical errors induced by the irregular particle spacing may dominate the results especially in the later stage of the numerical simulations. The same problem also happens in the PD field, as explained by Silling et al. [133]. To avoid the particle clustering phenomenon or the instability problem, the particle shifting technology (PST) [159] is widely applied in the fluid flow simulations [202-207]. The particles will be nearly uniformly distributed after shifting; thus, the singularity of the particle distribution will be reduced. Therefore the particle positions can be modified by using a shifting displacement [159]:

$$\left(\mathbf{x}_i^{n+1}\right)^{corrected} = \mathbf{x}_i^0 + \left(\mathbf{u}_i^{n+1}\right)^{shifted} \tag{6.46}$$

The shifting displacement for particle i can be found as

$$\left(\mathbf{u}_i^{n+1}\right)^{shifted} = \mathbf{u}_i^{n+1} + \left(\delta\mathbf{u}_i\right)^{PST} \tag{6.47}$$

In Eq. (6.47), the parameter $\left(\delta\mathbf{u}_i\right)^{PST}$ represents the shifting distance and it can be defined as

$$\left(\delta\mathbf{u}_i\right)^{PST} = C_{PST}\alpha_{PST}\mathbf{U}_i \tag{6.48}$$

where C_{PST} is a predefined constant ranging from 0.01 to 0.1 depending on the specific problem and α_{PST} is the shifting magnitude which can be defined as [159]

$$\alpha_{PST} = \left|\mathbf{V}_{\max}\right| \Delta t \tag{6.49}$$

where $\left|\mathbf{V}_{\max}\right|$ can be chosen as the magnitude of the largest velocity overall fluid particles or it can be estimated specifically according to the specific problem [159] .

In Eq. (6.48), the parameter $\mathbf{U}_i$ represents the displacement shift-vector which can be defined as [159]

$$\mathbf{U}_i = \sum_{j=1}^{N_i} \frac{\left|\overline{\xi}_i\right|^2}{\left|\boldsymbol{\xi}_{ij}^n\right|^2} \boldsymbol{\zeta}_{ij} \tag{6.50a}$$

with

$$\boldsymbol{\zeta}_{ij} = \frac{\boldsymbol{\xi}_{ij}^n}{\left|\boldsymbol{\xi}_{ij}^n\right|} \tag{6.50b}$$

$$\left|\overline{\xi}_i\right| = \frac{1}{N_i} \sum_{j=1}^{N_i} \left|\boldsymbol{\xi}_{ij}^n\right| \tag{6.50c}$$

where $\left|\overline{\xi}_i\right|$ represents the average spacing between the central point i and its family members (e.g. j) [159] and $\boldsymbol{\zeta}_{ij}$ represents the unit distance vector between particles i and j . Note that, the summation of $\boldsymbol{\zeta}_{ij}$ in Eq. (6.50a) can reflect the anisotropy of the current particle distribution [159] and the term $\left(\left|\overline{\xi}_i\right|^2 / \left|\boldsymbol{\xi}_{ij}^n\right|^2\right)$ acts as a weighted function in the formulation. According to [203], numerical errors will be induced if the shifting distance is much larger than the initial spacing distance Δx . Therefore, an upper limit for the particle shifting distance, $\left(\delta \mathbf{u}_i\right)^{PST}$, is imposed as $0.2\Delta x$ [203]. As an optional procedure, the velocity and pressure can also be corrected based on the displacement

shifting. The corresponding details are provided in Appendix E. The flowchart of the PST is provided in Fig. 6-4 as

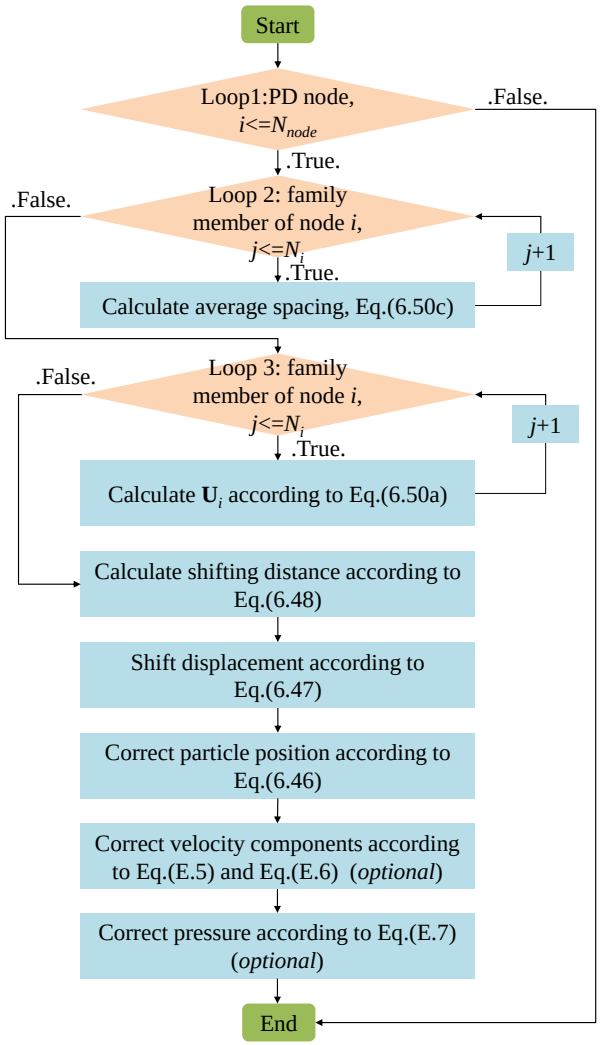

Fig. 6-4 Flowchart for PST algorithm

6.2.4. Moving least square algorithm for multiphase fluids

It is known that the free movement of the particles may create the "pressure instability" problems for Lagrangian particle methods, where the mass is not conserved and the great oscillation occurs in density and pressure [208, 209]. In order to overcome this problem, velocity, pressure and density values are smoothed by using moving least square (MLS) algorithm [153, 210]. The algorithm is introduced to hydrodynamics by Dilts [153]. In the present chapter, the first order MLS [154]

provided in Section 5.4.6.2 is modified for multi-phase fluids flow density smoothing as [208]

$$\left(\rho_i^n\right)^{smoothed} = \frac{\sum_j \left(\tilde{\rho}_j^n\right) w_{MLS}\left(\xi_{ij}^n\right) V_j}{\sum_j w_{MLS}\left(\xi_{ij}^n\right) V_j} \tag{6.51}$$

with

$$\left(\tilde{\rho}_j^n\right) = \left(\frac{\left(P_j^n\right) - P_0}{P_{ref}} + 1\right)^{\frac{1}{\gamma_i}} \rho_{0,i} \text{ and } \gamma_i = \begin{cases} \gamma_1 \text{ for fluid 1} \\ \gamma_2 \text{ for fluid 2} \end{cases}; \rho_{0,i} = \begin{cases} \rho_{0,1} \text{ for fluid 1} \\ \rho_{0,2} \text{ for fluid 2} \end{cases} \tag{6.52}$$

where $w_{MLS}\left(\xi_{ij}^n\right)$ is provided in Eq.(5.113). The parameter $\rho_{0,i}$ is the initial density of particle i. The correction in Eq. (6.52) can be considered as converting the phase of particle j into the phase of particle i [208].

6.2.5. XSPH displacement smoothing

Compared to the PST introduced in Section 6.2.3 for the large irregular particle distributions, a simpler XSPH method can be chosen for less irregular particle distributions to save computational time. The formulation in XSPH method [128] is adopted here to only update the displacements as

$$\left(\mathbf{u}_i^{n+1}\right)^{shifted} = \mathbf{u}_i^{n+1} + \left(\delta\mathbf{u}_i\right)^{XSPH} \tag{6.53a}$$

with

$$\left(\delta\mathbf{u}_i\right)^{XSPH} = \left(\chi \sum_j m_i \frac{\left(\rho_i^n + \rho_j^n\right)}{2\rho_i^n \rho_j^n} \left(\mathbf{v}_j^n - \mathbf{v}_i^n\right) w_0\left(\left|\xi_{ij}^n\right|\right)\right) \Delta t \tag{6.53b}$$

where χ is an adjustable parameter as $0 \le \chi \le 1$ [128] and m_i is the mass of particle i which can be calculated as

$$m_i = \rho_{0,i} V_i \tag{6.53c}$$

6.2.6. Artificial viscosity

To reduce the undesirable oscillations, the artificial viscosity, $\prod$, widely applied in SPH method [128] can be utilized and incorporated into the current PDDO model. According to [128, 211], the momentum equation Eq.(6.2) can be modified by including the artificial viscosity form as

$$\rho \frac{\partial \mathbf{v}}{\partial t} = -\nabla P + \mathbf{F}^V + \mathbf{F}^B + \mathbf{F}^S + \nabla \prod \tag{6.54}$$

where the SPH form of the gradient of artificial viscosity, $\prod_i$ for particle i is expressed as [189]

$$\nabla \prod_i = \begin{cases} \sum_{j=1}^{N_i} \dfrac{\alpha h c_{avg} \left(\mathbf{v}_j - \mathbf{v}_i \right) \cdot \boldsymbol{\xi}_{ij}}{\left| \boldsymbol{\xi}_{ij} \right|^2 + \left(0.1h \right)^2} \left(\nabla_i W_{ij} \right) V_j, & \text{for} \quad \left(\mathbf{v}_j - \mathbf{v}_i \right) \cdot \boldsymbol{\xi}_{ij} < 0 \\ 0, & \text{otherwise} \end{cases} \tag{6.55}$$

where W_{ij} represents a weighted function in SPH method.

In Eq.(6.55), c_{avg} is the average value of the artificial speeds of sound of particle i and j. Inspired by SPH method [128], the gradient of the artificial viscosity term $\prod_i$ is reformulated by replacing the SPH gradient operator with PDDO as

$$\nabla \prod_i = \begin{cases} \sum_{j=1}^{N_i} \dfrac{\alpha h c_{avg} \left(\mathbf{v}_j^n - \mathbf{v}_i^n \right) \cdot \boldsymbol{\xi}_{ij}^n}{\left| \boldsymbol{\xi}_{ij}^n \right|^2 + \left(0.1h \right)^2} \left(\mathbf{g}_1 \left(\boldsymbol{\xi}_{ij}^n \right) \right) V_j, & \text{for} \quad \left(\mathbf{v}_j^n - \mathbf{v}_i^n \right) \cdot \boldsymbol{\xi}_{ij}^n < 0 \\ 0, & \text{otherwise} \end{cases} \tag{6.56}$$

where $h = 1.2\Delta x$ (being same with the one in MLS scheme) [212] and the empirical constant α which generally ranges from 0.01 to 0.1 [128]. In this chapter, the empirical constant is chosen as $\alpha = 0.02$. Finally, the flowchart of the algorithm including surface tension calculation is provided in Fig. 6-5 [8].

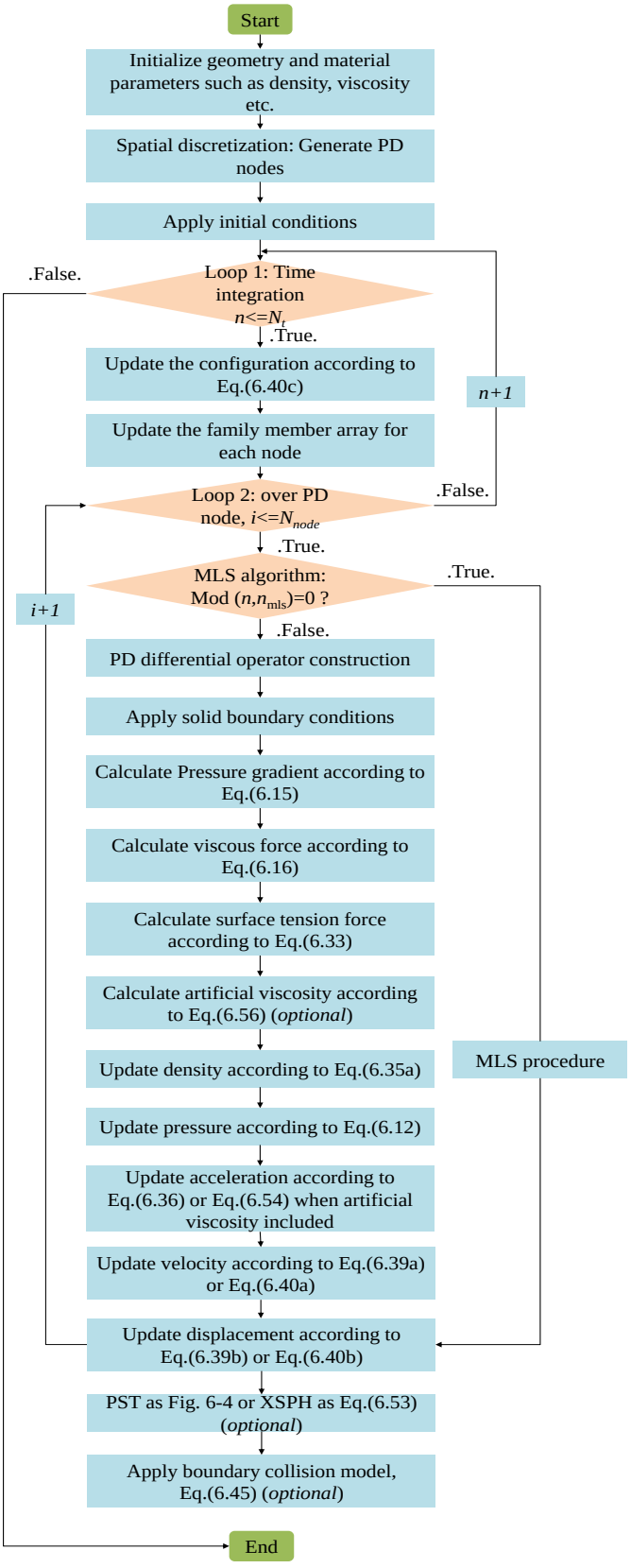

Fig. 6-5 Flowchart for the multi-phase fluid flow simulation by the PDDO model including the surface tension force calculation

6.3. Numerical simulations

In this section, some multi-phase fluid flow benchmark problems are solved by using the newly developed PDDO model. First, the two-phase fluids hydrostatic problem is simulated to validate the energy conservation of the PDDO model. Second, the two-phase Poiseuille flow simulation is conducted to validate the multi-viscosity coefficient treatment. Subsequently, the 2D droplet deformation under the surface tension force is simulated to validate the surface tension PDDO formulation.

6.3.1. Hydrostatic test

In the section, a hydrostatic simulation is conducted to study the energy conservation of the current PDDO model [208]. The stationary fluids with their properties being $\rho_{0,A}=3000\ \text{kg/m}^3$, $\rho_{0,B}=1000\ \text{kg/m}^3$ and $\mu_A=\mu_B=10^{-3}\ \text{kg/ms}$ [186] are in an open container with dimensions being $L\times W=0.05\,\text{m}\times 0.03\,\text{m}$, as shown in Fig. 6-6 (a). The gravitational acceleration is $|\mathbf{g}|=9.8\ \text{m/s}^2$. For fluid particle i, it is implemented as

$$\mathbf{F}_i^B=\begin{bmatrix}0\\-\rho_i|\mathbf{g}|\end{bmatrix} \tag{6.57}$$

The maximum velocity of the fluid is estimated as $|\mathbf{V}_{\max}|=\sqrt{|\mathbf{g}|W/2}\approx 0.383\ \text{m/s}$ [142] and the material constants are $\gamma_A=\gamma_B=1$. The artificial speeds of sound are hence chosen as 10 times of the maximum velocity as $c_A=c_B=10|\mathbf{V}_{\max}|=3.83\ \text{m/s}$ [183]. The background pressure is set as $P_0=0$ since the free surface is involved [195]. As shown in Fig. 6-6 (b), 40×24 PDDO particles are distributed in a uniform form with the initial particle spacing is set as $\Delta x=1.25\times 10^{-3}\ \text{m}$. The horizon size is chosen as $\delta=3.6\Delta x$. In order to save the computational time, only one fictitious layer is imposed to simulate the solid wall. The solid wall boundary conditions are

$$x=0,\ x=L,\ y=0: v_x=v_y=0 \tag{6.58}$$

where v_x and v_y are the horizontal and vertical components of velocity. Consequently, the boundary conditions are implemented by forcing the particles in the fictitious layer having the velocities calculated according to Eq.(6.42) with $\mathbf{v}_{wall}=0$. In addition, the pressures of the fictitious solid particles are calculated according to Eq.(6.43a).

The real fluid particles on the free surface are forced to have the constraint as

$$y=W:P=0 \tag{6.59}$$

The velocities of the free surface fluid particles are updated according to Eq.(6.36) and Eq.(6.39a).

The simulation time step size is chosen as $\Delta t=10^{-5}$ s with total simulation time as $t=1.0$ s. The MLS algorithm is performed every 20 time steps, i.e. $n_{MLS}=20$ [154]. The XSPH modification in Section 6.2.5 with the constant being $\chi=0.08$ [189]. The Velocity Verlet algorithm in Section 6.2.1 is adopted. The PST is not applied in this case. The surface tension force is not included since it is neglectable compared with the gravity force. The artificial viscosity is not used.

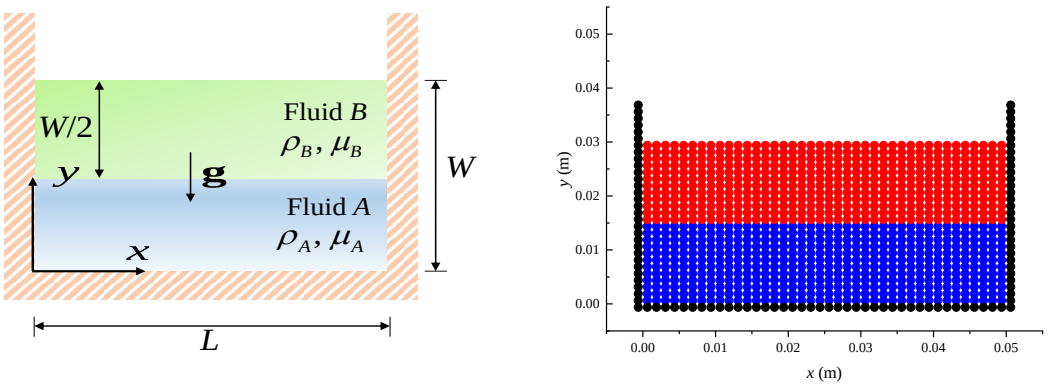

(a) (b)

Fig. 6-6 Schematic of hydrostatic problem: (a) Geometry illustration and (b) PDDO discretization

The analytical solution for hydrostatic pressure is calculated as

$$p_{B,analytical}=\rho_B|\mathbf{g}|(W-y) \tag{6.60}$$

$$p_{A,analytical} = \rho_B |\mathbf{g}|(W/2) + \rho_A |\mathbf{g}|(W/2 - y) \tag{6.61}$$

where y represents the vertical coordinate. The time history of the predicted pressure and kinetic energy at $(x, y) = (0.025, 0.015)$ are presented in Fig. 6-7. The PDDO results are compared with analytical solutions. The pressure profile along the mid vertical line $x = 2.5 \times 10^{-2}$ m is compared with the analytical solution, as shown in Fig. 6-8 (a). Furthermore, the deformed configuration at the final time is presented in Fig. 6-8 (b). It can be observed that the PDDO results agree well with the analytical solutions. Thus, the capability of the present PDDO model for solving the two-phase hydrostatic problem is demonstrated. Besides, the energy conservation of the model is also validated.

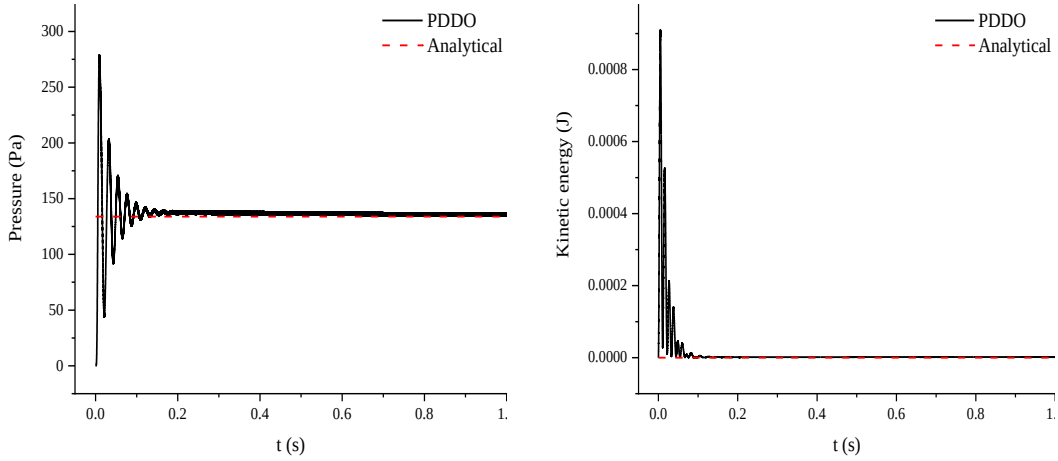

(a) (b)

Fig. 6-7 Time history of (a) pressure and (b) kinetic energy at $(x, y) = (0.025, 0.015)$.

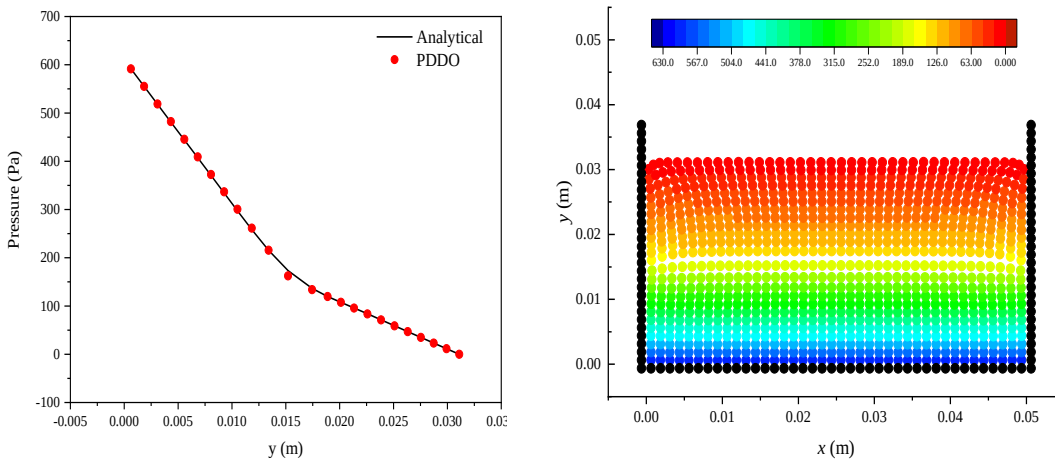

(a) (b)

Fig. 6-8 Variation of pressure distribution at (a) $x = 2.5\times10^{-2}$ m (b) deformed configuration at $t = 1$ s

6.3.2. Two-phase Poiseuille flow

The two-phase fluids laminar flow within two infinite plates has been studied [213] as a benchmark problem in the field of multi-phase fluid flows. As shown in Fig. 6-9, two adjacent immiscible fluids Poiseuille laminar flow is simulated by using the developed PDDO model. The flow domain has the dimensions as $L = 2b = 10^{-3}$ m. The top and bottom boundaries are stationary and non-slip. The boundary conditions are

At $y = -b$

$$v_x = v_y = 0 \tag{6.62}$$

At $y = b$

$$v_x = v_y = 0 \tag{6.63}$$

Consequently, the velocities of the fictitious solid particles are calculated according to Eq.(6.42) with $\mathbf{v}_{wall} = 0$. In addition, the pressures of the fictitious solid particles are calculated according to Eq.(6.43a).

The initial conditions for all particles including the fluid particles and the fictitious solid particles are:

$$v_x = v_y = 0 \tag{6.64}$$

A pressure gradient is applied as a body force per unit mass as $F = 2\times10^{-4}$ m/s^2 over both fluids in the x direction, as for particle i

$$\mathbf{F}_i^B = \begin{bmatrix} \rho_i F \\ 0 \end{bmatrix} \tag{6.65}$$

The densities of both fluids are the same as $\rho_{0,A} = \rho_{0,B} = 1000$ kg/m^3. The viscosity coefficient of fluid *B* is fixed as $\mu_B = 10^{-3}$ kg/ms. The viscosity coefficient of fluid *A* has three different values, namely, 2×10^{-3} kg/ms, 5×10^{-3} kg/ms and 10×10^{-3} kg/ms. The material constants both for fluid *A* and *B* are set as $\gamma_A = \gamma_B = 1$. The maximum velocity of the fluid is set as $|\mathbf{V}_{\max}| = 8.7\times10^{-6}$ m/s [188]. Hence, the artificial speeds of sound become $c_A = c_B = 8.7\times10^{-5}$ m/s [128]. The background pressure is not adopted for this simple laminar fluid flow case. In the PDDO simulation, an initial particle spacing of $\Delta x = 1\times10^{-5}$ m is adopted. The time step size is chosen as $\Delta t = 1\times10^{-5}$ s. The total simulation time is chosen as $t = 0.6$ s to achieve a steady state at the end of the simulation. The fluids are stationary at the initial state. Since the surface tension effect is small and neglectable compared to the applied body force, no surface tension force is applied. The PST, the MLS, the XSPH, and the artificial viscosity are not used in this case. The Euler forward scheme is used.

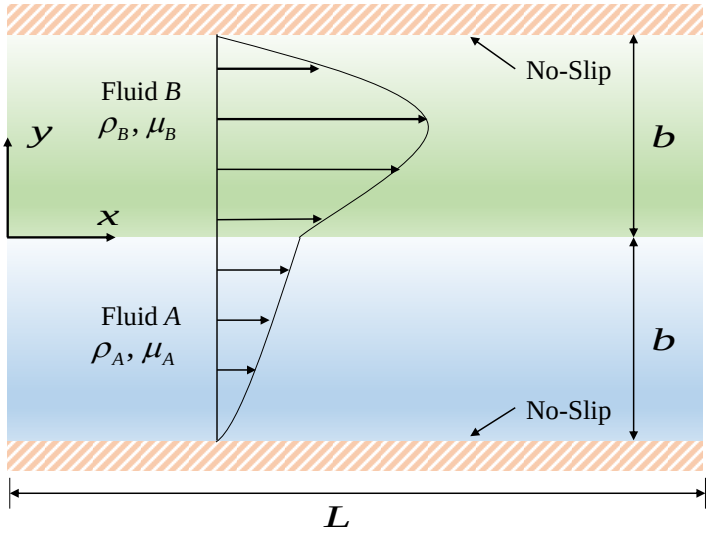

Fig. 6-9 Schematic of two-phase Poiseuille flow

The analytical solutions of the horizontal velocity for the two fluids are provided by Bird et al. [214] as

$$v_{A,x} = \frac{\rho_A F b^2}{2\mu_A}\left[\left(\frac{2\mu_A}{\mu_A+\mu_B}\right)+\left(\frac{\mu_A-\mu_B}{\mu_A+\mu_B}\right)\left(\frac{y}{b}\right)-\left(\frac{y}{b}\right)^2\right] \tag{6.66a}$$

$$v_{B,x} = \frac{\rho_B F b^2}{2\mu_B}\left[\left(\frac{2\mu_B}{\mu_A+\mu_B}\right)+\left(\frac{\mu_A-\mu_B}{\mu_A+\mu_B}\right)\left(\frac{y}{b}\right)-\left(\frac{y}{b}\right)^2\right] \tag{6.66b}$$

where $v_{A,x}$ and $v_{B,x}$ represent the horizontal velocity for fluid A and B respectively. The term y represents the vertical coordinate. The analytical average velocities are calculated as [214]

$$\bar{v}_{A,x} = \frac{1}{b}\int_{-b}^{0} v_{A,x}\mathrm{d}y = \frac{\rho F b^2}{12\mu_A}\left(\frac{7\mu_A+\mu_B}{\mu_A+\mu_B}\right) \tag{6.67a}$$

$$\bar{v}_{B,x} = \frac{1}{b}\int_{0}^{b} v_{B,x}\mathrm{d}y = \frac{\rho F b^2}{12\mu_B}\left(\frac{\mu_A+7\mu_B}{\mu_A+\mu_B}\right) \tag{6.67b}$$

$$\bar{v}_x = \left(\bar{v}_{A,x}+\bar{v}_{B,x}\right)/2 \tag{6.67c}$$

where $\bar{v}_{A,x}$ and $\bar{v}_{B,x}$ represent the average horizontal velocity for fluids A and B respectively. The average horizontal velocity over the whole flow domain, i.e. $\bar{v}_x$, is calculated according to Eq.(6.67c).

The comparison between the PDDO and analytical solutions of the normal velocity $v_x / \bar{v}_x$ at the steady-state is provided in Fig. 6-10. It can be inferred from the figure that the results agree well.

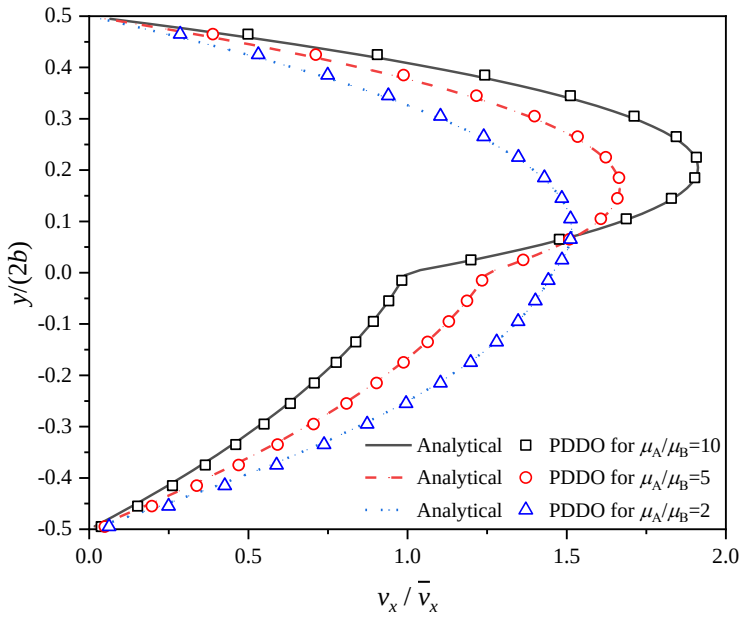

Fig. 6-10 Comparison of the horizontal velocity profile between the PDDO results and analytical solutions in three different viscosity coefficient ratios at $t = 0.6\,\mathrm{s}$.

A convergence study is also carried out for different resolutions and viscosity coefficients, namely $\Delta x = 5\times10^{-5}$ m, 3.3×10^{-5} m, 2×10^{-5} m, and 1×10^{-5} m for $\mu_A/\mu_B = 10, 5, 2$, respectively. The error can be calculated as

$$\varepsilon_r = \sqrt{\frac{\sum_i \left(v_{x,PDDO} - v_{x,analytical}\right)^2}{\sum_i \left(v_{x,analytical}\right)^2}} \tag{6.68}$$

From Fig. 6-11, it can be observed that the numerical simulation error decreases with increasing PDDO particles. Furthermore, the error becomes larger with larger viscosity ratios.

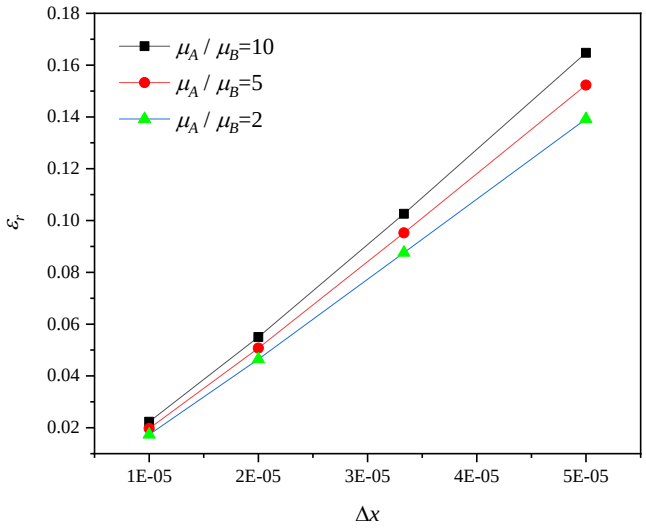

Fig. 6-11 Rate of convergence for two-phase Poiseuille flow in three viscosity ratios

6.3.3. 2D droplet deformation

To validate the surface tension model, a 2D square droplet deformation simulation is conducted as previous ones [186, 192, 195, 197]. A square droplet containing fluid A with sides $l_d = 0.6\,\mathrm{m}$ is located in the centre of a container with its sides being $L = 1\,\mathrm{m}$, as shown in Fig. 6-12 (a). The droplet is surrounded by fluid B. The two fluids have the same density and viscosity coefficient as $\rho_A = \rho_B = 1\,\mathrm{kg/m^3}$ and $\mu_A = \mu_B = 0.2\ \mathrm{Pa \cdot s}$. The surface tension coefficient is set as $\beta = 1\ \mathrm{N/m}$ [186, 192, 195, 197].

The initial condition is

$$\text{at } t = 0 : \mathbf{a} = 0,\ \mathbf{v} = 0,\ \mathbf{u} = 0 \tag{6.69}$$

The non-slip solid boundary condition is applied. As shown in Fig. 6-12 (b), the fluid domain is discretized by 80×80 particles and three layers of the fictitious particles are imposed to represent the fixed solid boundary as

$$x=-L/2,\ x=L/2,\ y=-W/2,\ y=W/2:v_x=v_y=0 \tag{6.70}$$

Therefore, the velocities of the fictitious solid particles are calculated according to Eq.(6.42) with $\mathbf{v}_{wall}=0$. The pressure of the fictitious solid particles is calculated according to Eq.(6.43a). On the fluids interface, the surface tension force is included.

The horizon size is chosen as $\delta=3.6\Delta x$. The speed of the sound is set as $c_A=c_B=10$ m/s and the material constants are $\gamma_A=\gamma_B=1$. The maximum velocity magnitude thus can be calculated as $|\mathbf{V}_{\max}|=c_A/10=1$ m/s [128]. Furthermore, the background pressure is calculated as $P_0=0.05P_{ref}=0.05\rho_{0,B}c_A^2/\gamma_A=5$ Pa as explained in Section 6.1.1. The time step size is chosen as $\Delta t=1\times10^{-4}$ s and the total simulation time is $t=1$ s. The MLS algorithm is performed every 20 time steps, i.e. $n_{MLS}=20$ [154]. The PST without pressure and velocity correction is performed as well. The constant in PST is chosen as $C_{PST}=0.01$. Besides, it can be calculated according to Eq.(6.49) as $\alpha_{PST}=1\times10^{-4}$ m. The artificial viscosity in Section 6.2.6 is adopted to make the simulation more stable. The velocity Verlet algorithm is used. The XSPH is not used in this case.

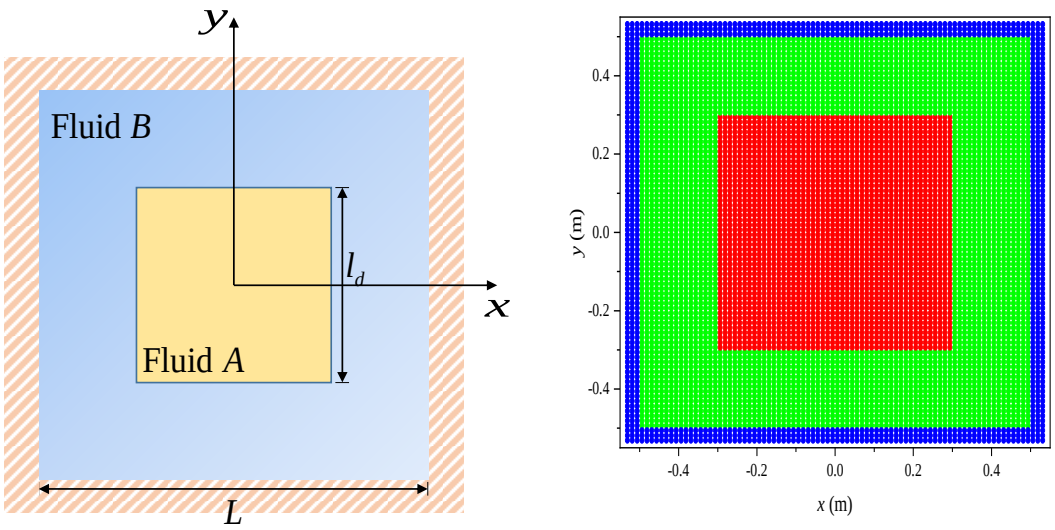

(a) (b)

Fig. 6-12 2D square droplet deformation under surface tension force (a) geometry sketch and (b) PDDO discretization with 80×80 nodes

The evolution of the droplet configuration is provided in Fig. 6-13. It can be observed from the figure that at the equilibrium state, the square droplet is transformed in a circular shape. The radius of the final circular droplet can be calculated as $R = l_d/\sqrt{\pi} \approx 0.338\,\text{m}$ ($\pi R^2 = l_d^2$ with incompressible hypothesis [186, 192, 195, 197]). Consequently, the pressure drop between the two phases is calculated according to Laplace's law as [208]

$$\Delta p = \beta\kappa = \frac{\beta}{R} \approx 2.954\,\text{Pa} \tag{6.71}$$

where the inner fluid has a higher pressure to balance the surface tension force. The pressure profile along the horizontal line $y = 0$ with different resolutions is provided in Fig. 6-14(a). The time history of the average pressure difference $\Delta P = \bar{P}_A - \bar{P}_B$ is provided in Fig. 6-14 (b) where $\bar{P}_A$ and $\bar{P}_B$ represent the average pressure of the fluid particles for fluid A and B which are not in the interface region, respectively. The pressure distribution is provided in Fig. 6-14(c). Due to the viscosity force, the kinetic energy of the square droplet will decrease with time increasing, leading to a steady state finally. The time history of the kinetic energy and the velocity distribution at the final stage are provided in Fig. 6-15. With the refinement of the resolution, the magnitude of the kinetic energy decreases at the quasi-equilibrium state, within the 1×10^{-5} level for 80×80 particles. However, it can also be observed from Fig. 6-15 (b) that even for the quasi-equilibrium state, the oscillation of the interface still exists. This oscillation, also can be noted as the spurious current, may be created by the slight variation of curvature because of the discrete nature of numerical approach according to the explanation given in [215]. The L_1 norm [215] defined as $L_1 = \sum_1^{N_{node}} |\mathbf{v}|/N_{node}$ is 3.3×10^{-3}, and L_2 norm [215] defined as $L_2 = \sqrt{\sum_1^{N_{node}} |\mathbf{v}|^2/N_{node}^2}$ is 7.9×10^{-5} at the final time.

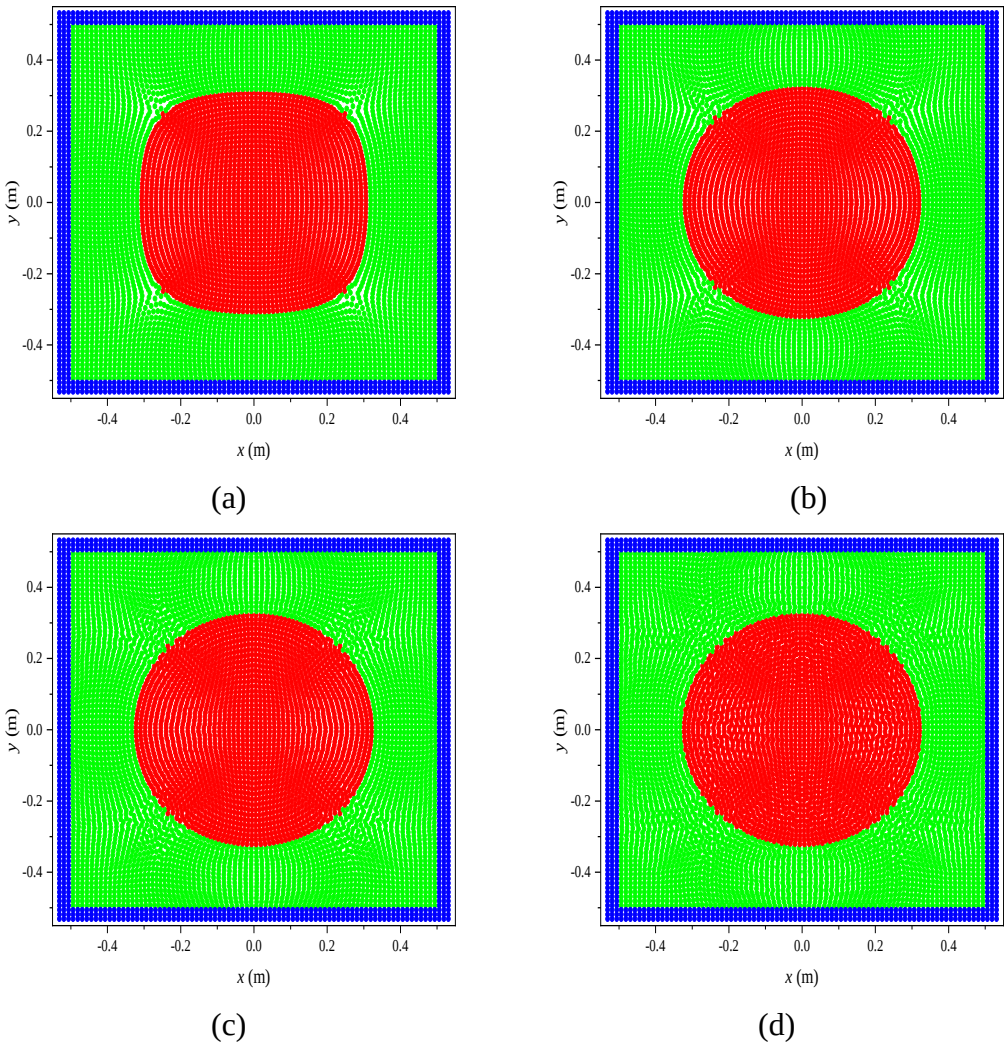

Fig. 6-13 Particle distribution at time (a) $t=0.1\,\mathrm{s}$, (b) $t=0.3\,\mathrm{s}$, (c) $t=0.5\,\mathrm{s}$, and (d) $t=1\,\mathrm{s}$ with 80×80 particles

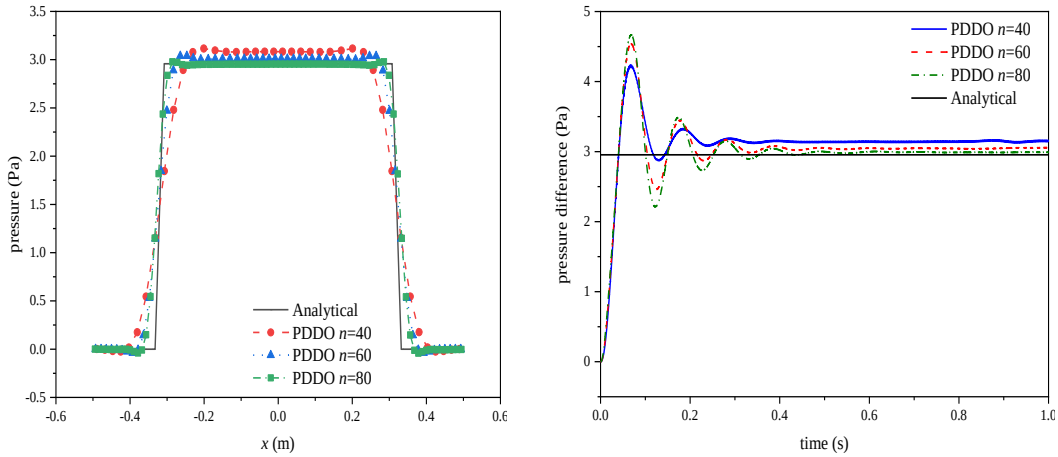

(a) (b)

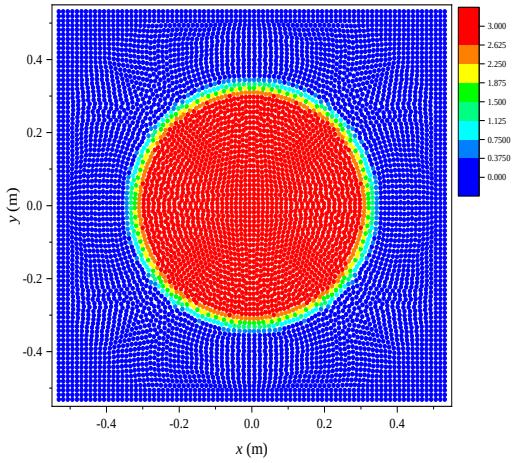

(c)

Fig. 6-14 Pressure profile (a) comparison with analytical solution along $y=0$, (b) time history of the average pressure difference, and (c) pressure distribution with 80×80 particles

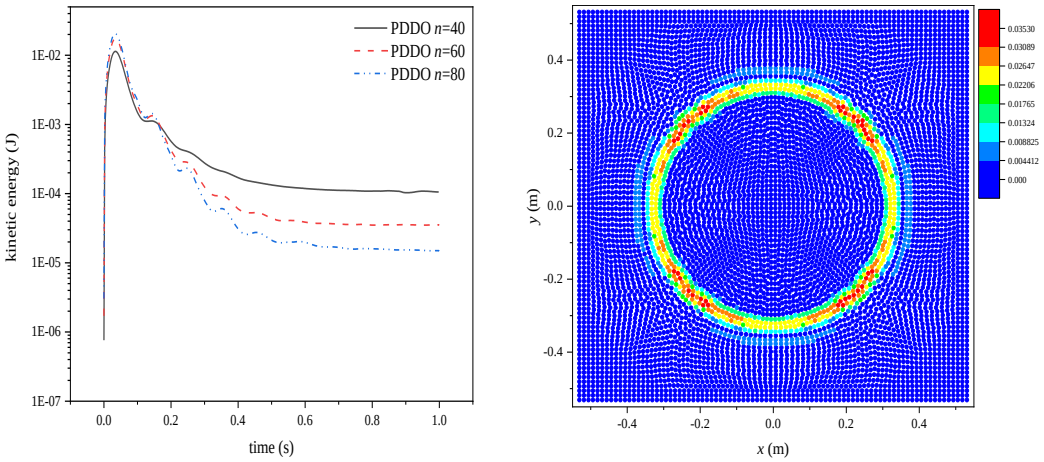

(a) (b)

Fig. 6-15 (a) Time history of the kinetic energy of the inner droplet and (b) velocity distribution at the final state for 80×80 resolution

The orientation and magnitude of the surface tension force obtained by the current PDDO model are provided in Fig. 6-16 (a). Besides, the SPH result [195] is provided in Fig. 6-16 (b) for comparison. It can be observed that all the surface tension forces are pointing to the centre of the inner droplet, being perpendicular to the interface. Because the interparticle index numbers used in this section are always positive, the normal vector always points out to the other fluid phase. In other words, the normal vector of fluid particle *A* points to fluid *B* and the normal vector of fluid particle *B*

points to fluid *A*. However, the curvatures on the two sides of the interface belonging to the two different fluid phases have opposite sign values, one being positive and the other being negative. As a result, the final surface tension forces always point to the centre. Also, the magnitude of the surface tension force decreases from the interface to the edge of the interface region.

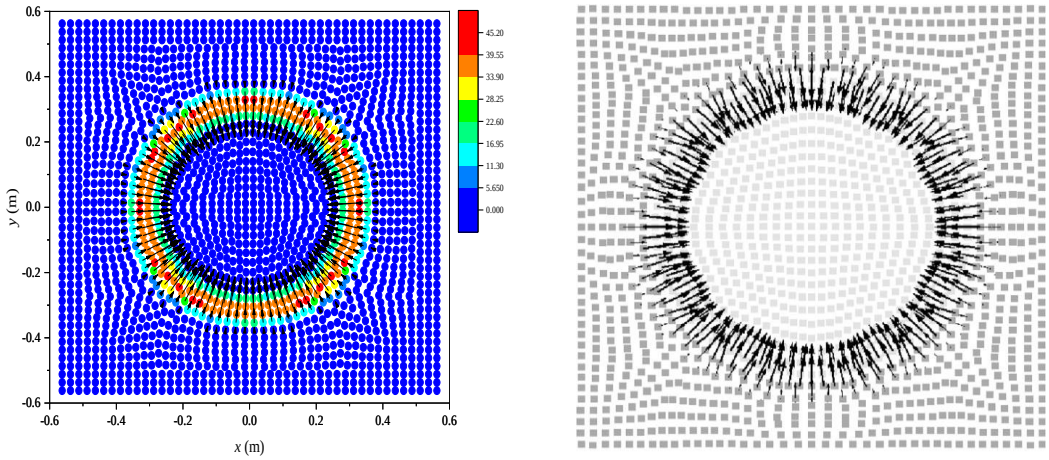

(a) (b)

Fig. 6-16 The direction of the surface tension force and magnitude (a) obtained by PDDO for 40×40 nodes and (b) obtained by SPH 40×40 nodes [195]

Furthermore, two more simulation cases are conducted: case 1 for $R_{ratio}=\mu_B/\mu_A=\rho_B/\rho_A=10$, and case 2 for $R_{ratio}=\mu_B/\mu_A=\rho_B/\rho_A=5$, as shown in Table 7.

Table 7 Density and viscosity values for different cases

Case number	$\rho_A\left(\mathrm{kg/m^3}\right)$	$\rho_B\left(\mathrm{kg/m^3}\right)$	$\mu_A\left(\mathrm{Pa\cdot s}\right)$	$\mu_B\left(\mathrm{Pa\cdot s}\right)$	R_{ratio}
0	1	1	0.2	0.2	1
1	1	5	0.2	1	5
2	1	10	0.2	2	10

The final configurations of the droplet for both cases are provided in Fig. 6-17 (a) and (b). The pressure profiles along $y=0$ for $R_{ratio}=1$, $R_{ratio}=5$, and $R_{ratio}=10$ are provided in Fig. 6-17 (c) for comparison. It is interesting to see that the case of

$R_{ratio}=5$ has the worst accuracy among all these three cases. According to the investigation in [195], both a smaller viscosity coefficient ratio and a larger density ratio can give less accurate results. In the current study, the accuracy of case 2 which has a relatively smaller viscosity coefficient ratio and a smaller density ratio is less than the one of case 1 which has a relatively larger viscosity coefficient ratio and a larger density ratio. Therefore, in the present work, the ratio of the viscosity coefficient has a larger effect than the ratio of density on the accuracy of the simulation results.

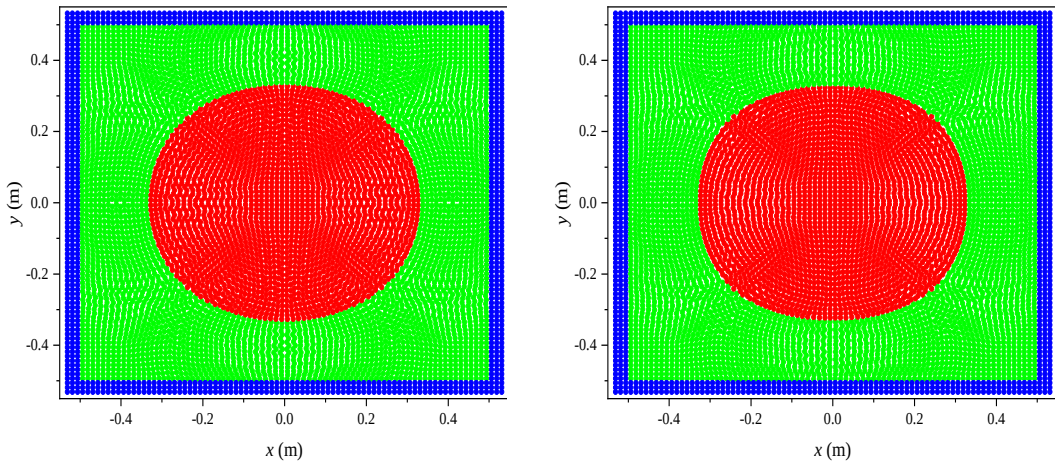

(a) (b)

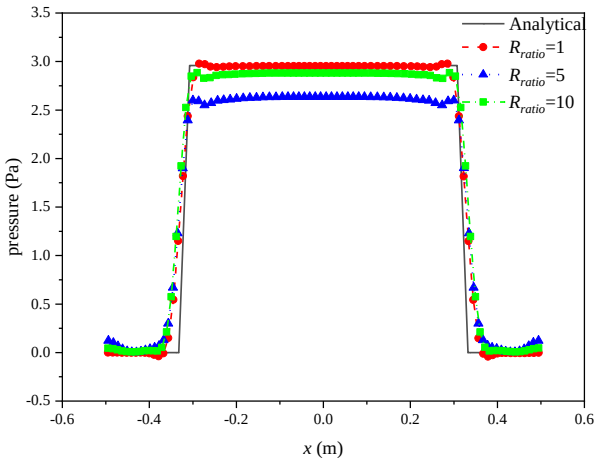

(c)

Fig. 6-17 Particle distributions at time $t=1\,\mathrm{s}$ with 80×80 particles for (a) case 1, and (b) case 2. (c) pressure profiles comparison

6.4. Summary

In this chapter, a multi-phase fluid laminar flow model is developed by using the peridynamic differential operator. The surface tension force originally from the Continuum Surface Force model is converted into a PDDO expression. The developed model is applied to solve the multi-phase fluid flow problems, e.g. two-phase hydrostatic problem, two-phase Poiseuille flow, 2D droplet deformation. The good agreements between the PDDO results and the existing results demonstrate the capability of the present model for the multi-phase fluid flow simulations.

7. Fluid-Structure Interaction Numerical Simulation

7.1. Introduction

Fluid-structure interaction (FSI) is a class of problems with mutual dependence between the fluid and structural mechanics parts [216]. The FSI phenomenon widely exists in the engineering field, e.g. liquid sloshing [120], slamming [217], etc.. Therefore, it has been extensively and intensively studied for years.

There are mainly two types of simulation methods, i.e. simultaneous methods and partitioned methods. When the coupling between the fluid and structure is strong, or the fluid motion and structure deformation are comparable, it is convenient to employ a simultaneous solution [218]. One popular method is the Arbitrary-Lagrangian-Eulerian (ALE) formulation for coupling the fluid described by Eulerian formulation and the structure described by Lagrangian formulation [219]. The immersed boundary method (IBM) couples the Eulerian fluid and the Lagrangian structure via interpolation in a bi-directional way [220]. Another promising solution falls into the category of fully Lagrangian description in which both the fluid and the structure are formulated in Lagrangian form. Taking the smoothing particle hydrodynamics (SPH) as an example, Antoci et al. [218] develop a coupled SPH-SPH model to simulate the behaviour of fluid and elastic structure by their SPH form governing equations. The SPH-SPH model predicted results are compared with the ones obtained by the experiment, achieving a good agreement. A multiphase SPH model has been employed by Ruben Paredes and Len Imas [221] to solve the fluid-structure interaction problems. The simulations of the sloshing problems and the elastic gate problem are conducted to verify their pure SPH model. Furthermore, a complex fluid-structure dam-breaking problem is studied in [222] with using the multi-phase SPH method coupled with Adaptive-Particle-Refinement (APR) technique. An enhanced incompressible SPH-SPH coupled method is proposed by Khayyer et al. [223] to simulate the incompressible fluid and elastic structure interactions. The divergence-free property of the fluid velocity field is guaranteed by solving the Poisson Pressure Equation (PPE). Besides, a dynamic stabilizer technique is employed [224] to overcome the tension instability issues. The state-of-art development of the SPH-SPH or SPH coupled with

other methods methodology for FSI problems is reviewed by Moubiu Liu and Zhiliang Zhang [225]. For example, the discrete element method (DEM) can be coupled with the SPH method for solving the FSI problems, where DEM is used for the structure modelling while SPH is adopted for the fluid modelling [226]. In the study of Wu et al. [226], the free surface flow, as well as the structural failure, is considered. Besides the application of SPH on FSI problems, the moving particle semi-implicit (MPS) method has also been utilized for the FSI problems. A multi-resolution MPS model is developed by Khayyer et al. [227] for the incompressible fluid-elastic structure interaction simulations. In their study, the problem of sloshing with an elastic baffle is simulated. The good agreement between the numerical results and the experiment results validates the accuracy of their model. Furthermore, an MPS model considering a dynamic equation of angular momentum conservation is proposed in [228] for FSI problems corresponding to the incompressible fluid flow and elastic structures.

Since the PD theory is initially proposed for solid mechanics, the published PD models for FSI problems are rare. A coupled PD-IBM methodology is developed by Barba et al. [229] for hydraulic fracture problems. The BB-PD theory is adopted for structure behaviour simulation and the open-source CaNS parallel code is utilized for fluid modelling [229]. Liu et al. [212] develop a PD model for FSI problems to simulate ice-water interactions. The BB-PD is also used for ice modelling with including the ice breakage [230-232]. The updated Lagrangian particle hydrodynamics (ULPH) proposed by Tu et al. [132] is utilized to simulate the fluid flow. Being different from the aforementioned PD models, this chapter discusses an FSI model where the elastic structure is simulated by OSB-PD and the fluid is modelled by PDDO. As a result, the elastic structure can have any material properties. At the same time, the integration of the non-local fluid governing equations, i.e. Navier-Stokes equations, can be only performed once since the PDDO can achieve higher-order derivatives converting [8].

7.2. Numerical implementations for fluid-structure simulation

The algorithm of the interaction implementation between the fluid and the elastic structure is a key issue in FSI problems. As illustrated in Fig. 7-1, two different sets of

PD particles are used to represent the structure and the fluid, i.e. green particles for structure and blue particles for fluid. For the particles near the fluid-structure interface, Γ, there are four kinds of PD interactions between them: structure-structure interaction (green colour), fluid-fluid interaction (blue colour), structure (central)-fluid (family member) interaction (red colour), and fluid (central)-structure (family member) interaction (yellow colour).

For the first two kinds of interactions (the single-phase interactions, the green one and blue one), the OSB-PD model and PDDO model can be utilized to simulate the solid and fluid, which is presented in Section 7.2.1. The numerical implementation for the other two kinds of PD interactions (the red one and the yellow one) is presented in Section 7.2.3.

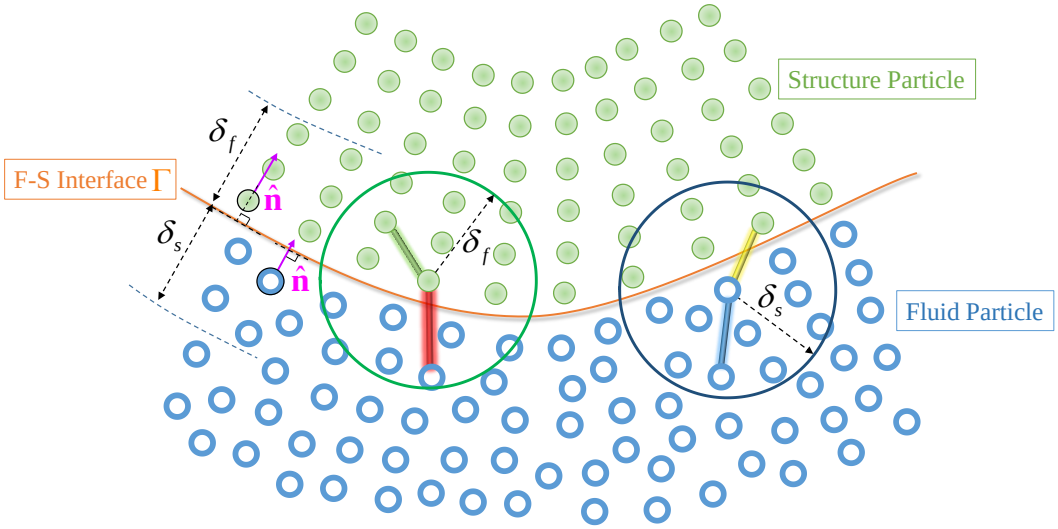

Fig. 7-1 Fluid-Structure interface illustration

7.2.1. Discretised form of PD governing equations

The governing equations are expressed by using the discretized forms.

Equation of motion for mechanical deformations:

$$\ddot{\mathbf{u}}_{s,i}^{n+1}=\frac{1}{\rho_s}\sum_{j=1}^{N_{s,i}}\left(\frac{2\delta_s ad\Lambda_{ij}}{\left|\mathbf{x}_{s,j}-\mathbf{x}_{s,i}\right|}\left(\theta_{s,i}+\theta_{s,j}\right)+4\delta_s bs_{ij}\right)\frac{\mathbf{y}_{s,j}-\mathbf{y}_{s,i}}{\left|\mathbf{y}_{s,j}-\mathbf{y}_{s,i}\right|}V_{s,j}+\frac{1}{\rho_s}\mathbf{b}_{s,i}^{n+1} \quad (7.1)$$

where $\ddot{\mathbf{u}}_{s,i}^{n+1}$ is the acceleration of solid particle i at time step $n+1$. $N_{s,i}$ is the total number of the family members belonging to solid of solid particle i. $\mathbf{x}_{s,i}$ and $\mathbf{x}_{s,j}$ are the initial positions of solid particle i and j. Correspondingly, $\mathbf{y}_{s,i}$ and $\mathbf{y}_{s,j}$ are the current positions of particle i and j. $\theta_{s,i}$ and $\theta_{s,j}$ are the dilatations of particle i and j, provided in Eq.(2.10). s_{ij} is the bond stretch between particle i and j, provided in Eq.(2.7). $V_{s,j}$ is the volume of the solid particle j. The subscript $\left(_s\right)$ denotes the solid particles. The superscript $\left(^{n+1}\right)$ denotes the updated configuration.

Navier-Stokes equations for fluid:

$$\rho_{f,i}^{n+1}=\rho_{f,i}^{n}-\rho_{f,i}^{n}\Delta t\sum_{j=1}^{N_{f,i}}\left[\left(\mathbf{v}_{f,j}^{n}-\mathbf{v}_{f,i}^{n}\right)\cdot\mathbf{g}_1\left(\left|\mathbf{y}_{f,j}^{n}-\mathbf{y}_{f,i}^{n}\right|\right)\right]V_{f,j}^{n} \tag{7.2}$$

$$\begin{aligned}\ddot{\mathbf{u}}_{f,i}^{n+1}=&\frac{1}{\rho_{f,i}^{n+1}}\left(\mu_f\sum_{j=1}^{N_{f,i}}\left(\mathbf{v}_{f,j}^{n}-\mathbf{v}_{f,i}^{n}\right)\mathrm{Tr}\left(\mathbf{g}_2\left(\left|\mathbf{y}_{f,j}^{n}-\mathbf{y}_{f,i}^{n}\right|\right)\right)V_{f,j}^{n}\right)\\&-\frac{1}{\rho_{f,i}^{n+1}}\left(\sum_{j=1}^{N_{f,i}}\left(P_{f,j}^{n}-P_{f,i}^{n}\right)\mathbf{g}_1\left(\left|\mathbf{y}_{f,j}^{n}-\mathbf{y}_{f,i}^{n}\right|\right)V_{f,j}^{n}\right)+\frac{1}{\rho_{f,i}^{n+1}}\mathbf{b}_{f,i}^{n+1}\end{aligned} \tag{7.3}$$

The subscript $\left(_f\right)$ denotes that the particles belong to fluids. $\rho_{f,i}^{n+1}$ and $\ddot{\mathbf{u}}_{f,i}^{n+1}$ represent the density and acceleration of fluid particle i in the updated configuration $t=t_{n+1}$. $N_{f,i}$ is the total number of the family members belonging to the fluid system of particle i. $V_{f,j}^{n}$ is the volume of fluid particle j in the current configuration.

The velocity, displacement, and position for solid and fluid particles are updated by the velocity Verlet algorithm (2nd order) [200] as

$$\mathbf{v}_{s,i}^{n+1}=\mathbf{v}_{s,i}^{n}+\frac{1}{2}\left(\ddot{\mathbf{u}}_{s,i}^{n+1}+\ddot{\mathbf{u}}_{s,i}^{n}\right)\Delta t\,,\ \mathbf{v}_{f,i}^{n+1}=\mathbf{v}_{f,i}^{n}+\frac{1}{2}\left(\ddot{\mathbf{u}}_{f,i}^{n+1}+\ddot{\mathbf{u}}_{f,i}^{n}\right)\Delta t \tag{7.4}$$

$$\mathbf{u}_{s,i}^{n+1}=\mathbf{u}_{s,i}^{n}+\mathbf{v}_{s,i}^{n+1}\Delta t+\frac{1}{2}\ddot{\mathbf{u}}_{s,i}^{n}\Delta t\ ,\mathbf{u}_{f,i}^{n+1}=\mathbf{u}_{f,i}^{n}+\mathbf{v}_{f,i}^{n}\Delta t+\frac{1}{2}\ddot{\mathbf{u}}_{f,i}^{n}\Delta t^2 \tag{7.5}$$

$$\mathbf{y}_{s,i}^{n+1} = \mathbf{x}_{s,i} + \mathbf{u}_{s,i}^{n+1},\ \mathbf{y}_{f,i}^{n+1} = \mathbf{x}_{f,i} + \mathbf{u}_{f,i}^{n+1} \tag{7.6}$$

In the present study, a uniform initial node spacing is adopted for both fluid and solid. Hence the horizon size for fluid δ_f and the horizon size for solid δ_s equal to each other, i.e. $\delta_f = \delta_s = \delta$.

7.2.2. Numerical treatment for the fluid model

7.2.2.1 Free surface detection

Similar to MPS scheme number density is calculated for detecting the free surface as proposed by Koshizuka et al. [233]. The number density can reflect the number of family members where a larger one represents more family members and a smaller represents fewer family members. The initial and current number density can reflect the level of the number of family members in the initial and current configuration, respectively. The initial and current number densities of particle i are calculated as [233]

$$d^{(0)}(i) = \sum_{j=1}^{N_i} \left(e^{-\left(|\mathbf{x}_j - \mathbf{x}_i|/h\right)^2} - e^{-9} \right) / \left(\pi h^2 \left(1 - 10e^{-9}\right) \right) \tag{7.7}$$

$$d^{(n)}(i) = \sum_{j=1}^{N_i} \left(e^{-\left(|\mathbf{y}_j - \mathbf{y}_i|/h\right)^2} - e^{-9} \right) / \left(\pi h^2 \left(1 - 10e^{-9}\right) \right) \tag{7.8}$$

where h is the smooth length defined as $h = 1.2\Delta x$ [139]. Particle i will become a free-surface fluid particle, and its pressure will be forced as $P_i = 0$, if the following criterion is satisfied [233]

$$d^{(n)}(i) < 0.9 d^{(0)}(i) \tag{7.9}$$

7.2.2.2 Fluid-structure interface collision model

The fluid-structure interface collision model is applied for preventing material points to enter the solid structure [234]. The solid wall is simulated as a reflective boundary condition.

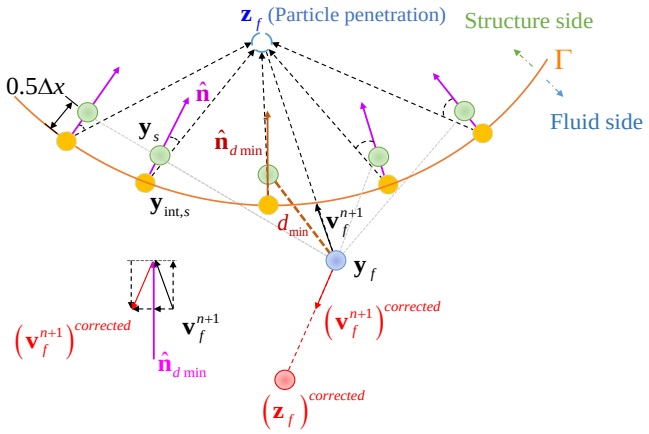

Fig. 7-2 Collision model for fluid-structure interface condition

In Fig. 7-2, the fluid particle at $\mathbf{y}_f$ is located within the fluid-structure interface region (defined in Fig. 7-1). The solid particles within the interface-nearest layer (these solid particles have the shortest distance to the interface) are considered here as the family members of fluid particle at $\mathbf{y}_f$, i.e. the solid particle at $\mathbf{y}_s$ belongs to the family members of fluid particle at $\mathbf{y}_f$.

A fictitious particle at $\mathbf{y}_{\text{int},s} = \mathbf{y}_s - 0.5\Delta x\hat{\mathbf{n}}(\mathbf{y}_s)$ is defined as the corresponding interface particle of solid particle at $\mathbf{y}_s$, shown as the yellow circle in Fig. 7-2. The position $\mathbf{y}_{\text{int},s}$ of this fictitious particle is assumed to be on the fluid-structure interface, as shown in Fig. 7-2.

Then the collision model is applied in two steps:

Step 1) The first step is to check if the fluid particle at $\mathbf{y}_f$ penetrates the interface Γ.

The new position of the fluid particle at $\mathbf{y}_f$ is updated according to Eq.(7.6). The new location of the fluid particle is denoted as $\mathbf{z}_f$. Then for all the solid family member particles considered in the collision model, e.g. solid particle at $\mathbf{y}_s$, the following criteria is checked

$$\hat{\mathbf{n}}(\mathbf{y}_s)\cdot(\mathbf{z}_f-\mathbf{y}_{\text{int},s})>0 \tag{7.10}$$

If the criterion in Eq.(7.10) is satisfied, it is concluded that the particle at $\mathbf{z}_f$ penetrates the solid (shown as dashed blue circle in Fig. 7-2).

Step 2) If the fluid particle penetrates the structure, its velocity should be corrected accordingly.

First, find the solid family member obtaining the shortest relative distance with fluid particle at $\mathbf{y}_f$ and its unit normal as

$$d_{\min}=\min\left(\left|\mathbf{y}_s-\mathbf{y}_f\right|\right),\ \mathbf{y}_s\in H_{\mathbf{y}_f}^{n+1} \tag{7.11a}$$

$$\hat{\mathbf{n}}_{d\min}=\hat{\mathbf{n}}(\mathbf{y}_{s,d\min}) \tag{7.11b}$$

Subsequently, the velocity of the fluid particle at $\mathbf{y}_f$ is corrected as

$$\left(\mathbf{v}_f^{n+1}\right)^{corrected}=\mathbf{v}_f^{n+1}-2\left(\mathbf{v}_f^{n+1}\cdot\hat{\mathbf{n}}_{d\min}\right)\hat{\mathbf{n}}_{d\min},\ \text{if}\ \mathbf{v}_f^{n+1}\cdot\hat{\mathbf{n}}_{d\min}>0 \tag{7.12}$$

Here $\mathbf{v}_f^{n+1}$ is the velocity predicted by Eq.(7.4). The updated corrected displacement and position become

$$\left(\mathbf{u}_{f,i}^{n+1}\right)^{corrected}=\mathbf{u}_{f,i}^{n}+\left(\mathbf{v}_f^{n+1}\right)^{corrected}\Delta t+\frac{1}{2}\ddot{\mathbf{u}}_f^n\Delta t^2 \tag{7.13}$$

$$\left(\mathbf{z}_f\right)^{corrected}=\mathbf{x}_f+\left(\mathbf{u}_f^{n+1}\right)^{corrected} \tag{7.14}$$

7.2.3. Boundary and FSI treatment

For flow simulation, the elastic structure serves as a moving boundary condition with the deformed configuration. The solid particle at $\mathbf{y}_s$ is treated as the boundary particle of fluid $\mathbf{y}_{f,boundary}$ which occupies the same position as $\mathbf{y}_s$.

On the other hand, the fluid effect on the structural deformation is considered via the fluid pressure field acting as an external force [218]. The details are provided in the following content in this section.

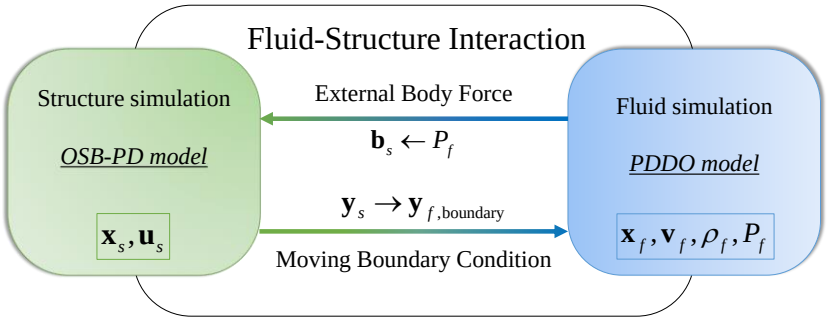

Fig. 7-3 FSI methodology scheme

7.2.3.1 Interface definition and its normal

In dealing with the interaction between the elastic structure and fluid particles, the definition of the interface domain and its normal is one of the key issues. Since the PD is a non-local theory, the interface region between the fluid and the elastic structure has a fixed thickness, being twice of the horizon size 2δ, as shown in Fig. 7-1. Because of the movement of the structure and the fluid particles, the interface, as well as its normal direction $\hat{\mathbf{n}}$ (see Fig. 7-1), changes with time integration. The colour function method which is adopted in the volume of fraction (VOF) [179] method is employed in the present study. The structure and the fluid particles are identified by a predefined colour function as

$$c(\mathbf{x}_i) = \begin{cases} 1, \text{ for particle } \mathbf{x} \text{ belonging to fluid, } \mathbf{x}_i = \mathbf{x}_f \\ 2, \text{ for particle } \mathbf{x} \text{ belonging to solid, } \mathbf{x}_i = \mathbf{x}_s \end{cases} \tag{7.15}$$

The colour function in Eq.(7.15) indicates if a particle belongs to the fluid or the structure. However, during the simulation process, particle $\mathbf{x}_i$ may move to its new position. Therefore, it is necessary to find out if the particle $\mathbf{x}_i$ is close to the interface region or not. This can be done by calculating the gradient of the colour function at point $\mathbf{x}_i$ by using the colour function values of its neighbours through PDDO [18] as

$$\mathbf{c}_g\left(\mathbf{x}_i\right)=\nabla c\left(\mathbf{x}_i\right)=\sum_{j=1}^{N_i}\left(c\left(\mathbf{x}_j\right)-c\left(\mathbf{x}_i\right)\right)\mathbf{g}_1\left(\left|\mathbf{y}_j-\mathbf{y}_i\right|\right)V_j \tag{7.16}$$

It can be inferred from Eq.(7.16) that if the neighbourhood of point $\mathbf{x}_i$ is fully located within the single-phase region, i.e. either the structure domain or the fluid domain, the value of the normal direction vector becomes zero $\mathbf{c}_g\left(\mathbf{x}_i\right)=0$. On the contrary, if the particle is in the interface region, the magnitude of its normal direction vector will not be zero, $\mathbf{c}_g\left(\mathbf{x}_i\right)\neq 0$. This can be used to find out if the material point $\mathbf{x}_i$ is at the interface region or not. The unit normal direction of the interface can also be calculated by using the gradient of colour function as

$$\hat{\mathbf{n}}\left(\mathbf{x}_i\right)=\frac{\mathbf{c}_g\left(\mathbf{x}_i\right)}{\left|\mathbf{c}_g\left(\mathbf{x}_i\right)\right|} \tag{7.17}$$

Being similar to Chapter 6, the unit normal direction vector $\hat{\mathbf{n}}\left(\mathbf{x}_i\right)$ can be calculated by using PDDO as

$$\hat{\mathbf{n}}\left(\mathbf{x}_i\right)=\begin{cases}\dfrac{\mathbf{c}_g\left(\mathbf{x}_i\right)}{\left|\mathbf{c}_g\left(\mathbf{x}_i\right)\right|}=\dfrac{\sum_{j=1}^{N_i}\left(c\left(\mathbf{x}_j\right)-c\left(\mathbf{x}_i\right)\right)\mathbf{g}_1\left(\left|\mathbf{y}_j-\mathbf{y}_i\right|\right)V_j}{\left|\sum_{j=1}^{N_i}\left(c\left(\mathbf{x}_j\right)-c\left(\mathbf{x}_i\right)\right)\mathbf{g}_1\left(\left|\mathbf{y}_j-\mathbf{y}_i\right|\right)V_j\right|}, \text{ if } \mathbb{N}\left(\mathbf{x}_i\right)=1 \\ 0, \text{ if } \mathbb{N}\left(\mathbf{x}_i\right)=0\end{cases} \tag{7.18}$$

where

$$\mathbb{N}\left(\mathbf{x}_i\right)=\begin{cases}1, \text{if } \left|\mathbf{c}_g\left(\mathbf{x}_i\right)\right|>\varepsilon \\ 0, \text{otherwise}\end{cases} \tag{7.19}$$

Being same as Eq. (6.24), a function $\mathbb{N}(\mathbf{x})$ is defined to indicate if the unit normal vector is zero. A cut-off value $\varepsilon=1.0\times10^{-2}/\Delta x$ [198] is set for the normal vector, smaller than which the unit normal becomes zero. Note that in Eq. (7.18) the term

$\left(c\left(\mathbf{x}_j\right)-c\left(\mathbf{x}_i\right)\right)$ can be positive or negative which leads to the unit normal direction always pointing from the fluid phase to the structure phase.

7.2.3.2 Effect of fluid flow on structure

The fluid effect on the structure deformation is simulated in terms of volumetric external body force. The similar approach developed by Antoci et al. [218] is adopted.

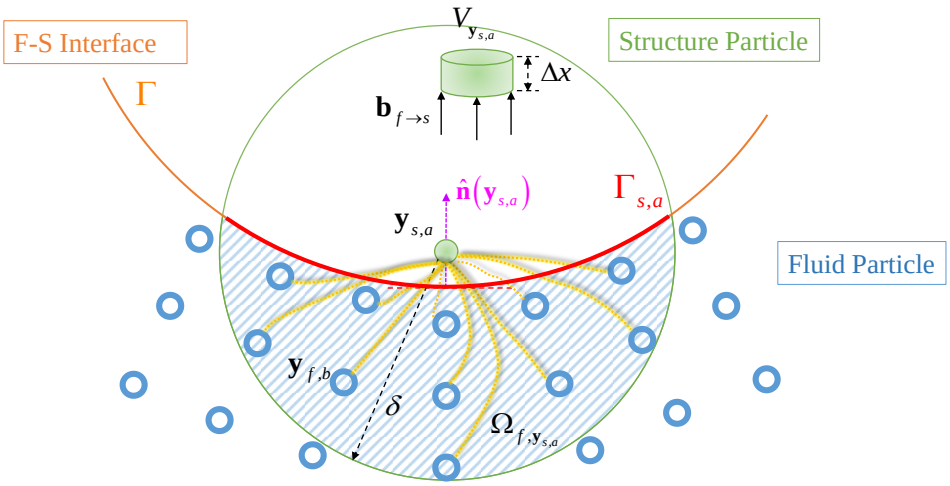

Fig. 7-4 PD Interactions of the interface structure particle at $\mathbf{y}_{s,a}$

The fluid pressure acting on solid particle at $\mathbf{y}_{s,a}$ can be approximated by the pressure of the fluid particles as

$$P_{s,a}=\frac{\sum_{b\in\Omega_{f,\mathbf{y}_{s,a}}}\frac{m_{f,b}}{\rho_{f,b}}P_{f,b}w_0\left(\left|\mathbf{y}_{f,b}-\mathbf{y}_{s,a}\right|\right)}{\sum_{b\in\Omega_{f,\mathbf{y}_{s,a}}}\frac{m_{f,b}}{\rho_{f,b}}w_0\left(\left|\mathbf{y}_{f,b}-\mathbf{y}_{s,a}\right|\right)} \tag{7.20}$$

where $\Omega_{f,\mathbf{y}_{s,a}}$ represents the interaction domain of solid particle at $\mathbf{y}_{s,a}$ within the fluid domain as shown in Fig. 7-4, and w_0 is the improved Gaussian weighted function. $P_{f,b}$ is the pressure, $m_{f,b}$ is the mass and $\rho_{f,b}$ is the density of fluid particle at $\mathbf{y}_{f,b}$. Note that particle at $\mathbf{y}_{f,b}$ belongs to the family members of the point at $\mathbf{x}_{s,a}$ as demonstrated in Fig. 7-4. The mass of the fluid particle, $m_{f,b}$, is calculated by using

the initial values of density and volume. It's assumed constant during the time integration as

$$m_{f,b} = \left(\rho_{f,b} V_{f,b}\right)_{t=0} \tag{7.21}$$

As explained by Antoci et al. [218], Eq.(7.20) can also be simplified as

$$P_{s,a} = 2 \sum_{b \in \Omega_{f,\mathbf{y}_{s,a}}} \frac{m_{f,b}}{\rho_{f,b}} P_{f,b} w_0 \left(\left| \mathbf{y}_{f,b} - \mathbf{y}_{s,a} \right| \right) \tag{7.22}$$

which provides a better and more stable solution.

The volumetric force exerted from the fluid particles to the structure particle at $\mathbf{y}_{s,a}$ can be approximated as

$$\mathbf{b}_{f \to s}\left(\mathbf{y}_{s,a}\right) = \frac{P_{s,a}}{\Delta x} \hat{\mathbf{n}}\left(\mathbf{y}_{s,a}\right) \tag{7.23}$$

where $\mathbf{b}_{f \to s}$ is the body force representing the effect of fluid on structural deformation, $\hat{\mathbf{n}}\left(\mathbf{y}_{s,a}\right)$ is the unit normal direction vector, Δx is the uniform initial node spacing (which is assumed same both for fluid and solid). In Eq.(7.23), the external volumetric pressure force is defined in the interface normal direction. The flowchart for the implementation of the fluid to structure effect is provided in Fig. 7-5.

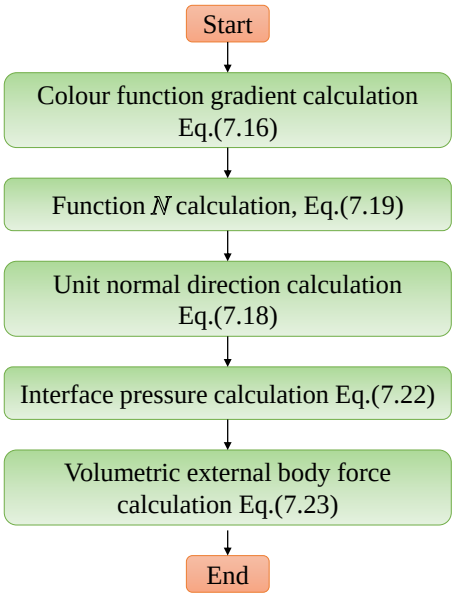

Fig. 7-5 Flowchart for calculating the effect of fluid force on the solid particle

7.2.3.3 Effect of structure on fluid

The solid in the FSI problems can be categorised as a deformable solid or a rigid solid. In the current FSI coupling model, both solid particles, i.e. either deformable solid particles or rigid solid particles, serve as a boundary condition for fluid flow. Therefore, after finding the structural deformations, the solid particles are treated as the fictitious flow boundary particles for flow simulation.

Non-slip velocity boundary condition for fluid: the effect of rigid wall

For the non-slip solid boundary condition, the velocity of the rigid wall particle for flow boundary is calculated as [152]

$$\mathbf{v}_{s,c} = 2\mathbf{v}_{\Gamma} - \left(\sum_{b \in fluid} w_0 \left(\left| \mathbf{y}_{s,c} - \mathbf{y}_{f,b} \right| \right) \mathbf{v}_{f,b} \right) \tag{7.24}$$

where $\mathbf{v}_{s,c}$ denotes the velocity of the rigid particle $\mathbf{y}_{s,c}$, $\mathbf{v}_{\Gamma}$ denotes the prescribed solid wall velocity. $\mathbf{v}_{f,b}$ is the fluid velocity at $\mathbf{y}_{f,b}$. The second term on the right-hand side of Eq.(7.24) is the weighted fluid particle velocity summation. The weighted function is constructed based on the current configuration.

slip velocity boundary condition for fluid: the effect of rigid wall

For the slip boundary condition, the velocity of the rigid particle for flow boundary can be set as

$$\mathbf{v}_{s,c} = \mathbf{v}_{\Gamma} \tag{7.25}$$

Slip and non-slip velocity boundary condition for fluid: the effect of deformable structure

The velocity of the elastic structural particle $\mathbf{y}_{s,a}$ for flow boundary is set as

$$\mathbf{v}_{s,a} = \mathbf{v}_{s,a}^{n} \tag{7.26}$$

where $\mathbf{v}_{s,a}^{n}$ is obtained from the structural model.

pressure boundary condition for fluid

The pressure of the solid particles acting on the fluid can be calculated as [152]

$$P_{s,a} = \frac{\sum_{b\in fluid} \left(P_{f,b} + \left(\mathbf{b}_{f,b} - \rho_{f,b}\ddot{\mathbf{u}}_{s,a}\right)\cdot\left(\mathbf{y}_{f,b} - \mathbf{y}_{s,a}\right)\right) w_0\left(\left|\mathbf{y}_{f,b} - \mathbf{y}_{s,a}\right|\right)\frac{m_{f,b}}{\rho_{f,b}}}{\sum_{b\in fluid} w_0\left(\left|\mathbf{y}_{f,b} - \mathbf{y}_{s,a}\right|\right)\frac{m_{f,b}}{\rho_{f,b}}} \tag{7.27a}$$

$$P_{s,c} = \frac{\sum_{b\in fluid} \left(P_{f,b} + \left(\mathbf{b}_{f,b} - \rho_{f,b}\ddot{\mathbf{u}}_{s,c}\right)\cdot\left(\mathbf{y}_{f,b} - \mathbf{y}_{s,c}\right)\right) w_0\left(\left|\mathbf{y}_{f,b} - \mathbf{y}_{s,c}\right|\right)\frac{m_{f,b}}{\rho_{f,b}}}{\sum_{b\in fluid} w_0\left(\left|\mathbf{y}_{f,b} - \mathbf{y}_{s,c}\right|\right)\frac{m_{f,b}}{\rho_{f,b}}} \tag{7.27b}$$

where $\mathbf{y}_{s,a}$ and $\mathbf{y}_{s,c}$ are the current positions of solid particles at $\mathbf{x}_{s,a}$ and $\mathbf{x}_{s,c}$, respectively. In this chapter, $\ddot{\mathbf{u}}_{s,a}$ is set as zero, which means that the acceleration of the elastic structure particle is not utilized in the fluid boundary simulation part, or the information of the structural acceleration is not transferred to the fluid part.

For the slip boundary condition, the viscous force between the fluid-solid particle interactions is neglected.

7.2.4. Numerical Procedure

The numerical procedure is provided in Fig. 7-6. In the most general fluid-structure interaction problems, there is usually a large difference between the initial configuration and the final configuration. Consequently, both for a structural particle or a fluid particle, the family members of it may change with the time variation. Therefore, for the FSI problems, the configuration updating according to Eq.(7.6) is performed before the family member array re-construction within each time step.

From the figure, it can also be observed that the density of the fluid particle changes, leading to weakly compressible material property. On the contrary, the density of the structure particle keeps constant during the time integration. Furthermore, the densities of the fluid and the structure may differ from each other. As a result, in the MLS density initialization procedure within the fluid part, the density of the structure particle (family member of a fluid particle) is considered to be the same as the fluid one, i.e. using a fake density as a fluid moving boundary particle. It also should be pointed out that the pressures of the deformable particles are fictitious, they are calculated just for the fluid boundary condition. Within the integration, the fluid-structure coupling is achieved by transferring the pressure information from the fluid to the structure as an external body force and transferring the position of the deformed structure particle as a moving boundary condition (shown in dashed arrow).

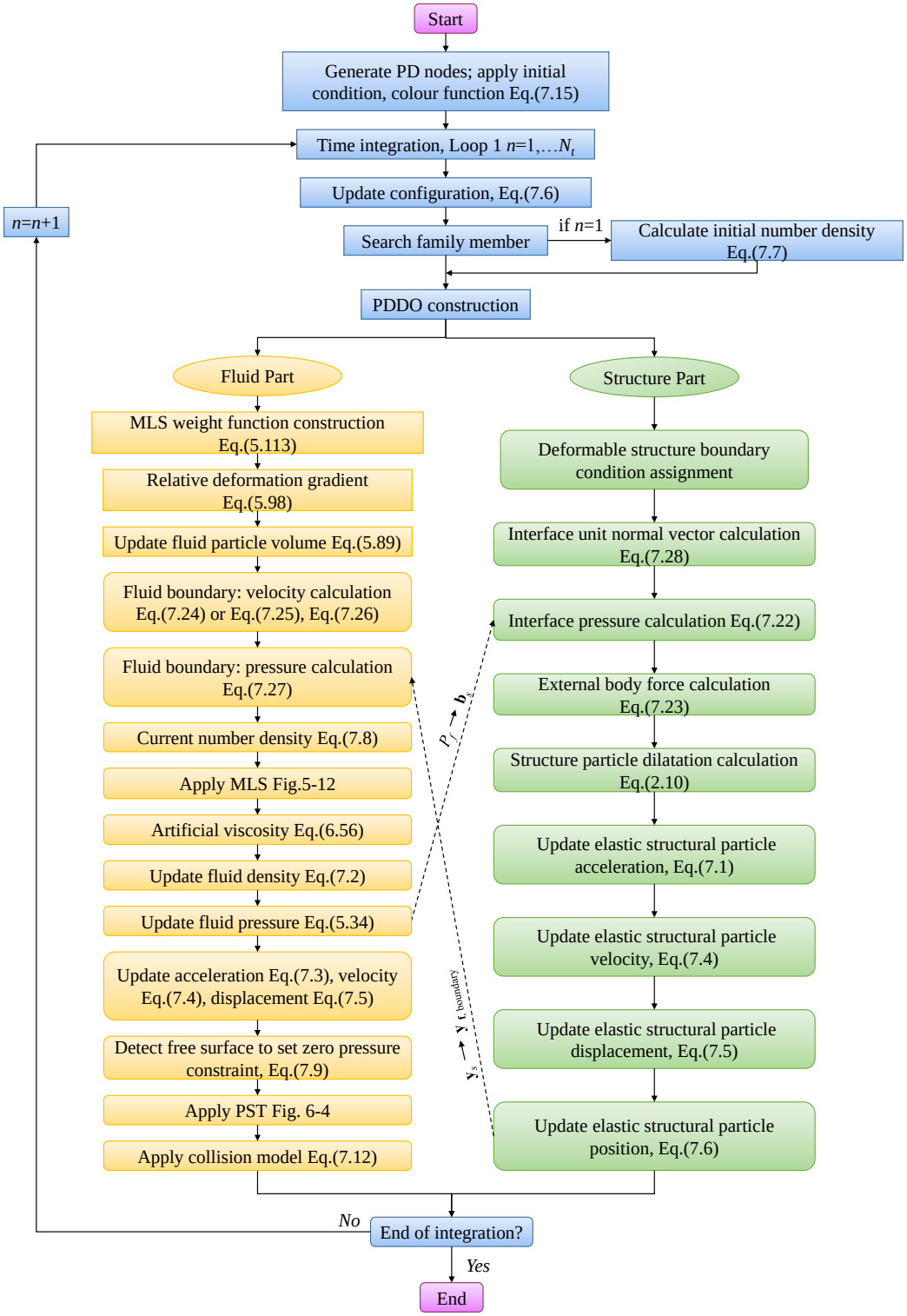

Fig. 7-6 Numerical procedure for FSI problems

7.3. Numerical simulations

7.3.1. Problem description

In this section, a numerical simulation of a dam collapse under an elastic rubber gate [218, 234, 235] is conducted to validate the proposed model. The material properties provided in Table 8 both for the fluid and the rubber are set the same as the ones in [218]. The geometry illustration of the problem is provided in Fig. 7-7. A fluid with dimensions being $L \times H = 0.1\,\mathrm{m} \times 0.14\,\mathrm{m}$ is within an upper open tank. The bottom, left and upper-right sides of the tank are assumed to be rigid. A rubber gate is located vertically adjacent to the right bottom corner of the fluid column with its dimensions being $0.005\,\mathrm{m} \times 0.079\,\mathrm{m}$. The upper end of the rubber is clamped by the right rigid wall and the bottom end is free to move. Then under the gravity effect, the fluid will move, and the rubber gate will open and deform under the fluid pressure effect.

Table 8 Fluid and rubber material properties

Parameters	Value
Fluid density $\rho_f \left(\mathrm{kg/m^3}\right)$	1000
Fluid viscosity $\mu_f \left(\mathrm{Pa \cdot s}\right)$	1×10^{-3}
Fluid material constant γ_f	7
Rubber density $\rho_s \left(\mathrm{kg/m^3}\right)$	1100
Rubber Poisson's ratio ν_s	0.4
Rubber elastic modulus $E \left(\mathrm{MPa}\right)$	12.0

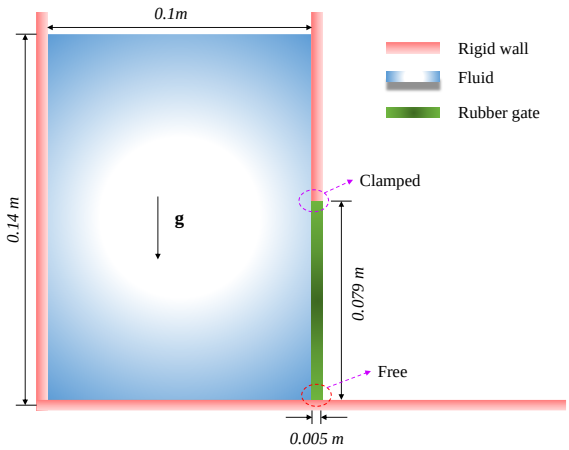

Fig. 7-7 Geometry illustration of dam collapse under a rubber gate

As to the PD discretization, the initial particle spacing is set as $\Delta x = 0.00125$ m (80×112 nodes for fluid). The horizon size is chosen as $\delta = 3.6\Delta x$ to be consistent with one in the MLS scheme. The gravity acceleration is set as $|\mathbf{g}| = 9.8\,\text{m/s}^2$. The maximum velocity of the fluid is estimated as $|\mathbf{v}_{f,\max}| = \sqrt{|\mathbf{g}|H} = 1.17$ m/s, leading to the artificial speed of sound being $c_f = 10|\mathbf{v}_{f,\max}| = 11.7$ m/s. The constant time step size is chosen as $\Delta t = 1\times10^{-5}$ s with the total simulation time being $t = 0.3$ s. The initial damping time is chosen as $t_{damp} = 100\Delta t$. The MLS scheme is performed every 20 time steps [154]. All the numerical treatments explained in Section 7.2.2 are adopted.

7.3.2. Numerical results

The comparison between the experimental results [218], the numerical results obtained by SPH method [218], and the PD predicted results are provided from Fig. 7-8 to Fig. 7-15 for every 0.04s. For the PD simulation results, the particles in blue colour represent the fluid, the pink particles represent the rigid wall, and the green particles represent the rubber gate. It can be inferred from this qualitative comparison that both the fluid motion and the rubber deformation are consistent from these three sources.

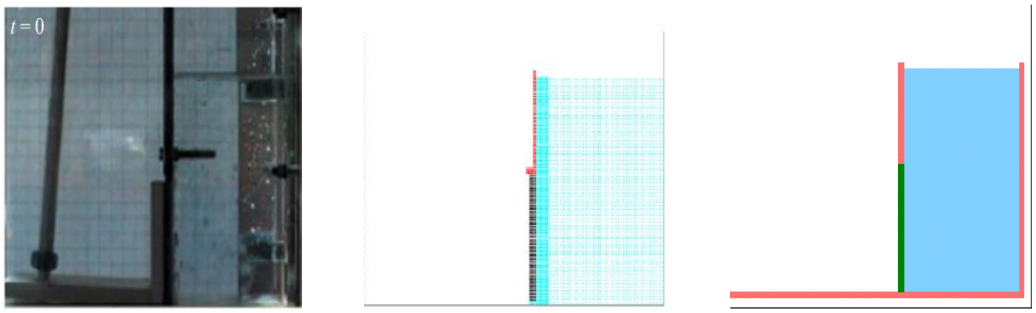

(a) (b) (c)

Fig. 7-8 Comparison between (a) the experiment image [218], (b) SPH results [218], and (c) PD result at t=0

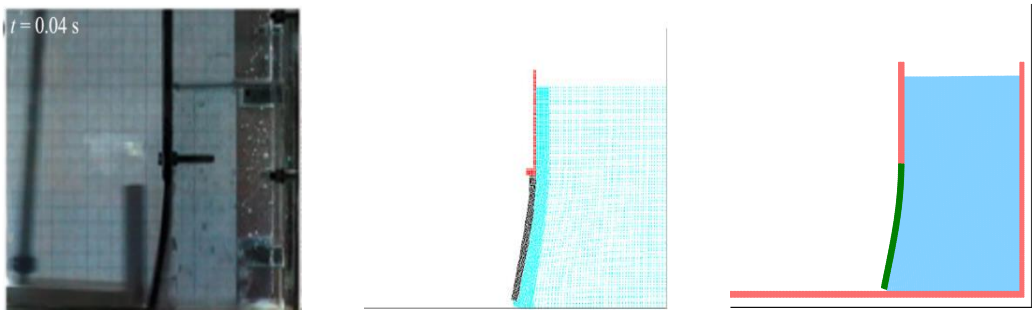

(a) (b) (c)

Fig. 7-9 Comparison between (a) the experiment image [218], (b) SPH results [218], and (c) PD result at t=0.04 s

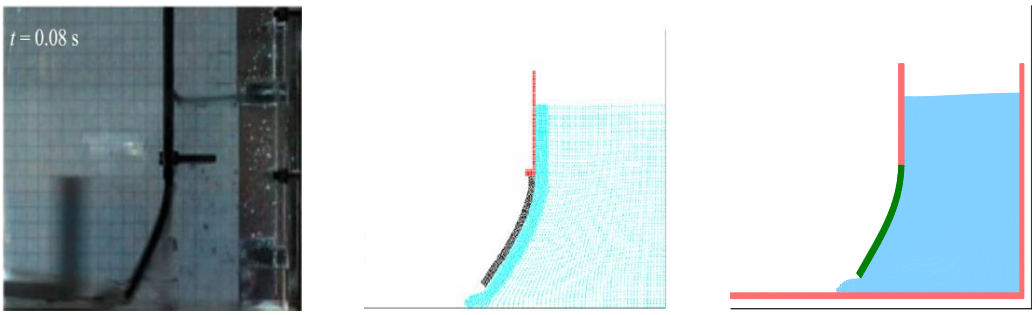

(a) (b) (c)

Fig. 7-10 Comparison between (a) the experiment image [218], (b) SPH results [218], and (c) PD result at t=0.08 s

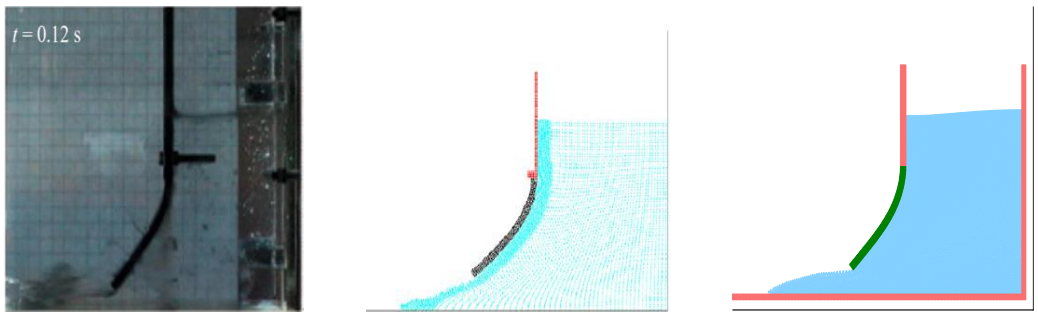

(a) (b) (c)

Fig. 7-11 Comparison between (a) the experiment image [218], (b) SPH results [218], and (c) PD result at t=0.12 s

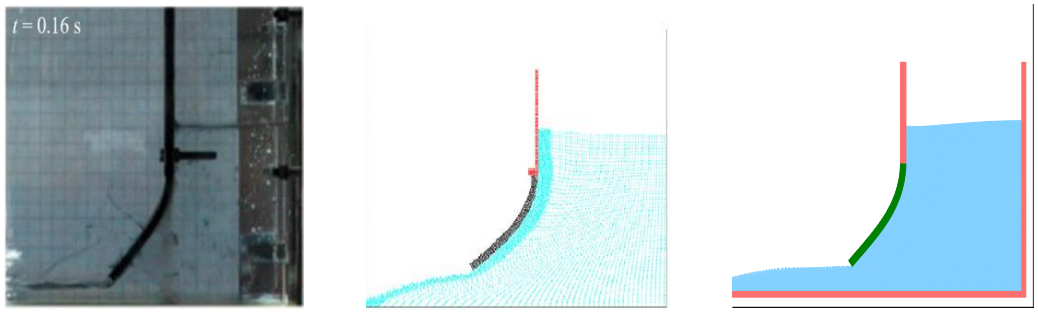

(a) (b) (c)

Fig. 7-12 Comparison between (a) the experiment image [218], (b) SPH results [218], and (c) PD result at t=0.16 s

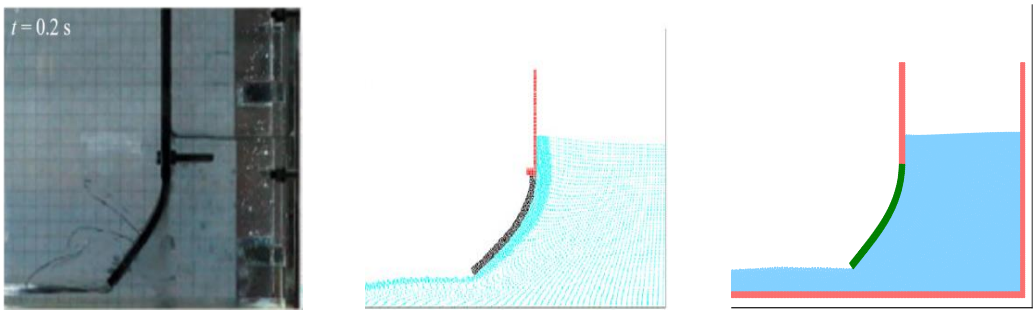

(a) (b) (c)

Fig. 7-13 Comparison between (a) the experiment image [218], (b) SPH results [218], and (c) PD result at t=0.2 s

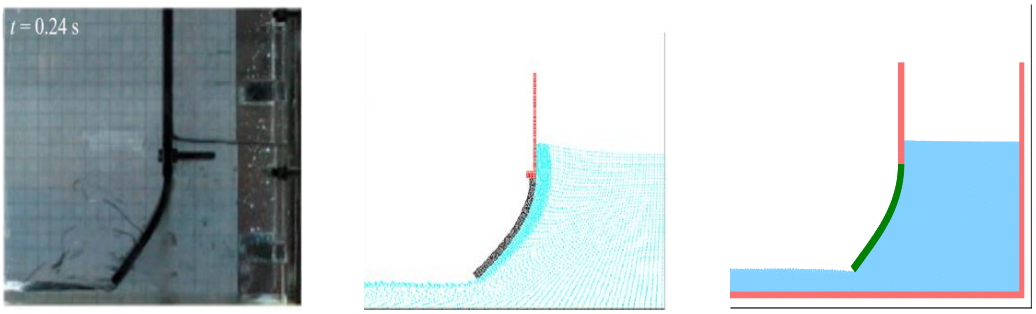

(a) (b) (c)

Fig. 7-14 Comparison between (a) the experiment image [218], (b) SPH results [218], and (c) PD result at t=0.24 s

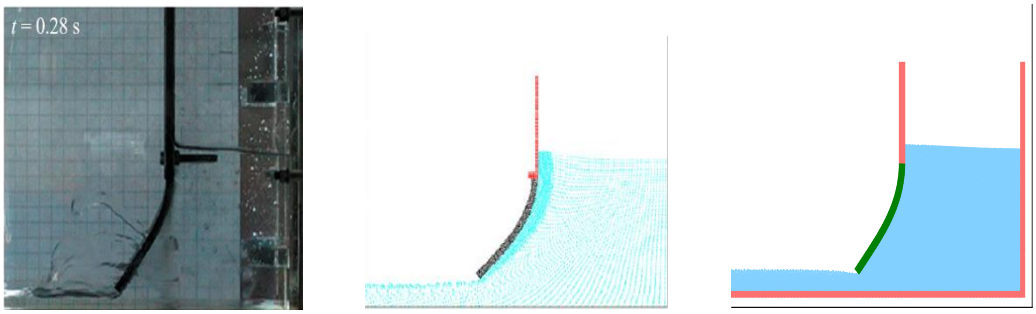

(a) (b) (c)

Fig. 7-15 Comparison between (a) the experiment image [218], (b) SPH results [218], and (c) PD result at t=0.28 s

The rubber gate is initiated to open due to the pressure of the stored water, leading to the water flowing out of the gate. Then with the decreasing of the water level behind the rubber gate, the water pressure acting on the rubber becomes smaller and smaller. Hence, the rubber gate gradually moves back under the resultant force of the gravity force and the water pressure.

A quantitative comparison is also performed to validate the proposed PD model. The simulation results from the following two PD cases are provided: case 1 for time step size $\Delta t = 1\times10^{-5}$ s and PD fluid nodes 80×112; cases 2 for time step size $\Delta t = 2\times10^{-5}$ s and PD fluid nodes 40×56. The time history of the displacement of the end of the plate, the water level near the rigid wall, and the water level with its distance from the rubber gate being $d = 0.05$ m are provided in Fig. 7-16 and Fig. 7-17.

Besides, the data obtained from the experiment and the SPH method [218] are presented for comparison.

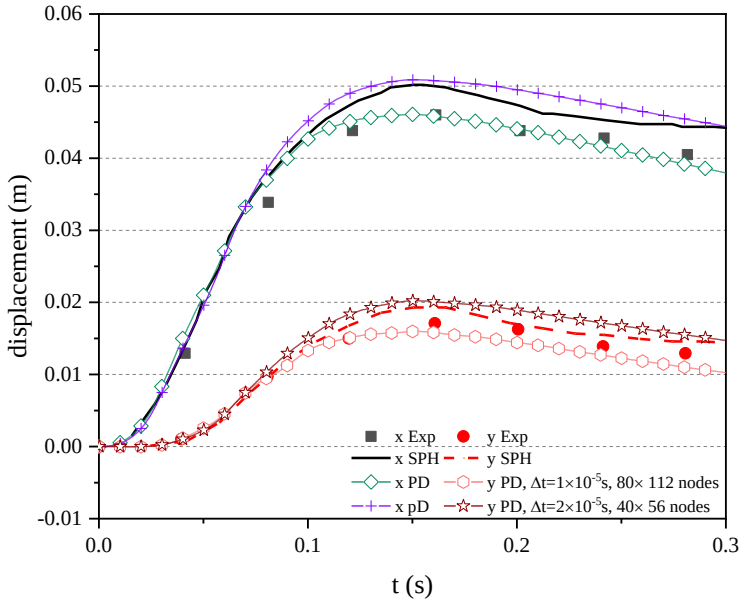

Fig. 7-16 Comparison for horizontal and vertical displacements (m) of the free end of the plate between the experiment results [218], SPH simulation result [218], and PD simulation results

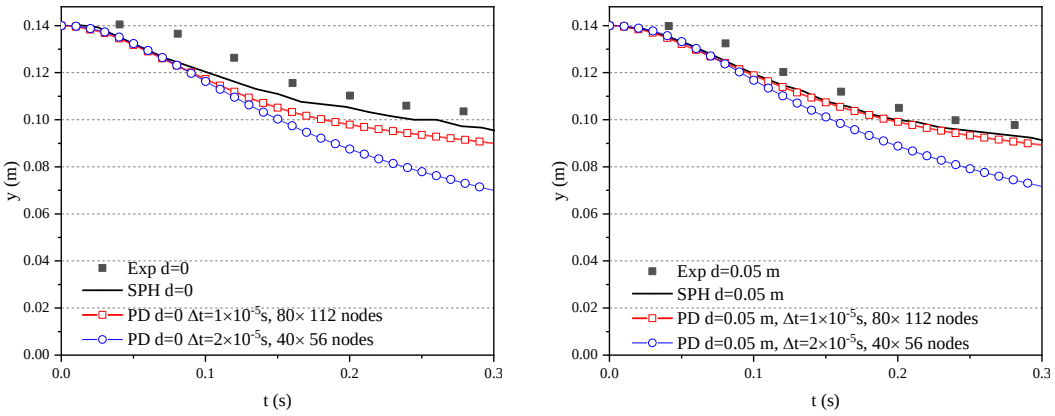

(a) (b)

Fig. 7-17 Water level (m) comparison just behind the gate (a) and 5 cm far from it (b) between the experiment results [218], SPH simulation result [218], and PD simulation results

It can be observed from Fig. 7-16, the displacements of the free end of the rubber gate increase until $t = 0.16\,\mathrm{s}$, which consistent with the observation from the qualitative comparison. Then after this peak point, the displacements both in the horizontal and vertical directions decrease until the end of the simulation, indicating

the moving back of the rubber gate to its initial shape. By analysing the time history of the water levels from the two locations ($d = 0$ and $d = 5\,\text{cm}$), the conclusion can be drawn that the velocity of the fluid volume increasing out of the rubber gate at the end of the simulation becomes much smaller than the one in the early stage. This is due to the smaller opening distance between the rubber gate and the bottom rigid plate compared with the one in the early stage. The quantitative study here agrees well with the previous qualitative study. In conclusion, from the quantitative comparison presented in Fig. 7-16 and Fig. 7-17, the current PD model is validated through the good agreement between the PD simulation results and the results from the experiment and SPH method. Besides, a smaller mesh size can be further utilized to achieve a more accurate result.

However, the discrepancies can also be observed both from PD and other numerical techniques. By investigating the sensitivity of the numerical parameters and techniques, the discrepancies may come from the following aspects. First, the PD node density and time step size may affect the accuracy of the final simulation results. In this case, the bending moment of the rubber gate acts an important role in the deformation process. For the rubber PD model, only 4 nodes exist in the thickness direction, indicating that all the 4 nodes experience the truncated integration domains. Therefore, the surface correction approach [10] which can improve the accuracy of the PD simulations, especially for the particles near the surface, can be utilized. However, the surface correction adopted in this PD equation of motion is a simple volume-based one as $s_c\left(\mathbf{x}_{s,i}\right) = \left(\pi h_{thick}\delta_s^2\right) / \sum_{j=1,\ j\in\Omega_s}^{N_i} V_{s,j}$, which may be not accurate enough. Besides, the smaller time step size can reduce the numerical discrepancies existing in the velocity Verlet algorithm. By comparing the PD predicted results from the two aforementioned different cases, the increasing of the number of the PD nodes and the decreasing of the time step size can give more accurate results. Second, the application of the MLS and PST provided in Section 7.2.2, on the one hand, can make the current approach more stable. On the other hand, they may decrease accuracy. For example, by comparing the time history of the displacement of the free rubber gate end, it can be observed that the application of the PST enlarges the discrepancy between the PD simulation result and

the experiment one. The PST applied in the current study does not have any modification regarding the free surface, which may decrease the accuracy of the numerical simulation [202].

The pressure and the velocity snapshots at the final state $t = 0.3\,\mathrm{s}$ are provided in Fig. 7-18. The pressure and velocity predicted by the PD approach present a similar distribution compared with the ones provided in [228, 234]. It should be mentioned that in Fig. 7-18 (a), the pressure of the rubber represents the fictitious solid pressure for boundary implementation, they are not from the constitutive equations of the solid rubber. Regarding the fluid pressure, the pressure inside the dam presents a similar hydrostatic pressure distribution. When only the free surface detecting approach provided in Section 7.2.2.1 is adopted, the fluid pressure outside the rubber gate may all become zero because of the over predicted number of free surface particles. The utilization of the PST in the current study can overcome this problem, which largely improves the accuracy of the pressure distribution of the fluid outside part.

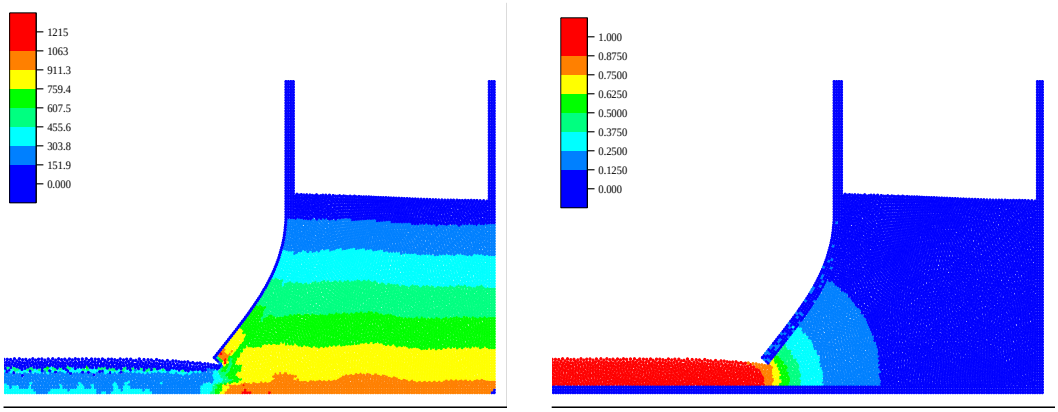

(a) (b)

Fig. 7-18 PD simulation results (a) Pressure and (b) velocity magnitude at the final state of $t = 0.3\,\mathrm{s}$

The configuration at the final stage $t = 0.3\,\mathrm{s}$ and its close view of the fluid-structure interface are provided in Fig. 7-19. The unit normal vector of the solid particles for the FSI interface is presented in Fig. 7-19 (b). The good agreement between the unit normal vector direction and the geometry indicates the capability of the proposed PD approach for accurately predicting the FSI interface. The interface normal direction approach provided in [218] has the limitation that it cannot be applied to the boundary

corner particles. However, the unit normal vectors of boundary rubber particles in the present study are also well represented because of the non-local property of the PD theory and the adoption of the colour function. Thus the aforementioned limitation in [218] is removed. In addition, it can also be observed from Fig. 7-19 (b) that no penetration occurs in the FSI interface region. Hence, the boundary collision model proposed in Section 7.2.2.2 is validated which has positive effects on the preventing penetration.

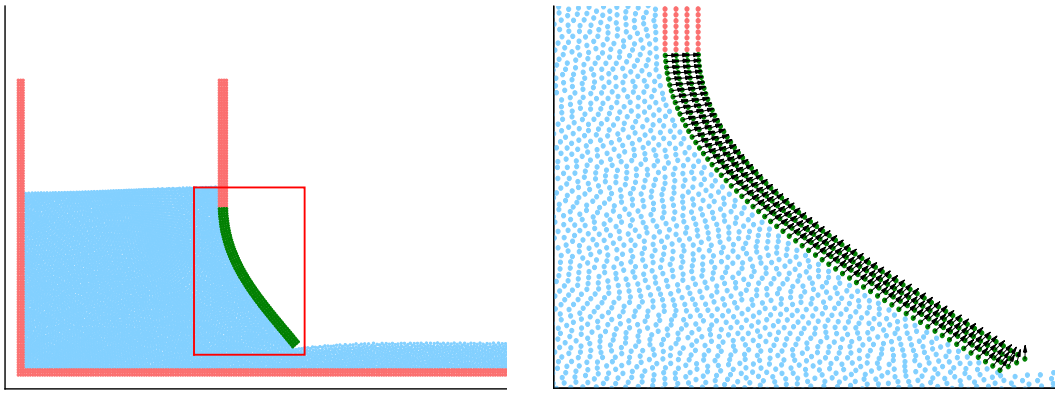

(a) (b)

Fig. 7-19 PD simulation results (a) configuration and (b) zoom view of the FSI interface state of $t = 0.3\,\mathrm{s}$

The largest PD bond stretch for each rubber particle at the time $t = 0.3\,\mathrm{s}$ is presented in Fig. 7-20. The regions with higher PD bond stretches show that these regions are more prone to failure.

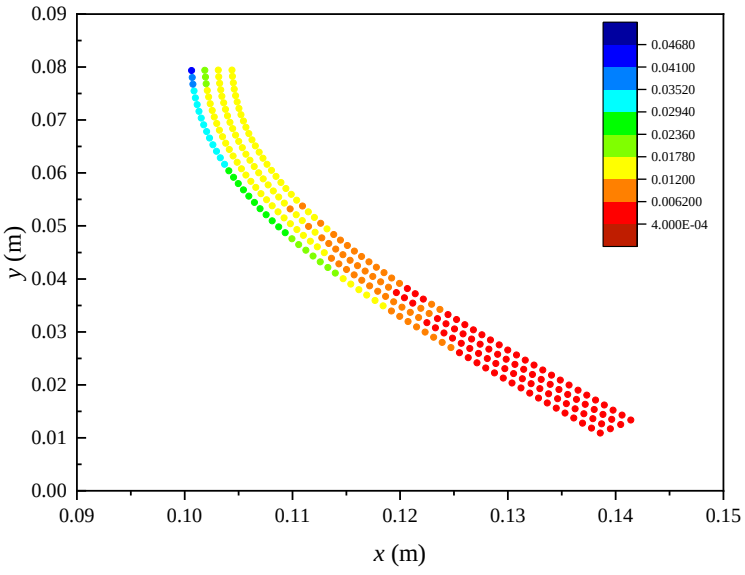

Fig. 7-20 The largest PD bond stretch for each rubber particle at time $t = 0.3\,\mathrm{s}$

7.4. Summary

In this chapter, a peridynamic based methodology for fluid-structure interaction problems is proposed for simultaneous numerical simulations. The structure model is developed by using the ordinary state-based peridynamic theory and the fluid model is developed by the peridynamic differential operator. The coupling scheme is performed bi-directionally. Then a dam collapse under an elastic rubber gate is simulated with the newly developed model. The PD predicted results are compared with the ones obtained by the experiment and other numerical simulation methods. The good agreement demonstrates the capability of the current model for accurately predicting the results of fluid-elastic structure interaction problems.

As the first PD model using the OSB-PD model for solid and PDDO model for fluid, the current study provides an alternative way for solving fluid-structure interaction problems. Besides, because of the intrinsic non-local property of PD theory, the FSI interface is easier to numerically implement.

8. Coupled Thermo-fluid-mechanical Peridynamic Model for Analysing Composite under Fire Scenarios

8.1. Introduction

The composite material response under fire load is a complex research topic since multidisciplinary fields are involved [3], e.g. thermodynamics, fluid mechanics, solid mechanics including composite material mechanics, chemical reaction theory, etc.[236]. Therefore, it would be a challenging task to numerically simulate this phenomenon by considering all aspects.

Regarding the modelling of the fire, understanding the mechanism and predicting the behaviour of fire is important and meaningful [237]. The fire can be considered as a summation of numerous flames [178]. Therefore, the flame can be treated as a basic element of fire. For the investigation of the flame in a physical aspect, the following fields are involved: the fluid field, the thermal field, the chemical reaction theory, and the species transport process.

- Fluid field: the flame can be categorized as being laminar flame and turbulent flame. In laminar flames, the burning gas flows in a regular pattern, which is contrary to the turbulent flames [237]. For laminar flames, the Navier-Stokes equation can be directly adopted by numerical methods to simulate their behaviour. On the other hand, the large eddy simulation (LES) method is usually utilized for a turbulent flame [238].
- Thermal field: the heat transfer and chemical reaction heat generation are the main two aspects in the numerical thermal model. Enthalpy is considered a primary variable in the heat transferring process. While the Arrhenius Law is usually employed in the heat generation due to chemical reaction [239].
- Chemical Reaction: the reaction model should be chosen which represents the reaction mechanism. Besides, the chemical kinetics of the elementary reactions [178] and their rates, e.g. chemical time scale, should also be decided [178]. A popular way to simulate the chemical reaction process is to use the commercial

software Chemkin III [240] and the open-source software Cantera developed by Python [241].

- Species transport: The flame is a multi-phase and multi-component fluid flow [242]. Consequently, a mixture fluid model which can predict the species diffusion process is required if all the solid components are considered [243].

As it is introduced above, the flame can be classified as a multi-component, multi-phase, chemical reactant, and heat transfer fluid flow [244]. As a result, the flames mechanism involves the knowledge of thermodynamics, thermochemistry, chemical kinetics, and fluid mechanics, etc. [245]. In other words, the mass transfer, heat transfer, momentum transfer, and species transfer exist in the flame motion.[246] Since the governing equations are often too complicated for analytical solutions, the technique of numerical simulation is widely applied [237]. There are various numerical methods for flame modelling, i.e. finite element method (FEM) [247], finite volume method (FVM)[242], finite difference methods (FDM) [248]. For these grid-based approaches, the space discretization should be fine enough for this complex combustion system. On the other hand, because of the presence of a high gradient of physical variables in the flame, special attention should be paid to time integration stability [242]. The computation time and memory requirements should be taken into consideration. On the contrary to the above grid-based approaches (FEM, FVM, FDM), Lagrangian methods can predict the non-linear convection term exactly [249]. Direct Lagrangian methods have been applied to simulate the reacting flows [250-252]. The remeshed smoothed particle hydrodynamics (SPH) in [249] is applied for the chemical reacting flows. A hydrogen/air opposed-jet burner numerical simulation is conducted with considering the Mach number effect [249]. The current existing numerical flame models cannot capture all the aforementioned aspects because of the fire's complex physical and chemical processes [237]. In the current study, the fire model is simplified as a heat-conducting single-phase fluid flow, ignoring the chemical reaction process and the diffusion of the components. In this way, the non-isothermal fluid flow PDDO model developed in [9] thus can be directly utilized to represent the fire physical model.

As to the investigation of composite response under fire loads which has been extensively studied [253-257], the key challenge to the modelling is the complexity of the thermal, chemical, physical, and failure process which control the composite

structure behaviour [258]. The firing process in the composites can be concluded as follows [258]:

- Thermal process: the heat conduction in composite materials from the fire [259], heat generation from decomposition and charring [260], convective heat loss, etc.
- Chemical process: viscous softening, melting, decomposition, and char-fibre reactions, etc.[3].
- Physical process: thermal expansion and contraction, matric cracking, fibre-matrix interface debonding, softening, delamination damage, etc.
- Failure process: charring, pores creation (creation of gas from resin decomposition) [261], thermal degradation of elasticity properties, micro-cracking, and delamination, etc.[2].

The current numerical models cannot capture all composites' responses as explained above. Therefore, simplification is applied in the numerical simulations [262]. For most researches regarding the composite response for fire scenarios, the decoupling of fire from composites is widely adopted in simulation approaches [263]. The fire is simply treated as a controlled heat flux or temperature boundary condition. The dynamics of fire are usually ignored. However, in the current study, the basic dynamics of fire motion, i.e. the thermal fluid flow, are considered during the composite response simulation. As a result, the physical problems belong to the field of thermal fluid-structure simulation of composite materials under the fire load. The thermal degradation of the composite properties [264], the matrix damage, and the fibre damage are taken into consideration in the composite model.

PD is originally developed for predicting damages in isotropic materials [4, 13]. Then, the formulation is extended for modelling damage in composite materials [10, 35, 75-78, 82, 86, 265-270]. The original form of PD is also extended for predicting thermal damages for both isotropic [40, 271-273] and composite materials [6, 7, 39, 46, 274]. Moreover, PD is also used for predicting corrosion and oxidation damage for both isotropic and composite materials [40, 274-278]. Therefore, due to the prediction capability of PD in many different applications, PD is used to predict the composite damage under the fire scenarios.

This chapter is organized as follows. The fire-induced temperature rising curve is provided in Section 8.2 to represent the fire effect in the thermal field. The thermal degradation properties of the composite material are also provided in Section 8.2. Section 8.3 describes the numerical implementations. Then, Section 8.4 describes the numerical simulations. In this section, composite damages due to direct contact with fire and composite damages due to hot gas induced by fire are investigated. Finally, the summary is provided in Section 8.5.

8.2. Composite material properties under fire

In this section, the temperature profile for fire and the thermal degradation properties of the composite material are provided.

8.2.1. Temperature profile of fire

The fire temperature profile as a function of time is used to represent the fire effect. In many thermal modelling approaches, fire is simulated as a controlled heat flux or temperature boundary conditions [258, 263], which brings simplification for the numerical simulations. Therefore, in the current study, the ISO 834 standard temperature-time curve [279] is utilized to represent the temperature fire profile as

$$T(t) = 20 + 345\log(8t/60 + 1) \tag{8.1}$$

where T represents the temperature in $^{\circ}\mathrm{C}$ and t represents the time in s. The temperature plot is provided in Fig. 8-1.

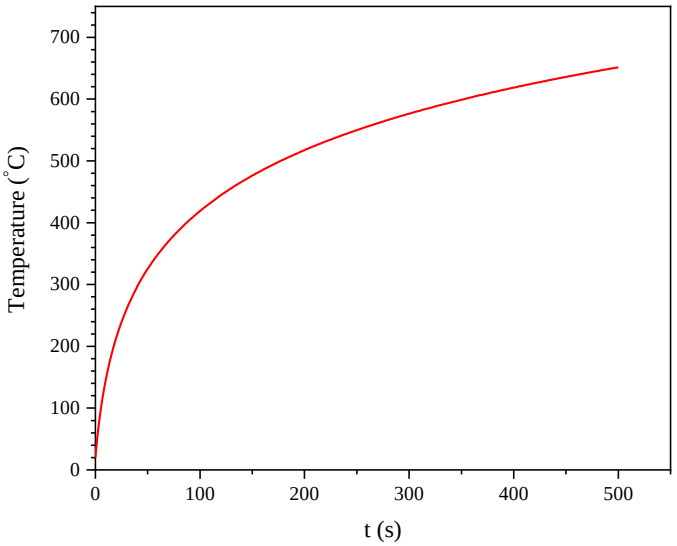

Fig. 8-1 ISO temperature-time curve represent fire [279]

8.2.2. Material degradation of composite material caused by fire

In the current study, a carbon fibre-epoxy composite material is considered. The material properties as functions of temperature are considered since material softening will occur under high temperature conditions. The thermal degradation properties from [280] are utilized and incorporated into the PD model. Regarding the material thermal properties, the thermal conductivity in the fibre direction, k_1, is assumed to be constant according to the experiment observation [259, 281].

The variation of transverse thermal conductivity, k_2, is shown in Fig. 8-2 (a). The temperature ranging from 348K to 373K in blue colour represents the glass transition region, as $T_{g\_low} = 348\,\mathrm{K}$ to represent the lower glass transition temperature and $T_{g\_high} = 373\,\mathrm{K}$ to represent the higher glass transition temperature. It can be observed that the transverse thermal conductivity decreases with temperature increasing in the glass transition region. When the temperature is higher than 573K ($T_{ignited} = 573\,\mathrm{K}$), the composite is ignited, and then the material property is assumed to be constant for $T > 573\,\mathrm{K}$ due to the lack of measured data. The variation of k_2 is represented as

$$k_2\left(\mathrm{W}/\left(\mathrm{m}\cdot\mathrm{K}\right)\right)=\begin{cases}0.362+7.57\times10^{-4}T, & 273\mathrm{K}<T\le348\mathrm{K}\\ 1.488-2.48\times10^{-3}T, & 348\mathrm{K}<T\le373\mathrm{K}\\ 0.104+1.23\times10^{-3}T, & 373\mathrm{K}<T\le573\mathrm{K}\\ 0.809, & 573\mathrm{K}<T\end{cases}\tag{8.2}$$

The variation of specific heat capacity, c_v, is shown in Fig. 8-2 (b) and represented as

$$c_v\left(\mathrm{J}/\left(\mathrm{Kg}\cdot\mathrm{K}\right)\right)=\begin{cases}-204+3.692T, & 273\mathrm{K}<T\le348\mathrm{K}\\ -2775+11.08T, & 348\mathrm{K}<T\le373\mathrm{K}\\ 665+1.858T, & 373\mathrm{K}<T\le573\mathrm{K}\\ 1730, & 573\mathrm{K}<T\end{cases}\tag{8.3}$$

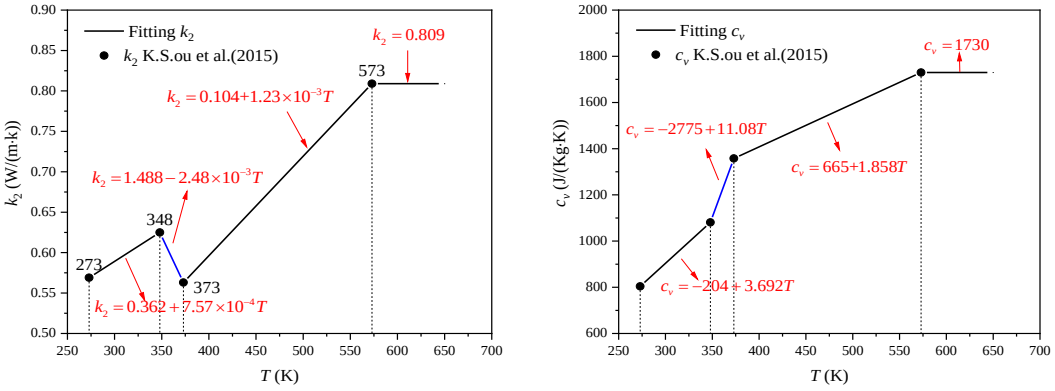

(a) (b)

Fig. 8-2 Temperature dependent (a) transverse thermal conductivity k_2 and (b) specific heat capacity c_v

To represent the mechanical material properties, the following function is used [264]

$$C(T)=\frac{C_0+C_\infty}{2}-\frac{C_0-C_\infty}{2}\tanh\left(C_1\left(T-T_{g\_high}\right)\right)\tag{8.4}$$

where C represents the material property, C_0 represents the unrelaxed (initial) material property and C_∞ the represents the relaxed (final) property. The term C_1 is a constant value and T_{g_high} represents the higher glass transition temperature as

$T_{g\_high} = 373\,\mathrm{K}$ in the current composite material. By using the Matlab curve fitting tool, the data is presented in Fig. 8-3:

The elastic modulus in the transverse direction, E_2, is presented as

$$E_2\left(\mathrm{GPa}\right) = \begin{cases} 4.645 - 4.529\tanh\left(0.02177\left(T-373\right)\right), & 273\mathrm{K} \le T < 475\mathrm{K} \\ 0.1, & 475\mathrm{K} \le T \end{cases} \tag{8.5}$$

The major shear modulus, G_{12}, is represented as

$$G_{12}\left(\mathrm{GPa}\right) = 2.29 - 2.238\tanh\left(0.0199\left(T-373\right)\right) \tag{8.6}$$

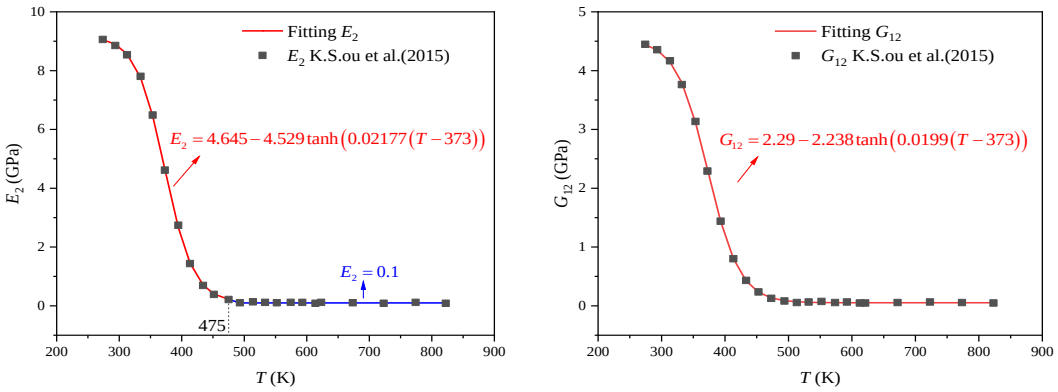

(a) (b)

Fig. 8-3 Temperature dependent (a) transverse elastic modulus E_2 and (b) major shear modulus G_{12}

Instead of using Eq.(8.4) for fitting the elastic modulus in the fibre direction, E_1 is fitted as Eq.(8.7) which can give a better fitting result as

$$E_1\left(\mathrm{GPa}\right) = \begin{cases} 146.64937 - 0.06535T, & 273\mathrm{K} \le T < 475\mathrm{K} \\ 110.86495 + 905.51983e^{\left(-T/91.34695\right)}, & 475\mathrm{K} \le T < 825\mathrm{K} \end{cases} \tag{8.7}$$

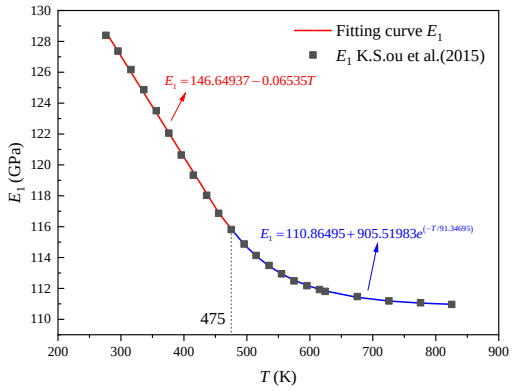

Fig. 8-4 Temperature dependent elastic modulus in fire direction

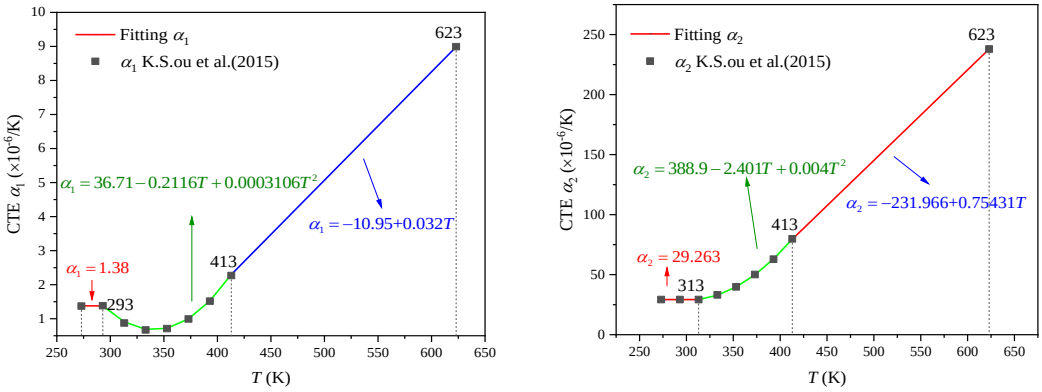

(a) (b)

Fig. 8-5 Temperature dependent (a) CTE in fibre direction α_1, (b) CTE in transverse direction α_2

The coefficients of the thermal expansion (CTE) both in fibre direction α_1 and in the transverse direction α_2 are segmented fitted as Fig. 8-5 and presented as

$$\alpha_1\left(\times 10^{-6}/\mathrm{K}\right)=\begin{cases}1.38, & 273\mathrm{K}<T\le 293\mathrm{K}\\ 36.71-0.2116T+0.0003106T^2, & 293\mathrm{K}<T\le 413\mathrm{K}\\ -10.95+0.032T, & 413\mathrm{K}<T\le 623\mathrm{K}\end{cases} \tag{8.8}$$

$$\alpha_2\left(\times 10^{-6}/\mathrm{K}\right)=\begin{cases}29.263, & 273\mathrm{K}<T\le 313\mathrm{K}\\ 388.9-2.401T+0.004T^2, & 313\mathrm{K}<T\le 413\mathrm{K}\\ -231.966+0.75431T, & 413\mathrm{K}<T\le 623\mathrm{K}\end{cases} \tag{8.9}$$

According to the PD failure criterion, the critical energy release rate is an important property in the damage simulation. The variation of energy release rate [282] is adopted as

$$G_{IC}\left(\mathrm{J/m^2}\right)=\begin{cases}265.568+3.49T-0.00745T^2, & 273\mathrm{K}\le T<535\mathrm{K}\\ 0, & 535\mathrm{K}\le T\end{cases} \tag{8.10}$$

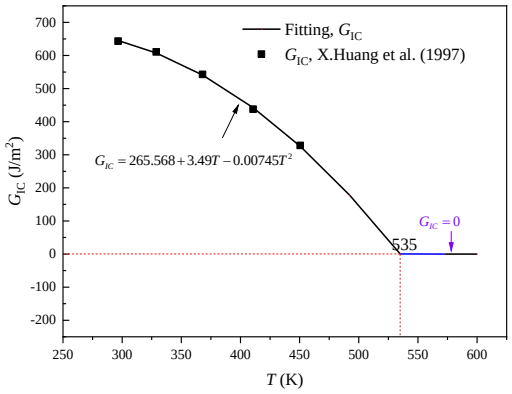

Fig. 8-6 Temperature dependent critical energy release rate G_{IC}

It is assumed that the bulk modulus $K_m\left(T\right)$ and Lamé constant $\mu_m\left(T\right)$ of the matrix material are linked to the transverse elastic modulus as [10]

$$K_m\left(T\right)=\frac{E_2\left(T\right)}{2\left(1-\nu_{12}\right)} \tag{8.11}$$

$$\mu_m\left(T\right)=\frac{E_2\left(T\right)}{2\left(1+\nu_{12}\right)} \tag{8.12}$$

with the major Poisson's ratio being assumed to be a constant as $\nu_{12}=0.33$.

8.3. PD Numerical implementations

The ordinary state-based thermomechanical PD composite model provided in Section 4.2.2 is utilized. The mechanical deformation of the composite is captured by using Eq.(4.17). The temperature change is obtained by using Eq.(4.25) with ignoring the coupling term in the heat conduction equation. The temperature degradation is

incorporated into the model [84], by incorporating temperature dependent material properties. The minor Poisson's ratio, v_{21}, is calculated at the initial temperature. On the other hand, the mechanical properties listed in Section 8.2 such as E_1, E_2, G_{12}, α_1, α_2 are temperature dependent as provided in Eqs.(8.5)-(8.9). Therefore the PD mechanical parameters a, b_{FT}, b_F, and b_T with their definitions in Eq.(4.6) become also temperature dependent. Moreover, the thermal conductivity in the fibre direction, k_1, is assumed constant. On the other hand, the thermal properties, k_2 and c_v are temperature dependent as provided in Eqs.(8.2)-(8.3). As a result, the corresponding PD thermal parameters κ_m and κ_f, provided in Eq.(4.10)-(4.11) also become temperature dependent. The PD critical stretches s_m, s_{ft}, s_{in}, and ϕ_{is} provided in Eq.(4.38)-(4.41) are functions of temperature due to the temperature dependent material properties G_{IC}, E_1, K_m, and μ_m as provided in Eq.(8.10)-(8.12). The critical energy release rates for the first and second failure mode are assumed the same, $G_{IIC} = G_{IC}$. On the other hand, the shear modulus for matrix material, G_m, is assumed constant.

The non-dimensional form of the PD thermo-fluid model provided in Section 5.3.5 is adopted to represent the fire heated air. Therefore, in order to couple the thermal-fluid model and the composite model, the non-dimensional form of the PD composite thermal model is used. It should be noted that the length, time, and temperature are cast into their non-dimensional values by using the same reference parameters both for the composite model and the fluid model. Furthermore, the temperature in the fitting functions of thermal degradation properties of composites is in a dimensional form. Therefore, the non-dimensional temperature should be converted into its dimensional value before the calculation of the composite material properties. The details are described as following.

8.3.1. Non-dimensional PD thermo-fluid model and composite thermal model

8.3.1.1 Non-dimensional PDDO fluid model

The PD thermo-fluid model [9] provided in Chapter 5 is used to represent the fire heated air. Furthermore, the fluid flow is assumed to be two-dimensional in the Eulerian description. The non-dimensional form of the non-local Naiver-Stokes equations [9] with Boussinesq approximation [175] by using the peridynamic differential operator [14] is adopted.

The thermo-fluid governing equations in the discretised form are:

Conservation of mass:

$$\begin{aligned}
&\rho_{f,i}^{*\,(n+1)} = \rho_{f,i}^{*\,(n)} \\
&-\Delta t^{*}\left(\begin{array}{l}
\rho_{f,i}^{*\,(n)}\sum_{j=1}^{N_{f,i}}\left(\mathbf{v}_{f,j}^{*\,(n)}-\mathbf{v}_{f,i}^{*\,(n)}\right)\cdot\mathbf{g}_1\left(\mathbf{x}_{f,j}^{*}-\mathbf{x}_{f,i}^{*}\right)V_{f,j}^{*} \\
-\sum_{j=1}^{N_{f,i}}\left(\rho_{f,j}^{*\,(n)}-\rho_{f,i}^{*\,(n)}\right)\left(\mathbf{v}_{f,i}^{*\,(n)}\cdot\mathbf{g}_1\left(\mathbf{x}_{f,j}^{*}-\mathbf{x}_{f,i}^{*}\right)\right)V_{f,j}^{*}
\end{array}\right)
\end{aligned} \tag{8.13}$$

Conservation of momentum:

$$\begin{aligned}
&\mathbf{v}_{f,i}^{*\,(n+1)} = \mathbf{v}_{f,i}^{*\,(n)} \\
&+\Delta t^{*}\left(\begin{array}{l}
-\sum_{j=1}^{N_{f,i}}\left(P_{f,j}^{*\,(n)}-P_{f,i}^{*\,(n)}\right)\mathbf{g}_1\left(\mathbf{x}_{f,j}^{*}-\mathbf{x}_{f,i}^{*}\right)V_{f,j}^{*} \\
+\sum_{j=1}^{N_{f,i}}\left(\mathbf{v}_{f,j}^{*\,(n)}-\mathbf{v}_{f,i}^{*\,(n)}\right)\left(\begin{array}{l}
\mathrm{Pr}\,\mu_{f,i}^{*\,(n)}\mathrm{Tr}\left(\mathbf{g}_2\left(\mathbf{x}_{f,j}^{*}-\mathbf{x}_{f,i}^{*}\right)\right) \\
-\left(\mathbf{v}_{f,i}^{*\,(n)}\cdot\mathbf{g}_1\left(\mathbf{x}_{f,j}^{*}-\mathbf{x}_{f,i}^{*}\right)\right)
\end{array}\right)V_{f,j}^{*} \\
+\mathrm{Ra}\,\mathrm{Pr}\,T_{f,i}^{*\,(n)}\begin{bmatrix}0\\1\end{bmatrix}
\end{array}\right)
\end{aligned} \tag{8.14}$$

Conservation of energy:

$$T_{f,i}^{*\,(n+1)} = T_{f,i}^{*\,(n)} + \Delta t^{*} \sum_{j=1}^{N_{f,i}} \left(T_{f,j}^{*\,(n)} - T_{f,i}^{*\,(n)} \right) \begin{pmatrix} k_{f,i}^{*\,(n)} \mathrm{Tr}\left(\mathbf{g}_2 \left(\mathbf{x}_{f,j}^{*} - \mathbf{x}_{f,i}^{*} \right) \right) \\ -\left(\mathbf{v}_{f,i}^{*\,(n)} \cdot \mathbf{g}_1 \left(\mathbf{x}_{f,j}^{*} - \mathbf{x}_{f,i}^{*} \right) \right) \end{pmatrix} V_{f,j}^{*} \tag{8.15}$$

pressure:

$$P_{f,i}^{*\,(n+1)} = \left(\frac{c_{sound}}{v_0} \right)^2 \left(\left(\rho_{f,i}^{*\,(n+1)} \right)^{\gamma_f} - 1 \right) \tag{8.16}$$

The non-dimensional parameters shown with $\left({}^{*} \right)$ are defined with respect to their reference parameters shown with $\left({}_{0} \right)$ as [144]

$$\mathbf{x}_f^{*} = \frac{\mathbf{x}_f}{L_0}; \mathbf{v}_f^{*} = \frac{\mathbf{v}_f}{v_0}; t^{*} = \frac{t}{\left(L_0 / v_0 \right)}; \rho_f^{*} = \frac{\rho_f}{\rho_{f,0}}; P_f^{*} = \frac{P_f}{\rho_f v_0^2}; T_f^{*} = \frac{T_f}{T_0}, \mu_f^{*} = \frac{\mu_f}{\mu_{f,0}}, k_f^{*} = \frac{k_f}{k_{f,0}} \tag{8.17}$$

where the parameters $\mathbf{x}_f$, $\mathbf{v}_f$, ρ_f, P_f, T_f, μ_f, and k_f represent the fluid particle position, velocity, density, pressure, temperature, viscous coefficient, and thermal conductivity. L_0, v_0, and T_0 are the reference length, velocity, and temperature. $\rho_{f,0}$, $\mu_{f,0}$, and $k_{f,0}$ are the reference fluid density, viscosity and thermal conductivity. t and t^{*} represent the time and non-dimensional time, respectively.

In Eqs.(8.13)-(8.16), the fluid point of interested is denoted by its coordinate as $\mathbf{x}_{f,i}^{*}$, and its family member is denoted by $\mathbf{x}_{f,j}^{*}$. $N_{f,i}$ is the total number of the fluid family members of fluid point $\mathbf{x}_{f,i}^{*}$. The volume of $\mathbf{x}_{f,j}^{*}$ is denoted by $V_{f,j}^{*}$. Tr represents the trace of a matrix. The parameters $\mathbf{v}_{f,i}^{*}$, $\rho_{f,i}^{*}$, $\mu_{f,i}^{*}$, $T_{f,i}^{*}$, and $k_{f,i}^{*}$ are defined at fluid location $\mathbf{x}_{f,i}^{*}$. The energy dissipated by the viscous force is ignored in Eq. (8.15) since it is too small compared with the energy increased by fire [283]. In Eq.(8.16), γ_f is

the ratio of specific heat capacity, c_{sound} is the artificial speed of sound. The ratio of specific heat capacity is chosen as $\gamma_f = 1$ for gas [141].

Furthermore, Sutherland's law [284-286] which reflects the temperature effect on the viscosity coefficient and the thermal conductivity is adopted in a non-dimensional form as

$$\mu_{f,i}^* = \left(T_{f,i}^*\right)^{1.5} \frac{1+S^*}{T_{f,i}^* + S^*}; \quad k_{f,i}^* = \left(T_{f,i}^*\right)^{1.5} \frac{1+S^*}{T_{f,i}^* + S^*}; \tag{8.18}$$

where $S^* = 111/T_0$ with T_0 being in unit K [284].

In the above equations, the current time step is denoted by the superscript $\left({}^{(n)}\right)$ and the updated time step is denoted by the superscript $\left({}^{(n+1)}\right)$. The non-dimensional time step size is denoted by Δt^*.

8.3.1.2 Non-dimensional OSB PD thermal model for composite

The non-dimensional parameters for PD composite thermal model are defined as

$$\mathbf{x}_s^* = \frac{\mathbf{x}_s}{L_0}; \mathbf{v}_s^* = \frac{\mathbf{v}_s}{v_0}; T_s^* = \frac{T_s}{T_0}; t^* = \frac{t}{\left(L_0/v_0\right)} \tag{8.19}$$

For both the composite thermal model and the thermo-fluid model, the reference velocity is chosen as

$$v_0 = \frac{\alpha_{df,0}}{L_0} \tag{8.20}$$

where $\alpha_{df,0}$ is the initial value of the thermal diffusivity of air as

$$\alpha_{df,0} = \frac{k_{f,0}}{\rho_{f,0} c_f} \tag{8.21}$$

Consequently, the nondimensional diffusivities of composites to the fluid are calculated as

$$\alpha_{ds1}^{*}=\frac{\alpha_{ds1}}{\alpha_{df,0}};\ \alpha_{ds2}^{*}=\frac{\alpha_{ds2}}{\alpha_{df,0}};\ \alpha_{dsm}^{*}=\frac{\alpha_{dsm}}{\alpha_{df,0}} \tag{8.22}$$

where α_{ds1} is the thermal diffusivity in the fibre direction, α_{ds2} is the thermal diffusivity in the transverse direction, and α_{dsm} is the thermal diffusivity of the matrix in the composite material.

By substituting Eqs.(8.19)-(8.22) into Eq.(4.25) and neglecting the coupling term, the non-dimensional form of the PD composite thermal model becomes

$$\begin{aligned}\frac{\partial T_{s,i}^{n,*}}{\partial t^{*}}=&\sum_{j=1}^{N_{s,ply,i}}\left[\left(\mu_F\chi_f\frac{\kappa_{f,i}^{n,*}+\kappa_{f,j}^{n,*}}{2}+\chi_m\frac{\kappa_{m,i}^{n,*}+\kappa_{m,j}^{n,*}}{2}\right)\frac{\left(T_{s,j}^{n,*}-T_{s,i}^{n,*}\right)}{\left|\mathbf{x}_{s,j}^{n,*}-\mathbf{x}_{s,i}^{n,*}\right|}\right]V_{s,j}^{n,*}\\&+\sum_{m=n+1,\,n-1}\left[\chi_{in}\kappa_{\text{inter},i}^{n,*}\frac{\left(T_{s,i}^{m,*}-T_{s,i}^{n,*}\right)}{\left|\mathbf{x}_{s,i}^{*,m}-\mathbf{x}_{s,i}^{n,*}\right|}\right]V_{s,i}^{m,*}\\&+\sum_{m=n+1,\,n-1}\sum_{j=1}^{N_{s,shear,i}}\left[\chi_{is}\kappa_{\text{inter},i}^{n,*}\frac{\left(T_{s,j}^{m,*}-T_{s,i}^{n,*}\right)}{\left|\mathbf{x}_{s,j}^{*,m}-\mathbf{x}_{s,i}^{n,*}\right|}\right]V_{s,j}^{m,*}+h_{s,i}^{n,*}\end{aligned} \tag{8.23}$$

The composite point of interested is denoted by its initial coordinate as $\mathbf{x}_{s,i}^{n,*}$, where the subscript $(_s)$ denotes the composite and $(_i)$ denotes the particle number. The superscript $(^n)$ represents the layer number. $N_{s,ply,i}$ represents the total number of family members which are in the same ply of the interested point $\mathbf{x}_{s,i}^{n,*}$. On the other hand, $N_{s,shear,i}$ represents the total number of the family members which interact with $\mathbf{x}_{s,i}^{n,*}$ through the interlayer shear bonds. $V_{s,j}^{n,*}$ represents the volume of material point at $\mathbf{x}_{s,j}^{n,*}$. By using Eqs.(4.10), (4.11), and (4.26), the non-dimensional PD thermal diffusivities are defined by as

$$\kappa_{f,i}^{n,*} = \frac{2\left(\alpha_{ds1}^{*} - \alpha_{ds2,i}^{*}\right)}{\sum_{j=1}^{N_{s,F,i}} \left|\mathbf{x}_{s,j}^{n,*} - \mathbf{x}_{s,i}^{n,*}\right| V_{s,j}^{n,*}} \tag{8.24}$$

$$\kappa_{m,i}^{n,*} = \frac{6\alpha_{ds2,i}^{*}}{\pi h_{thick}^{*}\left(\delta^{*}\right)^{3}} \tag{8.25}$$

$$\kappa_{\text{inter},i}^{n,*} = \frac{\alpha_{dsm}^{*}}{2\pi\left(h_{thick}^{*}\right)^{3}\left(\tilde{\delta}^{*} - h_{thick}^{*}\right)} \tag{8.26}$$

where the parameters $\kappa_{f,i}^{n,*}$, $\kappa_{m,i}^{n,*}$, and $\kappa_{\text{inter},i}^{n,*}$ are defined at location $\mathbf{x}_{s,i}^{n,*}$.

In Eq. (8.23), $h_{s,i}^{*}$ is the non-dimensional volumetric heat source, it can be represented as

$$h_{s,i}^{n,*} = \frac{h_{s,i}^{n} L_0}{\rho_s C_v T_0 v_0} \tag{8.27}$$

The non-dimensional composite temperature is updated according to Eq.(8.23) as:

$$\begin{aligned} T_{s,i}^{n,*\,(\mathrm{n}+1)} &= T_{s,i}^{n,*\,(\mathrm{n})} \\ &+\Delta t^{*}\left(\begin{array}{l} \sum_{j=1}^{N_{s,ply,i}}\left[\left(\mu_F \chi_f \frac{\kappa_{f,i}^{n,*\,(\mathrm{n})} + \kappa_{f,j}^{n,*\,(\mathrm{n})}}{2} + \chi_m \frac{\kappa_{m,i}^{n,*\,(\mathrm{n})} + \kappa_{m,j}^{n,*\,(\mathrm{n})}}{2}\right)\frac{\left(T_{s,j}^{n,*\,(\mathrm{n})} - T_{s,i}^{n,*\,(\mathrm{n})}\right)}{\left|\mathbf{x}_{s,j}^{n,*} - \mathbf{x}_{s,i}^{n,*}\right|}\right] V_{s,j}^{n,*} \\ + \sum_{m=n+1,\,n-1}\left[\chi_{in}\kappa_{\text{inter},i}^{n,*\,(\mathrm{n})}\frac{\left(T_{s,i}^{m,*\,(\mathrm{m})} - T_{s,i}^{n,*\,(\mathrm{n})}\right)}{\left|\mathbf{x}_{s,i}^{*,m} - \mathbf{x}_{s,i}^{n,*}\right|}\right] V_{s,i}^{m,*} + \\ \sum_{m=n+1,\,n-1}\sum_{j=1}^{N_{s,shear,i}}\left[\chi_{is}\kappa_{\text{inter},i}^{n,*\,(\mathrm{n})}\frac{\left(T_{s,j}^{m,*\,(\mathrm{m})} - T_{s,i}^{n,*\,(\mathrm{n})}\right)}{\left|\mathbf{x}_{s,j}^{*,m} - \mathbf{x}_{s,i}^{n,*}\right|}\right] V_{s,j}^{m,*} + h_{s,i}^{n,*\,(\mathrm{n})} \end{array}\right) \end{aligned} \tag{8.28}$$

8.3.1.3 Thermal and mechanical damage parameters

To represent the extent of damage due to ignition of composite material, a non-dimensional temperature, $\tilde{T}$, is defined as

$$\tilde{T} = \frac{T_{g\_high} - T_{s,i}^{n}}{T_{g\_high} - T_{s,ref}} \tag{8.29}$$

and

$$T_{s,i}^{n} = \begin{cases} T_{ignited} \rightarrow \tilde{T} = -2.5 \\ T_{s,ref} \rightarrow \tilde{T} = 1 \\ T_{g\_high} \rightarrow \tilde{T} = 0 \\ T_{g\_low} \rightarrow \tilde{T} = 0.3125 \end{cases} \tag{8.30}$$

where T_s is the temperature of the PD composite points, $T_{s,ref}$ is the reference temperature $T_{s,ref} = 293\,\mathrm{K}$, $T_{ignited}$ is the ignition temperature $T_{ignited} = 573\,\mathrm{K}$, T_{g_low} is the lower glass transition temperature $T_{g\_low} = 348\,\mathrm{K}$, and T_{g_high} is the higher glass transition temperature $T_{g\_high} = 373\,\mathrm{K}$ [280]. Therefore, $\tilde{T} \le -2.5$ represents that the material is ignited, $\tilde{T} = 1$ represents composite is at the reference temperature, $\tilde{T} \le 0$ represents the post glass transition period $\left(T_{s,i}^{n} > T_{g\_high}\right)$ as illustrated in Fig. 8-7.

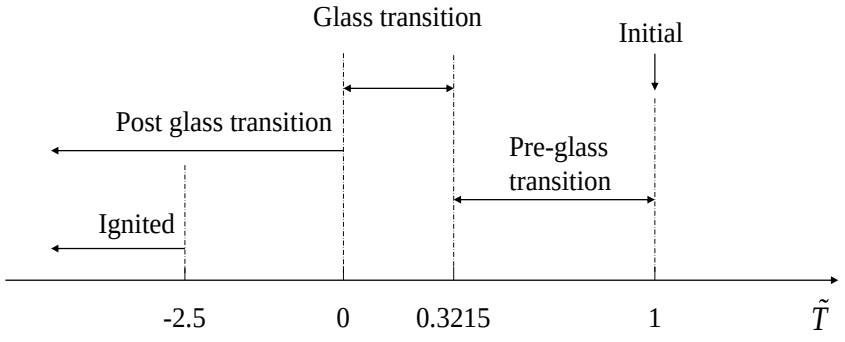

Fig. 8-7 Different domains distinguished by $\tilde{T}$ [280]

Regarding the mechanical damage parameter, the variation of the critical stretch for matrix bond, $s_{cm,i}$ as a function of temperature is plotted in Fig. 8-8. It can be observed from the figure that within the range of $273\,\mathrm{K} < T \le 348\,\mathrm{K}$, the material remains as a brittle material before the glass transition [3, 287]. Then the composite material becomes a rubber like ductile material [3, 287] for the approximate region

$348\ \mathrm{K}<T\leq 493\ \mathrm{K}$. Then when the temperature is larger than the critical value of 493 K, the critical stretch decreases as shown in Fig. 8-8. Finally the material totally fails (critical stretch equals to zero) when the temperature is higher than 535 K [287].

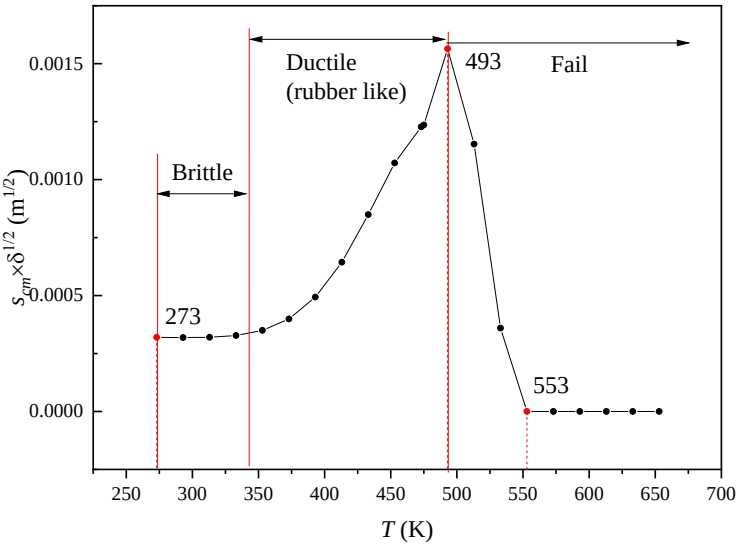

Fig. 8-8 The variation of $s_{cm}\delta^{1/2}$ as a function of temperature

8.3.2. Boundary conditions

8.3.2.1 Mechanical boundary conditions

The boundary condition involved in the composite mechanical model is applied by setting displacement values in the fictitious layer as [10]

$$\mathbf{u}_{s,bc}=0 \tag{8.31}$$

In Fig. 8-9, R_s represents the composite material, and $R_{s,bc}$ represents the fictitious region. The thickness of the fictitious layer is set as the size of the horizon (shown in black nodes in Fig. 8-9 (b)).

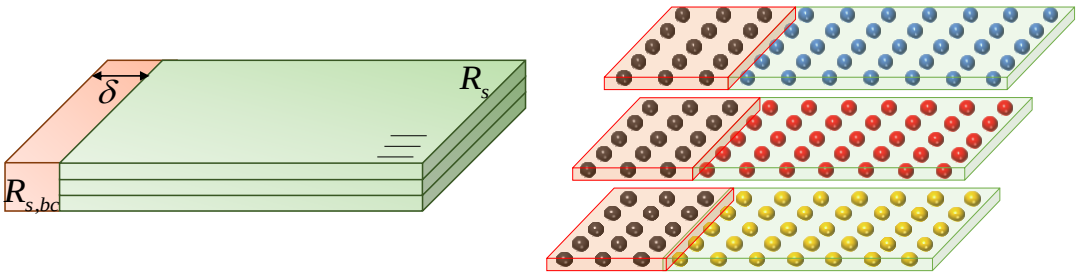

(a) (b)

Fig. 8-9 Fixed boundary implementation (a) geometry illustration and (b) PD implementation for $\delta = 3\Delta x$

8.3.2.2 Flow boundary conditions

The boundary condition involved in the fluid field is applied by setting non-dimensional velocity and displacement values in the fictitious layer as

$$\mathbf{v}_f^*\left(\mathbf{x}_{f,bc}^*\right) = 0; \mathbf{u}_f^*\left(\mathbf{x}_{f,bc}^*\right) = 0 \tag{8.32}$$

The pressure values at the fictitious particles in $R_{f,bc}$ are defined in the non-dimensional form as [9, 76]

$$P_f^*\left(\mathbf{x}_{f,bc}^*, t^*\right) = \frac{\sum_{j=1}^{N_{f,bc}} P_f^*\left(\mathbf{x}_{f,j}^*, t^*\right) w\left(\mathbf{x}_{f,j}^* - \mathbf{x}_{f,bc}^*\right)}{\sum_{j=1}^{N_{f,bc}} w\left(\mathbf{x}_{f,j}^* - \mathbf{x}_{f,bc}^*\right)} \tag{8.33}$$

where $\mathbf{x}_{f,bc}^*$ represents the fictitious rigid wall particle, $\mathbf{x}_{f,j}^*$ is its family member belonging to the fluid. $N_{f,bc}$ represents the total family members of point $\mathbf{x}_{f,bc}^*$ belonging to the fluid field, as shown in Fig. 8-10. $P_f^*\left(\mathbf{x}_{f,j}^*, t^*\right)$ represents the pressure of point $\mathbf{x}_{f,j}^*$. The weighted function w is provided in Eq.(2.25).

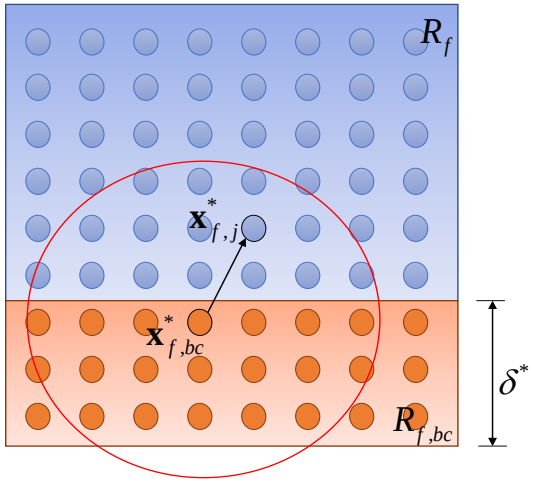

Fig. 8-10 Boundary condition implementation for fluid field with $\delta^* = 3\Delta x^*$

8.3.2.3 Thermal boundary conditions

The thermal boundary conditions are both involved in the composite model and fluid model. The temperature boundary condition is applied by adding fictitious layer as [43, 44]

$$T_i^*\left(t^*\right) = 2T_{bc}^*\left(t^*\right) - T_j^*\left(t^*\right) \tag{8.34}$$

where T_{bc}^* represents the non-dimensional boundary temperature. The parameters T_i^* and T_j^* represent the non-dimensional temperatures in the fictitious and real regions, respectively, as shown in Fig. 8-11.

No flux (insulated) boundary condition is applied by setting temperatures in the real region as [43, 44]

$$T_j^*\left(t^*\right) = T_k^*\left(t^*\right) \tag{8.35}$$

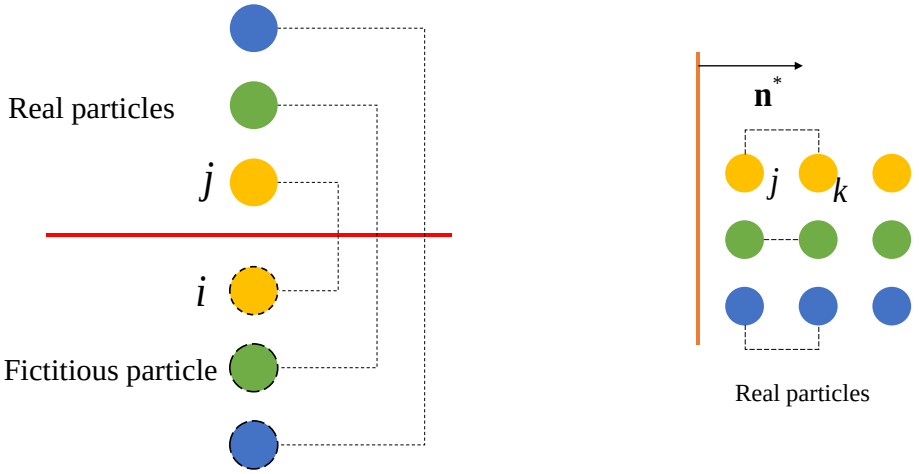

(a) (b)

Fig. 8-11 Thermal boundary condition implementation (a) temperature boundary condition, and (b) insulated boundary condition

8.3.3. Interface condition between composite and gas for thermal field

The convection boundary condition at the composite boundary is implemented by setting heat source at the boundary as [43, 44]

$$h_s^*\left(\mathbf{x}_{s,interface}^*,t^*\right)=-\frac{1}{\Delta x^*}h_{con}^*\left(T_s^*\left(\mathbf{x}_{s,interface}^*,t^*\right)-T_{f,local}^*\right) \tag{8.36}$$

where h_{con}^* is the non-dimensional convective heat transfer coefficient, $T_s^*\left(\mathbf{x}_{s,interface}^*,t^*\right)$ is the temperature in the composite region, and $T_{f,local}^*$ is the local fluid temperature which is calculated as the average temperature of the fluid particles which are within the horizon of $\mathbf{x}_{s,interface}^*$ as

$$T_{f,local}^*=\frac{\sum_{N_{s,interface,f}}T_f^*\left(\mathbf{x}_f^*,t^*\right)}{N_{s,interface,f}} \tag{8.37}$$

where $N_{s,interface,f}$ represents the total number of the family members of point $\mathbf{x}_{s,interface}^*$ which belongs to the fluid as shown in Fig. 8-12. $T_f^*\left(\mathbf{x}_f^*,t^*\right)$ is the non-dimensional fluid temperature predicted in the fluid model.

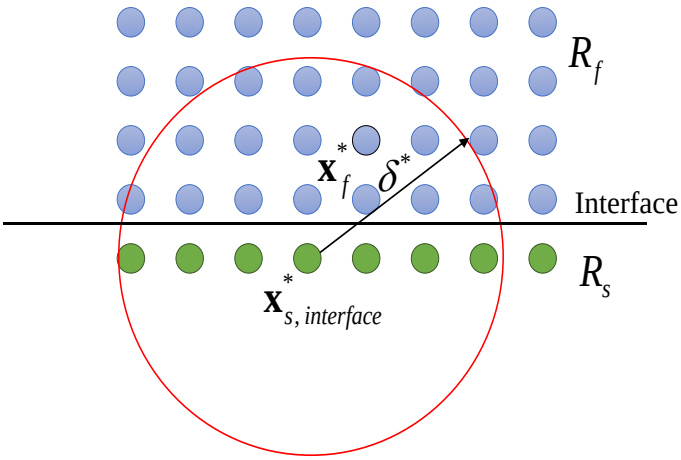

Fig. 8-12 Composite-gas interface illustration

The non-dimensional convection coefficient [286, 288] is

$$h^*_{con} = \max\left(\frac{C_{convection} T_0^{1/3} \left| T^*_s\left(\mathbf{x}^*_{s,interface}, t^*\right) - T^*_{f,i} \right|^{1/3}}{\rho_s c_v v_0}, \frac{k_{f,0}}{\rho_s c_v \alpha_{f,0}} \frac{k^*_f}{L^*_s} 0.0037\,\mathrm{Re}^{0.8}\,\mathrm{Pr}^{1/3} \right) \tag{8.38}$$

where $C_{convection}$ is a coefficient for natural convection which is $C_{convection} = 1.52\ \mathrm{W/\left(m^2K^{4/3}\right)}$ for a horizontal surface and $C_{convection} = 1.38\ \mathrm{W/\left(m^2K^{4/3}\right)}$ for a vertical surface. The parameter L^*_s is the non-dimensional length of the composite ply. c_v is the specific heat capacity of composites provided in Eq.(8.3).

Similarly, the radiation boundary condition for the composite thermal field is implemented by setting heat source at the boundary as [39]

$$h^*_s\left(\mathbf{x}^*_{s,interface}, t^*\right) = \sigma^*_{stefan-boltzmann} \varepsilon \frac{1}{\Delta x^*} \left(\left(T^*_{f,local}\right)^4 - \left(T_s\left(\mathbf{x}^*_{s,interface}, t^*\right)\right)^4 \right) \tag{8.39}$$

where $\sigma^*_{stefan-boltzmann}$ is the non-dimensional Stefan Boltzman constant defined as

$$\sigma^*_{stefan-boltzmann} = \frac{\sigma_{stefan-boltzmann} T_0^3 L_0}{\rho_s c_v \alpha_{f,0}} \tag{8.40}$$

with $\sigma_{stefan-boltzmann} = 5.67\times10^{-8}\ \mathrm{W/\left(m^2K^4\right)}$. The surface emissivity ε is assumed to be one as $\varepsilon = 1$ in the current study.

8.4. Numerical simulations

In this section, two cases are presented. The first case investigates the damage in composite due to direct contact with fire. This case belongs to the thermomechanical analysis where the heat conduction and composite deformation are included. The second case investigates the damage in composite due to hot gas induced by fire. The fire is simulated as a temperature boundary condition which heats the air. Then the heated air transfers the heat energy to the composite material via convection and radiation, indicating a one-way coupling thermal fluid and structure interaction.

8.4.1. Composite damage due to direct contact with the fire

8.4.1.1 Problem description

As illustrated in Fig. 8-13, a three-layer laminated composite material is investigated. The laminate is 0.1 m in length (L=0.1 m) and 0.1 m in width (W=0.1 m). Each layer has a uniform thickness as $h_{thick} = 0.001\,\mathrm{m}$. The fibre direction of each layer is chosen as $\left[0/90^{\circ}/0\right]$. The density of the composite is $\rho_s = 1620\ \mathrm{kg/m^3}$. The thermal conductivity in the fibre direction, k_1, is assumed constant as $k_1 = 8.3075\ \mathrm{W/\left(m\cdot K\right)}$ [259, 281]. The thermal conductivity of matrix material, k_m, is assumed constant as $k_m = 0.2\ \mathrm{W/\left(m\cdot K\right)}$ [6]. The CTE of matrix material α_m is $\alpha_m = 63\times10^{-6}/\mathrm{K}$ [6]. The tension strength in the fibre direction is chosen as $\sigma_{1t} = 2550MPa$ [289]. E_m and G_m are the elastic and shear modulus of the matrix material, which have the values as $E_m = 3.4\,\mathrm{GPa}$ and $G_m = 1.308\,\mathrm{GPa}$ [86]. The other composite material properties, k_2, c_v, E_1, E_2, G_{12}, α_1, α_2, G_{IC}, K_m, μ_m, ν_{12} are provided in Section 8.2.2.

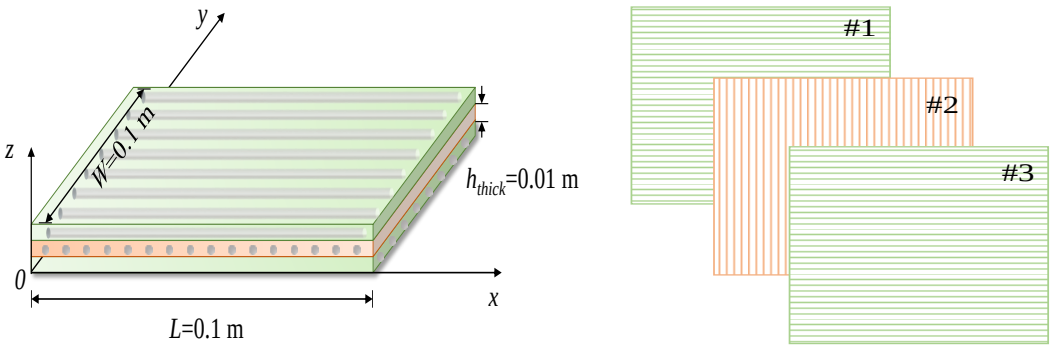

(a) (b)

Fig. 8-13 (a) Three layers laminate geometry illustration and (b) fibre direction illustration

A uniform initial temperature is set for the composites as $T_s^0 = T_{s,ref} = 293\,\mathrm{K}$. Besides, all composite nodes are static at the initial condition. The boundary conditions are provided as follows.

Thermal boundary conditions:

As shown in Fig. 8-14, the edge on $x = 0, \left|y - W/2\right| < W/8$ is under a temperature boundary condition induced by a localized fire. The other three edges $x = L$, $y = 0$, and $y = W$ are insulated.

At $x = 0$

$$\begin{aligned} &\left|y - W/2\right| < W/8 : T_s = T_{fire}\left(t\right) = 345\log\left(8t/60 + 1\right) + T_s^0 \\ &\left|y - W/2\right| \geq W/8 : \frac{\partial T_s}{\partial x} = 0 \end{aligned} \tag{8.41a}$$

At $x = L$

$$\frac{\partial T}{\partial x} = 0 \tag{8.41b}$$

At $y = 0$ and $y = W$

$$\frac{\partial T}{\partial y} = 0 \tag{8.41c}$$

Mechanical boundary condition:

As to the mechanical field, the right vertical edge is fixed, and the other three edges are free to deform as

At $x = L$

$$\mathbf{u}_s = 0 \tag{8.42}$$

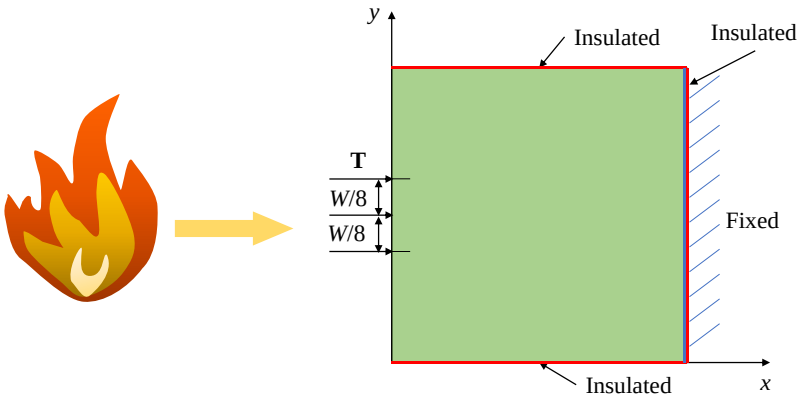

(a)

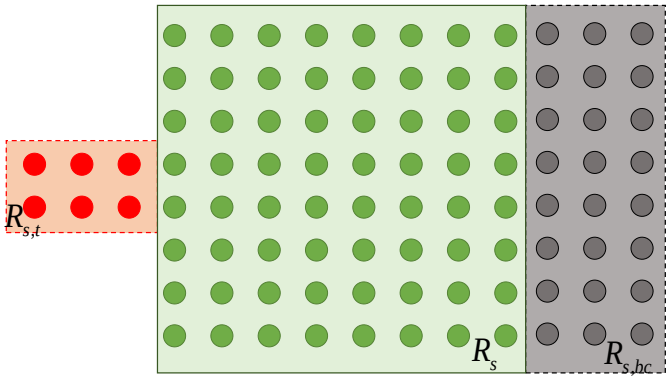

(b)

Fig. 8-14 Boundary sketch for composite directly under local fire (top view): (a) geometry illustration and (b) PD discretization

The top view of the PD discretization is illustrated in Fig. 8-14 (b). For the laminate ply, denoted by R_s, each layer is discretized by 40×40 nodes in the $x-y$ plane and one node in the z direction. Therefore, the laminate totally contains $40\times40\times3$ PD points and the initial in-plane node spacing is $\Delta x = 0.0025\,\text{m}$. The in-plane horizon is chosen as $\delta = 3.015\Delta x$. The region denoted by $R_{s,t}$ is the thermal fictitious layer

($10\times3\times3$ PD points) and $R_{s,bc}$ is the fictitious layer ($40\times3\times3$ PD points) representing the fixed boundary condition in the mechanical field. The value of related parameters to calculate the critical stretch σ_{1t}, G_{IC}, E_1, μ_m, K_m, E_m, and G_m are provided in this section and Section 8.2.2. Hence, the initial value of the critical stretches are calculated as $s_{cm}=3.39\times10^{-3}$, $s_{ft}=1.99\times10^{-2}$, $s_{in}=1.97\times10^{-2}$, and $s_{is}=2.25\times10^{-2}$.

The time step size for heat conduction analysis is set as $\Delta t=10^{-3}$ s. The mechanical deformation analysis is conducted in a quasi-static solution for each 50 seconds by using the adaptive dynamic relaxation (ADR) technique [87]. The total simulation time is 500 s.

8.4.1.2 Numerical Procedure

In this thermomechanical analysis, the heat conduction is performed in a transient process, while the mechanical analysis is performed as a static case for each 50 seconds. The numerical procedure for the thermomechanical problem 5.1 is provided in Fig. 8-15.

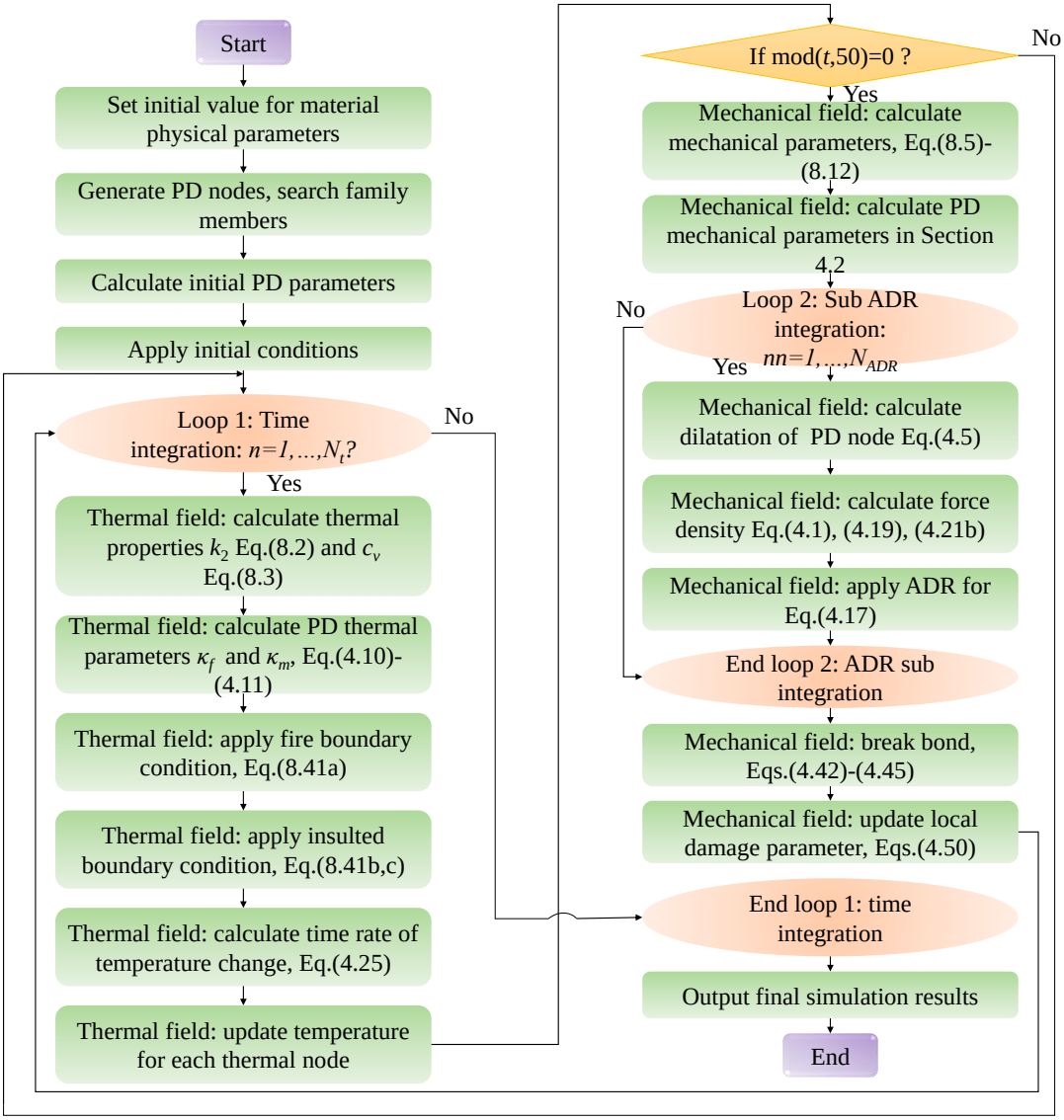

Fig. 8-15 Flowchart for thermo-mechanical model for composite for problem 8.4.1

8.4.1.3 Numerical results

The temperature change distributions of the laminate at different times are provided in Fig. 8-16. It can be observed that the temperature change distributions for the bottom and top plies are identical but differ from the distribution for the middle ply. The fibre direction which has a larger thermal conductivity is parallel to *x* direction for the bottom and top plies, leading to a faster heat transfer in the *x* direction compared to the middle ply. Therefore, the heated region of the top and bottom plies in the figure are more concentrated in the *x* direction than the middle ply.

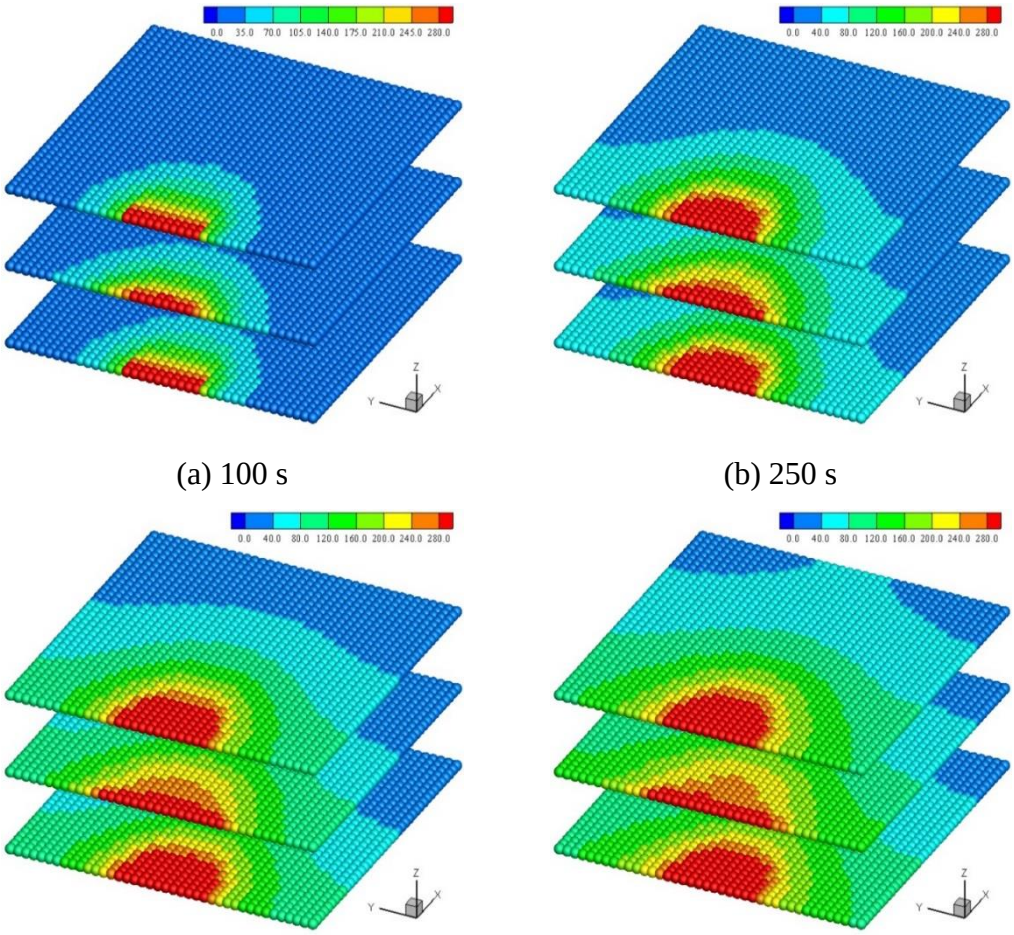

(a) 100 s (b) 250 s

(c) 400 s (d) 500 s

Fig. 8-16 The temperature change distributions at different times

Fig. 8-17 represents the distribution of $\tilde{T}$ according to Eq.(8.29) at $t = 500\,\mathrm{s}$. Red colour represents the post glass transition period, the white colour represents the glass transition period, and the blue colour represents the period before the glass transition. The composite particles where the ignition occurs, $\tilde{T} < -2.5$ are removed in the figure. It is observed from the figure that the composite is ignited near the location of the localized fire.

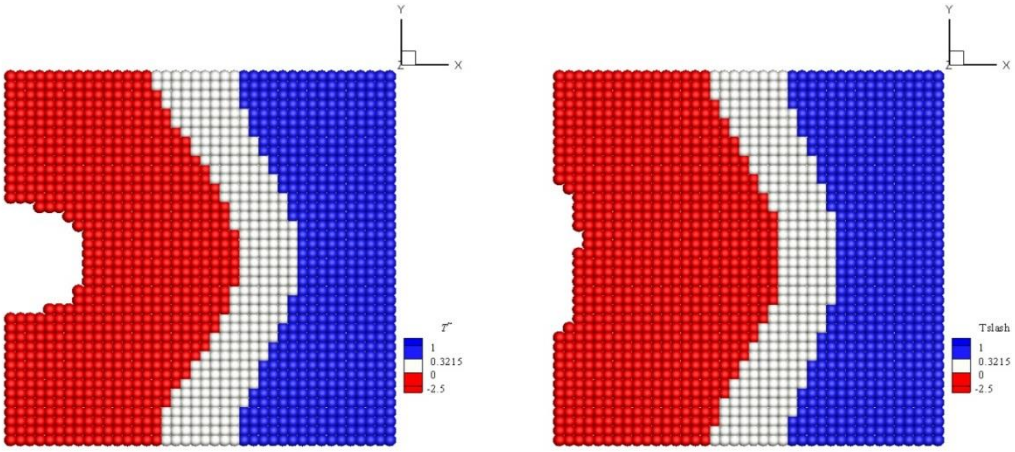

(a) bottom layer (b) middle layer

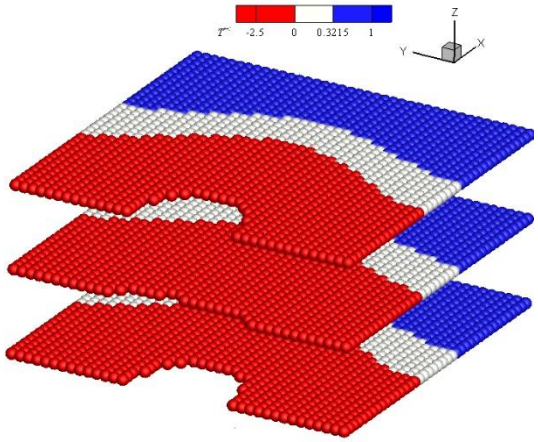

(c) 3D view of all the three layers

Fig. 8-17 The distribution of $\tilde{T}$ at $t = 500\,\mathrm{s}$

The matrix damage, interlayer normal damage, and interlayer shear damage in the mechanical field predicted at different times are provided in Fig. 8-18 and Fig. 8-19. During the early stage of the simulation, the crack does not occur until $t = 55\,\mathrm{s}$. Then the crack starts to propagate both in the plane and in the thickness direction.

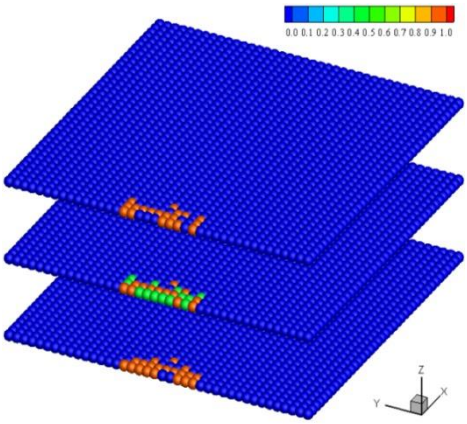

(a) Interlayer normal damage, φ_{in}

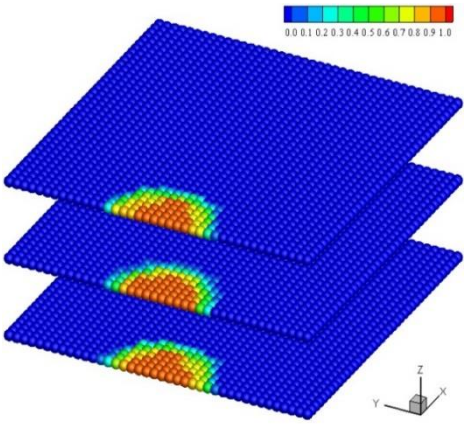

(b) Interlayer shear damage, φ_{is}

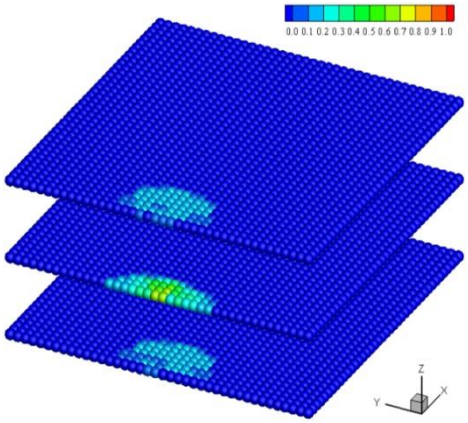

(c) Interlayer matrix damage, φ_m

Fig. 8-18 Composite mechanical local damage at 250 s

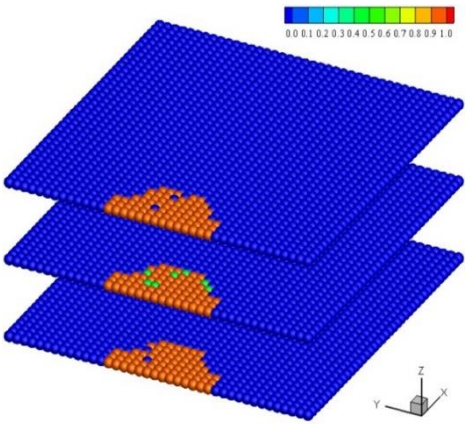

(a) Interlayer normal damage, φ_{in}

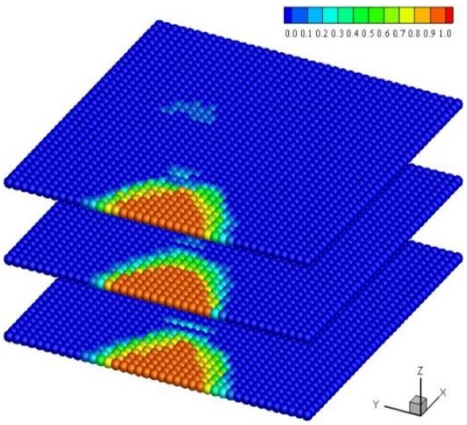

(b) Interlayer shear damage, φ_{is}

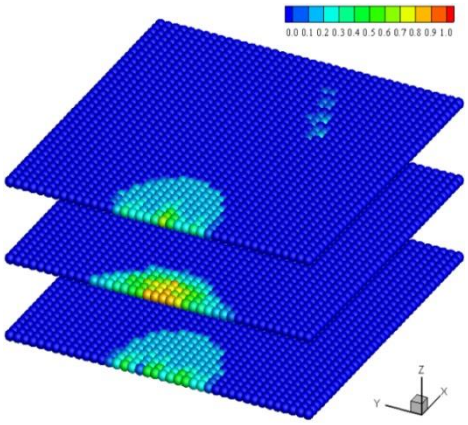

(c) Interlayer matrix damage, φ_m

Fig. 8-19 Composite mechanical local damage at 500 s

The displacements distributions at $t = 100\,\text{s}$ and $t = 500\,\text{s}$ are plotted in Fig. 8-20 and Fig. 8-21. Note that, the composite nodes where the ignition occurs, $\tilde{T} < -2.5$ and damage parameters, φ_m for matrix damage, φ_{in} for interlayer normal damage, and φ_{is} for interlayer shear damage are bigger than 0.5 are removed in both figures. It can be observed from the figures that the region near the local fire damages due to high temperature and mechanical deformation.

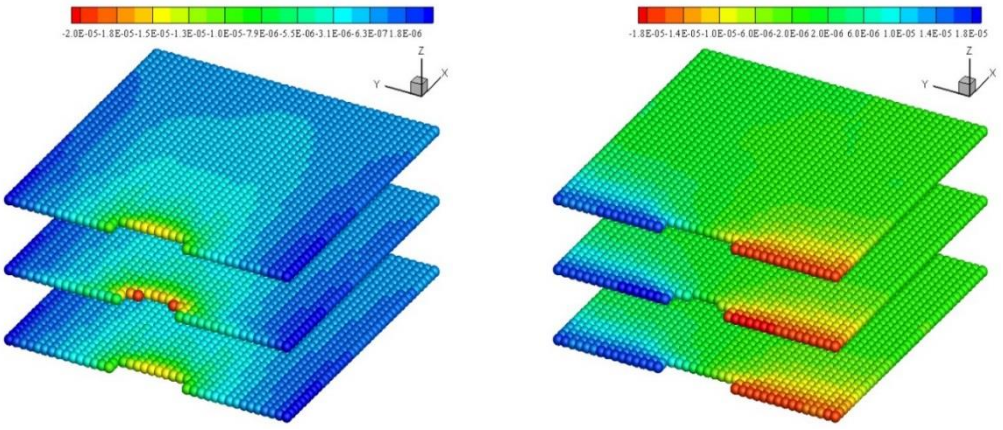

(a) (b)

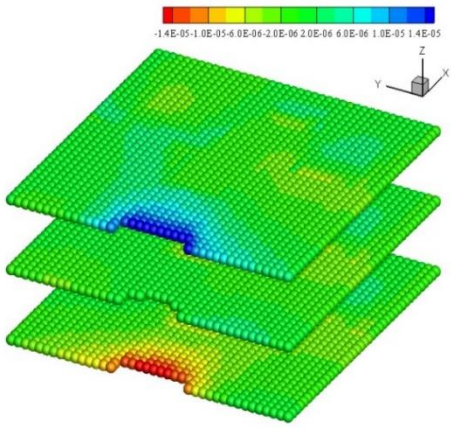

(c)

Fig. 8-20 Displacement distributions (m) at $t=100\,\mathrm{s}$: (a) in x direction, (b) in y direction, and (c) in z direction

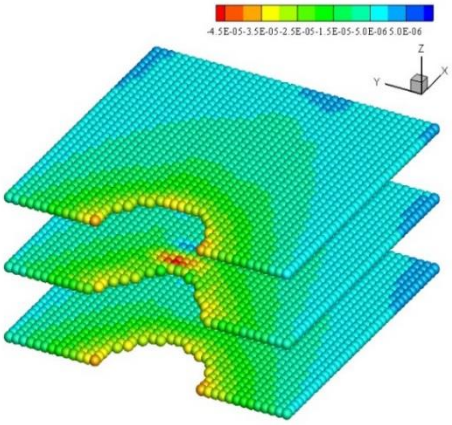

(a)

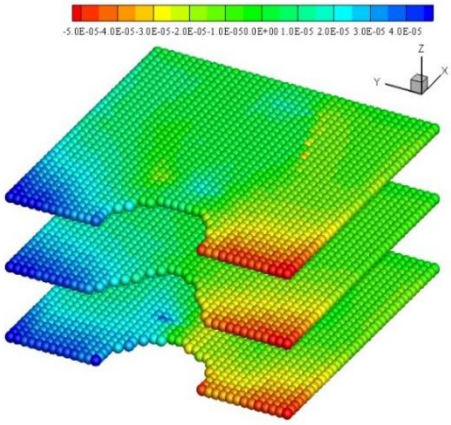

(b)

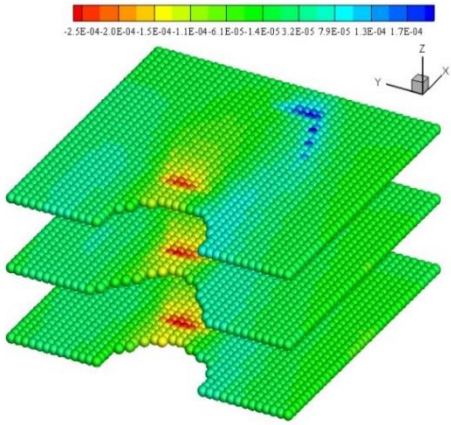

(c)

Fig. 8-21 Displacement distributions (m) at $t=500\,\mathrm{s}$: (a) in x direction, (b) in y direction, and (c) in z direction

8.4.2. Composite damage due to hot gas induced by fire

The moving fluid-structure interfaces are one of the typical features in many combustion applications, such as burning and melting surfaces [286]. In this example, the effect of hot gas induced by fire on the composite material is investigated. The hot gas fluid flow and composite model are coupled through the thermal field.

The composite material properties in Section 8.4.1 are used. The temperature profile provided in Eq.(8.1) is implemented at the boundary where fire is implemented. The air flow is assumed as two-dimensional. In this section, the one-way coupling approach for the thermal field is used. The heat transfer from composite to air is neglected, only heat transfer from air to composite is considered. It is assumed that the deformation of the composite does not affect the flow field. The composite deformation obtained in the previous problem is neglectable compared by its geometry dimensions, thus the composite mechanical deformation induced by the heated air is ignored in this problem.

8.4.2.1 Problem Description

The geometry of the problem is illustrated in Fig. 8-22. The air (shown in blue colour) is in a square solid cavity with its non-dimensional dimensions as L^*=W^*=1 and $h^*_{thick} = 0.015$. The three-layer composite laminate with the fibre orientation [0/90°/0] is clamped on the left vertical solid boundary (its top layer is illustrated in Fig. 8-22 by the green colour). The geometry length and width of the laminate are $L^*_s = W^*_s = 0.5$, and the thickness of each layer is $h^*_{thick,ply} = 0.005$. As shown in Fig. 8-22, the distance between the bottom boundary of the cavity and the bottom of the composite is $d^* = 0.25$. The length of the local fire region is set as $d^*_{fire} = 0.25$.

The horizon size is chosen as $\delta^* = 3.015\Delta x^*$ where the node spacing is $\Delta x^* = 0.0125$ for both composite and fluid flow simulations. The total time, $t^* = 0.25$, and time step size, $\Delta t^* = 1\times10^{-5}$ are chosen for simulating gas flow and heat conduction in composite material.

The non-dimensional parameters are set as Pr=0.713 and Ra=10^3 for air. The reference length is set as L_0=0.2 m. The reference velocity is calculated as $v_0 = \alpha_{f,0}/L_0 = 10^{-4}$ m/s with the viscous coefficient $\alpha_{f,0}$=2×10^{-5} m^2/s for air. Therefore, the non-dimensional simulation time $t^* = 0.25$ corresponds to 500 s. The artificial speed of sound is chosen as $c_{sound} = 10v_0$ [142].

The reference temperature and initial temperature are chosen as $T_s^0 = T_{s,ref} = 293\text{K}$, i.e. $T^* = 0$ for the initial condition. The boundary conditions are also provided in Fig. 8-22 with grey colour representing the insulated boundary condition, the red one representing the local fire boundary, and the yellow one representing the composite-fluid interface, expressed as

Thermal field:

$x^* = 0$ and $x^* = L^*$

$$\frac{\partial T^*}{\partial x^*} = 0 \tag{8.43}$$

$y^* = 0$

$$\begin{aligned} &x^* \le d_{fire}^* : T^* = T_{fire}^*\left(t^*\right) = \frac{345\log\left(8\times2000\times t^*/60+1\right)}{T_0};\ 0 < t^* < 0.25 \\ &x^* > d_{fire}^* : \frac{\partial T^*}{\partial x^*} = 0 \end{aligned} \tag{8.44}$$

$y^* = W^*$

$$\frac{\partial T^*}{\partial y^*} = 0 \tag{8.45}$$

Mechanical field:

$$x^* = 0;\ x^* = L^*;\ y^* = 0;\ y^* = W^* : \mathbf{u}^* = 0 \tag{8.46}$$

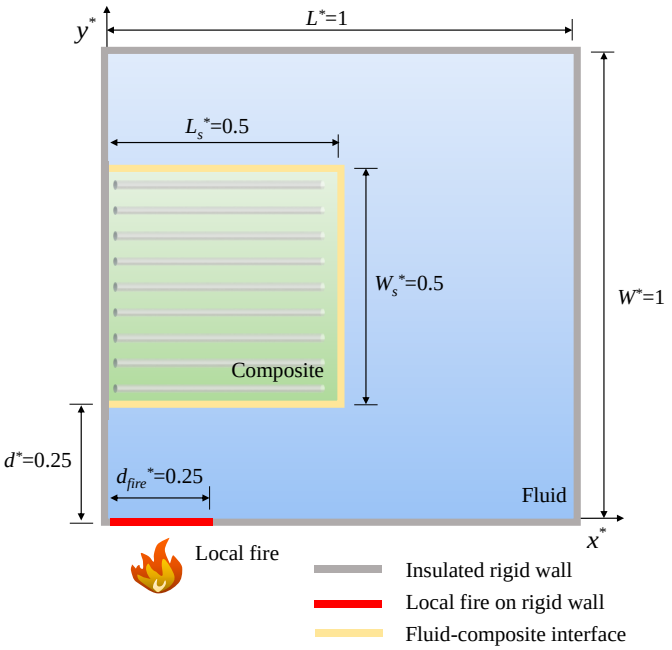

Fig. 8-22 Geometry illustration for composite and fluid coupling response under the fire scenario

As observed in Section 8.4.1, the deformation of composites under fire is relatively small in the in-plane layers compared to its geometry dimensions. Therefore, the composite deformation effect on the fluid field is ignored in the current study for simplicity. For flow simulations, the composite-fluid interface is assumed as a rigid solid wall, as shown in Fig. 8-23 (a).

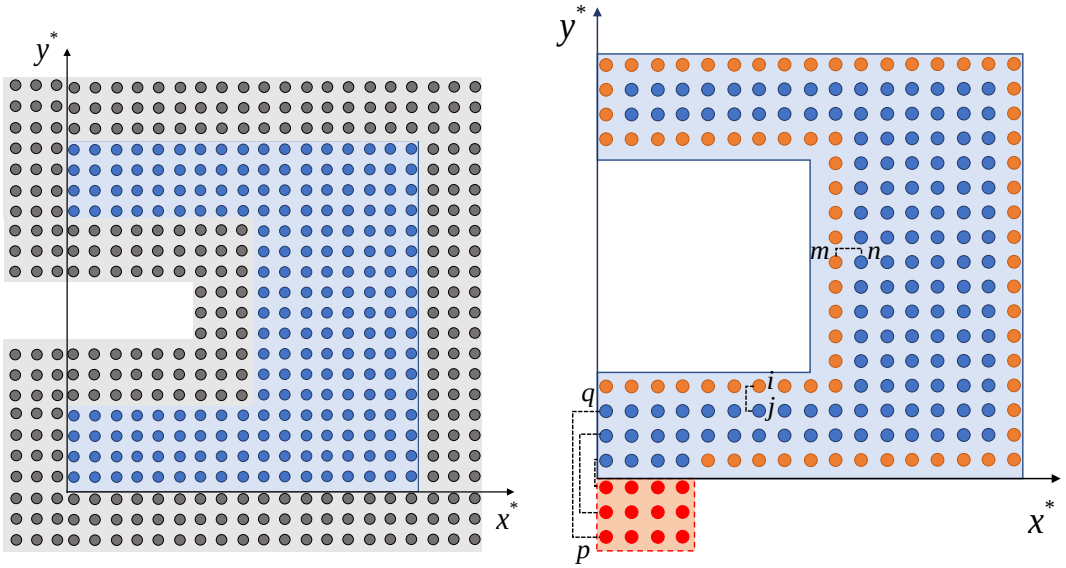

(a) (b)

Fig. 8-23 PD points for (a) fluid flow field and (b) thermal field

In the mechanical field, all the velocities and displacements of the particles belonging to the fictitious solid wall layers keep zero throughout the simulation process, i.e. the solid boundary conditions are (grey points in Fig. 8-23 (a)):

At $x^* = L^*$; $y^* = 0$; $y^* = W^*$; $x^* = 0, y^* < d^*$; $x^* = 0, y^* > W^* - d^*$; $x^* = L_s^*, d^* \le y^* \le W^* - d^*$; $0 < x^* \le L_s^*, y^* = d^*$ and $0 < x^* \le L_s^*, y^* = W^* - d^*$:

$$\mathbf{u}_f^* = 0 \tag{8.47}$$

In the fluid thermal field, the thermal boundary conditions are

At $x^* = 0, y^* < d^*$ '; $x^* = 0, y^* > W^* - d^*$; $x^* = L_s^*, d^* \le y^* \le W^* - d^*$ and $x^* = L^*$ (orange points in Fig. 8-23 (b)):

$$\frac{\partial T_f^*}{\partial x^*} = 0 : T_{f,m}^* = T_{f,n}^* \text{ for pairwise points} \tag{8.48}$$

At $0 < x^* \le L_s^*, y^* = d^*$; $0 < x^* \le L_s^*, y^* = W^* - d^*$; $y^* = W^*$; $y^* = 0, x^* \ge d_{fire}^*$ and $x^* = L^*$ (orange points in Fig. 8-23 (b)):

$$\frac{\partial T_f^*}{\partial y^*} = 0 : T_{f,i}^* = T_{f,j}^* \text{ for pairwise points} \tag{8.49}$$

At $y^* = 0, x^* < d_{fire}^*$ (for red points in Fig. 8-23 (b)):

$$T_{f,p}^* = 2T_{fire}^*\left(t^*\right) - T_{f,q}^* \tag{8.50}$$

The composite material is the same as the one in Section 8.4.1. Regarding the composite PD model, the composite points' initial spacing is the same as the fluid spacing, i.e. $\Delta x^* = 0.0125$ with $40 \times 40 \times 3$ nodes. The location $z = 0$ is in the midplane of the composite model.

The front view of the composite model for the mechanical field and thermal field is provided in Fig. 8-24, respectively. In Fig. 8-24 (a), the fictitious layers on the left represent the vertical solid wall, and the green points represent the composite laminate. In Fig. 8-24 (b), no fictitious layer is added in the thermal field. The orange points in Fig. 8-24 (b) are under insulated-boundary conditions while the purple points are under the convective and radiation condition related to the fluid flow.

Thermal boundary conditions are:

At $x^* = 0$

$$\frac{\partial T_s^*}{\partial x^*} = 0 : T_{s,i}^* = T_{s,j}^* \text{ for pairwaise points} \tag{8.51}$$

At $x^* = L_s^*$, $y^* = d^*$, and $y^* = W^* - d^*$

$$\begin{aligned} h_s^*\left(\mathbf{x}_{s,interface}^*, t^*\right) = &-\frac{1}{\Delta x^*} h_{con}^*\left(T_s^*\left(\mathbf{x}_{s,interface}^*, t^*\right) - T_{f,local}^*\right) \\ &+ \sigma_{stefan-boltzmann}^* \varepsilon \frac{1}{\Delta x^*}\left(\left(T_{f,local}^*\right)^4 - \left(T_s\left(\mathbf{x}_{s,interface}^*, t^*\right)\right)^4\right) \end{aligned} \tag{8.52}$$

Mechanical boundary conditions:

At $x^* = 0$

$$\mathbf{u}_s^* = 0 \tag{8.53}$$

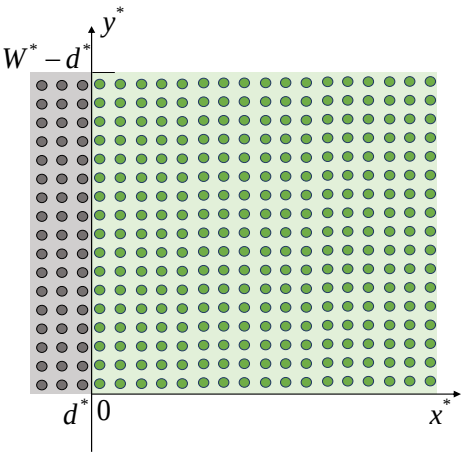

(a)

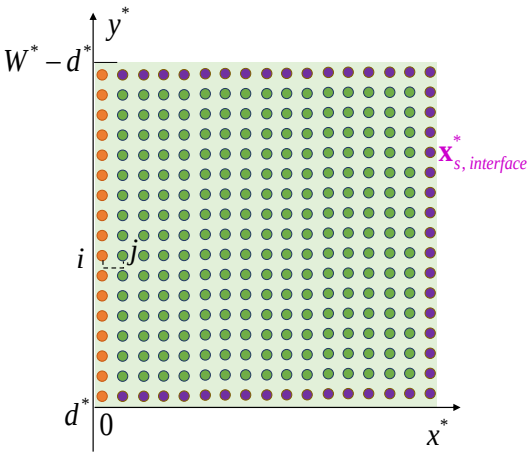

(b)

Fig. 8-24 PD material points for (a) composite mechanical field, (b) composite thermal field

8.4.2.2 Numerical Procedure

The flowchart for problem 8.4.2 is provided in Fig. 8-25. First, the thermo-fluid flow is simulated in a non-dimensional form under the fire boundary condition. Thus, the dimensionless temperature profiles of the fluid are predicted. Subsequently, the heat is transferred from the fluid field to the composite through the convection and radiation interface boundaries. The dimensionless temperature change in the composite is predicted by solving the composite heat conduction equation under the interface boundary condition. Then the dimensionless temperature of the composite is converted into its dimensional value, in order to update the composite material properties both including the thermal properties and the mechanical properties. This procedure, i.e. thermo-fluid flow and composite heat conduction, is performed every time step as a transient analysis. Subsequently, being same as Section 8.4.1, the deformation of the PD composite model due to the temperature change is predicted by using the ADR technique [87] for each 100 seconds as a quasi-static analysis. The composite mechanical analysis is performed in a dimensional form by using the converted dimensional temperature profiles. Besides, it should be noted that the non-dimensional values of the composite geometry are used in the composite mechanical analysis, which can be treated as a geometry scaled model. Therefore, the predicted deformation such as displacement is also scaled.

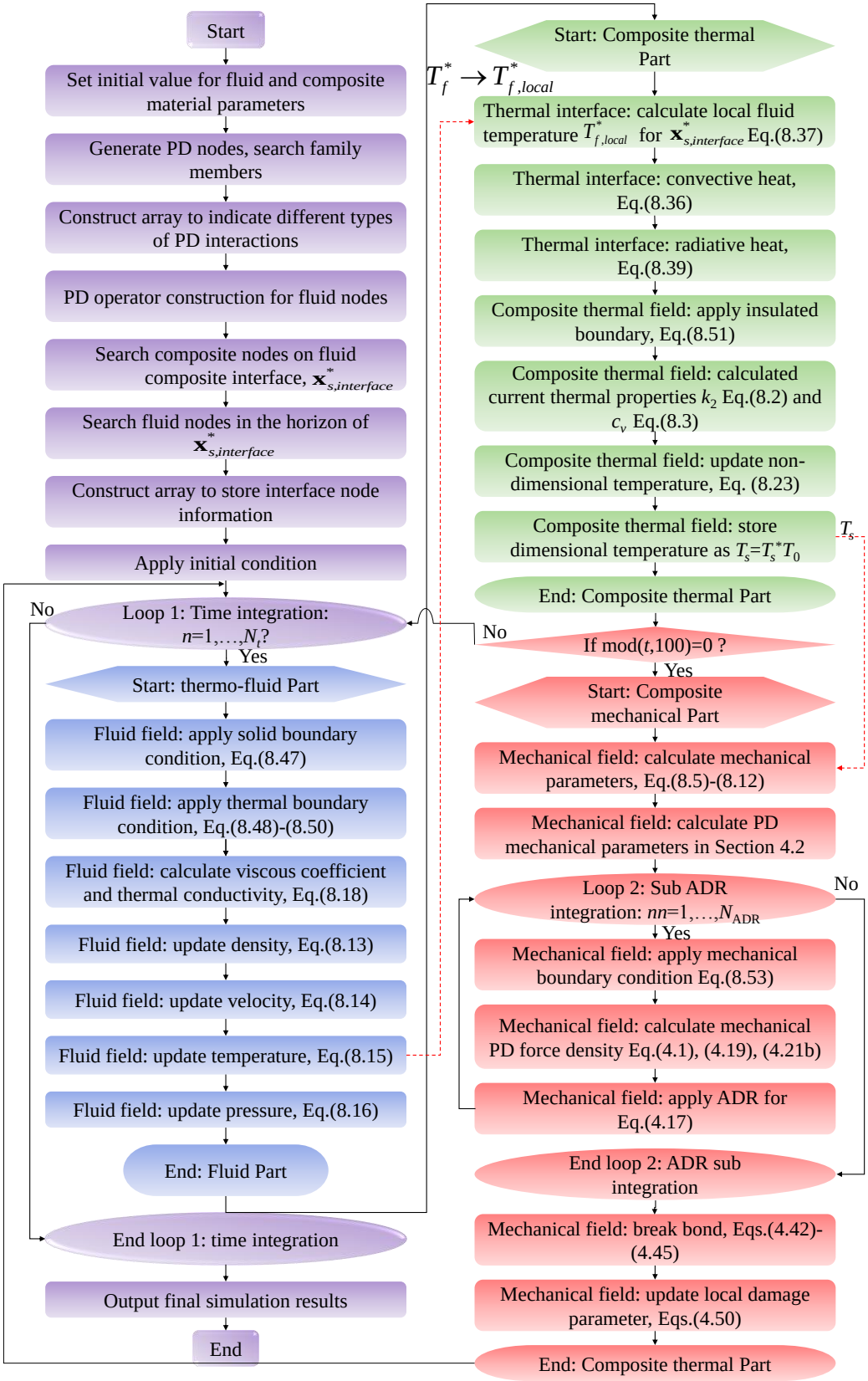

Fig. 8-25 Flowchart for the coupled thermo-fluid model for air and thermo-mechanical model for composite for problem 8.4.2

8.4.2.3 Numerical results

The temperature profiles in fluid with respect to the reference temperature, $\left(T_f - T_{ref}\right)$ are provided in Fig. 8-26. In order to be comparable to the fire temperature-time curve, the real values of the temperature at different times are provided. It can be observed from Fig. 8-26 that the interface between the composite bottom edge and fluid suffers the high temperature while the temperatures around other interfaces are relatively low.

Non-dimensional velocity profiles of fluid at different times are provided in Fig. 8-27. The fluid flows due to the temperature difference between boundaries. The largest velocity occurs just below the composite bottom edge at $t^* = 0.05$. Then the air will flow up due to the temperature difference between the high temperature on the bottom and the relatively low temperature on the top. In this example $\mathrm{Ra} = 10^3$ is used and it is much smaller than $\mathrm{Ra} = 10^6$ for turbulent flow [166], therefore the fluid flow shown in Fig. 8-27 is laminar.

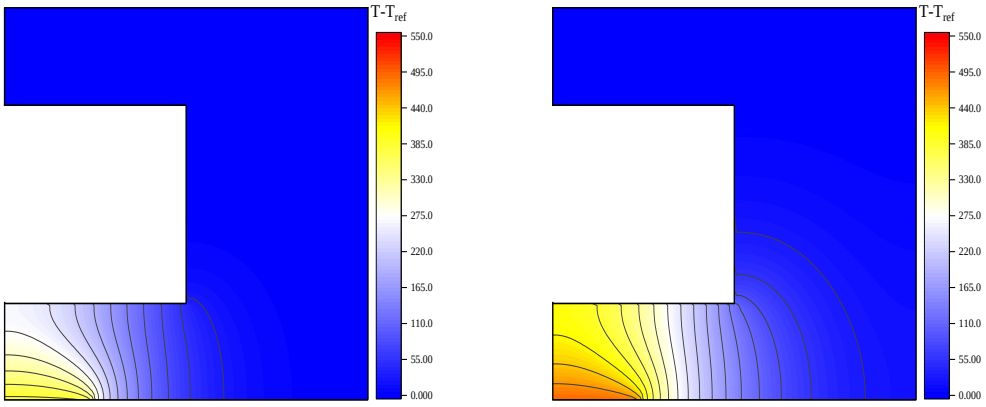

(a) (b)

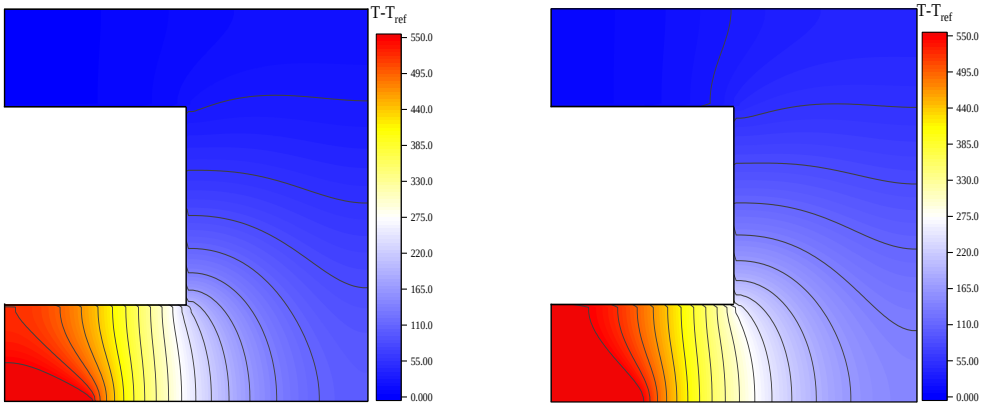

(c) (d)

Fig. 8-26 Temperature profiles in fluid with respect to reference temperature, $\left(T_f - T_{ref}\right)$ at time (a) $t = 100\,\text{s}\left(t^* = 0.05\right)$, (b) $t = 200\,\text{s}\left(t^* = 0.1\right)$, (c) $t = 400\,\text{s}\left(t^* = 0.2\right)$, and (d) $t = 500\,\text{s}\left(t^* = 0.25\right)$

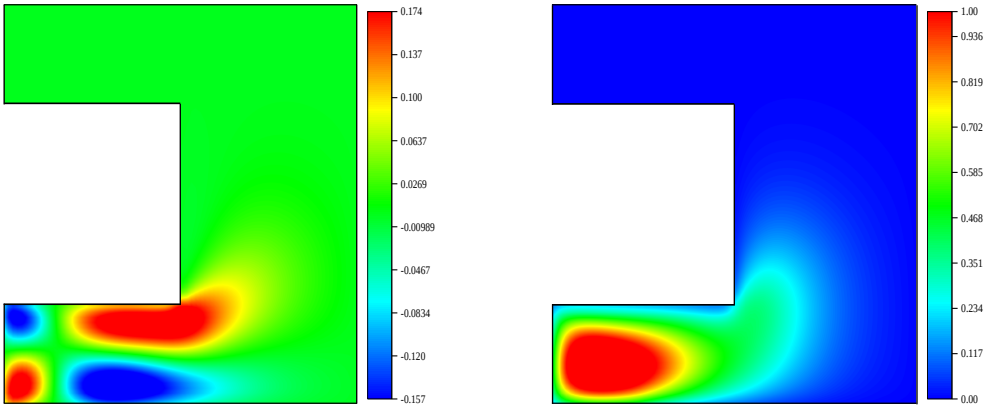

(a) v_x^*, at $t^* = 0.05$ (b) v_y^*, at $t^* = 0.05$

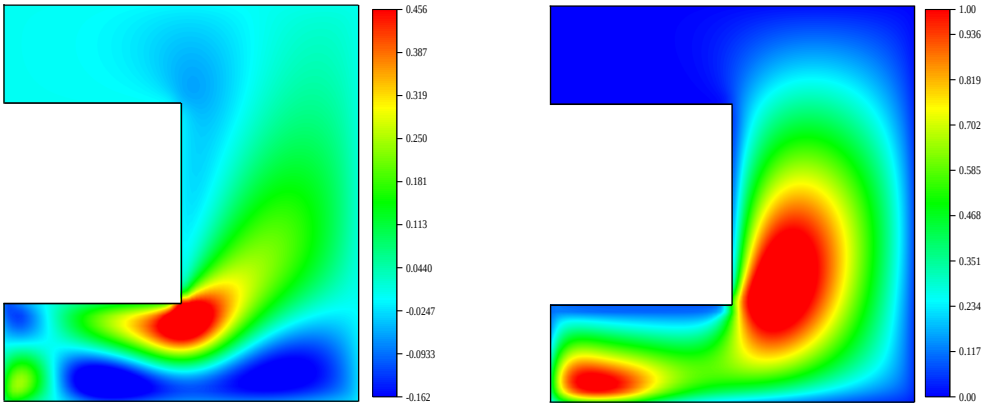

(c) v_x^*, at $t^* = 0.1$ (d) v_y^*, at $t^* = 0.1$

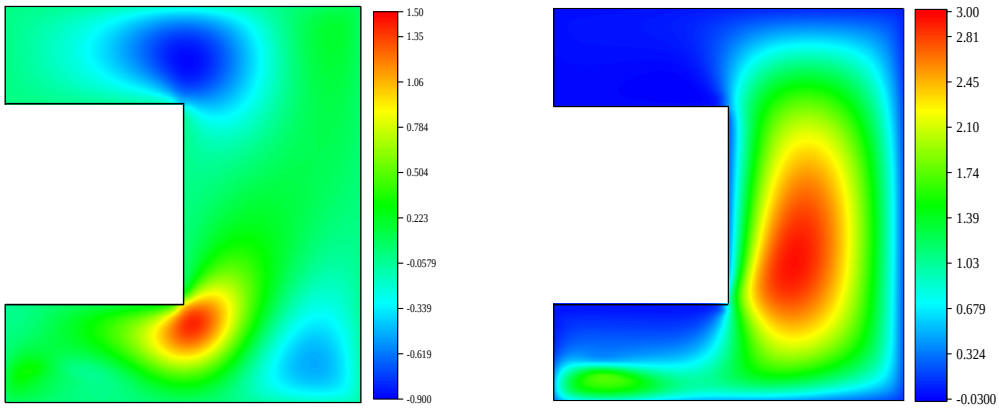

(e) v_x^*, at $t^* = 0.2$ (f) v_y^*, at $t^* = 0.2$

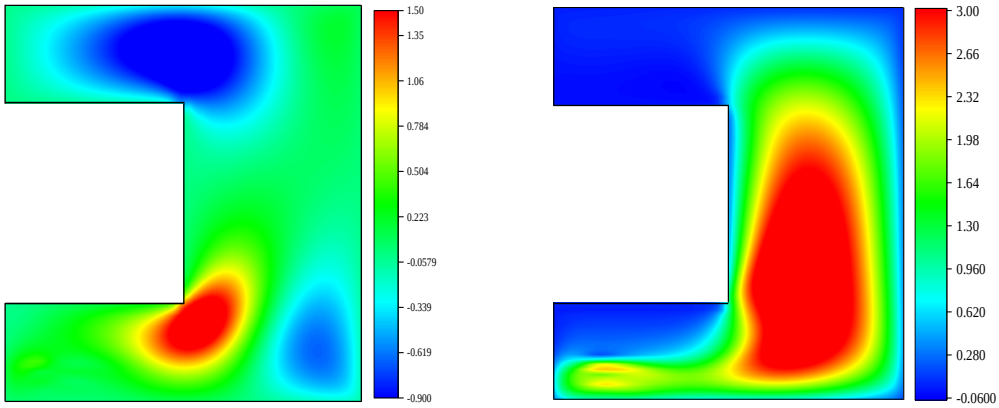

(g) v_x^*, at $t^* = 0.25$ (h) v_y^*, at $t^* = 0.25$

Fig. 8-27 Non-dimensional velocity profiles of fluid at different times

Regarding the thermal field of the composite laminate, the temperature profiles in composites with respect to the reference temperature are provided in Fig. 8-28 at different times. It can be observed from Fig. 8-28 that due to the anisotropic property and different stacking sequence of the laminates, the temperature distributions are different for different layers at the same time. The rate of temperature rise is relatively small due to the small local fired region and the low thermal conductivity of composite materials used in the present study. According to the investigation performed in [280], the temperature rising rate of the average temperature of the same composite material is only 0.07 K/s [280]. In this example, the rising rate is 0.085 K/s for the bottom layer and 0.061 K/s for the middle layer, which is consistent with the investigation in [280]. In the previous example in Section 8.4.1, the temperature rising rate of the average temperature of laminates is 0.21 K/s. Compared to the previous problem in which the composite is directly imposed under the fire-induced temperature boundary condition,

the temperature rise in this simulation case is much smaller. Furthermore, no damage due to melting of composite material is observed.

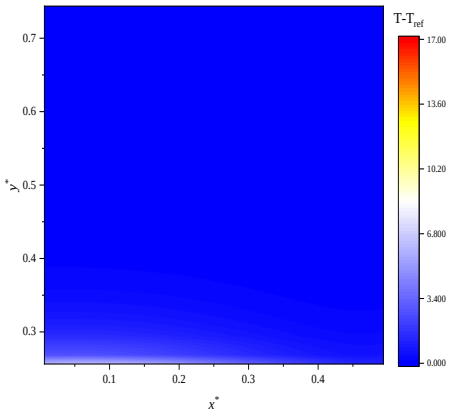

(a) bottom layer, at $t = 100$ s

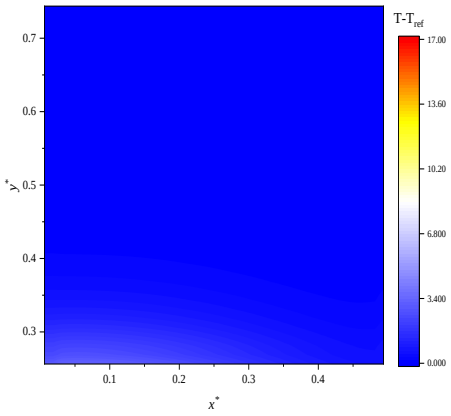

(b) middle layer, at $t = 100$ s

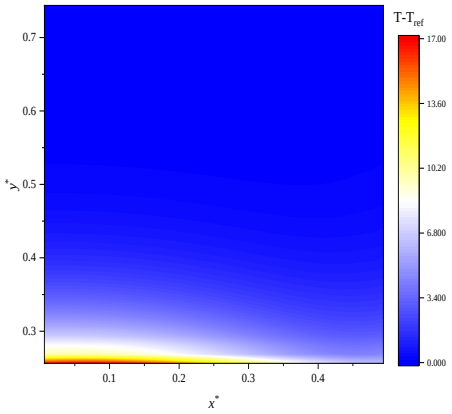

(c) bottom layer, at $t = 200$ s

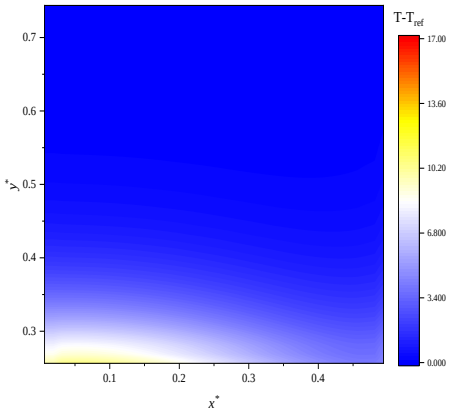

(d) middle layer, at $t = 200$ s

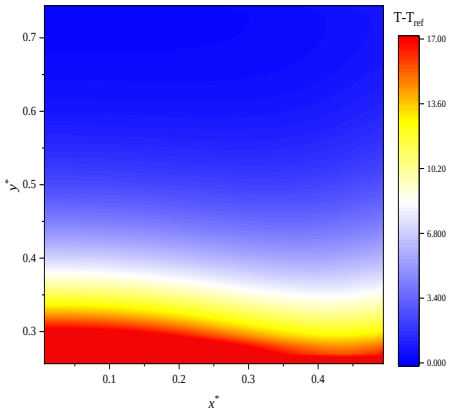

(e) bottom layer, at $t = 400$ s

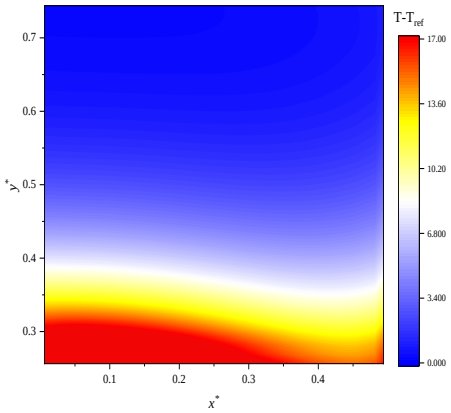

(f) middle layer, at $t = 400$ s

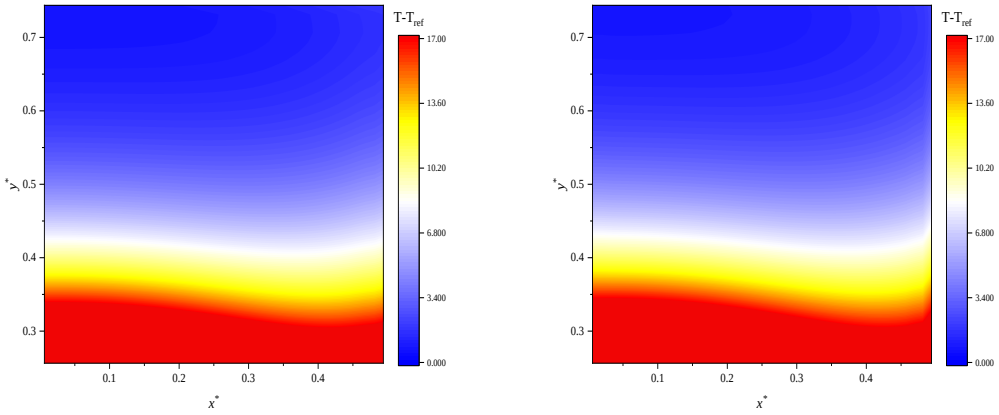

(g) bottom layer, at $t = 500\,\mathrm{s}$ (h) middle layer, at $t = 500\,\mathrm{s}$

Fig. 8-28 Temperature profiles in composite with respect to the reference temperature T_{ref}, $\left(T_s - T_{ref}\right)$, at different times

The deformation of the composite is predicted for each 100 seconds by using the ADR approach [87]. The total number of iterations in one ADR performance is $N_{ADR} = 4000$. Fig. 8-29 represents the convergence of displacement fields for ADR [87] simulations at time $t^* = 0.25$. The non-dimensional displacements of the three-layer composite at different times are provided in Fig. 8-30-Fig. 8-31. The deformed shape at the final stage is provided in Fig. 8-32. It can be observed from the figure that the delamination tends to occur in the heated region because of the thermal expansion.

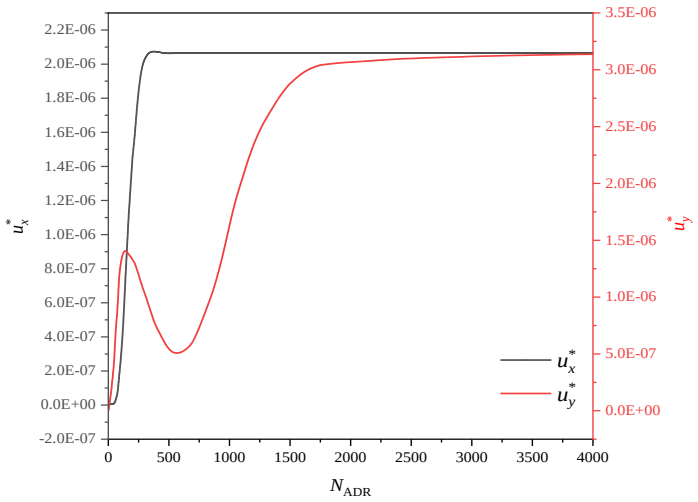

Fig. 8-29 Convergence of non-dimensional displacement fields for ADR [87] at $t^* = 0.25$

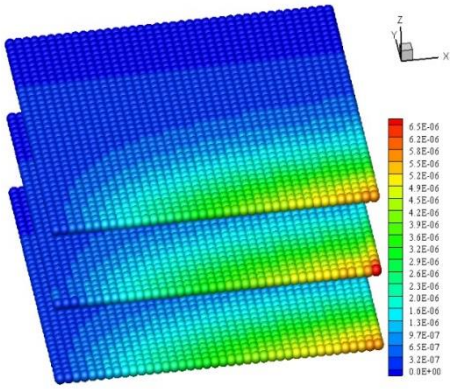

(a) u_x^*

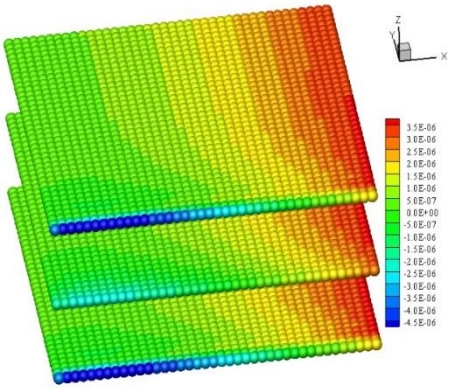

(b) u_y^*

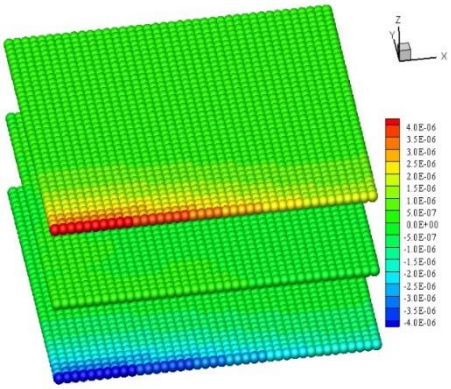

(c) u_z^*

Fig. 8-30 Non-dimensional displacement distribution at $t^* = 0.1$

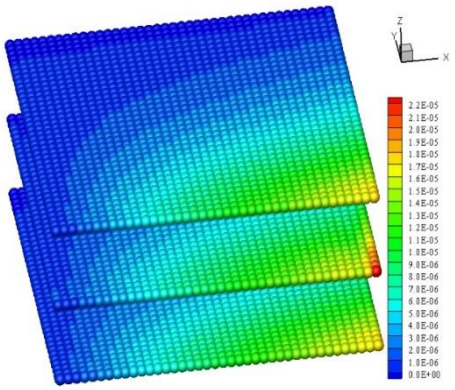

(a) u_x^*

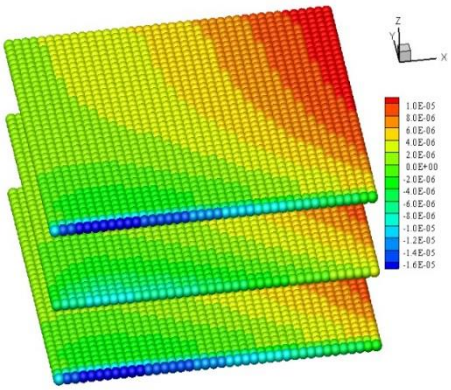

(b) u_y^*

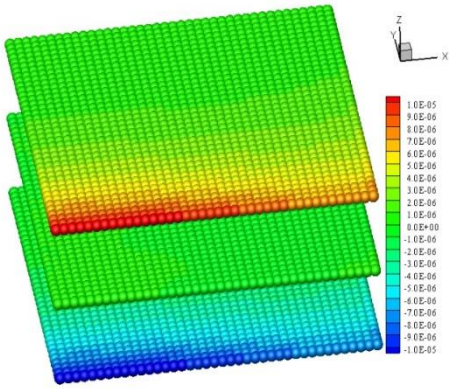

(c) u_z^*

Fig. 8-31 Non-dimensional displacement distribution at $t^* = 0.25$

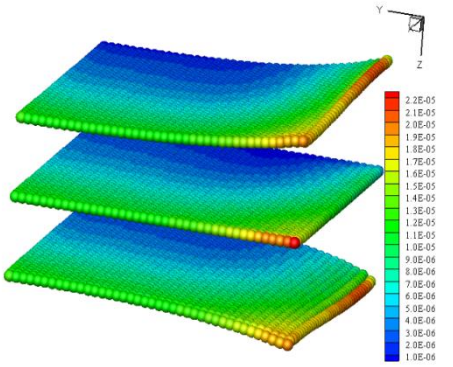

Fig. 8-32 Deformed shape at $t^* = 0.25$ (displacement scale factor 200 for deformed shape)

8.5. Summary

In this chapter, the developed PD composite model and thermo-fluid model are coupled together to predict the composite response under the fire scenario. The thermal degradations of composite material properties are incorporated into the peridynamic composite model. The ISO standard temperature-time curve is adopted to represent the fire-induced high temperature. The fluid model coupled with heat transfer is utilized to represent the physical fire model. Two problems are investigated in the present chapter, i.e. composite damage due to direct contact with fire and composite damage due to hot gas induced by fire. The convective and radiative boundary conditions are implemented by coupling the thermo-fluid model with the composite model.

9. Conclusion

9.1. Achievements against the objectives

The goal of this research is to predict the composite damage under fire scenario by using one methodology, i.e. peridynamic theory. Therefore, the peridynamic theory which is originally proposed for solid mechanics is extended to the fluid mechanics to model the fire physical properties. Furthermore, the fluid-structure interaction algorithm in the framework of peridynamic theory is also developed, which can be further generally applied to the FSI engineering problems. The main achievements against the research objectives are listed as follows:

- An OSB PD fully coupled thermomechanical model for isotropic material is developed. The coupling terms including the thermal effect on solid deformation and the mechanical deformation effect on temperature are involved in the OSB-PD model. The PD expressions of the thermal modulus for 1D, 2D, and 3D problems are first time derived in OSB-PD theory. Then several benchmark problems are solved by using the developed model, e.g. three-point bending problem, Kalthoff plate problem etc.
- An OSB PD fully coupled thermomechanical model for laminated composite materials is developed. The direction-dependent properties of the composite materials are taken into consideration. The PD thermal conductivity formulation for interlayer heat conduction is derived for the first time. Furthermore, the PD thermal modulus for composite materials in the OSB-PD framework is firstly derived.
- A single-phase fluid model is developed based on the peridynamic differential operator. The Navier-Stokes equations are reformulated into a non-local form expressed by the peridynamic differential operator. The developed model is applied to solve some benchmark problems in fluid mechanics including a free surface fluid flow.
- A heat-conducting fluid model is developed for fluid flow coupled with heat transfer problems by using the peridynamic differential operator. The heat conduction and fluid flow are simulated in a simultaneously way. The

developed model is applied to solve some benchmark problems, i.e. natural convection and mixed convection.

- A peridynamic model is developed for multiphase fluid flow problems by using the peridynamic differential operator. The surface tension force is included in the fluid flow governing equations. The developed model is applied to solve the classical problems, e.g. two-phase hydrostatic problem, two-phase Poiseuille flow, and 2D droplet deformation.
- A peridynamic model is developed for fluid-structure interaction problems. The structure is modelled by using the ordinary state-based peridynamic theory, while the fluid is modelled by using the peridynamic differential operator. The interface between the fluid and the structure is traced by using the colour function gradient. Then the developed model is applied to simulate the water column collapse under a rubber gate.
- The composite response under fire scenario is simulated by using the previous composite model and fluid model. The thermal degradation properties of the composite are incorporated into the original composite model. The problems of the composite are directly and indirectly under a fire-induced high-temperature boundary condition are investigated.

9.2. Novelty and contribution

The existing peridynamic model for fully coupled thermomechanical models is in the bond-based form. Therefore, the Poisson's ratio of the solid material is forced to be 1/3 for 2D problems and 1/4 for 3D problems. By using the ordinary state-based peridynamic theory, an OSB PD fully coupled thermomechanical model is developed to fill the gap. The developed model has been successfully applied to solve some benchmark problems in a fully coupled thermomechanical fashion, which is published in [5].

The composite materials are widely used in the engineering field, due to their high strength to weight ratio and other high-performance properties. The prediction of crack propagation of composite materials is important especially under extremely harsh conditions, e.g. high-temperature environments. The fully coupled thermomechanical

composite model in ordinary state-based peridynamic theory is not available in the published literature. Therefore, based on the previous fully coupled thermomechanical bond-based peridynamic model, an ordinary state-based peridynamic fully coupled thermomechanical model is developed for composite materials. In addition to involving the coupling terms between the mechanical field and the thermal field, the anisotropic material properties of the composites are also included in the developed model. The developed model is fully validated and applied to predict crack propagation in a fully coupled manner. The relevant study is published in [6]. As an application example, the crack propagation and temperature variation of a 13-layer laminate are simulated under underwater explosion pressure conditions. This study is published in [7].

The peridynamic theory is originally proposed for solid mechanics. Aa a result, as a computational mechanics method, its application on fluid mechanics field is still limited. A viscous fluid model in laminar flow condition is developed by using the PDDO for the first time. The fluid flow governing equations, i.e. Navier-Stokes equations, are reformulated into an integral form. Furthermore, the second-order derivatives in the N-S equations can be approximated by one integration with the help of high order PDDO. Some benchmark problems in fluid mechanics have been successfully solved by using the new PDDO fluid model, validating the capability of the developed model. The relevant study is published in [8].

The heat-conducting fluid flow is a multi-physics subject, involving the knowledge of fluid mechanics and thermodynamics. A peridynamic model which can be applied for the fluid flow coupled with heat transfer problems is not available in the published literature. Based on the fluid PDDO model, a heat-conducting fluid PDDO model is developed for the first time. The fluid flow governing equations and the heat conduction equation are coupled in the model. The classical problems, e.g. natural convection and mixed convection are solved by using the developed model on different Rayleigh numbers. The relevant work is published in [9].

The simulation of the multi-phase fluid flow is a complex task. Based on the PDDO single-phase fluid model, a multi-phase fluid PDDO model including the surface

tension force is developed for the first time. Furthermore, some numerical techniques such as particle shifting technique are reformulated by using the PDDO. The interface normal direction is calculated by using the colour function gradient which is also reformulated to a PDDO form. Some classical multi-fluid problems are solved, validating the accuracy of the multi-phase fluid PDDO model. The relevant work is written as a journal paper which is under review.

The fluid-structure interaction is often encountered in the engineering field. It will be convenient for one to use a single methodology to simulate these FSI problems. Furthermore, when structural damage is involved in the problem, it becomes more complex and challenging work. The peridynamic theory has the advantage over the classical continuum mechanics on the damage prediction, because of the integral form of the equation of motion. However, an FSI PD model which can simultaneously predict the solid deformation and fluid motion, as well as including the interactions, is not available in the published literature. Therefore, a peridynamic model is developed for fluid-structure interaction problems. The existing ordinary state-based PD model is adopted for the isotropic solid. The PDDO fluid model is utilized in the FSI PD model. Then an algorithm to couple the OSB-PD solid model and PDDO fluid model is developed. Furthermore, the interface is tracked simultaneously. The developed PD model is successfully applied to solve FSI problems. The relevant work is written as a journal paper which is under review.

The simulation of the response of composite material in fire environments is a meaningful research topic in terms of safety. Therefore, a numerical algorithm is developed to investigate the composite material response under fire boundary condition. However, no PD model is available for this case which belongs to the field of thermal fluid-structure interactions. Therefore, a novel PD model is developed for this problem. First, the thermal degradation properties of composites are implemented into the existing composite PD model. Then the composite response directly under fire-induced temperature boundary condition is investigated. The thermal status such as glass transition, the thermal expansion as well as the crack propagation of the composite is studied. Second, the fluid model is utilized to represent the physical model of the fire. The air is heated by the localized fire temperature boundary condition.

Then the composite deforms under the heated air. The heat conduction within the composite and the deformation of the composite are simulated. The convection and radiation between the air and the composite are considered. This study will be the first one to investigate the composite response under fire using the peridynamic theory. The related study is written as a journal paper which is under review.

9.3. Publications from PhD thesis

Journal Papers

[P1] Y. Gao, S. Oterkus, Peridynamic Analysis of Marine Composites under Shock Loads by Considering Thermomechanical Coupling Effects, Journal of Marine Science and Engineering, 6 (2018) 38.

[P2] Y. Gao, S. Oterkus, Ordinary state-based peridynamic modelling for fully coupled thermoelastic problems, Continuum Mechanics and Thermodynamics, 31 (2019) 907-937.

[P3] Y. Gao, S. Oterkus, Non-local modelling for fluid flow coupled with heat transfer by using peridynamic differential operator, Engineering Analysis with Boundary Elements, 105 (2019) 104-121.

[P4] Y. Gao, S. Oterkus, Nonlocal numerical simulation of low Reynolds number laminar fluid motion by using peridynamic differential operator, Ocean Engineering, 179 (2019) 135-158.

[P5] Y. Gao, S. Oterkus, Fully coupled thermomechanical analysis of laminated composites by using ordinary state-based peridynamic theory, Composite Structures, 207 (2019) 397-424.

[P6] Y. Gao, S. Oterkus, Multi-phase fluid flow simulation by using the peridynamic differential operator. (under review)

[P7] Y. Gao, S. Oterkus, Fluid-structure interaction simulation by using the peridynamic theory. (under review)

[P8] Y. Gao, S. Oterkus, Thermal fluid-structure simulation of composites under the fire scenario. (under review)

Conference Papers

[P9] Y. Gao, S. Oterkus, Thermomechanical Analysis of Composites Under Shock Load Using Peridynamics, in: The 28th International Ocean and Polar Engineering Conference, International Society of Offshore and Polar Engineers, Sapporo, Japan, 2018, pp. 8.

9.4. Gaps and recommended future work

Concerning the fully coupled thermomechanical PD models for composite materials, parallel computing can be adopted to save the computational time. For example, the numerical simulations for the 13 ply laminates take approximately 3 days for sequential computing. The computation time can be reduced to less than 1 day when parallel computing is used with 4 cores.

Concerning the PDDO single-phase fluid model, the model can be extended for high Reynolds number laminar flow. Even the turbulent flow can be investigated by incorporating the turbulent model into the governing equations. It should be noted that, for a high Reynolds number laminar flow or turbulent flow, a stable algorithm regarding the numerical implementation is required when the peridynamic particles are in a highly distorted distribution.

Concerning the PPDO heat-conducting fluid model, more numerical simulations can be done. For example, the effects of different type of boundary conditions, e.g. convective boundary, radiative boundary on the fluid flow can be investigated.

Concerning the PDDO multi-phase fluid model, more numerical simulations can be performed to validate the model, e.g. Rayleigh Taylor instability problem, air bubble rising in a water column.

Concerning the fluid-structure interaction PD model, more numerical simulations can be performed to validate the model. Furthermore, the structure failure can be

simply incorporated into the current model, which can reflect the advantages of the PD theory where the integral equations remain valid regardless of discontinuities. Besides, the current FSI PD model can be more efficient by setting different mesh sizes for critical regions and other regions. For example, the fluid and structure interaction region can have a fine mesh while the other parts with less motion or deformation can have a relatively coarse mesh, in order to make simulations more efficient.

The current fluid-related PDDO models, i.e. the single-phase fluid model, the heat-conducting fluid model, the multi-phase fluid model, and the fluid-structure interaction model, are all applied to 2D fluid flow simulations. Therefore, the 3D fluid flow can also be simulated by simply extending the current 2D fluid models.

Concerning the simulation of the composite response under fire scenario, the experimental validation is required. In addition, the following aspects can be considered for further PD study on this topic. Firstly, the fire can be represented by a multi-phase, multi-component, heat-conducting, and chemical reactive fluid flow. Currently, only the heat-conducting property is incorporated into the fluid flow to represent the fire. Consequently, the current fire model can be extended by involving the other properties to represent fire realistic properties. For example, the solid components can be considered within the fluid flow by using the multi-species fractions and diffusion velocity. The chemical reaction can also be included as a heat-generating source in the conservation of energy equation. Secondly, the thermal coupling between the composite model and the fluid model is considered in a one-way approach. Only the temperature of the fluid influences the thermal field of composites. Therefore, for further study, the two-way coupling can be considered which will be more realistic. Thirdly, because the deformation of the composite under fire is negligible, the coupling between the fluid flow and composite deformation is not considered in the thermal fluid-structure interaction simulation for composite under the fire scenario. Hence, the fluid-structure interaction algorithm developed in this thesis can be incorporated into the composite-fire simulation when the deformation coupling effect cannot be ignored.

9.5. Final remarks

The ultimate problem to be solved in this thesis is the prediction of the composite material response under fire scenario, which is a multifield topic including solid mechanics, thermodynamics, fluid mechanics, and their coupling terms. In order to solve this problem, the application field of the peridynamic theory is extended to the fluid mechanics, i.e. developing a single-phase fluid model, a multi-phase fluid model, a fluid flow coupled with heat transfer model, a fluid-structure interaction model. Furthermore, the ordinary state-based peridynamic model for fully coupled thermomechanics is developed both for isotropic materials and laminated composites. Finally, the investigation of composite response under fire scenario is conducted by combining the developed PD fluid model and composite model.

References

[1] Kaw AK. Mechanics of composite materials: CRC press, 2005.

[2] Luo C, Desjardin P. Thermo-mechanical damage modeling of a glass–phenolic composite material. Composites Science and Technology. 2007;67:1475-88.

[3] Mouritz AP, Gibson AG. Fire properties of polymer composite materials: Springer Science & Business Media, 2007.

[4] Silling SA. Reformulation of elasticity theory for discontinuities and long-range forces. Journal of the Mechanics and Physics of Solids. 2000;48:175-209.

[5] Gao Y, Oterkus S. Ordinary state-based peridynamic modelling for fully coupled thermoelastic problems. Continuum Mechanics and Thermodynamics. 2018;31:907-37.

[6] Gao Y, Oterkus S. Fully coupled thermomechanical analysis of laminated composites by using ordinary state based peridynamic theory. Composite Structures. 2019;207:397-424.

[7] Gao Y, Oterkus S. Peridynamic Analysis of Marine Composites under Shock Loads by Considering Thermomechanical Coupling Effects. Journal of Marine Science and Engineering. 2018;6:38.

[8] Gao Y, Oterkus S. Nonlocal numerical simulation of low Reynolds number laminar fluid motion by using peridynamic differential operator. Ocean Engineering. 2019;179:135-58.

[9] Gao Y, Oterkus S. Non-local modeling for fluid flow coupled with heat transfer by using peridynamic differential operator. Engineering Analysis with Boundary Elements. 2019;105:104-21.

[10] Madenci E, Oterkus E. Peridynamic theory and its applications: Springer, 2014.

[11] Silling SA, Epton M, Weckner O, Xu J, Askari E. Peridynamic States and Constitutive Modeling. Journal of Elasticity. 2007;88:151-84.

[12] Madenci E, Oterkus E. Damage Prediction. Peridynamic Theory and Its Applications. New York, NY: Springer New York; 2014. p. 115-24.

[13] Silling SA, Askari E. A meshfree method based on the peridynamic model of solid mechanics. Computers & Structures. 2005;83:1526-35.

[14] Madenci E, Barut A, Futch M. Peridynamic differential operator and its applications. Computer Methods in Applied Mechanics and Engineering. 2016;304:408-51.

[15] Adams JC, Brainerd WS, Martin JT, Smith BT, Wagener JL. Fortran 95 handbook: complete ISO/ANSI reference: MIT press, 1997.

[16] Spitsberg I, Steibel J. Thermal and environmental barrier coatings for SiC/Sic CMCs in aircraft engine applications. International Journal of Applied Ceramic Technology. 2004;1:291-301.

[17] Nali P, Carrera E, Calvi A. Advanced fully coupled thermo-mechanical plate elements for multilayered structures subjected to mechanical and thermal loading. International journal for numerical methods in engineering. 2011;85:896-919.

[18] Biot MA. Thermoelasticity and Irreversible Thermodynamics. Journal of Applied Physics. 1956;27:240-53.

[19] Herrmann G. On variational principles in thermoelasticity and heat conduction. Quarterly of Applied Mathematics. 1963;21:151-5.

[20] Jabbari M, Dehbani H, Eslami MR. An Exact Solution for Classic Coupled Thermoelasticity in Spherical Coordinates. Journal of Pressure Vessel Technology. 2010;132:031201--11.

[21] Jabbari M, Dehbani H, Eslami MR. An Exact Solution for Classic Coupled Thermoelasticity in Cylindrical Coordinates. Journal of Pressure Vessel Technology. 2011;133:051204--10.

[22] Dillon O, Tauchert T. The experimental technique for observing the temperatures due to the coupled thermoelastic effect. International Journal of Solids and Structures. 1966;2:385IN1389-388IN4391.

[23] BILEN EA. Computational reality : Solving Nonlinear and Coupled Problems in Continuum Mechanics: SPRINGER, 2018.

[24] Cannarozzi AA, Ubertini F. A mixed variational method for linear coupled thermoelastic analysis. International Journal of Solids and Structures. 2001;38:717-39.

[25] Tehrani PH, Eslami MR. Boundary Element Analysis of Coupled Thermoelasticity with Relaxation Times in Finite Domain. AIAA journal. 2000;38:534-41.

[26] Atkinson C, Craster RV. Fracture in fully coupled dynamic thermoelasticity. Journal of the Mechanics and Physics of Solids. 1992;40:1415-32.

[27] Weichert R, Schönert K. Heat generation at the tip of a moving crack. Journal of the Mechanics and Physics of Solids. 1978;26:151-61.

[28] Bhalla KS, Zehnder AT, Han X. Thermomechanics of slow stable crack growth: closing the loop between experiments and computational modeling. Engineering Fracture Mechanics. 2003;70:2439-58.

[29] Miehe C, Schänzel LM, Ulmer H. Phase field modeling of fracture in multi-physics problems. Part I. Balance of crack surface and failure criteria for brittle crack propagation in thermo-elastic solids. Computer Methods in Applied Mechanics and Engineering. 2015;294:449-85.

[30] dell'Isola F, Andreaus U, Placidi L. At the origins and in the vanguard of peridynamics, non-local and higher-gradient continuum mechanics: An underestimated and still topical contribution of Gabrio Piola. Mathematics and Mechanics of Solids. 2014;20:887-928.

[31] Demmie P, Silling S. An approach to modeling extreme loading of structures using peridynamics. Journal of Mechanics of Materials and Structures. 2007;2:1921-45.

[32] Silling SA, Weckner O, Askari E, Bobaru F. Crack nucleation in a peridynamic solid. International Journal of Fracture. 2010;162:219-27.

[33] Ha YD, Bobaru F. Characteristics of dynamic brittle fracture captured with peridynamics. Engineering Fracture Mechanics. 2011;78:1156-68.

[34] Huang D, Lu G, Qiao P. An improved peridynamic approach for quasi-static elastic deformation and brittle fracture analysis. International Journal of Mechanical Sciences. 2015;94-95:111-22.

[35] Hu W, Ha YD, Bobaru F. Peridynamic model for dynamic fracture in unidirectional fiber-reinforced composites. Computer Methods in Applied Mechanics and Engineering. 2012;217-220:247-61.

[36] Bobaru F, Hu W. The Meaning, Selection, and Use of the Peridynamic Horizon and its Relation to Crack Branching in Brittle Materials. International Journal of Fracture. 2012;176:215-22.

[37] Agwai A, Guven I, Madenci E. Predicting crack propagation with peridynamics: a comparative study. International Journal of Fracture. 2011;171:65-78.

[38] Oterkus S, Vazic B, Wang H, Diyaroglu C, Oterkus E. Dynamic propagation of a macrocrack interacting with parallel small cracks. AIMS Materials Science. 2017;4:118-36.

[39] Oterkus S, Madenci E, Agwai A. Peridynamic thermal diffusion. Journal of Computational Physics. 2014;265:71-96.

[40] Oterkus S, Madenci E. Peridynamic modeling of fuel pellet cracking. Engineering Fracture Mechanics. 2017;176:23-37.

[41] Bobaru F, Duangpanya M. A peridynamic formulation for transient heat conduction in bodies with evolving discontinuities. Journal of Computational Physics. 2012;231:2764-85.

[42] Bobaru F, Duangpanya M. The peridynamic formulation for transient heat conduction. International Journal of Heat and Mass Transfer. 2010;53:4047-59.

[43] Oterkus S, Madenci E, Agwai A. Fully coupled peridynamic thermomechanics. Journal of the Mechanics and Physics of Solids. 2014;64:1-23.

[44] Oterkus S. Peridynamics for the solution of multiphysics problems [Doctor of Philosophy]. Arizona: The University of Arizona, 2015.

[45] Madenci E, Oterkus S. Peridynamics for Coupled Field Equations. Handbook of Peridynamic Modeling2016.

[46] Oterkus S, Madenci E. Fully coupled thermomechanical analysis of fiber reinforced composites using peridynamics. 55th AIAA/ASMe/ASCE/AHS/SC Structures, Structural Dynamics, and Materials Conference-SciTech Forum and Exposition 20142014.

[47] Oterkus S, Madenci E. Crack growth prediction in fully-coupled thermal and deformation fields using peridynamic theory. 54th AIAA Structures, Structural Dynamics and MaterialsConference, Boston, Massachusetts. 2013.

[48] Agwai AG. A Peridynamic Approach for Coupled Fields [Doctor of philosophy]. Arizona: The University of Arizona., 2011.

[49] Oterkus S, Fox J, Madenci E. Simulation of electro-migration through peridynamics. Electronic Components and Technology Conference (ECTC), 2013 IEEE 63rd: IEEE; 2013. p. 1488-93.

[50] Silling SA. Linearized Theory of Peridynamic States. Journal of Elasticity. 2010;99:85-111.

[51] Lord HW, Shulman Y. A generalized dynamical theory of thermoelasticity. Journal of the Mechanics and Physics of Solids. 1967;15:299-309.

[52] SACKMAN J. Approximate Solutions in Linear, Coupled Thermoelasticity. Journal of Applied Mechanics. 1968.

[53] Hosseini-Tehrani P, Eslami MR. BEM analysis of thermal and mechanical shock in a two-dimensional finite domain considering coupled thermoelasticity. Engineering Analysis with Boundary Elements. 2000;24:249-57.

[54] Madenci E, Oterkus E. Peridynamic Theory. Peridynamic Theory and Its Applications. New York, NY: Springer New York; 2014. p. 19-43.

[55] Oterkus S, Madenci E, Oterkus E. Fully coupled poroelastic peridynamic formulation for fluid-filled fractures. Engineering Geology. 2017;225:19-28.

[56] Kalthoff JF. Modes of dynamic shear failure in solids. International Journal of Fracture. 2000;101:1-31.

[57] Chadwick P. Thermo-mechanics of rubberlike materials. Philosophical Transactions of the Royal Society of London A: Mathematical, Physical and Engineering Sciences. 1974;276:371-403.

[58] Kalthoff J, Winkler S. Failure mode transition at high rates of shear loading. DGM Informationsgesellschaft mbH, Impact Loading and Dynamic Behavior of Materials. 1988;1:185-95.

[59] Kalthoff JF. Shadow Optical Analysis Of Dynamic Shear Fracture. SPIE; 1988. p. 6.

[60] Borden MJ, Verhoosel CV, Scott MA, Hughes TJR, Landis CM. A phase-field description of dynamic brittle fracture. Computer Methods in Applied Mechanics and Engineering. 2012;217-220:77-95.

[61] Batra RC, Ravinsankar MVS. Three-dimensional numerical simulation of the Kalthoff experiment. International Journal of Fracture. 2000;105:161-86.

[62] Silling S. Peridynamic modeling of the Kalthoff–Winkler experiment. Submission for the. 2001.

[63] Dipasquale D, Zaccariotto M, Galvanetto U. Crack propagation with adaptive grid refinement in 2D peridynamics. International Journal of Fracture. 2014;190:1-22.

[64] Prewo KM, Brennan JJ. High-Strength Silicon-Carbide Fiber-Reinforced Glass-Matrix Composites. Journal of Materials Science. 1980;15:463-8.

[65] Carter JP, Booker JR. Finite-Element Analysis of Coupled Thermoelasticity. Computers & Structures. 1989;31:73-80.

[66] Stanley P. Applications and potential of thermoelastic stress analysis. Journal of materials processing technology. 1997;64:359-70.

[67] Ene HI. On Linear Thermoelasticity of Composite-Materials. International Journal of Engineering Science. 1983;21:443-8.

[68] Rao DM, Sinha PK. Finite element coupled thermostructural analysis of composite beams. Computers & Structures. 1997;63:539-49.

[69] Mukherjee N, Sinha PK. Thermal shocks in composite plates: a coupled thermoelastic finite element analysis. Composite Structures. 1996;34:1-12.

[70] Khan KA, Barello R, Muliana AH, Lévesque M. Coupled heat conduction and thermal stress analyses in particulate composites. Mechanics of Materials. 2011;43:608-25.

[71] Kogl M, Gaul L. A boundary element method for anisotropic coupled thermoelasticity. Archive of Applied Mechanics (Ingenieur Archiv). 2003;73:377-98.

[72] Brischetto S, Carrera E. Coupled thermo-mechanical analysis of one-layered and multilayered plates. Composite Structures. 2010;92:1793-812.

[73] Ghobadi A. Common Type of Damages in Composites and Their Inspections. World Journal of Mechanics. 2017;7:24-33.

[74] Richardson MOW, Wisheart MJ. Review of low-velocity impact properties of composite materials. Composites Part A: Applied Science and Manufacturing. 1996;27:1123-31.

[75] Diyaroglu C. Peridynamics and its applications in marine structures [Doctor of Philosophy]. Glasgow: University of Strathclyde, 2016.

[76] Oterkus E, Madenci E. Peridynamic analysis of fiber-reinforced composite materials. Journal of Mechanics of Materials and Structures. 2012;7:45-84.

[77] Oterkus E, Madenci E, Weckner O, Silling S, Bogert P, Tessler A. Combined finite element and peridynamic analyses for predicting failure in a stiffened composite curved panel with a central slot. Composite Structures. 2012;94:839-50.

[78] Oterkus E, Madenci E. Peridynamic Theory for Damage Initiation and Growth in Composite Laminate. Key Engineering Materials. 2011;488-489:355-8.

[79] Kilic B, Agwai A, Madenci E. Peridynamic theory for progressive damage prediction in center-cracked composite laminates. Composite Structures. 2009;90:141-51.

[80] Oterkus E. Peridynamic theory for modeling three-dimensional damage growth in metallic and composite structures [Doctor of philosophy]. Arizona: University of Arizona, 2010.

[81] Colavito KW. Peridynamics for Failure and Residual Strength Prediction of Fiber-Reinforced Composites [Doctor of Philosophy]. Arizona: The University of Arizona., 2013.

[82] Oterkus E, Madenci E. Peridynamics for Failure Prediction in Composites. 53rd AIAA/ASME/ASCE/AHS/ASC Structures, Structural Dynamics and Materials Conference: American Institute of Aeronautics and Astronautics; 2012.

[83] Nettles A. Basic mechanics of laminated composite plates. National Aeronautics and Space Administration, Huntsville, AL (United States). George C. Marshall Space Flight Center; 1994.

[84] Oterkus E. Peridynamic theory for modeling three-dimensional damage growth in metallic and composite structures: University of Arizona, 2010.

[85] Ayatollahi MR, Aliha MRM. Analysis of a new specimen for mixed mode fracture tests on brittle materials. Engineering Fracture Mechanics. 2009;76:1563-73.

[86] Diyaroglu C, Oterkus E, Madenci E, Rabczuk T, Siddiq A. Peridynamic modeling of composite laminates under explosive loading. Composite Structures. 2016;144:14-23.

[87] Kilic B, Madenci E. An adaptive dynamic relaxation method for quasi-static simulations using the peridynamic theory. Theoretical and Applied Fracture Mechanics. 2010;53:194-204.

[88] Berthelot J-M. Classical Laminate Theory. In: Berthelot J-M, editor. Composite Materials: Mechanical Behavior and Structural Analysis. New York, NY: Springer New York; 1999. p. 287-311.

[89] Staab G. Laminar composites: Butterworth-Heinemann, 2015.

[90] Le Q, Bobaru F. Surface corrections for peridynamic models in elasticity and fracture. Computational Mechanics. 2017:1-20.

[91] Madenci E, Guven I. The finite element method and applications in engineering using ANSYS®: Springer, 2015.

[92] Hetnarski RB, Eslami MR, Gladwell G. Thermal stresses: advanced theory and applications: Springer, 2009.

[93] King J. Failure in composite materials. Metals and Materials. 1989;5:720-6.

[94] Bogert P, Satyanarayana A, Chunchu P. Comparison of Damage Path Predictions for Composite Laminates by Explicit and Standard Finite Element Analysis Tools. 47th AIAA/ASME/ASCE/AHS/ASC Structures, Structural Dynamics, and Materials Conference: American Institute of Aeronautics and Astronautics; 2006.

[95] Alpay S, Madenci E. Crack Growth Prediction in Fully-Coupled Thermal and Deformation Fields Using Peridynamic Theory. 54th AIAA/ASME/ASCE/AHS/ASC Structures, Structural Dynamics, and Materials Conference2013. p. 1477.

[96] Wu EM, Reuter Jr R. Crack extension in fiberglass reinforced plastics. University of Illinois; 1965.

[97] Jose S, Ramesh Kumar R, Jana MK, Venkateswara Rao G. Intralaminar fracture toughness of a cross-ply laminate and its constituent sub-laminates. Composites Science and Technology. 2001;61:1115-22.

[98] Li X, Hallett SR, Wisnom MR, Zobeiry N, Vaziri R, Poursartip A. Experimental study of damage propagation in Over-height Compact Tension tests. Composites Part A: Applied Science and Manufacturing. 2009;40:1891-9.

[99] Manders PW, Chou T-W, Jones FR, Rock JW. Statistical analysis of multiple fracture in 0/90/0 glass fibre/epoxy resin laminates. Journal of Materials Science. 1983;18:2876-89.

[100] Mouritz AP. The damage to stitched GRP laminates by underwater explosion shock loading. Composites Science and Technology. 1995;55:365-74.

[101] Hellbratt S-E. Experiences from design and production of the 72 m CFRP-sandwich corvette visby. Proceedings of the 6th international conference on sandwich construction CRC Press, Fort Lauderdale2003. p. 15-24.

[102] Li HCH, Herszberg I, Davis CE, Mouritz AP, Galea SC. Health monitoring of marine composite structural joints using fibre optic sensors. Composite Structures. 2006;75:321-7.

[103] Baley C, Davies P, Grohens Y, Dolto G. Application of Interlaminar Tests to Marine Composites. A Literature Review. Applied Composite Materials. 2004;11:99-126.

[104] LeBlanc J, Shukla A. Dynamic response of curved composite panels to underwater explosive loading: Experimental and computational comparisons. Composite Structures. 2011;93:3072-81.

[105] Tagarielli VL, Schiffer A. The response to underwater blast. Dynamic Deformation, Damage and Fracture in Composite Materials and Structures: Woodhead Publishing; 2016. p. 279-307.

[106] Arora H, Rolfe E, Kelly M, Dear JP. Full-Scale Air and Underwater-Blast Loading of Composite Sandwich Panels. Explosion Blast Response of Composites: Woodhead Publishing; 2017. p. 161-99.

[107] Hall DJ. Examination of the effects of underwater blasts on sandwich composite structures. Composite Structures. 1989;11:101-20.

[108] Latourte F, Grégoire D, Zenkert D, Wei X, Espinosa HD. Failure mechanisms in composite panels subjected to underwater impulsive loads. Journal of the Mechanics and Physics of Solids. 2011;59:1623-46.

[109] LeBlanc J, Shukla A. Dynamic response and damage evolution in composite materials subjected to underwater explosive loading: An experimental and computational study. Composite Structures. 2010;92:2421-30.

[110] Wadley H, Dharmasena K, Chen Y, Dudt P, Knight D, Charette R, et al. Compressive response of multilayered pyramidal lattices during underwater shock loading. International Journal of Impact Engineering. 2008;35:1102-14.

[111] Rabczuk T, Samaniego E, Belytschko T. Simplified model for predicting impulsive loads on submerged structures to account for fluid-structure interaction. International Journal of Impact Engineering. 2007;34:163-77.

[112] Hoo Fatt MS, Palla L. Analytical Modeling of Composite Sandwich Panels under Blast Loads. Journal of Sandwich Structures & Materials. 2009;11:357-80.

[113] Kazancı Z. A review on the response of blast loaded laminated composite plates. Progress in Aerospace Sciences. 2016;81:49-59.

[114] Carrera E, Demasi L, Manganello M. Assessment of Plate Elements on Bending and Vibrations of Composite Structures. Mechanics of Advanced Materials and Structures. 2002;9:333-57.

[115] Liew KM, Zhao X, Ferreira AJM. A review of meshless methods for laminated and functionally graded plates and shells. Composite Structures. 2011;93:2031-41.

[116] Dawe DJ. Use of the finite strip method in predicting the behaviour of composite laminated structures. Composite Structures. 2002;57:11-36.

[117] Cimpoeru SJ, Ritzel DV, Brett JM. Physics of Explosive Loading of Structures. Explosion Blast Response of Composites: Woodhead Publishing; 2017. p. 1-22.

[118] Turkmen HS, Mecitoglu Z. Nonlinear structural response of laminated composite plates subjected to blast loading. AIAA journal. 1999;37:1639-47.

[119] Faltinsen O. Sea loads on ships and offshore structures: Cambridge university press, 1993.

[120] Cao XY, Ming FR, Zhang AM. Sloshing in a rectangular tank based on SPH simulation. Applied Ocean Research. 2014;47:241-54.

[121] Gómez-Gesteira M, Cerqueiro D, Crespo C, Dalrymple RA. Green water overtopping analyzed with a SPH model. Ocean Engineering. 2005;32:223-38.

[122] Ye LY, Wang C, Chang X, Zhang HY. Propeller-ice contact modeling with peridynamics. Ocean Engineering. 2017;139:54-64.

[123] Wang C, Xiong WP, Chang X, Ye LY, Li X. Analysis of variable working conditions for propeller-ice interaction. Ocean Engineering. 2018;156:277-93.

[124] Liu RW, Xue YZ, Lu XK, Cheng WX. Simulation of ship navigation in ice rubble based on peridynamics. Ocean Engineering. 2018;148:286-98.

[125] Anderson JD, Wendt J. Computational fluid dynamics: Springer, 1995.

[126] Lucy LB. A numerical approach to the testing of the fission hypothesis. The astronomical journal. 1977;82:1013-24.

[127] Gingold RA, Monaghan JJ. Smoothed particle hydrodynamics: theory and application to non-spherical stars. Monthly Notices of the Royal Astronomical Society. 1977;181:375-89.

[128] Monaghan JJ. Smoothed Particle Hydrodynamics. Annual Review of Astronomy and Astrophysics. 1992;30:543-74.

[129] Oterkus E, Madenci E. Peridynamic Theory for Damage Initiation and Growth in Composite Laminate. Advances in Fracture and Damage Mechanics X. 2012;488-489:355-8.

[130] Javili A, Morasata R, Oterkus E, Oterkus S. Peridynamics review. Mathematics and Mechanics of Solids. 2019;24:3714-39.

[131] Wang J, Zhang X. Modified Particle Method with integral Navier–Stokes formulation for incompressible flows. Journal of Computational Physics. 2018;366:1-13.

[132] Tu Q, Li S. An updated Lagrangian particle hydrodynamics (ULPH) for Newtonian fluids. Journal of Computational Physics. 2017;348:493-513.

[133] Silling SA, Parks ML, Kamm JR, Weckner O, Rassaian M. Modeling shockwaves and impact phenomena with Eulerian peridynamics. International Journal of Impact Engineering. 2017;107:47-57.

[134] Ouchi H, Katiyar A, York J, Foster JT, Sharma MM. A fully coupled porous flow and geomechanics model for fluid driven cracks: a peridynamics approach. Computational Mechanics. 2015;55:561-76.

[135] Katiyar A, Foster JT, Ouchi H, Sharma MM. A peridynamic formulation of pressure driven convective fluid transport in porous media. Journal of Computational Physics. 2014;261:209-29.

[136] Reddy JN, Gartling DK. The finite element method in heat transfer and fluid dynamics: CRC press, 2010.

[137] Morris JP, Fox PJ, Zhu Y. Modeling Low Reynolds Number Incompressible Flows Using SPH. Journal of Computational Physics. 1997;136:214-26.

[138] Liu G-R, Liu MB. Smoothed particle hydrodynamics: a meshfree particle method: World Scientific, 2003.

[139] Liu M-b, Liu G-r. Smoothed Particle Hydrodynamics (SPH): an Overview and Recent Developments. Archives of Computational Methods in Engineering. 2010;17:25-76.

[140] Drikakis D, Rider W. The artificial compressibility method. High-Resolution Methods for Incompressible and Low-Speed Flows. 2005:173-208.

[141] Batchelor GK. An introduction to fluid dynamics: Cambridge university press, 2000.

[142] Monaghan JJ. Simulating Free Surface Flows with SPH. Journal of Computational Physics. 1994;110:399-406.

[143] Becker M, Teschner M. Weakly compressible SPH for free surface flows. Proceedings of the 2007 ACM SIGGRAPH/Eurographics symposium on Computer animation: Eurographics Association; 2007. p. 209-17.

[144] Szewc K, Pozorski J, Tanière A. Modeling of natural convection with Smoothed Particle Hydrodynamics: Non-Boussinesq formulation. International Journal of Heat and Mass Transfer. 2011;54:4807-16.

[145] Bergel GL, Li S. The total and updated lagrangian formulations of state-based peridynamics. Computational Mechanics. 2016;58:351-70.

[146] Swope WC, Andersen HC, Berens PH, Wilson KR. A computer simulation method for the calculation of equilibrium constants for the formation of physical clusters of molecules: Application to small water clusters. The Journal of Chemical Physics. 1982;76:637-49.

[147] Intel R. Intel math kernel library reference manual. Tech. Rep. 630813-051US, 2012.[Online]. Available: http://software. intel. com/sites/products/documentation/hpc/mkl/mklman/mklman. pdf; 2011.

[148] Anderson E, Bai Z, Dongarra J, Greenbaum A, McKenney A, Du Croz J, et al. LAPACK: A portable linear algebra library for high-performance computers. Proceedings of the 1990 ACM/IEEE conference on Supercomputing: IEEE Computer Society Press; 1990. p. 2-11.

[149] Madenci E. Peridynamic integrals for strain invariants of homogeneous deformation. ZAMM - Journal of Applied Mathematics and Mechanics / Zeitschrift für Angewandte Mathematik und Mechanik. 2017;97:1236-51.

[150] Oterkus S, Madenci E. Peridynamics for Antiplane Shear and Torsional Deformations. Journal of Mechanics of Materials and Structures. 2015;10:167-93.

[151] Macek RW, Silling SA. Peridynamics via finite element analysis. Finite Elements in Analysis and Design. 2007;43:1169-78.

[152] Adami S, Hu XY, Adams NA. A generalized wall boundary condition for smoothed particle hydrodynamics. Journal of Computational Physics. 2012;231:7057-75.

[153] Dilts GA. Moving-least-squares-particle hydrodynamics—I. Consistency and stability. International journal for numerical methods in engineering. 1999;44:1115-55.

[154] Colagrossi A, Landrini M. Numerical simulation of interfacial flows by smoothed particle hydrodynamics. Journal of Computational Physics. 2003;191:448-75.

[155] Mao Z, Liu GR. A Lagrangian gradient smoothing method for solid-flow problems using simplicial mesh. International journal for numerical methods in engineering. 2018;113:858-90.

[156] Adami S, Hu XY, Adams NA. A transport-velocity formulation for smoothed particle hydrodynamics. Journal of Computational Physics. 2013;241:292-307.

[157] Chaniotis AK, Poulikakos D, Koumoutsakos P. Remeshed Smoothed Particle Hydrodynamics for the Simulation of Viscous and Heat Conducting Flows. Journal of Computational Physics. 2002;182:67-90.

[158] Liu GRLMB. SPH for General Dynamic Fluid Flows. Smoothed Particle Hydrodynamics: WORLD SCIENTIFIC; 2003. p. 103-76.

[159] Xu R, Stansby P, Laurence D. Accuracy and stability in incompressible SPH (ISPH) based on the projection method and a new approach. Journal of Computational Physics. 2009;228:6703-25.

[160] Koshizuka S, Oka Y. Moving-Particle Semi-Implicit Method for Fragmentation of Incompressible Fluid. Nuclear Science and Engineering. 2017;123:421-34.

[161] Koshizuka S. A particle method for incompressible viscous flow with fluid fragmentation. Computational Fluid Dynamics Journal. 1995;4:29.

[162] Martin JC, Moyce WJ, Penney WG, Price A, Thornhill C. Part IV. An experimental study of the collapse of liquid columns on a rigid horizontal plane. Philosophical Transactions of the Royal Society of London Series A, Mathematical and Physical Sciences. 1952;244:312-24.

[163] Corcione M. Effects of the thermal boundary conditions at the sidewalls upon natural convection in rectangular enclosures heated from below and cooled from above. International Journal of Thermal Sciences. 2003;42:199-208.

[164] Patankar S. Numerical heat transfer and fluid flow: CRC press, 1980.

[165] De Vahl Davis G. Natural convection of air in a square cavity: A bench mark numerical solution. International Journal for Numerical Methods in Fluids. 1983;3:249-64.

[166] Elder JW. Turbulent free convection in a vertical slot. Journal of Fluid Mechanics. 2006;23:99-&.

[167] Markatos NC, Pericleous KA. Laminar and turbulent natural convection in an enclosed cavity. International Journal of Heat and Mass Transfer. 1984;27:755-72.

[168] C. Wan BP, GW Wei, D. A new benchmark quality solution for the buoyancy-driven cavity by discrete singular convolution. Numerical Heat Transfer: Part B: Fundamentals. 2001;40:199-228.

[169] Danis ME, Orhan M, Ecder A. ISPH modelling of transient natural convection. International Journal of Computational Fluid Dynamics. 2013;27:15-31.

[170] Moallemi MK, Jang KS. Prandtl number effects on laminar mixed convection heat transfer in a lid-driven cavity. International Journal of Heat and Mass Transfer. 1992;35:1881-92.

[171] Iwatsu R, Hyun JM, Kuwahara K. Mixed convection in a driven cavity with a stable vertical temperature gradient. International Journal of Heat and Mass Transfer. 1993;36:1601-8.

[172] Wong JCF. Numerical simulation of two‐dimensional laminar mixed‐convection in a lid‐driven cavity using the mixed finite element consistent splitting scheme. International Journal of Numerical Methods for Heat & Fluid Flow. 2007;17:46-93.

[173] Oztop HF, Dagtekin I. Mixed convection in two-sided lid-driven differentially heated square cavity. International Journal of Heat and Mass Transfer. 2004;47:1761-9.

[174] Sharif MAR. Laminar mixed convection in shallow inclined driven cavities with hot moving lid on top and cooled from bottom. Applied Thermal Engineering. 2007;27:1036-42.

[175] Gray DD, Giorgini A. The validity of the boussinesq approximation for liquids and gases. International Journal of Heat and Mass Transfer. 1976;19:545-51.

[176] Barakos G, Mitsoulis E, Assimacopoulos D. Natural convection flow in a square cavity revisited: Laminar and turbulent models with wall functions. International Journal for Numerical Methods in Fluids. 1994;18:695-719.

[177] Aly AM, Chamkha AJ, Lee S-W, Al-Mudhaf A. On Mixed Convection in an Inclined Lid-Driven Cavity with Sinusoidal Heated Walls Using the Isph Method. Computational Thermal Sciences: An International Journal. 2016;8:337-54.

[178] Turns SR. An introduction to combustion: McGraw-hill New York, 1996.

[179] Hirt CW, Nichols BD. Volume of fluid (VOF) method for the dynamics of free boundaries. Journal of Computational Physics. 1981;39:201-25.

[180] van der Pijl SP, Segal A, Vuik C, Wesseling P. A mass-conserving Level-Set method for modelling of multi-phase flows. International Journal for Numerical Methods in Fluids. 2005;47:339-61.

[181] Yang Q, Yao J, Huang Z, Asif M. A comprehensive SPH model for three-dimensional multiphase interface simulation. Computers & Fluids. 2019;187:98-106.

[182] Wang Z-B, Chen R, Wang H, Liao Q, Zhu X, Li S-Z. An overview of smoothed particle hydrodynamics for simulating multiphase flow. Applied Mathematical Modelling. 2016;40:9625-55.

[183] Monaghan JJ, Rafiee A. A simple SPH algorithm for multi-fluid flow with high density ratios. International Journal for Numerical Methods in Fluids. 2013;71:537-61.

[184] Tartakovsky AM, Meakin P. A smoothed particle hydrodynamics model for miscible flow in three-dimensional fractures and the two-dimensional Rayleigh–Taylor instability. Journal of Computational Physics. 2005;207:610-24.

[185] Cummins SJ, Rudman M. An SPH Projection Method. Journal of Computational Physics. 1999;152:584-607.

[186] Guo K, Chen R, Qiu S, Tian W, Su G. An improved Multiphase Moving Particle Semi-implicit method in bubble rising simulations with large density ratios. Nuclear Engineering and Design. 2018;340:370-87.

[187] Wang J, Zhang X. Improved Moving Particle Semi-implicit method for multiphase flow with discontinuity. Computer Methods in Applied Mechanics and Engineering. 2019;346:312-31.

[188] Rezavand M, Taeibi-Rahni M, Rauch W. An ISPH scheme for numerical simulation of multiphase flows with complex interfaces and high density ratios. Computers & Mathematics with Applications. 2018;75:2658-77.

[189] Suresh P, Kumar SP, Pantaik B. A Comparative Study of Two Different Density Estimation Techniques for Multi-Phase Flow Simulations Using SPH. International Journal for Computational Methods in Engineering Science and Mechanics. 2019;20:29-47.

[190] Fürstenau J-P, Avci B, Wriggers P. A Numerical Review of Multi-Fluid SPH Algorithms for High Density Ratios. Advances in Computational Fluid-Structure Interaction and Flow Simulation: Springer; 2016. p. 139-50.

[191] TingYe, DingyiPan, CanHuang, MoubinLiu. Smoothed particle hydrodynamics (SPH) for complex fluid flows: Recent developments in methodology and applications. Physics of Fluids. 2019;31:011301.

[192] Yan J, Li S, Zhang AM, Kan X, Sun P-N. Updated Lagrangian Particle Hydrodynamics (ULPH) modeling and simulation of multiphase flows. Journal of Computational Physics. 2019;393:406-37.

[193] Zhang A, Sun P, Ming F. An SPH modeling of bubble rising and coalescing in three dimensions. Computer Methods in Applied Mechanics and Engineering. 2015;294:189-209.

[194] Brackbill JU, Kothe DB, Zemach C. A continuum method for modeling surface tension. Journal of Computational Physics. 1992;100:335-54.

[195] Krimi A, Rezoug M, Khelladi S, Nogueira X, Deligant M, Ramírez L. Smoothed Particle Hydrodynamics: A consistent model for interfacial multiphase fluid flow simulations. Journal of Computational Physics. 2018;358:53-87.

[196] Colagrossi A, Bouscasse B, Antuono M, Marrone S. Particle packing algorithm for SPH schemes. Computer Physics Communications. 2012;183:1641-53.

[197] Adami S, Hu XY, Adams NA. A new surface-tension formulation for multi-phase SPH using a reproducing divergence approximation. Journal of Computational Physics. 2010;229:5011-21.

[198] Morris JP. Simulating surface tension with smoothed particle hydrodynamics. International Journal for Numerical Methods in Fluids. 2000;33:333-53.

[199] Pahar G, Dhar A. Mixed miscible-immiscible fluid flow modelling with incompressible SPH framework. Engineering Analysis with Boundary Elements. 2016;73:50-60.

[200] Sloper KS, Dourmashkin RR, Bird RB, Slavin G, Webster ADB. Chronic Malabsorption Due to Cryptosporidiosis in a Child with Immunoglobulin Deficiency. Gut. 1982;23:80-2.

[201] Ren H, Zhuang X. A Nonlocal Formulation for Weakly Compressible Fluid. Singapore: Springer Singapore; 2018. p. 835-50.

[202] Akbari H. An improved particle shifting technique for incompressible smoothed particle hydrodynamics methods. International Journal for Numerical Methods in Fluids. 2019;90:603-31.

[203] Lind SJ, Xu R, Stansby PK, Rogers BD. Incompressible smoothed particle hydrodynamics for free-surface flows: A generalised diffusion-based algorithm for stability and validations for impulsive flows and propagating waves. Journal of Computational Physics. 2012;231:1499-523.

[204] Zhang ZL, Walayat K, Huang C, Chang JZ, Liu MB. A finite particle method with particle shifting technique for modeling particulate flows with thermal convection. International Journal of Heat and Mass Transfer. 2019;128:1245-62.

[205] Mokos A, Rogers BD, Stansby PK. A multi-phase particle shifting algorithm for SPH simulations of violent hydrodynamics with a large number of particles. Journal of Hydraulic Research. 2017;55:143-62.

[206] Vacondio R, Rogers BD, Stansby PK, Mignosa P, Feldman J. Variable resolution for SPH: A dynamic particle coalescing and splitting scheme. Computer Methods in Applied Mechanics and Engineering. 2013;256:132-48.

[207] Shadloo MS, Zainali A, Yildiz M. Simulation of single mode Rayleigh–Taylor instability by SPH method. Computational Mechanics. 2012;51:699-715.

[208] Chen Z, Zong Z, Liu MB, Zou L, Li HT, Shu C. An SPH model for multiphase flows with complex interfaces and large density differences. Journal of Computational Physics. 2015;283:169-88.

[209] Chen Z, Zong Z, Li HT, Li J. An investigation into the pressure on solid walls in 2D sloshing using SPH method. Ocean Engineering. 2013;59:129-41.

[210] Dilts GA. Moving least-squares particle hydrodynamics II: conservation and boundaries. International journal for numerical methods in engineering. 2000;48:1503-24.

[211] Monaghan JJ, Gingold RA. Shock simulation by the particle method SPH. Journal of Computational Physics. 1983;52:374-89.

[212] Liu R, Yan J, Li S. Modeling and simulation of ice–water interactions by coupling peridynamics with updated Lagrangian particle hydrodynamics. Computational Particle Mechanics. 2019;7:241-55.

[213] !!! INVALID CITATION !!! [186, 188, 213-217].

[214] Bird RB, Stewart WE, Lightfoot EN. Transport phenomena: John Wiley & Sons, 2007.

[215] Remington BA, Weber SV, Marinak MM, Haan SW, Kilkenny JD, Wallace RJ, et al. Single-mode and multimode Rayleigh–Taylor experiments on Nova. Physics of Plasmas. 1995;2:241-55.

[216] Bazilevs Y, Takizawa K, Tezduyar TE. Computational fluid-structure interaction: methods and applications: John Wiley & Sons, 2013.

[217] Faltinsen OM. Hydroelastic slamming. Journal of Marine Science and Technology. 2001;5:49-65.

[218] Antoci C, Gallati M, Sibilla S. Numerical simulation of fluid–structure interaction by SPH. Computers & Structures. 2007;85:879-90.

[219] Souli M, Ouahsine A, Lewin L. ALE formulation for fluid–structure interaction problems. Computer Methods in Applied Mechanics and Engineering. 2000;190:659-75.

[220] Zhu L, Peskin CS. Simulation of a Flapping Flexible Filament in a Flowing Soap Film by the Immersed Boundary Method. Journal of Computational Physics. 2002;179:452-68.

[221] Paredes RJ, Imas L. Application of multiphase SPH to fluid structure interaction problems. 9th international SPHERIC workshop CNAM Paris, France2014.

[222] Sun PN, Le Touzé D, Zhang AM. Study of a complex fluid-structure dam-breaking benchmark problem using a multi-phase SPH method with APR. Engineering Analysis with Boundary Elements. 2019;104:240-58.

[223] Khayyer A, Gotoh H, Falahaty H, Shimizu Y. An enhanced ISPH–SPH coupled method for simulation of incompressible fluid–elastic structure interactions. Computer Physics Communications. 2018;232:139-64.

[224] Khayyer A, Gotoh H, Shimizu Y. Comparative study on accuracy and conservation properties of two particle regularization schemes and proposal of an optimized particle shifting scheme in ISPH context. Journal of Computational Physics. 2017;332:236-56.

[225] Liu M, Zhang Z. Smoothed particle hydrodynamics (SPH) for modeling fluid-structure interactions. Science China Physics, Mechanics & Astronomy. 2019;62:984701.

[226] Wu K, Yang D, Wright N. A coupled SPH-DEM model for fluid-structure interaction problems with free-surface flow and structural failure. Computers & Structures. 2016;177:141-61.

[227] Khayyer A, Tsuruta N, Shimizu Y, Gotoh H. Multi-resolution MPS for incompressible fluid-elastic structure interactions in ocean engineering. Applied Ocean Research. 2019;82:397-414.

[228] Hwang S-C, Khayyer A, Gotoh H, Park J-C. Development of a fully Lagrangian MPS-based coupled method for simulation of fluid–structure interaction problems. Journal of Fluids and Structures. 2014;50:497-511.

[229] Dalla Barba F, Campagnari P, Zaccariotto M, Galvanetto U, Picano F. A Fluid-Structure Interaction model based on Peridynamics and Navier-Stokes equations for hydraulic fracture problems. 6th European Conference on Computational Mechanics (ECCM 6), 7th European Conference on Computational Fluid Dynamics (ECFD 7). Glasgow, UK2018.

[230] Vazic B, Oterkus E, Oterkus S. Peridynamic approach for modelling ice-structure interactions. Trends in the Analysis and Design of Marine Structures: Proceedings of the 7th International Conference on Marine Structures (MARSTRUCT 2019, Dubrovnik, Croatia, 6-8 May 2019): CRC Press; 2019. p. 55.

[231] Lu W, Li M, Vazic B, Oterkus S, Oterkus E, Wang Q. Peridynamic modelling of fracture in polycrystalline ice. Journal of Mechanics. 2019.

[232] Vazic B, Oterkus E, Oterkus S. In-plane and out-of plane failure of an ice sheet using peridynamics. Journal of Mechanics. 2019:1-7.

[233] Koshizuka S, Nobe A, Oka Y. Numerical analysis of breaking waves using the moving particle semi-implicit method. International Journal for Numerical Methods in Fluids. 1998;26:751-69.

[234] Yang Q, Jones V, McCue L. Free-surface flow interactions with deformable structures using an SPH–FEM model. Ocean Engineering. 2012;55:136-47.

[235] Liu M-b, Shao J-r, Li H-q. Numerical simulation of hydro-elastic problems with smoothed particle hydrodynamics method. Journal of Hydrodynamics. 2013;25:673-82.

[236] Cuoci A, Frassoldati A, Faravelli T, Ranzi E. Numerical Modeling of Laminar Flames with Detailed Kinetics Based on the Operator-Splitting Method. Energy & Fuels. 2013;27:7730-53.

[237] van't Hof B. Numerical aspects of laminar flame simulation: Technische Universiteit Eindhoven, 1998.

[238] Pierce CD, Moin P. Progress-variable approach for large-eddy simulation of non-premixed turbulent combustion. Journal of Fluid Mechanics. 2004;504:73-97.

[239] Amantini G, Frank JH, Smooke MD, Gomez A. Computational and experimental study of steady axisymmetric non-premixed methane counterflow flames. Combustion Theory and Modelling. 2007;11:47-72.

[240] Kee RJ, Rupley FM, Meeks E, Miller JA. CHEMKIN-III: A FORTRAN chemical kinetics package for the analysis of gas-phase chemical and plasma kinetics. Sandia National Labs., Livermore, CA (United States); 1996.

[241] Goodwin DG, Moffat HK, Speth RL. Cantera: An object-oriented software toolkit for chemical kinetics, thermodynamics, and transport processes. Caltech, Pasadena, CA. 2009.

[242] RConsul C, Claramunt K, Cadafalch J, Oliva A. Detailed numerical simulation of laminar flames by a parallel multiblock algorithm using loosely coupled computers. Combustion Theory and Modelling. 2003;7:525-44.

[243] Coffee T, Heimerl J. Transport algorithms for premixed, laminar steady-state flames. Combustion and Flame. 1981;43:273-89.

[244] Boonkkamp TJLnotJBcoc-A, Eindhoven University of Technology, Department of Mechanical Engineering. Numerical modelling of laminar flames: a concise introduction. 2003:55-69.

[245] Manninen M, Taivassalo V, Kallio S. On the mixture model for multiphase flow. Technical Research Centre of Finland Finland; 1996.

[246] De Ris JN. Spread of a laminar diffusion flame. Symposium (International) on Combustion. 1969;12:241-52.

[247] Becker R, Braack M, Rannacher R. Numerical simulation of laminar flames at low Mach number by adaptive finite elements: Taylor & Francis, 1999.

[248] ten Thije Boonkkamp J, Schreel K. Numerical modelling of laminar flames: a concise introduction. Lecture notes of the JM Burgerscentrum course on combustion: 19-22 April 2005, Eindhoven University of Technology, Department of Mechanical Engineering. 2003:55-69.

[249] Chaniotis AK, Frouzakis CE, Lee JC, Tomboulides AG, Poulikakos D, Boulouchos K. Remeshed smoothed particle hydrodynamics for the simulation of laminar chemically reactive flows. Journal of Computational Physics. 2003;191:1-17.

[250] Krishnan A, Ghoniem AF. Simulation of rollup and mixing in rayleigh-taylor flow using the transport-element method. Journal of Computational Physics. 1992;99:1-27.

[251] Soteriou MC, Ghoniem AF. Effects of the free-stream density ratio on free and forced spatially developing shear layers. Physics of Fluids. 1995;7:2036-51.

[252] Brown AL. Impact and Fire Modeling Considerations Employing SPH Coupling to a Dilute Spray Fire Code. ASME 2009 Heat Transfer Summer Conference collocated with the InterPACK09 and 3rd Energy Sustainability Conferences2009. p. 161-71.

[253] Dimitrienko YI. Thermomechanical behaviour of composite materials and structures under high temperatures: 1. Materials. Composites Part A: Applied Science and Manufacturing. 1997;28:453-61.

[254] Hopkins D, Quintiere JG. Material fire properties and predictions for thermoplastics. Fire Safety Journal. 1996;26:241-68.

[255] Gibson AG, Wright PNH, Wu YS, Mouritz AP, Mathys Z, Gardiner CP. The Integrity of Polymer Composites during and after Fire. Journal of Composite Materials. 2016;38:1283-307.

[256] Kim NK, Bhattacharyya D. Development of fire resistant wool polymer composites: Mechanical performance and fire simulation with design perspectives. Materials & Design. 2016;106:391-403.

[257] Feih S, Mathys Z, Gibson AG, Mouritz AP. Modeling Compressive Skin Failure of Sandwich Composites in Fire. Journal of Sandwich Structures & Materials. 2008;10:217-45.

[258] Mouritz AP, Feih S, Kandare E, Mathys Z, Gibson AG, Des Jardin PE, et al. Review of fire structural modelling of polymer composites. Composites Part A: Applied Science and Manufacturing. 2009;40:1800-14.

[259] Milke JA, Vizzini AJ. Thermal Response of Fire-Exposed Composites. Journal of Composites Technology & Research. 1991;13:145-51.

[260] Sullivan R, Salamon N. A finite element method for the thermochemical decomposition of polymeric materials—I. Theory. International Journal of Engineering Science. 1992;30:431-41.

[261] Mityushev V, Obnosov YU, Pesetskaya E, Rogosin S. Analytical Methods for Heat Conduction in Composites. Mathematical Modelling and Analysis. 2008;13:67-78.

[262] Mcmanus HL, Springer GSJJoCM. High temperature thermomechanical behavior of carbon-phenolic and carbon-carbon composites, i. analysis. 1992;26:206-29.

[263] Henderson JB, Wiebelt JA, Tant MR. A Model for the Thermal Response of Polymer Composite Materials with Experimental Verification. Journal of Composite Materials. 1985;19:579-95.

[264] Gibson AG, Wu YS, Evans JT, Mouritz AP. Laminate Theory Analysis of Composites under Load in Fire. Journal of Composite Materials. 2005;40:639-58.

[265] Oterkus E, Madenci E. Peridynamics for failure prediction in composites. 53rd AIAA/ASME/ASCE/AHS/ASC Structures, Structural Dynamics and Materials Conference 20th AIAA/ASME/AHS Adaptive Structures Conference 14th AIAA2012. p. 1692.

[266] Oterkus E, Barut A, Madenci E. Damage growth prediction from loaded composite fastener holes by using peridynamic theory. 51st AIAA/ASME/ASCE/AHS/ASC Structures, Structural Dynamics, and Materials Conference 18th AIAA/ASME/AHS Adaptive Structures Conference 12th2010. p. 3026.

[267] Mehrmashhadi J, Chen Z, Zhao J, Bobaru F. A stochastically homogenized peridynamic model for intraply fracture in fiber-reinforced composites. Composites Science and Technology. 2019;182:107770.

[268] Xu J, Askari A, Weckner O, Silling S. Peridynamic analysis of impact damage in composite laminates. Journal of Aerospace Engineering. 2008;21:187-94.

[269] Askari E, Xu J, Silling S. Peridynamic analysis of damage and failure in composites. 44th AIAA aerospace sciences meeting and exhibit2006. p. 88.

[270] Colavito K, Barut A, Madenci E, Phan N. Residual strength of composite laminates with a hole by using peridynamic theory. 54th AIAA/ASME/ASCE/AHS/ASC Structures, Structural Dynamics, and Materials Conference2013. p. 1761.

[271] Nguyen CT, Oterkus S. Peridynamics for the thermomechanical behavior of shell structures. Engineering Fracture Mechanics. 2019;219:106623.

[272] Wang H, Oterkus E, Oterkus S. Three-Dimensional Peridynamic Model for Predicting Fracture Evolution during the Lithiation Process. Energies. 2018;11:1461.

[273] Kilic B, Madenci E. Prediction of crack paths in a quenched glass plate by using peridynamic theory. International Journal of Fracture. 2009;156:165-77.

[274] Madenci E, Oterkus S. Peridynamic modeling of thermo-oxidative damage evolution in a composite lamina. 58th AIAA/ASCE/AHS/ASC Structures, Structural Dynamics, and Materials Conference2017. p. 0197.

[275] De Meo D, Oterkus E. Finite element implementation of a peridynamic pitting corrosion damage model. Ocean Engineering. 2017;135:76-83.

[276] De Meo D, Russo L, Oterkus E. Modeling of the onset, propagation, and interaction of multiple cracks generated from corrosion pits by using peridynamics. Journal of Engineering Materials and Technology. 2017;139.

[277] Jafarzadeh S, Chen Z, Bobaru F. Peridynamic modeling of repassivation in pitting corrosion of stainless steel. Corrosion. 2018;74:393-414.

[278] Jafarzadeh S, Chen Z, Bobaru F. Peridynamic modeling of intergranular corrosion damage. Journal of The Electrochemical Society. 2018;165:C362-C74.

[279] ISO IIOfS, Geneva, Switzerland. 834: Fire resistance tests-elements of building construction. 1999.

[280] Ou KS, Zheng J, Luo WJ, Li XF, Hu HS, Yang JB, et al. Heat and Mechanical Response Analysis of Composite Compressed Natural Gas Cylinders at Vehicle Fire Scenario. Procedia Engineering. 2015;130:1425-40.

[281] Gibson A, Browne T, Feih S, Mouritz A. Modeling composite high temperature behavior and fire response under load. Journal of Composite Materials. 2012;46:2005-22.

[282] Huang X, Gillespie JW, Eduljee RF. Effect of temperature on the transverse cracking behavior of cross-ply composite laminates. Composites Part B: Engineering. 1997;28:419-24.

[283] Merrikh AA, Lage JL. Natural convection in an enclosure with disconnected and conducting solid blocks. International Journal of Heat and Mass Transfer. 2005;48:1361-72.

[284] White FM, Corfield I. Viscous fluid flow: McGraw-Hill New York, 2006.

[285] Chenoweth DR, Paolucci S. Natural convection in an enclosed vertical air layer with large horizontal temperature differences. Journal of Fluid Mechanics. 2006;169:173-210.

[286] Luo C, Xie W, DesJardin PE. Fluid-Structure Simulations of Composite Material Response for Fire Environments. Fire technology. 2009;47:887-912.

[287] Gibson AG, Browne TNA, Feih S, Mouritz AP. Modeling composite high temperature behavior and fire response under load. Journal of Composite Materials. 2012;46:2005-22.

[288] McGrattan KB, Baum HR, Rehm RG, Hamins A, Forney GP. Fire dynamics simulator--Technical reference guide: National Institute of Standards and Technology, Building and Fire Research, 2000.

[289] Rahmani H, Najafi SHM, Ashori A. Mechanical performance of epoxy/carbon fiber laminated composites. Journal of Reinforced Plastics and Composites. 2014;33:733-40.

[290] Nowinski JL. Theory of thermoelasticity with applications: Sijthoff & Noordhoff International Publishers, 1978.

[291] Madenci E, Oterkus S. Ordinary state-based peridynamics for plastic deformation according to von Mises yield criteria with isotropic hardening. Journal of the Mechanics and Physics of Solids. 2016;86:192-219.

[292] Madenci E, Oterkus S. Ordinary state-based peridynamics for thermoviscoelastic deformation. Engineering Fracture Mechanics. 2017;175:31-45.

[293] Heck A. Introduction to MAPLE: Springer-Verlag New York, 1993.

Appendix A. Thermal Modulus for Isotropic Material

The thermal modulus for a material point can be obtained by using the PD local thermal modulus formulation provided in Eq.(3.8) as follows:

When small deformation approximation is adopted, Λ_{ij} provided in Eq. (2.9d) results in $\Lambda_{ij}=1$. Consequently, the integration term in Eq. (3.8) becomes

$$\sum_{j=1}^{N_i}\Lambda_{ij}V_j = V_{H_{\mathbf{x}}} \tag{A.1}$$

with $V_{H_{\mathbf{x}}}$ representing the integration volume.

For 2D problems, the integration domain is a circle disk with its radius, δ and thickness, h_{thick}. On the other hand, the integration domain for 3D problems is a sphere, thus the volume in Eq. (A.1) can be calculated as

$$V_{H_{\mathbf{x}}} = \pi h_{thick}\delta^2 \text{ for 2D} \tag{A.2a}$$

$$V_{H_{\mathbf{x}}} = \frac{4\pi\delta^3}{3} \text{ for 3D} \tag{A.2b}$$

An average value of relative position can also be evaluated by using weighted integration as

$$\left|\boldsymbol{\xi}\right|_{avg} = \frac{\int_{H_{\mathbf{x}}}\left|\boldsymbol{\xi}\right|\mathrm{d}V'}{\int_{H_{\mathbf{x}}}\mathrm{d}V'} = \frac{\int_0^{2\pi}\int_0^{\delta}\left|\boldsymbol{\xi}\right|h_{thick}\left|\boldsymbol{\xi}\right|\mathrm{d}\left|\boldsymbol{\xi}\right|\mathrm{d}\vartheta}{V_{H_{\mathbf{x}}}} = \frac{2\pi h_{thick}\delta^3/3}{\pi h_{thick}\delta^2} = \frac{2\delta}{3} \text{ for 2D} \tag{A.3a}$$

$$\left|\boldsymbol{\xi}\right|_{avg} = \frac{\int_{H_{\mathbf{x}}}\left|\boldsymbol{\xi}\right|\mathrm{d}V'}{\int_{H_{\mathbf{x}}}\mathrm{d}V'} = \frac{\int_0^{\delta}\int_0^{2\pi}\int_0^{\pi}\left|\boldsymbol{\xi}\right|\left|\boldsymbol{\xi}\right|^2\sin(\phi)\,d\phi\mathrm{d}\vartheta\mathrm{d}\left|\boldsymbol{\xi}\right|}{V_{H_{\mathbf{x}}}} = \frac{\pi\delta^4}{4\pi\delta^3/3} = \frac{3\delta}{4} \text{ for 3D} \tag{A.3b}$$

In Eq. (A.3), ϑ represents the bond angle with respect to x axis for 2D cases and ϕ represents the bond angle with respect to the x-y plane for 3D cases.

Recalling the classical material constants

$$K_\theta = \frac{E}{2(1-\nu)},\ \mu = \frac{E}{2(1+\nu)} \text{ for 2D} \tag{A.4a}$$

$$K_\theta = \frac{E}{3(1-2\nu)},\ \mu = \frac{E}{2(1+\nu)} \text{ for 3D} \tag{A.4b}$$

Finally, by substituting Eq. (A.2), Eq. (A.3) and Eq. (A.4) into Eq. (3.6), average PD thermal modulus for a material point can be calculated as

$$\bar{\beta} = \frac{3E\alpha}{\pi h_{thick}\delta^3(1-\nu)} \text{ for 2D} \tag{A.5a}$$

$$\bar{\beta} = \frac{3E\alpha}{\pi\delta^4(1-2\nu)} \text{ for 3D} \tag{A.5b}$$

PD thermal modulus for ordinary state-based form reduces to bond-based form by plugging in $\nu = 1/3$ for 2D and $\nu = 1/4$ for 3D in Eq. (A.5) [43, 44] as

$$\beta_b = \frac{c\alpha}{2} \tag{A.6}$$

with the definition of c being provided in Chapter 2.1.1. As can be seen from the above formulations, bond-based PD has a limitation on Poisson's ratio [10, 11].

Reduced form as Bond-Based PD:

Equation of motion:

In bond-based PD by applying the restriction $a = 0$ in [10], the corresponding PD force functions provided in Eq. (2.9) becomes

$$\mathbf{t}\left(\mathbf{u}_j-\mathbf{u}_i,\mathbf{x}_j-\mathbf{x}_i,t\right)=2\delta b\left(s_{ij}-\alpha T_i\right)\frac{\mathbf{y}_j-\mathbf{y}_i}{\left|\mathbf{y}_j-\mathbf{y}_i\right|} \tag{A.7a}$$

$$\mathbf{t}\left(\mathbf{u}_i-\mathbf{u}_j,\mathbf{x}_i-\mathbf{x}_j,t\right)=-2\delta b\left(s_{ij}-\alpha T_j\right)\frac{\mathbf{y}_j-\mathbf{y}_i}{\left|\mathbf{y}_j-\mathbf{y}_i\right|} \tag{A.7b}$$

By enforcing the magnitude of PD force density provided in Eq. (A.7a) and Eq.(A.7b) to be equal to each other as

$$\mathbf{t}\left(\mathbf{u}_j-\mathbf{u}_i,\mathbf{x}_j-\mathbf{x}_i,t\right)=2\delta b\left(s_{ij}-\alpha\frac{\left(T_i+T_j\right)}{2}\right)\frac{\mathbf{y}_j-\mathbf{y}_i}{\left|\mathbf{y}_j-\mathbf{y}_i\right|} \tag{A.8a}$$

$$\mathbf{t}\left(\mathbf{u}_i-\mathbf{u}_j,\mathbf{x}_i-\mathbf{x}_j,t\right)=-2\delta b\left(s_{ij}-\alpha\frac{\left(T_i+T_j\right)}{2}\right)\frac{\mathbf{y}_j-\mathbf{y}_i}{\left|\mathbf{y}_j-\mathbf{y}_i\right|} \tag{A.8b}$$

it results in $\mathbf{t}\left(\mathbf{u}_j-\mathbf{u}_i,\mathbf{x}_j-\mathbf{x}_i,t\right)=-\mathbf{t}\left(\mathbf{u}_i-\mathbf{u}_j,\mathbf{x}_i-\mathbf{x}_j,t\right)$. By plugging Eq. (A.8) into Eq.(2.3), the equation of motion becomes [43]

$$\rho\ddot{\mathbf{u}}\left(\mathbf{x}_i,t\right)=\sum_{j=1}^{N_i}\left(4\delta bs_{ij}-2b\delta\alpha\left(T_i+T_j\right)\right)\left(\frac{\mathbf{y}_j-\mathbf{y}_i}{\left|\mathbf{y}_j-\mathbf{y}_i\right|}\right)V_j+\mathbf{b}\left(\mathbf{x}_i,t\right) \tag{A.9a}$$

or

$$\rho\ddot{\mathbf{u}}\left(\mathbf{x}_i,t\right)=\sum_{j=1}^{N_i}\left(cs_{ij}-\beta_b\left(T_i+T_j\right)\right)\left(\frac{\mathbf{y}_j-\mathbf{y}_i}{\left|\mathbf{y}_j-\mathbf{y}_i\right|}\right)V_j+\mathbf{b}\left(\mathbf{x}_i,t\right) \tag{A.9b}$$

with bond-based thermal modulus as

$$\beta_b=2b\alpha \tag{A.10a}$$

or

$$\beta_b=\frac{c\alpha}{2} \tag{A.10b}$$

Heat Equation:

The form of the heat conduction equation in bond-based peridynamics remain same as Eq. (3.1) [43]

$$\rho c_v \dot{T}\left(\mathbf{x}_i,t\right)=\sum_{j=1}^{N_i}\left(\kappa\frac{\Theta\left(\mathbf{x}_j,t\right)-\Theta\left(\mathbf{x}_i,t\right)}{\left|\mathbf{x}_j-\mathbf{x}_i\right|}-\Theta_0\beta\left(\mathbf{x}_j-\mathbf{x}_i\right)\dot{e}\left(\mathbf{x}_j-\mathbf{x}_i\right)\right)V_j+h_s\left(\mathbf{x}_i,t\right) \tag{A.11}$$

with bond-based thermal modulus provided in Eq. (A.10).

Appendix B. PD Thermal Parameters for Composites

B.1 PD thermal micro conductivities for composites

The heat conduction equation for a single layer composite provided by Oterkus and Madenci [46] is modified for multi-layer composites as

$$\begin{aligned}\rho c_v \dot{T}_k^n = &\sum_{j=1}^{N_{ply}} \left[\left(\mu_F \kappa_f + \kappa_m \right) \frac{\Theta\left(\mathbf{x}_j^n, t\right) - \Theta\left(\mathbf{x}_k^n, t\right)}{\left|\mathbf{x}_j^n - \mathbf{x}_k^n\right|} \right] V_j^n \\ &+ \sum_{m=n+1, n-1} \sum_{j=1}^{N_{inter}} \left[\kappa_{inter} \frac{\Theta\left(\mathbf{x}_j^m, t\right) - \Theta\left(\mathbf{x}_k^n, t\right)}{\left|\mathbf{x}_j^m - \mathbf{x}_k^n\right|} \right] V_j^m + \rho q_b\left(\mathbf{x}_k^n, t\right)\end{aligned} \tag{B.1}$$

The first term on the right side of Eq. (B.1) represents the in-plane heat conduction in a lamina [46] and the second term represents the heat conduction between the neighbouring layers.

The PD thermal micro conductivities can be determined by applying simple loading conditions and by comparing thermal potentials with classical formulations [43, 44]. The thermal micro conductivities for a lamina provided by Oterkus and Madenci [46] are given in Eq. (4.10)-(4.11). Similarly, the thermal micro conductivity through the thickness direction can be calculated by applying simple loading condition as

$$\Theta\left(x, y, z\right) = z \tag{B.2}$$

The thermal potential in the classical formulation can be calculated under the given loading condition as [10, 39, 44]

$$Z_C = \frac{1}{2} k_m \left(\frac{\partial \Theta}{\partial z} \right)^2 = \frac{1}{2} k_m \tag{B.3}$$

where k_m is the thermal conductivity in the thickness direction. In a resin-rich laminate, the material property in the thickness direction can be assumed to be same as the matrix material property.

The corresponding PD thermal micro-potential developed by the central point **x** and its family member $\mathbf{x}'$ can be evaluated as [39]

$$z_{PD} = \kappa_{inter} \frac{\left[\Theta - \Theta'\right]^2}{2\left|\mathbf{x} - \mathbf{x}'\right|} \tag{B.4}$$

The PD thermal potential is the summation of all microthermal potential with the point, calculated as

$$Z_{PD} = \frac{1}{2}\int_H \kappa_{inter} \frac{\left[\Theta - \Theta'\right]^2}{2\left|\mathbf{x} - \mathbf{x}'\right|} \mathrm{d}V' \tag{B.5}$$

where κ_{inter} is the PD thermal bond constant in the thickness direction. The integration domain, H, for the interlayer thermal bonds between n^{th} ply and m^{th} ply is a circular disk with the thickness being equal to h_{thick}. For the given loading condition, the temperature difference becomes

$$\Theta' - \Theta = h_{thick} \tag{B.6}$$

Therefore, Eq.(B.5) can be evaluated as

$$\begin{aligned} Z_{PD} &= 2\left(\frac{1}{2}\int_0^{2\pi}\int_0^{\delta} \kappa_{inter} \frac{{h_{thick}}^2}{2\sqrt{\left|\xi'\right|^2 + {h_{thick}}^2}} h_{thick} \left|\xi'\right| d\left|\xi'\right| d\varphi \right) \\ &= \pi \kappa_{inter} {h_{thick}}^3 \left(\tilde{\delta} - h_{thick}\right) \end{aligned} \tag{B.7}$$

where ξ' represents the projection of the relative position ξ on the layer in which **x** is located, i.e. $\left|\xi\right| = \sqrt{\left|\xi'\right| + h_{thick}^2}$. By equating the thermal potential from both the classical theory Eq.(B.3) and peridynamic theory Eq.(B.7), the peridynamic bond constant for interlayer interactions can be found as

$$\kappa_{inter} = \frac{k_m}{2\pi {h_{thick}}^3 \left(\tilde{\delta} - h_{thick}\right)} \tag{B.8}$$

where $\tilde{\delta}$ is the horizon for interlayer shear bonds with $\tilde{\delta} = \sqrt{\delta^2 + h_{thick}^2}$ (see Fig. 4-4(b)).

B.2 PD thermal modulus for composites

Free Energy density

The free energy density in classical continuum mechanics for small deformation can be represented by the summation of internal energy density or strain energy and dissipated energy density into heat [290] as

$$\Psi_{CCM} = W_{CCM}^{M} - W_{CCM}^{T} \tag{B.9a}$$

with

$$W_{CCM}^{M} = \frac{1}{2}\{\sigma\}\{\varepsilon\} \tag{B.9b}$$

$$W_{CCM}^{T} = \left[\{\beta_{cl}\}\{\varepsilon\}T + \frac{c_v}{2\Theta_0}T^2\right] \tag{B.9c}$$

where $\{\beta_{cl}\}$ is the thermal modulus vector in classical continuum mechanics, $\{\sigma\}$ is the stress tensor, $\{\varepsilon\}$ is the strain vector and Ψ_{CCM} is the free energy density. Similarly, the PD free energy density can be written [43] as

$$\Psi_{PD} = W_{PD}^{M} - W_{PD}^{T} \tag{B.10a}$$

where

$$W_{PD}^{M} = \frac{1}{2}\underline{\mathbf{U}} \bullet \mathrm{K} \bullet \underline{\mathbf{U}} \tag{B.10b}$$

$$W_{PD}^{T} = \left[\underline{\mathbf{B}} \bullet \underline{\mathbf{U}}T + \frac{c_v}{2\Theta_0}T^2\right] \tag{B.10c}$$

where $\underline{\mathbf{B}}$ is the thermal modulus and $\underline{\mathbf{U}}$ is the displacement in PD theory. Also, $\mathtt{K}$ is the modulus state [50]. Eq. (B.9c) and (B.10c) include the coupling term between mechanical and thermal field.

PD mechanical model is developed by equating the strain energy densities from both theories as [10, 80, 291, 292]

$$W_{CCM}^{M} = W_{PD}^{M} \tag{B.11}$$

Similarly, PD thermal modulus can be found by equating the free energy densities i.e. $\Psi_{CCM} = \Psi_{PD}$, which results in

$$W_{CCM}^{T} = W_{PD}^{T} \tag{B.12}$$

PD thermal modulus expression for single-layer/ lamina model

The peridynamic representation of thermal modulus is determined by applying 2 simple loading conditions as:

Loading 1:

$$\varepsilon_{11} = \zeta, \varepsilon_{22} = \gamma_{12} = 0 \tag{B.13a}$$

Loading 2:

$$\varepsilon_{22} = \zeta, \varepsilon_{11} = \gamma_{12} = 0 \tag{B.13b}$$

According to CCM:

In classical continuum mechanics, with respect to the material coordinate system, the thermal modulus for a lamina is defined as

$$\{\beta_{cl}\} = [Q]\{\alpha\} \tag{B.14}$$

where $[Q]$ is the reduced stiffness matrix given in Eq. (4.7). The thermal expansion coefficient vector, $\{\alpha\}$, is defined as

$$\{\alpha\} = \begin{Bmatrix} \alpha_1 \\ \alpha_2 \\ 0 \end{Bmatrix} \tag{B.15}$$

Under the given two loading conditions, the first term on the right-hand side of Eq. (B.9c) can be obtained as:

Loading 1:

$$\{\beta_{cl}\}\{\varepsilon\}T = [Q]\{\alpha\}\{\varepsilon\}T = \begin{Bmatrix} Q_{11}\alpha_1 + Q_{12}\alpha_2 \\ Q_{12}\alpha_1 + Q_{22}\alpha_2 \\ 0 \end{Bmatrix} \cdot \begin{Bmatrix} \zeta \\ 0 \\ 0 \end{Bmatrix} T = \left(Q_{11}\alpha_1 + Q_{12}\alpha_2\right)\zeta T \tag{B.16a}$$

Loading 2:

$$\{\beta_{cl}\}\{\varepsilon\}T = [Q]\{\alpha\}\{\varepsilon\}T = \begin{Bmatrix} Q_{11}\alpha_1 + Q_{12}\alpha_2 \\ Q_{12}\alpha_1 + Q_{22}\alpha_2 \\ 0 \end{Bmatrix} \cdot \begin{Bmatrix} 0 \\ \zeta \\ 0 \end{Bmatrix} T = \left(Q_{12}\alpha_1 + Q_{22}\alpha_2\right)\zeta T \tag{B.16b}$$

According to PD theory:

Corresponding PD representation can be defined as:

$$\underline{\mathbf{B}} \bullet \underline{\mathbf{U}} T = T \int_H \beta \left(\frac{\mathbf{y}' - \mathbf{y}}{|\mathbf{y}' - \mathbf{y}|} \right) \cdot \mathbf{u}\left(\mathbf{x}' - \mathbf{x}\right) \mathrm{d}H \tag{B.17}$$

By using small-angle approximation Eq. (B.17) becomes as (See Figure B-1):

$$\underline{\mathbf{B}} \bullet \underline{\mathbf{U}} T = T \int_H \beta \eta_X \mathrm{d}H = T \int_H \beta \left(|\mathbf{y}' - \mathbf{y}| - |\mathbf{x}' - \mathbf{x}| \right) \mathrm{d}H \tag{B.18}$$

with

$$\eta_X = u'_X - u_X = \cos(\varphi)\left(u'_x - u_x\right) + \sin(\varphi)\left(u'_y - u_y\right) \tag{B.19}$$

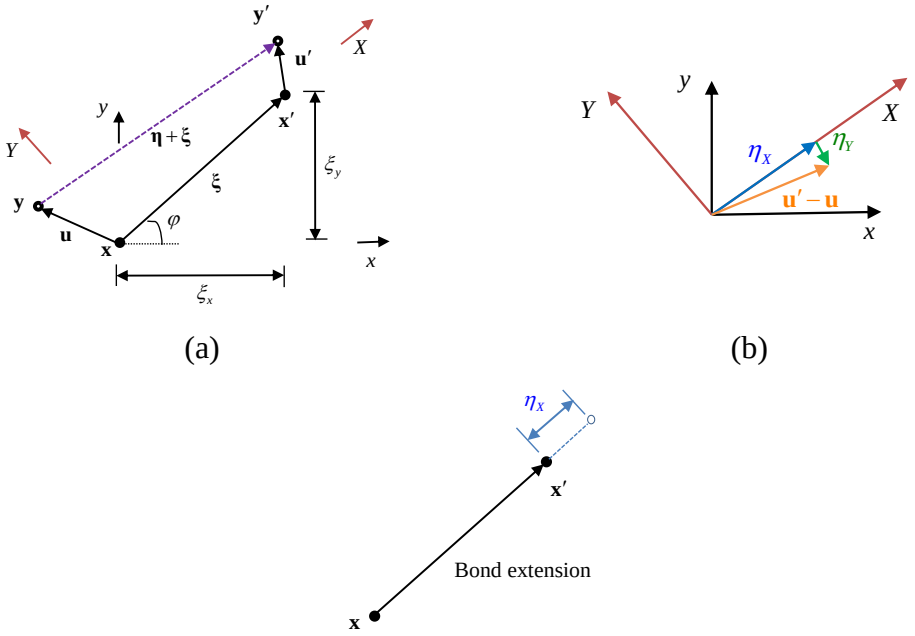

Figure B-1 Relative displacement between points $\mathbf{x}$ and $\mathbf{x}'$ in different coordinates [76].

The relative distances in deformed configuration between the material points $\mathbf{x}$ and $\mathbf{x}'$ for given loading conditions are,

Loading 1:

$$\left|\mathbf{y}' - \mathbf{y}\right| = \left[1 + \zeta\cos^2(\varphi)\right]\left|\mathbf{x}' - \mathbf{x}\right| \tag{B.20a}$$

Loading 2:

$$\left|\mathbf{y}' - \mathbf{y}\right| = \left[1 + \zeta\sin^2(\varphi)\right]\left|\mathbf{x}' - \mathbf{x}\right| \tag{B.20b}$$

Eq. (B.18) for given loading conditions can be defined as:

Loading 1:

$$\underline{\mathbf{B}} \cdot \underline{\mathbf{U}}T = T\int_H \left(\mu_F \beta_f + \beta_m\right)\left|\mathbf{x}' - \mathbf{x}\right|\left(\zeta\cos^2(\varphi)\right)\mathrm{d}H \tag{B.21a}$$

Loading 2:

$$\underline{\mathbf{B}} \cdot \underline{\mathbf{U}} T = T \int_H \left(\mu_F \beta_f + \beta_m \right) \left| \mathbf{x}' - \mathbf{x} \right| \left(\zeta \sin^2 \left(\varphi \right) \right) \mathrm{d}H \tag{B.21b}$$

By plugging the relative distance between the material points **x** and **x**′ into Eq.(B.21), Eq.(B.21) becomes

Loading 1:

$$\begin{aligned} \underline{\mathbf{B}} \cdot \underline{\mathbf{U}} T &= T \int_H \left(\mu_F \beta_f + \beta_m \right) \zeta \cos^2 \left(\varphi \right) \left| \underline{\xi} \right| \mathrm{d}H \\ &= T \int_0^{2\pi} \int_0^{\delta} \left(\mu_F \beta_f + \beta_m \right) \zeta \cos^2 \left(\varphi \right) \left| \underline{\xi} \right| h_{thick} \left| \underline{\xi} \right| d \left| \underline{\xi} \right| d\varphi \\ &= \zeta T \left[\sum_{\mathbf{x}'=1}^{N_F} \beta_f \left| \underline{\xi} \right| V' + \frac{\pi h_{thick} \delta^3}{3} \beta_m \right] \end{aligned} \tag{B.22a}$$

Loading 2:

$$\begin{aligned} \underline{\mathbf{B}} \cdot \underline{\mathbf{U}} T &= T \int_H \left(\mu_F \beta_f + \beta_m \right) \zeta \sin^2 \left(\varphi \right) \left| \underline{\xi} \right| \mathrm{d}H \\ &= T \int_0^{2\pi} \int_0^{\delta} \left(\mu_F \beta_f + \beta_m \right) \zeta \sin^2 \left(\varphi \right) \left| \underline{\xi} \right| h_{thick} \left| \underline{\xi} \right| d \left| \underline{\xi} \right| d\varphi \\ &= \zeta T \left(\frac{\pi h_{thick} \delta^3}{3} \beta_m \right) \end{aligned} \tag{B.22b}$$

By equating the expressions Eq. (B.16) and Eq. (B.22), the following relations are obtained as

$$\sum_{\mathbf{x}'=1}^{N_f} \beta_f \left| \underline{\xi} \right| V' + \frac{\pi h_{thick} \delta^3}{3} \beta_m = Q_{11} \alpha_1 + Q_{12} \alpha_2 \tag{B.23a}$$

and

$$\frac{\pi h_{thick} \delta^3}{3} \beta_m = Q_{12} \alpha_1 + Q_{22} \alpha_2 \tag{B.23b}$$

Finally, the expressions of β_f and β_f are defined as

$$\beta_f = \frac{\left(Q_{11}\alpha_1 + Q_{12}\alpha_2\right) - \left(Q_{12}\alpha_1 + Q_{22}\alpha_2\right)}{\sum_{\mathbf{x}'=1}^{N_F} |\boldsymbol{\xi}| V'} \tag{B.24a}$$

and

$$\beta_m = \frac{3\left(Q_{12}\alpha_1 + Q_{22}\alpha_2\right)}{\pi h_{thick}\delta^3} \tag{B.24b}$$

PD thermal modulus for a 2D isotropic material Eq. (B.24) becomes

$$\beta_f = 0 \tag{B.25a}$$

$$\beta_m = \frac{6K_\theta\alpha}{\pi h_{thick}\delta^3} = \frac{3E\alpha}{\pi h_{thick}\delta^3(1-\nu)} = \frac{3\beta_{cl}}{\pi h_{thick}\delta^3} \tag{B.25b}$$

with

$$\alpha_1 = \alpha_2 = \alpha, Q_{11} = Q_{22} = K_\theta + \mu, Q_{12} = K_\theta - \mu \tag{B.26}$$

where K_θ and μ are bulk modulus and Lamé constant, respectively. The PD parameters provided in Eq. (B.25) are consistent with the ones in [5].

Furthermore, for bond-based peridynamic theory the PD thermal modulus will reduce to [43];

$$\beta_f = 0 \tag{B.27a}$$

$$\beta_m = \frac{1}{2}c\alpha \tag{B.27b}$$

with

$$c = \frac{9E}{\pi h_{thick}\delta^3} \text{ for 2D} \tag{B.27c}$$

PD thermal modulus expression for multi-layer/ laminate model

In a multi-layer/laminate model, the expressions of the PD thermal modulus associated with in-plane bonds remain the same as the ones in the lamina model (Appendix B.2). The PD thermal model for multi-layer composites including coupling effects can be written as

$$\begin{aligned}\rho c_v \dot{T}_k^n = &\sum_{j=1}^{N_{ply}} \left[\left(\mu_F \kappa_f + \kappa_m \right) \frac{\Theta\left(\mathbf{x}_j^n, t\right) - \Theta\left(\mathbf{x}_k^n, t\right)}{\left|\mathbf{x}_j^n - \mathbf{x}_k^n\right|} - \Theta_0 \left(\mu_F \beta_f + \beta_m \right) \dot{e}_{kj}^n \right] V_j^n \\ &+ \sum_{m=n+1,n-1} \sum_{j=1}^{N_{inter}} \left[\kappa_{inter} \frac{\Theta\left(\mathbf{x}_j^m, t\right) - \Theta\left(\mathbf{x}_k^n, t\right)}{\left|\mathbf{x}_j^m - \mathbf{x}_k^n\right|} - \Theta_0 \beta_{inter} \dot{e}_{kj,z}^{nm} \right] V_j^m + \rho q_b \left(\mathbf{x}_k^n, t\right)\end{aligned} \tag{B.28}$$

Similarly, PD thermal modulus can be found by equating the free energy densities from PD theory and CCM as given in Eq. (B.12) for simple loading conditions.

In order to derive the expression of PD thermal modulus, a uniform transverse normal stretch is applied as

$$\varepsilon_{33} = \zeta \tag{B.29}$$

According to CCM:

Under the given loading condition, the first term on the right-hand side of Eq. (B.9c) can be obtained as:

$$\{\beta_{cl}\}\{\varepsilon\} T = \{E_m \alpha_m\}\{\zeta\} T = E_m \alpha_m \zeta T \tag{B.30}$$

According to PD theory:

Under the given loading condition, as illustrated in Figure B-2, for the material point $\mathbf{x}_k^n$ of interest, the relative positions in undeformed and deformed configurations are

$$\left|\mathbf{x}_j^m - \mathbf{x}_k^n\right| = \sqrt{h_{thick}^2 + l^2} \tag{B.31a}$$

$$\left|\mathbf{y}_j^m-\mathbf{y}_k^n\right|=\sqrt{\left(1+\zeta\right)^2 h_{thick}^2+l^2} \tag{B.31b}$$

with $l=\left|\mathbf{y}_j^m-\mathbf{y}_k^n\right|$ and $m=\left(n+1,n-1\right)$

Consequently, the relative displacement becomes

$$\left|\mathbf{y}_j^m-\mathbf{y}_k^n\right|-\left|\mathbf{x}_j^m-\mathbf{x}_k^n\right|=\sqrt{\left(1+\zeta\right)^2 h_{thick}^2+l^2}-\sqrt{h_{thick}^2+l^2}\approx\frac{\zeta h_{thick}^2}{\sqrt{h_{thick}^2+l^2}} \tag{B.32}$$

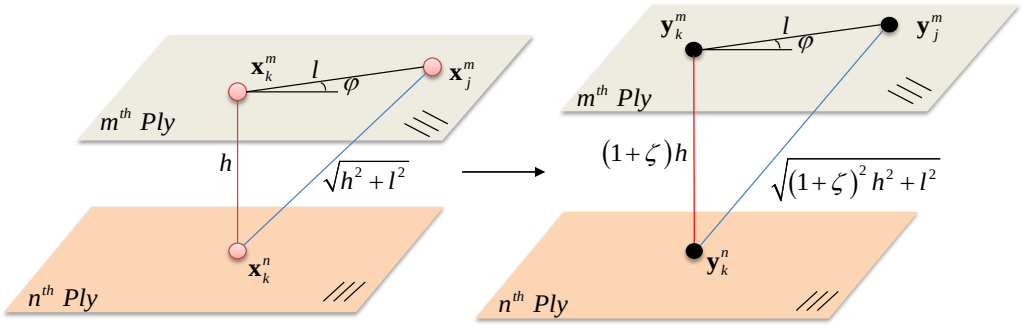

Figure B-2 Illustration of relative positions in undeform and deformed configurations.

The integration domain, H, is a circular disk with radius being δ and thickness being h_{thick}. Therefore, by considering the two adjacent plies $m=\left(n+1,n-1\right)$, Eq. (B.17) can be calculated as

$$\begin{aligned}\underline{\mathbf{B}}\cdot\underline{\mathbf{U}}T&=2\int_H\beta_{inter}\frac{\zeta h_{thick}^2}{\sqrt{h_{thick}^2+l^2}}\mathrm{d}H\\&=2\int_0^{2\pi}\int_0^{\delta}\beta_{inter}\frac{\zeta h_{thick}^2}{\sqrt{h_{thick}^2+l^2}}h_{thick}l\mathrm{d}l\mathrm{d}\varphi=4\pi\beta_{inter}\zeta h_{thick}^3\left(\tilde{\delta}-h_{thick}\right)\end{aligned} \tag{B.33}$$

By equating Eq.(B.30) and Eq.(B.33), the expression of β_{inter} can be obtained as

$$\beta_{inter}=\frac{E_m\alpha_m}{4\pi h_{thick}^3\left(\tilde{\delta}-h_{thick}\right)} \tag{B.34}$$

Appendix C. Surface Correction Factor for Composites

The values of the PD parameters depend on the domain of integration which is decided by the horizon. Therefore, surface correction factors are needed when the material points are located near the free surface. The surface correction factors for mechanical parameters for composite materials and isotropic materials have already been provided in [10, 44, 291]. The surface correction factors for PD micro conductivity κ and PD thermal modulus β will be discussed in here.

The surface correction factors of the PD micro conductivity are achieved by comparing the thermal potential obtained from PD and classical formulations under simple loading conditions [43, 44]. The correctors of thermal modulus can be obtained by equating the free energy densities calculated from the two theories.

C.1 Surface correction factors for PD micro conductivity

Surface correction factors for single-layer/lamina model

As illustrated in Figure C-1, the coordinates of the material point $\mathbf{x}_k$ are denoted as (x_k, y_k) for the global coordinate system and (X_k^1, X_k^2) for the material coordinate system.

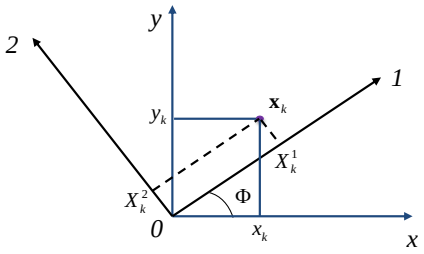

Figure C-1 Coordinate system illustrations.

A simple linear temperature field, $\Theta = X^1 + X^2$, is applied to the lamina. The corresponding temperature difference between two material points is

$$\Theta_j - \Theta_k = \left(X_j^1 + X_j^2\right) - \left(X_k^1 + X_k^2\right) \tag{C.1}$$

The PD thermal potential at material point $\mathbf{x}_k$ can be expressed as

$$Z_k^{PD} = Z_{k,F}^{PD} + Z_{k,M}^{PD} \tag{C.2}$$

where $Z_{k,F}^{PD}$ and $Z_{k,M}^{PD}$ represent the contributions from fibre thermal bonds and the matrix thermal bonds. By using the expression given in Eq.(B.5), the PD thermal potential can also be expressed as [39, 43]

$$Z_{k,F}^{PD} = \frac{1}{2}\sum_{j=1}^{N_F} \kappa_f \frac{\left(\left(X_j^1 + X_j^2\right) - \left(X_k^1 + X_k^2\right)\right)^2}{2\left|\mathbf{x}_j - \mathbf{x}_k\right|} \tag{C.3a}$$

and

$$Z_{k,M}^{PD}\left(\mathbf{x}_k\right) = \frac{1}{2}\sum_{j=1}^{N_{ply}} \kappa_m \frac{\left(\left(X_j^1 + X_j^2\right) - \left(X_k^1 + X_k^2\right)\right)^2}{2\left|\mathbf{x}_j - \mathbf{x}_k\right|} \tag{C.3b}$$

On the other hand, corresponding thermal potential can be calculated as [10, 43, 44]

$$Z = \frac{1}{2}\left(k_1\left(\frac{\partial\Theta}{\partial X_1}\right)^2 + k_2\left(\frac{\partial\Theta}{\partial X_2}\right)^2\right) = \frac{1}{2}\left(k_1 + k_2\right) \tag{C.4}$$

The lamina will become a matrix material when $k_1 = k_2$, then the corresponding thermal potential is

$$Z_M = \frac{1}{2}\left(k_2\left(\frac{\partial\Theta}{\partial X_1}\right)^2 + k_2\left(\frac{\partial\Theta}{\partial X_2}\right)^2\right) = k_2 \tag{C.5}$$

Therefore, the thermal potential given in Eq.(C.4) can be expressed as

$$Z = Z_M + Z_F \tag{C.6}$$

with

$$Z_F = \frac{1}{2}\left(k_1 - k_2\right) \tag{C.7a}$$

and

$$Z_M = k_2 \tag{C.7b}$$

where Z_F and Z_M are the thermal potentials related to the fibre material and matrix material, respectively.

Consequently, the surface correction factors of κ_f and κ_m at point $\mathbf{x}_k$ can be calculated as

$$S_F\left(\mathbf{x}_k\right) = \frac{Z_F}{Z_{k,F}^{PD}} = \frac{\frac{1}{2}\left(k_1 - k_2\right)}{\frac{1}{2}\sum_{j=1}^{N_F}\kappa_f \frac{\left(\left(X_j^1 + X_j^2\right) - \left(X_k^1 + X_k^2\right)\right)^2}{2\left|\mathbf{x}_j - \mathbf{x}_k\right|}} \tag{C.8a}$$

and

$$S_M\left(\mathbf{x}_k\right) = \frac{Z_M}{Z_{k,M}^{PD}} = \frac{k_2}{\frac{1}{2}\sum_{j=1}^{N_{ply}}\kappa_m \frac{\left(\left(X_j^1 + X_j^2\right) - \left(X_k^1 + X_k^2\right)\right)^2}{2\left|\mathbf{x}_j - \mathbf{x}_k\right|}} \tag{C.8b}$$

Surface correction factors for multi-layer composite model

For a multi-layer thermal composite model, the surface correction factors for κ_f and κ_m remain the same. Thus, only the derivation of the surface correction factors for the interlayer micro conductivity κ_{inter} is explained in this section. A linear temperature field $\Theta\left(x, y, z\right) = z$ is applied to all the plies with respect to the global coordinate system. Subsequently, the temperature difference is calculated as

$$\Theta_j^m - \Theta_k^n = z_j^m - z_k^n \tag{C.9}$$

where the point $\mathbf{x}_k^n$ is in the n^{th} and $\mathbf{x}_j^m$ is in the m^{th} ply. Therefore, the temperature difference is zero between $\mathbf{x}_j^n$ and $\mathbf{x}_k^n$. The thermal potential of point $\mathbf{x}_k^n$ can be calculated as

$$\begin{aligned} Z_{inter}^{PD} &= \sum_{m=n+1,n-1} \frac{1}{2} \sum_{j=1}^{N_{inter}} \kappa_{inter} \frac{\left(z_j^m - z_k^n\right)^2}{2\left|\xi\right|} \\ &= \begin{cases} \dfrac{1}{2} \displaystyle\sum_{j=1}^{N_{inter}} \kappa_{inter} \frac{h_{thick}^2}{2\left|\mathbf{x}_j^m - \mathbf{x}_k^n\right|} & for\ n = 1, N \\ \displaystyle\sum_{m=n-1,\, n+1} \frac{1}{2} \sum_{j=1}^{N_{inter}} \kappa_{inter} \frac{h_{thick}^2}{2\left|\mathbf{x}_j^m - \mathbf{x}_k^n\right|} & for\ n = 2, 3, \cdots N-1 \end{cases} \end{aligned} \tag{C.10}$$

where N is the total number of plies in a laminate (see Fig. 4-4(a)).

Corresponding thermal potential in CCM can be calculated as

$$Z_{inter} = \frac{1}{2}\left(k_3 \left(\frac{\partial \Theta}{\partial z} \right)^2 \right) = \frac{1}{2} k_3 \tag{C.11}$$

There is only one adjacent layer for the bottom and top ply. However, the value of κ_{inter} is calculated by summing the thermal potential energy developed by two plies. Therefore, to calculate the surface correction factors for the points in the bottom and top plies, the PD thermal potential developed by interlayer thermal bonds are doubled. In conclusion, the surface correction factors for κ_{inter} are given as

$$S_{inter}\left(\mathbf{x}_k^n\right)=\frac{Z_{inter}}{Z_{inter}^{PD}}=\begin{cases}\dfrac{\frac{1}{2}k_3}{2\left(\frac{1}{2}\sum_{j=1}^{N_{inter}}\kappa_{inter}\dfrac{h_{thick}^2}{2\left|\mathbf{x}_j^m-\mathbf{x}_k^n\right|}\right)} & \text{for } n=1,\ N\\ \dfrac{\frac{1}{2}k_3}{\sum_{m=n-1,\ n+1}\frac{1}{2}\sum_{j=1}^{N_{inter}}\kappa_{inter}\dfrac{h_{thick}^2}{2\left|\mathbf{x}_j^m-\mathbf{x}_k^n\right|}} & \textit{for } n=2,3,\cdots N-1\end{cases} \tag{C.12}$$

where h_{thick} is the thickness of a single layer.

C.2 Surface correction factors for PD thermal modulus

Surface correction factors for the single-layer composite model

The surface correction factors for PD thermal moduli β_f and β_m are determined by applying two different loading conditions as in the fibre direction then in the transverse direction as:

Loading 1:

$$\mathbf{u}_1=\left\{\zeta x_1 \quad 0\right\} \tag{C.13a}$$

Loading 2:

$$\mathbf{u}_2=\left\{0 \quad \zeta x_2\right\} \tag{C.13b}$$

The orthotropic property of a single layer composite is assumed as the summation of a matrix material and a fibre material that only exists in the fibre direction. In analogy with the PD thermal modulus components, the classical thermal modulus β_{cl} is assumed to be

$$\beta_{cl}=\begin{Bmatrix}\beta_{cl}^f+\beta_{cl}^m\\ \beta_{cl}^m\\ 0\end{Bmatrix}=\begin{Bmatrix}Q_{11}\alpha_1+Q_{12}\alpha_2\\ Q_{12}\alpha_1+Q_{22}\alpha_2\\ 0\end{Bmatrix} \tag{C.14a}$$

with

$$\beta_{cl}^{f} = \left(Q_{11}\alpha_1 + Q_{12}\alpha_2\right) - \left(Q_{12}\alpha_1 + Q_{22}\alpha_2\right) \tag{C.14b}$$

$$\beta_{cl}^{m} = Q_{12}\alpha_1 + Q_{22}\alpha_2 \tag{C.14c}$$

Under given loading conditions, the first term on the right-hand side of Eq. (B.9c) can be obtained as:

Load 1:

$$\{\beta_{cl}\}\{\varepsilon\}T = [Q]\{\alpha\}\{\varepsilon\}T = \begin{Bmatrix} Q_{11}\alpha_1 + Q_{12}\alpha_2 \\ Q_{12}\alpha_1 + Q_{22}\alpha_2 \\ 0 \end{Bmatrix} \cdot \begin{Bmatrix} \zeta \\ 0 \\ 0 \end{Bmatrix} T = \left(Q_{11}\alpha_1 + Q_{12}\alpha_2\right)\zeta T \tag{C.15a}$$

with

$$\left\{\beta_{cl}^{f,1}\right\}\{\varepsilon\}T = \left[\left(Q_{11}\alpha_1 + Q_{12}\alpha_2\right) - \left(Q_{12}\alpha_1 + Q_{22}\alpha_2\right)\right]\zeta T \tag{C.15b}$$

$$\left\{\beta_{cl}^{m,1}\right\}\{\varepsilon\}T = \left[Q_{12}\alpha_1 + Q_{22}\alpha_2\right]\zeta T \tag{C.15c}$$

Load 2:

$$\{\beta_{cl}\}\{\varepsilon\}T = [Q]\{\alpha\}\{\varepsilon\}T = \begin{Bmatrix} Q_{11}\alpha_1 + Q_{12}\alpha_2 \\ Q_{12}\alpha_1 + Q_{22}\alpha_2 \\ 0 \end{Bmatrix} \cdot \begin{Bmatrix} 0 \\ \zeta \\ 0 \end{Bmatrix} T = \left(Q_{12}\alpha_1 + Q_{22}\alpha_2\right)\zeta T \tag{C.16a}$$

with

$$\left\{\beta_{cl}^{f,2}\right\}\{\varepsilon\}T = 0 \tag{C.16b}$$

$$\left\{\beta_{cl}^{m,2}\right\}\{\varepsilon\}T = \left[Q_{12}\alpha_1 + Q_{22}\alpha_2\right]\zeta T \tag{C.16c}$$

Since there is no deformation in the fibre direction, the fibres do not deform under load 2. Therefore, the deformation effect of fibre on temperature is zero.

Corresponding PD representation can be defined by using Eq. (B.18) as:

Load 1:

$$\left(\underline{\mathbf{B}}\bullet\underline{\mathbf{U}}\right)^{f,1}T=T\sum_{j=1}^{N_f}\beta_f\left(\mathbf{u}_1\left(\mathbf{x}_j\right)-\mathbf{u}_1\left(\mathbf{x}_k\right)\right)\cdot\frac{\mathbf{y}_j-\mathbf{y}_k}{\left|\mathbf{y}_j-\mathbf{y}_k\right|}V_j \tag{C.17a}$$

$$\left(\underline{\mathbf{B}}\bullet\underline{\mathbf{U}}\right)^{m,1}T=T\sum_{j=1}^{N_{ply}}\beta_m\left(\mathbf{u}_1\left(\mathbf{x}_j\right)-\mathbf{u}_1\left(\mathbf{x}_k\right)\right)\cdot\frac{\mathbf{y}_j-\mathbf{y}_k}{\left|\mathbf{y}_j-\mathbf{y}_k\right|}V_j \tag{C.17b}$$

Load 2:

$$\left(\underline{\mathbf{B}}\bullet\underline{\mathbf{U}}\right)^{f,2}T=0 \tag{C.18a}$$

$$\left(\underline{\mathbf{B}}\bullet\underline{\mathbf{U}}\right)^{m,2}T=T\sum_{j=1}^{N_{ply}}\beta_m\left(\mathbf{u}_2\left(\mathbf{x}_j\right)-\mathbf{u}_2\left(\mathbf{x}_k\right)\right)\cdot\frac{\mathbf{y}_j-\mathbf{y}_k}{\left|\mathbf{y}_j-\mathbf{y}_k\right|}V_j \tag{C.18b}$$

As a result, the surface correction factors are

$$S_F^1\left(\mathbf{x}_k,\mathbf{x}_j\right)=\frac{\left\{\beta_{cl}^{f,1}\right\}\left\{\varepsilon\right\}T}{\left(\underline{\mathbf{B}}\bullet\underline{\mathbf{U}}\right)^{f,1}T}=\frac{\left[\left(Q_{11}\alpha_1+Q_{12}\alpha_2\right)-\left(Q_{12}\alpha_1+Q_{22}\alpha_2\right)\right]\zeta}{\sum_{j=1}^{N_F}\beta_f\left(\mathbf{u}_1\left(\mathbf{x}_j\right)-\mathbf{u}_1\left(\mathbf{x}_k\right)\right)\cdot\frac{\mathbf{y}_j-\mathbf{y}_k}{\left|\mathbf{y}_j-\mathbf{y}_k\right|}V_j} \tag{C.19a}$$

$$S_M^1\left(\mathbf{x}_k,\mathbf{x}_j\right)=\frac{\left\{\beta_{cl}^{m,1}\right\}\left\{\varepsilon\right\}T}{\left(\underline{\mathbf{B}}\bullet\underline{\mathbf{U}}\right)^{m,1}T}=\frac{\left[Q_{12}\alpha_1+Q_{22}\alpha_2\right]\zeta}{\sum_{j=1}^{N_{ply}}\beta_m\left(\mathbf{u}_1\left(\mathbf{x}_j\right)-\mathbf{u}_1\left(\mathbf{x}_k\right)\right)\cdot\frac{\mathbf{y}_j-\mathbf{y}_k}{\left|\mathbf{y}_j-\mathbf{y}_k\right|}V_j} \tag{C.19b}$$

$$S_F^2\left(\mathbf{x}_k,\mathbf{x}_j\right)=1 \tag{C.19c}$$

$$S_M^2\left(\mathbf{x}_k,\mathbf{x}_j\right)=\frac{\left\{\beta_{cl}^{m,2}\right\}\left\{\varepsilon\right\}T}{\left(\underline{\mathbf{B}}\bullet\underline{\mathbf{U}}\right)^{m,2}T}=\frac{\left[Q_{12}\alpha_1+Q_{22}\alpha_2\right]\zeta}{\sum_{j=1}^{N_{ply}}\beta_m\left(\mathbf{u}_2\left(\mathbf{x}_j\right)-\mathbf{u}_2\left(\mathbf{x}_k\right)\right)\cdot\frac{\mathbf{y}_j-\mathbf{y}_k}{\left|\mathbf{y}_j-\mathbf{y}_k\right|}V_j} \tag{C.19d}$$

It should be noted that these correction factors are validated for the fibre and transverse directions. They can act as the principal values of an ellipse [10] to approximate the surface corrections in any other directions as

$$S_F\left(\mathbf{x}_k,\mathbf{x}_j\right)=1/\sqrt{\left(n_1/S_F^1\left(\mathbf{x}_k,\mathbf{x}_j\right)\right)^2+\left(n_2/S_F^2\left(\mathbf{x}_k,\mathbf{x}_j\right)\right)^2} \tag{C.20a}$$

and

$$S_M\left(\mathbf{x}_k,\mathbf{x}_j\right)=1/\sqrt{\left(n_1/S_M^1\left(\mathbf{x}_k\right)\right)^2+\left(n_2/S_M^2\left(\mathbf{x}_k\right)\right)^2}, \tag{C.20b}$$

where n_1 and n_2 are the projections of the relative position vector between $\mathbf{x}_k$ and $\mathbf{x}_j$ in fibre and transverse directions.

Surface correction factors for multi-layer composite model

For a multi-layer composite model, the surface correction factors for in-plane directions remain the same as the ones calculated in lamina model. The surface correction factor for the thickness direction is developed. A third loading condition is applied as

Load 3:

$$\mathbf{u}_3=\{0 \quad 0 \quad \zeta z\} \tag{C.21}$$

Under the given loading condition, the second term on the right-hand side in Eq. (B.9c) can be obtained as:

$$\{\beta_{cl}\}\{\varepsilon\}T=E_m\alpha_m\zeta T \tag{C.22}$$

Corresponding PD representation can be defined by using Eq. (B.18) as

$$\underline{\mathbf{B}}\bullet\underline{\mathbf{U}}T=T\sum_{m=n+1,n-1}\sum_{j=1}^{N_{inter}}\beta_{inter}\left(\mathbf{u}_z\left(\mathbf{x}_j\right)-\mathbf{u}_z\left(\mathbf{x}_k\right)\right)\cdot\frac{\mathbf{y}_j-\mathbf{y}_k}{\left|\mathbf{y}_j-\mathbf{y}_k\right|}V_j^m \tag{C.23}$$

Then the surface correction factor for β_{inter} is

$$S_z^{\beta}\left(\mathbf{x}_k^n, \mathbf{x}_j^m\right) = \frac{\{\beta_{cl}\}\{\varepsilon\}T}{\underline{\mathbf{B}} \bullet \underline{\mathbf{U}}T}$$

$$= \begin{cases} \dfrac{E_m \alpha_m \zeta}{2\sum_{j=1}^{N_{inter}} \beta_{inter}\left(\mathbf{u}_z\left(\mathbf{x}_j\right) - \mathbf{u}_z\left(\mathbf{x}_k\right)\right) \cdot \dfrac{\mathbf{y}_j - \mathbf{y}_k}{\left|\mathbf{y}_j - \mathbf{y}_k\right|} V_j^m} & \text{for } n = 1, N \\ \dfrac{E_m \alpha_m \zeta}{\sum_{m=n+1,n-1} \sum_{j=1}^{N_{inter}} \beta_{inter}\left(\mathbf{u}_z\left(\mathbf{x}_j\right) - \mathbf{u}_z\left(\mathbf{x}_k\right)\right) \cdot \dfrac{\mathbf{y}_j - \mathbf{y}_k}{\left|\mathbf{y}_j - \mathbf{y}_k\right|} V_j^m} & n = 2, 3, \cdots N-1 \end{cases}$$

(C.24)

Appendix D. Analytical solution for 2D PDDO

For 2D PD differential operator, the integration domain, $H_{\mathbf{x}}$, is set to be a disk with its radius being horizon δ and thickness being h_{thick}, analytical form of PD differential operator can also be calculated.

By utilizing the weighted function

$$w(\xi) = e^{-(2\xi/\delta)^2} \tag{D.1}$$

and substituting $\xi = |\boldsymbol{\xi}|$, $\xi_1 = \xi\cos(\theta)$, and $\xi_2 = \xi\sin(\theta)$ with θ being the bond direction with respect to the positive x_1 direction into Eq.(2.28a), the analytical form of shape matrix, $\mathbf{A}$, can be obtained as

$$\mathbf{A} = \int_0^{2\pi}\int_0^{\delta} e^{-(2\xi/\delta)^2} \begin{bmatrix} \xi^2\mathrm{c}^2 & \xi^2\mathrm{cs} & \xi^3\mathrm{c}^3 & \xi^3\mathrm{cs}^2 & \xi^3\mathrm{c}^2\mathrm{s} \\ \xi^2\mathrm{cs} & \xi^2\mathrm{s}^2 & \xi^3\mathrm{c}^2\mathrm{s} & \xi^3\mathrm{s}^3 & \xi^3\mathrm{cs}^2 \\ \xi^3\mathrm{c}^3 & \xi^3\mathrm{c}^2\mathrm{s} & \xi^4\mathrm{c}^4 & \xi^4\mathrm{c}^2\mathrm{s}^2 & \xi^4\mathrm{c}^3\mathrm{s} \\ \xi^3\mathrm{cs}^2 & \xi^3\mathrm{s}^3 & \xi^4\mathrm{c}^2\mathrm{s}^2 & \xi^4\mathrm{s}^4 & \xi^4\mathrm{cs}^3 \\ \xi^3\mathrm{c}^2\mathrm{s} & \xi^3\mathrm{cs}^2 & \xi^4\mathrm{c}^3\mathrm{s} & \xi^4\mathrm{cs}^3 & \xi^4\mathrm{c}^2\mathrm{s}^2 \end{bmatrix} h_{thick}\xi\,\mathrm{d}\xi\,\mathrm{d}\theta \tag{D.2}$$

where $\mathrm{c} = \cos(\theta)$ and $\mathrm{s} = \sin(\theta)$. After performing the integrations, Eq.(D.2) results in

$$\mathbf{A} = \frac{\pi h_{thick}\delta^4}{32e^4} \begin{bmatrix} (e^4-5) & 0 & 0 & 0 & 0 \\ 0 & (e^4-5) & 0 & 0 & 0 \\ 0 & 0 & \frac{3(e^4-13)\delta^2}{8} & \frac{(e^4-13)\delta^2}{8} & 0 \\ 0 & 0 & \frac{(e^4-13)\delta^2}{8} & \frac{3(e^4-13)\delta^2}{8} & 0 \\ 0 & 0 & 0 & 0 & \frac{(e^4-13)\delta^2}{8} \end{bmatrix} \tag{D.3}$$

After substituting **A** into Eq.(2.27), the expression of the matrix **a** can be obtained as

$$\mathbf{a}=\frac{32e^4}{\pi h_{thick}\delta^4}\begin{bmatrix} \frac{1}{\left(e^4-5\right)} & 0 & 0 & 0 & 0 \\ 0 & \frac{1}{\left(e^4-5\right)} & 0 & 0 & 0 \\ 0 & 0 & \frac{6}{\left(e^4-13\right)\delta^2} & \frac{-2}{\left(e^4-13\right)\delta^2} & 0 \\ 0 & 0 & \frac{-2}{\left(e^4-13\right)\delta^2} & \frac{6}{\left(e^4-13\right)\delta^2} & 0 \\ 0 & 0 & 0 & 0 & \frac{8}{\left(e^4-13\right)\delta^2} \end{bmatrix} \tag{D.4}$$

Consequently, by substituting Eq. (D.4) and Eq. (D.1) into Eq.(2.24), the analytical expression of the PD differential operator for the 2D problem is obtained as

$$\begin{Bmatrix} g^{10}(\xi) \\ g^{01}(\xi) \\ g^{20}(\xi) \\ g^{02}(\xi) \\ g^{11}(\xi) \end{Bmatrix}=\frac{32\xi e^{-(2\xi/\delta)^2+4}}{\pi h_{thick}\delta^4}\begin{Bmatrix} \frac{\cos(\theta)}{\left(e^4-5\right)} \\ \frac{\sin(\theta)}{\left(e^4-5\right)} \\ \frac{2\xi\left(4\cos^2(\theta)-1\right)}{\left(e^4-13\right)\delta^2} \\ \frac{2\xi\left(4\sin^2(\theta)-1\right)}{\left(e^4-13\right)\delta^2} \\ \frac{8\xi\cos(\theta)\sin(\theta)}{\left(e^4-13\right)\delta^2} \end{Bmatrix} \tag{D.5}$$

Finally, the partial derivatives will be converted into their non-local forms as

$$\begin{Bmatrix} \dfrac{\partial f(\mathbf{x})}{\partial x_1} \\ \dfrac{\partial f(\mathbf{x})}{\partial x_2} \\ \dfrac{\partial^2 f(\mathbf{x})}{\partial x_1^2} \\ \dfrac{\partial^2 f(\mathbf{x})}{\partial x_2^2} \\ \dfrac{\partial^2 f(\mathbf{x})}{\partial x_1 \partial x_2} \end{Bmatrix} = \int_{H_x} \frac{32\xi e^{-(2\xi/\delta)^2+4}}{\pi h_{thick}\delta^4} \begin{Bmatrix} \dfrac{\cos(\theta)}{(e^4-5)} \\ \dfrac{\sin(\theta)}{(e^4-5)} \\ \dfrac{2\xi(4\cos^2(\theta)-1)}{(e^4-13)\delta^2} \\ \dfrac{2\xi(4\sin^2(\theta)-1)}{(e^4-13)\delta^2} \\ \dfrac{8\xi\cos(\theta)\sin(\theta)}{(e^4-13)\delta^2} \end{Bmatrix} (f(\mathbf{x}+\boldsymbol{\xi})-f(\mathbf{x}))\,dV' \qquad (D.6)$$

It should be mentioned that for the numerical simulations, the PD differential operator is computed numerically.

Appendix E. PST corrections for physical variables except displacement

Regarding the PST, after the particle position being shifted, the fluid velocity $\mathbf{v}_i$, pressure P_i and density ρ_i for particle i, represented by ϕ_i, can be corrected according to the Taylor series expansion. Originally, the Taylor series expansion used in the PST [159] only has second-order accuracy. In the present work, the second-order derivatives are already calculated by using PPDO. Therefore, Taylor series expansion with a third-order error term can easily be adopted as [293]

$$\left(\phi_i^{n+1}\right)^{corrected} = \phi_i^{n+1} + \left(\nabla\phi\right)_i^n \cdot \left(\delta\mathbf{u}_i\right)^{PST} + \frac{1}{2}\left(\left(\delta\mathbf{u}_i\right)^{PST}\right)^T \mathbf{H}_i \left(\delta\mathbf{u}_i\right)^{PST} + o\left(\left|\left(\delta\mathbf{u}_i\right)^{PST}\right|^3\right) \quad \text{(E.1)}$$

where $\mathbf{H}_i$ represents the Hessian matrix as [293]

$$\mathbf{H}_i = \begin{bmatrix} \dfrac{\partial^2\phi_i}{\partial x_1^2} & \dfrac{\partial^2\phi_i}{\partial x_1\partial x_2} \\ \dfrac{\partial^2\phi_i}{\partial x_1\partial x_2} & \dfrac{\partial^2\phi_i}{\partial x_2^2} \end{bmatrix} \quad \text{(E.2)}$$

Consequently, the non-local form of the Hessian matrix can be derived as

$$\begin{aligned} \mathbf{H}_i = \begin{bmatrix} \dfrac{\partial^2\phi_i}{\partial x_1^2} & \dfrac{\partial^2\phi_i}{\partial x_1\partial x_2} \\ \dfrac{\partial^2\phi_i}{\partial x_1\partial x_2} & \dfrac{\partial^2\phi_i}{\partial x_2^2} \end{bmatrix} &= \sum_{j=1}^{N_i}\left(\phi\left(\mathbf{x}_j^n\right) - \phi\left(\mathbf{x}_i^n\right)\right)\begin{bmatrix} \mathrm{g}^{20}\left(\boldsymbol{\xi}_{ij}^n\right) & \mathrm{g}^{11}\left(\boldsymbol{\xi}_{ij}^n\right) \\ \mathrm{g}^{11}\left(\boldsymbol{\xi}_{ij}^n\right) & \mathrm{g}^{02}\left(\boldsymbol{\xi}_{ij}^n\right) \end{bmatrix} V_j \\ &= \sum_{j=1}^{N_i}\left(\phi\left(\mathbf{x}_j^n\right) - \phi\left(\mathbf{x}_i^n\right)\right)\mathbf{g}_2\left(\boldsymbol{\xi}_{ij}^n\right) V_j \end{aligned} \quad \text{(E.3)}$$

The PPDO form of Eq.(E.1) can be derived by replacing the PDDO gradient operator provided in Eq.(5.1d) and PDDO form of the Hessian matrix in Eq.(E.3), resulting in

$$\begin{aligned}\left(\phi_i^{n+1}\right)^{corrected} &= \phi_i^{n+1} + \left[\sum_{j=1}^{N_i}\left(\phi\left(\mathbf{x}_j^n\right)-\phi\left(\mathbf{x}_i^n\right)\right)\mathbf{g}_1\left(\xi_{ij}^n\right)V_j\right]\cdot\left(\delta\mathbf{u}_i\right)^{PST} \\ &+\frac{1}{2}\left(\left(\delta\mathbf{u}_i\right)^{PST}\right)^T\left[\sum_{j=1}^{N_i}\left(\phi\left(\mathbf{x}_j^n\right)-\phi\left(\mathbf{x}_i^n\right)\right)\mathbf{g}_2\left(\xi_{ij}^n\right)V_j\right]\left(\delta\mathbf{u}_i\right)^{PST}\end{aligned} \tag{E.4}$$

where the expression of $\left(\delta\mathbf{u}_i\right)^{PST}$ is provided in Eq.(6.48).

Therefore, the corrected velocity components become

$$\begin{aligned}\left(v_{i,x}^{n+1}\right)^{corrected} &= v_{i,x}^{n+1} + \left[\sum_{j=1}^{N_i}\left(v_x\left(\mathbf{x}_j^n\right)-v_x\left(\mathbf{x}_i^n\right)\right)\mathbf{g}_1\left(\xi_{ij}^n\right)V_j\right]\cdot\left(\delta\mathbf{u}_i\right)^{PST} \\ &+\frac{1}{2}\left(\left(\delta\mathbf{u}_i\right)^{PST}\right)^T\left[\sum_{j=1}^{N_i}\left(v_x\left(\mathbf{x}_j^n\right)-v_x\left(\mathbf{x}_i^n\right)\right)\mathbf{g}_2\left(\xi_{ij}^n\right)V_j\right]\left(\delta\mathbf{u}_i\right)^{PST}\end{aligned} \tag{E.5}$$

$$\begin{aligned}\left(v_{i,y}^{n+1}\right)^{corrected} &= v_{i,y}^{n+1} + \left[\sum_{j=1}^{N_i}\left(v_y\left(\mathbf{x}_j^n\right)-v_y\left(\mathbf{x}_i^n\right)\right)\mathbf{g}_1\left(\xi_{ij}^n\right)V_j\right]\cdot\left(\delta\mathbf{u}_i\right)^{PST} \\ &+\frac{1}{2}\left(\left(\delta\mathbf{u}_i\right)^{PST}\right)^T\left[\sum_{j=1}^{N_i}\left(v_y\left(\mathbf{x}_j^n\right)-v_y\left(\mathbf{x}_i^n\right)\right)\mathbf{g}_2\left(\xi_{ij}^n\right)V_j\right]\left(\delta\mathbf{u}_i\right)^{PST}\end{aligned} \tag{E.6}$$

The corrected pressure values become

$$\begin{aligned}\left(P_i^{n+1}\right)^{corrected} &= P_i^{n+1} + \left[\sum_{j=1}^{N_i}\left(P\left(\mathbf{x}_j^n\right)-P\left(\mathbf{x}_i^n\right)\right)\mathbf{g}_1\left(\xi_{ij}^n\right)V_j\right]\cdot\left(\delta\mathbf{u}_i\right)^{PST} \\ &+\frac{1}{2}\left(\left(\delta\mathbf{u}_i\right)^{PST}\right)^T\left[\sum_{j=1}^{N_i}\left(P\left(\mathbf{x}_j^n\right)-P\left(\mathbf{x}_i^n\right)\right)\mathbf{g}_2\left(\xi_{ij}^n\right)V_j\right]\left(\delta\mathbf{u}_i\right)^{PST}\end{aligned} \tag{E.7}$$

It should be noted that the corrections for velocity components and pressure have limit effects on the accuracy improvement of the numerical results, less than 10% [205]. Therefore, the PST corrections for velocity and pressure provided from Eqs. (E.5) to (E.7) can be neglected for saving the computational time. Since in this study second-order PDDO equations are used, the higher-order terms in Eq. (E.1) can be easily adopted to increase the numerical accuracy of the PST method.

Furthermore, it should be noted that the PST applied here is only applicable to the fluid flow without free surface. If the free surface is involved, the improved version of PST by using Fick's law [203] should be adopted.